Environmental & Orientation Effects on the Ultrasonic Fatigue of a Single-crystal Nickel Superalloy.



Robin J. Scales

Mansfield College

University of Oxford

A thesis submitted for the degree of

Doctor of Philosophy in Materials

Trinity 2024

Abstract

Single-crystal superalloys are used in the high-pressure turbine blades of jet engines. Their fatigue performance is important for safety and cost. A better understanding of their fatigue lives to higher cycle numbers will aid this. Two key under-explored areas in the research are #1 lower temperature ($\approx 450\,^{\circ}\mathrm{C}$) as the focus has been placed on higher temperatures; #2 results from substantial and consistently controlled single-crystal orientations other than ubiquitous $\langle 100 \rangle$.

A novel ultrasonic fatigue method using meso-scale cantilevers was used to assess the fatigue performance of CMSX-4 from 10^4 to 10^9 cycles to failure, generating S-N curves.

The small-scale nature of the samples with this ultrasonic fatigue method allowed for the novel investigation of the fatigue crack initiation behaviour under different conditions. This is important as initiation dominates the high cycle fatigue life.

All results showed values greater than expected from the literature, which was proposed to be from a combination of bending fatigue and small-scale testing.

The $450\,^{\circ}\mathrm{C}$ results showed an improved fatigue performance compared to room temperature due to the anomalous yield strength phenomenon. The failure changed from shearing mode at room temperature to both shearing and opening at $450\,^{\circ}\mathrm{C}$. ECCI micrographs showed the dislocation behaviour changing from planar slip to homogeneous slip.

The in-vacuum room temperature fatigue performance improved compared to the air-in tests. Unexpectedly, the fractographs suggest that opening mode fracture occurred under vacuum, likely linked to the enhanced performance, and proposed to be from significant localised heating around the crack tip under vacuum.

The crystal orientations of the samples from EBSD were consistent and close to the intended orientations. Cantilevers orientated near $\langle 110 \rangle$ showed similar in-air room temperature S-N curves compared to those orientated near $\langle 100 \rangle$. Both showed shearing mode fracture but had different fracture paths correlating with crystal plasticity finite element models and the literature. The slip behaviour of the two orientations was captured in ECCI and was compared with each other, the fracture behaviour, and the literature.

A novel method was developed and used to obtain/determine ECCI diffraction conditions with greater accuracy; this can impact other materials and applications.

Acknowledgements

To my parents thank you for putting up with me chatting about my research and codes, helping me battle my verbose writing style, and being supportive through this turbulent time and welcoming me home to recover from burnout. To my sister for having my back always. To my dogs, Pippin & Fudge, for being my best friends and the best listeners. Thanks to my loving aunts, uncles, grandparents, and cousins, you mean the world to me.

A big thank you to my supervisors Angus Wilkinson & Jicheng Gong for the four years working on this fun research. Thank you, Jicheng, for helping me when I came across experimental issues, and you would either help rapidly in the lab or ping me back on MS Teams. Especially for helping the foil preparation when I was stuck for weeks. Thank you, Angus, for being the nice and supportive helping hand when I was struggling. Your support on the literature and the results was invaluable. I need to practice my bowling in the future to become as good as you. This thesis would not have been possible without you two and I wish you the best in the future.

Thank you to Becs for helping me find Angus and organising important meetings with him. Thank you all for being such a lovely person; never stop.

Thank you to Matt Appleton, Jane Woolrich, and Julian Mason-Flucke from Rolls-Royce PLC, who listened to my work and gave me feedback over the years.

Many thanks to Eralp Demir who has been super helpful (and patient) with my crystal plasticity modelling questions and for helping brainstorm research ideas.

I want to thank my work colleagues and friends for tolerating me for making coffee in the office, chatting about my codes, and for many great memories. To the best office mates you could have: Brad Young, Jack Aspinall, Johann Perrera, Pedr Charlesworth, Benjamin Evans, Rob Kerr, Shatha Almarri, Anna Kareer, Andrew Bulla, and Keivan Samani. I hope that wherever our paths take us, we can keep in touch and all meet once again.

To the fatigue grouplet for surpassing the VHCF of our degrees: Laz Pujilaksono, Chris Magazzeni, Rory Rose, Hanqing Liu, Oliver Clement, and Sujay.

Thank you to Dave Armstrong and Roger Reed for being my assessors during my degree and giving me feedback on my progression and work.

To the other amazing people in the materials department and OMG group: Sophia Ungermann (couldn't have asked for a better housemate too). Kieran Rivers & Holly Thompson (for encouraging breaks away from work and BBQs). Phani Karamched, Graham Wyatt, and DCCEM for being superstars when it comes to electron microscopy and for being lovely people. Zhaoying Ma, Yvonne Chart, Lizzie Jones, Joseph Zhong, Leon Tenassia, George Tebbutt, Ryan Schofield, Laura Wheatley, Xinrui Huang, Sean Telford, Marcus Williamson, Emma & Harry, and Shona Macnab. Jack Haley. Gareth Jones, for helping many times with coding and getting *EMsoft* to install and understand it. Bo-shiuan Li (my first supervisor and good friend). Kay Song, Ed Darnbrough, Zihao Wang, Yige Sun, Kay Davies (for always being helpful and lovely). Helena Cotterill (for allowing me to do outreach and show my passion towards the subject). To Chris Hamlett and the rest of Discover Materials who are doing amazing outreach work.

Thank you to the tutorial fellows at Mansfield and Queen's and to Jonathan Yates for allowing me to teach materials science to the undergraduates. I wish the best for you and to all who I have taught.

The Oxford institutions that supported me and propped up my moral over the years: G&D's, especially the incredible Sally at Little Clarendon Street. When I was going through tough times in research and in life you and G&D's were a reliable lighthouse of support and helped me when I genuinely needed it. Jolly Farmers and Staff for being one of my favourite pubs in all of Oxford. I wish I had found you sooner, as the pub and the LGBTQ+ community you have fostered have been a social lifeline and a home away from home. I am currently writing the acknowledgements in there now. Tasha and Ruby at Blushes for being amazing hair stylists and working their magic to boost my mood. *I'm Japanese* food van for being the happiest and welcoming of people, and giving the karaage curry chicken just when I need it. To The Castle Jericho Coffee Traders cafe, Common Ground, and Tree Artisan cafes for being amazing people, supplying me the much-needed coffee, and hosting me whilst I write my thesis.

Finally, to my Oxford and home friends. Sophia, Josh, and Morgan for being great friends and the nicest of housemates. You made my year so smooth and it has been a pleasure living with you three and all the good memories. Ryan & Alex, for being partners in crime with me in many social situations; I love you both. To Karim, Johanna, Alec, Jess, and Wilder, thank you for being good friends and company (let's do another hot pot in the future). To Chris, Caroline, Amir, Johnathan, Emma, Taly and Maritsa at Mansfield, I hope to see you soon! To

Khazna, Laura, Elise, and Kara, I love you all lots and our little meetups. To Ed Kaine and Dan Webster, thank you for being supportive and good friends when I pop down to Reading or you to Oxford. To Svenja, Poppy, Alison, Jessie, and Sophie, thank you for many good memories and parties! Svenja and Poppy, I wish you the best, especially with your PhDs. Thank you to Mimes, Immy, and Holly for being Jolly Farmers buddies, one day we will hang outside of there haha.

To the Rock Music Society, having been involved since 2016 and being part of the committee for long durations, it is great to see it still alive and thriving. Thank you for allowing me to be involved despite being an elder. I want to thank you all, but I want to specifically thank the following: to the previous and current presidents, especially those during my DPhil of Lucy, Conrad, Danann, Adrian, and now Meg. Your hard work has kept our wonderful and welcoming community going. Conrad, you were my best friend during lockdown; you deserve the world. Danann, you're a star and a good friend. Adrian, you have the best of conversations and moments, it will be interesting to see where the winds will take you. To Cat & Adrian for supporting me in my rough times. To the current and future committees, I wish you well.

To all who are reading this, thank you, I hope it proves of interest and use.

Contents

Abbreviations **viii**

1 Introduction **1**

2 Literature Review **7**
2.1 Materials Details (CMSX-4) 8
2.2 Fatigue Introduction 17
2.3 Fatigue Fracture 19
2.4 Temperature Effect 32
2.5 Fatigue Method Effects 34
2.6 SXO S-N Dependence 41
2.7 Environment Effect 47
2.8 Similar Fatigue Methodologies 57

3 Aims &Objectives **62**

4 Methodology **66**
4.1 Ultrasonic Fatigue Rig 67
4.2 Sample Preparation 83
4.3 Crystal Plasticity 88
4.4 Sample Measurement 91
4.5 Electron Microscopy 92
4.6 Radiography 96

5 Method Developments **99**
5.1 Porosity Assessment 100
5.2 Failure Detection &Tracking 109
5.3 ECCI Technique Development 112

6 Environment Testing **130**
6.1 Introduction 131
6.2 Ambient Electropolishing Effect 133
6.3 Room Temperature Air vs Vacuum 141

6.4 Room Temperature ECCI . . . 162
6.5 Intermediate Temperature . . . 183
6.6 Chapter Summary . . . 233

7 Single Crystal Orientation Testing &Modelling 236
7.1 Cantilever Design Development . . . 237
7.2 Sample Preparation . . . 243
7.3 S-N . . . 247
7.4 Fractography . . . 252
7.5 Simulations vs Experiments . . . 273
7.6 <110> ECCI Micrographs . . . 281
7.7 Discussion . . . 304
7.8 Chapter Summary . . . 311

8 Final Remarks 314

Appendices

A Room Temperature Oxidation (glaze) 321
A.1 Fretting Fatigue Literature . . . 321
A.2 Experimental Observations . . . 324

B Methods 336
B.1 Development: Laser Streak Length Measurement . . . 336
B.2 Convergence Studies . . . 337
B.3 Height Micrometer Part List . . . 340
B.4 IT Vacuum Resonance Issues . . . 341

C Calculations &Equations 342
C.1 Pore Distribution Fitting Equations . . . 342
C.2 Oxygen Partial Pressure . . . 343
C.3 ECCI Probe Depth . . . 344
C.4 Stage Tilt Correction . . . 344
C.5 Plastic Zone . . . 345

D Supplementary Micrographs 348
D.1 Radiographs . . . 348
D.2 EDX . . . 350
D.3 ECCI . . . 351
D.4 MTEX Orientation on Micrographs . . . 361

References 363

Abbreviations

α_{amp}	Bending Angle Amplitude.
ε_{amp}	Strain Amplitude.
ρ_{GND}	Geometrically Necessary Dislocation Density.
σ_{amp}	Stress Amplitude.
σ_y	Yield stress.
σ_w	Classical Fatigue Limit.
σ_{vm}	Von Mises' Stress.
ω	Stress-per-Angle (aka SPA) in MPa/mrad.
$\underline{b}$	Burgers Vector.
c	Fatigue Crack Length.
f	Frequency.
f_D	Driving Frequency.
$\underline{g}$	Diffraction Vector.
K	Stress Intensity Factor.
ΔK	Stress Intensity Factor Range.
ΔK_{th}	Threshold Stress Intensity Factor Range.
L	Laser Length.
N_f	Number of Cycles to Failure.
$p_{\mathbf{O_2}}$	Oxygen Partial Pressure.
$P_f(50\%)$	50% Probability of Failure.
R	Fatigue Ratio ($= {}^{\sigma_{min}}/_{\sigma_{max}}$).
R_{stage}	SEM Stage Rotation.
ΔR_{mtex}	Change in Stage Rotation in MTEX.
t_g	Probe depth for a given diffraction condition in ECCI.
T	Temperature.

T_{stage} . . . . . SEM Stage Tilt.

ΔT_{mtex} . . . . . Change in Stage Tilt in MTEX.

WD . . . . . Working Distance.

A-N . . . . . Bending Angle Amplitude vs Number of Cycles.

APB . . . . . Anti-phase Boundary.

BSE . . . . . Back-scattered Electron.

CC . . . . . Cross-correlation.

CD . . . . . Cantilever Direction. The crystallographic direction in which the cantilever axis is orientated.

CPFE . . . . . Crystal Plasticity Finite Element.

CRSS . . . . . Critical Resolved Shear Stress.

CT . . . . . Compact Tension.

cECCI . . . . . Controlled-ECCI.

EBSD . . . . . Electron Back-scatter Diffraction.

ECCI . . . . . Electron Contrast Channelling Imaging.

eCHORD . . . Electron Channelling Orientation Determination.

ECP . . . . . Electron Channelling Pattern.

EDM . . . . . Electron Discharge Machining.

EDX . . . . . Energy Dispersive X-ray Analysis.

EM . . . . . Electron Microscopy.

EP . . . . . Electropolished.

EV . . . . . Extreme Value.

FCC . . . . . Face-Centred Cubic.

FCG . . . . . Fatigue Crack Growth.

FCGR . . . . . Fatigue Crack Growth Rate.

FEG . . . . . Field Emission Gun.

FEM . . . . . Finite Element Modelling.

FIB . . . . . Focused Ion Beam.

FN . . . . . Foil normal, i.e. the crystallographic direction correlating to the surface normal of the foil from which the fatigue samples are machined.

GEV . . . . . Generalised Extreme Value.

GND . . . . . Geometrically Necessary Dislocation.

HCF . . . . . High Cycle Fatigue.

HH . . . . . Horizontal Holder.

HR-EBSD . . High Angular Resolution EBSD.

IT . . . . . Intermediate Temperature.

K-T . . . . . Kitagawa-Takahashi.

KW locks . . . Kear-Wilsdorf Locks.

LCF . . . . . Low Cycle Fatigue.

LHS . . . . . Left Hand Side.

OM . . . . . Optical Microscopy.

PX . . . . . Polycrystalline.

R-ECCI . . . . Rotational-ECCI.

RF . . . . . Resonant frequency.

RHS . . . . . Right Hand Side.

ROI . . . . . Region of Interest.

RT . . . . . Room Temperature.

SAECP . . . . Selected-area Electron Channelling Pattern.

S-N . . . . . Stress Amplitude vs Number of Cycles.

SEM . . . . . Scanning Electron Microscopy.

SE . . . . . Secondary Electron.

SF . . . . . Stacking Fault.

SSF . . . . . Superlattice stacking fault.

SX . . . . . Single-crystal.

SXO . . . . . Single-crystal Orientation.

SXNBS . . . . Single-crystal Nickel-Based Superalloy.

TEM . . . . . Transmission Electron Microscopy.

TOCA . . . . . Tools for Orientation Determination and Crystallographic Analysis.

UFR . . . . . Ultrasonic Fatigue Rig.

UFT . . . . . Ultrasonic Fatigue Testing.

VH . . . . . Vertical Holder.

VHCF . . . . . Very High Cycle Fatigue (aka Gigacycle Fatigue).

w.r.t. . . . . . with respect to.

1 Introduction

Aviation Industry

The aviation industry is a key part of modern society and has a market value of US$ 841 billion (2023) [1]. In 2022, US$ 92 billion of this revenue was generated by engine original equipment manufacturers [2]. A schematic of a jet engine is shown in fig. 1.1.

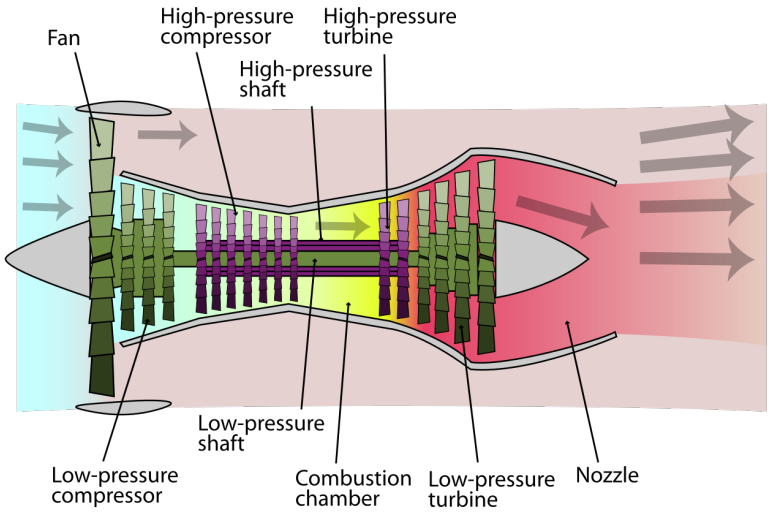


Figure 1.1: Jet engine schematic. Figure from [3] (CC BY-SA 3.0).

Turbine Blades

This thesis focuses on the high-pressure turbine blades, as shown in fig. 1.2. They are typically made from single-crystal nickel-based superalloys (SXNBSs) due to

their excellent mechanical and oxidation performances at the operating conditions [4, 5][6, p. 28]. Greater engine efficiencies are achieved with greater turbine entry temperatures, which can be above the melting point of SXNBSs such as ≈ 1600 °C. Therefore, they are typically covered in a thermal barrier coating and have internal cooling channels [7, p. 138-140] to reduce the temperature and oxidation [5, p. 1].

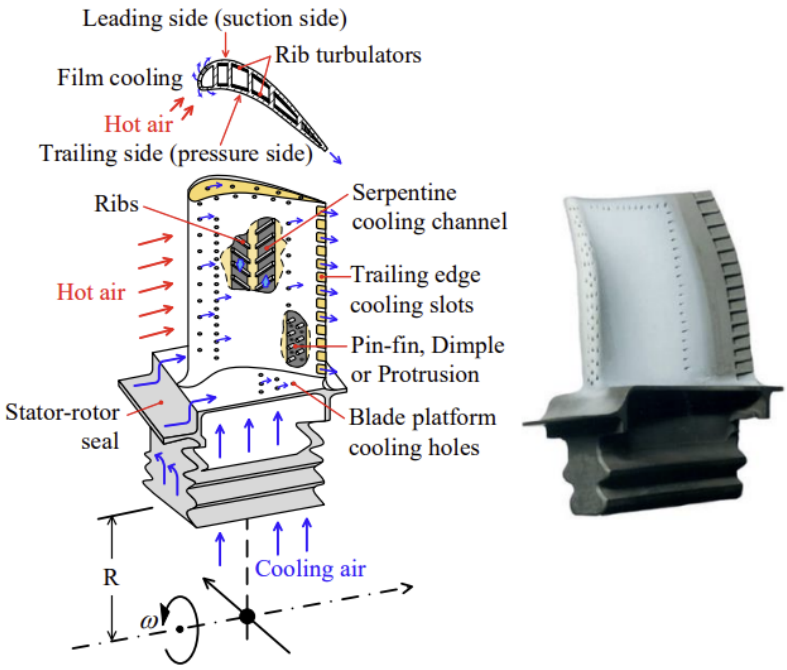


Figure 1.2: Thermal barrier coated high-pressure turbine blades. Figure from [8] (CC BY 3.0).

The mechanical properties of SXNBSs are desirable for the blades' harsh in-service conditions. Exposure to hot combustion gases causes the blades to experience temperatures ranging from 400 °C to 1000 °C [9, p. 28]. The blades also experience high centrifugal forces (e.g., 66×10^3 g [7, p. 142]) and bending forces [7, p. 144]. Hence, their high creep strength is desirable [10].

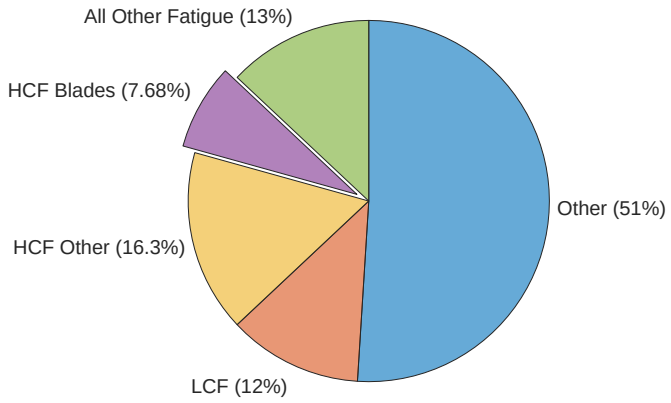
The single-crystal (SX) blades are grown via a grain selector or seeding, where ⟨100⟩ is easiest to form as the primary orientation [6, p. 129] whereas other non-standard primary orientations are difficult to obtain [11][6, p. 129]. Their SX nature makes their mechanical behaviour anisotropic where the ⟨100⟩ crystallographic direction has the best balance of mechanical properties, e.g., good creep performance [12],

and low-cycle thermal fatigue resistance [6, p. 190].

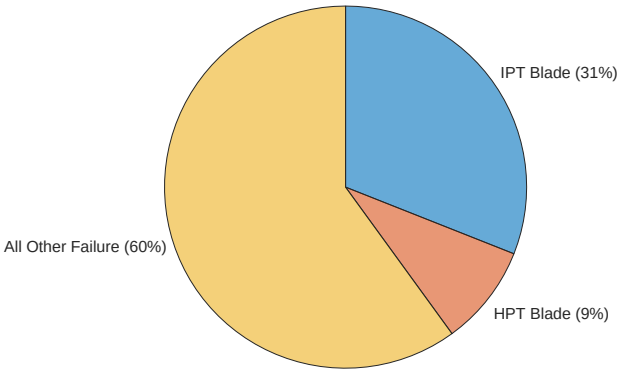
Fatigue is important to consider for the turbine blades as it accounts for a significant portion of recorded failures [13, p. 131]. High cycle fatigue (HCF) is particularly important due to the high proportion of recorded failures (fig. 1.3) and costing US$ 100 million per year for inspections and maintenance [13, p. 130]. The HCF originates from the blades vibrating at their natural frequencies with a low stress amplitude (σ_{amp}) [13, p. 131]. The natural frequencies of the blades range from 1 kHz to 10 kHz [4, p. 251]. Blade vibrations originate from either forced vibration or flutter, where the blades can undergo a flexural (flap) mode deformation akin to cantilever bending [13, p. 134] at ≈ 7.29 kHz [14], with higher frequencies required for torsional and axial modes [13, p. 134]. Therefore, the stress state on the blades is near steady-state stress from centrifugal forces (max. at the fir-tree) and gas flow bending with alternating stresses from various sources like the aforementioned vibrations [13, p. 134-135]. The high-frequency/low-stress causes fatigue failures to occur in the HCF and very high cycle fatigue (VHCF) regimes [4], and as such, the modern recommendation for aerospace components is to have a fatigue lifetime of at least 10^9 cycles [15–17] which is in VHCF regime.

The blade design life is estimated to be between 3×10^4 h and 1×10^5 h [20, p. 863], which is around a minimum of six years for a commercial aeroplane before being "overhauled or replaced" [7, p. 144].

CMSX-4 is a 2$^{\text{nd}}$ generation SXNBS, which, despite its age, is still "widely used as blade materials for aircraft jet engines" [21, p. 3] it has been extensively researched due to its continuing relevance and suitability to compare with similar SXNBSs. A 2007 paper noted the lack of fatigue research into the alloy compared with its creep behaviour for 750 °C to 1000 °C [22].



(a) Gas turbine engine (1996). Adapted from [18].



(b) Turboprop engine (2022). Adapted from [19].

Figure 1.3: Aircraft engine failure/withdrawal statistics.

Experimentally, the most time-efficient method to investigate the HCF and VHCF regimes is to use an ultrasonic fatigue rig (UFR) operating at $> 20\,\text{kHz}$ to achieve the required number of cycles to failure (N_f) [17]. Extrapolating to those regimes from low cycle fatigue (LCF) is not advised because of potential changes in fatigue failure mechanisms, which may form a duplex stress amplitude vs number of cycles (S-N) curve [23]; direct measurement is advised. An additional benefit of ultrasonic testing is that their frequencies are comparable to the blades' kHz vibratory fatigue (c.f. conventional fatigue frequencies) [4, 17].

Environment

Recently, there has been research interest in uncoated SXNBS behaviour. This is because the fir tree region and cooling passages are not coated, and the thermal barrier coating can become damaged, exposing the superalloy to oxidation [24,

p. 1679]. The fir tree and cooling passages are also at lower temperatures than the aerofoil, being $< 650\,^{\circ}\mathrm{C}$ [24, p. 1679] and can experience relatively high stresses. Regions of the main section of the blade itself can also be cooler due to the coating and cooling passage [5, p. 2].

A significant amount of research has focused on fatigue at around the maximum blade temperature ($1150\,^{\circ}\mathrm{C}$ [21, p. 2]). However, a better understanding of fatigue in the $400 - 700\,^{\circ}\mathrm{C}$ range for superalloys is needed for improved fatigue life predictions [25, p. 17]. Research into temperatures lower than typically investigated can offer further insight into these regions of the high-pressure blade [5, p. 1].

As shown in the literature review (chapter 2), research has shown oxygen to be beneficial and detrimental to the fatigue performance of SXNBSs with conflicts in results between the sources. Considering that the turbine blade can be exposed to oxygen at significant temperatures, it is valuable to understand the effect of oxygen on fatigue by testing in low and high partial oxygen pressure (p_{O_2}) conditions at these relatively low temperatures.

Single-crystal Orientation (SXO)

SXNBSs are mechanically highly anisotropic [21, p. 2]. Recent literature has shown that the effect of single-crystal orientation (SXO) on the S-N curve and fatigue behaviour up to the VHCF regime for CMSX-4 and other superalloys needs to be better understood [11]. Most of the VHCF research has focused on the $\langle 100 \rangle$ primary orientation [11] or other SXOs in the LCF regime. Most research involves macroscale samples, limiting both the number of samples and the SXO consistency. For superalloys, the [100] primary orientation deviation can be $< 5^{\circ}$ [26, p. 2] and is typically permitted up to 12° for blades [20, p. 863]. Subsequently, understanding the SXO effect on fatigue is vital in modelling due to these deviations and that the complex blade geometry means the peak stresses and fatigue cracks are not always associated with $\langle 100 \rangle$ loading [20, p. 863] [5, p. 1]. Recent VHCF work highlighted the need to obtain more $\langle 110 \rangle$ primary orientation data due to the difficulty of obtaining that primary orientation [11].

Therefore, a method to better complete the SXO dependence on fatigue for non-standard orientations will be valuable for the blade as a whole and for the regions of more complex stress states (e.g., cooling passages and fir-tree).

Research Statement

A novel UFR is used in this thesis, allowing meso-scale CMSX-4 cantilevers to undergo fully-reversed bending fatigue; this is the first full investigation using this UFR on single crystals. This thesis is subdivided into three main chapters based on the research aims generated after reviewing the literature and identifying key areas to investigate:

- Chapter 5: Developed methods to aid in analysing the fatigue results, e.g., a novel electron contrast channelling imaging (ECCI) technique.
- Chapter 6: Assessing the environmental effects on fatigue when altering the temperature (room temperature vs 450 °C) and the medium (air vs vacuum).
- Chapter 7: Improving the understanding of SXO on fatigue in ambient conditions.

These investigations involve S-N curves, extensive fractography, and electron microscopy (EM) techniques to compare effects and understand fatigue mechanisms.

2

Literature Review

Contents

2.1 Materials Details (CMSX-4) 8
2.1.1 As-Supplied Microstructure 8
2.1.2 Elastic Properties 10
2.1.3 Plastic Properties 13
2.2 Fatigue Introduction 17
2.2.1 S-N Curves 17
2.2.2 Fatigue Crack Dislocation Emission 18
2.3 Fatigue Fracture 19
2.3.1 Fracture Modes 19
2.3.2 Fatigue Crack Growth Rate 28
2.3.3 CMSX-4 Cantilevers Fatigue Fractography 30
2.4 Temperature Effect 32
2.5 Fatigue Method Effects 34
2.5.1 Size Effect 35
2.5.2 Frequency Effect 39
2.6 SXO S-N Dependence 41
2.6.1 Conventional Fatigue Regime 41
2.6.2 Very High Cycle Fatigue 43
2.7 Environment Effect 47
2.7.1 Oxides 48
2.7.2 Air Effect on Fatigue 49
2.7.3 Ni Microbeam results 55
2.7.4 Water Effect on Fatigue Response 56
2.8 Similar Fatigue Methodologies 57

2.1 Materials Details (CMSX-4)

The single-crystal nickel-based superalloy (SXNBS) investigated in this thesis was CMSX-4.

2.1.1 As-Supplied Microstructure

The alloy was grown as a single-crystal and heat-treated by the supplier. Reported compositions from literature for CMSX-4 are outlined in table 2.1. The as-supplied material had not undergone any hot-isostatic pressing to mitigate porosity. The primary crystallographic orientation can be controlled to $< 5°$ from the cube orientation along the growth direction, whereas the secondary orientation is often uncontrolled [26, p. 162].

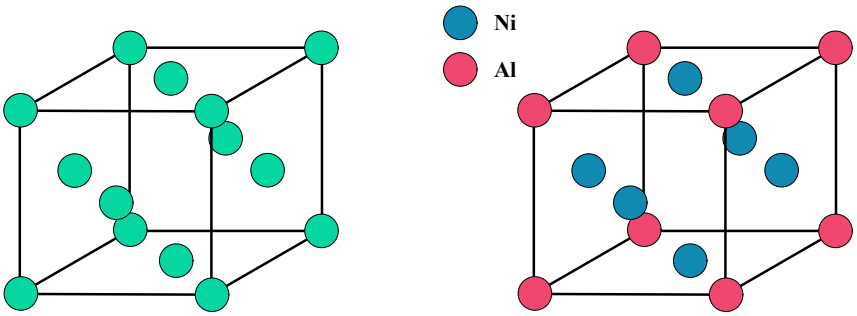
Table 2.1: CMSX-4 composition in atomic percent (at.%) and weight percent (wt.%).

	Al	Ti	Cr	Co	Ni	Mo	Ta	W	Re	Hf
at.% [27]	12.71	1.34	7.47	9.99	62.86	0.39	2.18	2.11	0.95	N/A
wt.% [11, 28]	5.6	1.0	6.5	9.0	-	0.6	6.4	6.0	3.0	0.1
wt.% [29]	6.2	1.1	6.4	9.5	59.0	0.8	7.3	7.1	2.6	N/A

The proprietary heat treatment procedure produces the typical cuboidal $\gamma - \gamma'$ microstructure (fig. 2.1). The γ phase is a face-centred cubic (FCC) solid solution, whereas γ' is an $L1_2$ (Ni_3Al) intermetallic and forms cubes with $\{100\}$ habit planes. The resulting structure is a matrix of thin channels of γ with cubic γ' precipitates [27], appearing bright and dark respectively under back-scattered electron (BSE) imaging.

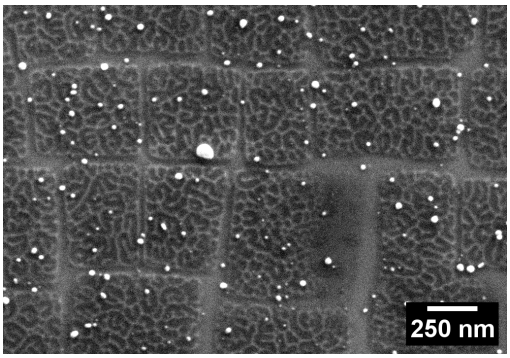
Despite γ and γ' being different phases, they both have similar lattice parameters [27] & crystal structures, and with γ' being coherent with γ means that they can be treated as a single-crystal macroscopically (apart from the microplasticity).

γ' occupies a significant volume fraction of the alloy ($\approx 70\%$ [27, 30]) and has cubic edge lengths of $\approx 0.35 - 0.45$µm [27].

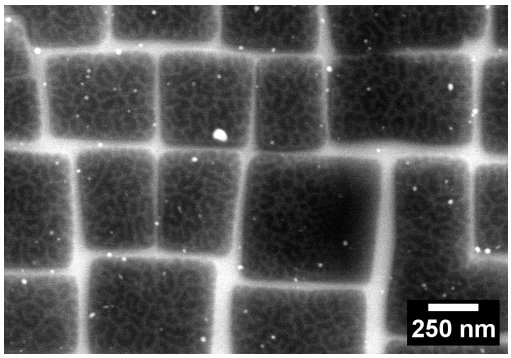


(a) γ FCC crystal structure.

(b) γ' $L1_2$ crystal structure.



(c) Secondary electron (SE).



(d) Back-scattered electron (BSE).

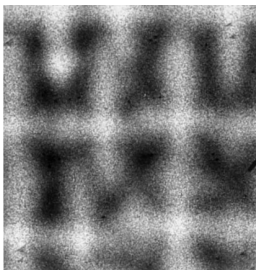
Figure 2.1: Crystal structure and phase morphologies of the γ & γ' phases in nickel superalloys. The micrographs are of an electropolished, then mildly oxidised CMSX-4 from sample C9 (IT Vacuum) with a surface normal near [001].

The dendritic solidification nature of the sample causes various features:

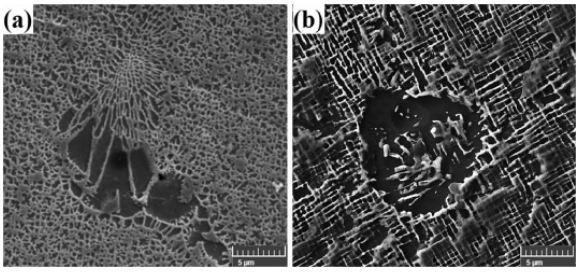
- Microsegregation - more refractory alloying additions are richer in dendrite cores [27, 28] (fig. 2.2a). It is not entirely removed during heat treatments due to the cost of further reducing it.
- Eutectic pools can occur [28] (fig. 2.2b), with a typical volume fraction around 1 % to 6 % [30].
- Low-angle grain boundaries occur because despite the alloy being considered a single crystal, small crystal misorientations ($1-3°$ [21]) exist between separate dendrites (fig. 2.2c), essentially low-angle grain boundaries [31].
- Porosity forms in the interdendritic regions during the casting process [6, p. 186], being shrinkage pores or spherical gas pores (fig. 2.2d). They account for a low volume fraction between 0.1% and 0.26% [30]. However, “porosity

considerably deteriorates the fatigue properties of superalloys, due to the stress concentration effect" [30] (discussed in section 2.5.1).

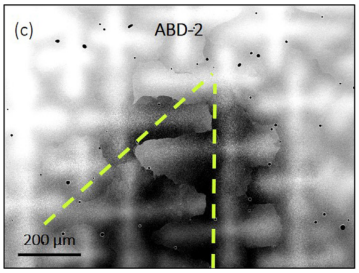
- Ta-rich MC-type carbides can also form in the interdendritic regions and have morphologies as shown in fig. 2.2e.



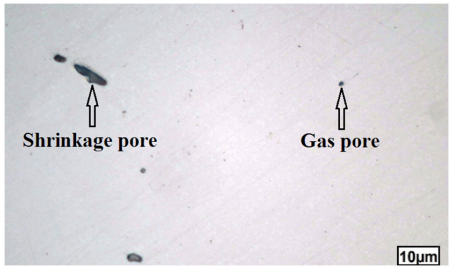
(a) Re coring microsegregation [27].



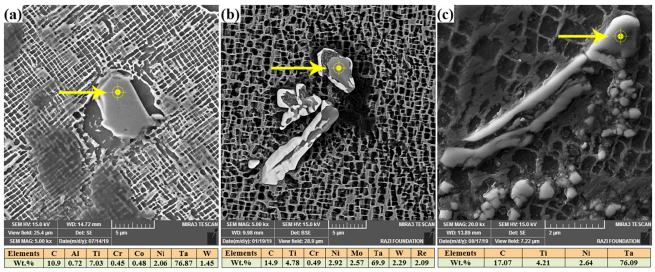
(b) Eutectic pool types before and after heat treatment [30].



(c) BSE micrograph showing low-angle grain boundaries and coring [31].



(d) Interdendritic casting pores [30].



(e) MC carbide morphologies at three different withdrawal rates [30].

Figure 2.2: Examples of microstructural features of CMSX-4.

2.1.2 Elastic Properties

Like other SXNBSs, CMSX-4 is highly anisotropic in its elastic behaviour [6, 21], which is "important to consider" [6] in its engineering application. For a perfectly elastically isotropic material, its Zener factor is 1. CMSX-4, on the other hand, is strongly anisotropic, having values of 2.9 & 4.7 at 20 °C & 1300 °C, respectively [21].

The compliance tensor ($\underline{\underline{S}}$) relates the stress and strain tensors (2^{nd} rank) to each other [21] and hence contains the alloy's elastic anisotropic information. Due to the cubic symmetry of γ and γ', only three elastic constants are required to describe $\underline{\underline{S}}$ [6, 21, 32] as shown in eq. (2.1) [32].

$$\underline{\underline{S}} = \begin{bmatrix} s_{11} & s_{12} & s_{12} & 0 & 0 & 0 \\ s_{12} & s_{11} & s_{12} & 0 & 0 & 0 \\ s_{12} & s_{12} & s_{11} & 0 & 0 & 0 \\ 0 & 0 & 0 & s_{44} & 0 & 0 \\ 0 & 0 & 0 & 0 & s_{44} & 0 \\ 0 & 0 & 0 & 0 & 0 & s_{44} \end{bmatrix} \tag{2.1}$$

The three elastic constants are s_{11}, s_{12}, & s_{44}, and where the above tensor is in the principal axis orientation where indices 1, 2, and 3 correlate to the [100], [010], and the [001] crystallographic directions, respectively [6]. The designation of $\underline{\underline{S}}$ above is orthotropic and has been used in fatigue studies on CMSX-4 to account for crystal orientation [11].

Epishin et al. [21] obtained the elastic constants of CMSX-4 as a function of temperature from 24°C to 1300°C using the sonic resonance method (fig. 2.3). From this elastic tensor under the principal orientation, one can find the elastic response under other crystal orientations using direction cosine [6] or by using tools such as MTEX to rotate the tensor.

For the three main crystallographic directions, their Young's modulus follows as $E_{100} < E_{110} < E_{111}$ [6, 11, 21] (table 2.2 & fig. 2.4). Like other SXNBSs, they all monotonically decrease with increasing temperature [6, p. 106], where under low enough temperatures, they vary nearly linearly with temperature [6, 33].

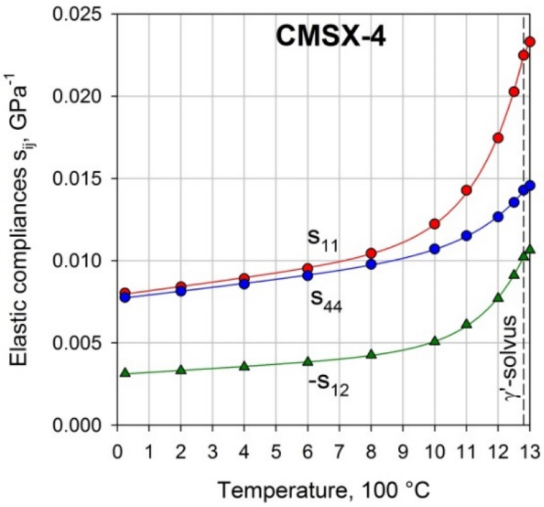


Figure 2.3: Variation of the three compliance elastic constants with temperature for CMSX-4. Figure from [21] (CC BY 4.0).

Table 2.2: Young's modulus (E [GPa]) and $\underline{\underline{S}}$ component values [$10^{-3}\times$GPa^{-1}] for CMSX-4 as a function of temperature (T [°C]). Modulus calculated using MTEX with $\underline{\underline{S}}$ from Ref [21].

T	s_{11}	$-s_{12}$	s_{44}	$\langle 100\rangle E$	$\langle 110\rangle E$	$\langle 111\rangle E$
20	7.95	3.10	7.73	126	230	317
20 [11]	-	-	-	127	230	311
100	8.16	3.20	7.91	123	224	310
400	8.96	3.56	8.62	112	206	287
450	9.10	3.63	8.74	110	203	283
650	9.74	3.92	9.27	103	191	268
750	9.94	4.00	9.41	98	185	265
750 [11]	-	-	-	98	189	261

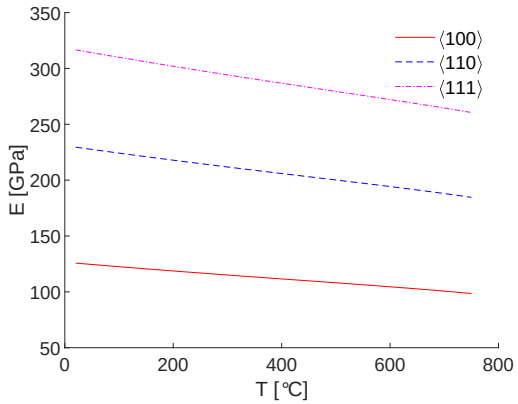


Figure 2.4: Calculated Young's modulus for CMSX-4 for the three major crystallographic directions against temperature. Generated in MTEX using $\underline{\underline{S}}$ from Ref [21].

2.1.3 Plastic Properties

Dislocation Structures

The plastic response of the sample, mediated mostly by dislocations, is paramount in understanding the fatigue response of a sample under a given condition.

For SXNBSs, there are three possible different slip systems, as designated by Cervellon et al. (2021) [11] and visualised schematically in fig. 2.5:

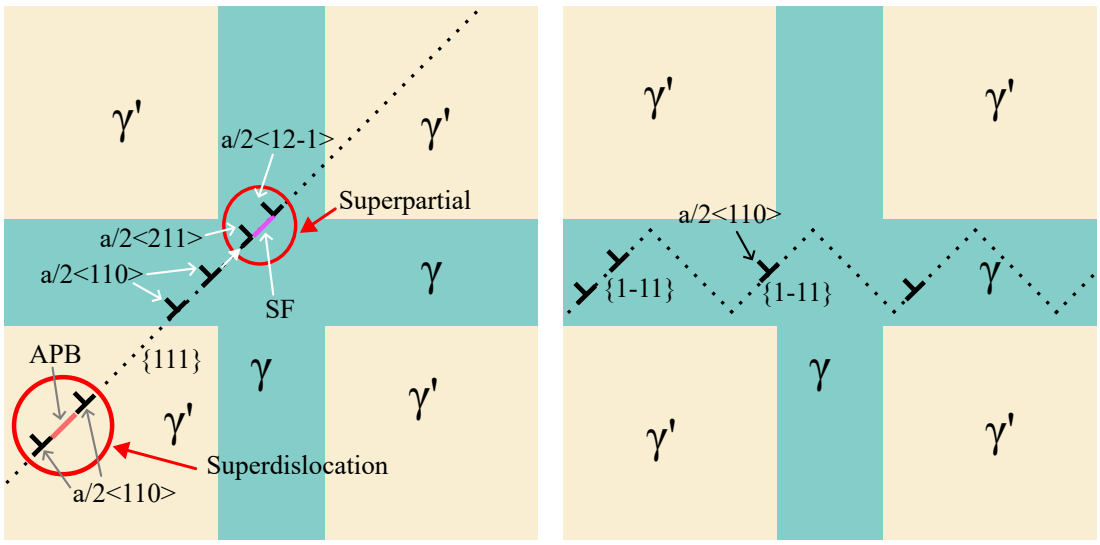
- **Octahedral slip**. The microscopic slip plane and the macroscopic fracture plane lie on a {111} plane (hence, octahedral). The $\{111\}\langle 110\rangle$ slip system is the expected form for a FCC metal.
- **Cubic slip**. The microscopic slip plane and the macroscopic fracture plane lie on a {001} plane (hence, cubic). Formally cubic slip is $\{100\}\langle 110\rangle$ [11, p. 8].
- **Pseudo-cubic slip**. The microscopic slip plane follows alternating {111} planes in γ channels, which makes the macroscopic fracture plane normal to {001}. Its origin is "still discussed" but is thought to be from cross-slip and dislocation glide reactions [11, p. 8].

The nature of the dislocation structures within a SXNBS is not trivial like in most other FCC metallic alloys. The dislocations can exist as Shockley partials in the γ channels (RHS of eq. (2.2)), called a *superpartial*, which macroscopically act as the sum of the two partials (LHS) [6].

$$\frac{a}{2}\langle 110\rangle\{\bar{1}11\} \rightarrow \frac{a}{6}\langle 211\rangle\{\bar{1}11\} + \frac{a}{6}\langle 12\bar{1}\rangle\{\bar{1}11\} \tag{2.2}$$

Superpartials travel in pairs (called *superdislocations*) where the trailing superpartial removes the planar stacking faults generated by the leading superpartial [6]. The ideal slip system in γ' is $a\langle 100\rangle\{\bar{1}11\}$, so as a single superpartial form an energetically costly anti-phase boundary (APB) in γ', two are then needed [6].

The spacing of the superpartials in the superdislocation can be greater than the precipitate diameter (weak coupling) or smaller and virtually always within the



(a) Octahedral **(b)** Pseudo-cubic

Figure 2.5: Schematics of octahedral slip and pseudo-cubic slip in the γ and γ' microstructure. The γ' is one possible combination of dislocation dissociation (see Ref [6] for more).

same γ' precipitate (strong coupling) [6].

Prof Wang's (Sichuan University) research group has looked into the dislocation structures of monotonic uniaxial loading of CMSX-4 from room temperature (RT) up to 1100°C under compression [34] and under tension [35]. Their mechanical results are shown in fig. 2.6.

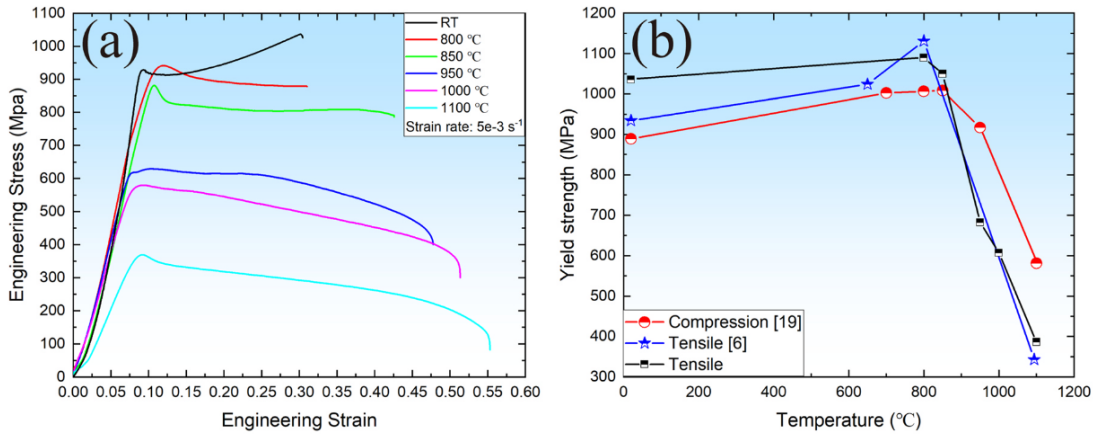


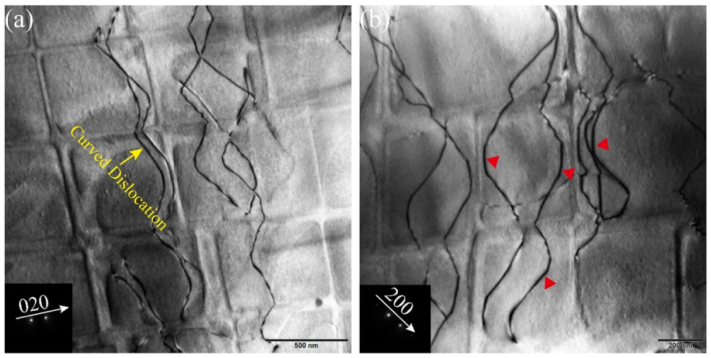
Figure 2.6: Tensile stress-strain curve and yield stress as a function of temperature for CMSX-4 along the <100> direction. Compression yield strength is also plotted. Figure from [35].

At RT, tension [29, 35] and compression [34] results identified the dislocations as two $^{a}/_{2}\langle 110\rangle\{\bar{1}11\}$ superpartials that cut and shear the γ & γ', with an APB linking them in γ' (fig. 2.7a).

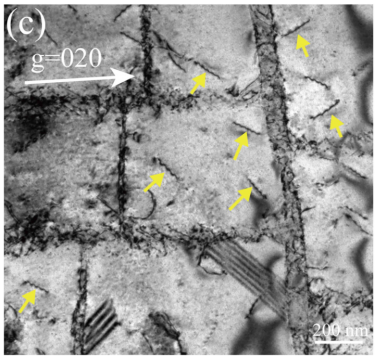
Figure 2.7b shows other defects at elevated temperatures. One of them is the superlattice stacking fault (SSF), which is another form of dissociation of the superpartial for entering the γ' [35] and can occur in γ & γ' [34]. Occurring in the γ channels only at 800°C and also in γ' when $\geq$ 800°C [35]. SSFs are rare at RT but dominate between 800°C and 850°C (no temperatures investigated between) [35]. They appear as parallel, broad dark lines [35].

Kear-Wilsdorf (KW) locks also occur in that temperature range in the γ' precipitates and look like kinks in the superdislocation due to local cross-slip [35].

The domination of APBs vs SSFs depends on alloy composition and temperature. The alloy composition affects these defects' respective energies, so there is a transition from one to the other in dominance for each alloy, e.g., SSFs to APBs with temperature in a novel SXNBS in Ref [36].



(a) Curved and long cutting superdislocations. APBs shown by red triangles. Tested under compression at 20°C along the ⟨100⟩ direction. [34].



(b) Defect appearance for SSF (parallel bands) and KW locks (yellow arrows). Tested under tension at 850°C along the ⟨100⟩ direction. [35].

Figure 2.7: Dislocations and defects in two-beam TEM for CMSX-4 under various temperatures.

Yield Strength

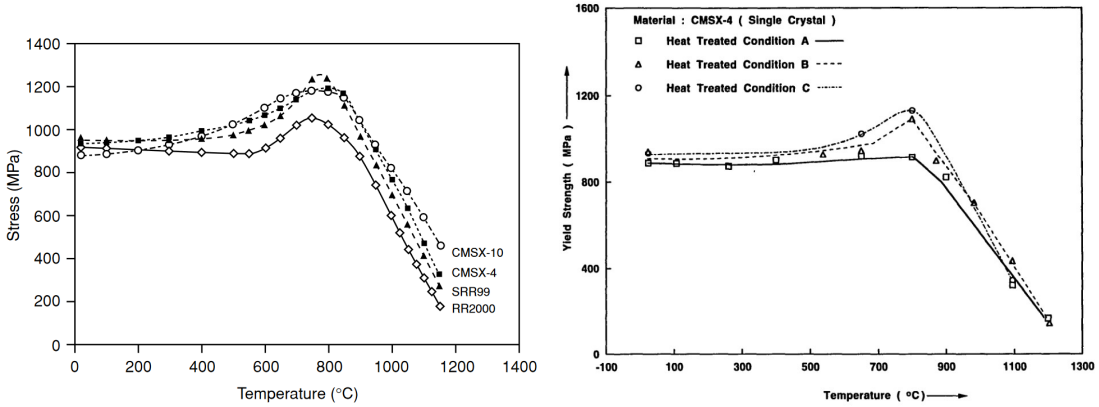
CMSX-4 and many SXNBSs unusually have an increasing yield stress (σ_y) with temperature up to ≈ 800°C [33], known as the anomalous yield strength phenomenon [6], which can be seen in the tensile data in figs. 2.6 and 2.8 for CMSX-4. Note the typical asymmetry in superalloys of the tensile and compression σ_y behaviour in fig. 2.6 [6, p 86].

The increase of σ_y and ultimate tensile strength from RT to ≈ 800°C is caused by the strengthening of the γ' phase as superpartials inside it have thermally activated cross-slip from {111} to {100} planes under applied stress [6, 33]. So higher temperatures promote more cross-slip to {100} planes; however, these cross-slipped sections are immobile due to their APBs and are the KW locks [6]. The

KW locks increase the resistance to dislocation motion within γ' up until cubic slip ($\frac{a}{2}\langle 1\bar{1}0\rangle\{001\}$) dominates above $\approx$ 800°C [6].

As γ' is the $\approx 70 vol.\%$ phase in the alloys, its strengthening supersedes the decreasing strength of the γ phase [33].

Thus, below $\approx$ 800°C, the dominant yielding mechanisms is γ' shearing, but above it the bypass of the γ' dominates [33]. The alloy's σ_y increases with temperature due to the increasing the γ' strength with temperature with the shearing mechanism.



(a) SXNBSs (incl.CMSX-4). [6] **(b)** Different heat treatments. [33]

Figure 2.8: CMSX-4 σ_y vs temperature along <100> loading direction.

2.2 Fatigue Introduction

2.2.1 S-N Curves

Table 2.3 summarises the three empirical fatigue regimes of N_f in an S-N plot: LCF, HCF, and VHCF.

Table 2.3: Summary of the three different fatigue regimes, how they behave, and how the fatigue results are collected and analysed. "Pre." stands for predominant.

Regime [37]	LCF	HCF	VHCF
N_f [37]	$\leq 10^5$	$10^5 - 10^7$	$\geq 10^7$
Pred. Process [38]	Crack Growth	initiation + short-crack behaviour	
S-N ($R = -1$)	$\varepsilon_a - N_f$	$\sigma_a - N_f$	
Equation	Coffin-Manson [37]	Palmgren [39]	(Duplex) Basquin [23]

Palmgren's Basquin equation (eq. (2.3)) accounts for the plateau in fatigue data of the classical fatigue limit (σ_w) [39] and a similar equation has been used with the same ultrasonic fatigue rig (UFR) [40].

$$\sigma_a = C_1(C_2 N_f + C_3)^{C_4} + \sigma_w \tag{2.3}$$

Equation (2.3) works for the conventional fatigue regime, but it cannot describe the duplex S-N behaviour (fig. 2.9). It is proposed that combining two curves can explain the S-N curves into the VHCF regime [23].

A probabilistic S-N curve can also be defined, which uses statistics to plot curves of a given failure probability, and has been looked into for the novel UFR by Magazzeni in Refs [40, 41].

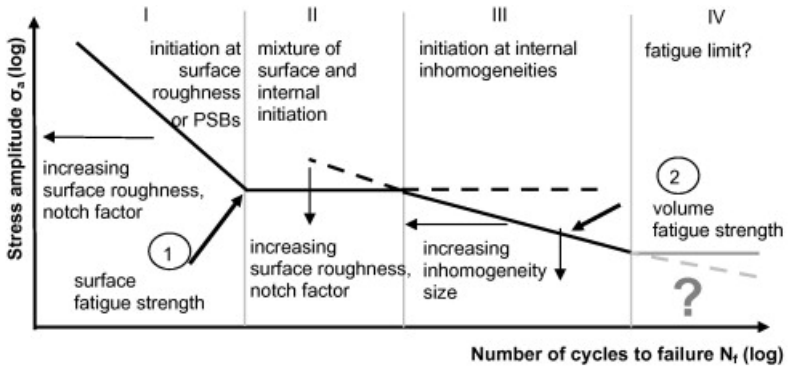


Figure 2.9: Schematic duplex S-N showing two curves. Figure from [23].

2.2.2 Fatigue Crack Dislocation Emission

Figure 2.10 depicts the distribution and type of dislocations expected from theory ahead of the fatigue crack tip for the three types of crack-tip loading [42, 43].

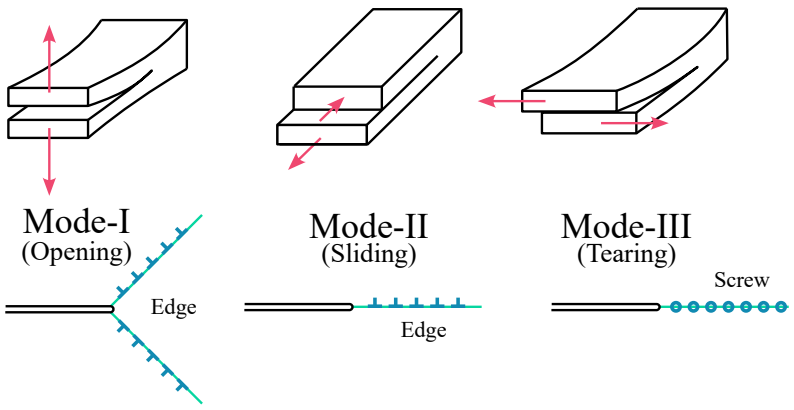


Figure 2.10: Expected dislocation types emitted ahead of a fatigue crack tip under the three different types of loading with plastic crack propagation. Adapted from Ref [42].

A dislocation-free zone is expected to form ahead of the fatigue crack tip and has to occur at all times [42, p. 30]. A component of it is due to some of the emitted dislocations returning to the crack tip on the reverse cycle [42, p. 25]. Edge dislocations tend to return to the crack tip, whereas screws tend not to because lattice frictional stress (i.e. σ_y) causes them to bunch a distance away [42, p. 25]. See Ref [42] for more details on the dislocation-free zone.

2.3 Fatigue Fracture

2.3.1 Fracture Modes

SXNBSs, unlike most materials, can initiate cracks under opening rather than shearing [44] (fig. 2.11), however this typically occurs under high temperatures.

Shearing mode is crystallographic in that the γ' precipitates are sheared along a {111} slip plane (fig. 2.12). This tends to happen more at lower temperatures (e.g. RT) due to the lower critical resolved shear stress (CRSS) in γ' [44, 45]. It has been observed at all driving frequencies (including ultrasonic) at RT [44].

Opening mode occurs when shear is restricted to the γ channels in the microstructure, with the crack propagating then microscopically along these channels to macroscopically propagate like a mode-I crack (i.e. opening crack) w.r.t. the fatigue loading [44, 45] (fig. 2.12).

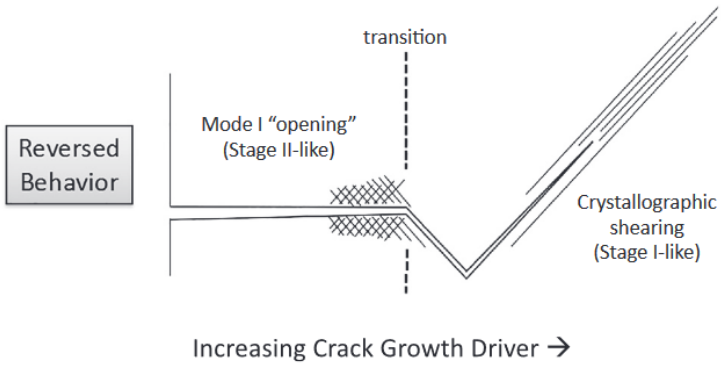


Figure 2.11: Schematic of the two types of SXNBS fatigue fracture surfaces. Representative of a typical high-temperature response. Figure from [44].

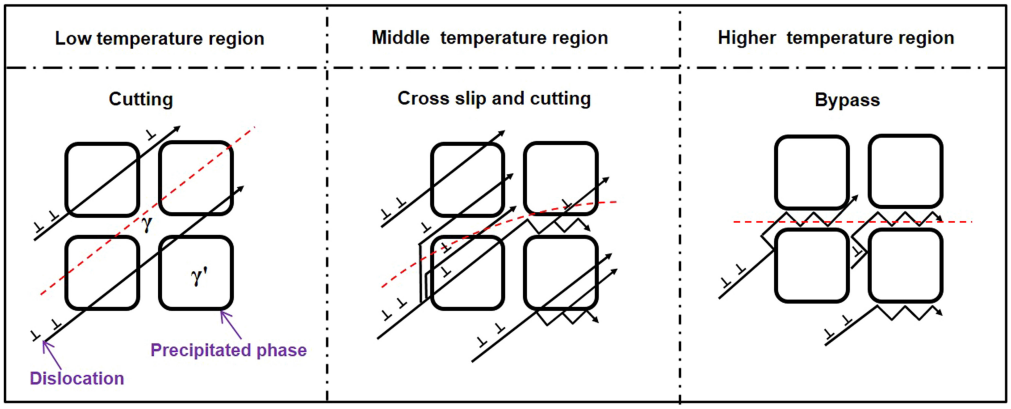


Figure 2.12: Plastic response with temperature in a DS superalloy, associated with a change in fracture mode and fractography. Associated with $T < 600°C$, $T = 600 - 700°C$, and above peak fatigue performance when $T > 700°C$. Figure from [46].

Homogeneous slip, the opposite of inhomogeneous slip, describes when the dislocations are no longer localised around one singular slip plane. Inhomogeneous slip often occurs when the precipitates can be cut (sheared), so the dislocations continue along the same slip plane. Homogeneous and inhomogeneous slips are associated with opening and shearing modes, respectively.

Some terms describe different aspects of slip but are associated. Sengupta & Putatunda (1994) describe it well in the following: "high temperatures and low strain rates resulted in wavy, homogeneous slip (stage II), whereas low temperatures and high strain rates produced planar heterogeneous slip and crystallographic fatigue crack growth along {111} type of planes (stage I) in this material." [48, p. 1166]. The quote describes opening and shearing modes, respectively. They are

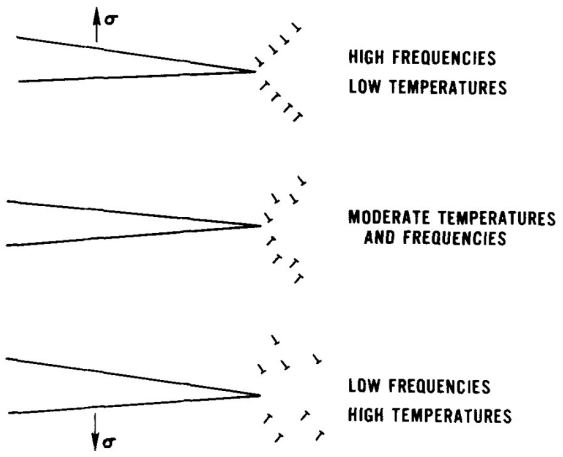


Figure 2.13: Dislocation response in fatigue in a SXNBS with respect to temperature & frequency diagram. Transitioning from developing to shearing mode (inhomogeneous/planar) to opening mode (homogeneous) from top to bottom, respectively. Figure from [47].

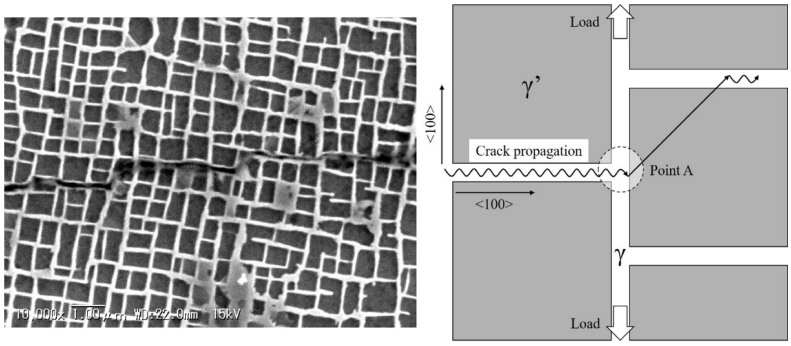
due to shearing and Orowan looping of γ' mechanisms respectively [49]. MacLachlan & Knowles (2001) [50] also found this response for CMSX-4 under $R = 0$ loading.

The wavy in "wavy slip" describes the dislocations having a zigzag-like appearance in the microstructure as seen in RT compression of CMSX-4 (fig. 2.7a) and SRR99 at 700 °C (Ref [51]).

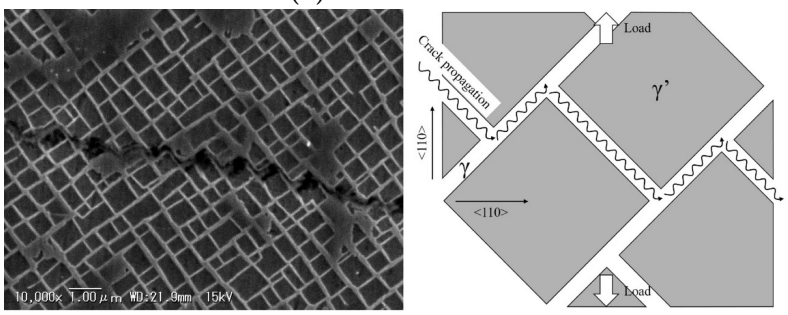
Opening Fracture

Opening mode preferentially occurs over shearing mode under higher temperatures, lower frequencies, and lower ΔK_I values. It occurs when the resolved shear stress is insufficient for shear fracture. For CMSX-4 at 450 °C, fig. 2.14 shows the pseudo-cubic slip caused by the anomalous yield phenomenon and the weaker γ channels; hence most slip is octahedral in the channels with the possibility of occasional γ' shearing like in <100><100> [45]. Thus, cubic features with little steps can be seen depending on your viewing angle due to this pseudo-cubic slip.

Opening mode can occur at RT under low ΔK_I values (e.g., < 8 MPa$\sqrt{\text{m}}$), and the less tortuous path it takes through the γ channels increases the fatigue crack growth rate (FCGR) [44].



(a) <100><100>



(b) <110><110>

Figure 2.14: Opening mode fracture (via pseudo-cubic slip) for CMSX-4 at 450 °C under different loading and crack orientations. The stress intensity factor range (ΔK) is low enough to be in the opening mode regime. The first Miller indices indicate the loading direction, and the second indicates the crack propagation direction. Figure from [45].

Transition

The transition from opening to shearing modes depends on temperature, alloy, frequency, and environment, making it difficult to establish a criterion for it [44]. A 2020 paper on this topic said that more work needs to be done to form a robust criterion [52]. Still, they indicated that the resolved shear stress intensity factor was the most suitable stress intensity factor criterion as the FCGR is unreliable [52].

Generally, for SXNBS, the opening fracture mode is expected at low driving frequencies, high temperatures, and oxidising environments [44]. However, when under ultrasonic frequencies or vacuum, shearing fracture is observed due to kinetics or lack of oxidising species to eliminate/reduce the embrittlement of the material ahead of the crack tip [44]. Figure 2.13 shows the slip behaviour for this.

The most relevant research for CMSX-4's fatigue fracture behaviour comes

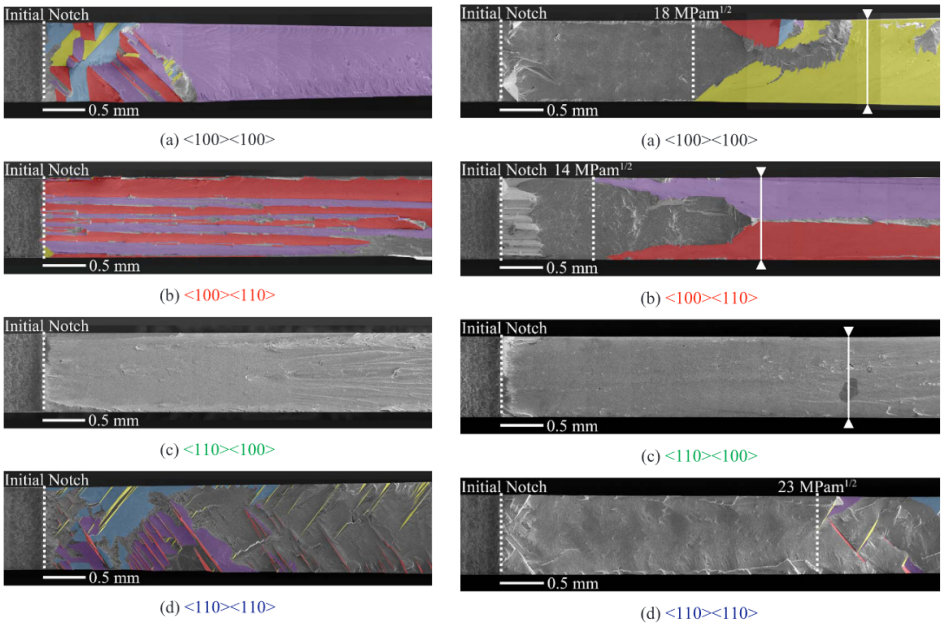
from Inoue & Sakaguchi's group (Refs [45, 53]). They performed macro-scale compact tension (CT) tests of different SXOs at RT [45, 53], 450°C and 700°C [45]. However, no S-N data was collected as they focused on the FCGR. Their labelling convention is that the 1st Miller index is the loading direction, and the 2nd is the crack propagation direction. Table 2.4 shows that shearing mode dominates at RT, whereas higher temperatures become dominated by opening mode transitioning when under a high enough ΔK_I. Figure 2.15 shows their 20 °C and 450 °C fractographs.

A recent paper found similar results and found the 300 °C response was intermediate between 20 °C and 450 °C in both length of opening mode and of the ΔK_I for shearing [54].

An alloy's σ_y, which is temperature and strain rate dependent, correlates with its fatigue resistance, as the microplasticity determines the rate of fatigue crack initiation [50].

Table 2.4: Fracture mode as a function of temperature and ΔK_I from [45, 54] . Mixed means Open→Shear. <110><110>. *In Ref [54] mixed up to 450 °C.

	<100><100>	<100><110>	<110><100>	<110><110>
RT	Shearing	Shearing	Opening	Shearing*
300 °C [54]	Mixed	Mixed	Opening	Mixed*
450 °C	Mixed	Mixed	Opening	Mixed*
750 °C	Mixed	Mixed	Opening	Opening



(a) $T \approx 20°C$ **(b)** $T = 450°C$

Figure 2.15: CT fractography for RT and 450 °C under $R = 0.4$ and 10 Hz fatigue conditions. Crystallographic planes (i.e., shearing mode fracture) have been coloured, whereas opening mode has not been. Figure from [45].

Figure 2.16 shows the different mode surfaces under high magnification. The opening mode shows the cuboidal structure well and with the crack following the γ channels to create the {100} ledges. The shearing mode shows no ledges, and the γ' precipitates have been cut along a {111} plane to form triangular projections of the cuboids.

Ref [42] looked at the fracture modes with temperature @ 10 Hz. The RT fracture path was described as "zigzag", fracturing along {111} planes, shearing the γ' [42, p. 60-61] (i.e. shearing mode), with river patterns occurring [42, p. 79]. Whereas at 650 °C, a flat smooth fracture surface with pseudo-cubic slip (i.e. opening mode) was observed before transitioning to shearing mode under a higher ΔK [42, p. 64-66]. The 650 °C fatigue showed dislocation dipoles, sheared γ', interfacial dislocations from lattice mismatch, and Orowan loops [42, p. 66-67].

To predict the fracture path through modelling, Ref [56] modelled a microstruc-

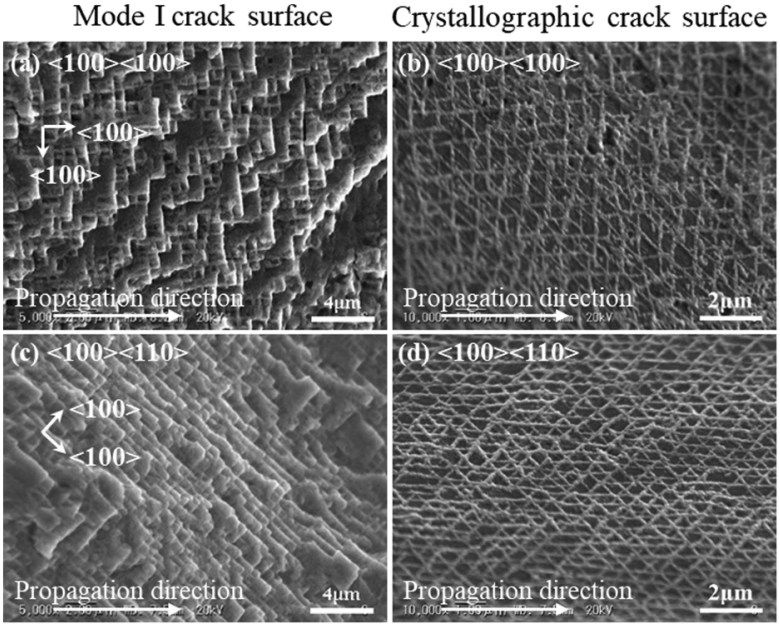


Figure 2.16: Opening (1st column) and shearing (2nd column) fatigue fracture paths under high magnification in CMSX-4 at 450°C, $R = 0.4$, $f = 10$Hz. Figure from [55].

ture similar to CMSX-4 at 20 °C & 700 °C at low and high σ_{amp} under $R = 0.1$ & 2.5×10^{-2} Hz. They found that the crack path follows the pseudo-cubic slip in the γ-channels at high temperatures and low σ_{amp} (can transition to shearing at long enough cracks), and that typical γ' shearing happens at low temperatures [56, p. 14].

Shearing Fracture

Figure 2.17 shows how these shearing mode fracture paths appear in 3D also for CMSX-4 for different loading and crack propagation directions [53], and fig. 2.18 shows this under high magnification. The 2nd form (i.e. b) is typically referred to as "factory roof" in the literature [45]. Table 2.5 summarises the stress intensity components in the fatigue crack.

Neu's interpretation of the results from Ref [45] (i.e. fig. 2.15) is that shearing mode occurs if the crack has enough drive and follows the plane of the highest resolved shear stress, with the path being weakly influenced by pores and remnant eutectics [44].

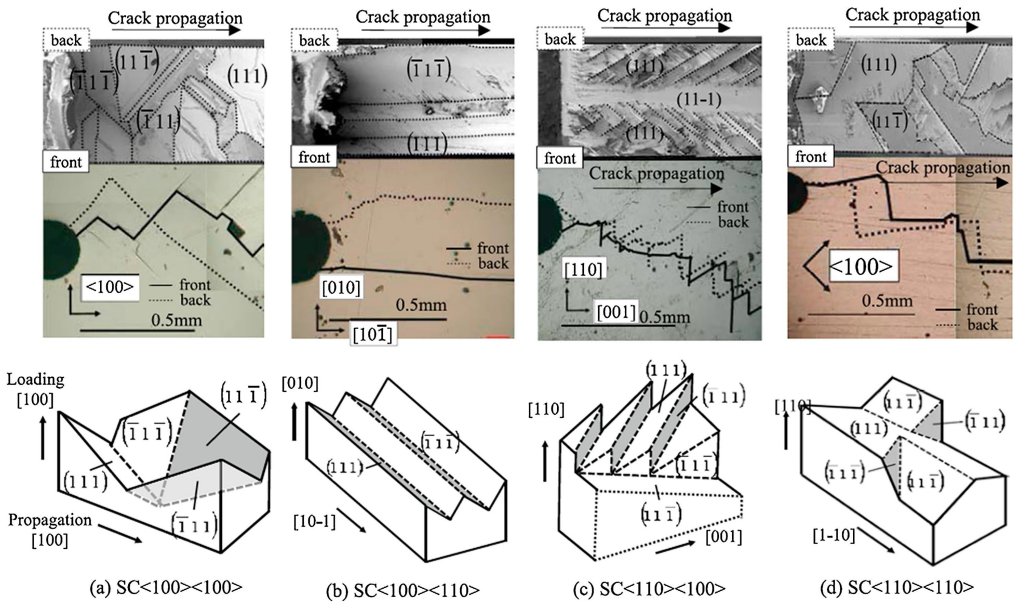


Figure 2.17: Forms of shearing mode (i.e. crystallographic) fatigue fracture paths in CMSX-4 at RT. Figure from [53].

Table 2.5: Stress intensity modes associated with the forms of shearing cracks in fig. 2.17 [53].

Mode	⟨100⟩⟨100⟩	⟨100⟩⟨110⟩	⟨110⟩⟨100⟩	⟨110⟩⟨110⟩
I	✓	✓	✓	✓
II	✓		✓	
III	✓	✓		✓

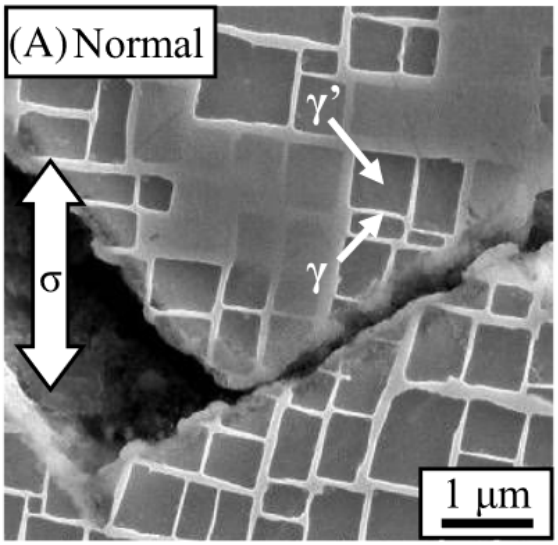
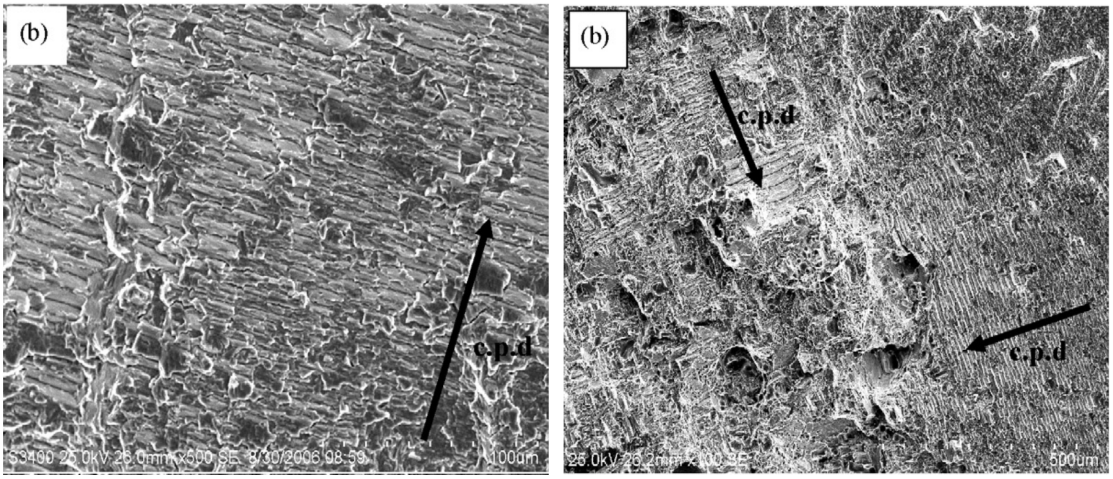


Figure 2.18: CMSX-4 fatigue fracture under a <100><100> orientation, with an SE micrograph. Figure from [57] (CC BY 4.0).

Shearing Fracture Steps

A feature of shearing fracture is shearing fracture steps (a.k.a steps). Figure 2.19 shows they are fine and extensive step-like features often normal to the fatigue crack growth (FCG) direction. They have been associated with {111} planes in the final fast fracture (rotary fatigue test in Ref [58]).



(a) Smooth specimen **(b)** Notched specimen

Figure 2.19: Fractography for SRR99 SXNBS under 700 °C under $R = -1$ and 83.3 Hz fatigue conditions. [001] is the growth direction normal to the viewing plane. The FCG directions are shown by the black arrows, which the "steps" seem to be aligned with. Figure from [51].

Figure 2.20 shows steps in CMSX-4 (air & vacuum at 650°C [59]). "Cleavage steps", are likely the same feature but with larger facets, have also been seen in the RT tensile test fracture surface for CMSX-4 [35] and a novel SXNBS [36].

In the pre-crept plate-like γ' CMSX-4, the very fine steps among darker flat regions of opening mode fracture at RT fatigue under a <100><100> orientation are associated with shearing mode fracture within the γ' [57].

It has been noted that plane stress conditions promote shearing mode fracture, whereas plane strain promotes opening mode fracture [44, 60, 61]. Ref [61] found that for their near <100><100> PWA 1480 SXNBS CT test specimens that on the outer surfaces large {111} shearing facets occurred on two planes (i.e. under

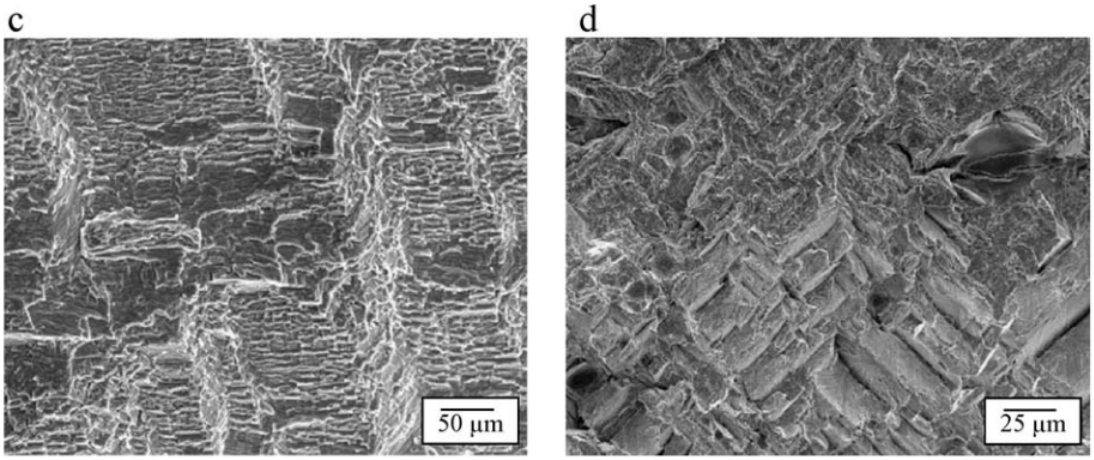


Figure 2.20: Forms of shearing mode fatigue fracture paths in CMSX-4 at 650°C. (c) and (d) were found in air under high ΔK but under <001><110> and <001><001> orientations, respectively. They both show extensive but fine faceting. Figure from [59].

plane stress), but under mid-thickness (i.e. plane strain) and intermediate-to-high ΔK four {111} fracture facets occur.

The mid-thickness facets are smaller and look step-like under high ΔK and in the schematic, and this could be why they are associated with the final fast fracture in Ref [58].

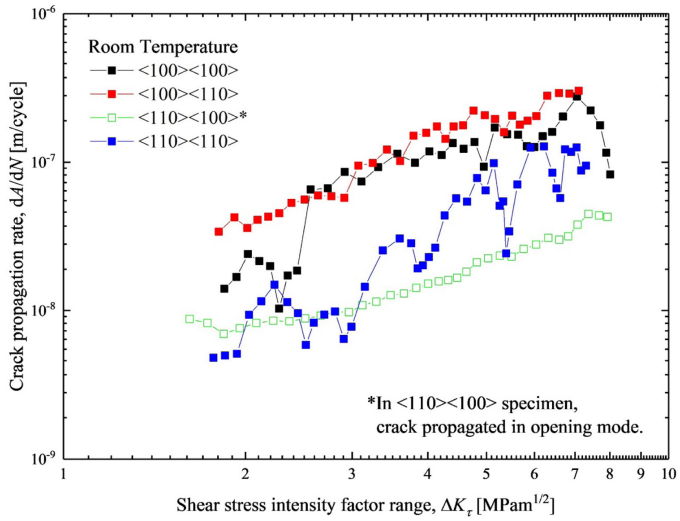
2.3.2 Fatigue Crack Growth Rate

The RT Paris plots from the shearing mode failure of CMSX-4 are in fig. 2.21a, showing the fastest to slowest orientations are <100><110>(b), <100><100>(a), <110><100>(c), and <110><110>(d); with form (b) is slightly faster than (a). Ref [53] from the same research group shows more clearly that form (b) (aka roof-top) is faster than form (a).

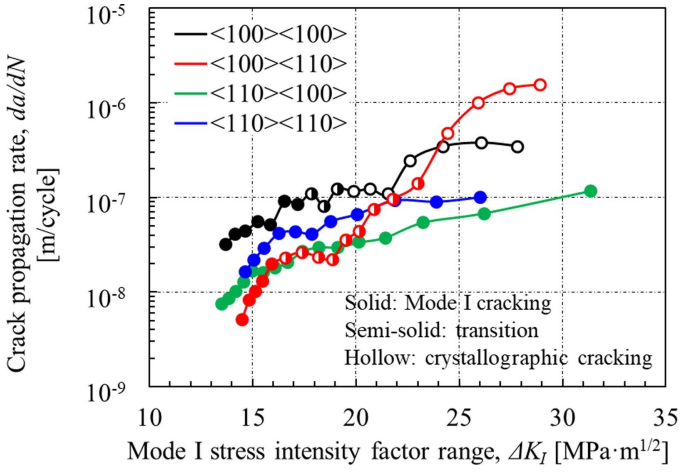
Roof-top being the fastest agrees with Ref [44] in that infrequent crack deflection, which roof-top has little-to-none, leads to a less tortuous crack path, which increases the FCGR. Quoting Neu, "the FCG rates are significantly influenced by the primary and secondary crystallographic orientations". The irregular zigzag shearing mode crack path of ⟨100⟩ orientated CMSX-4, causes a high crack closure, which lowers the FCGR [42, p. 61-62].

Therefore, when varying the SXO of the mesocantilevers in this thesis, the fractography may give an insight into the FCGR.

Figure 2.21b shows CMSX-4 at 450 °C indicating the shearing mode has a greater FCGR than the opening mode [55]. Interestingly, the order of fastest FCGR changes when under the initial opening mode fracture, as shown in fig. 2.14 with <100><100> being the fastest, followed by <110><110>, which makes logical sense with their convenient crack paths.



(a) 20°C [45]. Related to fig. 2.15.



(b) 450°C [55].

Figure 2.21: FCGRs for CMSX-4 under 20 °C & 450 °C as a function of ΔK. Both tested under $R = 0.4$ & $f = 10$Hz conditions.

For CMSX-4 at 650 °C & 725 °C, it was found that the FCGR was affected by the

SXO due to how much shearing mode can be slowed via the orientation-dependent interdendritic porosity and by the elastic + plastic anisotropy [22].

There is a contradiction on which failure mode has the faster FCGR in Neu's review [44]. Page 271 states that opening fracture has a greater FCGR than shearing as the path through the γ channels is less torturous; however, fig. 2.22 on page 277 & fig. 2.21 depict opening fracture with a slower rate.

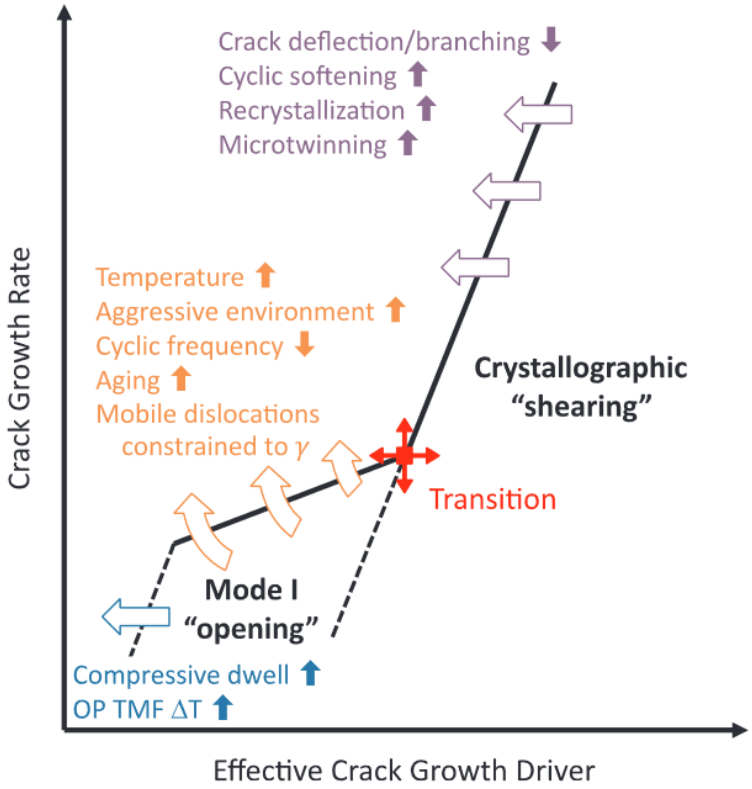


Figure 2.22: Schematic of FCGR vs driving force and the two types of SXNBS fatigue fracture surfaces. Figure from [44].

2.3.3 CMSX-4 Cantilevers Fatigue Fractography

Ref [62] fatigued a notched microcantilever of CMSX-4 to investigate the size effect, shearing fracture, and slip behaviour. They tested a $10 \times 10 \times 42.5\,\mu m^3$ cantilever under $R_{disp} = -0.8$ (asymmetric to attempt crack initiation on the notched side only).

Dislocations piled up at the neutral axis of the beam, with their back stress affecting the crack tip (dislocation source), causing an initial deceleration with crack

progression before temporarily changing the slip plane, later reverting due to pile up on the secondary plane. The neutral axis shifted further from the crack due to pile-up stress, and an alternating "zig-zag" crack path formed [62]. The zig-zag appears to begin when the crack is near the initial neutral axis.

The shifting of the neutral axis location occurs when the fatigue crack spans the breadth of the cantilever and the K_{tip} is not altered [38, p. 1298].

It is not mentioned, but despite the low surface roughness and damage, multiple samples exhibit crack initiation on the opposite side of the remaining ligament. A reason for this is indicated in their finite element modelling (FEM), which exhibits a high Tresca stress in that region ahead of the crack. This *exit side* fracture has also been found in Rene-N5 (SXNBS) microcantilever bending fatigue, where it was observed to initiate from extrusions/intrusions [63, p. 161] (fig. 2.24).

Ref [62] concludes that the neutral axis pile-up effect improves not only the fatigue lifetime (c.f. uniaxial) but also affects the FCGR & the threshold stress intensity factor range (ΔK_{th}) through a lack of crack closure.

The bending fatigue of the Rene-N5 microcantilevers showed that fatigue cracks initiated as $\{111\}$ shearing facets at stress concentrations (for $N_f < 10^6$) and typically grew along a $\{100\}$ plane [63, p. 161] (fig. 2.24).

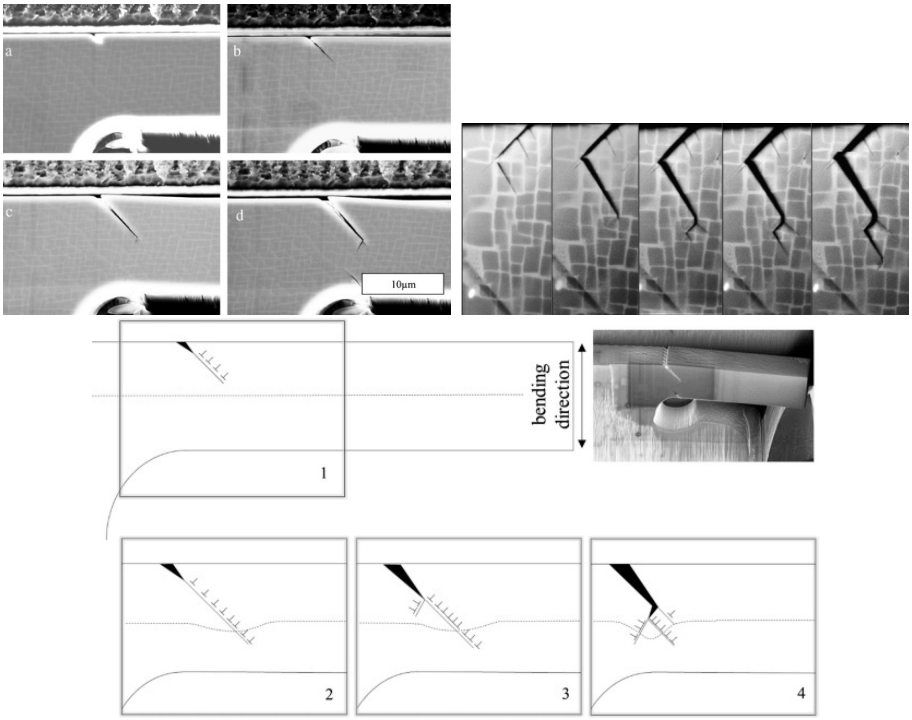


Figure 2.23: CMSX-4 bending microcantilever fatigue at RT. Two examples of crack propagation and a schematic of the dislocation pile-up mechanism. Figures from [62].

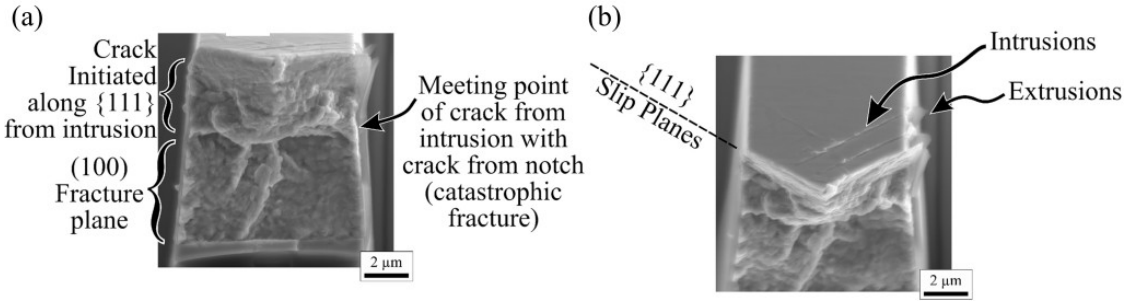


Figure 2.24: Fractography of SXNBS Rene-N5 bending fatigue. Figure from [63].

2.4 Temperature Effect

The following discussion will be important to distinguish between responses under LCF and HCF, and it is important to keep in mind the σ_y response with temperature (T). The effects of oxidation will be discussed in section 2.7.

Fatigue

For CMSX-4 in air, when approaching the peak σ_y temperature $\approx 800\,^{\circ}\mathrm{C}$ from below it, an improvement in fatigue response occurs (HCF in fig. 2.25), but worsens when

going above it (HCF in fig. 2.25 & fig. 2.26). This is attributed to the strengthening, and then the weakening of the alloy in [64], concurring with figs. 2.6 and 2.8a.

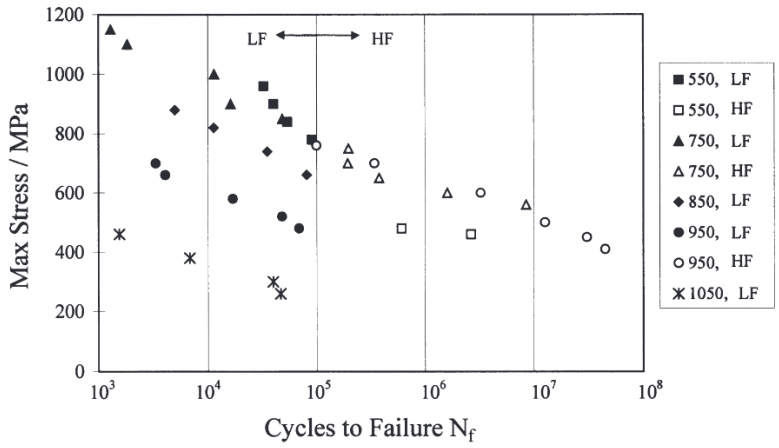


Figure 2.25: Un-coated CMSX-4 S-N results with temperature tested in air and with $R = 0$. The two testing frequencies were $LF = 0.25\,\text{Hz}$ & $HF = 100\,\text{Hz}$. Figure from [50].

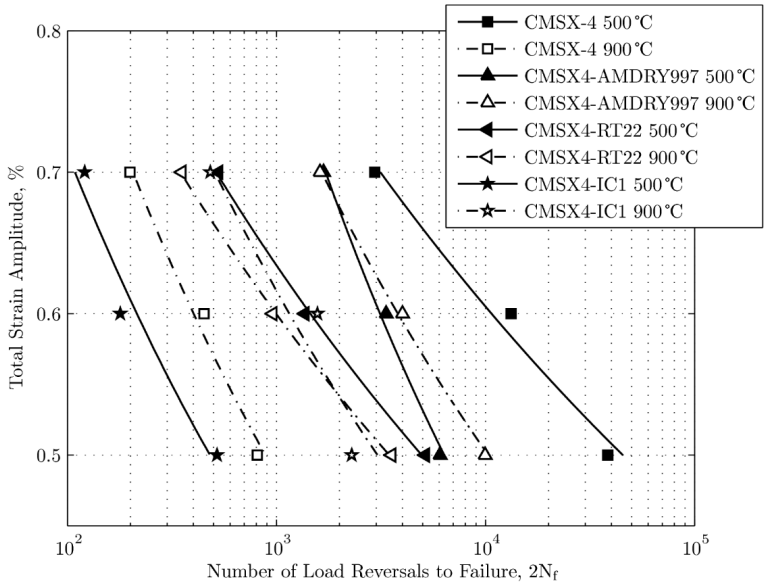


Figure 2.26: CMSX-4 under $R = -1$ with decreasing fatigue strength with increasing temperature. Tested either coated or uncoated. Figure from [64].

CMSX-4's strain hardening exponent increases with temperature because it increases the presence of stacking faults, which hinders cross-slip [42, p. 55, 80].

Figure 2.27 shows that for polycrystalline (PX) Inconel 718 in air, the run-out performance increases with temperature but peaks at 500 °C from RT around

$N_f = 10^6 - 10^7$. It is associated with "crack stagnation" of cracks around 20-30µm as the higher temperatures cause both oxide-induced and plasticity-induced crack closure [65]. Oxide-induced crack closure arises from volume expansion from oxidation, bridging the crack, and plasticity-induced crack closure is when the plastic zone in the crack wake or crack tip acts to close the crack [5, p. 20]. Figure 2.27 also highlights the non-trivial S-N behaviour, as RT & 300 °C outperform 500 °C at low enough N_f [65]. Note, these PX sample results are not directly comparable to the SX samples in this thesis.

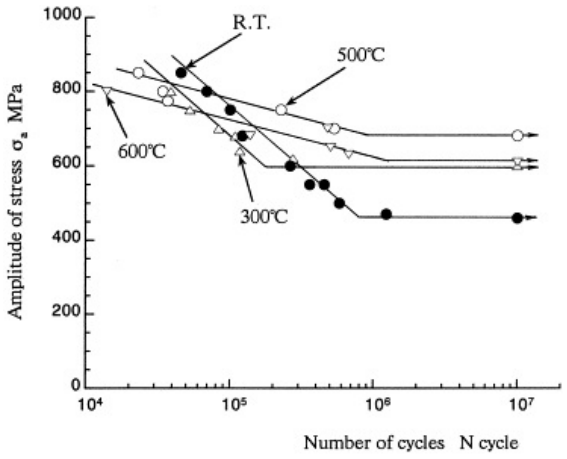


Figure 2.27: PX Inconel 718 S-N curve at various temperatures in air. Achieved with rotary bending of a specimen with a diameter and gauge length of 8 mm and 10 mm respectively. Figure from [65].

Creep

Creep's effect on fatigue was found to be negligible for CMSX-4 at RT and very low at 650 °C even under positive fatigue ratio $\sigma_{min}/\sigma_{max}$ (R) values [42, p. 58&70].

Hence, creep should be negligible in this work due to fully reversed fatigue (i.e. $R = -1$) and under ultrasonic frequencies.

2.5 Fatigue Method Effects

The novel UFR in this work uses ultrasonic frequencies and small specimen geometries, so this section will address the effects that these might cause.

2.5.1 Size Effect

The nature of decreasing the stressed volume of a fatigue specimen changes the defect population within it, naturally pushing the pore size distribution lower, giving rise to statistically better fatigue performances compared to their larger counterparts [66, p. 20]. This increase in fatigue strength is a classic fatigue size effect phenomenon [67, p. 1].

The "risk volume" metric is often used in fatigue size effect, and it is the "most influencing factor" in the VHCF regime [68]. A useful & reasonable metric is the fractional metric of V_{90}, the total volume where $\sigma_a \geq 0.9\sigma_{a,max}$ (N.B. arbitrary fraction), but doesn't account for σ_{amp} distribution within the test component like other metrics [68].

A list of potential causes of size effect in these mesoscale bending samples are:

1. Porosity [5]
2. Biaxial vs triaxial stress [61, 69]
3. Dislocation pile-up [62]
4. Strain-gradient + geometrically necessary dislocations (GNDs) [70]

Review papers have touched on the size effect, with focuses on the VHCF regime [68], defects [71], and the microstructure & geometrical contributions [67].

Porosity

Porosity is the most crucial size effect, as work done for CMSX-4 under similar testing conditions for this work said "porosity distribution is a key parameter as these inherent defects have been shown to control fatigue crack initiation and should be included in life prediction models" [5, § 5.5]. Numerous papers state the importance of porosity on fatigue performance (Refs. [58, 72]), placing the focus of their effect on the VHCF regime (Refs [73, 74]).

For CMSX-4, it is reported that its fatigue crack initiation can be dominated by porosity depending on the testing conditions [22, p. 1439].

Hot-isostatic pressing treatment showed a 20-fold life improvement in the VHCF regime for CMSX-4 and other SXNBS [73]. This decreased the pore distribution, showing that the casting pores dominated the fatigue performance [73]. Ref [75, ch. 3] similar results in SXNBSs.

A Kitagawa-Takahashi (K-T) diagram (fig. 2.28) can be used to explain how the fatigue limit depends on the critical pore size as done for SXNBS DD5 [72]. Metrics of the pore size can be the *Feret diameter* or $\sqrt{area}$, with the former being preferred due to its more conservative nature [72]. A population frequency histogram of the Feret diameter results in a log-normal distribution, which can estimate the maximum pore size using the *statistical extreme value* method [72].

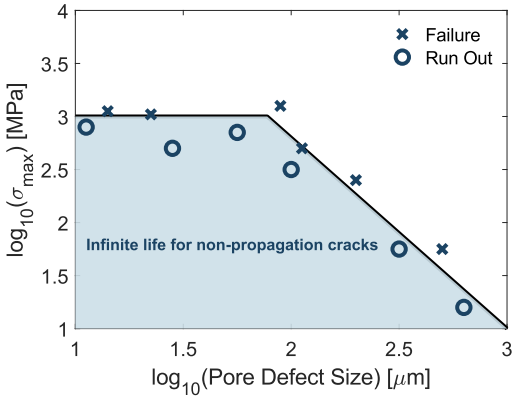


Figure 2.28: Schematic K-T plot for a single N_f.

The physically smaller sample size also creates a larger degree of scatter within the fatigue results. Extreme examples are a sample with no pore and a sample with a pore almost the size of the stressed volume, therefore giving great and poor fatigue strengths, respectively.

General

In the current literature, the study of size effect on single crystals is primarily in the LCF regime, and so there is a lack of higher lifetime regime behaviour [67, p. 18]. It has been noted that in single crystals, the size effect is more significant for fatigue crack initiation than growth, owing to the plasticity dependence on size, which causes initiation [67, p. 7].

Biaxial vs triaxial Stress

A transition from opening to shearing going from triaxial to biaxial stressed regions was found for SXNBS PWA 1480 at $R = 0.5$, 20 Hz, at RT, in air [61]. The change in fracture mode is thought to alter the FCGR and hence the N_f [61]. However, in a W microcantilever, it shows that despite its size, it transitions from biaxial to triaxial stress from its surface to its centre [69, p. 410].

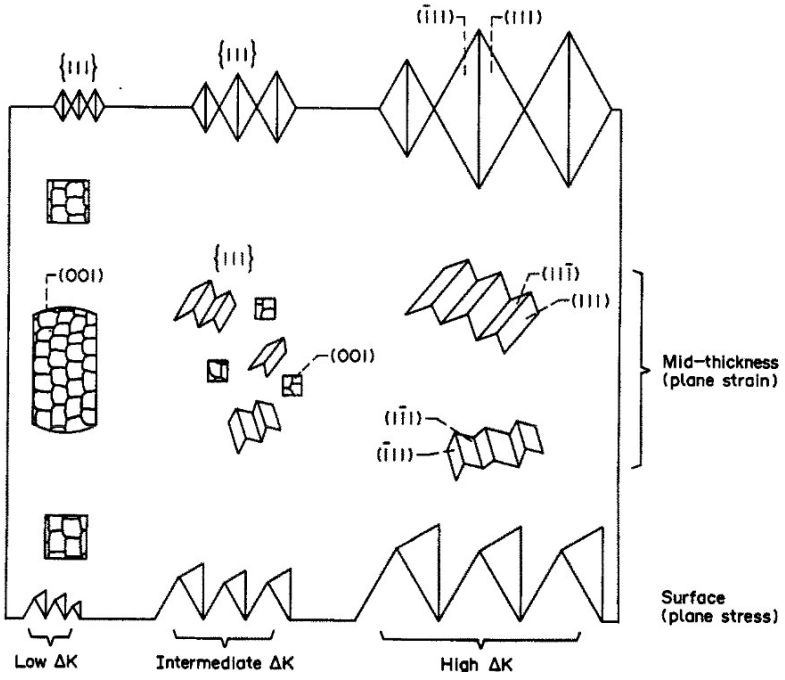


Figure 2.29: Biaxial & triaxial stress state's effect on fractography along with ΔK. (001) & {111} indicate opening and shearing mode fracture paths respectively. Figure from [61].

Dislocations

In a 10 µm thick CMSX-4 microcantilever, the FCGR was affected by dislocation pile-up and lack of crack closure (discussed in section 2.3.3). The smaller size allows for significant back stress from pile-up, reducing the propagation rate and crack plane [62]. As thickness decreases, the flow stress increases due to the greater degree of back stress [62, p. 131], having a reciprocal relationship for SX Cu microcantilevers [76]. A larger strain gradient (%/µm) will cause the GNDs to be denser and increase the flow stress [70, p. 3048].

N.B., a 15 µm thick uncracked CMSX-4 microcantilever is considered thick enough to mitigate the strain gradient and pile-up size effects. Once cracked though, the remaining ligament will increase the strain gradient [70, p. 3048]. Based on SX Cu microcantilever flow stress vs thickness, a ligament (thickness) less than 50 µm thick would have >5% flow stress increase compared to a 150 µm thick cantilever [77, §3.2].

Crack Closure

Figure 2.30 shows that the FCGR differs depending on the specimen size, with the authors discussing the effect of crack closure [70, p. 3047]. A significant source of size effect in smaller samples is plasticity-induced crack closure due to plane stress being more dominant [70, p. 3047]. Blades in service will be substantially larger in size, and so the fatigue crack behaviour will be less dominated by plane stress but may be more relevant to thin section regions.

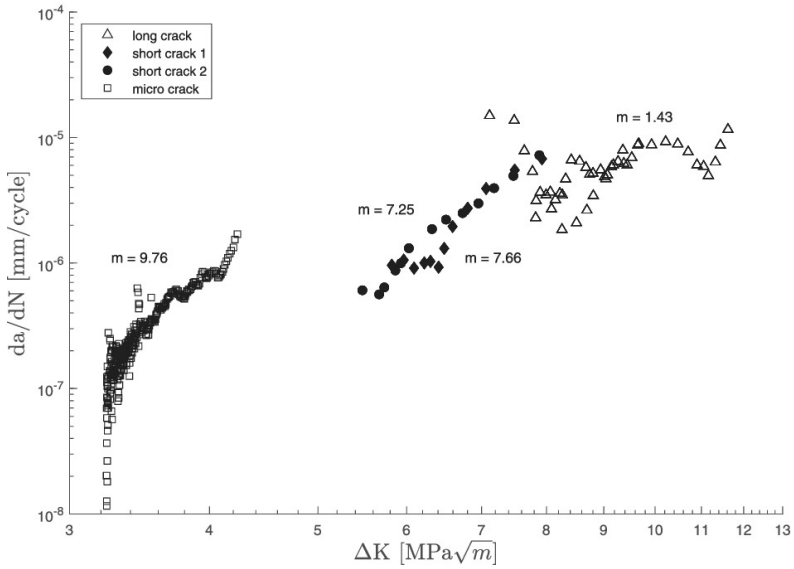


Figure 2.30: Paris plot for three different CMSX-4 specimen sizes. The long, short, and micro-cracks correspond to the lower mm, upper µm, and lower µm ranges respectively. Similarly, from "micro specimen, a tensile specimen with focused ion beam (FIB) notch, and tensile specimen with a long fatigue crack", respectively. Figure from [70] (CC BY 4.0).

2.5.2 Frequency Effect

Examples of intrinsic and extrinsic frequency dependencies are deformation mechanisms and environmental processes, respectively [66].

Intrinsic

A 2016 review on ultrasonic fatigue [66] concluded (based on the limited data at the time), that Ni-based superalloys exhibit a weak dependency with frequency due to the strain rate insensitivity of FCC metals. For SXNBS tested with UFRs a little-to-no frequency response and no fatigue limit in the $N_f = 1 \times 10^7 - 5 \times 10^8$ range [66]. Ni microcantilevers also lacked a frequency dependence when comparing results collected at 8 kHz and at 0.5 Hz [78, p. 2340]

At RT, SXNBSs are not strain rate sensitive, so increasing the frequency will not change the slip mode [79, p. 1].

Ultrasonic frequencies limit dislocation cross-slip and motion, causing less damage at each cycle [9, p. 19-20]. Additionally, the cross-slip of screw dislocations

is a cause of kinematic irreversibility of cyclic slip [80, § 4.7], which promotes fatigue crack initiation.

Extrinsic

A 2023 review paper [9] indicates that FCC metals (specifically an Al alloy) do show an extrinsic frequency effect, showing a strong fatigue performance improvement in air and a weak one in Ar when going from $< 400\,\text{Hz}$ to $20\,\text{kHz}$. In Al it is postulated that higher frequencies reduce the interactions with the environment, which reduces the oxidation damage that decreases the fatigue life [81, p. 230].
The testing environment can affect tests even under ultrasonic frequencies, and there is a frequency dependency when there are kinetic processes [9]. They conclude that complementary vacuum data is needed to assess frequency effects fully [9]

For SXNBS MAR-M200, ultrasonic frequencies hindered the negative environment effects on its fatigue performance, responding similarly to that of vacuum conditions with conventional frequencies [79]. The ultrasonic air tests showed dimples (local ductile failure) like conventional frequency vacuum tests [79].

Internal Heating

Internal heating is caused by anelasticity and stress-strain hysteresis during the fatigue cycling process for elastic ([82]) and plastic ([66]) deformation regimes, respectively. It is typically worsened by the degree of deformation, volume, and testing frequency.

Internal heating is thought to be negligible for $\approx 10\,\mu\text{m}$ PX Ni microcantilevers under high-frequency ($8\,\text{kHz}$) and low-frequency ($0.5\,\text{Hz}$) bending fatigue [78, p. 2340].

For macroscale SXNBS MAR-M200, despite the low internal heating under conventional UFR attributed to SXNBSs having low internal friction and lack of grain boundaries, cooling was still required during fatigue [79, p. 2]. It was proposed that the local heating at the crack tip is negligible for the ultrasonic fatigue testing (UFT) macroscale samples due to the same slip behaviour as conventional frequency tests [79, p. 1935].

2.6 SXO S-N Dependence

A 2021 paper states that the SXO effect of the fatigue performance on SXNBSs, especially HCF, has received much less attention, with creep performance being the focus [83].

2.6.1 Conventional Fatigue Regime

LCF is typically reported as ε_a-N_f (i.e. Coffin-Manson), as reported for the SXO at elevated temperatures for two SXNBSs in Refs [26, 84]. Ref [26] finds that secondary orientation has a "pronounced effect on fatigue life", but with no conclusion for primary orientation. The secondary orientation is also of interest as it is "neither specified nor controlled" for manufacturing of the blades [26, p. 162].
In strain control LCF tests [84] the best strain fatigue performance in decreasing order are $\langle 001 \rangle$, $\langle 011 \rangle$, then $\langle 111 \rangle$, which when accounting for stiffness (orientation factor [85]) the strain fatigue performances virtually reduce down to one curve.

In recent load control tests on a SXNBS it was found that the fatigue performance significantly depended on the primary orientation at elevated temperatures (fig. 2.31) [83]. With the best performance when closest to $\langle 111 \rangle$, with a reduction when approaching either $\langle 001 \rangle$ or $\langle 011 \rangle$ with different mechanisms for all.

These different mechanisms are: $\langle 111 \rangle$ has multiple octahedral slip systems contained within the γ channels; and similarly approaching $\langle 001 \rangle$ it becomes two octahedral slip systems; whereas approaching $\langle 011 \rangle$ causes stacking faults to form from octahedral slip interactions [83].

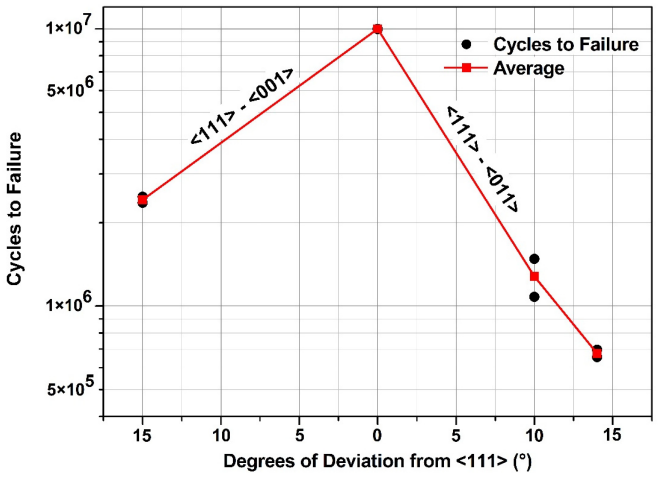


Figure 2.31: Model SXNBS SXO fatigue performance dependence at 850°C, σ_a = 445MPa, & $R = -1$. Orientation varied near the inverse pole figure edges. Figure from [83] (CC BY 4.0).

Figure 2.32 shows the rotary HCF on SRR99 (@ 700°C, $f = 83.3$Hz, $R = -1$) seeded to form $\langle 001 \rangle$, $\langle 011 \rangle$, and $\langle 111 \rangle$ samples (with <6° deviation) [86]. They conclude from their linear extrapolations that the fatigue limit (i.e. $N_f = 10^7$) order of the orientations is $\sigma_{011} > \sigma_{111} > \sigma_{100}$. However, this is questionable, as each curve exhibits a large scatter across a small N_f regime and a significant overlap, and the linear fit extrapolation is likely a poor metric to exhibit their differences in behaviour.

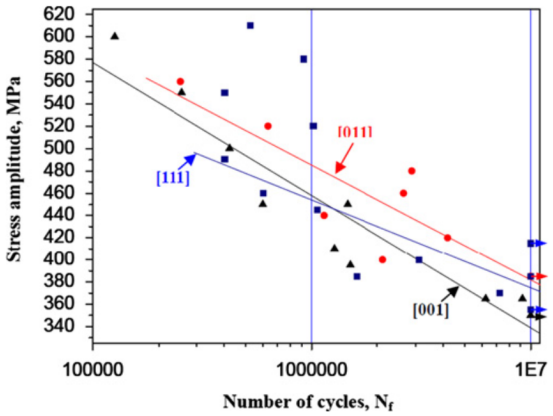


Figure 2.32: Rotary bending S-N curve for SRR99 @ $T = 700$°C for different crystal orientations via seeding. Figure from [86].

Figure 2.33 shows the ε_a-N_f curves at $R = -1$ at 950 °C for for CMSX-4 [20]. The authors conclude the best to worst fatigue performance orientations for all

temperatures at $R = -1$ are $\langle 001 \rangle$, $\langle 011 \rangle$, then $\langle 111 \rangle$ in stain amplitude (ε_{amp}). They attribute this order to an increasing Young's modulus value (i.e. elastic anisotropy dominated) [20, § 5]. The authors conclude that for $N_f \geq 10^3$, the fatigue performance can be accounted for using the relevant Young's modulus for that orientation [20, § 8].

It is worth noting that the LCF in Refs [26, 84] from different alloys show $\langle 001 \rangle$ being better than $\langle 111 \rangle$, but this is the opposite in fig. 2.33. This could be due to CMSX-4 being different to the other two alloys or that 950 °C behaves differently to 649-760 °C.

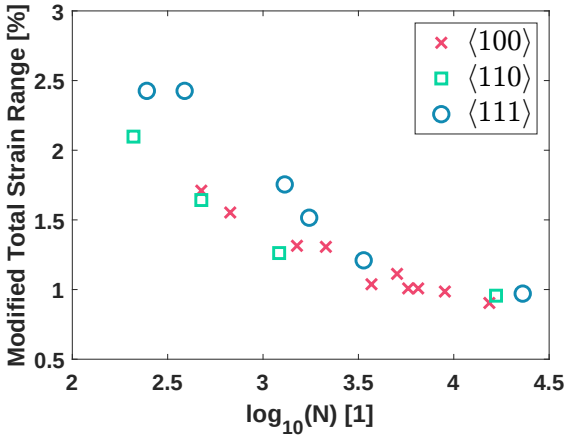


Figure 2.33: CMSX-4 A-N at $R = -1$ & 950 °C as a function of SXO, the relevant points are coloured. Adapted from Ref [20].

2.6.2 Very High Cycle Fatigue

The most relevant paper was by Cervellon et al. (2021) [11], investigating the fatigue performance of CMSX-4, MC-NG, and AM1 from the HCF to the VHCF regimes. They performed these tests with a standard uniaxial UFR at 750 °C and $R = -1$. The gauges of the hourglass specimens had minimum diameters of 3 mm and volumes of 34 mm^3 for both $\langle 100 \rangle$ + $\langle 110 \rangle$, and 46 mm^3 for $\langle 111 \rangle$. The disorientations (deviations) for $\langle 100 \rangle$ were mostly <5° (CMSX-4), $\langle 110 \rangle$ was ≈ 10°, and $\langle 111 \rangle$ was either unknown or <2°.

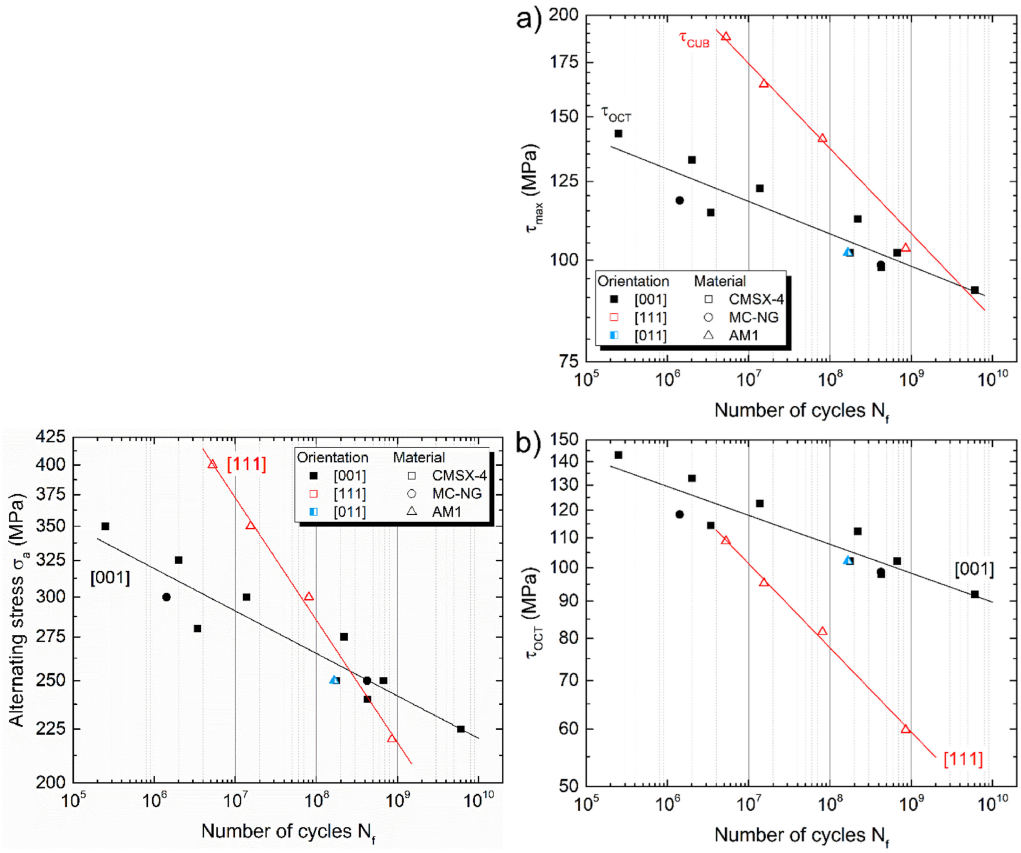
Their S-N curves for the three different orientations in fig. 2.34 ignore alloy dependencies, based on earlier work (under the same conditions) that found

processing dominated the VHCF response rather than alloy due to changes in pore sizes [73, p. 3941&3949] in numerous SXNBSs. They assume that orientation dominates the fatigue response over chemical differences between the alloys due to their similar microstructures [11, p. 2]. However, conflicting evidence has been found that alloy differences drastically vary the fatigue responses [60].

The paper admits to having no proper characterisation of the $\langle 011 \rangle$ fatigue response as only one data point was collected [11, p. 3]. They speculate that as the $\langle 011 \rangle$ point overlaps with the $\langle 001 \rangle$ curve, the $\langle 011 \rangle$ response would be similar to $\langle 001 \rangle$ as they both have octahedral slip systems [11, p. 8]. However, fig. 2.34b shows that the $\langle 001 \rangle$ & $\langle 111 \rangle$ curves could not be resolved when using the shear fatigue failure criterion alone; not concurring with their proposed theory. Additionally, in fig. 2.34a, the $\langle 110 \rangle$ point is near the $\langle 001 \rangle$ & $\langle 111 \rangle$ transition point, making it less clear.

In fig. 2.34a, ignoring alloy differences, for $N_f \leq 10^8$ the $\langle 001 \rangle$ performance is worse, but when $N_f \geq 10^9$ it is superior. The authors note this and liken their switch in performance to the results in fig. 2.32 [11, p. 8]. Ref [86] differs from Ref [11]. Firstly, they say the $\langle 011 \rangle$ performance is different to $\langle 001 \rangle$'s. Secondly, it shows $\langle 001 \rangle$ being better than $\langle 111 \rangle$ before the transition N_f, the opposite of Ref [11].

The results from fig. 2.31 are $N_f > 10^5$ & $T = 850°\text{C}$ are not an S-N curve but show that $\langle 111 \rangle$ outperforms $\langle 001 \rangle$ and $\langle 011 \rangle$, so this could be after the transition period due to the larger N_f through a lower σ_a which concurs with Cervellon et al. [11] or because of the higher temperature.



(a) Normal stress. **(b)** Resolved stress.

Figure 2.34: SXO fatigue dependence for SXNBS (incl. CMSX-4) at 750°C $R = -1$. Figures from [11].

The authors propose that FCGR during initiation is orientation dependent based on the near-constant ΔK at which the rough zone ends [11, p. 9]. The rough zone being a localised region around stress concentrations of: high dislocation density; intense $\gamma - \gamma'$ shearing slip bands; recrystallization; and the formation TCP and/or carbides; and cavities [87].

The $\langle 100 \rangle$ primary orientation has multiple heterogeneous octahedral slip systems and shears the γ' precipitates. The $\langle 110 \rangle$ orientation is similar apart from having one or two dominant slip systems depending on if it is off-axis or on-axis. In $\langle 111 \rangle$, non-localised (homogeneous) pseudo-cubic slip occurs due to the low octahedral Schmid factor, reducing the hardening by avoiding the γ' precipitates, but in the VHCF regime the homogeneous nature promotes fatigue crack initiation thought to

be causing the worse ⟨111⟩ to ⟨100⟩ transition in best performance.

The authors state that the exact mechanism of pseudo-cubic slip is still undecided in the literature but has been postulated to be caused by cross-slip and also dislocation reactions [11, p. 10].

From their discussion, it would appear that shearing mode fracture occurs in both ⟨001⟩ & ⟨011⟩, with ⟨001⟩ having multiple {111} facets, whereas ⟨011⟩ has one {111} facet. The authors, however, indicate that the ⟨111⟩ primary orientation exhibits a mixed mode response, having an opening mode via pseudo-cubic slip initially before becoming heterogeneous octahedral slip later and likely then {111} facet(s) [11].

The lack of an opening mode for ⟨001⟩ and ⟨011⟩ in Cervellon's work is different to Inoue-Sakaguchi's work (section 2.3.1 & table 2.4). Cervellon found that opening followed by potential shearing occurred for all tested orientations at elevated temperatures. The large difference in frequencies is the likely cause as they are both at similar temperatures (fig. 2.13), as Ref [47] found the transition frequency from opening to shearing at 760 °C to be 600 Hz. Hence, Cervellon's 20 kHz would suggest a strong shearing mode tendency. The frequency-temperature relationship for the slip and fractography has also been found in CMSX-4 [48, p. 1166] and is schematically shown in fig. 2.13.

Table 2.6: Summary of the literature discussing the effect of SXO on fatigue life (excluding A-N experiments). "RB" is rotating bending. "A" is ⟨100⟩, "B" is ⟨110⟩, and "C" is ⟨111⟩. "Disp." is displacement. All tests are $R = -1$.

Ref	[83]	[86]	[11]	[88]
SXNBS	Model	SRR99	AM1, CMSX-4, MC-NG	DD6
T [°C]	800	700	750	760,1000
Experiment	RB	RB	UFR	UFR
Control Variable	Load	Load	Disp.	Disp.
f [Hz]	83.3	83.3	20k	20k
Specimen Dia. [mm]	4.00	6.25	3.00	5.00
Specimen Length [mm]	52	52	24.0 A 27.5 B 34.6 C	48
σ range [MPa]	445	340-620	200-425	175-375
N_f range	10^5 to 10^6	10^5 to 10^7	10^5 to 10^9	10^7 to 10^9
SXO Results & N_f Range	C>A&B	B>A>C, $< 10^6$ B>C>A, $> 10^6$	C>A, $< 3 \times 10^8$ A>C, $> 3 \times 10^8$ B≈A, $\approx 2 \times 10^8$	C>A, $\lessapprox 10^9$

2.7 Environment Effect

The effect of the environment on fatigue is often studied through FCGR experiments, resulting in Paris plots, e.g. Refs [9, 22, 59, 61, 66]. However, tests that take into account environmental effects in the S-N curves are less common but have been done as discussed in this section.

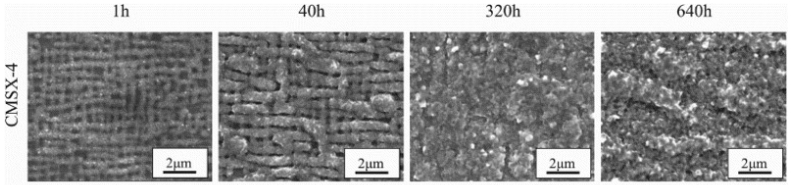
The focus will be on $O_{2(g)}$ for room temperature (RT) SXNBSs fatigue it has been "well documented" in its adsorption to the {111} planes [79], whereas $N_{2(g)}$ [24, 79] and $H_2O_{(g)}$ [89] were found to be insignificant to their fatigue .

Suppose oxygen can diffuse readily to the crack tip (promoted by high temperatures and low frequencies). In that case, one must consider oxygen's role in the plasticity at the crack tip, etc. and thus its effect on fatigue performance. Even at lower temperatures, less preferential oxides can form and thus be detrimental [24].

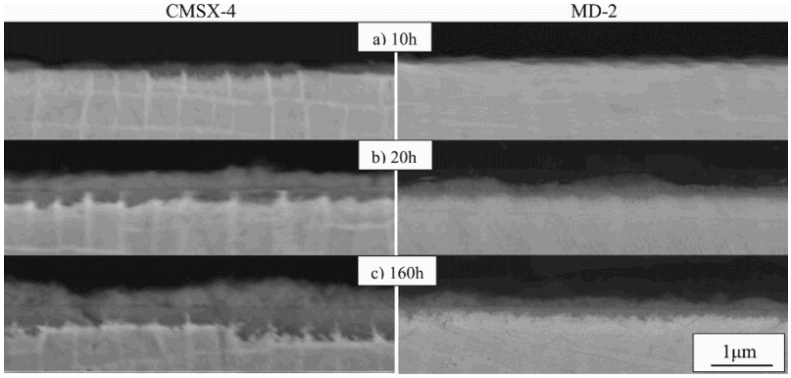
2.7.1 Oxides

Research on CMSX-4's oxides was limited in 2007, which was thought to be due to the alloy being coated when in service [22]. Later work looked into the oxidation behaviour of CMSX-4 between 450 °C-550 °C in laboratory air [24] which is relevant to the 450 °C testing in this thesis. The oxygen consumption doubled going from 450 °C to 550 °C [24]. Hence, if the total oxide scale thickness were $< 1\,\mu m$ thick after 200 h [24, p. 1682], then it could be half as thick at 450 °C. Elevated temperatures also lower the minimum p_{O_2} for oxides formation, e.g., 10^{-19}mbar for NiO at 550 °C [5, p. 132].

Figure 2.35 shows the development of the oxide with time. Note that the equilibrium phases formed here may differ from those formed in fatigue due to kinetics [24]. For times < 40 h at at 550 °C, the surface (fig. 2.35a) shows the preferential porous NiO oxidation of the γ channels with a thin discrete Al-rich oxide (likely Al_2O_3) over the γ' precipitates [24]. NiO γ oxidation is seen in Ref [22] and in the fatigue extrusion of PX Ni [38, p. 1294]. Mild inner oxidation (via depletion of Ni) is seen at 10 h with a more significant form at 20 h in fig. 2.35b. The authors note a lack of Cr containing oxides at these temperatures [24].



(a) Outer oxidation.



(b) Cross-section of oxidation.

Figure 2.35: Oxidation characterisation at 550 °C in air for CMSX-4. Figure from [24]

2.7.2 Air Effect on Fatigue

Table 2.7 summarises the effect that air has on fatigue performance in the literature for two SXNBSs and PX-Ni; it is in order from most to least reliable. It shows that, generally, air lowers fatigue performance unless surface pores can be plugged by oxidation (oxide plugs) in Refs [5, 22]. Additionally, how the fatigue crack initiates, and its mode is dependent on "strain rate/frequency, strain range, temperature and time for oxidation to occur" [5, p. 138].

Table 2.7: Table summarising whether air was found to be beneficial or not to fatigue performance. "✓" and "✗" means it was beneficial and not respectively, and "✓?" means air was maybe beneficial. "**V**" is vacuum, "**N**" is gaseous nitrogen, and "C" is gold coated. "Disp." is displacement control. "TA" is the tensile axis.

Parameter	PX-Ni	MAR-M200	CMSX-4
Fatigue method	Cantilever bending [90] Microresonator bending [91, 92]	Axial [89, 93]	Notched bending bar [5, 22]
Control variable	Disp. [90]	Load [89, 93]	Load [5, 22]
R	-1 [90–92]	$0.03 < R \leq 0.11$ [89, 93]	0.1 [5, 22]
Frequency	20 Hz [90] 9.5 kHz [91], 8 kHz [92]	10 Hz [89], 5 Hz [93]	0.25 Hz [5, 22]
SXO	-	⟨100⟩ TA [89, 93]	⟨100⟩⟨100⟩ TA/notch [5, 22] ⟨100⟩⟨110⟩ [22]
N_f	10^4 to 10^7 [90] 10^5 to 10^9 [91], 10^3 to 10^{10} [92]	10^3 to 10^7 [89, 93]	10^3 to 10^4 [5, 22]
Dimensions	26×250 µm [90] $\approx 60 \times 12 \times 20$ µm [91, 92]	0.32×1.27 cm, 0.64×3.81 cm [89] 0.25×1.27 cm, 0.64×3.81 cm [93]	$50 \times 8 \times 8$ mm [22] $66 \times 4 \times 9$ mm S-N [5] $40 \times 9 \times 9$ mm FCGR [5]
Temps. air is beneficial to N_f	✗ RT [90–92]	✗ RT-437 °C [89, 93] ✓? 437-659 °C [93] ✗ ≥649 °C [93]	✓ RT & 450 °C, ✗ 550 °C [5] ✗ 650 & 725 °C [22]
Low p_{O_2} environment medium	V [90, 92], C [91]	V [89, 93]	V [22] N [5]
S-N Collected?	✓ [90–92]	✓ [89, 93]	✓ [5, 22]
Paris(/FCGR) Collected?	✗ [90–92]	✗ [89, 93]	✓ [5, 22]

Room Temperature

Figure 2.36 shows that depending on temperature for MAR-M200, air can be detrimental or beneficial, being initially detrimental from 21 °C to 427 °C, and then becoming generally beneficial above that.

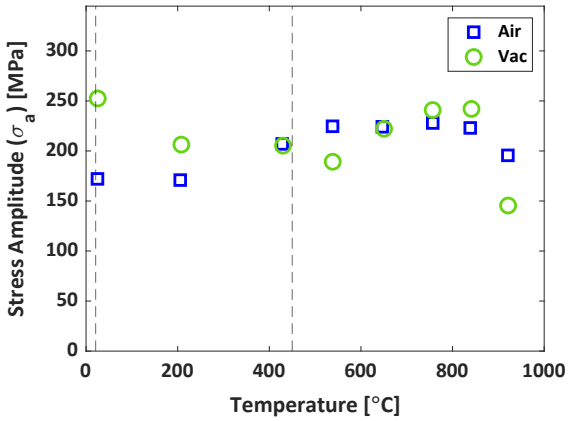


Figure 2.36: MAR-M200 $N_f = 10^6$ S-N data as a function of temperature for air vs vacuum. Adapted from [93].

At RT, there was no appreciable difference in the fatigue responses between lab air, dry air, and humid air (e.g. fig. 2.37) [89]. The authors believe that RT vacuum propagates shearing mode cracks with more plasticity (forming dimples), and RT air does this too at higher σ_a. However, at lower σ_a, they propose that oxygen embrittles the material ahead of the crack (chemisorption lowering surface energy), causing cleavage fracture, and thus increasing FCGR [89].

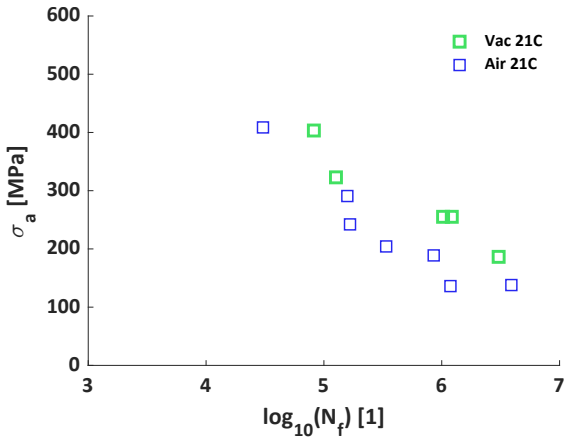


Figure 2.37: MAR-M200 SXNBS at 21 °C in different environments. Adapted from [89].

Ref [89] argues that ultrasonic air tests would behave similarly to low-frequency vacuum tests, including fractography, due to the kinetic limitation of oxygen interaction with the high FCGR [89]. Later research comparing ultrasonic & conventional frequencies in air & vacuum on RT MARM-M200 found that ultrasonic fatigue in air was similar in fractography to conventional frequency air for its crack initiation [79, p. 1935]. However, later in its growth, it became similar to vacuum (presence of dimples fig. 2.38) [79, p. 1935]. The authors attribute this to the higher frequency kinetically hindering the oxygen's detrimental effect on the FCGR for surface-initiated cracks, and its fatigue response is more similar to vacuum [79, p. 1933]. For a short enough crack, the diffusion rate is fast enough to counteract the high frequency.
The critical frequency for a crack to not be affected by diffusing $O_{2(g)}$ at RT was calculated to be 3 kHz [79, p. 1937].

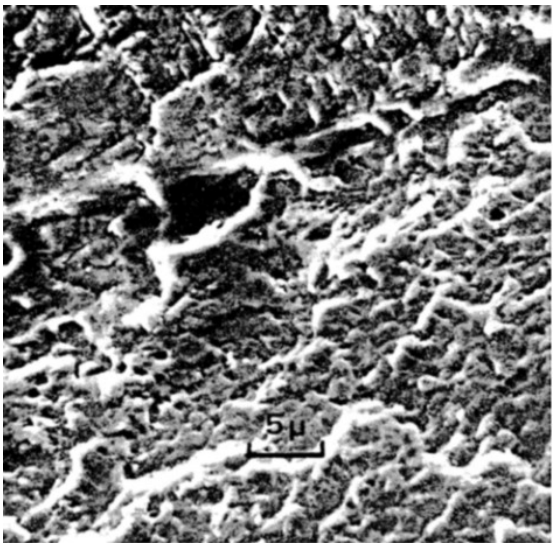
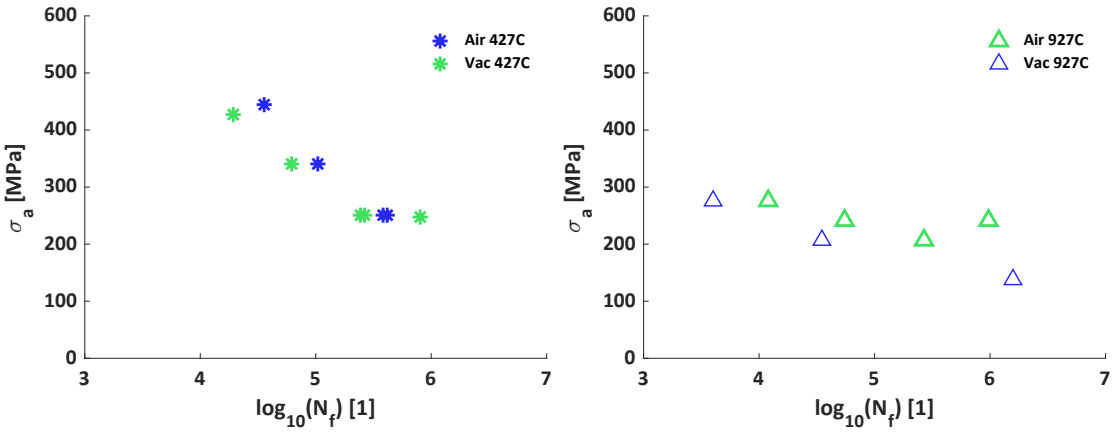


Figure 2.38: Dimples along long cracks for MAR-M200 tested in RT air in an UFR. Figure from [79].

Therefore, it is expected that at RT, the fatigue performance should be improved by less dislocation pinning from gaseous oxygen.

Elevated Temperature

Figures 2.36 and 2.39 indicates that air can be beneficial or similar to vacuum at elevated temperatures ($> 427\,^{\circ}C$) for MAR-M200 with conventional fatigue testing.



(a) 427 °C. **(b)** 927 °C

Figure 2.39: MAR-M200 $10^4 \leq N_f \leq 10^7$ S-N data as a function of temperature & environment. Adapted from [93].

Ref [22] found at 650 °C & 725 °C opening mode was dominant in air due to the high-temperature and low-frequency conditions and that more shearing facets occurred under vacuum (+ planar slip). They also proposed that oxygen affects slip reversibility and/or embrittles the superalloy ahead of the crack tip. Additionally, they propose the slip homogenisation from oxidation suppresses shearing mode cracks and causes oxide crack closure, reducing the FCGR [22]. However, the authors mention fatigue life in vacuum is typically greater than in air (144% better for single crack initiation) despite the greater FCGR but do not elaborate why [22].

For CMSX-4 at 650 °C, the diffusing oxygen to the crack tip is thought to diffuse along dislocations, pinning them, causing embrittlement [42, p. 70]. In CMSX-2 (@ 650 °C, $R = 0.1$, & $f = 2$ Hz), it is suggested that oxygen can pin dislocations, restricting them to γ channels, and thus promote opening mode whereas in vacuum shearing mode occurred [94].

Oxide plugs in CMSX-4 have been found in pre-oxidised [5] (tested at 450 °C & 550 °C) and not pre-oxidised (tested at 650 °C) in air fatigue [22]. It is thought that plugs reduce the local strain and cause initiation to be from internal pores rather than surface pores [5, p. 127, 137]. Despite the plugs, Ref [22] indicates vacuum shows a better fatigue life.

Therefore, the benefit of air is temperature dependent [93], the initiation mechanism change is temperature dependent [5], and is dependent on the kinetics [5, p. 138].

Evangelou Fractography

Evangelou's thesis [5] investigated the fatigue of CMSX-4 at RT and 450 °C and 550 °C, however, the fractographs are more useful than the limited fatigue life data. The FCGR experiments showed a transition from opening to shearing in 450 °C air, 550 °C air, and 450 °C vacuum with increasing ΔK [5, p. 163-164].

The micromechanics at intermediate temperatures (ITs) are complex due to the oxidation and slip characteristics. The oxidation showed no embrittlement ahead of the crack tip but enough to oxidise around it locally [5, Ch. 5, 6]. Octahedral and pseudo-cubic slip are both active, promoting shearing mode and opening mode fracture, respectively [5, p. 173]. Both modes are particularly active at 450 °C [5, p. 140].

In strongly oxidising environments, subsurface pore initiation forms a "halo" in a localised transient low p_{O_2} environment. It is a smooth circular region that grows until it reaches the surface from which air can now enter. The halo is absent in low p_{O_2} environments, and the whole surface is similar to the halo [5]. At low enough temperatures and under N_2 environment, fatigue initiates at surface pores with shear mode fracture [5].

Under low ΔK, opening mode occurred for all conditions, with it being caused by climb, cross-slip, and slip homogenisation via oxygen [5, p. 163]. Promoted also by the low testing frequency (0.25 Hz), which allows dislocations enough time to "diffuse out of planar bands before the crack manages to grow along them" [5, p. 164]. The opening mode regions of low ΔK where initiation occurs can be seen on the top fracture surfaces [5, p. 130, 174]. It is more extensive at 550 °C air than 450 °C air. At 450 °C air shearing mode {111} facets can also occur on the top surface near the initiation site [5, p. 130].

A "herring-bone" pattern occurs under high enough ΔK (lower in 450 °C air) caused when "extended slip band crack" occurs [5, p. 172], i.e. extended {111} shearing mode facets.

In fatigue crack initiation, the higher and more complex stress state regions at initiation sites (e.g. pores) promote opening mode fracture via homogenous slip from oxidation [5, p. 140]. In fatigue crack growth, pores (depending on their size) can also promotes planar slip and hence {111} fracture nearby them due to their complex stress states [5, p. 164].

It is proposed shearing mode is promoted by a combination of lower temperature (450 °C vs 550 °C) and low p_{O_2} [5, p. 132, 141].

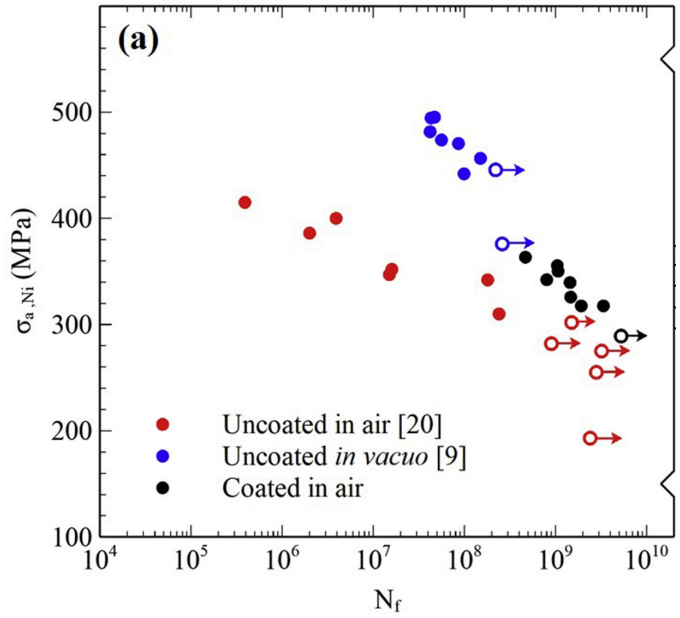
Oxides

In addition to oxygen affecting the plasticity at the crack tip, it has also been found to form oxides at the fatigue fracture surfaces, which embrittle the region ahead of the crack tip and act to increase the FCGR [5, p. 166, 169][95, §4.2]. In dwell fatigue of CMSX-4, it has been found that fracture surface oxide formation, depending on the kinetics, can also form thick enough to bridge the fatigue crack at the tip, acting beneficially to fatigue performance in that case [5, p. 173]. Additionally, in the same tests, the oxide formation ahead of the crack tip did not embrittle the region at the crack tip at 450 °C & 550 °C [5, p. 173].

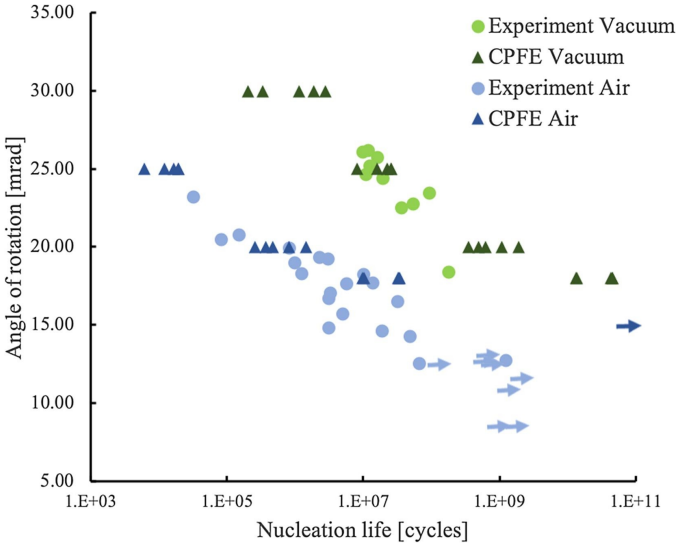
2.7.3 Ni Microbeam results

Pierron has been involved in high-frequency bending fatigue of PX Ni microcantilevers [78, 91, 96, 97]. Note, direct comparisons cannot be made between the PX samples in their work with the SX samples in this thesis. Figure 2.40 shows the lower fatigue life (by three decades) in air (c.f. vacuum) due to the frequency-independent stabilisation of microvoids failure mechanism in the HCF/VHCF regimes at RT in air [78, 91].

Another research group worked on micro-beam Ni and found that the persistent slip bands [90] and slip bands [97] allow oxides to form below the native oxide as



(a) 2018 data [91].



(b) 2020 data [92]

Figure 2.40: Pierron group microresonator cantilever S-N data for PX Ni for air vs vacuum conditions.

thick as 400 nm (thicker than the native) at RT [90] and the fatigue performance can be improved by a decade in a low p_{O_2} due to the lower rate of oxide-thickening [90].

2.7.4 Water Effect on Fatigue Response

$H_2O_{(g)}$ has been found to aid the thickening of the oxide [97]. In humid (90% R.H.) room temperature air PWA1383 & N5 (both SXNBS) the Al in γ' reacted with

$H_2O_{(g)}$ to produce H_{sol} that embrittled the {100} planes in the early stages of the crack, ultimately reducing the LCF life [98].

2.8 Similar Fatigue Methodologies

The following section is to discuss primarily work done outside of the Oxford Micromechanics Group's UFT methodology (Refs [41, 99, 100]).

A 2019 paper reviews micro-scale fatigue in metals, summarising the collected literature based on specimen size and the N_f range [101]. Where the closest method in size, N_f, and loading type was Straub et al. (2015) [38]. Thus, in 2019, the literature was limited for mesoscale bending tests in the HCF and beyond.

Straub et al. 2015

Straub's method, as shown in fig. 2.41, involves the strain-controlled, $R = -1$ capable, inertia-induced bending and/or torsion of a 200 µm thick mesocantilever via piezoelectric actuators attached to the gripped base [38].

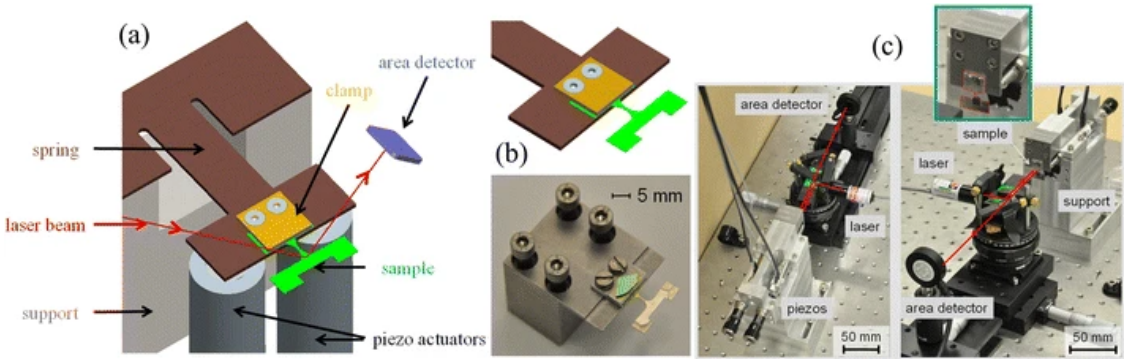


Figure 2.41: Straub's mesoscale bending fatigue setup. Figure from [38] (CC BY 4.0).

Strain is measured using a laser deflection system on the large free-end of the cantilever, with the deflection measured with a position-sensitive detector [38, p. 1290].

An unspecified frequency sweep procedure is used before each test to ascertain the undamaged sample's resonant frequency (RF) via displacement amplitude

[38, p. 1293]. Tracking frequency with time allowed for a frequency-based failure detection criterion (i.e. $^{\Delta f}/_{f_{initial}} = 10^{-3}$) [38, p. 1297].

The highest attainable frequency via resonance was 1.18 kHz for PX Cu, allowing the HCF and VHCF regimes to be investigated.

An advantage of this technique is that the sample size and high-stress gradient (due to bending) allow the results to be focused on initiation and short-crack growth, which is of great importance to HCF & VHCF (see section 2.2), whilst not permitting the less relevant long fatigue crack analysis [38, p. 1299]. Also, unlike larger samples, their small sample size benefited from a higher signal-to-noise ratio of elastic changes to the cantilever due to microcrack formation [38, p. 1295].

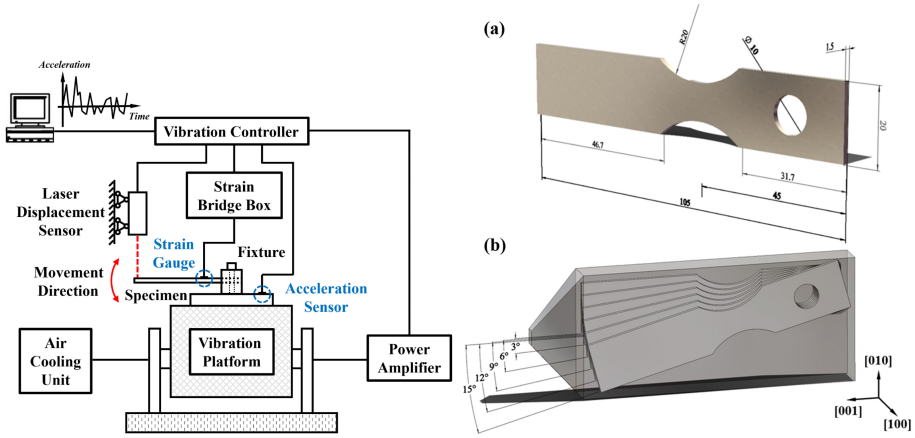
A benefit to the smaller sample size (volume V) is that intrinsic damping is $\propto V^3$ and surface crack initiation is $\propto V^2$ [38, p. 1295].

Later works derived from Straub (Refs [102, 103]) mainly differ by working on thicker (357 µm) samples and the inclusion of a stroboscopic optical microscopy (OM) system to take images in-situ.

Lu et al. 2023

Lu et al. (2023) developed a low-frequency fatigue rig to fatigue a macroscale (1.5 mm thick) SXNBS of DD6 (fig. 2.42b) via inertial-induced 1$^{\text{st}}$ mode bending (fig. 2.42a) at RT. It is similar to Straub [38] but without torsion, uses a laser displacement sensor, and a lower frequency actuator to vibrate the sample's clamped end.

The primary focus was the effect of SXO on random vibration fatigue rather than generating S-N curves, therefore frequency and σ_{amp} were not constant [104, p. 6]. Consequently, the R ratio was not necessarily -1 for the random fatigue tests [104, p. 9].



(a) Fatigue rig. **(b)** Macroscale sample design.

Figure 2.42: Lu et al.'s experimental setup. Figure from [104].

Figure 2.43, shows the one S-N curve at RT & $R = -1$ conditions. It was driven at resonance (i.e. 80 Hz to 160 Hz) for a very limited N_f (i.e. $\approx 1.0 \times 10^5 - 1.3 \times 10^5$). The S-N dependence on SXO could have been collected, but the authors assumed it is indifferent to SXO; hence why only one S-N curve was generated with undefined orientations.

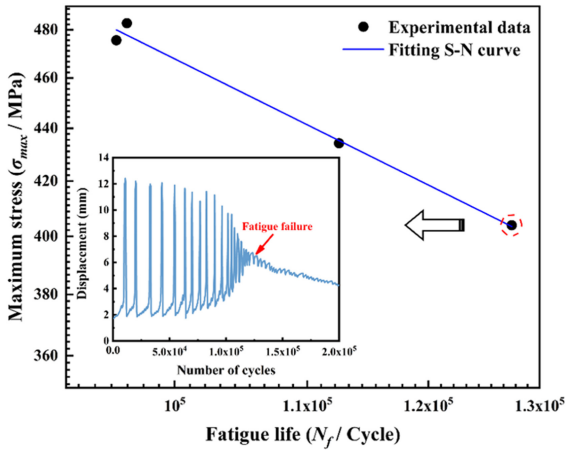


Figure 2.43: Inertial bending S-N for DD6 SXNBS @ $T = 20°C$ of unknown orientations. Figure from [104].

The random fatigue life decreases linearly for all three g^2/Hz values when going from a cantilever direction (CD) of [001] towards [011] (i.e. $0° \rightarrow 15°$) with a foil normal (FN) of [100]. The linear decrease breaks down at the highest vibration signal intensity though [104, p. 9].

The scanning electron microscopy (SEM) fractographs collected (figs. 2.44 and 2.45) show changes with crack progression and with deviation angle.

The crack initiation is associated with a "wavy, wrinkled morphology" region on a {111} plane in the corner of the cantilever (fig. 2.44) [104]. The region just underneath the surface propagating crack is the "fatigue crack propagation zone", which, due to the more stressed surfaces, causes them to spread horizontally near the surface. The propagation region is highly dissimilar to the rough and non-crystallographic appearing "final fracture zone" that occurs towards the centre in fig. 2.44. The equal degree of propagation zones on both sides of the cantilever indicates fracture initiated at roughly the same time for both sides, which is dubious.

The observed facets in figs. 2.44 and 2.45 were found to be associated {111} octahedral slip [104], and they are reminiscent of the RT results in Ref [45] (section 2.3.1).

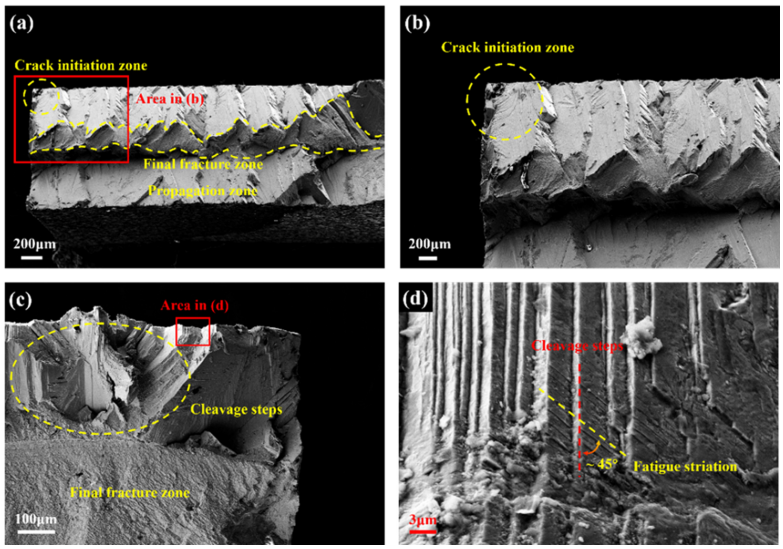


Figure 2.44: Unspecified SEM fractography of RT random fatigue of DD6 SXNBS. Figure from [104].

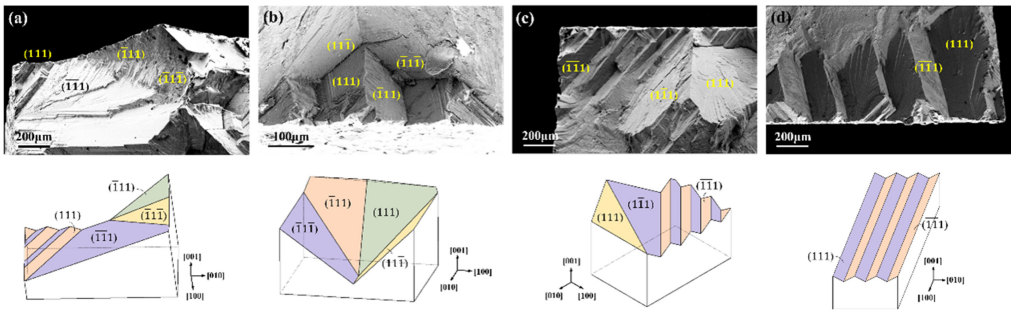


Figure 2.45: SEM fractography of RT random fatigue of DD6 SXNBS at $1\,g^2$/Hz with deviation angles from 0°, 3°, 6° and 12° from left to right. Figure from [104].

3
Aims & Objectives

After reviewing the literature in chapter 2, the following aims and objectives were identified from it. In brief, the fatigue technique used in this thesis can help investigate the fatigue behaviour of SXNBSs at low temperatures (RT & 550 °C) to help confirm whether air is beneficial or not to fatigue performance at these temperatures. Additionally, the literature is not unanimous on whether the fatigue performance of the ⟨110⟩ tensile axis fatigue performance is better or the same as ⟨100⟩, and the orientation (primary and secondary) of the tests is often not repeatable. Hence, use the novel fatigue method in this thesis to assess the fatigue performance of cantilevers with beam axes parallel to those orientations and with reproducible orientations. The full list of aims & objectives are separated by the chapters where they will be addressed.

Method Development (Chapter 5)

1. The mesoscale UFR used in this thesis fills a testing niche [101], especially for a SXNBS, which can assess any size effect at that scale.
2. Porosity is detrimental to fatigue life and may cause a size effect. So, can pore distribution be assessed using radiography for these mesoscale samples before testing (like those done on macroscale samples [72])? Can the relatively small

fracture surfaces help identify the initiating defects (e.g., casting pores) using SEM based fractography and correlate them to the fatigue performance?

3. There is a lack of cantilever bending fractographs for SXNBSs, especially for this scale, range of N_f values, and under different environmental and temperature conditions. The closest found was Ref [104], and so an aim is to expand on the available fractographs.
4. Develop ECCI protocols as a more convenient alternative to transmission electron microscopy (TEM) to aid in identifying and obtaining specific diffraction vectors ($\underline{g}$) (i.e. Bragg condition) for analysing the fatigue damage on a larger scale. Thus, characterise dislocations associated with fatigue, which for this material and conditions will be novel. In conjunction, use crystal plasticity finite element (CPFE) modelling and Schmid factor calculations to predict the dominant slip systems to aid in Burgers vector ($\underline{b}$) determination in ECCI.
5. Ultrasonic frequencies may prevent screw dislocation cross slip [9]. Can ECCI show the degree of homogeneous slip of screw dislocations in these ultrasonic tests (no example was found in the literature) and help understand the effects on fatigue?
6. The nature of the fatigue technique focuses on initiation and short crack growth due to the mesoscale sample size and theoretically unstable crack growth after initiation. So, unlike the long crack total failure of conventional macroscale samples, can an initiation and/or short crack growth S-N curve be generated? These S-N curves can be used to better inform fatigue models on initiation behaviour such as in FEM. They could help determine the required timing of part inspections (e.g., blades), allowing fatigue cracks to be detected earlier without excessively frequent inspections.

Environmental (Chapter 6)

The mesoscale size of the samples increases the area-to-volume ratio compared to macroscale samples, which is known for reducing self-heating and potentially

enhancing environment-fatigue contributions.

7. Will vacuum conditions lead to an improvement (Refs [79, 89, 93]) or a detriment (Ref [5]) to fatigue performance at ultrasonic test frequencies? Can SEM analysis techniques see if mechanisms (e.g., oxygen dislocation pinning, etc.) are observed in air conditions but not under vacuum? Performing tests under vacuum rather than noble gases is of research interest as internal crack formation is similar to vacuum conditions [5, p. 140][22, p. 1443]. Additionally, the available UFRs were not yet developed for using noble gas environments, planned be done after the vacuum and 450 °C fatigue tests.
8. Environment-fatigue interactions have been seen in the early stages of crack growth for ultrasonic fatigue in air [79]. No ultrasonic fatigue of a SXNBS under vacuum was found in the literature. Hence, will novel ultrasonic vacuum fatigue experiments show the expected lack of environment-fatigue fractography?
9. Investigate the under-explored intermediate temperature range ($\approx 450 - 550\,^{\circ}\mathrm{C}$) for SXNBSs (especially CMSX-4 [5, 50]) and help settle the dispute on whether it improves or lessens the fatigue performance compared to RT (see table 2.7).
10. The shearing vs opening mode failure propensity depends on alloy, temperature, frequency, SXO, and ΔK. Will ultrasonic fatigue with $R = -1$ for CMSX-4 at intermediate temperatures also unexpectedly show a lack of opening mode like at 1000 °C in Ref [11]? Ref [11] differs from lower frequency experiments in air (e.g., Refs [45, 65]). If so, this indicates the dominance of frequency over temperature.

Single-crystal Orientation (Chapter 7)

The novel UFT method has the potential for a high degree of repeatability and control of the SXO. The following aims exploit that.

11. Explore the under-investigated SXO effect on S-N curves (especially $\langle 110 \rangle$) rather than the numerous fatigue crack growth rate (FCGR) experiments.

Push past the LCF regime with highly controlled SXO. This will help in the accurate modelling of the deformation behaviour of SXNBSs [20]. S-N curves are important to collect as FCGR experiments can show discrepancies with N_f, as seen in the higher FCGR but improved N_f under vacuum conditions in Ref [59, p. 1444].

12. Compare the fractography dependency of SXO on the mesoscale with similar macroscale and microscale SXNBS results. If there is a difference, it could indicate a convolution of size effect with SXO.
13. The cantilever fractography for SXNBSs at other SXOs is under-explored, the literature reporting up to 12° disorientations from [100] for the CD [104]. Hence, perform tests with near $\langle 100 \rangle$ & $\langle 110 \rangle$ CDs to see how they differ. Then, study the differences in crack progression with increasing crack depth (i.e. increasing ΔK & σ_{amp}) and the slip behaviour ahead of the crack tip across the surface (e.g., ECCI).

4
Methodology

Contents

4.1 Ultrasonic Fatigue Rig 67
4.1.1 Sample Design 68
4.1.2 Holder Design 68
4.1.3 Bending Angle Determination 69
4.1.4 FEM Fundamentals 77
4.1.5 Fatigue Protocol 78
4.1.6 S-N Curves 80
4.2 Sample Preparation 83
4.2.1 Foil Preparation 84
4.2.2 Sample Machining 86
4.2.3 Electropolishing 86
4.3 Crystal Plasticity 88
4.4 Sample Measurement 91
4.5 Electron Microscopy 92
4.5.1 EDX 92
4.5.2 (HR-)EBSD 93
4.5.3 ECCI 95
4.6 Radiography 96

4.1 Ultrasonic Fatigue Rig

Figure 4.1 is a schematic of the meso-scale sample UFR used in this thesis and in previous works (e.g. [41, 99, 100]). It was developed from the conventional uniaxial UFRs by Dr Gong. Conventional UFRs are discussed in detail in review papers [15, 66].

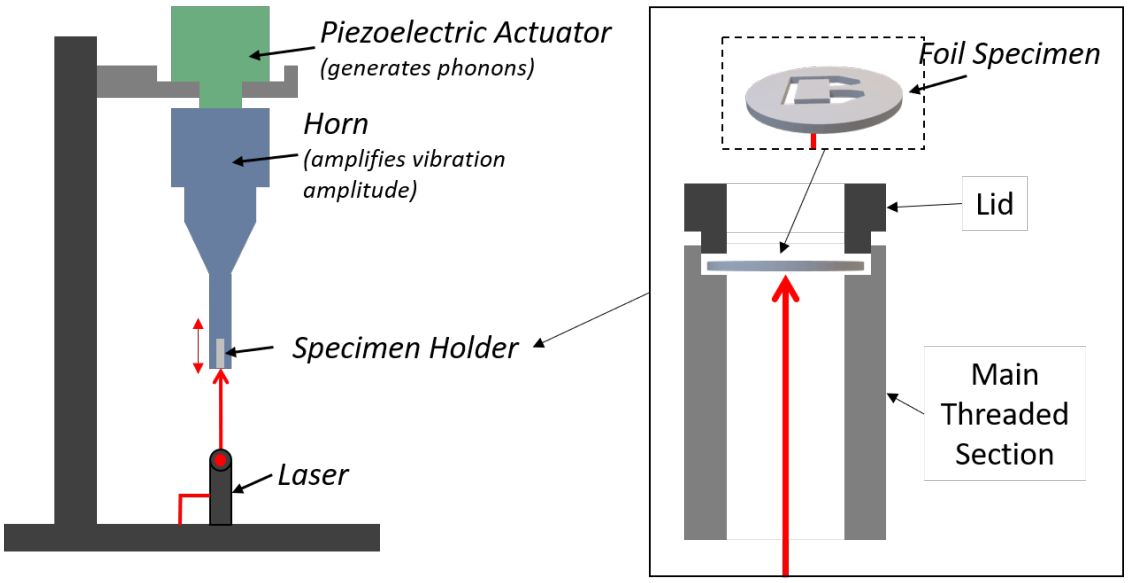


Figure 4.1: Typical research group UFR schematic.

In general, for UFRs, a piezoelectric actuator (aka ultrasonic converter) generates longitudinal sinusoidal vibrations through the horn (aka acoustic horn), forming a standing wave when the load train is designed correctly. In a conventional UFR, a macro-scale hourglass-shaped sample is affixed to the horn's tip, so the specimen design has to be accommodated for the standing wave condition [15]. However, this is less crucial for meso-scale samples.

The horn increases the vibration amplitude generated by the piezoelectric actuator to relevant vibration amplitudes, and its design affects the vibration amplitude gain.

The meso-scale samples are inserted just above the anti-node at the horn's tip and held within a modified grub screw that grips its surrounding ring. Vibrating the

sample bends the cantilever out of phase along the axial direction due to inertial lag. An unimpeded cantilever performs fully reversed bending ($R = -1$) at a frequency dominated by the driving frequency of the UFR (i.e. $\approx$ 20kHz). The transference of energy from the horn's vibration to the bending of the cantilever is called **coupling**.

4.1.1 Sample Design

Figure 4.2 shows the standard meso-scale cantilever design. Meso-scale as the dimensions are 100s of microns in length (e.g., $\approx$ 150 µm to 600 µm). The base, sides, and top are all gripped by a grub screw sample holder during the fatigue test, thus allowing the cantilever and hammer to move.

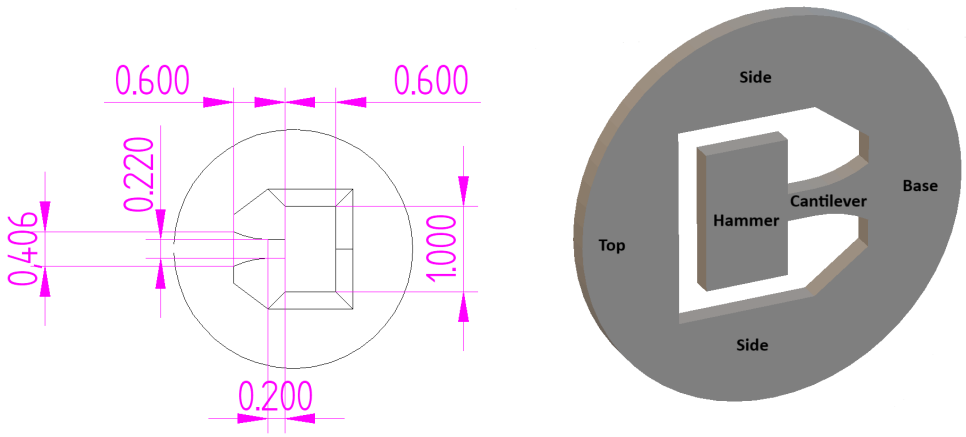
The design in fig. 4.2 is the 2nd generation developed in Ref [99] that reduced stress concentrations and stress homogeneity by making the cantilever taper to the base. A 3rd generation design was developed later in Ref [41] to further improve this, but it was not adopted in later work.

The hammer is intended not to deform but to reduce the resonant frequency (RF) to achieve appreciable coupling. Initially, it was thought that the RF should be "as far as possible from 20 kHz" to reduce the sensitivity of the samples' coupling with minor dimension variations so that they behave similarly. However, if the RF is too high (e.g. $\geq$ 32.5 kHz), the coupling is too low for sufficient cantilever bending at safe vibration amplitudes [41].

4.1.2 Holder Design

The design for mounting the samples (fig. 4.3) has remained unchanged since the development of the technique by Dr Gong.

A hollowed-out steel grub screw and lid (2.40 mm diameter) grip the sides, top, and base by $\approx$ 0.3 mm from the sample edge. Hollowing it out allows the cantilever to deflect and a laser to reflect off the hammer during fatigue to assess its deflection.



(a) 2D CAD (units in mm). **(b)** Labelled 3D final form.

Figure 4.2: Standard research group meso-scale cantilever design. Typically $\approx 150\,\mu m$ thick.

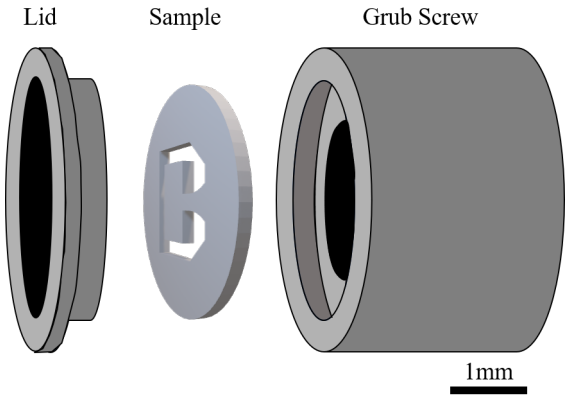


Figure 4.3: Machined steel grub screw to mount sample inside the horn tip. Adapted from [41] (CC BY 4.0).

4.1.3 Bending Angle Determination

Fundamentals

The UFR in this thesis employs an in-situ, non-contact method for measuring the sample's deformation, unlike the laser vibrometer methods used in similar but macroscale techniques [104, 105]. Instead of measuring the displacement amplitude at a point in the cantilever, a scientific laser pointer is shone onto the hammer's centre before fatigue testing.

FEM simulations show that the 1st eigenmode of deformation (i.e. out-of-plane bending) dominates. The deformation is concentrated within the cantilever, and the hammer is virtually undeformed, instead making an angle α with the cantilever's

rest state. Figure 4.4 is a schematic of the cantilever's steady-state fully reversed bending ($R = -1$) at a bending angle amplitude (α_{amp}). If the laser pointer is normally incident to the rest-state cantilever, the laser path will return to the source. However, an angular arc over a vibration cycle of approximately $4\alpha_{amp}$ is described during fatigue, which, on a horizontal plane under enough camera exposure (& human vision), appears as a laser streak called the laser length (L), the value of which depends on both α_{amp} and the working distance (WD).

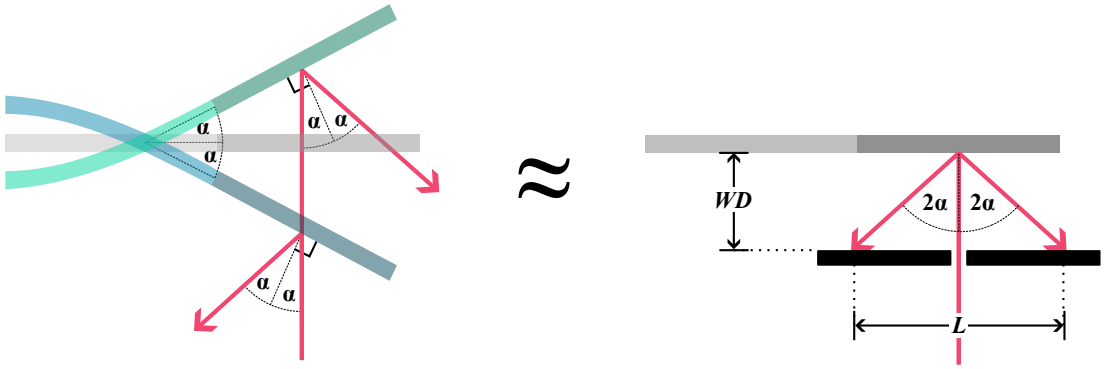


Figure 4.4: Ideal case α_{amp} determination of the cantilever during fatigue.

The ideal case mathematics with the assumptions described produces eq. (4.1) for the α_{amp} from L and WD.

$$\alpha_{amp} = \frac{1}{2} \cdot \arctan\left(\frac{L/2}{WD}\right) \tag{4.1}$$

In this work, the value of L was typically captured using a Thorcam scientific camera (model CS895CU) and, less frequently, the USB wide-view webcam. Unlike the Thorcam, the webcam had greater distortion and was harder to control the exposure and focus.

WD is measured using a measuring tape and/or a ruler sticker added to the optical tower of the rig. Both had a 1 mm resolution, but the latter allowed for simple arithmetic to determine the various WDs and assisted consistent placement.

Prior Method

Figure 4.5 shows the prior method to obtain L within the research group, using an aligned 30 mm ruler against the laser streak and manually capturing photos with a webcam.

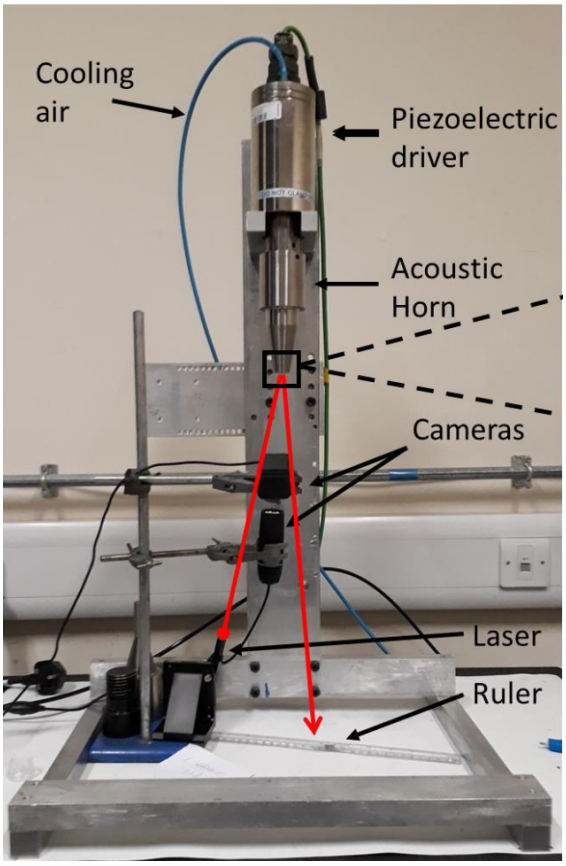


Figure 4.5: Prior method setup of the UFR to obtain L. Figure from [100].

The ruler avoids correcting for image distortion in measuring L; however, this technique has multiple downsides:

- L's resolution is ± 2 mm, limiting the α_{amp} resolution.
- A dark environment or lower exposure is beneficial in better capturing the laser streak, but that makes the ruler harder to read.
- Manually capturing and measuring from photos is tedious and limits the number of L measurements. So, significant statistical uncertainty in L and capturing changes in L are harder.

- Tilting the laser is required to project the laser streak away from its source to see it clearly. However, tilting breaks the ideal geometry assumptions of eq. (4.1); the greater the tilt, the greater the overestimation.

Development: Measuring Laser Streak Length

A MATLAB^{TM} script was used to measure L, accounting for lens distortion and location using the *Camera Calibrator* (Image Processing & Computer Vision toolbox). See appendix B.1.

The Thorcam's low-distortion lenses made the difference between calibrating the pixel-to-mm value manually and the corrected image minimal; however, calibrating with MATLAB is preferred.

Corrected images have the correct proportions, and each pixel correlates to a spatial coordinate in units of mm. Hence, the two end coordinates of the laser streak are used to determine L in mm using image analysis.

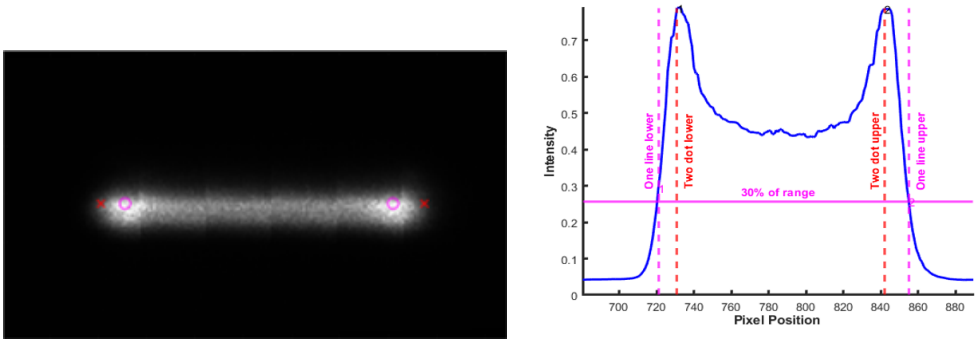
When the laser reflects as a singular dot, then two methods can be done to measure L:

1. One-line method: Choosing a brightness threshold so the laser streak becomes thin but continuous, then L is taken as the two ends of this threshold region.

2. Two-dot method: A brightness threshold is used so two small regions occur. L is then the distance between their centroids. Alternatively, the distance between the two most prominent peaks in brightness along a line can be used.

Prof James Marrow suggested using a pseudo-intensity profile method to determine L by rotating the captured image to make the laser streak horizontal and then summing the pixel values in each column to get the pseudo-intensity profile (see fig. 4.6). The method allows a messier pattern to be still analysed and avoids image thresholding.

A further adaptation was used in the first set of IT air tests. The same line profile is taken over each frame from a video, and the alternative two-dot method



(a) Rotated grey-scaled input frame with end points of the one-line (red crosses) and two-dot (magnet circles).

(b) Annotated plot of the intensity profile used to derive the one-line and two-dot methods.

Figure 4.6: Example visualisation of the one-line (magenta) and two-dot (red) methods.

is used. It is less computationally expensive and allows the same laser streak to be analysed if there are multiple as shown in fig. 4.7.

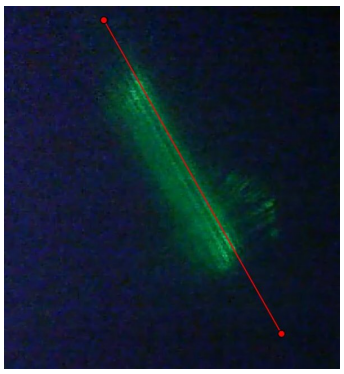
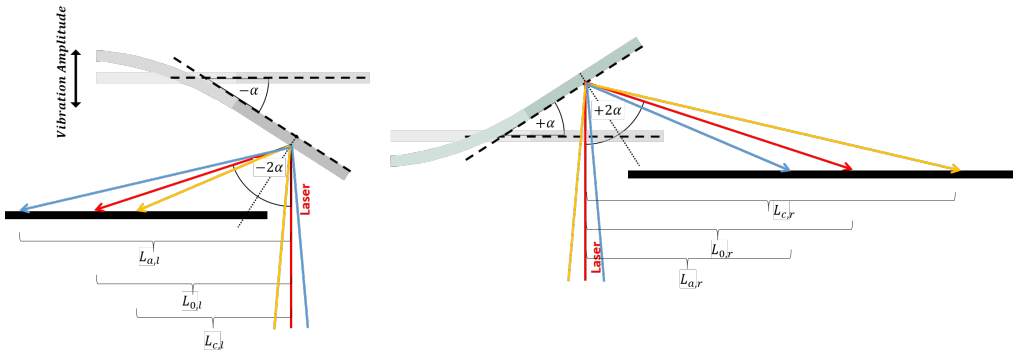


Figure 4.7: Manual line profile extraction method used in an intermediate air test where multiple parallel laser streaks occurred.

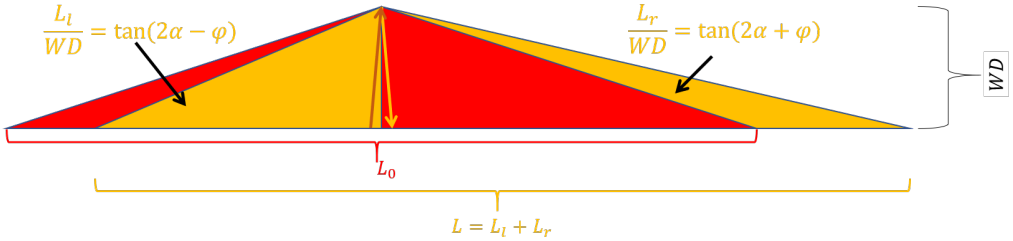
Laser Tilt Overestimation

The reflected laser travels longer distances when the laser source is tilted, increasing L under the same conditions and overestimating α_{amp} when using eq. (4.1) i.e. β_a. There are two orthogonal laser tilt axes, ϕ and θ, where in the ideal case, both are 90° to the ground.

ϕ-tilt is shown in fig. 4.8, and it shows how it is worse than θ-tilt because of the unequal spread of the laser streak (i.e. $L_l \neq L_r$). At $\phi = 0°$, $L_l = L_r = {}^{L}/_{2}$. From fig. 4.8, the calculated value of α_{amp} (i.e. β_a) can be derived (eq. (4.2)).



(a) Origin of ϕ tilt, showing its effects on the two extremes of the bending cycle.



(b) The method to calculate the measured L compared to the ideal value when $\phi = 0°$.

Figure 4.8: ϕ tilt diagrams.

$$\beta_a(\phi) = \frac{1}{2} \cdot \arctan\left(\frac{\tan(2\alpha_{amp} - \phi) + \tan(2\alpha_{amp} + \phi)}{2}\right) \tag{4.2}$$

Figure 4.10a shows the θ-tilt case with $\phi = 0°$. Here, the true distance travelled is H $(> WD)$ and causes L to increase.

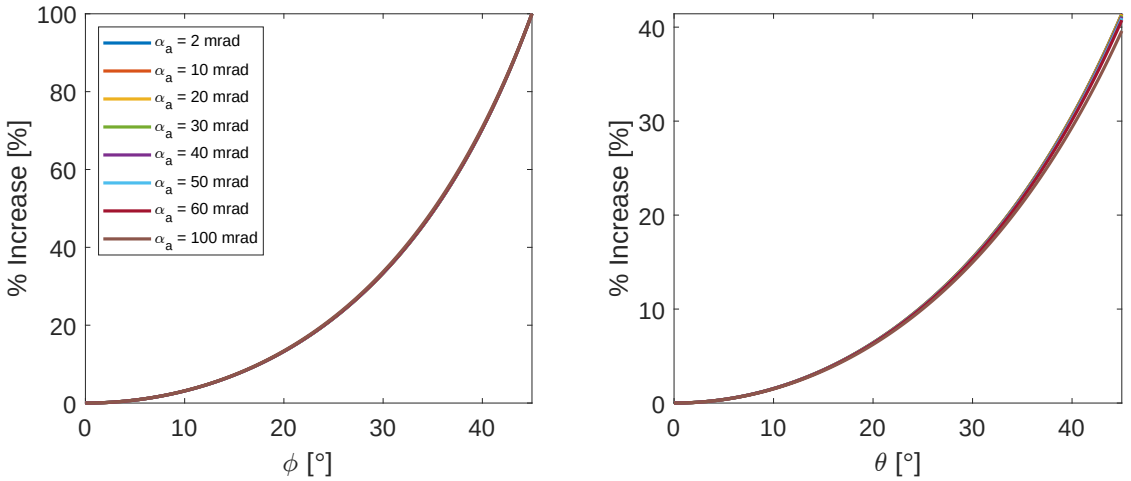
$$H = \frac{WD}{\cos(\theta)} \tag{4.3}$$

From geometry, the θ-tilt case is described by eq. (4.4).

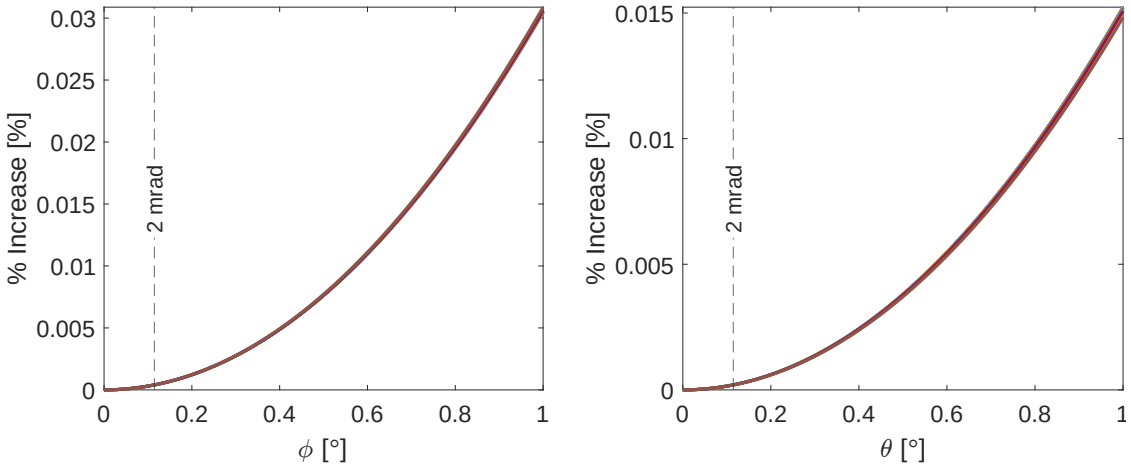
$$\beta_a(\theta) = \frac{1}{2} \cdot \arctan\left(\frac{\tan(2\alpha)}{\cos(\theta)}\right) \tag{4.4}$$

The percentage overestimate of α_{amp} with the two tilt axes is shown in fig. 4.9. θ-tilt is around $2\times$ less severe than ϕ-tilt, and an inclination that is less than $\approx 12.6°$ ($\equiv$ 220mrad) will have $\leq 5\%$ overestimation.

If the laser is level to within $\pm$2mrad using a bullseye spirit level (like in the aperture method), this predicts a maximum overestimation of $4.02 \times 10^{-4}\,\%$. Thus showing the benefit of using the aperture method.



(a) Up to 45° laser tilt in ϕ or θ.



(b) Up to 1° laser tilt in ϕ or θ.

Figure 4.9: Overestimation of different cantilever α_{amp} when the laser source is tilted in two tilt axes of ϕ and θ. Normalising to percentage increase brings the different α_{amp} curves together.

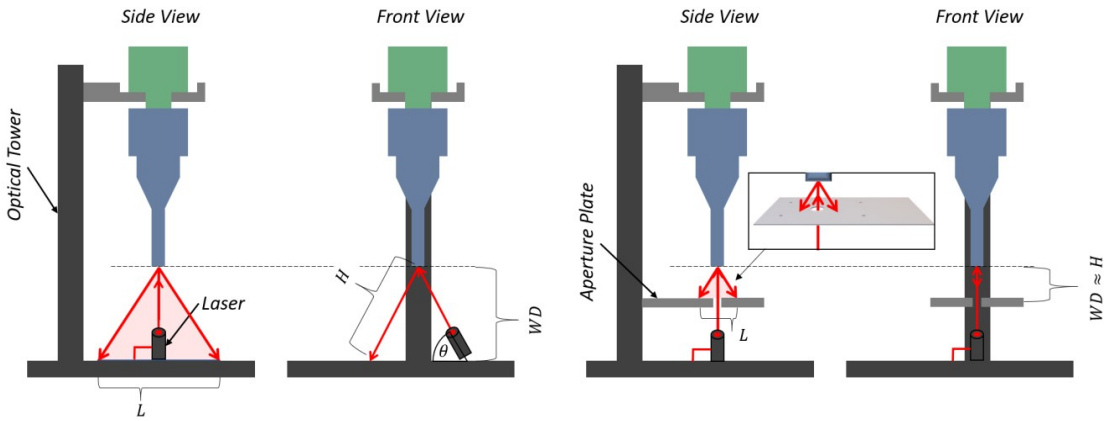
New Development: Aperture Method

The aperture plane was later developed to minimise and increase the consistency of the α_{amp} calculations (section 4.1.3). Figure 4.10a shows the θ-tilt case (i.e., $\theta \neq 90°$) in the standard setup, which causes α_{amp} to be overestimated according to fig. 4.9.

The aperture method in fig. 4.10b has the laser orientated within ± 2 mrad normal incidence with a bulls-eye spirit level meter (*RS Components Ltd*) on a glass slide. The laser passes through the aperture (a plate attached to the optical tower) and reaches the cantilever and this significantly reduces the α_{amp} overestimation (see fig. 4.9).

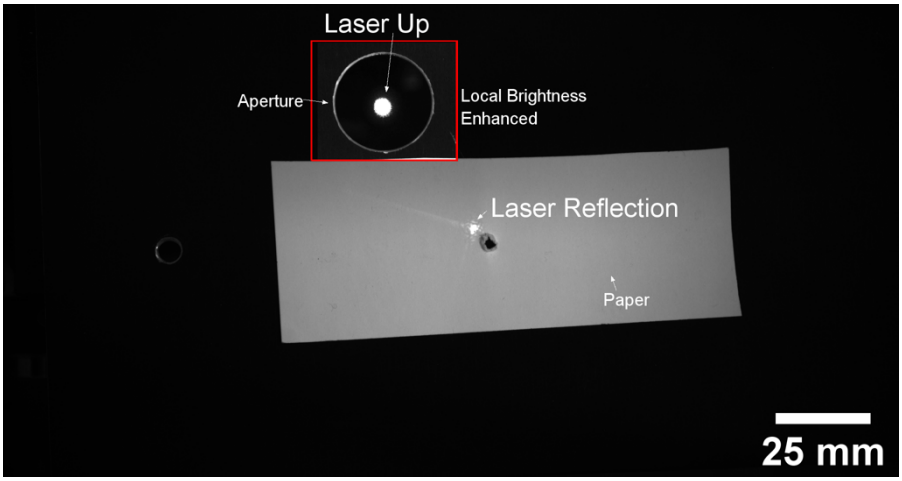
The aperture plate height determines the WD, making it shorter increases the confidence of normal incidence but decreases the maximum measurable L. A smaller aperture gives less scope for error in placement.

The aperture limits the minimum measurable α_{amp} but this is not a concern as the WD and the aperture can be changed (e.g., adding a small hole in a sheet of paper). Slight misorientations elsewhere can also lead to the reflection spot being translated away from the aperture hole, as seen in this work (fig. 4.11). Additionally, the consistency is increased as the geometrical constraint improves reproducibility.

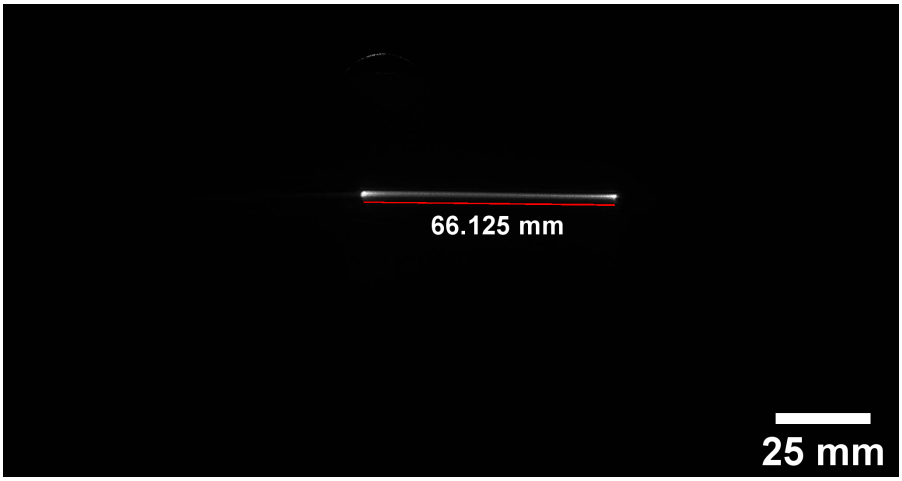


(a) Non-ideal geometry schematic. **(b)** Aperture method schematic.

Figure 4.10: Schematics of the laser paths in the non-ideal original and the aperture methods. Two perspectives are for path clarity.



(a) Off state. Small geometric deviations cause the reflected spot to deviate from the aperture.



(b) On state. Manual L measurement. Lower exposure than in (a).

Figure 4.11: Photograph from the aperture method (fig. 4.10b) to determine L when (a) off and (b) on.

4.1.4 FEM Fundamentals

The σ_{amp} from experimental α_{amp} is calculated using eq. (4.5).

$$\sigma_{amp} = \omega \cdot \alpha_{amp} \tag{4.5}$$

Where σ_{amp} is the nominal fatigue stress amplitude, α_{amp} is the cantilever bending angle made by the hammer, and the constant of proportionality is known as the stress-per-angle (ω).

The value of ω is calculated purely through FEM, whereby in bending, a nominal stress value is divided by the hammer's tilt angle. Equation (4.5) is valid up to $\alpha_{amp} < 300\,\text{mrad}$ (from elastic FEM of Ti-6Al-4V meso-cantilevers [41, p. 69]).

Unlike uniaxial fatigue testing or samples with simpler geometries, the choice of nominal stress from FEM is not trivial. One can take the axial bending stress along the cantilever or the Von Mises' stress (σ_{vm}), where the former is better in convergence studies and the latter being an "indicator of the body stress" [41, p. 80]. The σ_{vm} is chosen in this work as it accounts for all the principal stresses, rather than just one (axial stress) and it is a better indicator of yield.

The FEM models to calculate ω do not account for cracks, so the L values after crack formation can lead to significantly inaccurate σ_{amp} values. The predicted α_{amp} values (see section 5.2) are used instead once cracks have formed. As crack growth reduces the cantilever compliance, its resonant frequency decreases, which increases the cantilever's displacement amplitude. These correlations has led to successful crack formation detected by change in sample resonant frequency, and there is ongoing work in calibrating the cantilever displacement increase with its fatigue crack length.

Convergence studies in FEM are done to balance the better accuracy from mesh refinement with the computational time increase (further details in appendix B.2).

C3D20R (quadratic reduced hex) elements reduced the error from 5% to below 1% in mesocantilever FEM (c.f. C3D8R, aka linear reduced hex elements) in Ref [100]. C3D20 (quadratic hex elements) are chosen in this work for more accurate modelling by reducing the shear locking phenomenon [106] and not being reduced elements.

4.1.5 Fatigue Protocol

Figures 4.12 and 4.13 visualise how the standard staircase and the accelerated step loading (aka stress step) fatigue protocols differ. Ref [40, 107] describe the benefits of the stress step protocol.

Staircase uses linearly spaced σ_{amp} values. The samples are tested to the same N_f (e.g. $N_f = 10^7$), survivals (aka run-outs) increase the next test's σ_{amp}, whereas failures lower it, causing a fluctuation around the mean σ_{amp}.

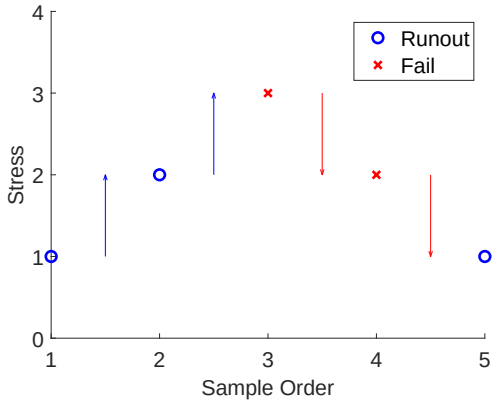
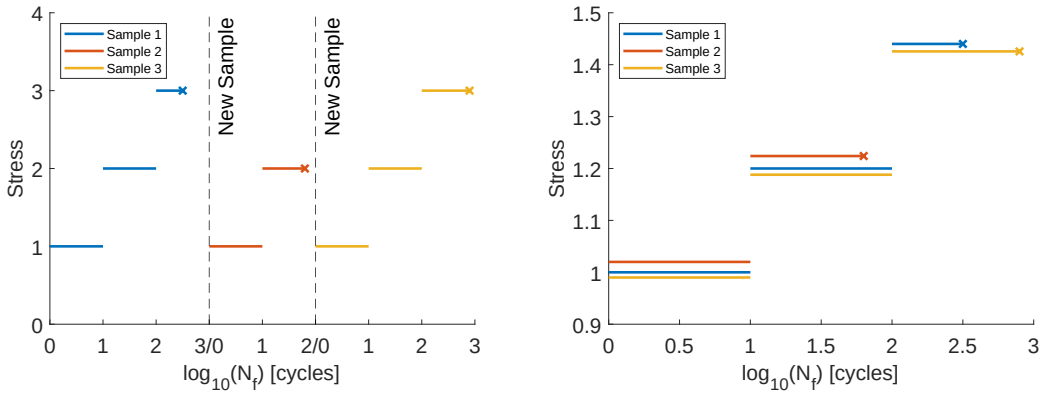


Figure 4.12: Staircase - linear-spacing.

For stress step, the stress space can be divided linearly [40] or geometrically [107], and the same sample is tested for a fixed number of cycles, starting below the estimated mean σ_{amp} and increasing σ_{amp} until failure. Performing incremental steps on the same sample leads to concerns about coaxing and accumulated damage, however "no appreciable difference" has been found between its results with the staircase protocol [40] and with the constant σ_{amp} protocol [107].

The stress step protocol leads to a more conservative assessment of the fatigue data, as it has a higher probability of finding defects than staircase [107], and the greater amount of information gained per sample can lower the required number of samples to test [100].

This thesis used the stress step method with geometrically spaced stress levels with at least a 10% increase (i.e. $\sigma_{a,i+1} \geq 1.1 \cdot \sigma_{a,i}$). Geometric was chosen over linear due to the decreasing gradient with N_f in an S-N curve, thus being fine enough to capture near plateaus at high N_f but spaced enough to minimise the influence of prior steps via a Miner's rule perspective. Starting σ_{amp} values and geometric factors were varied to refine the S-N curve (see fig. 4.13b).



(a) Step - linear-spacing.

(b) Step - geometric-spacing (ratio= 1.2) with non-identical starting stresses.

Figure 4.13: Schematics of the staircase and stress step protocols for obtaining fatigue data for a specific N_f. "x" represents failure.

4.1.6 S-N Curves

Plotting a single S-N curve with the stress step protocol differs from the other fatigue testing protocols. Within the group, this have varied from simply plotting the drastic failure points to complex probabilistic S-N curves involving integration limits and Bayesian statistics (see Ref [40]).

In this work, points are designated as survive, cracking, and drastic failure, corresponding to uncracked, lightly cracked, and heavily cracked/broken samples, respectively. Further details are in section 5.2.

Typically, within the research group, only each sample's last survival and drastic failure steps are plotted. However, Ref [107] uses more than one survival step because the last step represents the stress with energy just low enough for cracks not to propagate to cause drastic failure (unlike the drastic failure step), despite cracks arresting in previous stress steps in the sample.

Binomial Logistical S-N Analysis

As the stress-step protocol generates more data than the staircase protocol [107], the following explains the new statistical approach in this thesis to obtain 50%

probability of failure (i.e. P_f) S-N curves from the data.

Figures 4.14 to 4.16 show the order-independent schematic of how the fatigue data is analysed. The 1st sample (fig. 4.14) shows how for samples which have been tested to high number of cycles to failure (N_f), each survived step (circle markers) has technically also survived values of N_f lower than that (e.g., 10^8, 10^7, 10^6, etc. fig. 4.14). Therefore, these survival steps can be back-propagated to earlier lives. The final drastic failure step (star marker) is a record that the sample failed at or before that point, so after that N_f the sample would have failed.

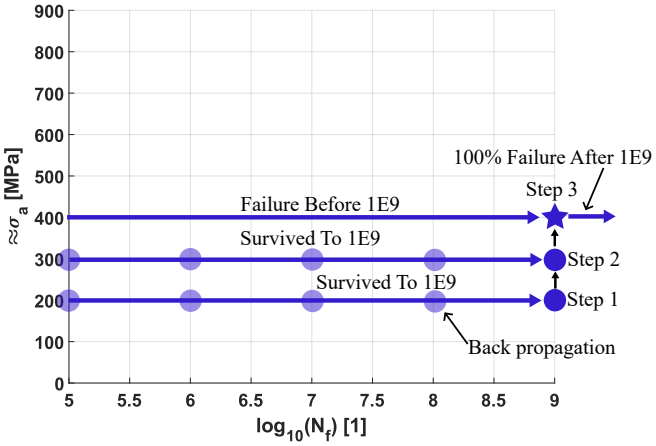


Figure 4.14: Schematic propagated S-N plot with just the 1st sample.

Following this, the 2nd sample (fig. 4.15) shows how the drastic failure points can be forward propagated. So, if it had failed by 10^7 cycles, then it would have failed by 10^8, 10^9 cycles, etc.

The propagation accounts for the known information of the whole dataset, making use of the fact that S-N curves monotonically decrease or remain constant (plateau) with increasing N_f. The statistics of the whole data set are shown by an example for a 3rd sample (fig. 4.16), where it fails on the first step at a lower than expected value based on the 1st and 2nd samples.

The information of the survival region of the S-N curve is greater than its failure region as there can be multiple survival steps but only one failure step per sample.

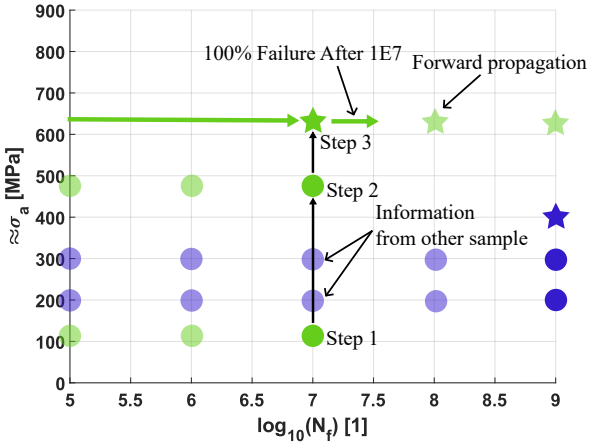


Figure 4.15: Schematic propagated S-N plot with the 1st and 2nd samples.

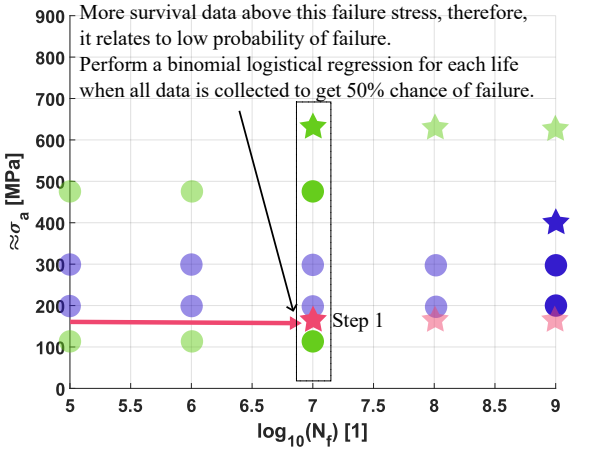
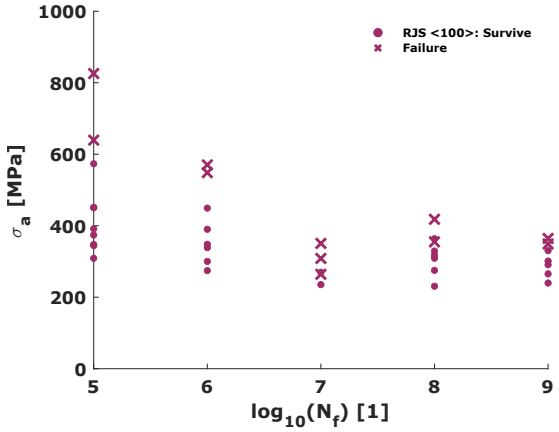


Figure 4.16: Schematic propagated S-N plot with the 1st, 2nd, and 3rd samples.

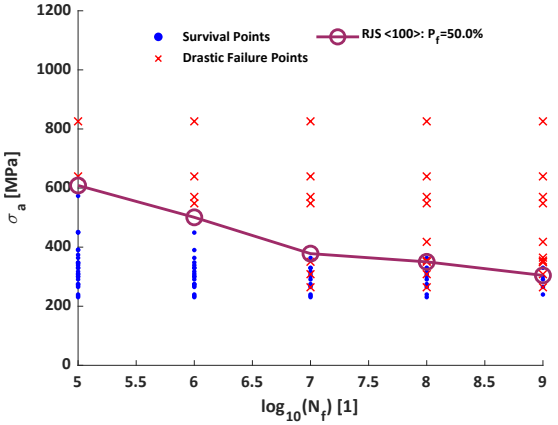
In this work, this is included by back-propagating the top 5 highest survival steps for each sample. Ideally, all survival steps are used; however, only the top 5 were recorded in this work's results spreadsheet. Therefore, this will bias the P_f of that S-N curve higher than taking just last survival step, but this accounts for more known values of survival for that N_f that exist within the dataset. Figure 4.16 shows how doing this makes the 3rd sample failure point a statistical outlier but still valid because of the non-zero distribution of failure.

To quantify this, a binomial logistical regression is taken for each N_f value, like the bounding box around 10^7 cycles in fig. 4.16. An example of this process is shown in fig. 4.17, where at $N_f = 10^7$ the two lower failure stress samples have a

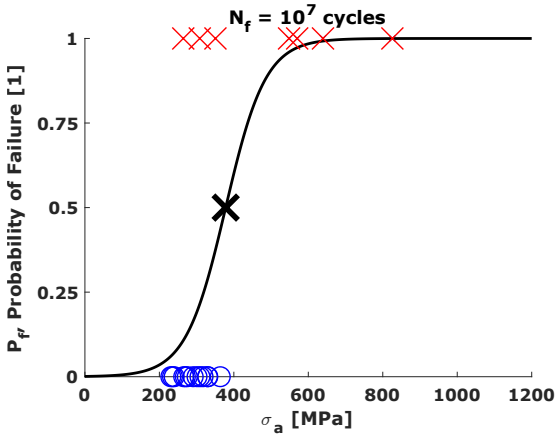
statistically low P_f due to the propagation of known survival data.



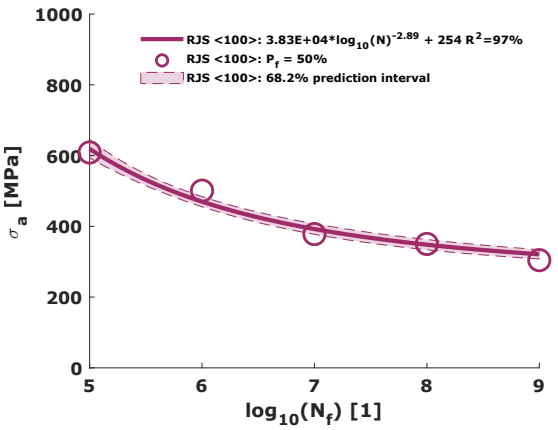
(a) Raw data of top 5 survive steps (circles) and failure steps (crosses).



(b) Propagated plot with $P_f = 50\%$ plotted.



(c) Logistical regression @ $N_f = 10^7$ from fig. 4.17b.



(d) Fitted $P_f = 50\%$ with ± 1 standard deviation prediction interval.

Figure 4.17: Applied statistical process using logistic regression and propagation for the RJS ⟨100⟩ samples. Starting from raw data in (a) to propagating data in (b), where red crosses are failures and blue circles are survival. Logistical regressions per life generate a 50% probability of failure for each life, generating which are plotted in (b,d) and fitted with a Basquin-like function in (d). The Jeffreys prior parameter is set to `none` in MATLAB 2024a.

4.2 Sample Preparation

The fatigue samples are machined from foils, which have the following requirements:

1. The foil thickness must be around 150 µm with minimal variation ($\leq$ 5µm) across the span of the foil. Minimising thickness variation maximises planarity within a sample and consistency between the samples across the same foil.

2. Residual stresses in the foil must be minimised to avoid affecting the fatigue results.
3. The maximum stress of the bent cantilever will be at the top and bottom surfaces [104]. So, the surface roughness must be minimised to avoid initiation from scratches.
4. In this thesis, the crystal orientation of the foil normal (FN) is preferred if it is near an orientation that allows for multiple desirable crystallographic directions along the cantilever direction (CD) via design rotation.

4.2.1 Foil Preparation

The supplied single-crystal CMSX-4 came as a rod, with its axis (the casting growth direction) near the ⟨100⟩.

Foil Machining

Electron discharge machining (EDM) cut parallel foils from the rod (fig. 4.18), chosen due to its accuracy, consistency, and thermal damage minimisation [41].

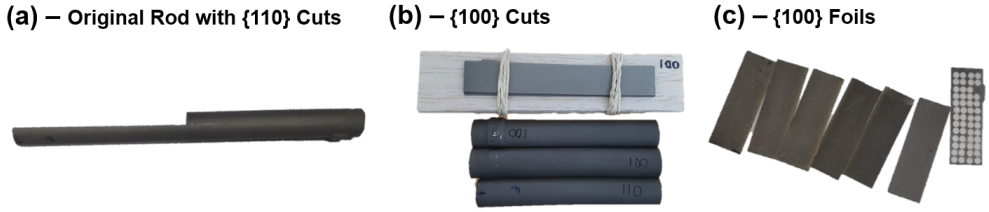


Figure 4.18: (a) shows the original bar that cut near ⟨110⟩ foils. (b) shows the collection of near ⟨100⟩ foils from the same rod via EDM. (c) depicts the ⟨100⟩ foils halved and with one finished foil with no samples left.

Like in titanium alloy foils [41], EDM forms a damage layer consisting of a thin, dark, rough surface layer and a residual stress layer in the foil surfaces. In the titanium alloy, the damage layer was around 20-40 µm thick and with compressive residual stresses [41]. Hence, the foils are initially 300 µm thick, to be thinned on both sides to the desired thickness to remove the damage layer and have a higher quality surface.

Figure 4.18 shows the initial EDM cut with a FN near ⟨110⟩. Further foils were prepared 45° to the initial cuts to obtain foils with FNs near ⟨100⟩ as shown in fig. 4.19.

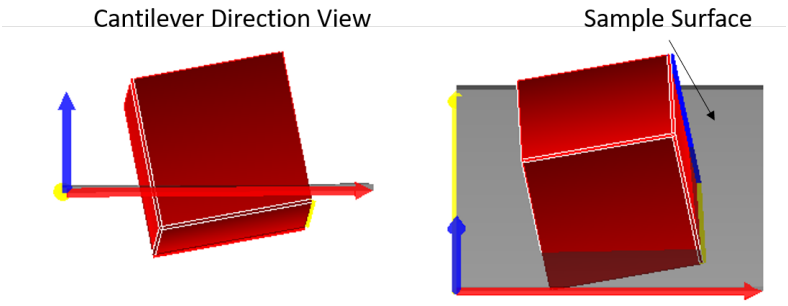


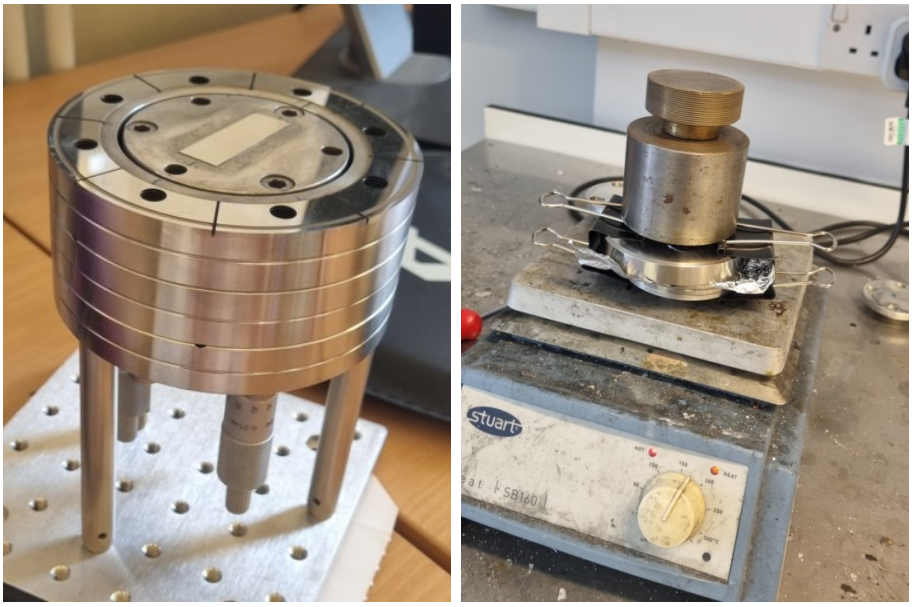
Figure 4.19: EBSD crystal orientation (sample RJSM10) produced with Bruker ESPRIT software. The blue axis is the FN, which is near ⟨100⟩, and the yellow axis is the cantilever and growth directions, showing that they are near ⟨100⟩.

Foil Polishing

The sample preparation method shares similarities with those in Ref [41]. However, a new grinding mount design was employed (fig. 4.20) called the tripod polisher.

The sample can be mounted onto a plate with a thin layer of crystal wax [41], with its height and orientation controlled by three micrometers. A sacrificial ring helps ensure the planarity and stability of the sample during preparation. Reducing the human skill in foil preparation made obtaining a foil with planar surfaces, parallel sides, and near the desired thickness easier.

The grinding steps are as follows. The height micrometer makes the foil parallel with the sacrificial ring. 600 grit SiC paper with 50 rpm removes the visible EDM damage layer and makes the foil planar. Successively finer grits up to 4000 grit are used, with the thickness and planarity tracked with the height micrometer. Remove the puck and the sample using the hot plate. Remount with the unpolished side exposed, and repeat the process until a thickness of 150 µm + 5 µm is measured (+5 µm to account for the crystal wax thickness). Finally, dismount the foil and remove the crystal wax with acetone.



(a) Photograph of tripod polisher **(b)** Mounting onto detachable disc procedure.

Figure 4.20: Tripod polisher used to produce the CMSX-4 foils in this thesis.

The finished foil ideally has a mirror finish with no distortion and virtually no visible scratches on the surface. A higher quality surface roughness was essential for the non-electropolished samples.

4.2.2 Sample Machining

An in-house laser machining setup was used in this thesis to machine the mesocantilevers, unlike the outsourced laser machining in previous works [41, 99], which allowed for on-demand machining and greater control of quality, i.e. less tapering of lateral profiles with increasing depth and less lateral re-deposition. The re-deposition was found to be poorly adhered to the cantilever, so it was of less concern.

4.2.3 Electropolishing

The samples were electropolished for EM analysis and/or to thin the samples. The physical setup of the procedure is shown in figs. 4.21 and 4.22 and was based on the successful electropolishing of titanium alloys within the research group [41, 99].

The electrolyte recipe is in table 4.1 and is cooled using the methanol bath via liquid nitrogen to $-50 \pm 5°C$ during electropolishing. A power source with variable

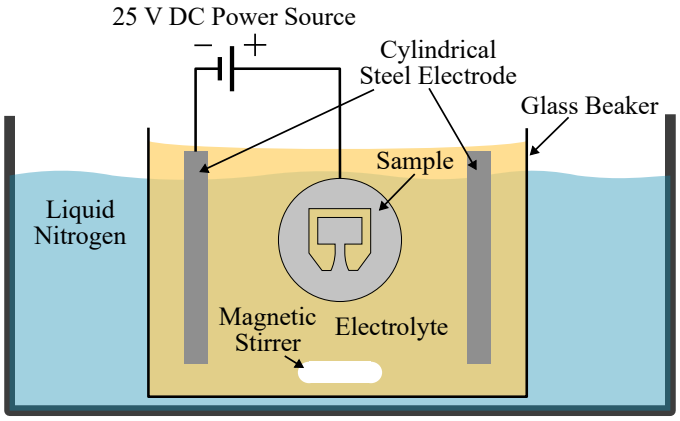


Figure 4.21: Electropolishing schematic. Adapted from [41] (CC BY 4.0).

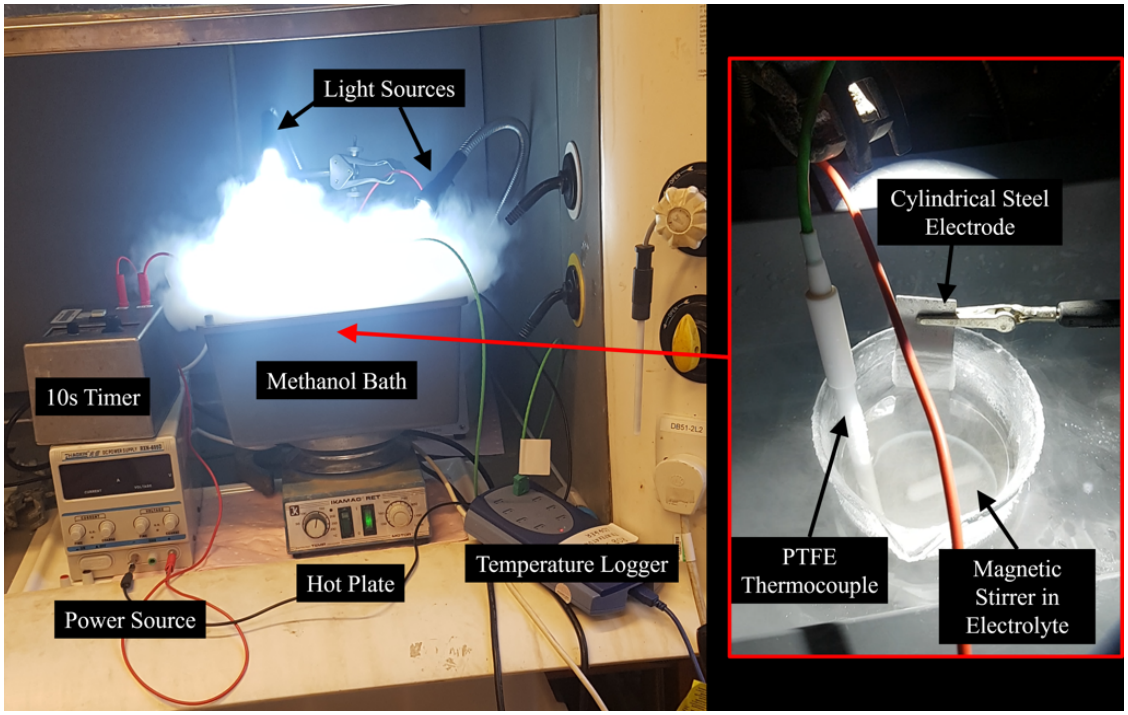


Figure 4.22: Physical electropolishing setup.

current and a 10 s interval timer is connected up such that the positive (anode) is connected to a Pt-tipped fine reverse-action tweezer. The negative (cathode) is connected to the submerged steel cage cathode.

Table 4.1: Electropolishing Solution Recipe

Order	Chemicals	Volume [ml]	Volume [%]
1st	Methanol	118	59
2nd	Ethylene Glycol	70	35
3rd	Perchloric Acid	12	6

Preparing solution:

1. To a lab-ware glass beaker, add the methanol, steel cathode cage, non-reactive magnetic stirrer, and PTFE thermocouple.
2. Slowly add the ethylene glycol (minor heat generation).
3. Cool methanol bath to $\leq 0\,^{\circ}\mathrm{C}$ with liquid nitrogen.
4. Set stirrer to 300 rpm to form a vortex in the centre.
5. Slowly add perchloric acid (significant heat generation).
6. Cool to $-50 \pm 5^{\circ}\mathrm{C}$.

Electropolishing procedure:

1. Maintain $-50 \pm 5^{\circ}\mathrm{C}$. Hotter/colder will make the electropolishing rate too fast/slow.
2. Grip a clean sample with the tweezers opposite the cantilever base (fig. 4.2).
3. Fully submerge just the sample and place it away from the vortex and where the curvature is flat with a high flow rate.
4. Electropolish in 10 s increments.
5. After every two increments, dip in two successive small methanol beakers in a consistent order.
6. When done, clean in the small methanol beakers and dry the sample with compressed inert gas after and/or medical wipe tissues.

4.3 Crystal Plasticity

CPFE modelling was used to assess the cantilevers' plastic deformation and single-crystal anisotropy. It has been used to determine the slip for the fatigue of

a SXNBS, which correlated well with experimentally observed slip traces and fatigue crack paths [108].

CPFE modelling was achieved in this work using ABAQUS CAE (2016, later 2022) with the UMAT and subroutines from the Tarleton Group's publicly accessible GitHub repository called CrystalPlasticity v2.5. Refer to Ref [109] and the GitHub repository documentation for further details on the CPFE calculations.

The meso-cantilever CPFE models were simulated using the settings described in table 4.2. Dynamic simulations cannot run with CPFE; hence, static simulations were used as an approximation. The face of the sample's base is encastred, and the hammer edge parallel to x is displaced in z to simulate mode one bending. Displacing the hammer edge by 20 µm quickly assesses elastic response, whereas 60 µm is enough deflection to determine the plastic response.

Using the mesh settings in table 4.2 produces a relatively fine mesh (fig. 4.23). The global seed size was informed by a convergence study (appendix B.2).

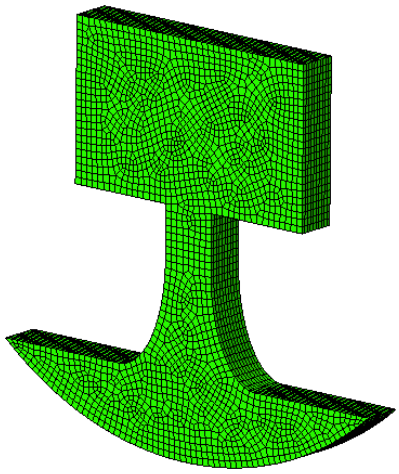


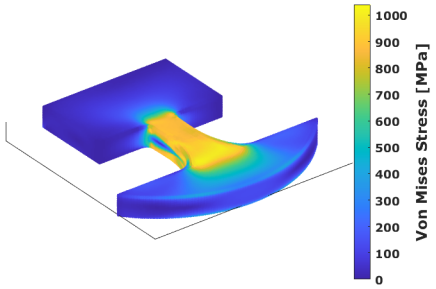
Figure 4.23: Typical crystal plasticity FEM mesh used in the CPFE modelling. Image generated in ABAQUS CAE.

Table 4.2: Crystal Plasticity FEM Setup. τ_c is CRSS. The C_{xy} are the components of the elastic stiffness matrix $\underline{\underline{C}}$. "*el.*" is elastic and "*pl.*" is plastic.

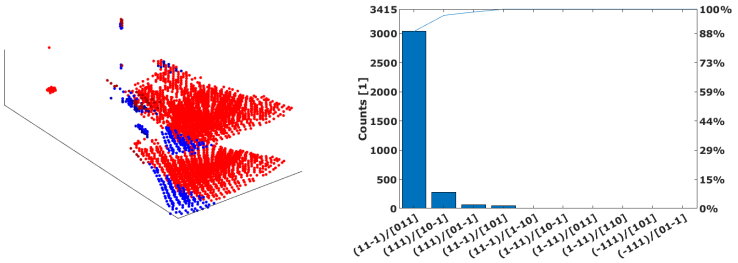
Name	Value
UMAT Case	Default 7 (i.e. CMSX-4)
Bunge (aka Euler) Angles	(ϕ_1, Φ, ϕ_2)
Max. Hammer Deflection	20µm (*el.*), 60µm (*el.* + *pl.*)
Step	General, Static
Amplitude	20% per 0.2 s
Run-time	$\approx$ 20min (*el.*), $\approx$ 50min (*el.* + *pl.*)
Element Type	C3D20
Mesh Controls	Hex $\Rightarrow$ Sweep $\Rightarrow$ Advancing Front
Number of Elements in Thickness	10
Maximum Deviation Factor	0.1
Minimum Seed Size	0.1 of Global Size
Global Seed Size	25µm
Default CMSX-4 UMAT (v2.5) Values	
τ_c Octahedral 23 °C	449 MPa
τ_c Octahedral 450 °C	461 MPa
τ_c Cubic 450 °C	498 MPa
$[C_{11}, C_{12}, C_{44}]$ 23 °C	[250.4,160.6,129.0] GPa
$[C_{11}, C_{12}, C_{44}]$ 450 °C	[232.9,154.5,115.1] GPa
$[C_{11}, C_{12}, C_{44}]$ 23 °C [21]	[251.3,160.9,129.4] GPa
$[C_{11}, C_{12}, C_{44}]$ 450 °C[21]	[232.3,153.7,113.4] GPa

In the elastic regime in ABAQUS, one can use the orthotropic elastic material property, but CPFE can do that and plasticity.

Inspired by Ref [108], fig. 4.24 shows how the dominant slip system can be calculated for each integration point by finding the slip system with the highest absolute slip.



(a) Scatter plot of Von Mises stress at each integration point.



(b) Dominant slip system of the top 10% VM stress visualised as a scatter plot and a Pareto chart.

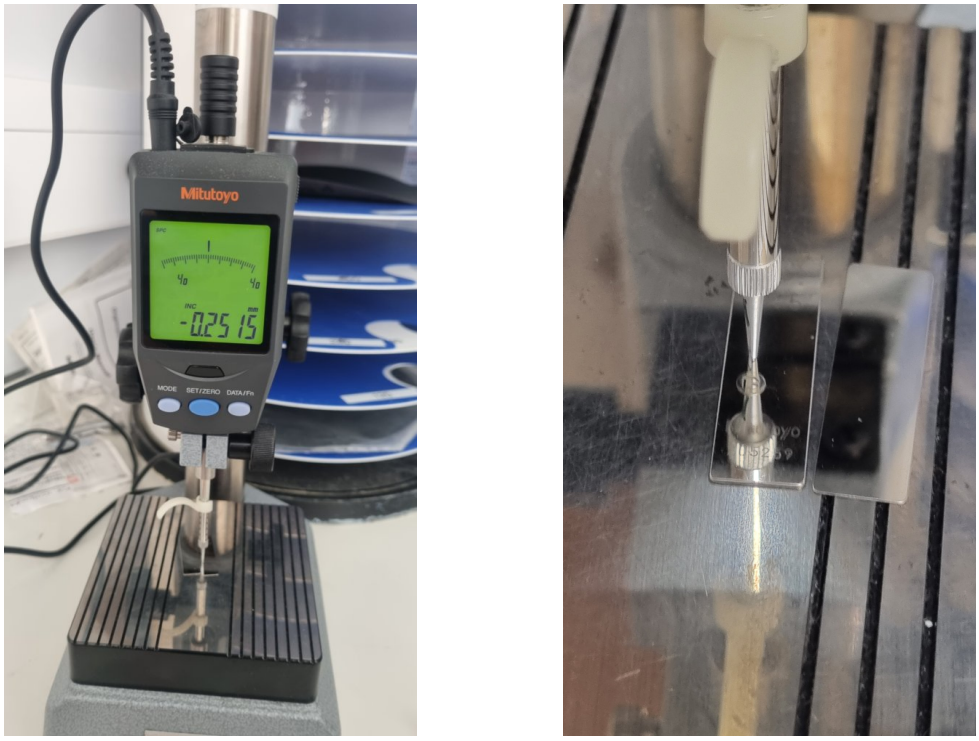
Figure 4.24: Dominant slip system obtainment of the top 10% risk-volume for a real sample (RJSN1) with CPFE modelling.

4.4 Sample Measurement

Lateral dimensions were measured using a *Zeiss Axiophot* optical microscope, fitted with initially a *Nikon* camera and later a *Zeiss Axiocam 506 color*.

A *Mitutoyo* height micrometer measured sample thicknesses due to concerns that standard micrometers cause scratches and overestimate the sample thickness as they measure the thickest part of the sample. The micrometer had a readout resolution of 0.1 µm. However, comparing the 0.5 mm and the 0.25 mm gauge blocks from *Mitutoyo*, there was at most ≈ 2 µm error between the expected thickness difference read between the two blocks. This uncertainty is reasonable considering the ± 1.5 µm accuracy of the digital readout and that the gauge blocks should have an accuracy of tolerance of ± 0.8 µm assuming Grade 1 is equivalent to 1 in the international tolerance grading system [1].

[1] Engineers Edge's International Tolerance Grades Table Chart ISO 286-1



(a) Micrometer setup and readout. **(b)** Higher magnification near probe tip.

Figure 4.25: Height micrometer with 0.25 mm and 0.50 mm gauge blocks and a mesocantilever on one.

The sample thickness was calculated from the mean of thicknesses measured from at least four locations (with repeats) and with the micrometer zeroed on the gauge block the sample was on.

4.5 Electron Microscopy

Unless stated otherwise, the electron microscopy (EM) data was collected on a *Zeiss Merlin* field emission gun (FEG) scanning electron microscopy (SEM).

4.5.1 EDX

Energy dispersive x-ray analysis (EDX) is an EM technique that uses the characteristic x-rays generated by interactions with the incoming electrons from an excitation volume near the sample surface to qualitatively and quantitatively assess the local chemical composition of microstructural features. For further details see Ref [110,

Ch. 10].

The data was collected with an annular four-channel silicon drift EDX detector (*XFlash FlatQUAD 5060F*), and cooled to around −25 °C.

Different acceleration voltages and windows were used depending on the elements of interest. A 20 kV window was chosen for comparing the metallic elements and 6 kV for the lighter element (C,N,O). Typically, scans were run for ≥ 15 min for sufficient counts per pixel for good quantification and accurate count maps. Analysis and quantification were done on Bruker's ESPRIT v2.3 software, and HyperSpy to generate EDX count maps with the Viridis colourmap.

4.5.2 (HR-)EBSD

EBSD

Electron back-scatter diffraction (EBSD) is an SEM technique that rasters the electron beam across the sample surface, capturing the electron back-scatter patterns with a CCD camera, allowing both the phase and crystal orientation to be mapped for a crystalline sample from the observed Kikuchi bands [110, 111]. The stage (& sample) are typically tilted near 70° [112] to increase the yield of BSEs [113]. See Refs [111, 113, 114] for details on diffraction pattern generation and analysis.

The angular resolution within an EBSD map has an accuracy of ≈ 0.5° [111, 114, 115] or less. However, in terms of absolute orientation accuracy, systematic errors can lead to larger discrepancies with the actual orientation [112], reported to be ≈ 2.0° [111, 116]. It could be as bad as 4.0° [112] or 3.0° − 5.0° [117]. 5.0° was used as the upper threshold for obtaining the correct crystal orientation [117].

EBSD is used to ascertain and confirm the intended crystal orientation of the samples, which can then be extended to other samples within the same batch/cantilever orientation. EBSD also confirms that the samples are single crystals within the technique's limits. The orientation is used in CPFE models, MTEX Schmid factor calculations, and to aid ECCI $\underline{g}$ determination.

HR-EBSD

High-angular-resolution EBSD (HR-EBSD) post-processes high-quality EBSD data to calculate the small lattice strains within each grain (< 0.1 mrad in rotation [114]) using cross-correlation-based analysis of the electron backscattered patterns in comparison with an appropriately chosen "strain-free" reference pattern. These sensitive strain measurements allow maps of strain, stress, and defect populations to be generated [111].

It is used in this work to assess the local state of remnant geometrically necessary dislocation density (ρ_{GND}) around the fatigue cracks.

Due to the higher angular resolution (θ_{min}) of the HR-EBSD technique compared to Hough-based techniques ($\pm 0.006^\circ \equiv \pm 0.105$mrad c.f. $\approx 0.5^\circ$), the noise floor (ρ_{min}) is lower for a given raster step-size (L_{step}) and Burgers vector magnitude ($|\underline{b}|$) according to eq. (4.6) [114]:

$$\rho_{min} = \frac{\theta_{min}}{L_{step} \cdot |\underline{b}|} \tag{4.6}$$

There is also the physically feasible measurable dislocation density ($= L_{step}.^{-2}$) to account for as well. So, with all factors, choosing the correct step size is complex, as smaller step sizes overestimate the density (via the increase in the noise floor), but larger step sizes underestimate the dislocation density (via capturing multiple dislocation dipoles) [114]. The effect of measured ρ_{GND} vs L_{step} is discussed in Ref [114]. In practice, the step size has a minimum value due to the minimum probe size of the electron beam, which in this SEM is $\approx$ 40nm [2], around the value typically chosen L_{step} in this thesis.

This work used the latest private version of the HR-EBSD code developed by Wilkinson et al. called **xEBSDv3**, and the typical operating conditions are outlined in table 4.3.

When the dislocation density is too low, HR-EBSD struggles to capture the dislocations and ECCI becomes more appropriate. Conversely ECCI struggles under high dislocation densities.

[2] Private conversation with Dr P Karamched

Table 4.3: Typical HR-EBSD conditions used.

Parameter	Value
Accelerating Voltage	20 kV
Probe Current	10 nA
T_{stage}	70°
Working Distance	≈ 18mm
Detector Distance	≈ 18mm
Camera Exposure	Variable
Pixel Size	≈ 40nm
EBSP resolution	800 × 600

4.5.3 ECCI

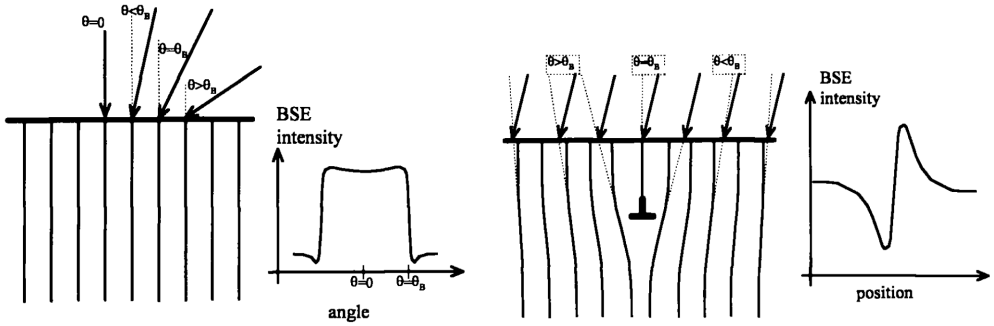
Electron contrast channelling imaging (ECCI) makes use of the electron channelling of the BSEs, which is the variation of the intensity due to the relative orientation relationship between the incident electron beam and the crystalline sample [118].

The origin of this contrast can be described with a Bloch wave model, which describes two Bloch-wave states, high reflection and high channelling BSE states. Figure 4.26 shows at the Bragg angle (θ_B) (i.e. maximum gradient), both populations of Bloch waves are equal. However, at lower angles, reflection dominates, and at higher angles, channelling dominates. Rotations in the crystal lattice allow defects such as dislocations to be imaged when at or near the Bragg condition as depicted in fig. 4.26b, with the contrast being sensitive to even a few mrad away from θ_B [112].

Similar to analysing defects in a TEM, $\underline{g} \cdot \underline{b}$ analysis can be used in ECCI if the diffraction vector ($\underline{g}$) is known. The value of $\underline{g}$ can be selected by orientating the grain to the Bragg condition for a set of crystal planes (associated with $\underline{g}$). For a large enough crystal and low image magnification, the electron channelling pattern (ECP) can be seen and used to aid this orientation [118].

Existing methods in the literature to obtain $\underline{g}$ in ECCI are discussed in section 5.3.

In this work, the samples are meso-scale single crystals, so an ECP can be visualised under BSE imaging, and a novel approach to determining crystal orientation and $\underline{g}$ conditions has been developed (see section 5.3).



(a) BSE intensity variation in an SEM with varying incident beam approach angle (θ).

(b) Example of the BSE intensity of a non-threading edge dislocation when the sample is orientated to the Bragg condition $\theta = \theta_B$ for a crystallographic plane.

Figure 4.26: Schematics explaining the origin of varying BSE intensity with varying crystal orientation and an example of defect contrast. Figures from [112].

An example of non-threading dislocations imaged in ECCI is shown in fig. 4.27.

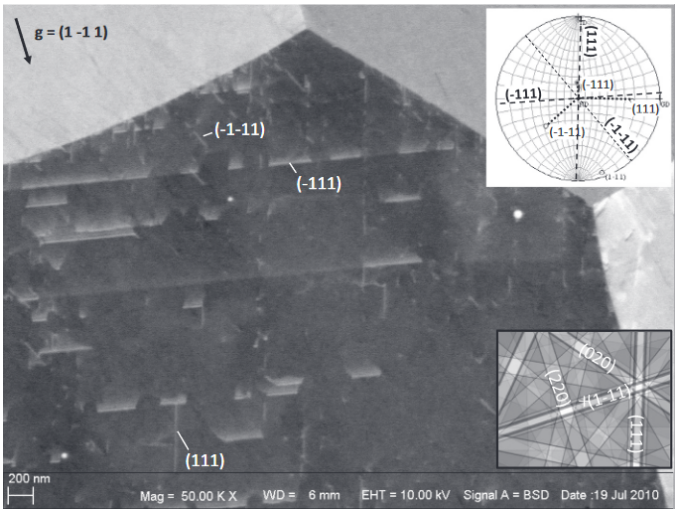


Figure 4.27: Example ECCI of TWIP steel. The non-threading dislocations are imaged under $\underline{g} = [1\bar{1}1]$. Figure from [119].

4.6 Radiography

The thin nature of the meso-cantilevers ($\approx 150\,\mu m$) allows the use of lab-based (low energy) X-ray computed tomography (XCT) to quickly capture radiographs.

The radiographs show:

1. It can assess sample thickness consistency as significant thickness variation

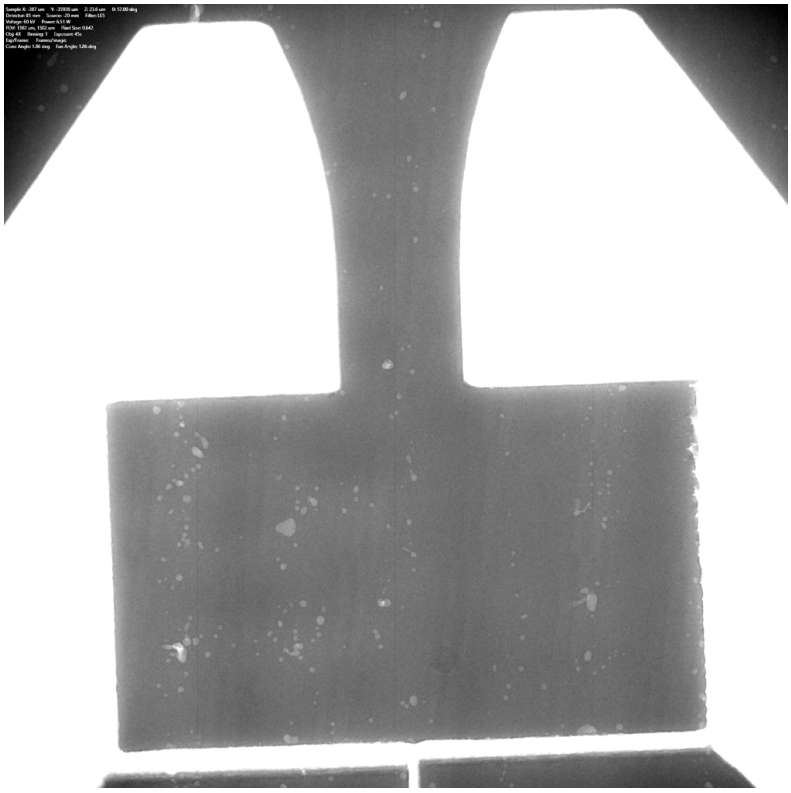


Figure 4.28: Radiograph of a CMSX-4 mesocantilever.

will cause changes in the attenuation and, thus, brightness. This also includes surface roughness on the lateral parts of the cantilever.

2. Interdendritic pores attenuate the X-rays less, appearing as bright globular features along the dendrite boundaries. This can be used to estimate the pore size distribution and predict the initiating pore before testing.
3. The growth direction of the single-crystal alloy can be estimated from the interdendritic region's orientation. The dendrites can be made out by interdendritic porosity and by microsegregation.

Using the *Zeiss Xradia Versa 510* XCT from Prof Marrow (Department of Materials, University of Oxford) with the help of his student Marcus Williamson, some samples had their radiographs taken under optimum conditions as detailed in (table 4.4).

Table 4.4: XRadia radiograph parameters used.

Parameter	Value
θ	57.00°
Detector	85 mm
Source	−20 mm
Filter	LE5
Voltage	60 kV
Power	6.5 W
Pixel Size	0.642 µm
Obj	4x
Exposure	45 s

5
Method Developments

Contents

5.1 Porosity Assessment 100
5.1.1 Radiography 100
5.1.2 Post-Mortem Comparison 105
5.1.3 Conclusions 109
5.2 Failure Detection &Tracking 109
5.3 ECCI Technique Development 112
5.3.1 Background 112
5.3.2 Method 114
5.3.3 Worked Example: Grown GaN Single Crystal 116
5.3.4 Worked Example: Fatigue Sample 120
5.3.5 Example ECCI Micrograph 126
5.3.6 Summary 128

5.1 Porosity Assessment

The following section addresses Aim 2, which is to see if radiography can aid the understanding of the individual and collective porosity in the samples, can those pores be found in SEM fractography, and can the initiating defect be correlated to the fatigue performance?

5.1.1 Radiography

Using the methodology as outlined in section 4.6, it was possible to obtain through-thickness radiographs of $\approx 150\,\mu m$ thick mesoscale CMSX-4 cantilevers.

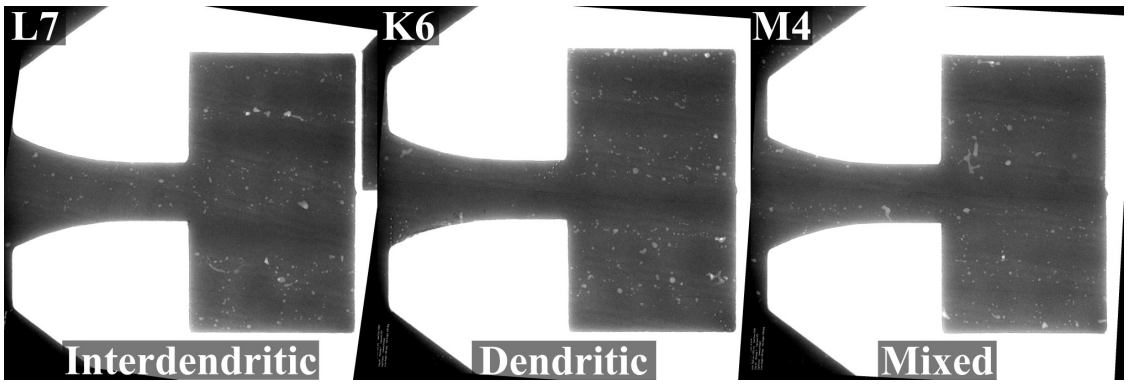
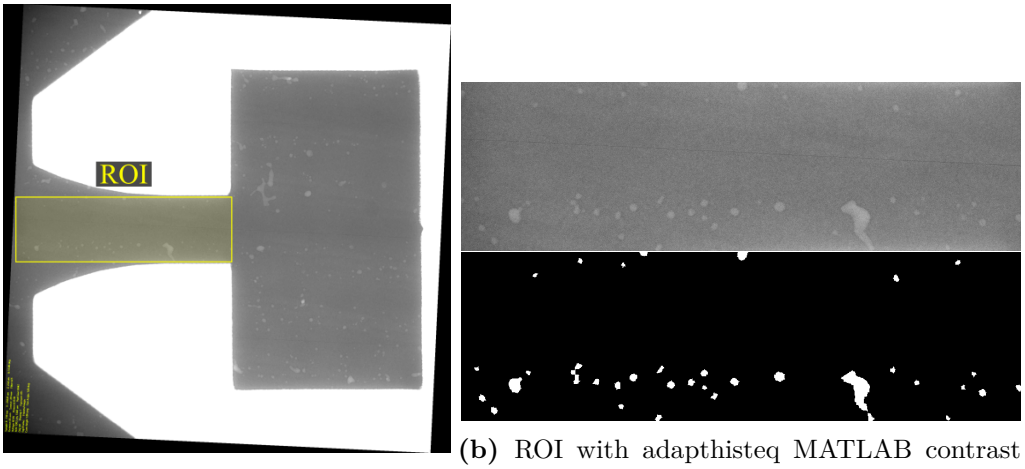


Figure 5.1: Contrast-enhanced example radiographs of non-electropolished RT air mesocantilevers. Examples of the dendritic, mixed, and interdendritic mesocantilevers are shown with their sample names.

Figure 5.2 shows how the radiographs are rotated so the rectangular region of interest (ROI) is drawn over the cantilever region only. Subsequently, the ROI undergoes a contrast enhancement (`adapthisteq`) followed by an intensity threshold (adaptive `imbinarize`). Dilation and erosion (`imclose`) are performed using a three-pixel radius disk structuring element. Finally, the pore size and shape were analysed with `regionprops`. Some of the brighter features could also be intermetallics, but as none have been identified in chapters 6 and 7, they all will be treated as pores in this analysis.

Figure 5.3 shows the pore geometry analysis, which gave similar results across all of the samples. Hence, the overall results should represent the bulk population more. Distribution fits were done in MATLAB (fig. 5.4), with those fits being the

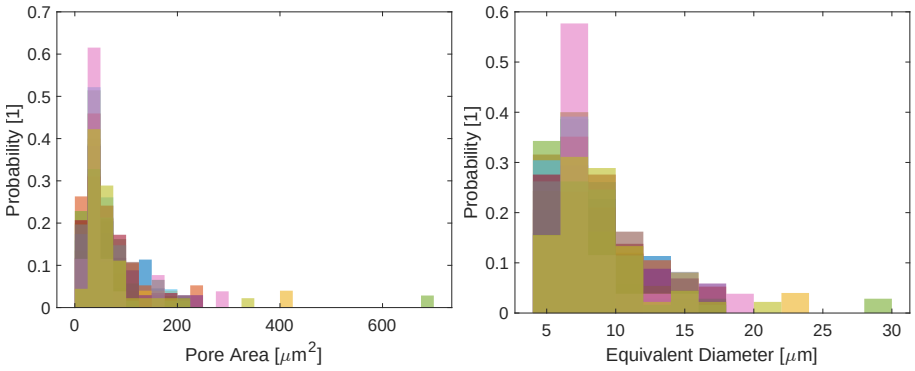


(a) Radiograph of M4 with ROI.

(b) ROI with adapthisteq MATLAB contrast improvement, followed by thresholding.

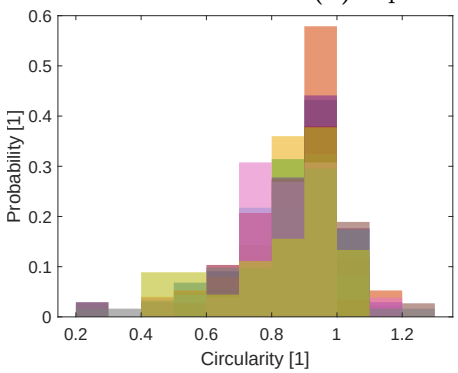
Figure 5.2: Radiograph pore analysis process.

generalised extreme value (GEV), extreme value (EV), and log-normal distributions. Log-normal was used to obtain the Feret diameter in Ref [72]. For further details on the fit equations, see appendix C.1.



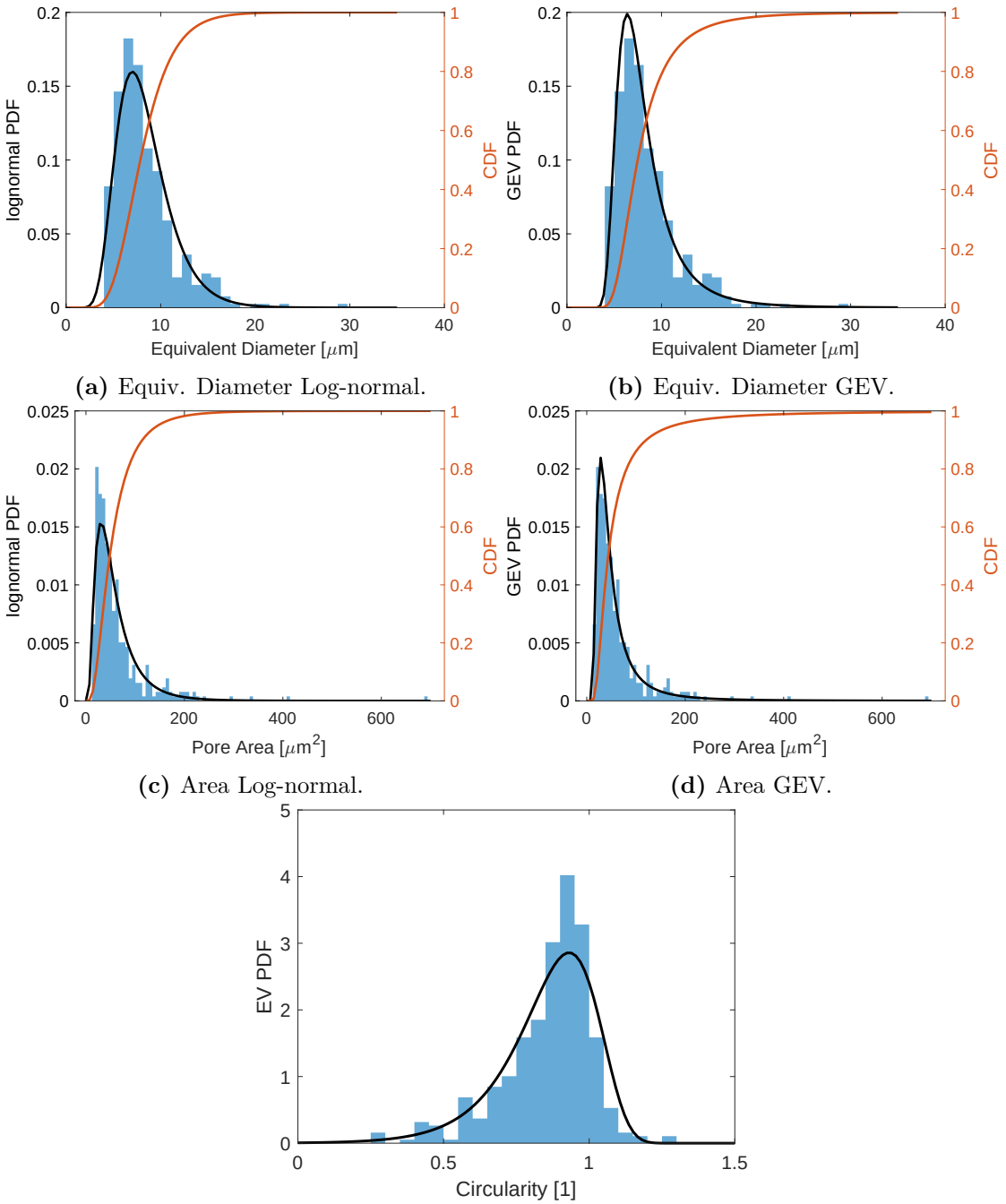
(a) Pore area.

(b) Equivalent diameter.



(c) Pore circularity.

Figure 5.3: Radiograph pore analysis histograms for each sample.



(a) Equiv. Diameter Log-normal.

(b) Equiv. Diameter GEV.

(c) Area Log-normal.

(d) Area GEV.

(e) Circularity EV.

Figure 5.4: Fitting of metrics of all samples different distributions.

The fitting parameters of the diameters are shown in table 5.1, including DD5 [72] for comparison. The pore circularity from this radiograph perspective (i.e. the FN) is highly circular with a μ of 0.931. The GEV distribution produced similar but better fits with the binned data than the log-normal distribution for equivalent

diameter and pore area. This is possibly due to GEV having one more parameter.

Table 5.1: Porosity distribution analysis via MATLAB.

Metric	Distribution	μ	σ	k	Max.
Ref [72] Feret Dia. [µm]	lognormal	2.50	0.22		$\approx 90\,\mu m$
Equiv. Dia. [µm]	lognormal	2.06	0.337		$29.7\,\mu m$
Equiv. Dia. [µm]	GEV	6.75	1.89	0.226	$29.7\,\mu m$
Area [µm^2]	GEV	35.5	19.8	0.528	$693\,\mu m^2$
Circularity [1]	EV	0.931	0.129		

By using the thresholded pores' equivalent diameters, their volume can be approximated to spheres, which figs. 5.2 and 5.3c show is reasonable. As each sample's thickness was recorded, their volume fraction porosity can be calculated (see fig. 5.5). These values agree with the lower bound of the reported porosity fraction of 0.10 % to 0.26 % for CMSX-4 From Ref [30]. Ref [30] estimated the area fraction porosity from optical micrographs taken parallel to the growth axis, unlike the radiographs taken approximately orthogonal to the growth axis (i.e. dendrites). The lower fractional porosity in this work could be due to a higher quality supplied material or an insufficient total area analysed.

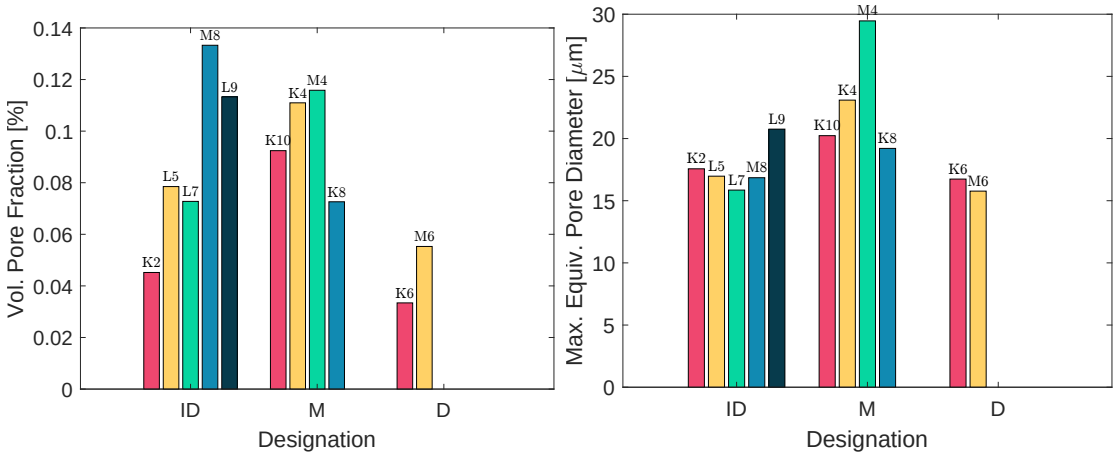
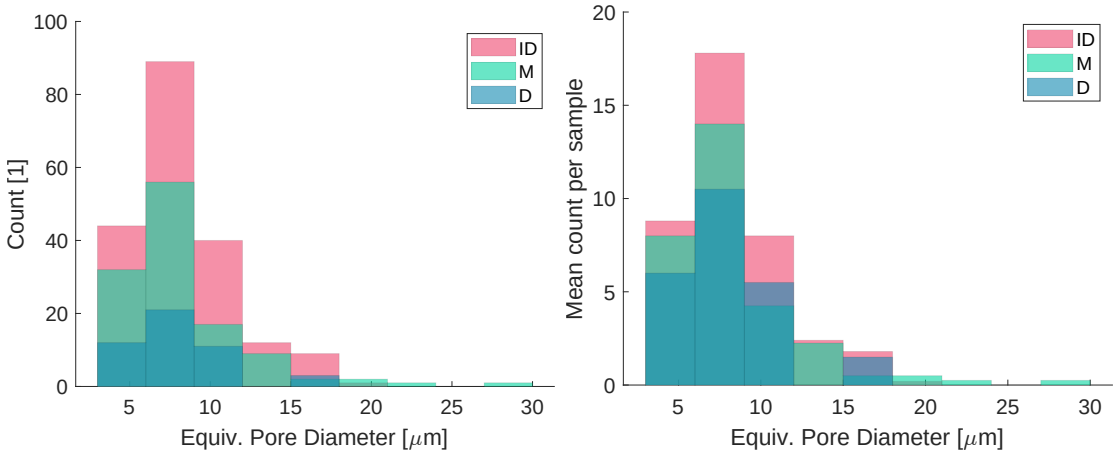


Figure 5.5: Cantilever porosity statistics in terms of area fraction porosity and maximum equivalent pore diameter. "ID" is interdendritic, "M" is mixed, and "D" is dendritic.

Figure 5.1 shows how the cantilevers can be machined primarily within the darker dendritic or the brighter & more porous interdendritic areas. Figure 5.5 shows that this has led to estimated mean volume fraction porosity values of 0.0886% for

interdendritic, 0.0980% for mixed, and 0.0444% for dendritic. The dendritic region showing the lowest average porosity of the three regions is expected [6, 30]. For the maximum pore diameter, there is a less significant difference between interdendritic and dendritic; however, mixed shows larger values. There are three explanations for this. 1st, it is more likely to have a whole pore contained within a cantilever rather than being cut off by the ROI or cantilever edge. 2nd, the sample study is too small to draw conclusions between interdendritic and mixed. Evidence of this is shown in the larger pores seen in a sample's hammer region rather than its main body. 3rd, some samples are borderline in their designation between mixed and interdendritic.

The greater tail for mixed in the high diameter regions in fig. 5.6b helps explain the greater mean average volume fraction porosity and maximum equivalent diameter for the mixed region compared to the other regions. Note the expected decrease in peak height going from ID to M to D fig. 5.6b. So, the 2nd and 3rd reasons best explain this result, as indicated by only two pores being found between 21 µm and 30 µm which are in the mixed group (fig. 5.6a).



(a) Total count. **(b)** Normalised count.

Figure 5.6: Equivalent pore diameters for the interdendritic (ID), mixed (M), and dendritic (D) regions. (a) The equivalent pore diameter counts are grouped by type. (b) To normalise the results, the total count was divided by the number of samples in each group.

5.1.2 Post-Mortem Comparison

The following investigates the correlation between the radiograph pores, post-fatigue fractographs, and fatigue performance.

Figure 5.7 shows the S-N coloured by %-porosity, showing no strong trends apart from lower %-porosity with N_f. However, as samples were randomly chosen, this is most likely a coincidence. Figure 5.8 similarly doesn't show a strong trend either, with even the larger pore result showing a lower σ_{amp} than the smaller pore at $N_f = 10^7$.

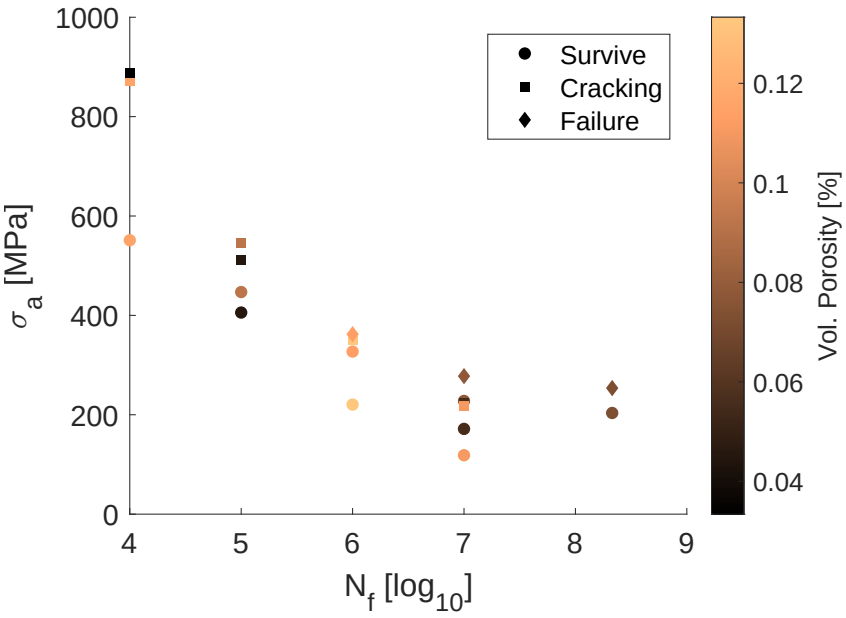


Figure 5.7: S-N of ambient samples with %-porosity.

The K-T diagram in fig. 5.9 is similar to that done in Ref [72] for a SXNBS. Designating the boundaries is challenging as there are not enough data points for all N_f, there is not a large pore size range, and step-loading was used. In fig. 5.9, it is expected that N_f should decrease in value from the bottom-left to the top-right [72, p. 13].

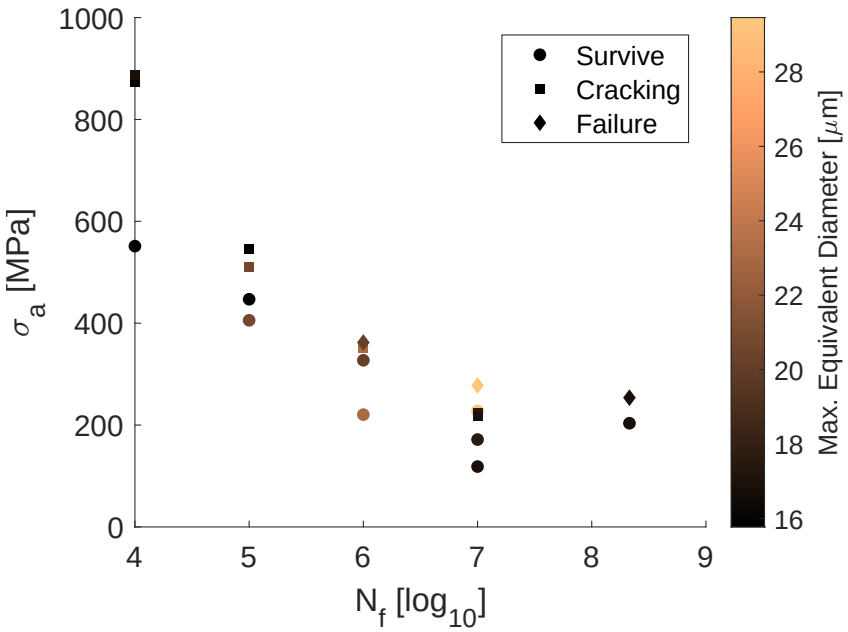


Figure 5.8: S-N of ambient samples with maximum equivalent diameter.

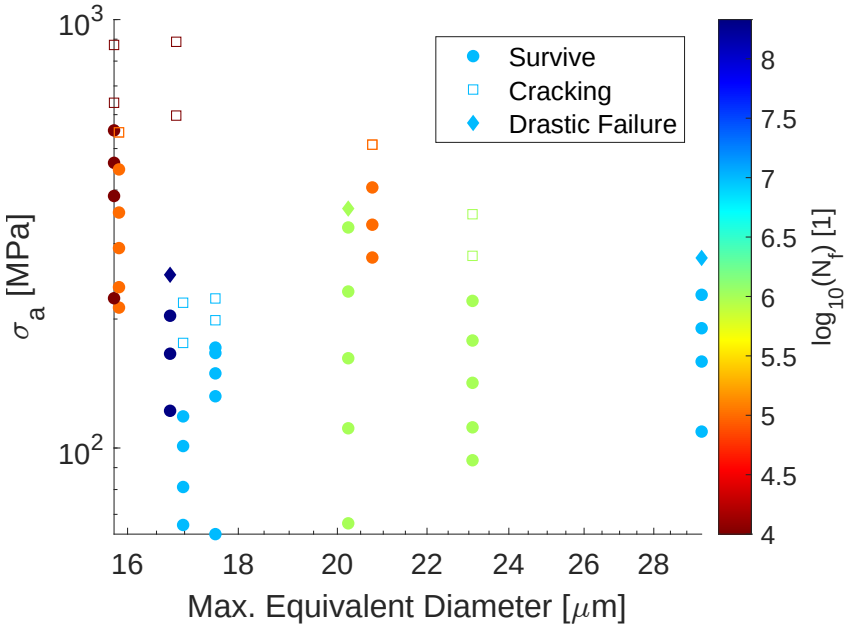
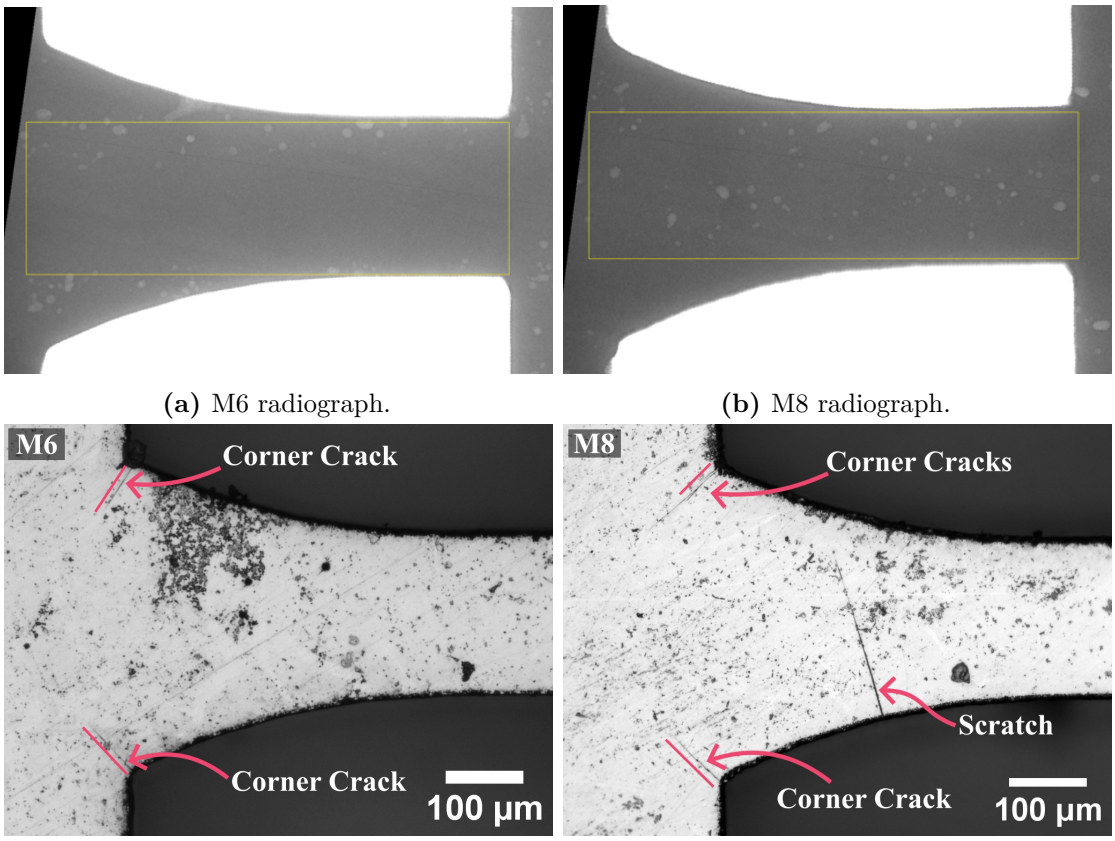


Figure 5.9: K-T plot with the observed maximum equivalent pore diameter. Filled circles are all survive steps, squares are cracking steps, and diamonds are a drastic failure.

%-Porosity Effect

M6 and M8 are the two N_f 10^4 data, but M8 has $\times 2.21$ more porosity as it is more interdendritic (see fig. 5.10). Despite this, the post-mortem OM shows that both samples exhibited corner cracking where the cantilever attaches to the base

and not from the pores in the radiographs. The radiographs capture the corner regions, but the rectangular ROI does not.



(a) M6 radiograph. **(b)** M8 radiograph.

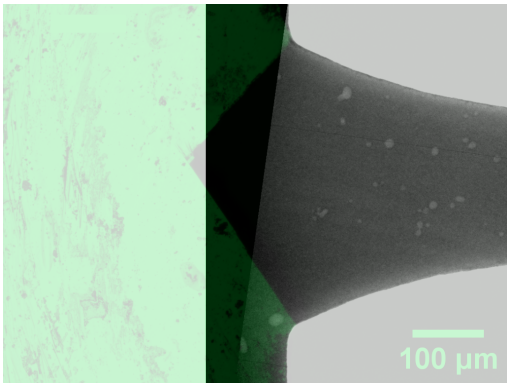
(c) M6 OM post-mortem. **(d)** M8 OM post-mortem.

Figure 5.10: Comparison before and after testing for M6 (red) vs M8 (yellow). Arrows and nearby parallel lines indicate the corner cracks. OM images grey-scaled.

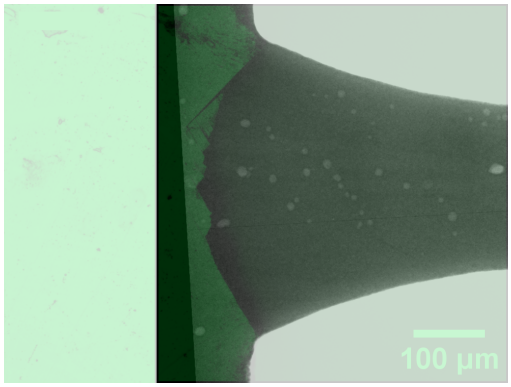
Corner cracking

Both samples ($N_f = 10^5$) exhibited failure via cracking into the cantilever base, so they are comparable. The optical micrographs in fig. 5.11 show that L7 has just two large {111} apparent facets that start from the corners, whereas L9 is similar apart from the more complex {111} faceting at its centre near the higher porosity in that sample. The SEM fractograph in fig. 5.11e shows around three or more spherical pores internally in the final failure region and a feature at the top surface; these could have influenced the fracture behaviour, but they are unlikely to be the ones in the radiograph as the fracture surface is deeper into the base. All available

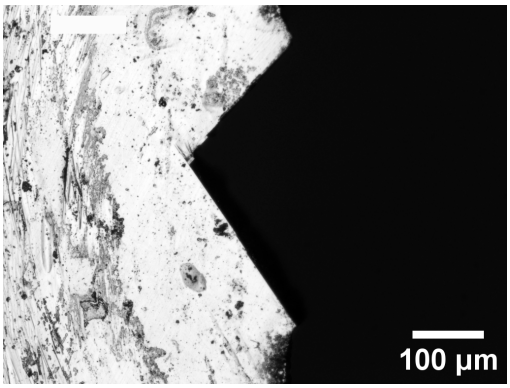
fractographs can be found in fig. 6.7. The stress concentration factor around the corners is assessed in section 6.3.2, finding it can be as high as ×3.



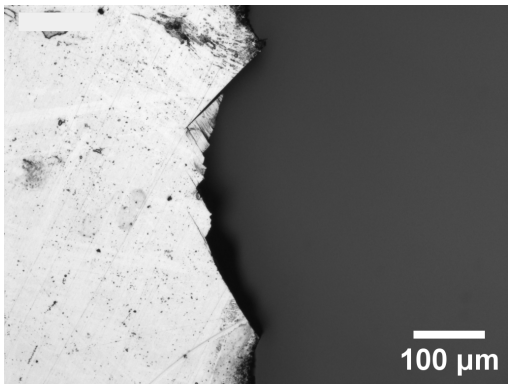
(a) L7 radiograph with OM post-mortem superimposed. Base failure.



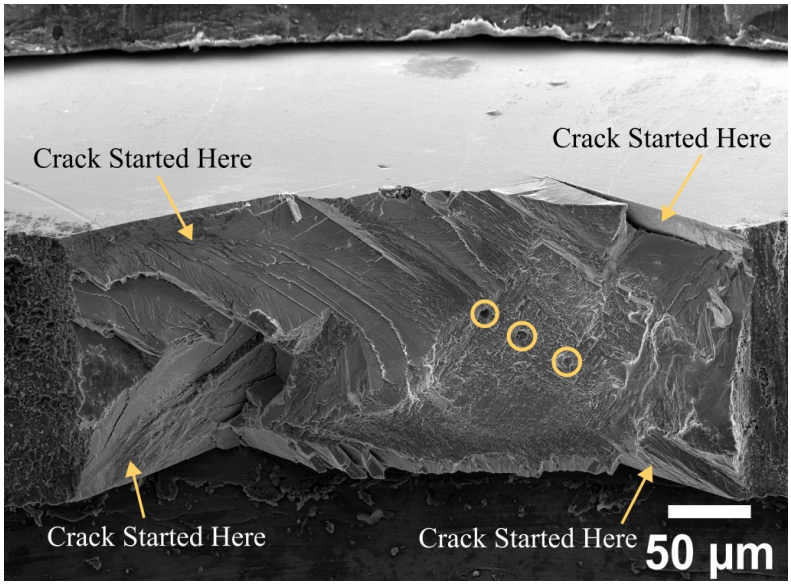
(b) L9 radiograph with OM post-mortem superimposed. Base failure.



(c) L7 OM post-mortem. Base failure.



(d) L9 OM post-mortem. Base failure.



(e) SEM fractograph of L9. Pores have been circled. Four fatigue crack initiation points have been labelled.

Figure 5.11: Comparison before and after testing for L7 vs L9. OM images grey-scaled.

5.1.3 Conclusions

- Porosity can be assessed throughout the captured regions within radiographs, allowing for more pores to be seen than could be via OM. The composition and interdendritic porosity can be qualitatively assessed. The cantilevers do not exist purely within a dendrite core or in an interdendritic region. Hence, the size effect due to porosity differences is unlikely to be strong in this work. Reducing the cantilever dimensions in future work could be done to investigate microsegregation and the porosity effect.
- Future X-ray computerised tomography is possible for these mesocantilevers, which would be useful for defect analysis as it quantifies pore location & dimensions (as 3D).
- The measured pore sizes for all samples can be fitted well with the generalised extreme value (GEV) distribution for their area and equivalent diameter.
- There is no strong correlation with the measured porosity in the S-N and K-T plots. Instead, by comparing micrographs, most initiation occurred at the corners where the cantilever attaches to the base rather than at the pores (further discussed later in chapter 7).

5.2 Failure Detection & Tracking

The following section addresses Aim 6, which is to assess the capability of crack detection and growth for the fatigue method used in this thesis.

Figure 5.13 shows how L-vs-time data can give information about the state of the sample. Multiple brief bursts of low amplitude cycling (calibration in fig. 5.13a) can be used as a calibration, as an uncracked sample's α_{amp}-vs-amplitude is linear, as shown in the calibration region in fig. 5.13b. The gradient of the linear region is dependent on the sample's resonance in the untracked state. Not shown here, but it was found to vary with sample thickness variation and with the cantilever direction orientation (e.g., lower for along $\langle 110 \rangle$ samples than $\langle 100 \rangle$).

Survive data points follow the linear calibration trend closely (fig. 5.13b) and have a virtually constant α_{amp}-vs-time (fig. 5.13a).

Cracking data points have a positive α_{amp}-vs-time gradient, as this experimental setup has greater coupling with crack growth, increasing the α_{amp}. The α_{amp} increases at a near-constant rate, and usually, the initial α_{amp} coincides with the calibration line at or within tolerance.

Drastic failure's initial α_{amp} starts above the calibration line and has an increasing α_{amp} rate. It completely fractures the sample, or the cracks are comparable to the cantilever dimensions. It can manifest in the laser streak as a "figure of eight" form (fig. 5.12) from an increased torsion component (e.g., 45° {111} shearing cracks in ⟨100⟩ samples) and as a significant translation when the UFR is on or off.

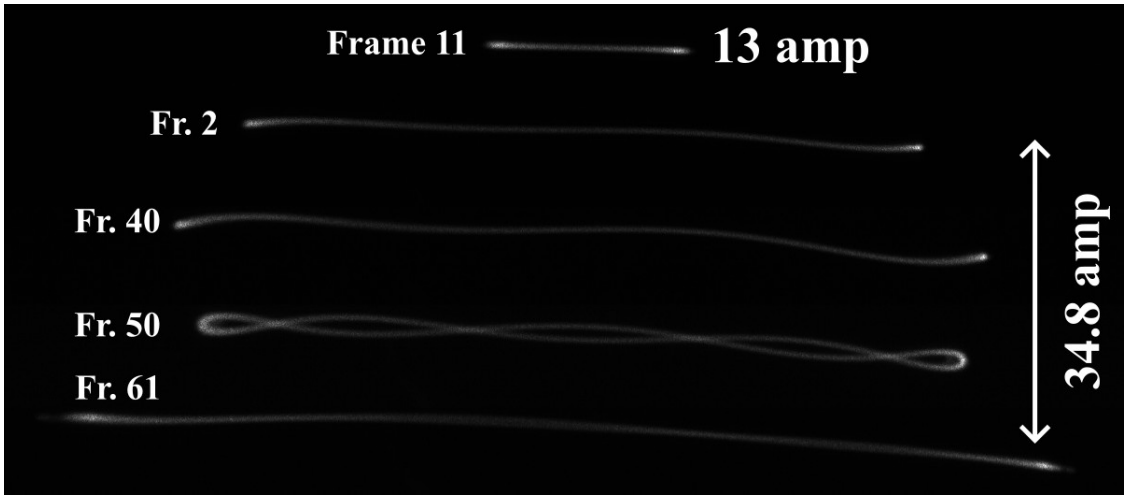
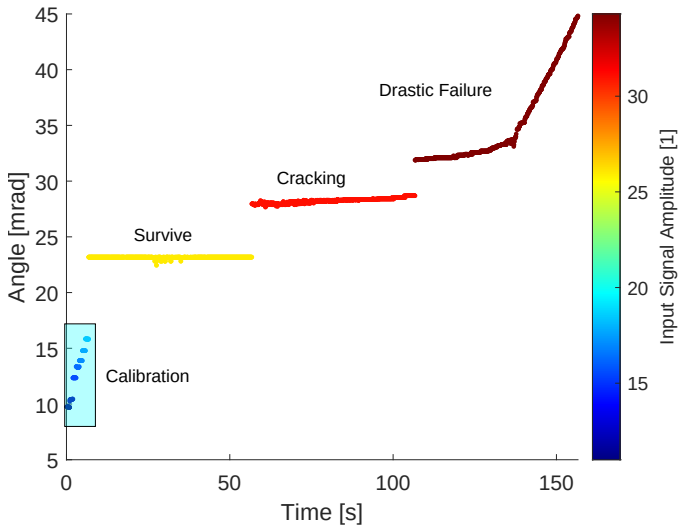
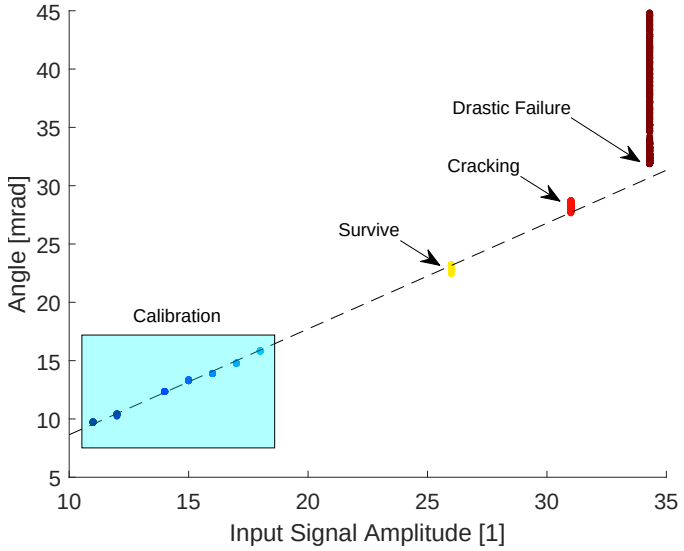


Figure 5.12: Stitched frames of survival and drastic failure steps laser streaks for a ⟨100⟩ CD ⟨100⟩ FN orientated sample. The input signal amplitude of 13 is a survival step. In the final step of a 34.8 input signal, the streak transitions from wavy to a "figure of eight" and then back to wavy before it rapidly completely fractures. An exposure of 30 ms was used.



(a) α_{amp} vs time.



(b) α_{amp} vs input vibration amplitude.

Figure 5.13: Failure detection and designation via L derived α_{amp} values.

The survival data points can be reported with an average α_{amp} (& σ_{amp}) with an uncertainty. However, the cracking and drastic failure points can be reported with their first α_{amp} value (as those are closest to the calibration line) or the calibration line predicted value at that amplitude. The justification for the latter is that if virgin samples were tested at those amplitudes, their extrapolated calibration line values would represent the σ_{amp} of their initially uncracked state. The σ_{amp} is calculated from experimental α_{amp} values using a simulation derived ω. As ω is determined from an uncracked simulation, then accurate σ_{amp} values when the

sample is significantly cracked cannot be obtained, only uncracked σ_{amp} values.

The benefit of obtaining a calibration is two-fold: designation of the fatigue step data point based on an uncracked response and extrapolation of uncracked σ_{amp} for all steps.

5.3 ECCI Technique Development

This section will address Aim 4 in developing a technique and software for obtaining diffraction conditions in ECCI. This work uses it to assess the plasticity involved in the fatigue of the meso-scale cantilever samples.

Detecting defects using ECCI is "well established", but "defect identification by ECCI is not well established" [118]. To determine the Burgers vector ($\underline{b}$) of a defect, one must first be confident with the diffraction vector ($\underline{g}$) used and, secondly, capture the same region under different $\underline{g}$.

Capturing defects under more than one $\underline{g}$ condition allows one to predict the nature of the defect using the $\underline{g} \cdot \underline{b} = 0$ & $\underline{g} \cdot (\underline{b} \times \underline{u}) = 0$ invisibility criterion equations (the latter for pure edge dislocations) [120]. Where $\underline{u}$ is the line unit vector of the dislocation. These equations neglect the surface relaxation derived contrast for threading dislocations [118].

This section summarises the development of a new method to obtain $\underline{g}$ conditions and interpret the observed ECP bands. The procedure is explained and applied to two worked examples of a simple sample (single-crystal GaN) and a more complex sample (fatigued SXNBS meso-cantilever).

5.3.1 Background

There are three main methods in the current literature for achieving specific $\underline{g}$ conditions in ECCI by tilting and rotating to calculated values:

1. Using selected-area electron channelling pattern (SAECP) [121]. However, SAECP is not commonly available on modern SEMs.

2. Controlled ECCI (cECCI) [119]
3. Rotational-ECCI (R-ECCI) [122]

cECCI is a technique that relies on a software called Tools for Orientation Determination and Crystallographic Analysis (TOCA). TOCA simulates the kinematical ECP for a "given crystal structure, orientation, and beam energy"[119]. To achieve cECCI, subsequent calculations are needed to calculate brightness and band widths to achieve the desired diffraction conditions [119], from which the tilt and rotation for a desired $\underline{g}$ are predicted. TOCA and their software are not publicly available; it can only do kinematical simulations, and it purely relies on input orientation only (e.g. via EBSD). The latter point is of concern as they even mention the true value inaccuracy of EBSD orientation can be "several degrees"[119], which can lead to inaccuracies in the simulated ECP intensity path. However, tilt and rotations away from the calculated values are required in practice to get to the correct $\underline{g}$.

R-ECCI, unlike cECCI, tilts and then rotates the sample, using the BSE intensity profile to get an orientation by comparing with theoretical profiles (from a simulated ECP). This is the electron channelling orientation determination (eCHORD) [123] method to determine crystal orientation. Once this is done, it is then rotated to the desired $\underline{g}$. EMsoft (open-source) generates the theoretical ECPs in eCHORD. Neither the R-ECCI or cECCI codes are publicly available, and EMsoft is challenging to install. R-ECCI removes the EBSD orientation uncertainty, where the orientation of the highest match metric should theoretically be the correct solution. The authors state a "unique signature" can be obtained using their technique [123, p. 147]. However, theoretical and experimental ECPs typically differ, and the crystal's orientation and/or symmetry mean that other orientations can produce high match metrics despite being inaccurate, producing inaccurate solutions.

Therefore, combining methods 2 & 3 by performing BSE intensity profile matching but limiting the solutions within the EBSD orientation and its experimental

uncertainty is a novel[1] self-consistent approach that improves accuracy and reduces the run time. The code is also written in the MATLAB programming language, so the installation and use are comparatively simpler.
Furthermore, in this thesis, another level of self-consistency is done for the SX meso-cantilevers by using the Kikuchi bands of the low magnification ECP (as described well in Refs [116, 118, 124]).

5.3.2 Method

Using the eCHORD method in Ref [123], the SEM stage tilt (T_{stage}) is set to a low value ($\approx 10°$) and rotated 360°, recording BSE micrographs at intervals. The stage is calibrated to keep the image centre as constant as possible. The BSE intensity at the optic axis is theoretically described by a small circle on a stereographic projection on the ECP. The circle's centre is the untilted orientation, its radius is the T_{stage} value, and changing the SEM stage rotation (R_{stage}) is a rotation about this circle. If the intensity is taken from regions away from the image centre, then the circular path in the stereographic ECP projection is not as strictly followed or invalid if far enough away [125].

eCHORD compares the experimental BSE intensity profile with 1 million theoretical profiles, with the best match being determined with a dot product metric [123]. It is worth noting that each profile was from one simulated ECP each (taking 60 minutes), with image processing and best match indexing taking $>$ 30 minutes and 5 minutes, respectively [123]. The best-matched theoretical and smoothed experimental profiles are similar but not identical.

The disorientation between the crystal orientations obtained in EBSD compared with eCHORD follows a gamma distribution with a peak at 0.74° [123].

From the best match solution, the $\underline{g}$ conditions available are where its circular path crosses the ECP channelling lines [122].

[1] As of 03/12/2023

The original eCHORD paper used $EHT = 15\,\text{kV}$, $I = 2\,\text{nA}$, $T_{stage} = 10°$ [123], but typically in this work $EHT = 30\,\text{kV}$, $I = 2 - 5\text{nA}$, $T_{stage} \approx 10°$, with a working distance $\approx 10\,\text{mm}$. The R_{stage} increments are varied between 1° and 10° due to time constraints of the microscope session and if the sample has been previously analysed. The recommended value for eCHORD for accuracy is 1° [123], but 2° has been used [125].

Method Developments

Where this work develops from that done in R-ECCI is the introduction of a few key features:

1. BSE profiles from small circles within the fundamental region of a master stereographic projection (from Bruker DynamicS in this thesis), which is faster than generating an ECP per profile and allows for non-circular paths.
2. A cross-correlation (CC) metric for matching is used (c.f. dot product), which is phase shift insensitive and gives the best phase shift for each profile.
3. The assessed orientations are done by a square grid on the ECP rather than equal angles in spherical coordinates, removing the bias towards the +ve z-axis, and allows for CC heat maps, which are good for interpretation and could ease future refinement methods to give better accuracy.
4. CC heat maps can indicate if the BSE intensity path is not a circle. A circle will have a circular distribution around the solution's peak in the CC map but will be highly non-circular otherwise (e.g. linear) [2].
5. The best-match solution is pre-informed by the EBSD orientation within the tolerance of the technique. Therefore, a reasonable solution is obtained rather than choosing an erroneous solution from other hot spots of high CC far away and reducing the computation time. The sub-region is a small circle centred about the EBSD orientation, with the radius being the typical absolute orientation uncertainty. 2° was chosen (see section 4.5.2), as it is comparable

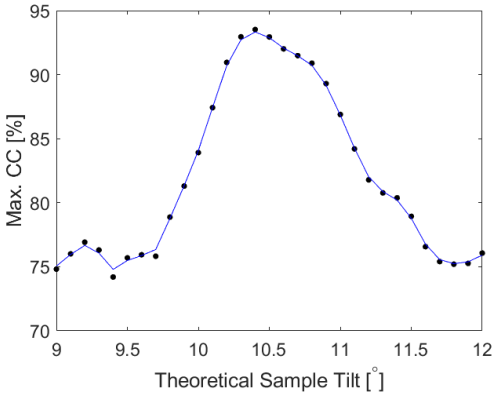
[2]Personal communication with Associate Prof Ben Britton (University of British Columbia) 10/11/2023

with the peak disorientation in eCHORD [123] and is within experimental error [116].

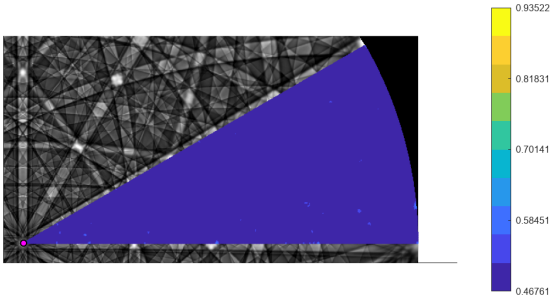
5.3.3 Worked Example: Grown GaN Single Crystal

An undeformed lab-grown single-crystal GaN had BSE micrographs captured with a tilted stage and rotated 360°. The micrographs were collected by Dr Karamched (University of Oxford). The crystal's surface normal is near [001], so the analysis should produce solutions at or near this orientation.

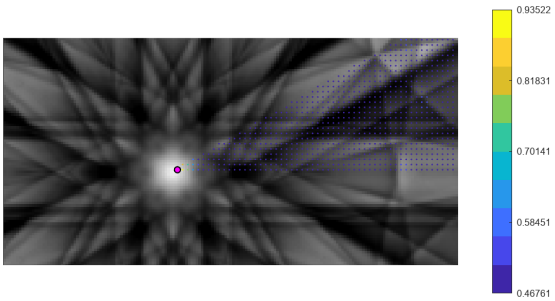
Figure 5.14 shows the analysis over the entire fundamental region with a small circle radius sweep from 9° to 12°. The results not only show that the calculated orientation is near [001] but that the peak CC occurs near 10°, being around 10.40° (fig. 5.14a).



(a) CC as a function of small circle radius (i.e. T_{stage}).



(b) CC heat map under optimum T_{stage}.



(c) CC heat map for optimum T_{stage} magnified around solution.

Figure 5.14: Results for the full fundamental region for [100] GaN sample. "Full" in table 5.2.

Using a sub-region about [001] with a higher resolution shows how the maximum CC profile increases by 1.66% but with similar computational expense (fig. 5.15). Figure 5.15b shows how quickly its value drops away from the expected solution, as 70% is still within good agreement with the correct answer.

Even in this simple case, despite a great visual matching on the ECP, there are discrepancies in z-score normalised intensities, causing the CC not to reach 100%.

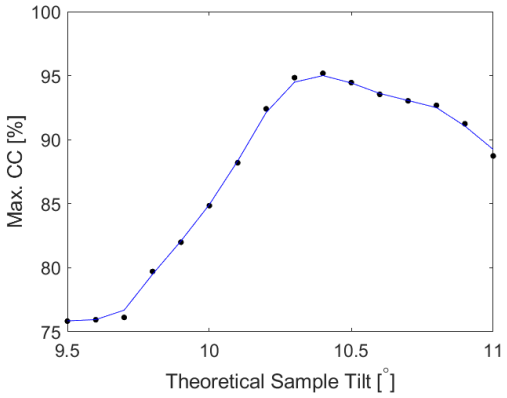
Figure 5.15d is an overlay plot where the experimental profile is overlaid onto the best-match's small circle. The magenta point is the small circle centre (i.e. orientation), and the green point represents the $R_{stage} = 0°$ point unless stated otherwise.

Figure 5.16 shows the CC improves using $T_{stage} = 10.40°$ (c.f. $T_{stage} = 10°$) under the same resolution. However, visually, there is an insignificant improvement when comparing the ECP paths.

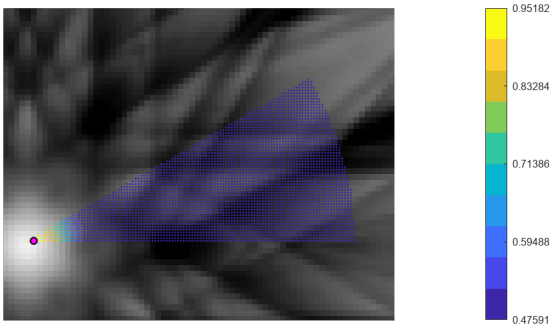
The "original tilt" and "high res." cases in table 5.2 show that refining the resolution and allowing slight deviations in T_{stage} increases CC and gives a lower disorientation.

It is important to note that good matching of the experimental orientation from the new method with the expected orientation can be down to:

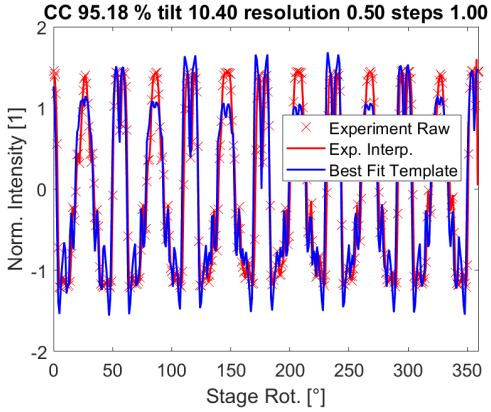
1. A lack of microstructural features.
2. High quality BSE images taken at every 1° stage rotation.
3. A high degree of symmetry in the BSE intensity, which only an orientation close to a zone axis can achieve. Thus, the solution is highly localised in the fundamental region, with that being the appropriate zone axis.



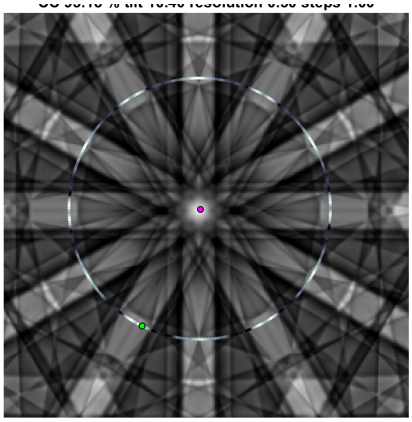
(a) CC as a function of small circle radius (i.e. stage tilt).



(b) CC heat map for optimum T_{stage}.



(c) Experimental BSE with the best match intensity profile.

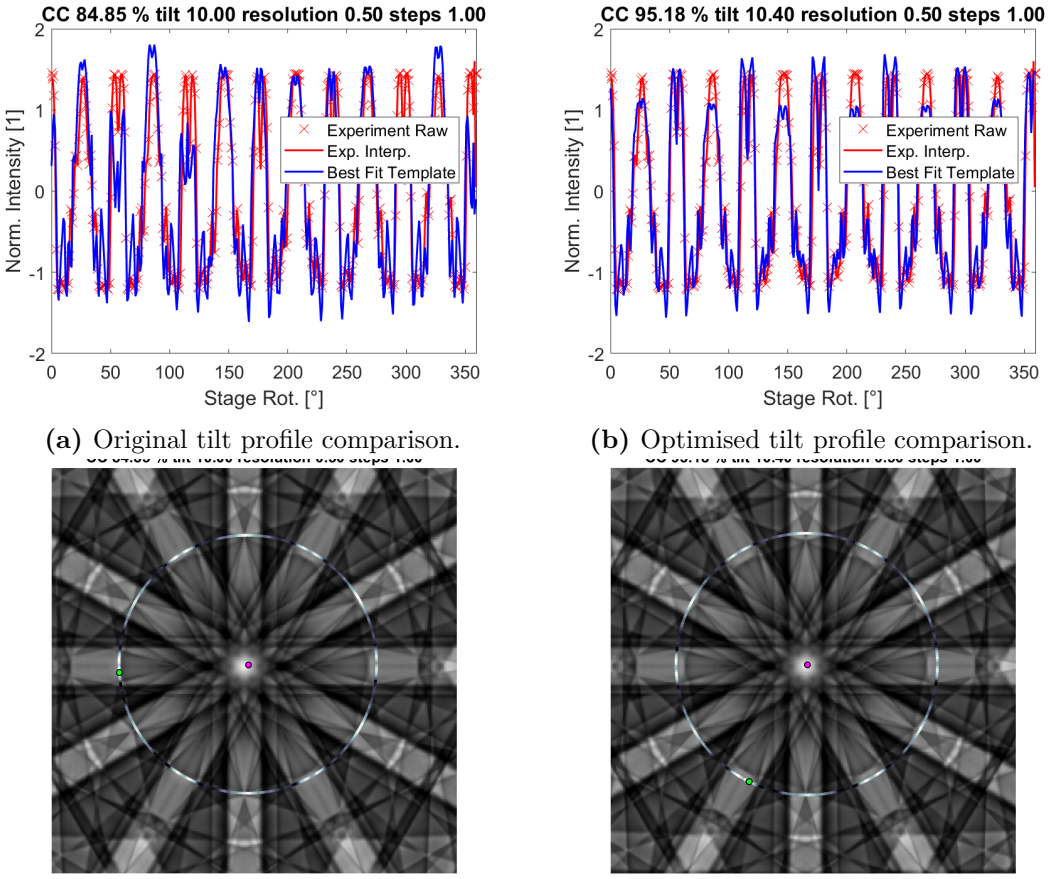


(d) Experimental BSE over best match small circle path.

Figure 5.15: Higher resolution sub-region around [100] for the [100] grown GaN sample. "Refined" in table 5.2.

Table 5.2: GaN new method analysis results under different parameters. The T_{stage} during collection was 10°, and in bold is the optimised value to which the CC is related.

Case ID	Grid Spacing [pixels]	T_{stage} [°]	CC [%]	Disorientation [°]
Full	2.0	9-12 **10.4**	93.5	
Refined	0.5	9.5-11 **10.4**	95.2	
Original Tilt	0.5	10	84.9	0.325
High Res.	0.1	**10.35**	95.4	0.180



(a) Original tilt profile comparison.

(b) Optimised tilt profile comparison.

(c) Original tilt overlay.

(d) Optimised tilt overlay.

Figure 5.16: Results for the grown GaN sample under the high resolution under a fixed tilt and an optimised tilt.

5.3.4 Worked Example: Fatigue Sample

The following is from sample RJSN1, tested in RT air until drastic failure. Figure 5.17 shows the broken cantilever (cantilever direction facing downwards) where its FN is near ⟨100⟩, and its CD is near ⟨110⟩.

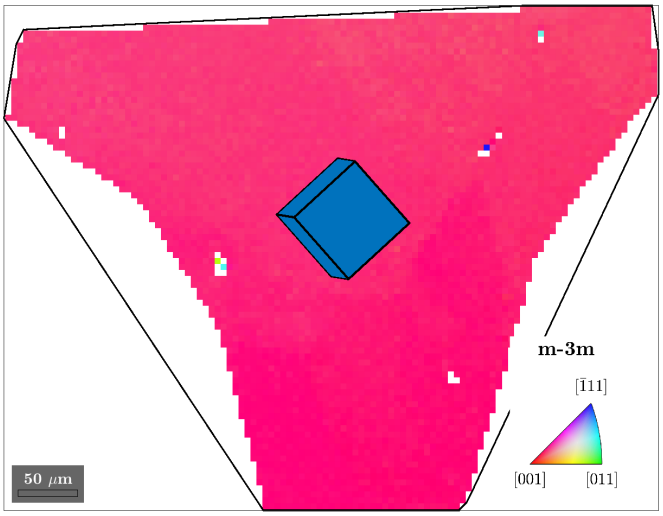


Figure 5.17: MTEX orientation plot for sample RJSN1 after fatigue failure (broken cantilever at the bottom), showing the surface normal's orientation (see the inset inverse pole figure) with a superimposed cubic orientation representation of the crystal orientation. x is set to west, and z is out of plane.

The collected BSE profile was taken at R_{stage} intervals of 1°/5° at 30kV, 2nA, and with $T_{stage} = 10°$.

Complete Fundamental Region vs ROI Analysis

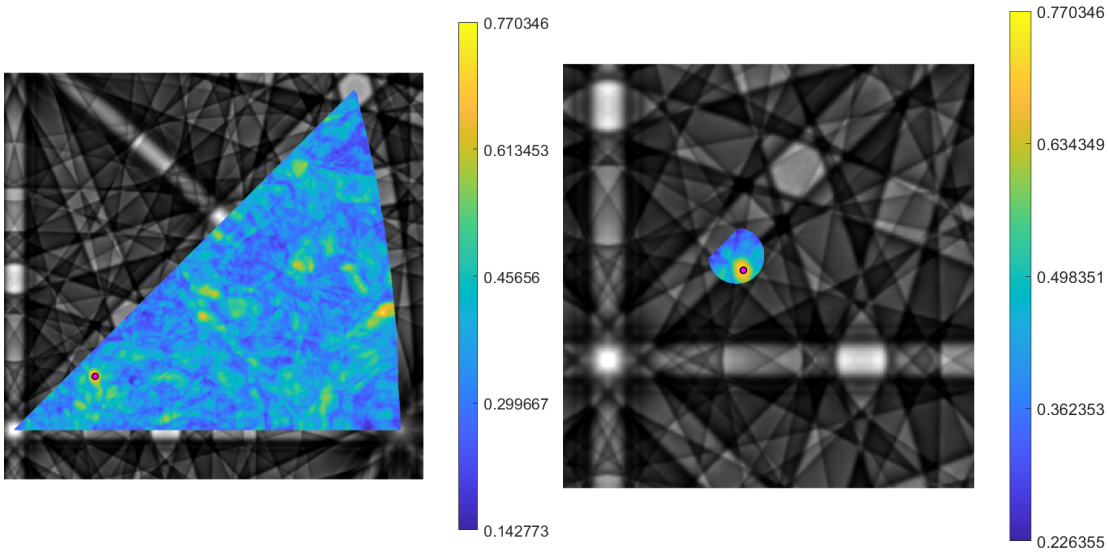
Figure 5.18 compares the analysis over the full fundamental region ("Full") and within a 2° ROI around the EBSD orientation for the same conditions. It shows that the same result emerges in both cases. However, in table 5.3, the sub-region method was ×92.1 faster (performed on a personal laptop with a 2.10GHz CPU & 16 GB RAM).

It is good that both cases are close to the EBSD orientation. However, the presence of other hot spots in fig. 5.18a indicates the importance of pre-informing the analysis to choose an appropriate solution in the case of ambiguity or an erroneous solution having a technically higher CC.

Table 5.3: RJSN1 analysis results under different parameters.

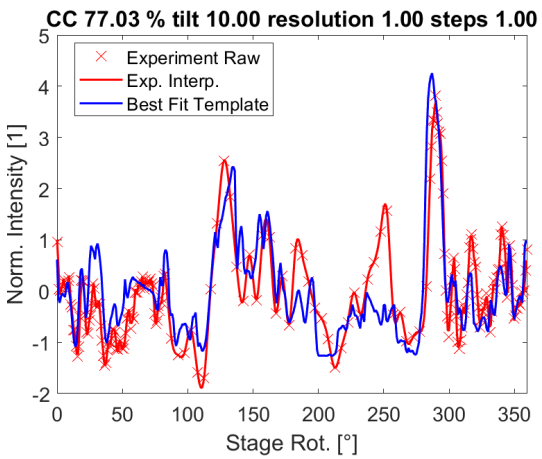
Case ID	Resolution [pixels]	Profiles	T_{stage} [°]	CC [%]	Time [s]
Full	1.00	329,793	10	77.0	120.6
2°	1.00	3,579	10	77.0	2.6
2° tilt coarse	1.00	3579×200	9-11 **10.27**	84.1	237.4
2° tilt fine	0.25	57,597	10.27	84.1	11.9
EBSD Solution	1.00	N/A	10	41.8	N/A

Comparing the z-score profiles (fig. 5.18c), many features are shared with mostly minor discrepancies. The superposition of the experimental profile onto the matched path in fig. 5.18d shows good agreement, where the main discrepancy is the higher brightness seen in the lower region of the small circle (i.e. ≈200-260° in fig. 5.18c).

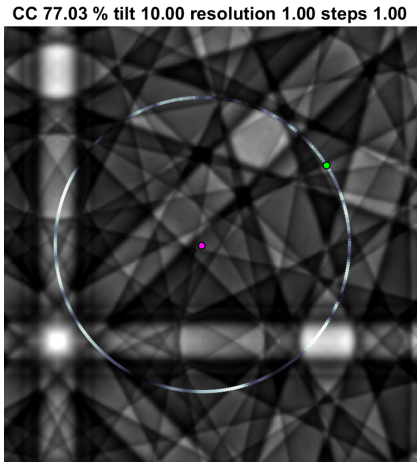


(a) CC heat map - fundamental region.

(b) CC heat map - EBSD 2° small circle.



(c) Experimental and matched theoretical profiles.



(d) Overlay plot.

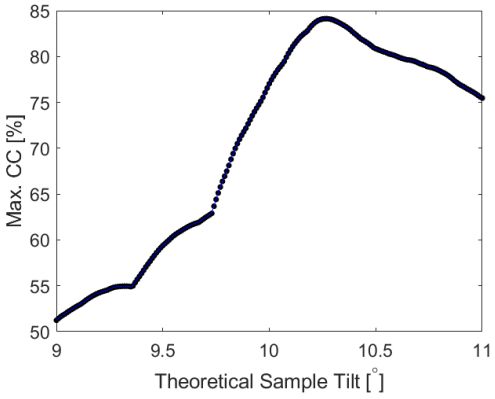
Figure 5.18: Results from novel ECCI orientation method when (a) analysing all orientations across the fundamental region ("Full" in table) and (b) analysing within a 2° small circle around the EBSD orientation ("2°" in table).

Tilt Angle Optimisation & Refinement

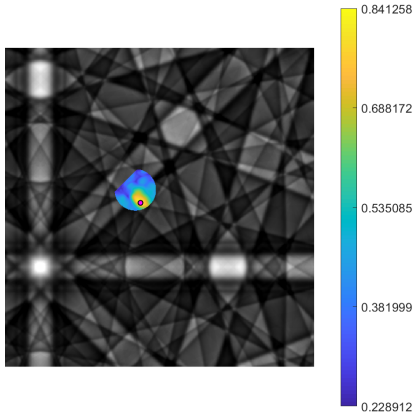
An optimum T_{stage} can be found from the best CC value when sweeping T_{stage} values. This can account for potential geometric inaccuracies (e.g., slopes in the sample, sample holder, etc.). Minor discrepancies between the intended and optimum tilts are not concerning, as the GaN case showed it too. Otherwise, using the same parameters as in section 5.3.4, optimising the T_{stage} substantially increasing the CC by 7.1% (see fig. 5.19). The minor increase of 0.27° in T_{stage} causes a mild

change in the CC heat map distribution and overlay.

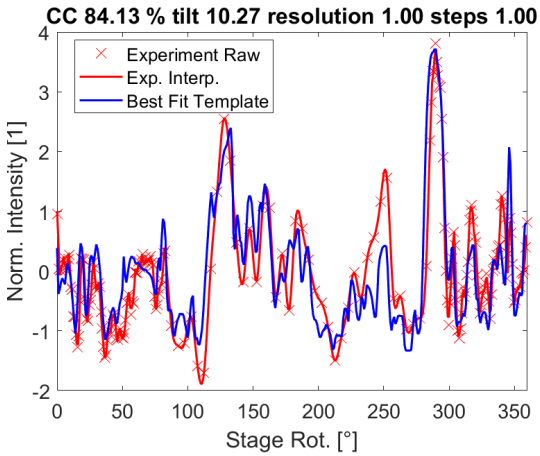
A 1-pixel grid spacing produced similar results but was ≈ 4.5× faster than a 0.25-pixel spacing.



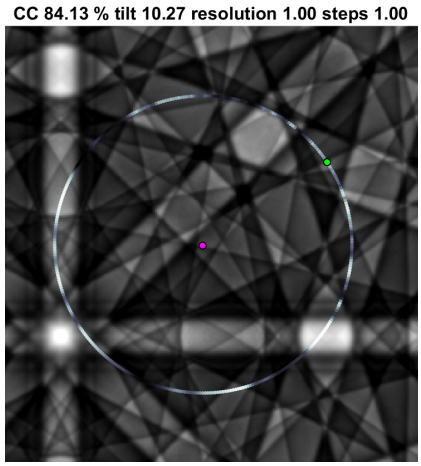
(a) Cross-correlation as a function of small circle radius.



(b) CC heat map.



(c) Profile comparison.



(d) Overlay.

Figure 5.19: Results from novel ECCI orientation method when analysing points within the 2° small circle from the EBSD orientation. Grid spacing in (a) is 1 × 1 pixels.

Validation

To create a self-consistent model of the best orientation estimate and the rotational alignment (magenta & green points respectively in fig. 5.18d). There are two other methods of validating the result.

The first is to tilt the EBSD orientation along the tilt axis in MTEX by the T_{stage} to compare where that lies with the equivalent point in the matched profile,

thus validating both phase and orientation. However, this method propagates any uncertainty obtained from EBSD, making it convenient but not completely reliable.

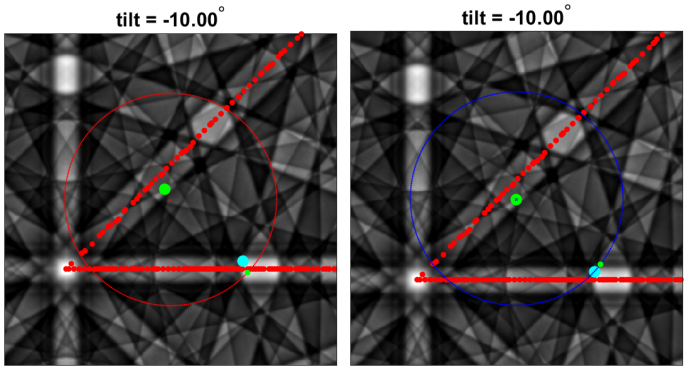
Secondly, see if the observed Kikuchi bands in the low magnification ECP agree with the best match. This is more useful, but it is only viable in large-grained or single-crystal samples.

These two methods are described next.

MTEX Tilt Validation

Figure 5.20 shows how a tilt of $-10°$ in MTEX (x west & z out of plane) on the EBSD orientation produces results which best match with that obtained by the profile matching used in fig. 5.18, as a tilt of $+10°$ would move the cyan points to the diametric opposite location on the small circle.

One can compare the MTEX tilt result when the surface normals are from the best-matched orientation (fig. 5.20a) and when from the EBSD surface normal (fig. 5.20b). Both cases agree well with the MTEX tilt results, with the EBSD version unsurprisingly agreeing better as its errors are propagated.



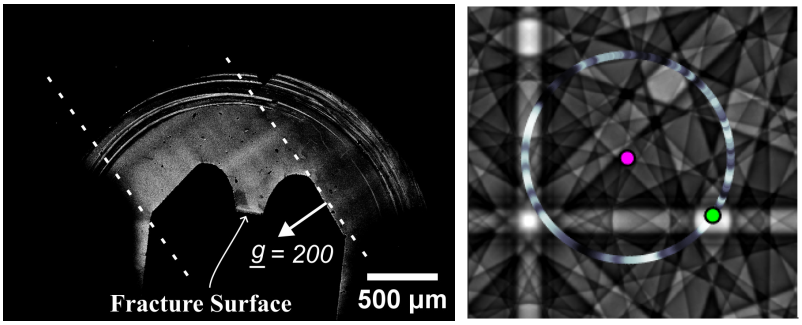
(a) Highest CC matched profile path.

(b) Mean EBSD orientation profile path.

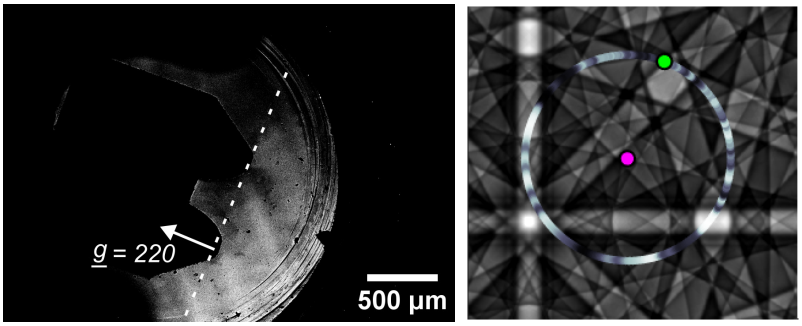
Figure 5.20: MTEX tilt validation under the same conditions as fig. 5.18 i.e. $T_{stage} = 10°$. The small green highlighted points on the small circles correlate with the nearest point to $R_{stage} = 285.5°$. The large green point represents the EBSD orientation small circle centre, with its value when tilted by $-10°$ in MTEX the large cyan point.

ECP Validation

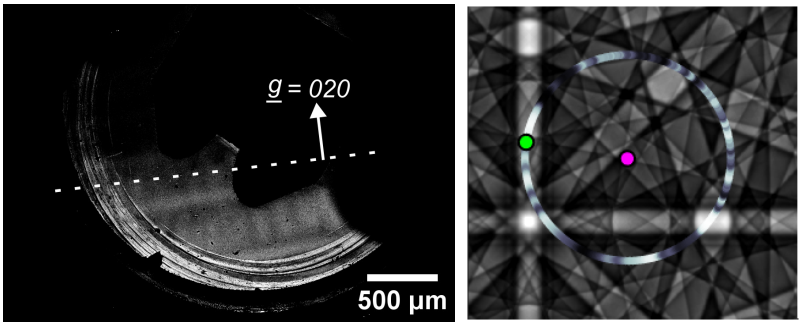
Using the "2° tilt fine" case in table 5.3, the Kikuchi bands observed in the ECPs in fig. 5.21 match with their respective $\underline{g}$ conditions from the novel method. By rotating the EBSD map in MTEX to match the stage rotation, the specific $\underline{g}$ vectors can be found. The channelling lines are perpendicular to their respective $\underline{g}$ vector.



(a) [200] Kikuchi band.



(b) [220] channelling line.

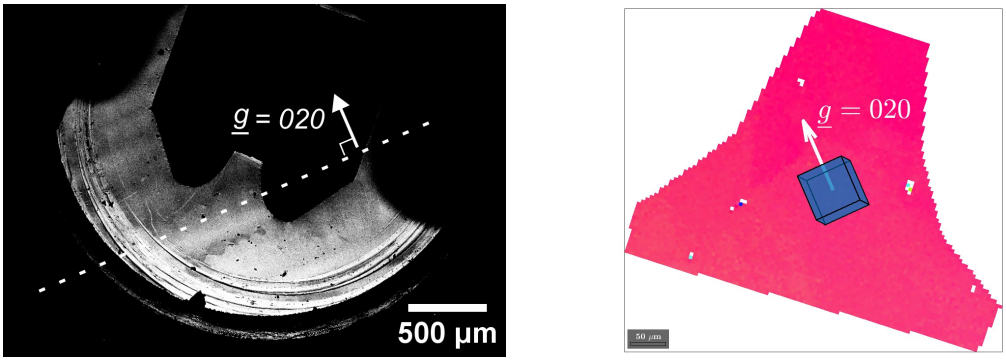


(c) Near the [020] channelling line.

Figure 5.21: BSE images (left) with their matched BSE signal small circle paths (right). The $\underline{g}$ and the channelling lines (dashed lines) are found by rotating the MTEX EBSD map.

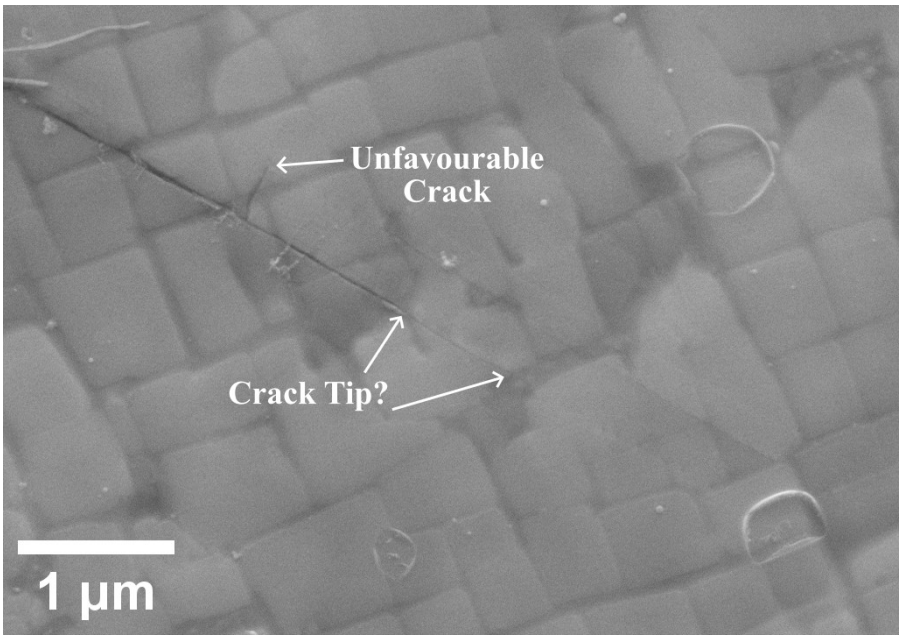
5.3.5 Example ECCI Micrograph

ECCI was done under the $\underline{g} = 020$ diffraction (fig. 5.22) (similar to fig. 5.21c), and the collected SE and BSE (i.e., ECCI) micrographs around a crack tip are in fig. 5.23. By comparing the two micrographs, the dislocations and defects are distinguished as they have greater contrast in the BSE signal than in the SE signal.

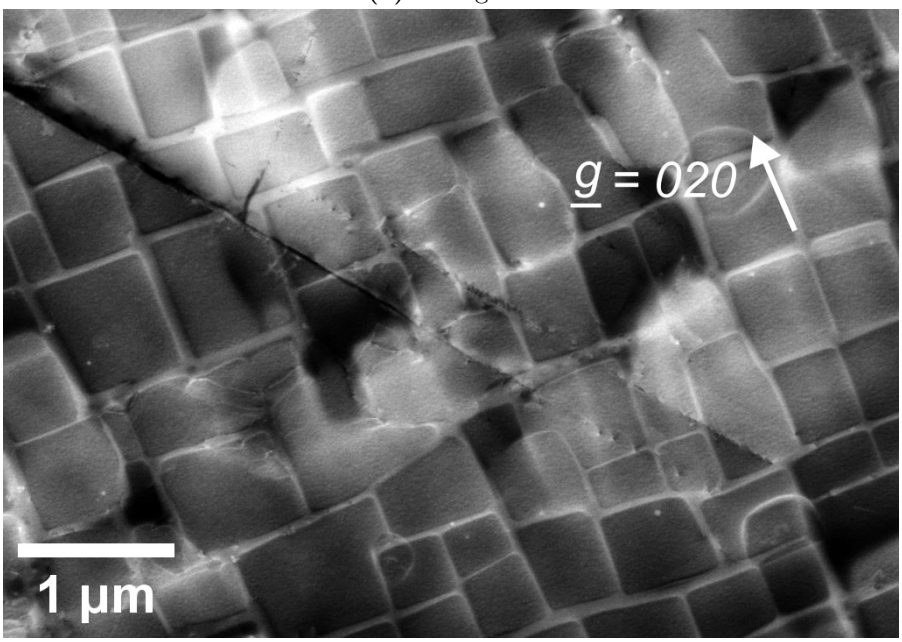


(a) BSE ECP. **(b)** Rotated EBSD map in MTEX.

Figure 5.22: ECCI diffraction on RJSN1 where (a) is the ECP channelling line in the BSE signal, and (b) is the $\underline{g} = 020$ determination from MTEX



(a) SE signal.



(b) BSE signal.

Figure 5.23: Micrographs of a fatigue crack in sample RJSN1 under the $\underline{g} = 020$ diffraction condition.

5.3.6 Summary

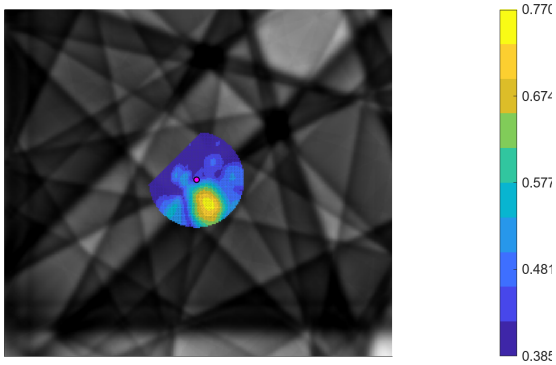
The disorientation from the EBSD crystal orientation is 1.177° for the first two cases where $T_{stage} = 10°$, and then becomes near 1.386° when $T_{stage} = 10.27°$. These disorientation values are not too dissimilar from those measured in the original eCHORD paper [123]. The increase in angular discrepancy from the EBSD orientation would indicate a worse match; however, the cross-correlation increases from 77.03% to 84.14%, which is still within the acceptable angular discrepancy range based on the GaN case.

Pre-informing the analysis with an EBSD orientation significantly increases the performance, which is not a feature in eCHORD. It is also beneficial in selecting a result within the absolute orientation accuracy of EBSD. Figure 5.24 shows the results if only the EBSD orientation and intended T_{stage} were used, like in cECCI, but with subsequent profile phase matching via CC. Using this process results in a significantly lower CC value.

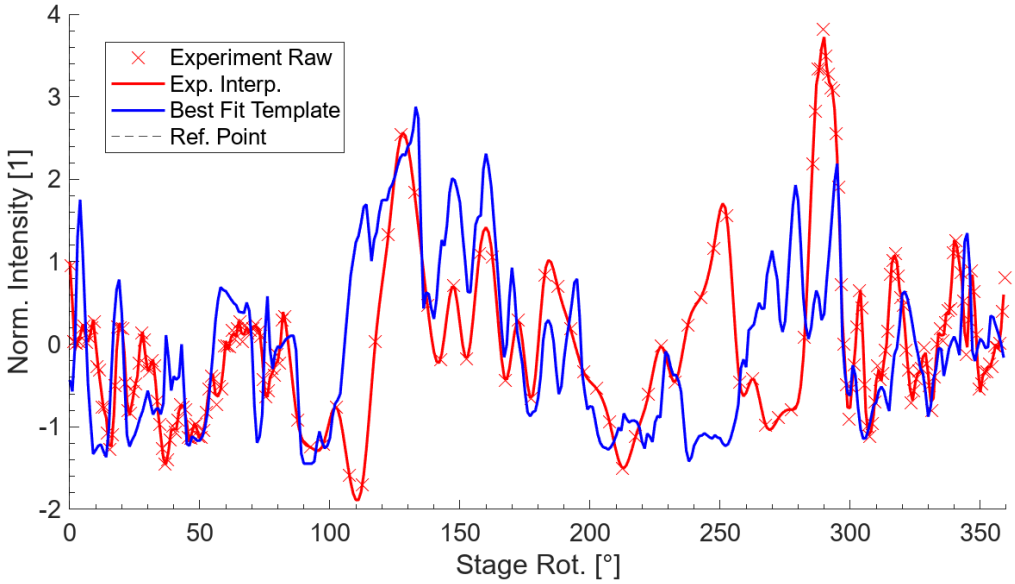
Future Work

Further development is planned for this code, and the following are some of these ideas:

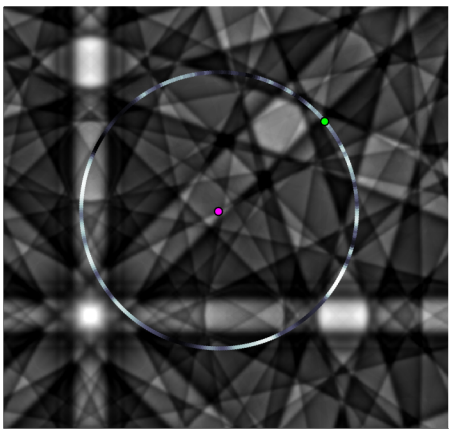
- Using the EBSD identified grains to automatically extract and match the BSE intensities to speed up analysing polycrystals.
- Optimise code to improve the time to match a grain.
- Use two intensity profiles from two different tilts for the same crystal to improve accuracy and reliability.



(a) CC map.



(b) Intensity profiles.



(c) Intensity superimposed onto matched ECP path.

Figure 5.24: The predicted results using the EBSD derived orientation and inputted stage tilt ($T_{stage} = 10°$).

6
Environment Testing

Contents

6.1 Introduction 131
6.1.1 Common Fractography Features 131
6.2 Ambient Electropolishing Effect 133
6.2.1 Sample Preparation 134
6.2.2 S-N 135
6.2.3 Conclusions 140
6.3 Room Temperature Air vs Vacuum 141
6.3.1 Room Temperature Vacuum Rig 141
6.3.2 S-N 142
6.3.3 Fractography Air 146
6.3.4 Fractography Vacuum 151
6.3.5 Discussion 157
6.3.6 Conclusions 161
6.4 Room Temperature ECCI 162
6.4.1 Sample I5 162
6.4.2 Sample RJSK2 173
6.4.3 Conclusions 181
6.5 Intermediate Temperature 183
6.5.1 Intermediate Temperature Rig 183
6.5.2 Intermediate Temperature Air 186
6.5.3 IT Air Discussion 204
6.5.4 Intermediate Temperature Vacuum 208
6.5.5 ECCI 217
6.5.6 IT Vacuum Discussion 229
6.5.7 IT Conclusions 231
6.6 Chapter Summary 233

6.1 Introduction

This chapter addresses the many environmental effects, both temperature and gaseous medium, that are unexplored or can be enriched by the opportunities given by the fatigue technique used in this thesis.

Two temperatures were investigated, those being room temperature (RT) & intermediate temperature (IT). Similarly, the two gaseous environments tested were air and vacuum to investigate the effect of p_{O_2}. The samples were electropolished (EP) or not (i.e. No-EP). The seven testing combinations are summarised in the testing rubric table 6.1.

Those samples tested under RT air are also known as *ambient* due to being in laboratory conditions.

Table 6.1: Environmental Testing Rubric.

	RT	**IT**
Air	No-EP, EP	EP
Vacuum	No-EP	EP

Before discussing the results, section 6.1.1 first explains how this thesis decides on the initiation and final exit sides, as this is used throughout each condition.

6.1.1 Common Fractography Features

Fracture Initiation & Exit

Samples that have not fully fractured give insight into features that indicate which side of the sample the fatigue crack initiated from (i.e. *initiation* side) and which side it has grown towards and eventually exits (i.e. *exit* side).

RJSK2 is a clear example, as only one side has an open crack. The initiation side (fig. 6.1a) has shearing mode cracks with minimal surface plasticity but with bifurcation. The exit side (fig. 6.1b) has no open crack and shows extensive surface

plasticity via slip traces. The extensive slip on the bottom side associated with the large plastic zone can be explained by the larger stress ahead of the long fatigue crack. As fracture leads to greater coupling, this bends the cantilever more, increasing the stress.

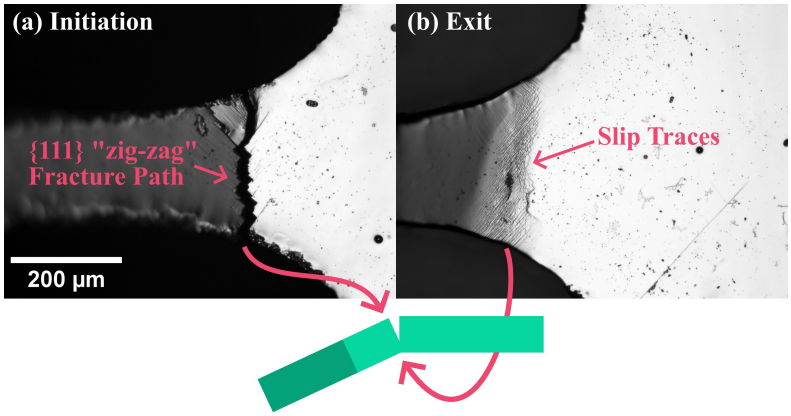
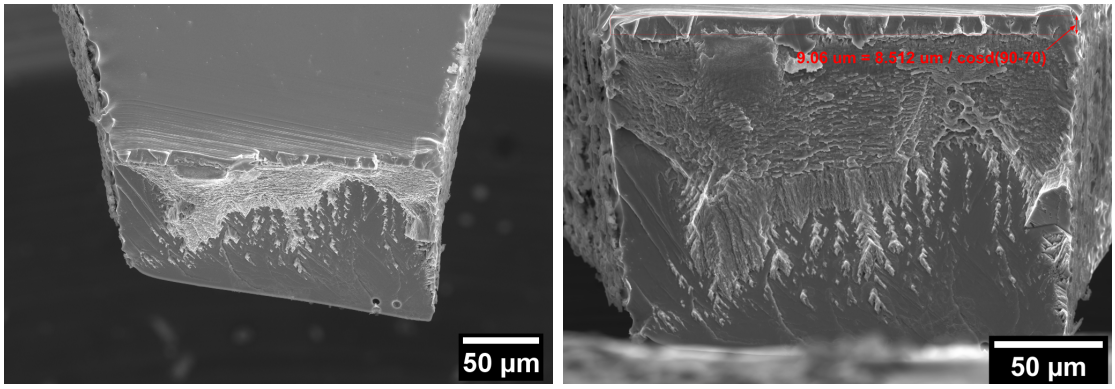


Figure 6.1: Optical images after drastic failure for sample RJSK2 on both sides with a schematic shown in (c). Its crystal orientation is CD⟨100⟩ FN⟨100⟩.

Exit Side Facets

One feature to note is the frequent facets that appear on the heavily slipped exit side of the fracture surface. Figure 6.2 shows an example of this in an RJS ⟨110⟩ sample where the general depth of these facets is around 9.06 µm. They are highly similar to those sometimes seen for conventional frequency bending fatigue of SXNBS microcantilevers as in Refs [62, 63] (see section 2.3.3), even in the approximate proportion of the fracture surface depth. Cracks can initiate from surface intrusions on the opposite side of the first initiated primary fatigue crack and join it [63, §4.3]. The tests in Ref [63] were run at resonance ($R = -1$ is assumed).

Hence, the proposed mechanism in this work for exit facet formation is that they initiate from intrusions sometime after the critical crack initiates; it could also be aided by damage build-up along these {111} planes. Therefore, it propagates from the free surface to the main fatigue crack tip.



(a) Low 20° tilt showing the substantial {111} slip bands.

(b) 70° tilt showing the exit facets following along the {111} slip bands.

Figure 6.2: SE fractography of sample RJSN1 (CD⟨110⟩ FN⟨100⟩) under two stage tilts and with exit facets towards the top fracture exit surface.

6.2 Ambient Electropolishing Effect

Prior work in the research group has found no significant differences in ambient fatigue performance between electropolished (EP) and not electropolished (No-EP) for CMSX-4, Ti-6Al-4V, and stainless steel mesocantilevers. The CMSX-4 samples were of a ⟨100⟩ CD & ⟨110⟩ FN[1]. However, this investigation still was done for two reasons:

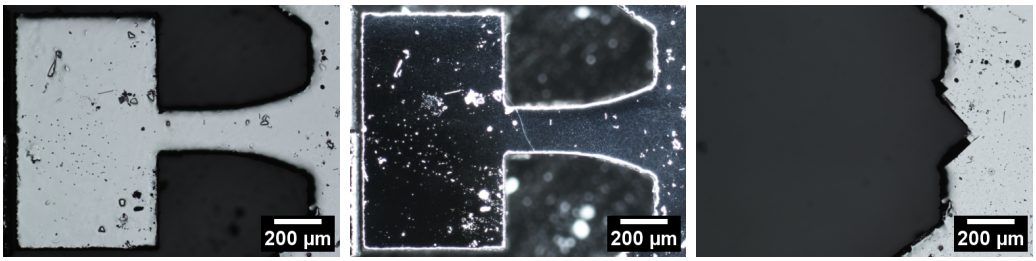
- To ascertain whether electropolishing had a strong effect on the S-N results for the ⟨100⟩ CD ⟨100⟩ FN samples in this work. This is important as some SEM techniques relied on an electropolished surface.
- The ⟨100⟩ CD ⟨100⟩ FN samples frequently had fatigue cracks initiate on the corners where the base and cantilever attach (aka *corner cracking*). So, electropolishing was done to see if it could mitigate this phenomenon.

To investigate this, a good baseline of 20 No-EP samples was collected to compare with the 10 EP samples and 8 RT Vacuum No-EP samples (section 6.3).

[1]Dr J Gong, unpublished work.

6.2.1 Sample Preparation

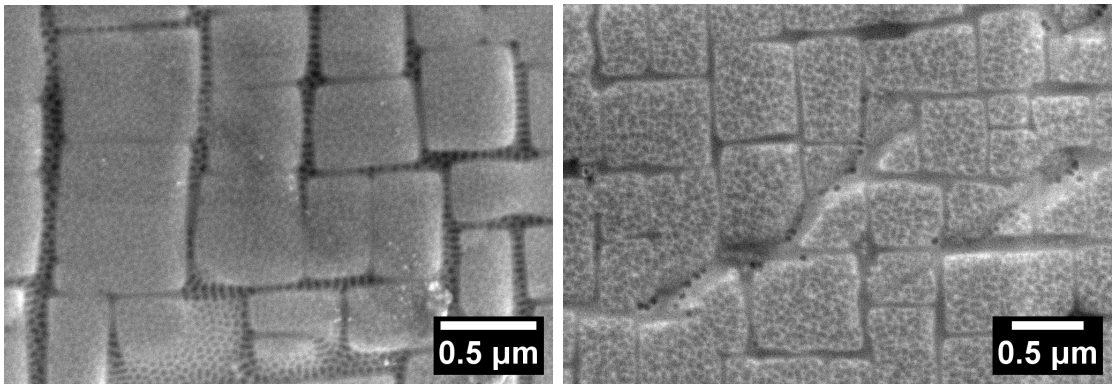
The EP samples were from another foil from the same batch as the No-EP samples, so they should have similar SXOs of near ⟨100⟩ CD and FN. The same mesocantilever design was used in both, and they were electropolished for 60 s (one was 30 s). The optical micrographs (fig. 6.3) show that electropolishing successfully removed/reduced the scratches from previous grinding steps during the sample preparation. Electropolishing exposed and enlarged surface and subsurface pores, and formed mild and smooth undulations of the surface and near the edges.



(a) Bright-field. **(b)** Dark-field. **(c)** Bright-Field Fatigued.

Figure 6.3: OM images of an electropolished sample (sample I3).

As fig. 6.4 shows, electropolishing causes preferential etching of the γ channels, highlighting the cuboidal $\gamma-\gamma'$ microstructure. Electropolishing artefacts sometimes occurred, whose exact origins were not investigated but could be related to initial oxide formation.



(a) Parallel banding or dots in the γ. Interconnect between γ and γ' can occur.

(b) Script-like features within γ' and dots at $\gamma-\gamma'$ interface.

Figure 6.4: SEM images of polishing artefacts examples surface (EP sample I9).

6.2.2 S-N

The FEM for both campaigns in fig. 6.5 show that statistically, the median cantilever stress-per-angle (ω) distribution of the EP samples is shifted slightly lower than the No-EP samples. A lower ω is expected due to their reduced thicknesses.

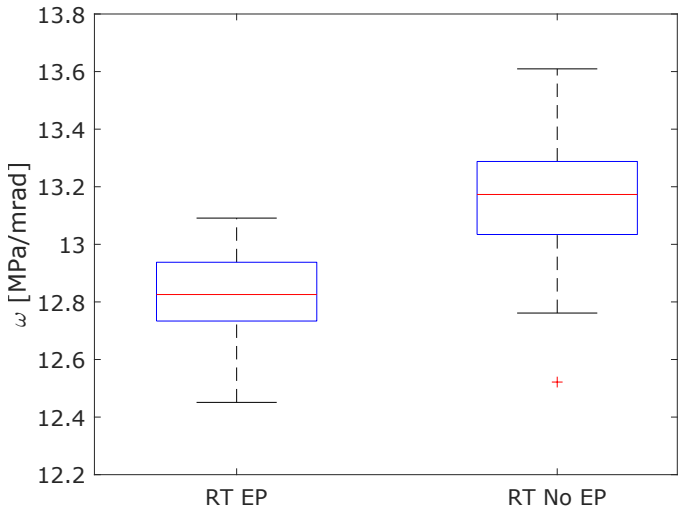
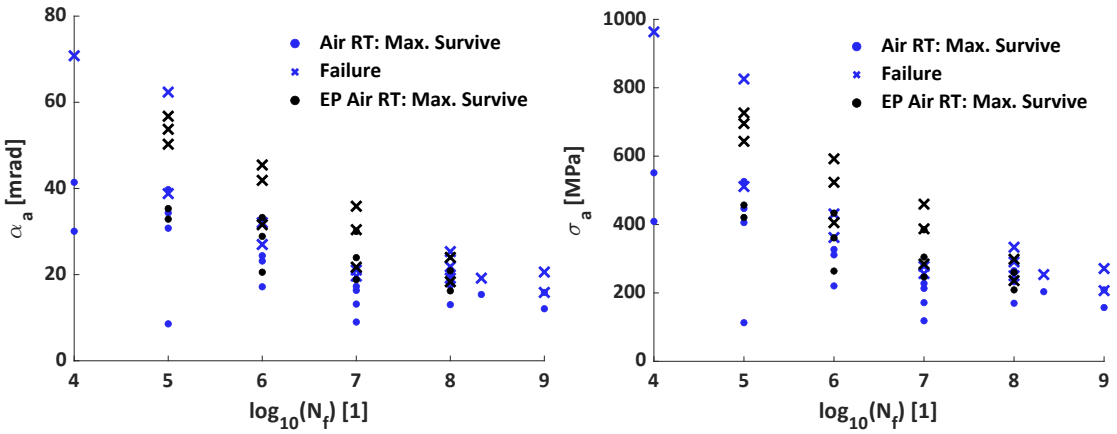


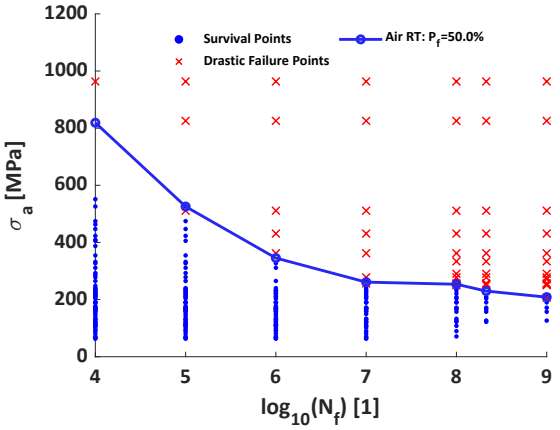
Figure 6.5: The stress-per-angle (ω) box plots of the median ω values of the samples for RT EP and RT No-EP.

In the bending angle amplitude vs number of cycles (A-N) plot (fig. 6.6a), the EP performance is similar if slightly improved than No-EP. However, the slightly lower ω (fig. 6.5) does not bring the two S-N data points significantly closer together in fig. 6.6e. The Basquin curves show that the EP data is within error with the No-EP results but is systematically higher by 56 MPa (mean average for $N_f = 10^5 - 10^8$).

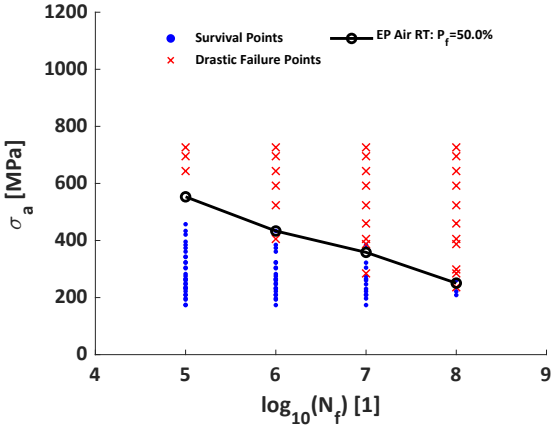


(a) A-N

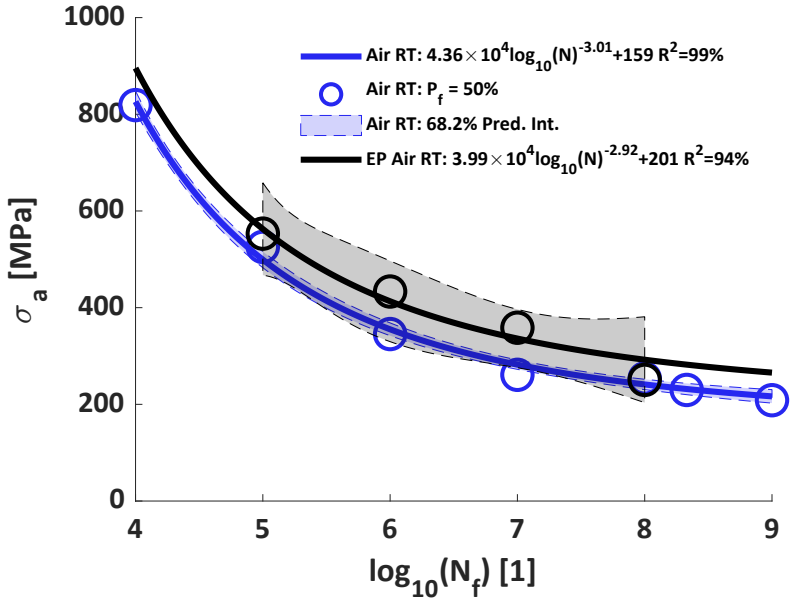
(b) S-N



(c) Propagated No-EP S-N



(d) Propagated EP S-N



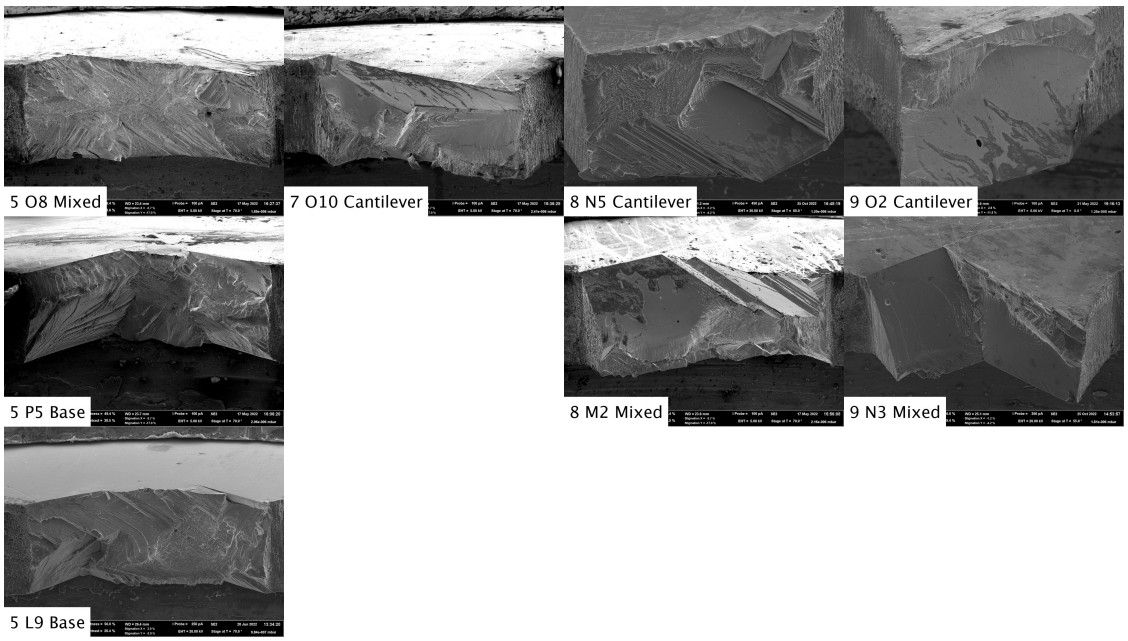
(e) S-N with Basquin-like curve fits

Figure 6.6: Fatigue results for RT air EP vs No-EP.

Table 6.2: RT air No-EP vs EP fatigue results. Basquin-like fits are of the form $\sigma_a = a \cdot \log_{10}(N)^b + c$. Jeffrey's prior was set to 'none'.

	No. Samples	a [MPa]	b [1]	c [MPa]	R^2
RT Air No EP	20	4.36×10^4	-3.01	159	99%
RT Air EP	10	3.99×10^4	-2.92	201	94%

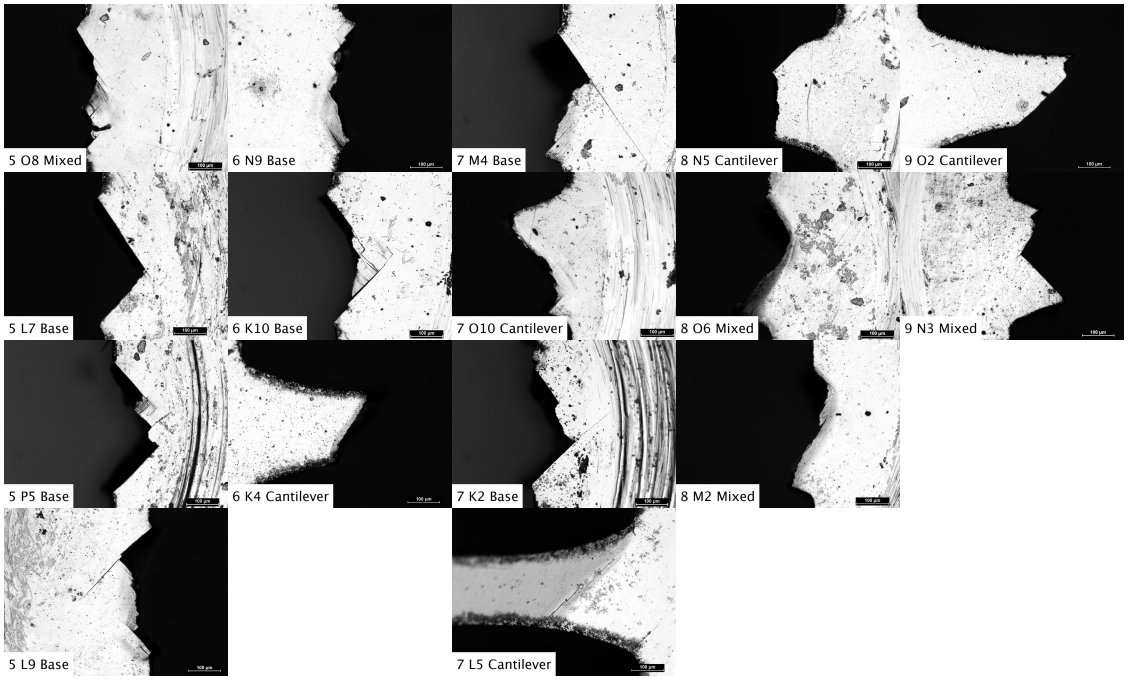
Comparing the optical micrographs in figs. 6.7 and 6.8, the proportion of the critical fracture path occurring within the main body of the cantilever ("cantilever" type) has not significantly increased after electropolishing, and corner cracking is still prevalent, leading to failure located completely within the base ("base") and a mixture of cantilever and base ("mixed"). Additionally, the SEM fractographs of the EP samples were similar to their No-EP counterparts (more details in section 6.3.3), indicating that fatigue and fracture mechanisms have not been altered.



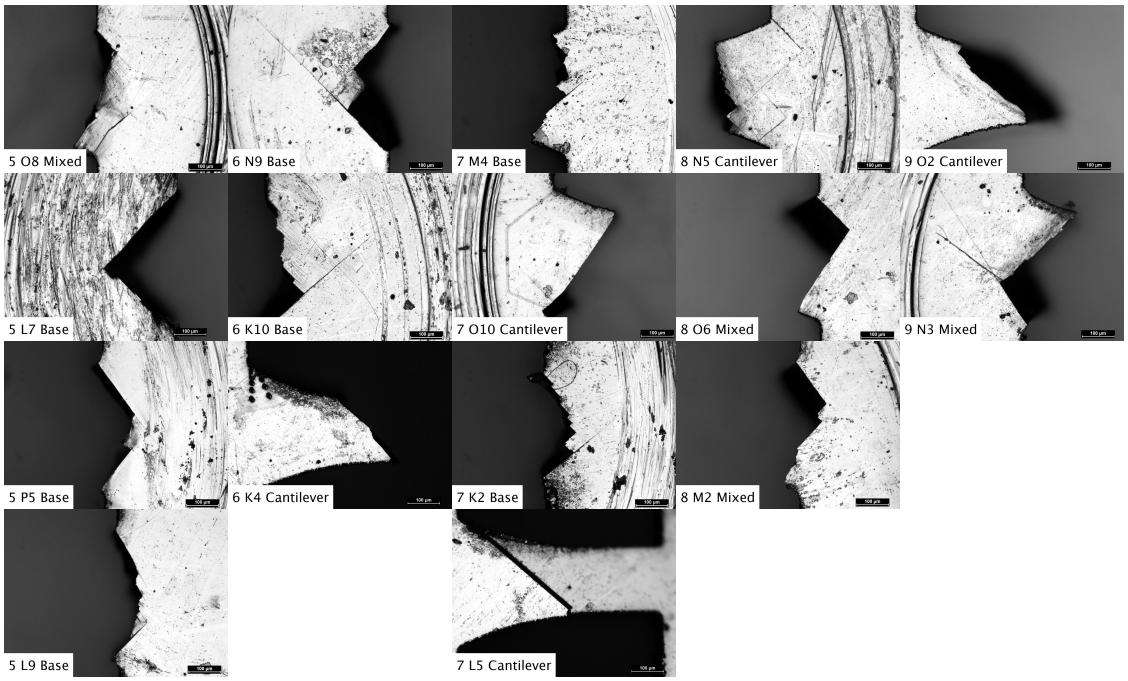
(a) SEM

Figure 6.7: RT air **no-EP** SEM fractography Results. Top-to-bottom indicates highest-to-lowest sample fatigue stress, the numbers and columns indicate the decade (i.e. $N_f = 10^x$), the letter-number combination is the sample ID, and the type of failure is at the end. OM has been grey-scaled.

(Cont. Next Page)

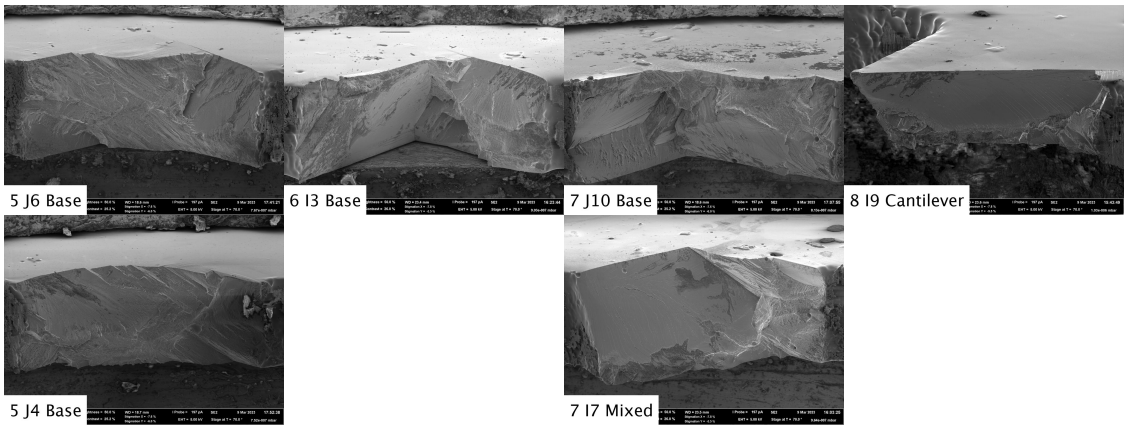


(b) OM side 1

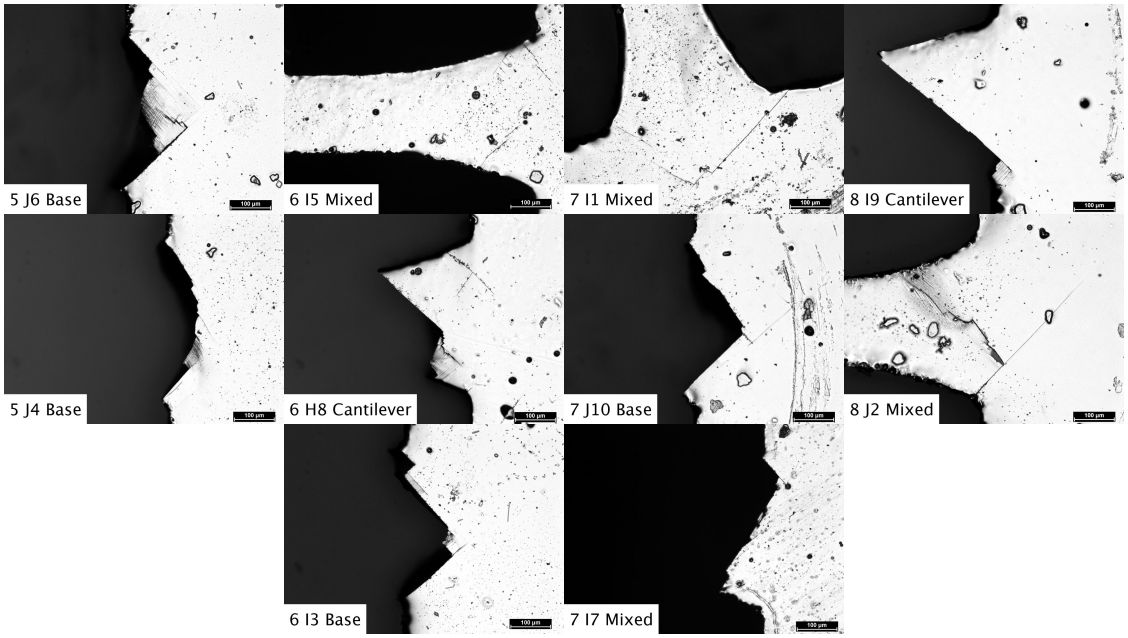


(c) OM side 2

Figure 6.7: RT air **no-EP** SEM fractography Results. Top-to-bottom indicates highest-to-lowest sample fatigue stress, the numbers and columns indicate the decade (i.e. $N_f = 10^x$), the letter-number combination is the sample ID, and the type of failure is at the end. OM has been grey-scaled.



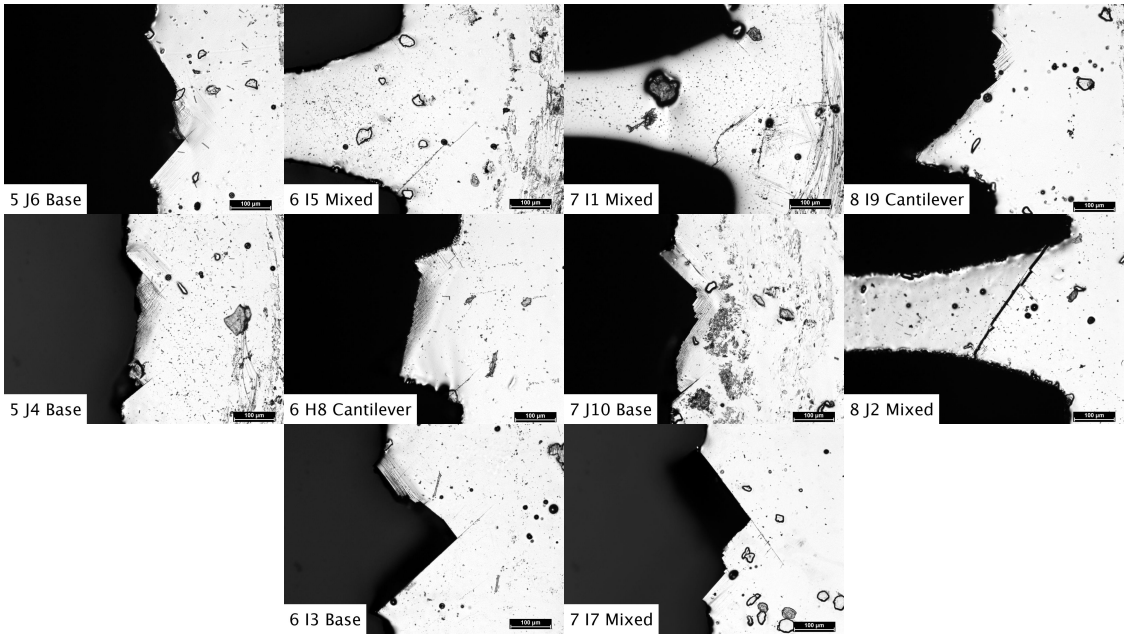
(a) SEM



(b) OM side 1

Figure 6.8: RT air **EP** fractography Results. Top-to-bottom indicates highest-to-lowest sample fatigue stress, the numbers and columns indicate the decade (i.e. $N_f = 10^x$), the letter-number combination is the sample ID, and the type of failure is at the end. OM has been grey-scaled.

(Cont. Next Page)



(c) OM side 2

Figure 6.8: RT air **EP** fractography Results. Top-to-bottom indicates highest-to-lowest sample fatigue stress, the numbers and columns indicate the decade (i.e. $N_f = 10^x$), the letter-number combination is the sample ID, and the type of failure is at the end. OM has been grey-scaled.

6.2.3 Conclusions

Electropolishing smooths out sharp features like scratches and exposes subsurface pores.

A negative consequence is that it introduces greater sample dimension variation, making comparing samples and testing campaigns more complex. Therefore, minimising the degree of electropolishing is recommended. The samples' failure did not change greatly from the un-electropolished equivalent. They had similar fractography and were still strongly affected by initiation at the corners. Importantly, electropolishing did not alleviate this corner cracking issue, indicating it is not due to surface quality. The minor improvement in the S-N could be due to reduced sharpness of features, so despite similar fracture behaviour, the same features that cause failure now take a greater σ_{amp} to initiate and fail.

6.3 Room Temperature Air vs Vacuum

6.3.1 Room Temperature Vacuum Rig

Figure 6.9 shows that the RT vacuum rig consists of 3 main parts: the UFT rig, a small steel chamber with four ports, and a two-stage vacuum pump. A spirit level was used to ensure the setup was level during testing.

The chamber has a window attached opposite the horn's end. The entrance for the horn has an o-ring and vacuum grease to ensure an air-tight seal. One port is attached to the vacuum pump (via a bellow), and the final port is blanked off.

The small chamber achieves 10^{-6} mbar pressure after around 15 min and a high vacuum of 10^{-8} mbar is achievable under a few hours. The p_{O_2} in ambient conditions is estimated to be 209.83 mbar whereas under vacuum it's estimated to be 2.07×10^{-9} to 2.07×10^{-7}mbar (see appendix C).

Two spots are generated by the window when the laser is aimed at the sample within the chamber due to its two surfaces. These reflections are easily accounted for in the analysis because they are stationary during testing.

It should also be noted that this setup does not actively cool or heat the sample or the horn, though compressed air is used to cool the actuator.

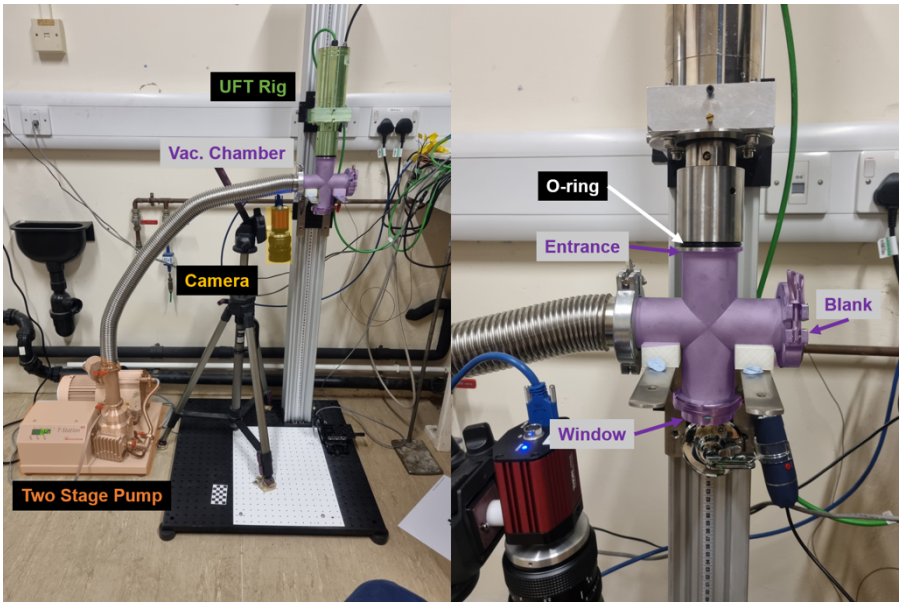


Figure 6.9: The room temperature vacuum UFT rig setup. The different components are labelled.

6.3.2 S-N

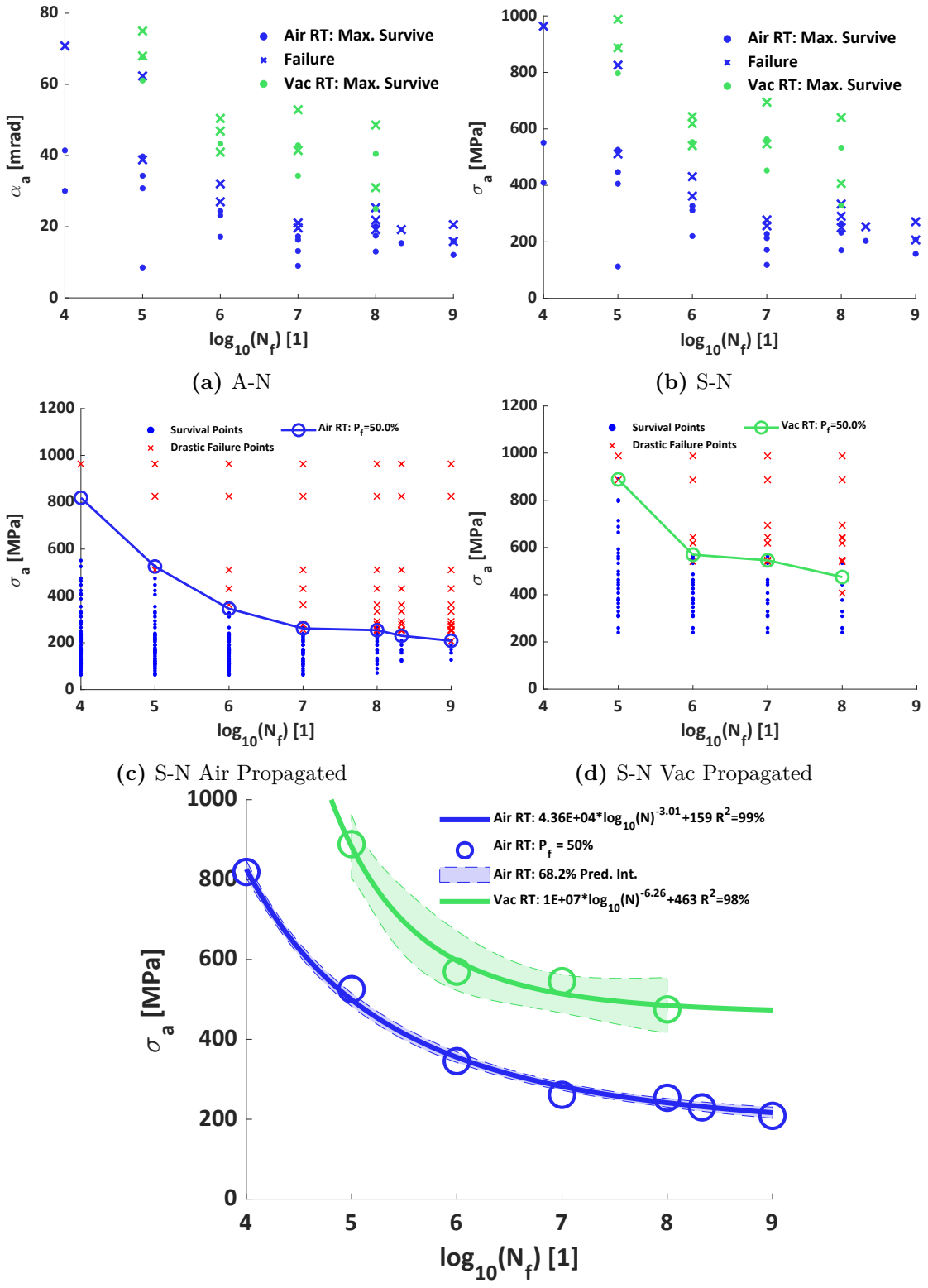
Both testing campaigns were done with the standard mesocantilever design, un-electropolished samples (i.e., 4000-grit finish), with a ⟨100⟩ CD ⟨100⟩ FN.

The RT air campaign used 20 samples, and the RT vacuum used 8; the discrepancy is because the RT air results are used as the baseline, so it needed a high degree of confidence.

Figure 6.10 shows the fatigue results from raw A-N data through to binomial logistic Basquin S-N curves. As both campaigns weren't electropolished, sample dimension variability is low, and the samples have similar ω values, making their S-N and A-N data comparable (fig. 6.10). Figure 6.10e shows a systematic and significant performance improvement when going from air to vacuum by 256 MPa (mean average for $N_f = 10^5 - 10^8$). The difference is more significant than seen in section 6.2.

Table 6.3: RT air & RT vacuum fatigue results (both no electropolishing). Basquin-like fits are of the form $\sigma_a = a \cdot \log_{10}(N)^b + c$. Jeffrey's prior was set to 'none'.

	No. Samples	a [MPa]	b [1]	c [MPa]	R^2
RT Air No EP	20	4.36×10^4	-3.01	159	99%
RT Vac. No EP	8	1.00×10^7	-6.26	463	98%



(a) A-N

(b) S-N

(c) S-N Air Propagated

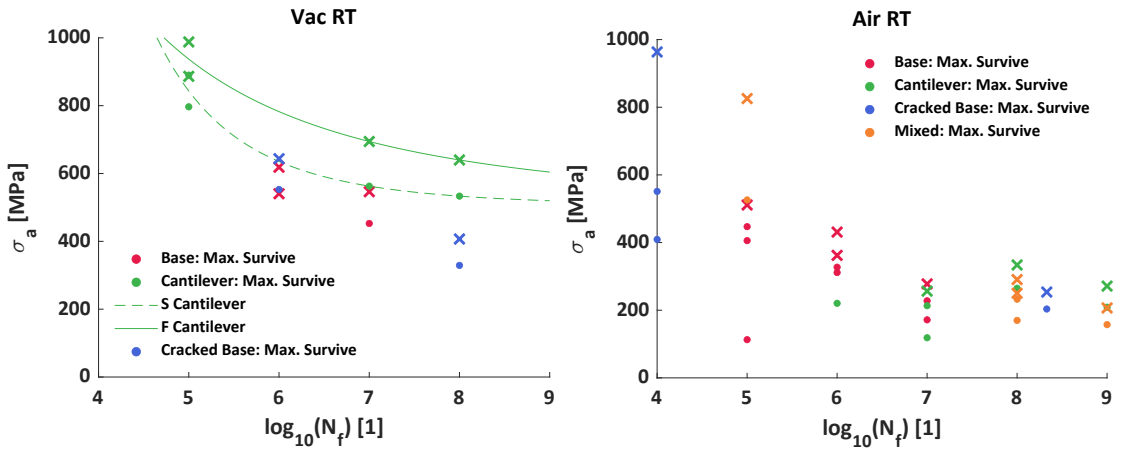
(d) S-N Vac Propagated

(e) S-N + Basquin-like curves

Figure 6.10: A-N & S-N data for RT air and vacuum.

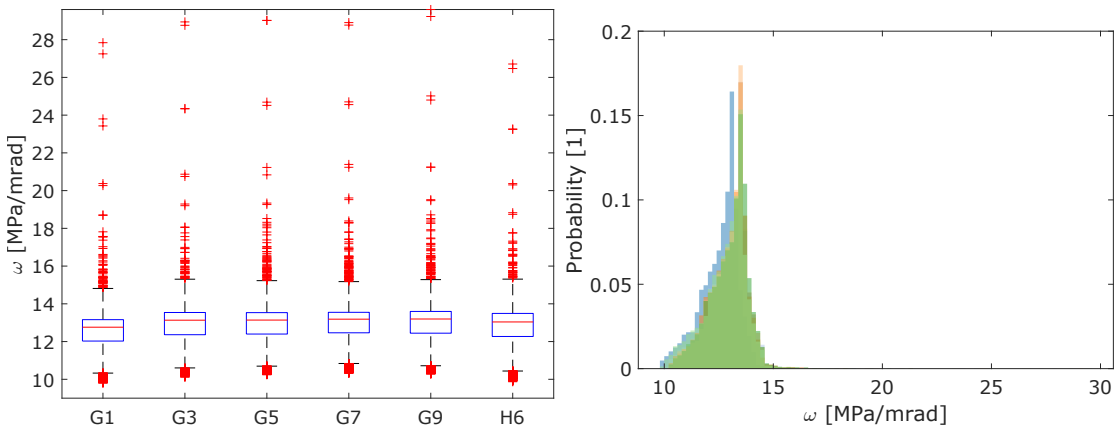
The spread in the vacuum data is larger. Separating the data by the failure location (fig. 6.11a) shows those within the main section of the cantilever have a greater α_{amp} than those which failed at the base or cracked at the base. The RT air results show a weaker effect when doing this, but it still generally performs better when the failure is more within the cantilever, i.e. cantilever/mixed over cracked base and base.

To explain this, fig. 6.13a shows the variation of ω on a part of the cantilever surface for this testing condition, showing stress concentrations at the corners. Analysing the ω of the two regions produces figs. 6.13b and 6.13c, showing that failure at the corners will have an actual ω value likely greater than that of the cantilever (aka main body) whose value is similar to the calculated nominal ω.



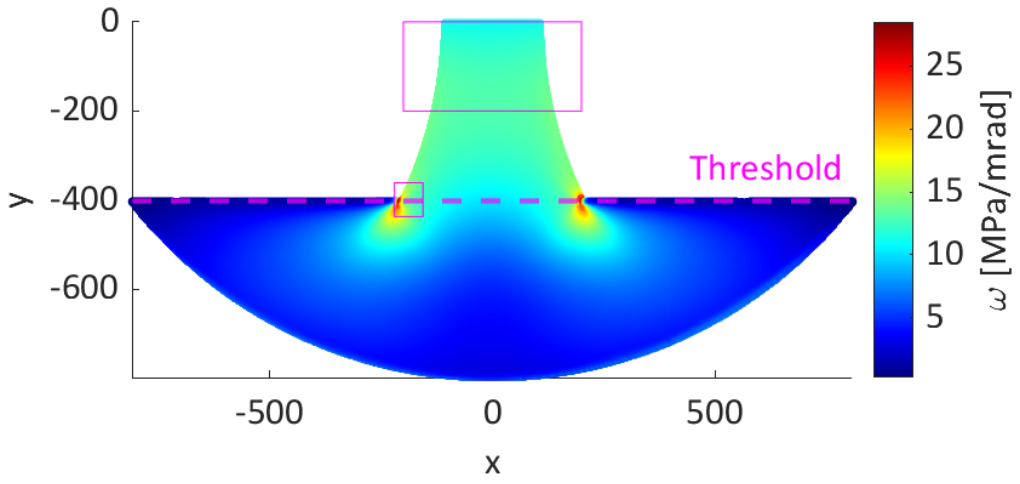
(a) RT Vacuum. **(b)** RT Air

Figure 6.11: S-Ns for RT air and vacuum separated by failure location within the mesocantilever.

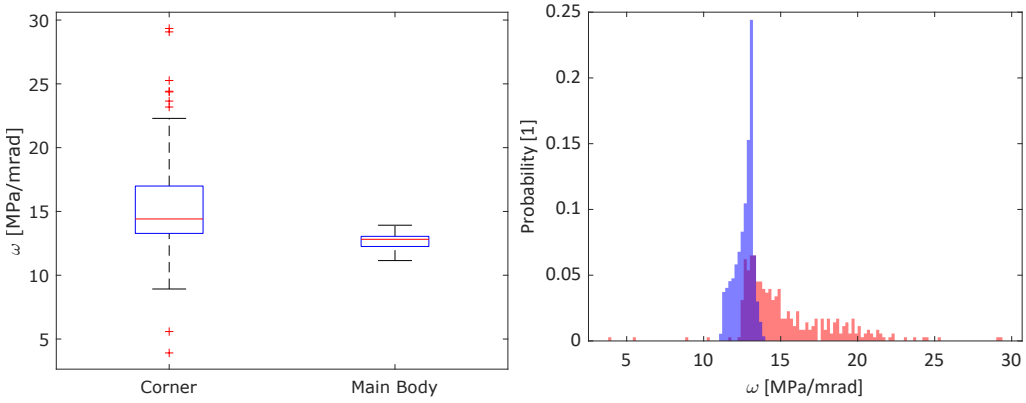


(a) ω box plot **(b)** ω histogram

Figure 6.12: RT vacuum ω further analysis with the σ_{vm} variation within the main cantilever body's surface.



(a) Whole surface.



(b) Box plot corner vs main body. **(c)** Histogram corner vs main body.

Figure 6.13: FEM derived RT vacuum ω on the surface in the corner and main cantilever body regions. Integration point ω values are plotted along with the interpolations. Above the threshold is what is considered for the nominal calculated ω results.

Figure 6.14 shows that the greater upper bound values of the interquartile range and adjacents can bring the corner (aka base) failure data points within the cantilever data. Calculating a precise ω based on the corner failure locations per sample is challenging due to the large stress gradients and the difficult-to-measure curvature at the corners.

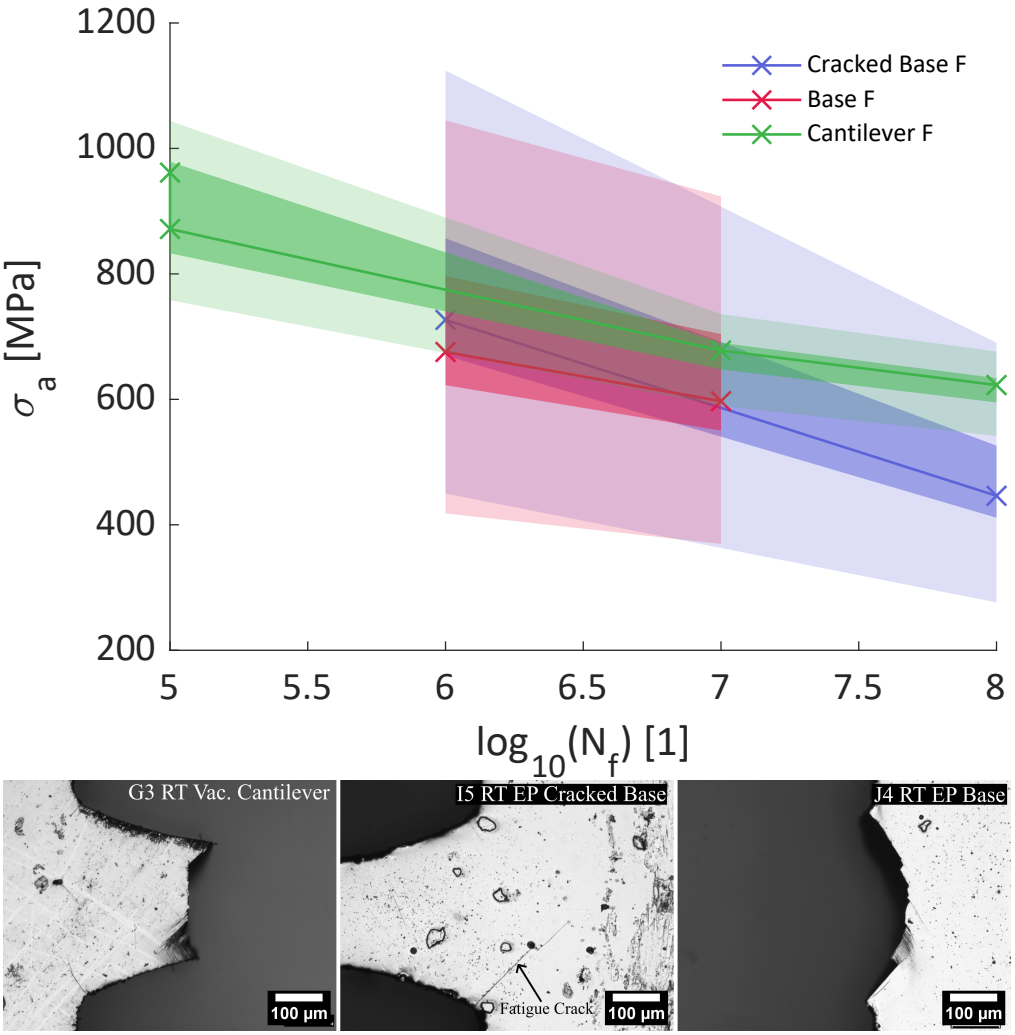


Figure 6.14: Drastic failure (F) S-N with statistical ranges as error bars and shaded. The paler shaded regions are the upper and lower adjacent values. The more opaque regions are the interquartile ranges. Example grey-scaled and contrast-enhanced optical micrographs of the failure designations are shown below the plot.

6.3.3 Fractography Air

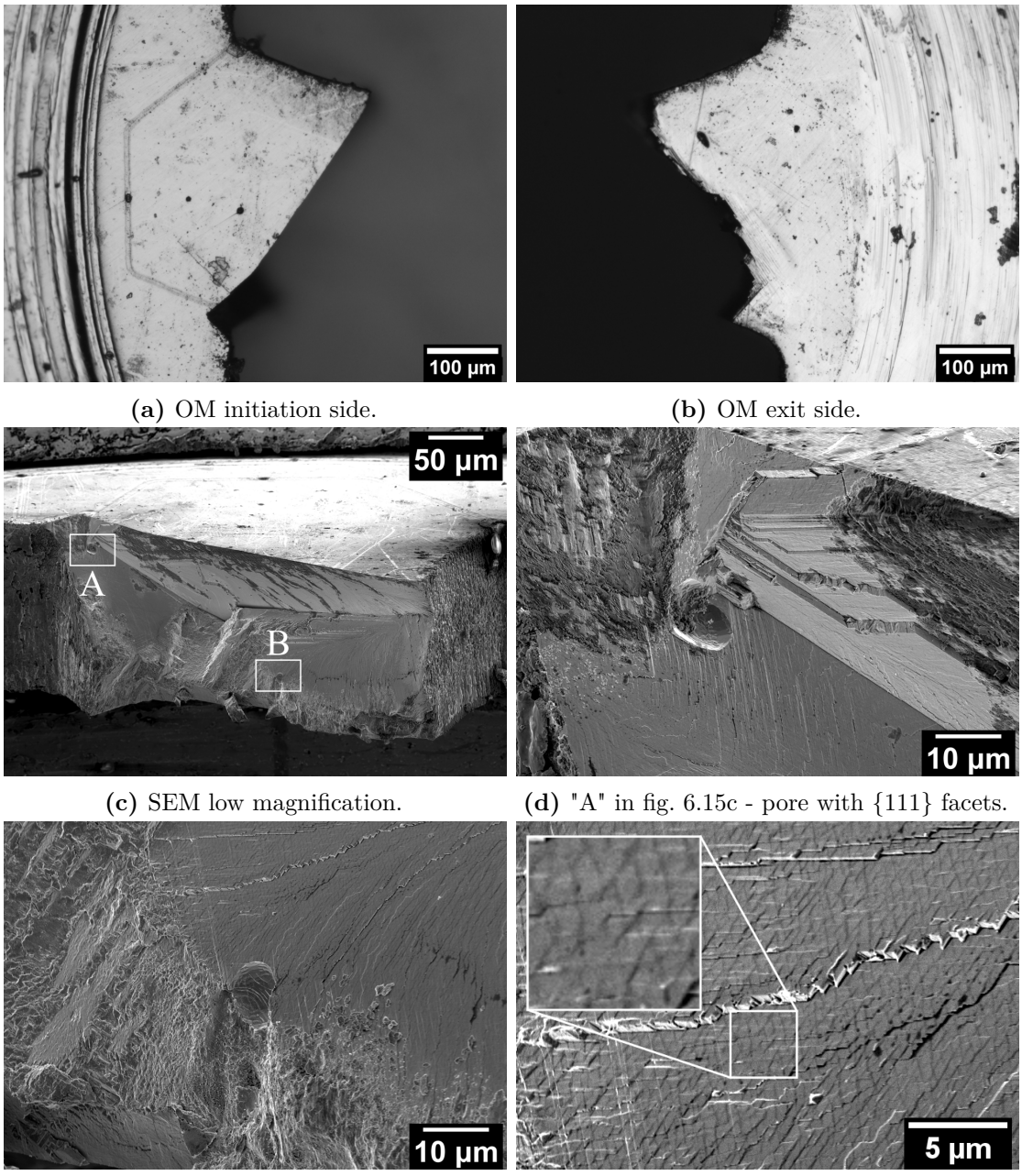
In this testing campaign, failure typically occurred close to, if not in, the cantilever base, with extensive {111} slip lines and fracture paths. The {111} slip traces make

a 45° angle to the cantilever direction due to the crystal orientation of these samples.

The following samples show features shared across the other RT air samples.
Sample **O10** (fig. 6.15) is an exemplary case where the fractography shows a few dominant but large {111} facets with a clear initiation side and a strong asymmetry on the two faces.
P5 (fig. 6.16) is more symmetrical and is virtually completely within the cantilever base, making it more challenging to define a single initiation side using the metrics in section 6.1.1. Hence, the side with slightly less surface slip is dubbed the "primarily initiation side".
N5 (fig. 6.17) shows how the finer alternating {111} facets in the “rooftop” morphology can appear like opening mode under OM and how cracks can still occur in the base despite the final failure being within the cantilever.
O2 (fig. 6.18) is a rare case of fracture only within the cantilever, and there is also a clear fatigue crack initiating pore with the growth of an almost singular fracture surface. Many {111} exit facets on the exit side can also be seen on the initiation side for O2.
No trend was observed on whether the exit facets formed preferentially on the top or bottom sides of the samples respective to their placement in the fatigue rig.

For sample **O10**, the initiation side (fig. 6.15a) shows very distinct and large shearing mode {111} facets with few slip lines, whereas the exit side (fig. 6.15b) shows more {111} slip lines and smaller {111} facets with the larger scale path appearing less crystallographic.

The SEM fracture surfaces show that multiple {111} facets, both big and small, can occur. The larger facets often have river lines. The triangular $\gamma - \gamma'$ morphology along the {111} plane can be seen in an SEM (e.g., fig. 6.15f), confirming they are shearing mode cracks.



(a) OM initiation side.

(b) OM exit side.

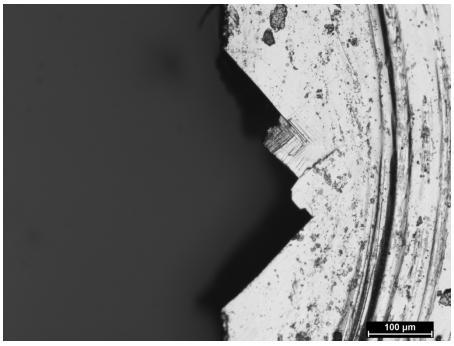
(c) SEM low magnification.

(d) "A" in fig. 6.15c - pore with {111} facets.

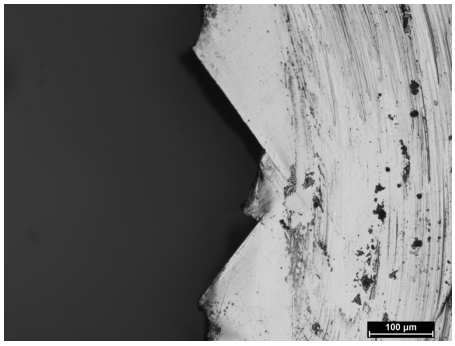
(e) "B" in fig. 6.15c - end of large {111} facet.

(f) Triangular $\gamma - \gamma'$ fracture on {111} facet in fig. 6.15e.

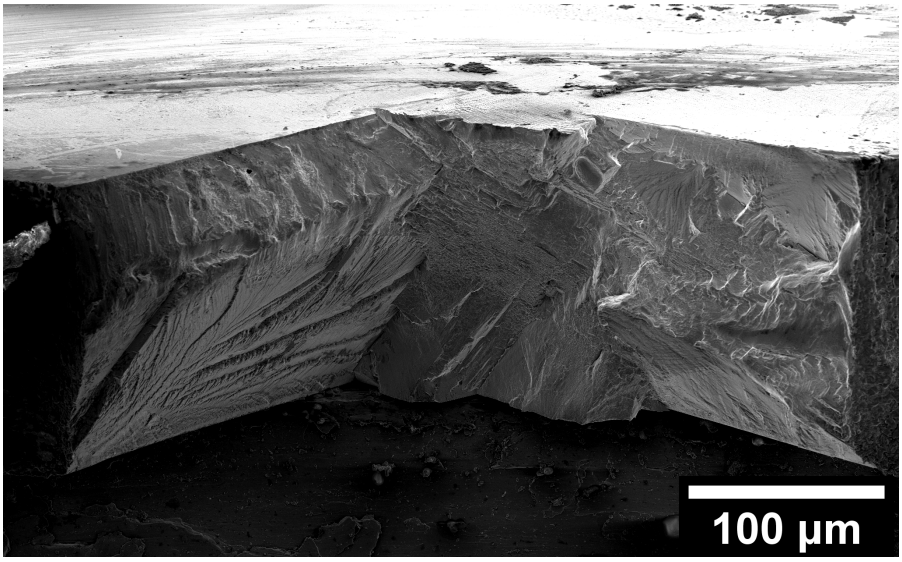
Figure 6.15: Fractography of O10, a RT air no-EP sample. OM has been grey-scaled.



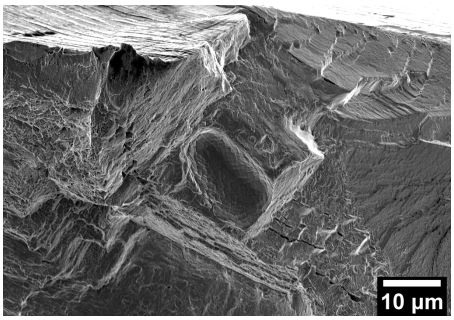
(a) Primarily OM initiation side.



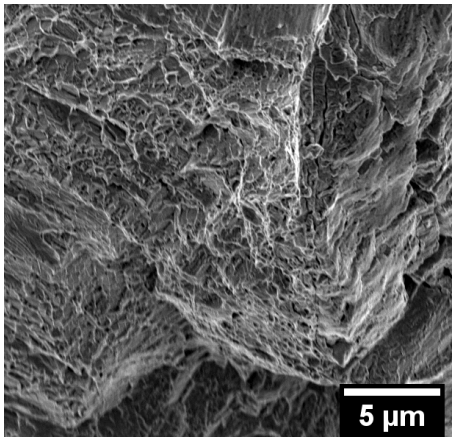
(b) Primarily OM exit side.



(c) SEM low magnification. Exit side on top.

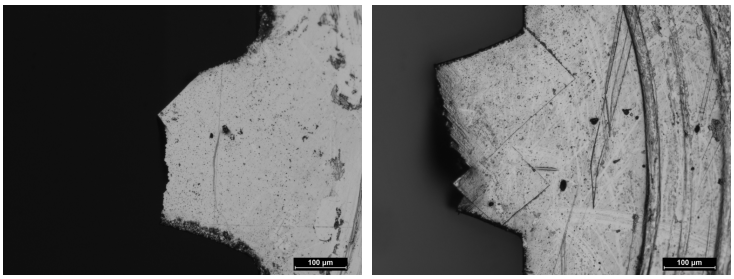


(d) Middle of the exit side.

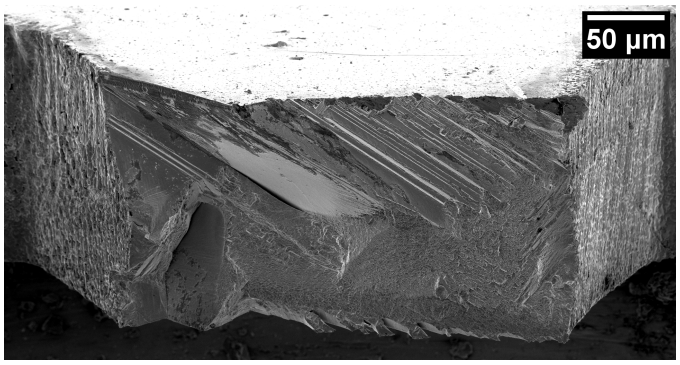


(e) Ductile region of the middle exit side.

Figure 6.16: Fractography of P5, a RT air no-EP sample. OM has been grey-scaled.

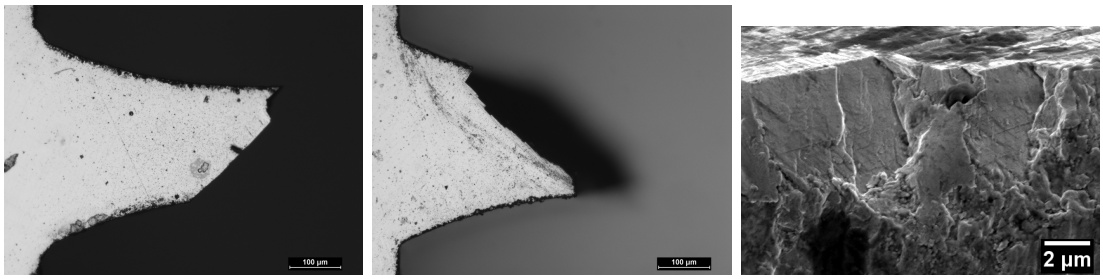


(a) OM initiation side. **(b)** OM exit side.

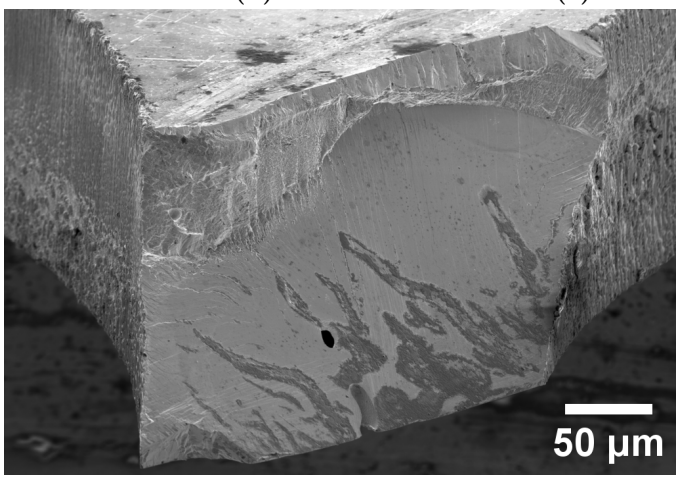


(c) SEM initiation side up.

Figure 6.17: Fractography of N5, a RT air no-EP sample. OM has been grey-scaled.



(a) OM initiation side. **(b)** OM exit side. **(c)** SEM exit {111} facet.



(d) SEM exit side up.

Figure 6.18: Fractography of O2, a RT air no-EP sample. OM has been grey-scaled.

6.3.4 Fractography Vacuum

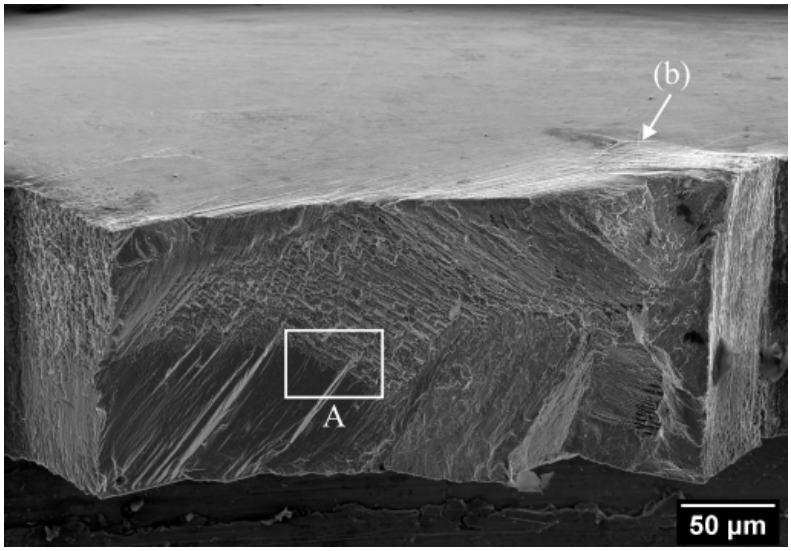
Evidence for opening mode fracture (via pseudo-cubic slip) has been observed in RT vacuum but not in air.

Near the corners of the fracture surface, there are dark circular features in 3/6 of the samples, which have a pore associated with them. Under higher magnification SEM, they show pseudo-cubic slip opening mode fracture with the crack plane showing what appears to be squares (aka cuboidal) rather than triangles. Samples H6 & G3 below are good examples of this feature.

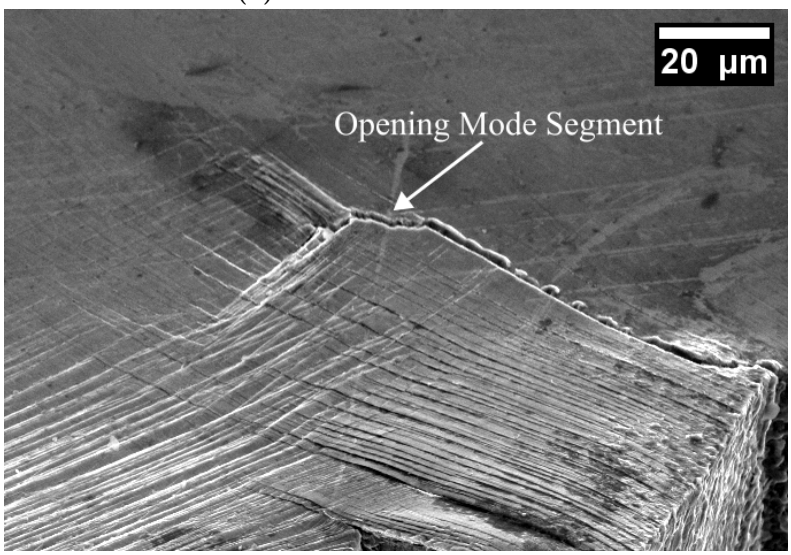
Sample H6 shows how distinctive the dark circular region is in a SEM fractograph (fig. 6.19a), and how it transitions into ductile steps with extensive dimpling (fig. 6.19c). The cuboidal nature of the opening mode fracture is clearer in fig. 6.19d, where occasional cutting of the γ' creates ledges parallel to the FCG direction. The fine fatigue striations in fig. 6.19d also indicate that the FCG direction is northeasterly.

As the dark circular region centres around the pore in the bottom LHS corner, it likely initiated the crack, and so this feature is associated with early FCG. The edge of this circular region is the transition to steps, which is seen in fast FCG rate shearing mode fracture. They also exhibit ductile dimples often seen in ductile fracture (fig. 6.19e), making the surface less planar under high magnification but still appear step-like under low magnification.

Sample G3 shows the opening mode circle separated by a {111} shearing mode facet. Figure 6.20e shows that the opening mode fracture does not always show a clear square cuboidal $\gamma - \gamma'$ morphology, and the fine striations indicate that the FCG direction is between the surface and the pores.

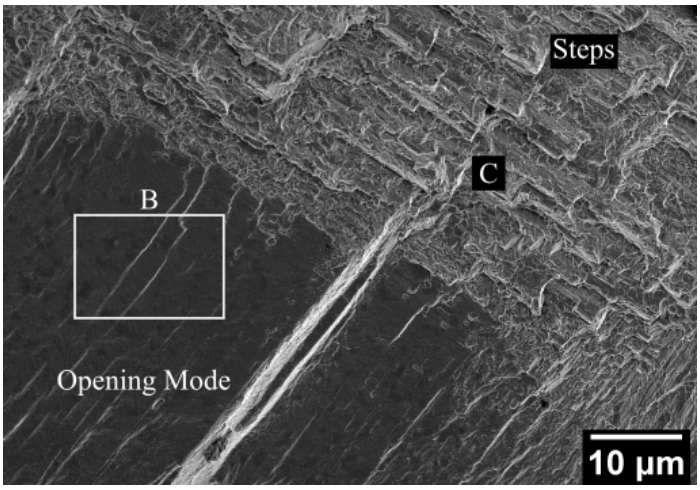


(a) Tilted fracture surface.

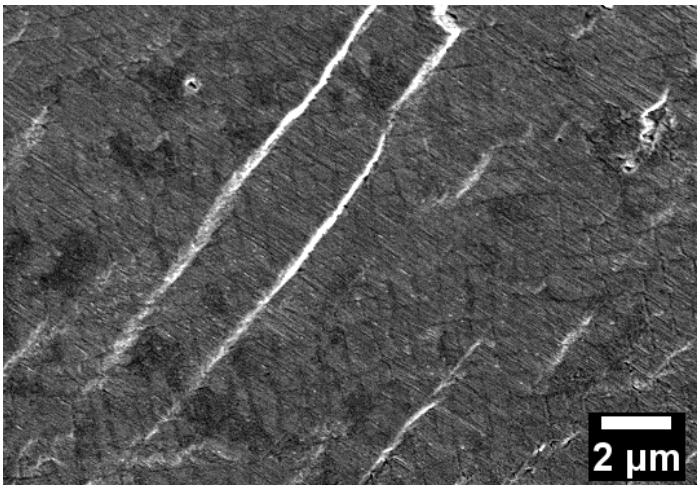


(b) "(b)" in fig. 6.19a - opening mode crack.

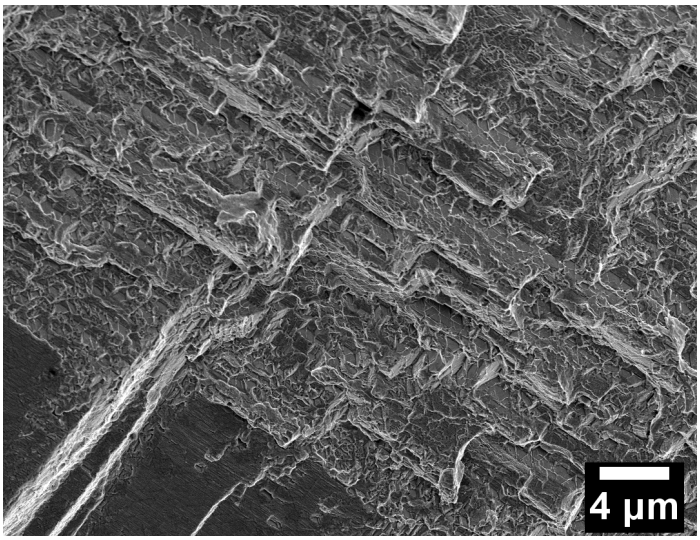
Figure 6.19: Fractography of H6, a RT vacuum no-EP sample.
(Cont. Next Page)



(c) "A" in fig. 6.19a - Transition.

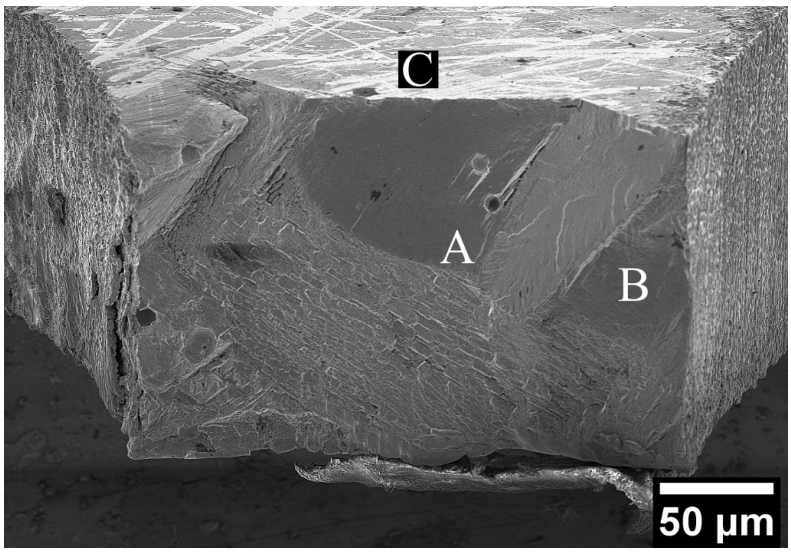


(d) "B" in fig. 6.19c - Dark opening-mode magnified.

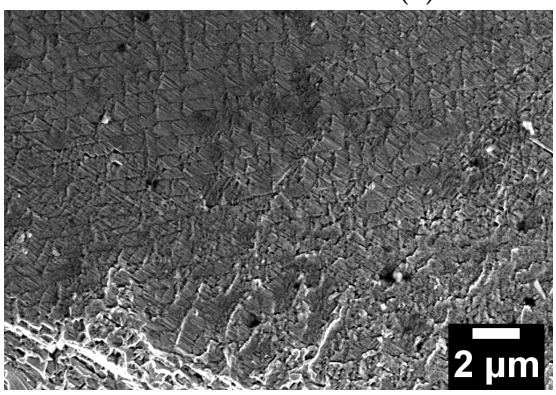


(e) "C" in fig. 6.19c - Ductile steps magnified.

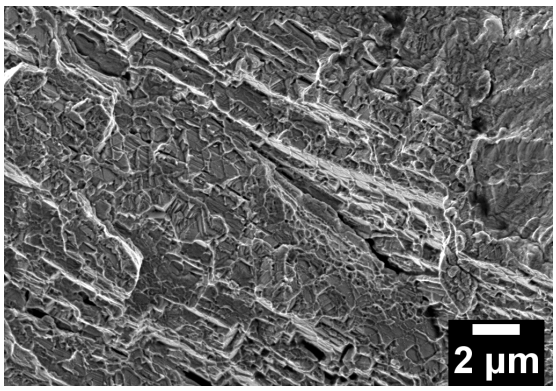
Figure 6.19: Fractography of H6, a RT vacuum no-EP sample.



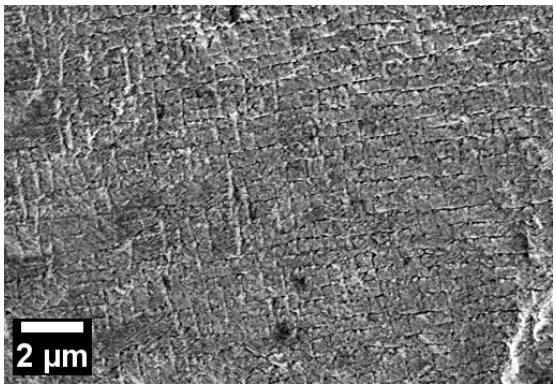
(a) Tilted fracture surface.



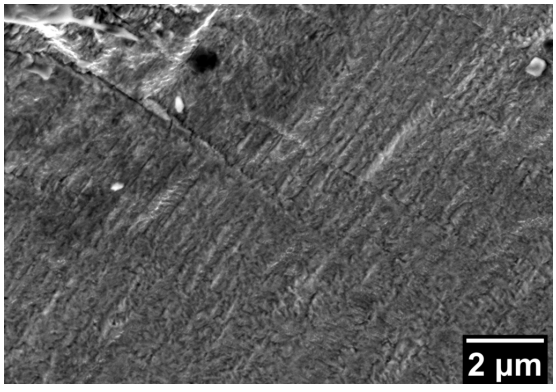
(b) "A" - Opening mode.



(c) "A" - Ductile region below.



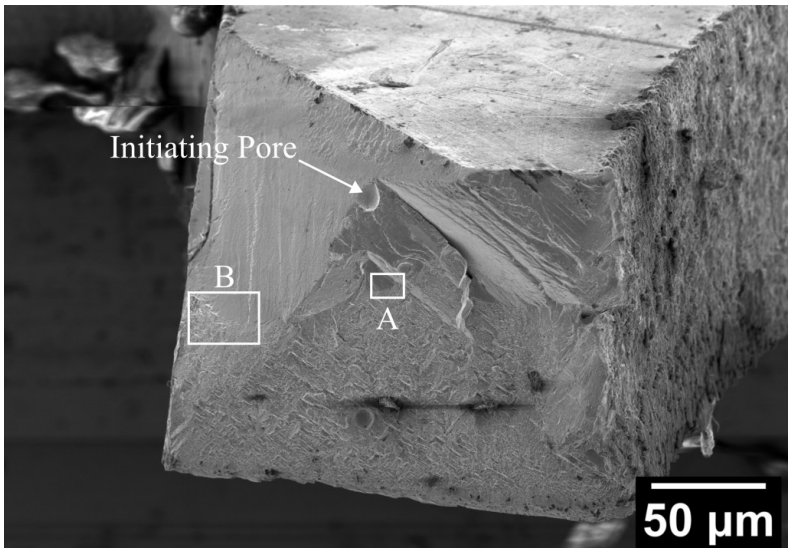
(d) "B" - Opening region.



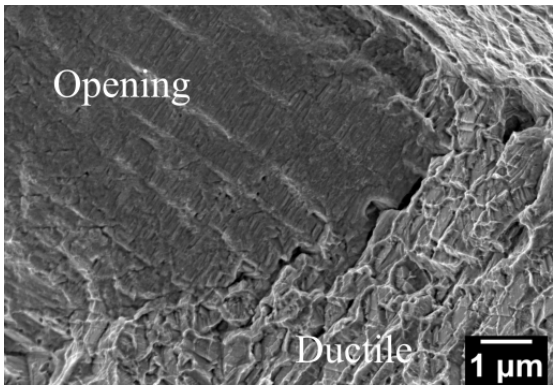
(e) Near "C" - Opening mode.

Figure 6.20: Fractography of G3, a RT vacuum no-EP sample.

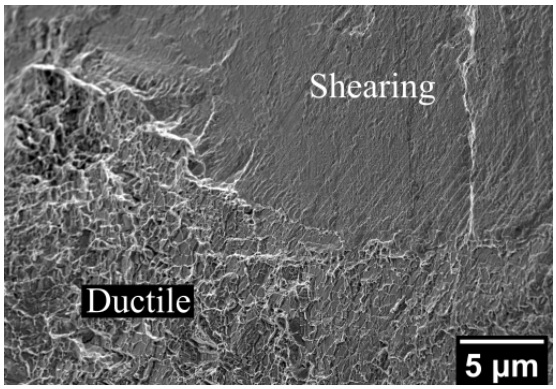
Sample H4 in fig. 6.21 shows a pore on the boundary of a {111} facet and an opening mode facet. However, the {111} facet does not show a $\gamma - \gamma'$ morphology but an undulating morphology with an even distribution of sub-micron voids. The typical dark circular transition to ductile-shearing on {111} can be seen, with a similar morphology to fig. 6.20e on the opening mode region. Interestingly, fig. 6.21c indicates that the large {111} facet shows more ductility later in its growth.



(a) Tilted fracture surface.

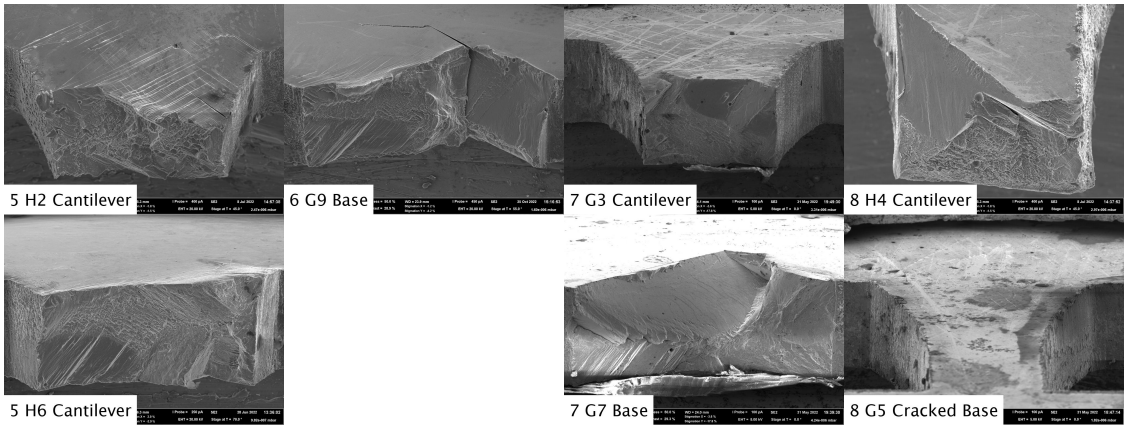


(b) "A" - Opening to ductile-shearing boundary.

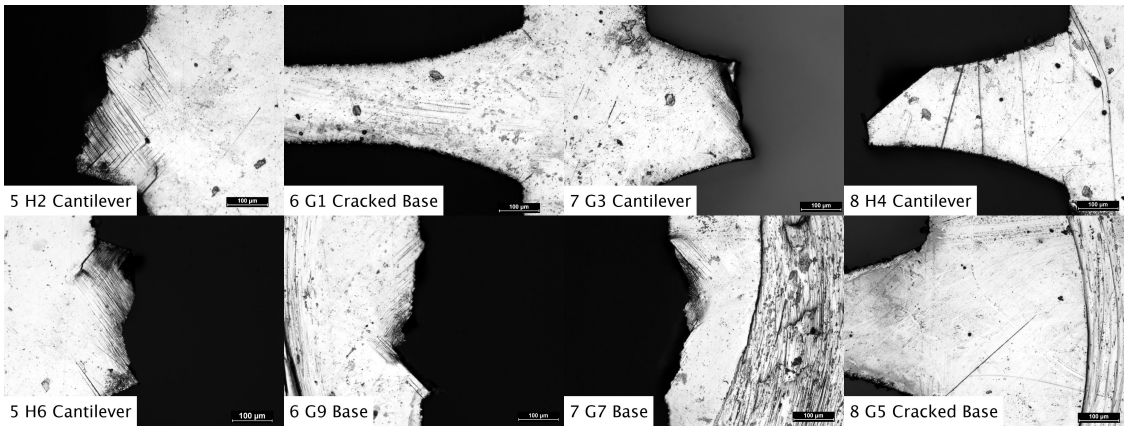


(c) "B" - Shearing {111} transition to ductile dimples.

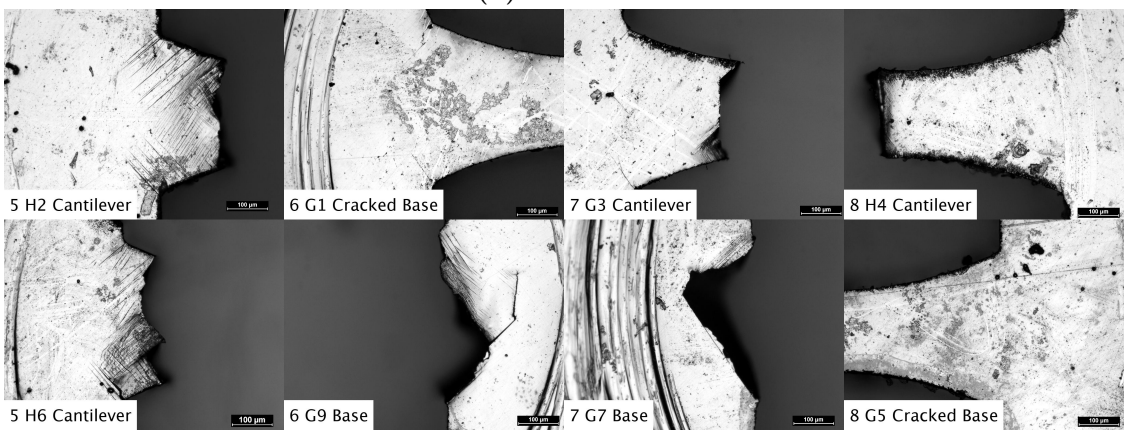
Figure 6.21: Fractography of H4, a RT vacuum no-EP sample.



(a) SEM



(b) OM side 1



(c) OM side 2

Figure 6.22: RT vacuum no-EP fractography Results. Top-to-bottom indicates highest-to-lowest sample fatigue stress, the numbers and columns indicate the decade (i.e. $N_f = 10^x$), the letter-number combination is the sample ID, and the type of failure is at the end. OM has been grey-scaled.

6.3.5 Discussion

Both the cracks and fracture surface only exhibited shearing mode {111} fracture in RT air, as expected considering the low temperature and high frequency [44, 45, 48]. Tests at ambient conditions and low frequencies for CMSX-4 tend to show shearing mode facets [45], which higher fatigue frequencies should further promote [44].

However, the observation of opening mode and pseudo-cubic slip for RT vacuum was unforeseen, as it was expected that the lower p_{O_2} should help further promote shearing mode fracture over opening mode [89].

Opening mode fracture via pseudo-cubic slip is often associated with increased σ_y, leading to a better fatigue performance [50]. Hence, the observed performance improvement corroborates that opening mode is occurring. Also, the significantly greater degree of {111} slip traces for the same N_f (e.g. 10^5) in the OM images of the vacuum tests compared to the air tests supports the higher σ_{amp} values used during testing.

Opening mode fracture is promoted by a low ΔK [44, 45, 54]. A mode-I bent cantilever is described by eq. (6.1) [126].

$$\Delta K_I = f\left(\frac{c}{H}\right)\Delta\sigma_b\sqrt{\pi c} \tag{6.1}$$

Where c is the fatigue crack length, H is the cantilever thickness, $\Delta\sigma_b$ is the cantilever axial stress range, and $f(c/H)$ is a geometric function.

Hence, eq. (6.1) says, for a given c, that $\sigma_{amp} \propto \Delta\sigma_b \propto \Delta K_I$. Then, considering that RT air initiates cracks at a lower σ_{amp}, it should have a lower ΔK than under vacuum. This indicates that the difference in ΔK between the two conditions does not cause the opening mode fracture. However, it does explains the transition from opening to shearing under vacuum when c increases to higher values, i.e., the end of the dark circular region.

Ductile dimple features can be seen on the shearing mode fracture surfaces under both conditions. In RT air, it is associated with high σ_{amp} values and possibly

multiple active octahedral slip systems (fig. 6.16). This would explain its occurrence in vacuum due to the higher σ_{amp} at drastic failure, and that pseudo-cubic slip is thought to be potentially from multiple octahedral slip systems. The occurrence of ductile dimples is not unexpected as Ref [79] found that conventional ultrasonic air tests showed ductile dimples (like in low-frequency vacuum tests).

As for why opening mode fracture via pseudo-cubic slip occurs, if the only known difference is the lack of air, it must be due to environmental interactions or increased heating. Anelastic heating may be more significant under a vacuum than in air. It is thought within the research group that most of the small amount of anelastic heat (small due to small volume) is lost through the conduction into the horn, explaining the low heating of the sample seen with low-magnification infrared cameras. The anelastic self-heating of SXNBSs is comparatively low, but the RT macroscale fatigue experiments still use active cooling [79]. However, the cantilever bending in this work likely leads to high fracture surface abrasion, which may lead to very localised self-heating [42, 127], which under vacuum may be heightened enough to cause the temperature to rise where opening mode fracture occurs.

It is challenging to compare and conclude the slip trace step heights between the air and vacuum conditions at similar σ_{amp} values from the captured optical micrographs ($N_f = 10^5$ in air compared with $N_f = 10^6 - 10^8$ vacuum).

Figure 6.23 compares the RT S-N curves of SXNBSs from literature. It shows that the No-EP performance is comparable to the ultrasonic data collected for MAR-M200 [79], if not better, especially in the VHCF regime. Compared to the conventional frequency tests [5, 89], it is significantly greater. However, the RT air EP sample showed a greater strength, and failure was often "corner crack" related for both conditions; hence, the fatigue strength for this condition is likely to be greater than the ultrasonic MAR-M200 data.

Figure 6.25 shows that the RT air No-EP results are similar if not stronger than the ultrasonic fatigue of $\langle 100 \rangle$ CMSX-4 at 750 °C in air [11]. This is interesting

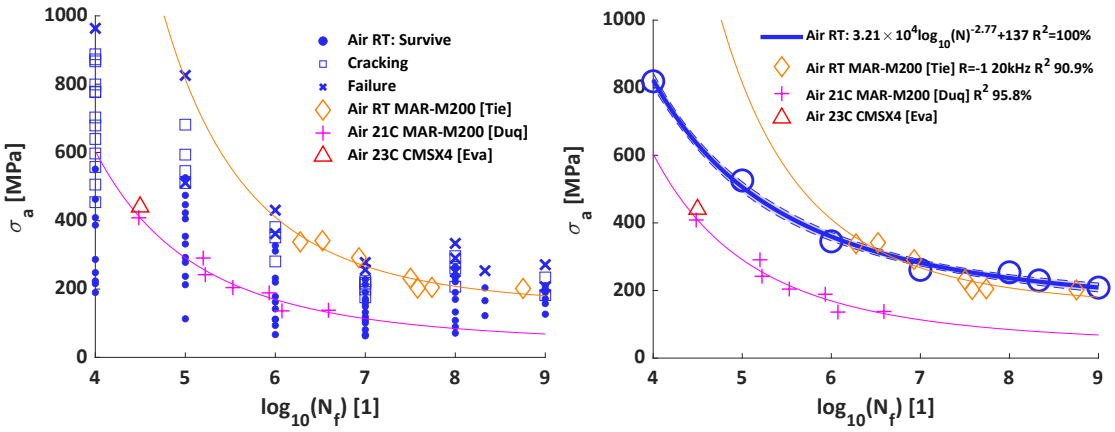


Figure 6.23: Comparison of RT fatigue data of ⟨100⟩ SXNBSs in air from the literature with the RT air No-EP data collected in this thesis. Raw data and fitted 50% failure are shown. [Tie] is standard $R = -1$ ultrasonic tests from [79]. [Duq] is $R > 0$ uniaxial fatigue at 5 Hz from [89]. [Eva] is U-notched bend specimens at 0.25 Hz with $R = 0.1$ from [5].

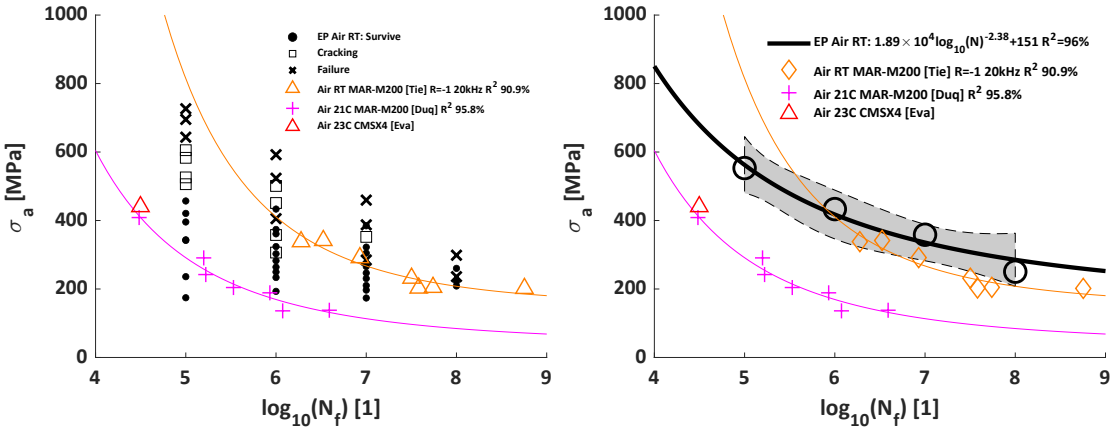


Figure 6.24: Same as fig. 6.23 but with the RT air EP samples from this work.

as 750 °C is near the peak σ_y [6, 42], and so it should show a greater fatigue performance than RT [50], as seen in the air data fig. 2.36 [93]. The 750 °C literature data appears to be both alloy and frequency-independent, which is interesting as the RT literature data indicates a strong frequency effect accounts for most of the discrepancy between this thesis and conventional frequency tests.

The results in this work indicate a better fatigue performance than the RT data in the literature [5, 79, 89], which is likely from the lower risk-volume size-effect of the mesocantilever samples.

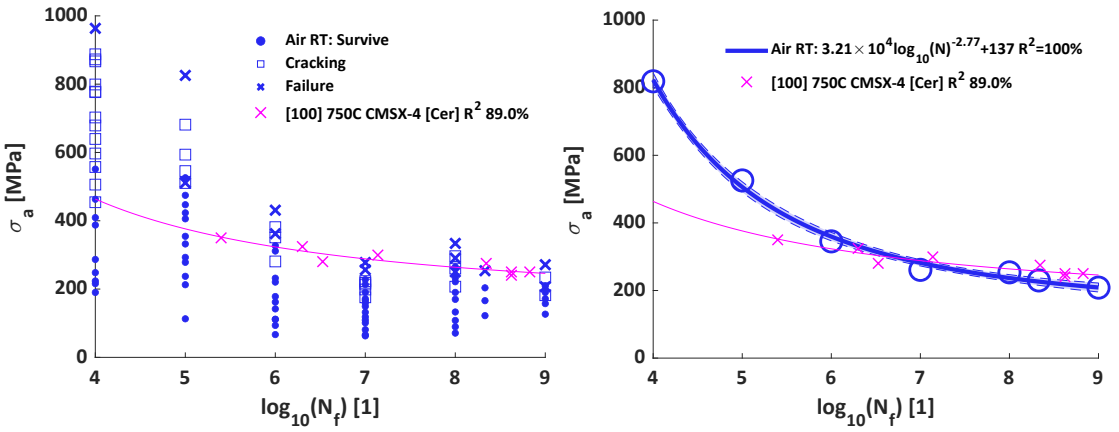


Figure 6.25: Comparison of macroscale uniaxial UFT failure data of ⟨100⟩ CMSX-4 in 750 °C air from [Cer] ([11]) with the RT air No-EP data collected in this thesis. Raw data and fitted 50% failure are shown.

The vacuum results show an improvement more significant than seen in RT MAR-M200 at 5 Hz in Ref [89] and in Ref [5]. The vacuum levels in Ref [89] range from 6.7×10^{-6} mbar to 1.6×10^{-5} mbar, which are orders of magnitude higher than in this work. The 1.25×10^{-3} mbar p_{O_2} in Ref [5] does not appear to have a strong effect on the fatigue performance. However, the estimated p_{O_2} in this work is a factor of $10^{3.8}$ lower than that work. Additionally, ultrasonic frequencies are thought to hinder oxidation kinetics in Ref [79]. Hence, the significantly greater increase in the fatigue performance going from air to vacuum in this work is likely due to the better vacuum levels and could be linked to the opening mode fracture.

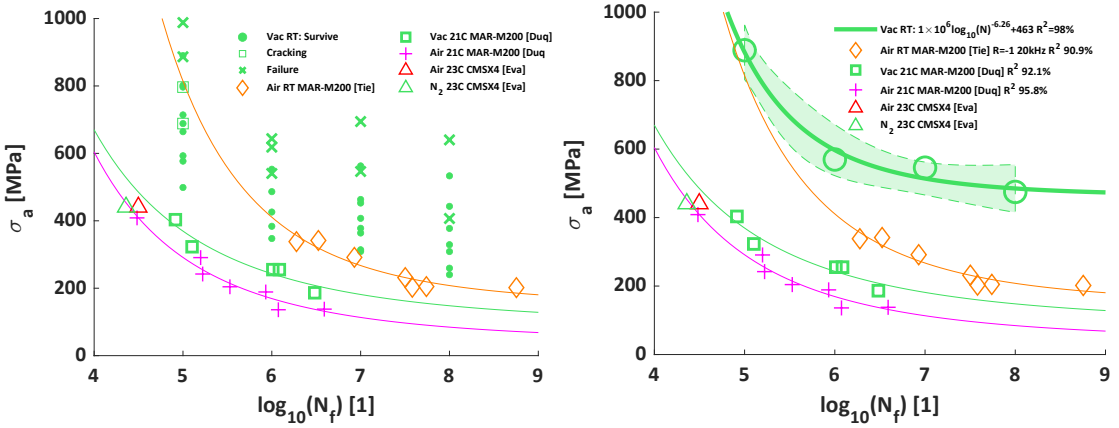


Figure 6.26: RT vacuum No-EP samples from this work. [Tie] is [79], [Duq] is [89], and [Eva] is [5].

6.3.6 Conclusions

1. Fractographs of RT air and vacuum fatigued CMSX-4 have been obtained. As expected, only shearing mode fractures were found in air, and unexpectedly, some opening mode fractures were found under vacuum.
2. Lower p_{O_2}, higher ΔK_I, and higher frequencies are thought to promote shearing mode over opening mode fracture. Hence, the leading proposed theory for the unexpected opening mode fracture occurring in the vacuum conditions but not in air is the occurrence of localised heating around the fracture surface through self-abrasion, which increases the temperature more significantly under vacuum.
3. Vacuum improves the fatigue performance compared to air. The leading proposed theories, which could all be occurring simultaneously, are:
   (a) Oxygen reduces slip reversibility by pinning dislocations ahead of the crack tip, then the damage along the slip planes per cycle will be higher, reducing the fatigue life [22, p. 1442][89, p. 1329]. Vacuum then has a lower FCGR compared to air [89, p. 1327]. The oxygen pinning of the dislocations has been though to promote slip homogenisation, however potentially the ultrasonic frequencies used have acted to hinder slip diffusion out of the slip plane at these low temperatures [5, p. 163-164].
   (b) Embrittlement of the material locally ahead of the fatigue crack tip from the gas adsorption in air [79, p. 1937] and oxidation [5, p. 169][95, p. 42].
   (c) The occurrence of opening mode would improve fatigue performance as it indicates slip homogenisation occurred [79, p. 1938].
4. Size effect (via smaller risk-volume) is the most likely reason for the improved fatigue performance of the RT air results (c.f. Refs [5, 79, 89]), being more comparable to the macroscale fatigue results of Ref [11] near the peak σ_y temperature.

6.4 Room Temperature ECCI

Only electropolished samples will have a surface sufficient to perform ECCI analysis on, and so the EP RT air samples are the only testing campaign so far in which this can be performed. However, for completeness, the ECCI results from the SXO campaign in chapter 7 ("RJS" prefix) will be included in this, as they will have been performed under the same environmental conditions but with a different cantilever design.

6.4.1 Sample I5

Sample I5 is a RT Air EP sample, where five cracks on the initiation side were analysed (fig. 6.27). Cracks 1 to 4 had HR-EBSD performed on their crack tips to compliment the ECCI results and to assess the local ρ_{GND} & plastic deformation information. Table 6.4 summarises the three ECCI conditions used on this sample.

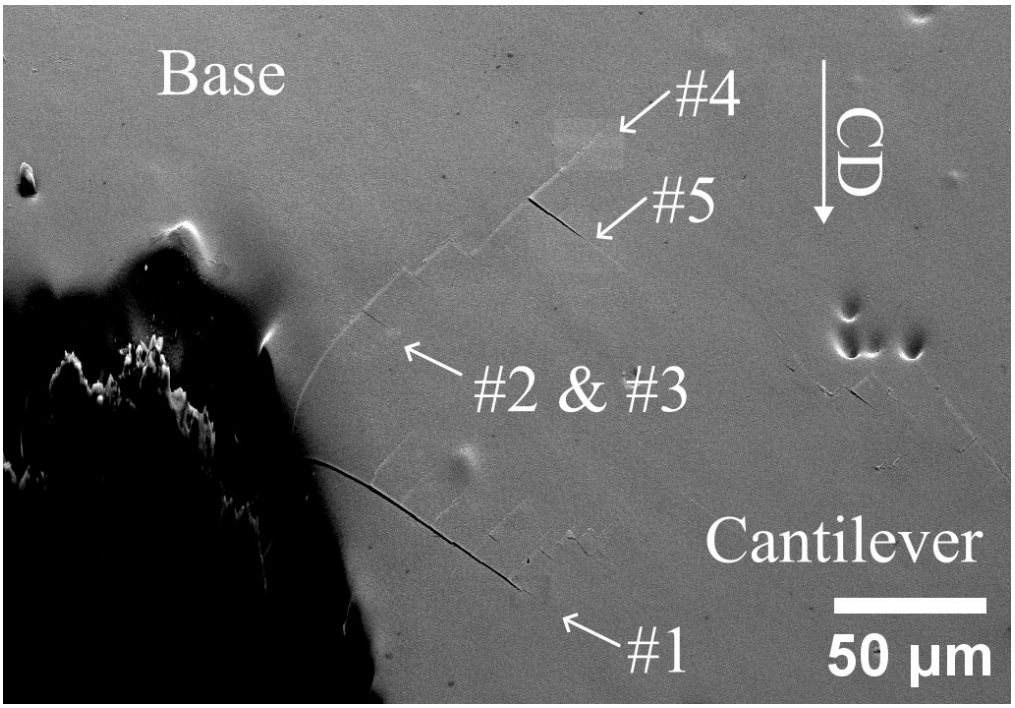


Figure 6.27: SE micrograph of all five cracks analysed in ECCI for sample I5.

Crack 2

Crack 2 is a shearing mode crack as shown in fig. 6.28.

Table 6.4: I5 ECCI conditions. $\underline{g}$ is estimated from channelling lines.

ID	T_{stage} [°]	$\underline{g}$
1	8	⟨220⟩
2	7	[200]
3	4	⟨220⟩

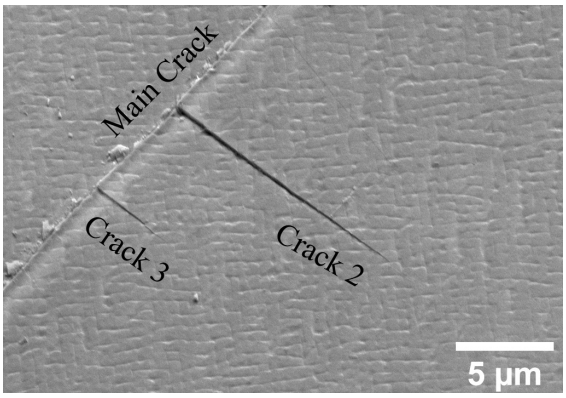
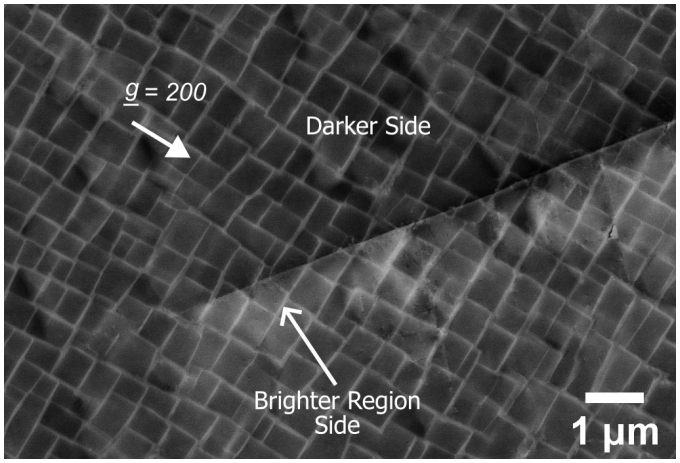


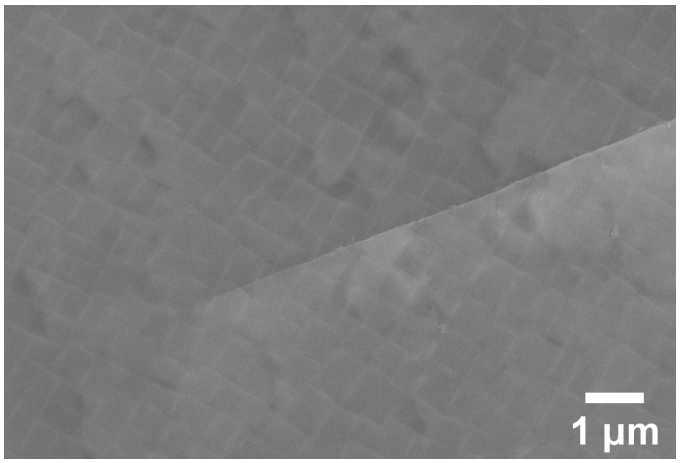
Figure 6.28: Cracks 2 & 3 shearing mode cracks from fig. 6.27.

In ECCI, the tearing mode component causes one side to be preferentially brighter (fig. 6.29). Figure 6.30 shows that the threading dislocations are prevalent, primarily occurring along the secondary slip system from the crack path. Threading dislocations are also found microns ahead of the crack tip. In the BSE, one side of the crack is dark, and its other side is bright, so with SE, the crack tip is seen to end at a γ channel.

The ECCI micrograph quality is high enough that the dark-bright splits of the threading dislocations can be observed (fig. 6.30).



(a) BSE micrograph.



(b) SE micrograph.

Figure 6.29: ECCI analysis of crack 2 showing the increased brightness due to the tearing mode component of the crack. Condition ID 2.

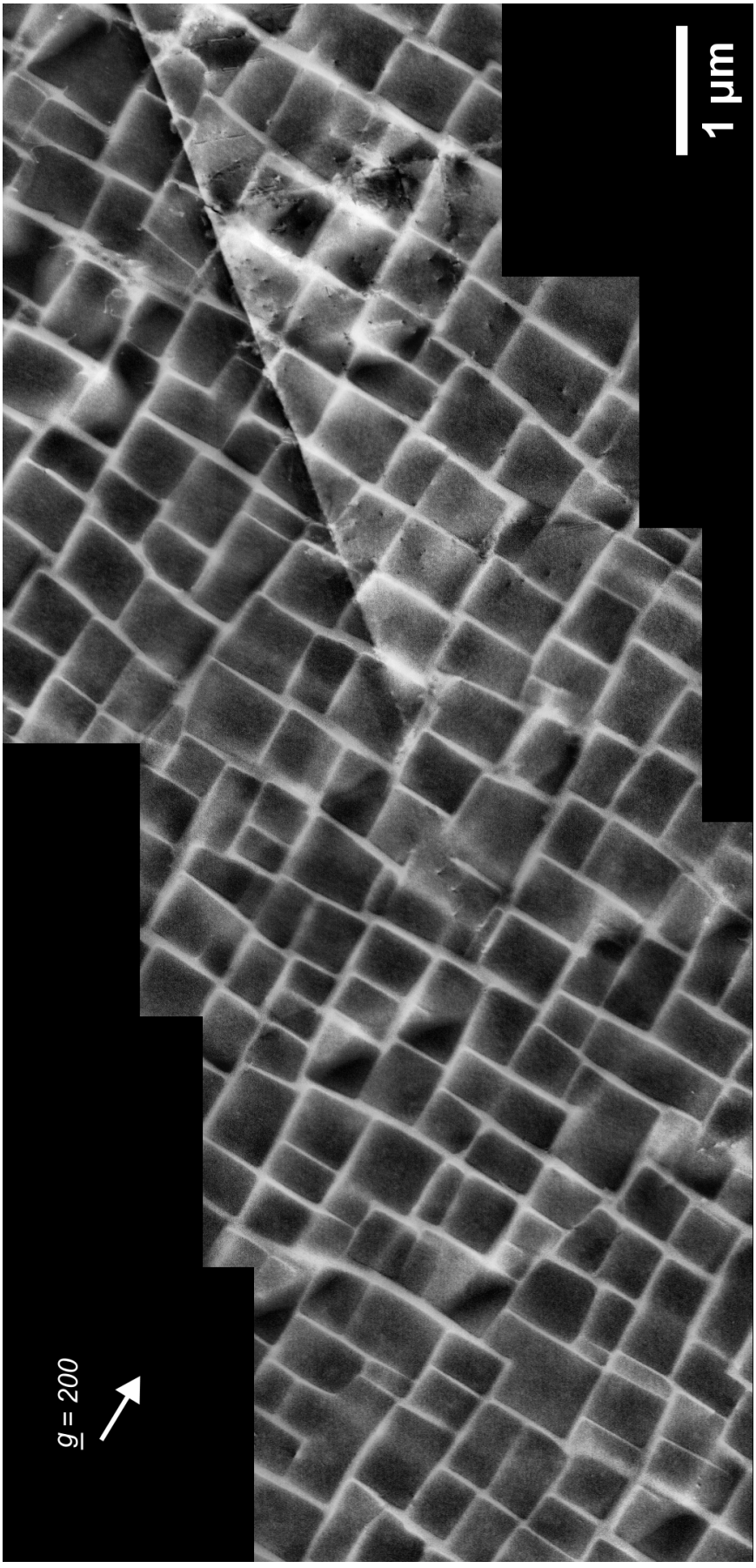
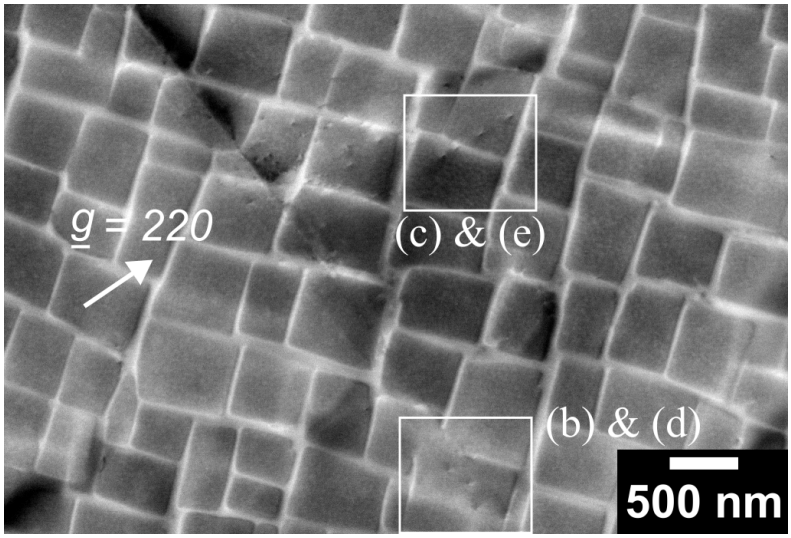
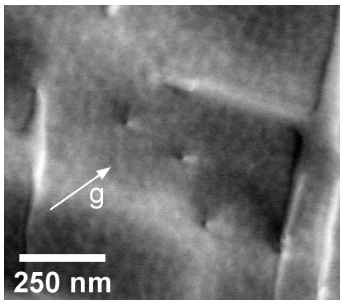


Figure 6.30: Crack 2 BSE ECCI stitched image with CLAHE image enhancement for contrast. Condition ID 2.

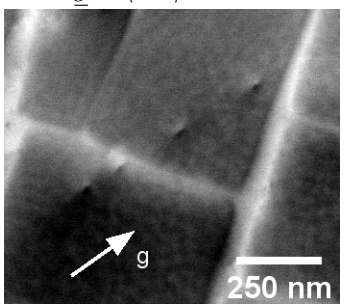
Figure 6.31 shows high-resolution, low-noise ECCI micrographs collected in diffraction condition ID 3. The three threading dislocations ahead of the crack tip shown in fig. 6.31b and in fig. 6.31c have changed contrasts with the different $\underline{g}$ condition.



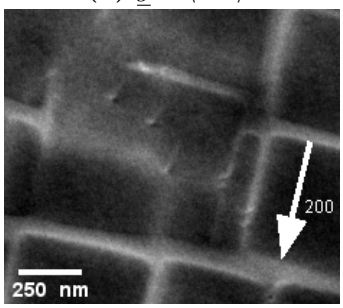
(a) Low magnification $\underline{g} = \langle 220 \rangle$.



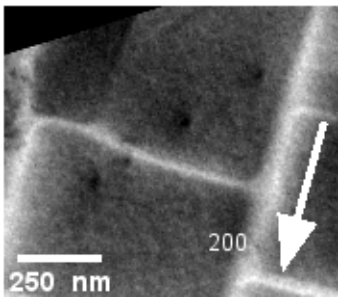
(b) $\underline{g} = \langle 220 \rangle$.



(c) $\underline{g} = \langle 220 \rangle$.



(d) $\underline{g} = [200]$. From fig. 6.30.



(e) $\underline{g} = [200]$. From fig. 6.30.

Figure 6.31: Crack 2 under $\underline{g}$ condition ID 3 (i.e., $\underline{g} = \langle 220 \rangle$). Auto brightness-contrast enhanced.

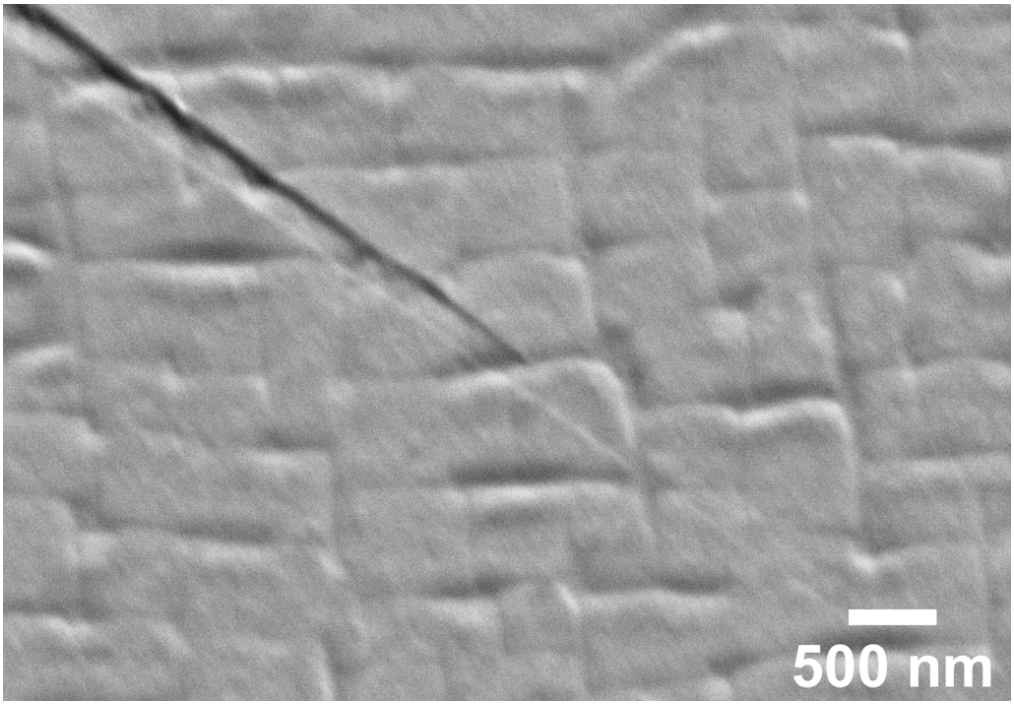
HR-EBSD of the crack shows a higher ρ_{GND} (fig. 6.32b) on the side where slip primarily is seen in ECCI (i.e., the brighter side in fig. 6.29a).

In fig. 6.34b, the vertical and horizontal areas of higher ρ_{GND} count near the crack tip also correlate well with the γ phase in the ECCI micrograph. These higher ρ_{GND} γ channels also appear brighter than average in the original ECCI micrograph but are enhanced with optimised brightness-contrast and CLAHE enhancements. The higher ρ_{GND} and ECCI brightness are likely interlinked.

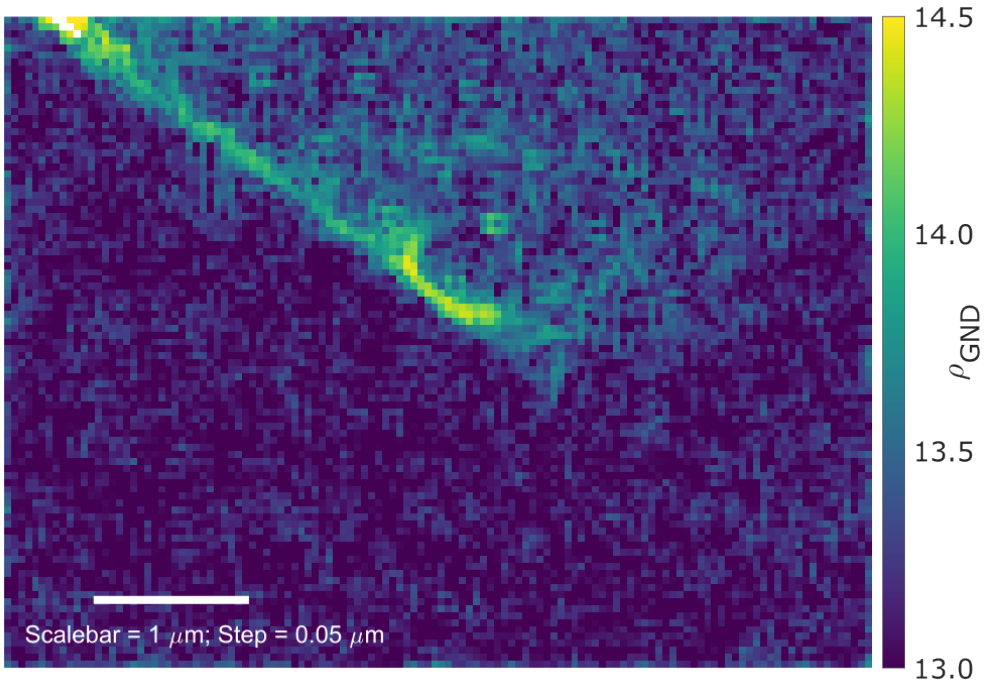
The threading dislocations circled in the ECCI micrograph (fig. 6.34b) cannot be distinguished in the ρ_{GND} map (fig. 6.34d). Figure 6.35 shows that the HR-EBSD's 45 nm step size can contain a singular threading dislocation in the ECCI micrograph unless it contains close dipoles (e.g., potentially the pairs on the right in fig. 6.35).

Therefore, the HR-EBSD noise floor is likely too large to resolve these dislocations at this small step size, but having a larger step size risks capturing dislocation dipoles. Hence, these comparisons show the benefits of ECCI in imaging dislocation where their density is low, but HR-EBSD can obtain dislocation information where ECCI cannot distinguish the individual dislocations due to their high density.

The estimated minimum ρ_{GND} from eq. (4.6) using the full and partial dislocations are $10^{12.97}\mathrm{m}^{-2}$ and $10^{13.21}\mathrm{m}^{-2}$ respectively, but $\rho = {}^{1}\!/\!_{L^2} = {}^{1}\!/\!_{45.1\,\mathrm{nm}^2} = 10^{14.69}\mathrm{m}^{-2}$. The variation below $10^{14.69}\mathrm{m}^{-2}$ in this work can be explained by Burgers vectors inclined to the sample surface plane.



(a) SE micrograph.



(b) ρ_{GND} map. Range = $10^{13} - 10^{14.5}\mathrm{m}^2$.

Figure 6.32: HR-EBSD analysis of crack tip 2. 1 µm scale bar, 45 nm step size.

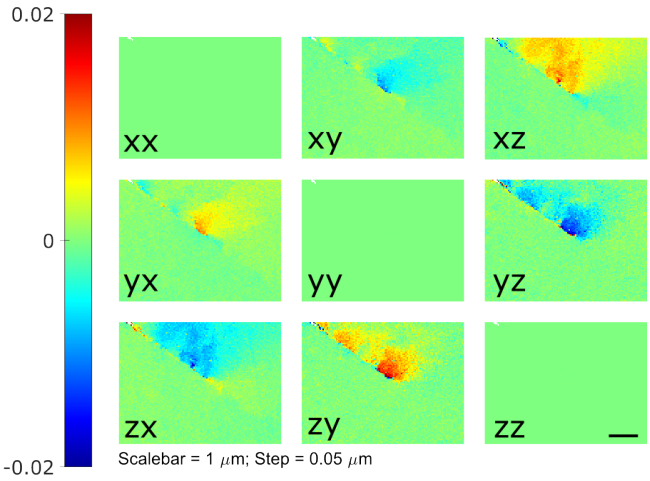
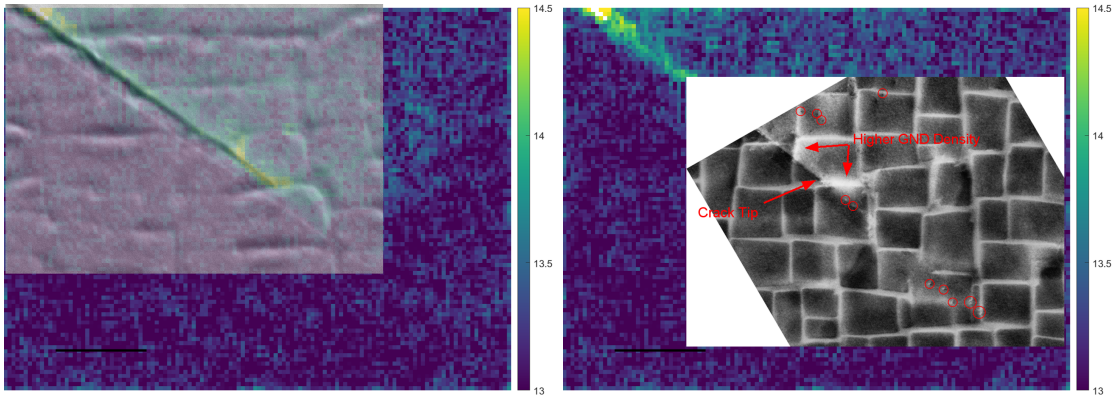
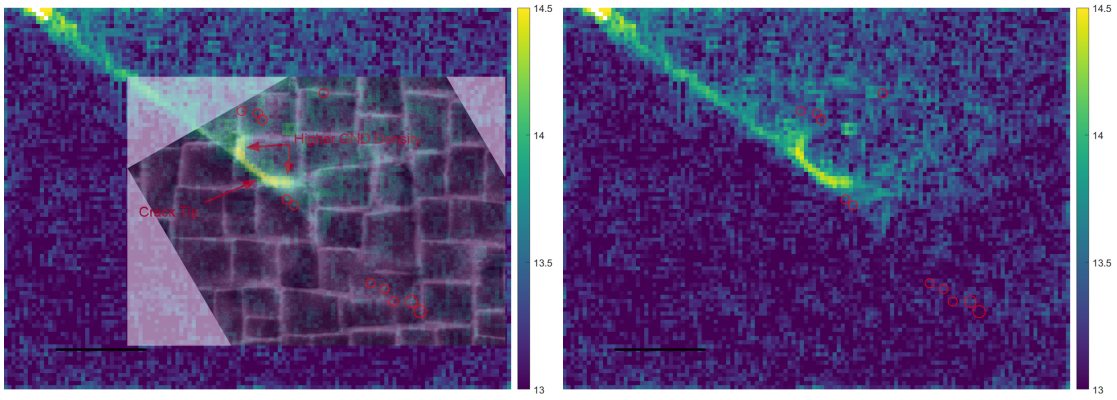


Figure 6.33: Calculated rotations from the HR-EBSD analysis of crack tip 2 in fig. 6.32.



(a) SE vs ρ_{GND} map. 30% transparency.

(b) ECCI vs ρ_{GND} map. 0% transparency.



(c) ECCI vs ρ_{GND} map. 50% transparency.

(d) ECCI vs ρ_{GND} map. 100% transparency.

Figure 6.34: Comparison of the HR-EBSD analysis of crack tip 2 with SE and ECCI micrographs.

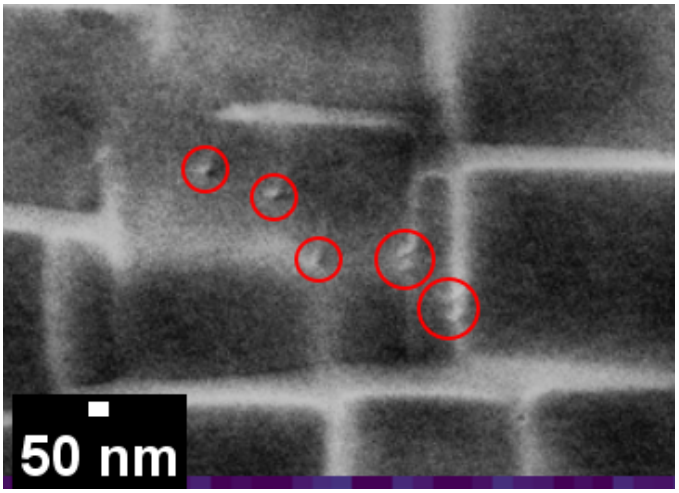
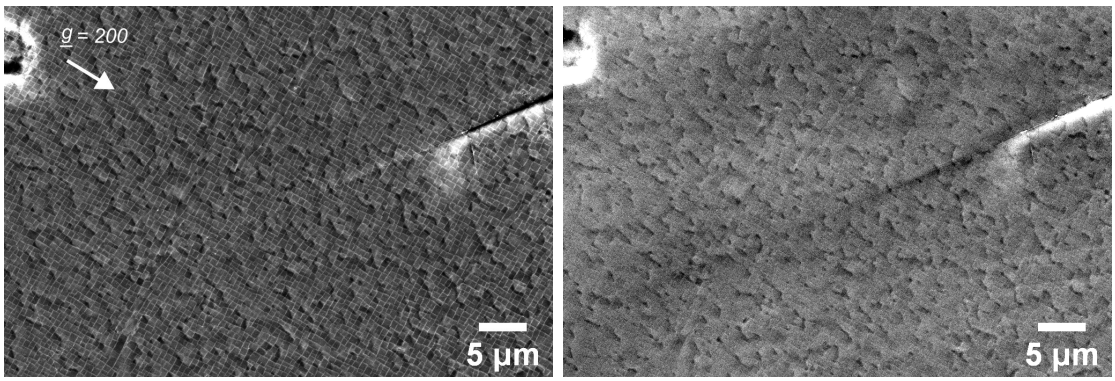


Figure 6.35: HR-EBSD 45 nm step size comparison with ECCI micrograph threading dislocations.

Crack 5

The dark region in the contrast-enhanced SE micrographs that extend out from the crack tip correlate with the brighter region in the BSE/ECCI micrographs. Figure 6.37 shows how the dislocation activity mostly occurs along the crack path or the other slip system parallel to the primary crack's path on one side. Like other shearing cracks, the slip ahead of the crack tip extends out ahead for at least $\approx 21\,\mu m$ (fig. 6.38). The dark "mottling" like features seen in the micrographs have been observed in other similar SXNBSs (heat-treated) and are not related to γ' coarsening from creep [128, 129].



(a) BSE micrograph. **(b)** SE micrograph.

Figure 6.36: Low magnification ECCI analysis of crack 5. Condition ID 2.

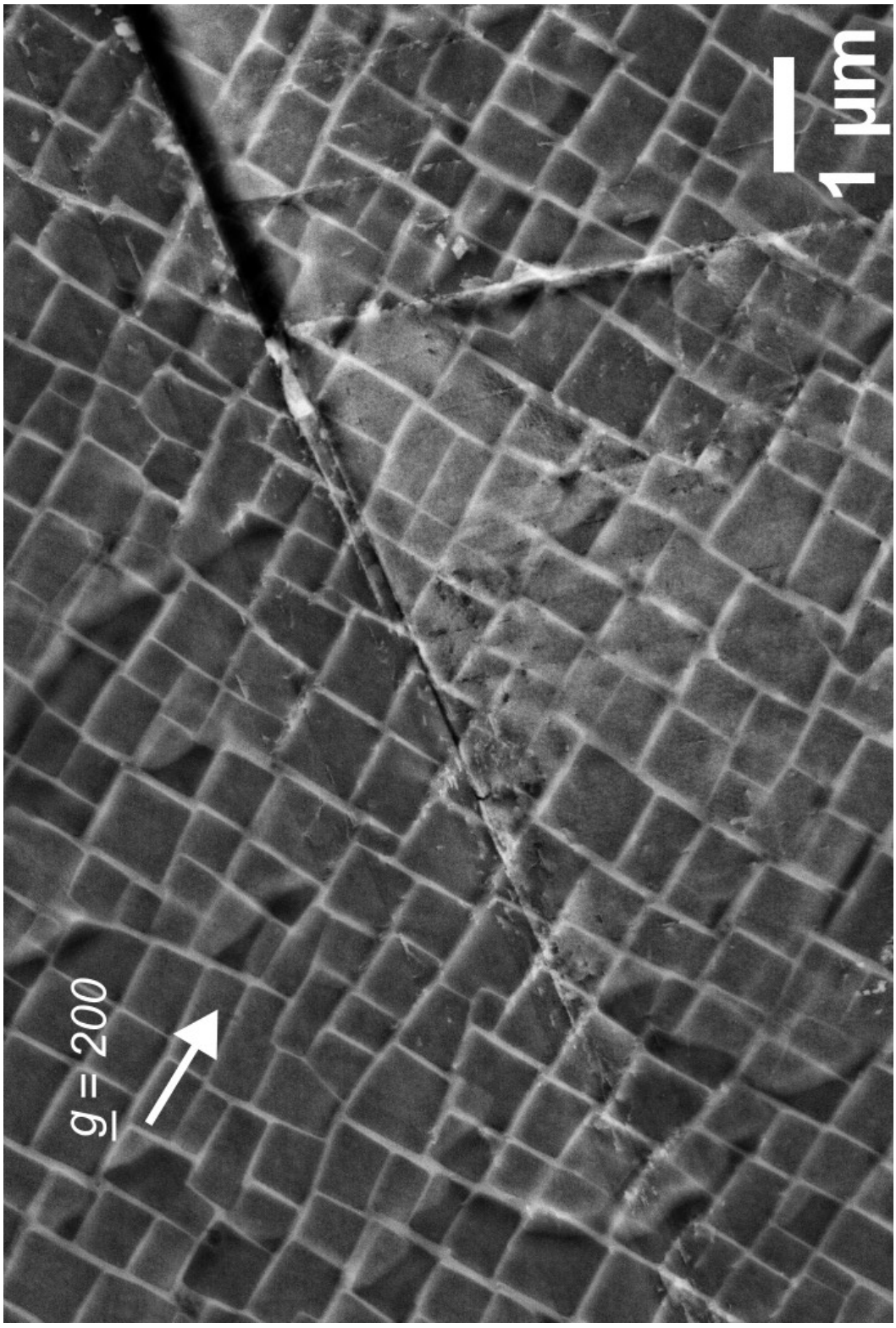


Figure 6.37: High resolution ECCI micrograph of crack 5. CLAHE enhancement was used.

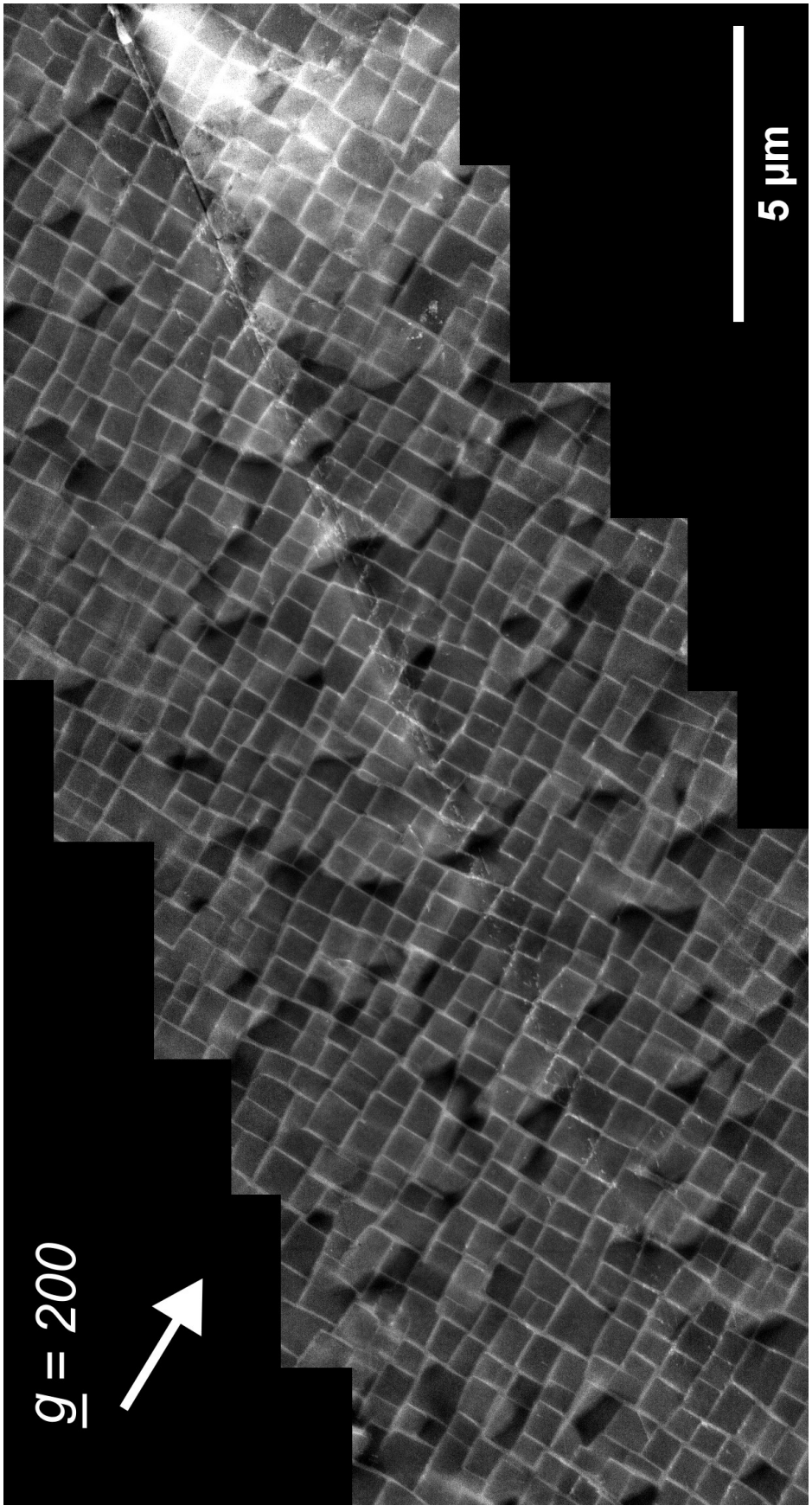
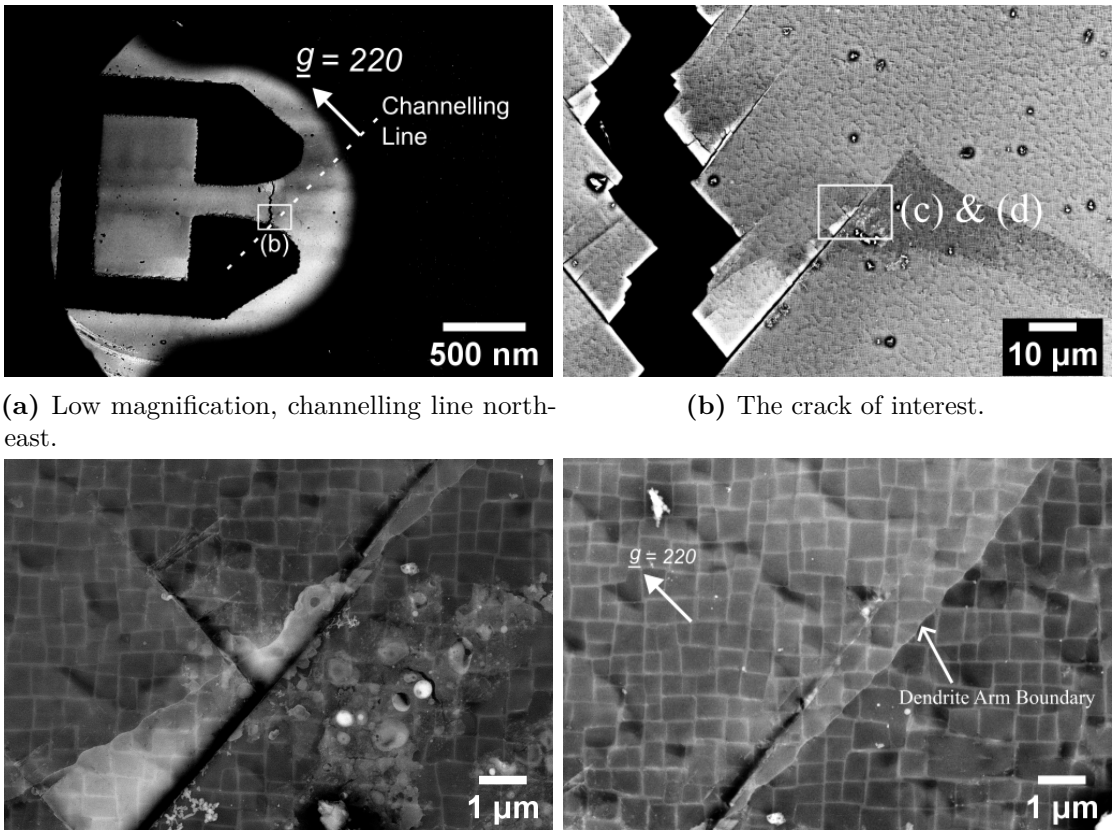


Figure 6.38: Stitch of ECCI micrograph of crack 5. Auto brightness-contrast enhancement was used.

6.4.2 Sample RJSK2

RJSK2 was tested in the SXO testing campaign to $N_f = 10^6$. It was orientated into a Bragg condition based on a likely $\underline{g} = \langle 220 \rangle$ channelling line, which has also been observed for similar conditions in RJSK4 from the same foil. A dendrite arm boundary occurs across the crack of interest, seen in the ECCI micrographs because of the small misorientation between the two dendrites.



(a) Low magnification, channelling line north-east.

(b) The crack of interest.

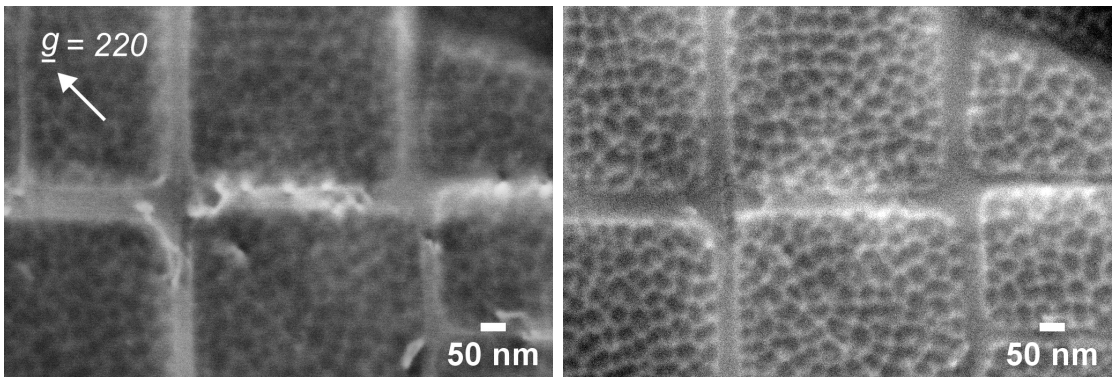
(c) Sub-crack.

(d) Primary crack tip.

Figure 6.39: ECCI micrographs of the cracks of interest in sample RJSK2.

Figure 6.40 demonstrates how the BSE signal in ECCI has stronger defect contrast than the SE signal, showing dislocations are seen at the $\gamma - \gamma'$ interfaces and the γ channels. Non-threading segments of the dislocations appear to connect threading segments at their ends. In the γ', the non-threading appears to have dark-bright parts on either side, whereas, in the γ phase, they appear bright.

Those whose dark-bright splits follow northwest also follow the estimated $\underline{g}$, but many dislocations do not exhibit this.



(a) BSE with 127-pixel block size CLAHE enhancement.

(b) SE with auto brightness-contrast.

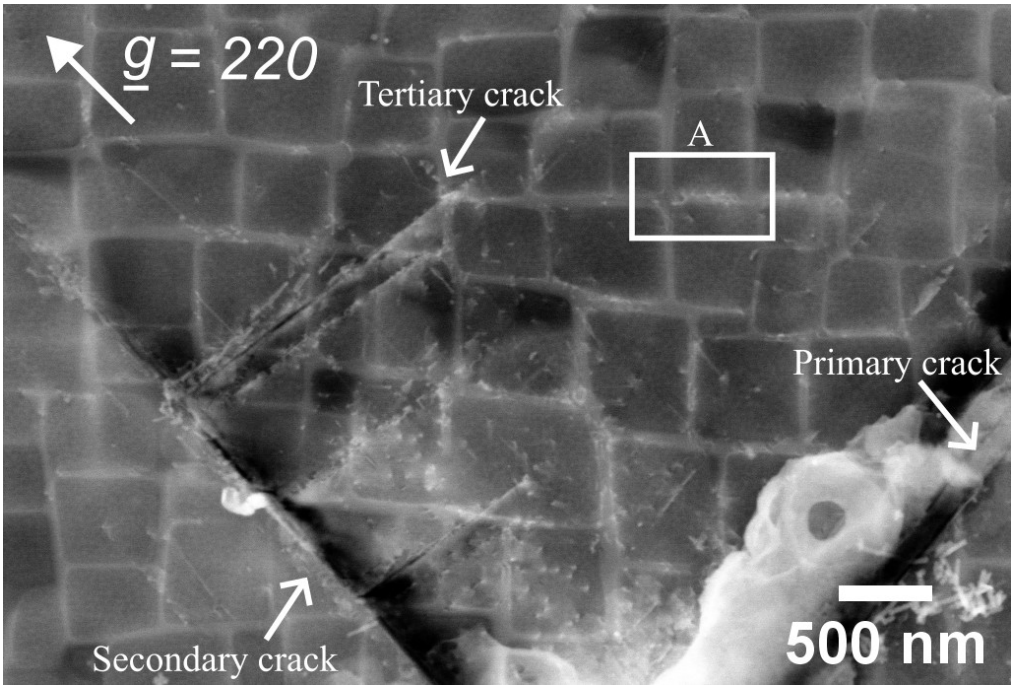
Figure 6.40: Comparison of SE with BSE (i.e. ECCI) micrographs under high magnification in sample RJSK2. From fig. 6.41a.

In the region between the secondary crack and the primary crack in fig. 6.41a, many threading dislocations can occur along {111} slip traces. The threading dislocation density increases closer to where the two cracks meet. Non-threading dislocations can also be observed but are less frequent.

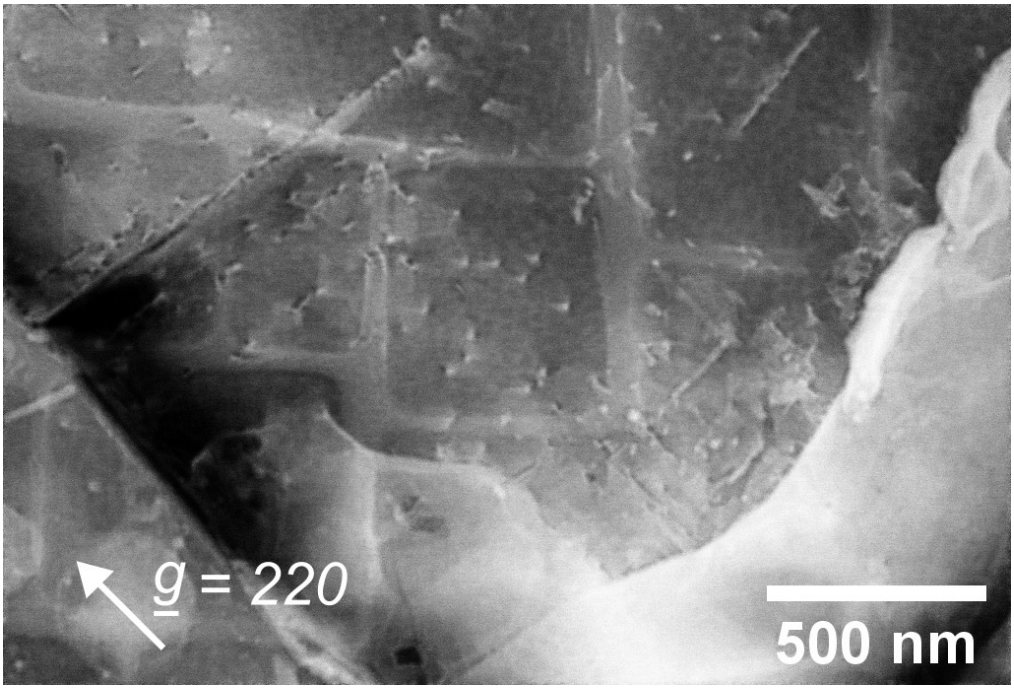
The dislocation density is locally higher around either side of the secondary and tertiary cracks.

The physical secondary crack tip is discerned in SE image (fig. 6.41d) and shows that dislocations are emitted along a {111} slip trace parallel to the crack path for microns (the yellow boundary in fig. 6.41e). A dislocation in fig. 6.41f has a trace parallel to the tertiary crack paths and could be the early stages of one of these cracks once the secondary crack grows further.

Some non-threading dislocations have bright-dark splits that appear to follow their line vectors, so, they either have splits normal or parallel to $\underline{g}$.



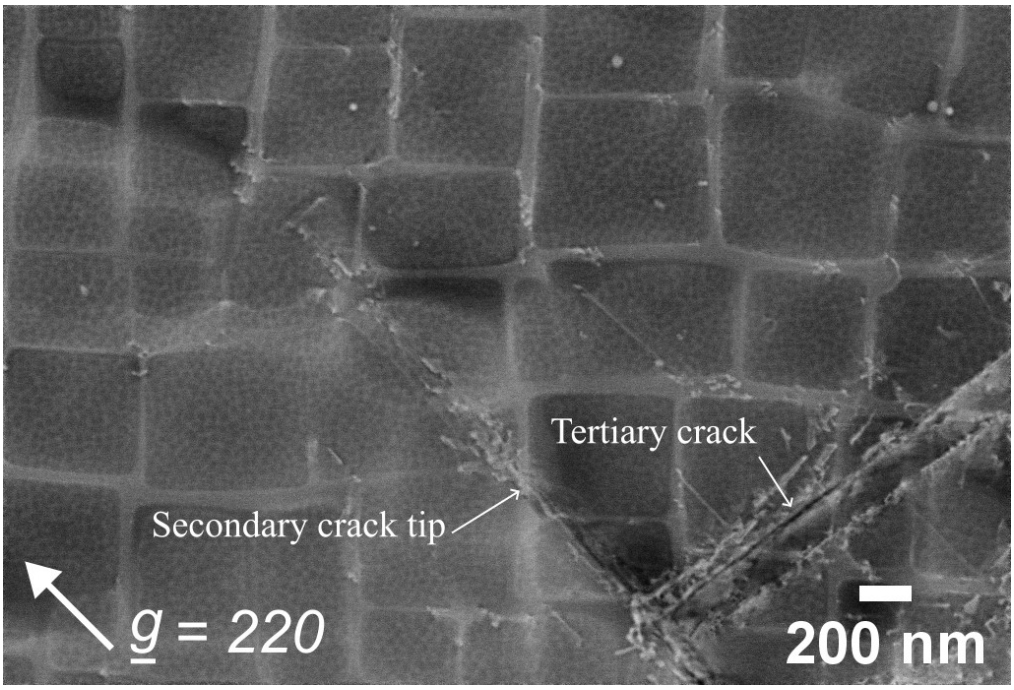
(a) ECCI of the bifurcation region from the crack of interest.



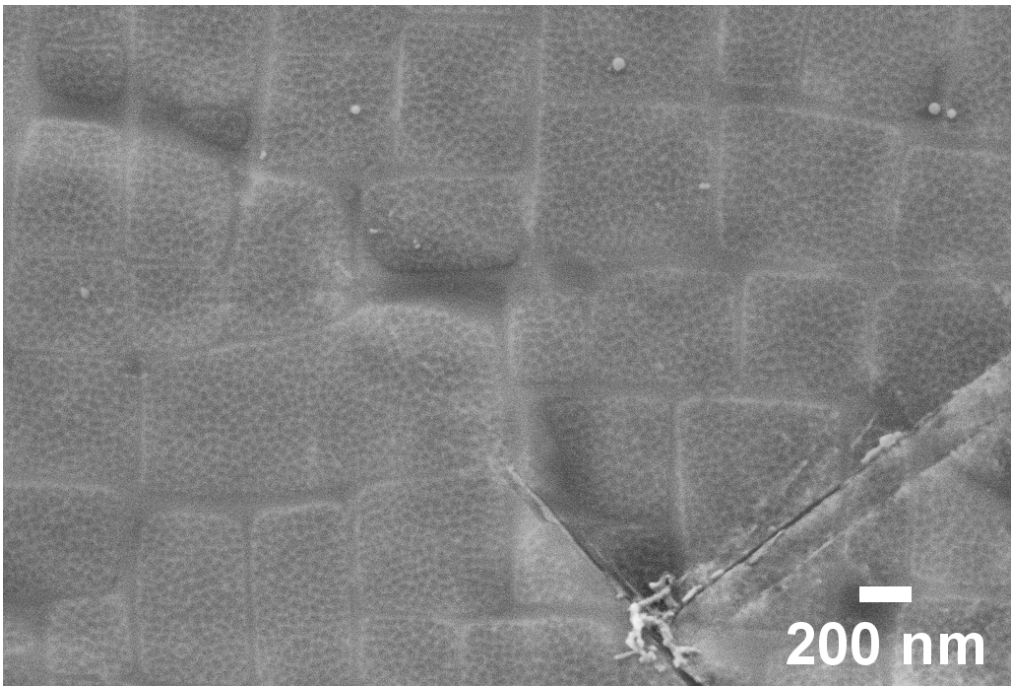
(b) The region between the primary and 1st tertiary crack. CLAHE with an 11-pixel block size.

Figure 6.41: ECCI analysis of the secondary crack region of sample RJSK2. CLAHE enhancements on 1024-pixel wide micrographs.

(Cont. Next Page)



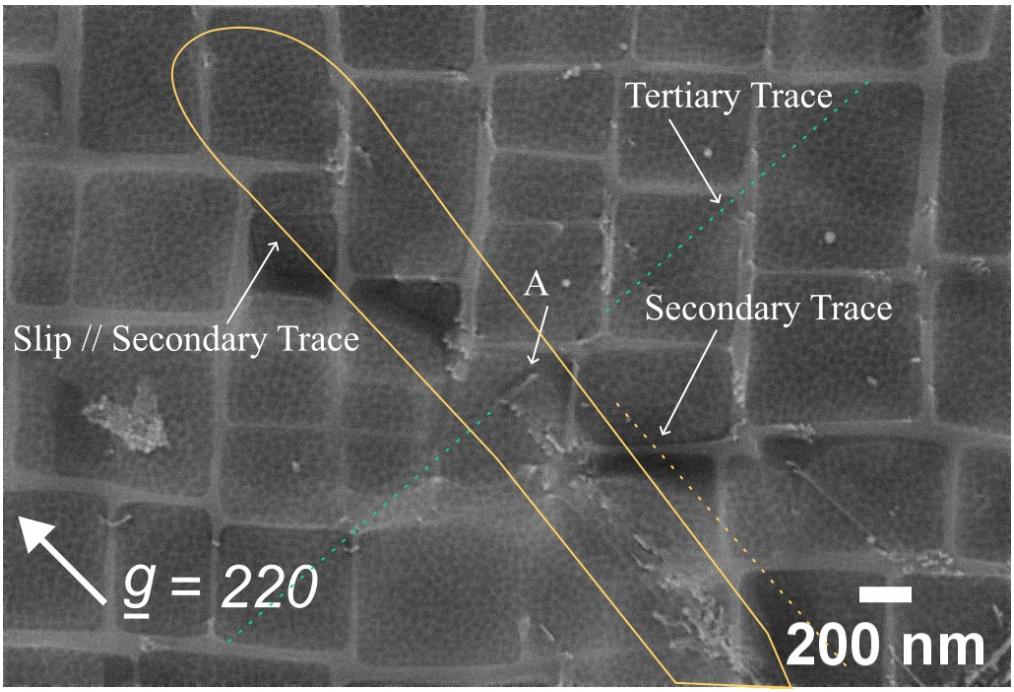
(c) ECCI around secondary crack tip. CLAHE with an 11-pixel block size.



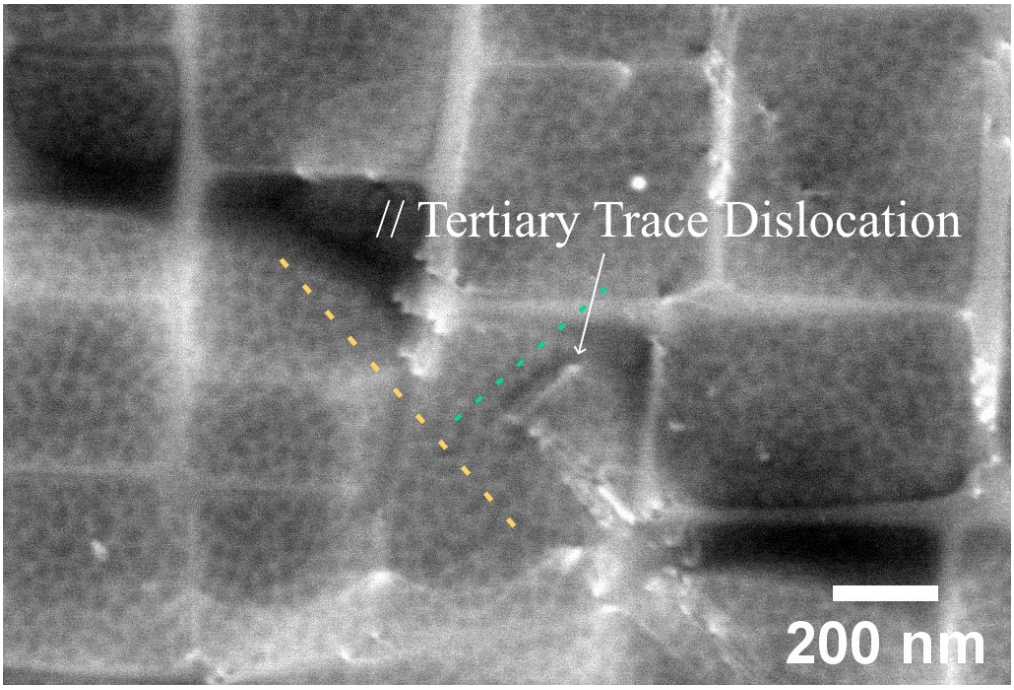
(d) SE around secondary crack tip. CLAHE with a 127-pixel block size.

Figure 6.41: ECCI analysis of the secondary crack region of sample RJSK2. CLAHE enhancements on 1024-pixel wide micrographs.

(Cont. Next Page)



(e) ECCI ahead of secondary crack tip in fig. 6.41c. CLAHE with an 11-pixel block size.



(f) ECCI around "A" in fig. 6.41e with just auto brightness-contrast enhancement.

Figure 6.41: ECCI analysis of the secondary crack region of sample RJSK2. CLAHE enhancements on 1024-pixel wide micrographs.

Comparing the SE and ECCI micrographs of the primary crack tip in fig. 6.42, the large contrast in the low magnification image appears to be a high dislocation density on a secondary slip system, exhibiting both threading and non-threading types. The intense brightness could be from a high non-threading dislocation density, or significant crystal rotations could cause the dark and bright regions. The bright region is associated with a $\approx 200\,\text{nm}$ long crack on the secondary slip system, and the dark region could be the start of a crack; these crystal rotations could be due to a tearing mode deformation from those cracks / proto-cracks.

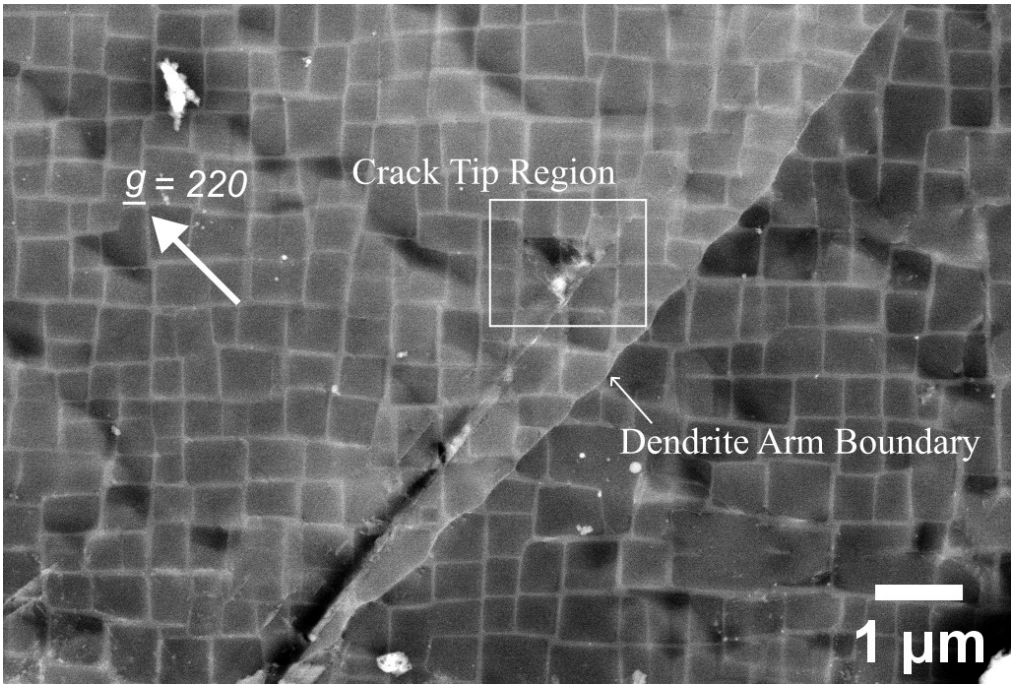
Ahead of the primary crack tip in fig. 6.42c, threading dislocations can be seen in pairs. Figure 6.42e shows that they become less frequent further along the slip plane. In fig. 6.42a, as one side of the crack is darker, this indicates rotation on one side and hence a tearing mode component to the crack propagation, so these dislocations could be related to a threading screw dislocation slip. Their dark-bright splits are parallel to $\langle 100 \rangle$ and not $\underline{g}$, indicating that they are not pure screws, and so they may be dislocation reactions from a pure screw, or they were/are not screw dislocations.

The lack of in-plane cutting of the precipitates seen in the micrographs are thought to be due to the following reasons (can act together):

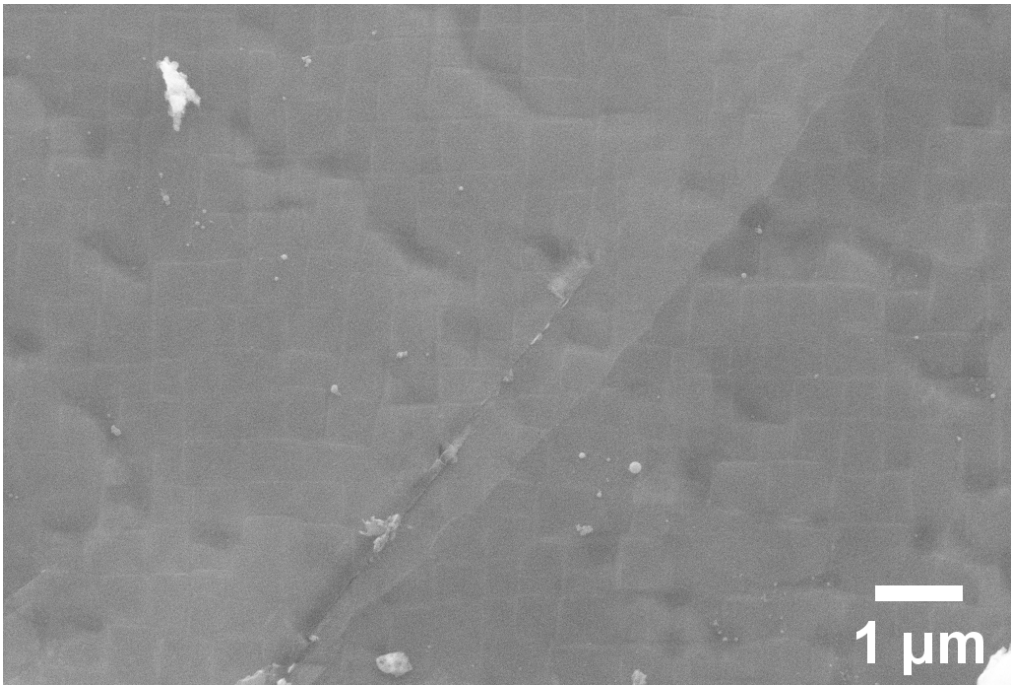
1. Fatigue is fully reversed, so there is low local irreversibility of the slip in comparison to fatigue tests where $R > 0$ and their significant degree of precipitate cutting.
2. The less likely reason is that $\underline{b}$ is near normal to the viewing plane normal (i.e. [001]) and so would not result in less strong shearing in the micrograph.

Non-threading dislocations on a parallel slip plane can be seen in fig. 6.42e that have an opposite dark-bright split to the aforementioned threading dislocations; likely having an opposite $\underline{b}$.

Threading dislocation-like contrast can be found along the dendrite boundary in fig. 6.42e (shown in inset), possibly due to its very low-angle grain boundary or because gliding dislocations are caught at the boundary.

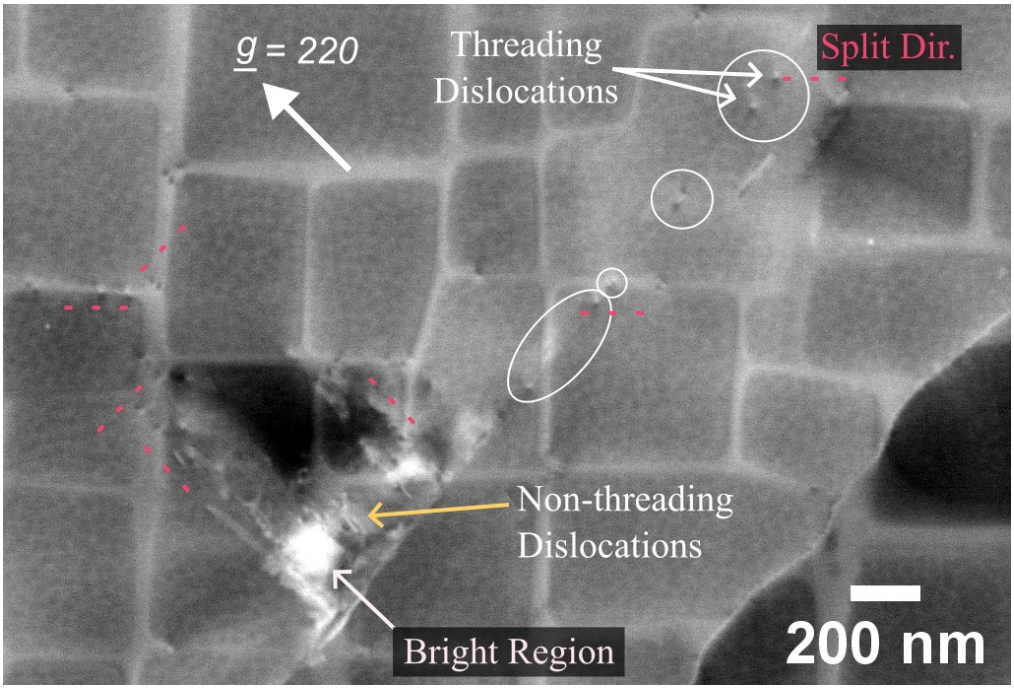


(a) Low mag. ECCI at the primary crack tip.

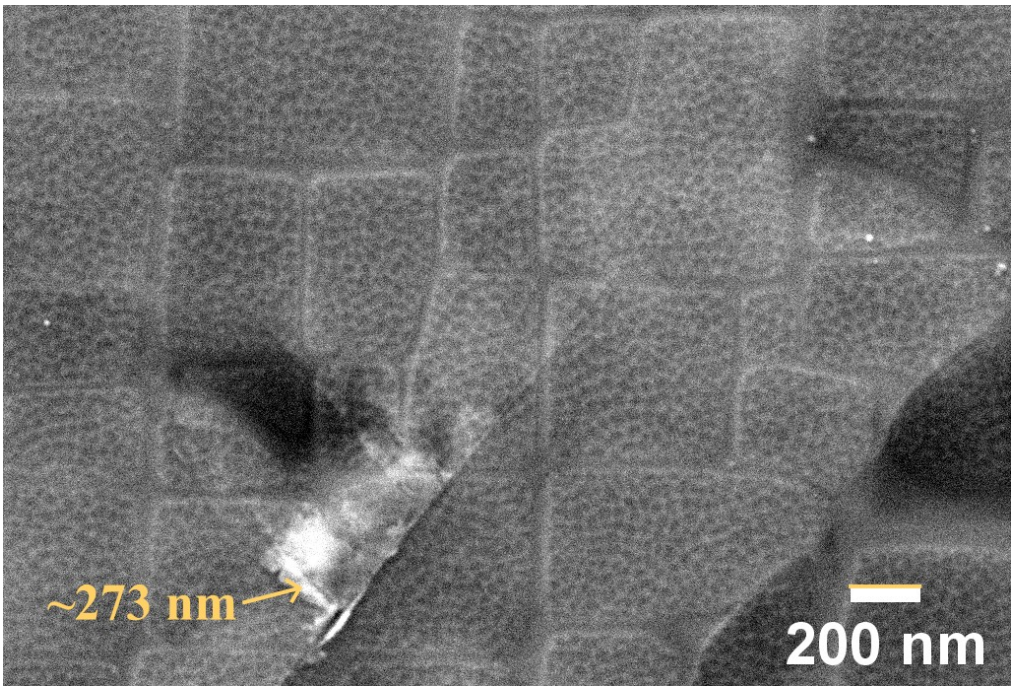


(b) Low mag. SE at the primary crack tip.

Figure 6.42: ECCI analysis of the primary crack region of sample RJSK2.
(Cont. Next Page)

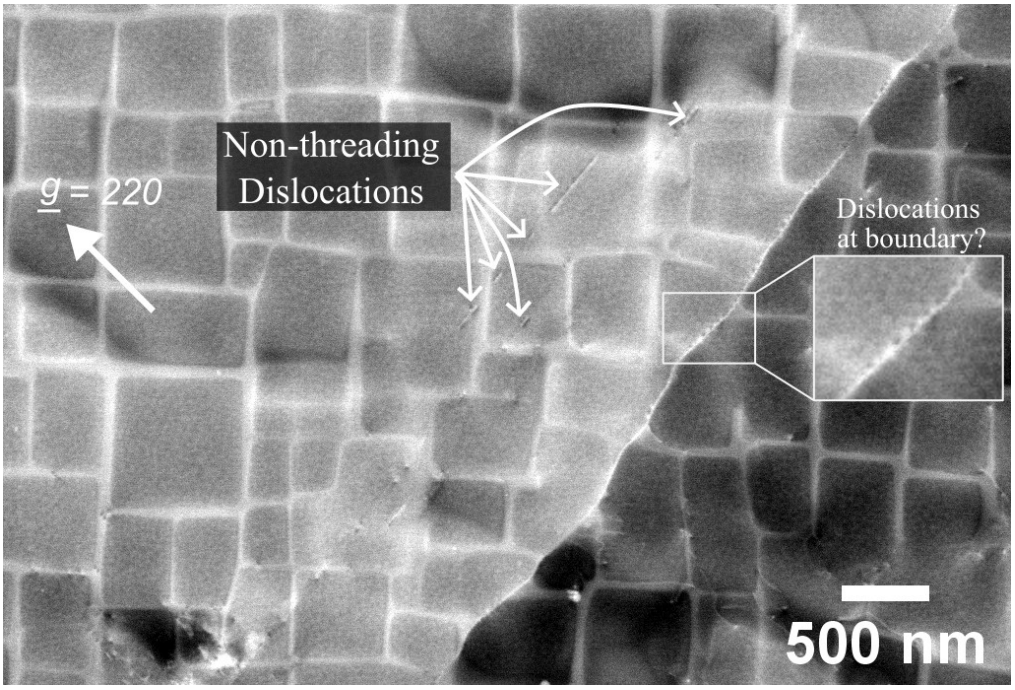


(c) ECCI at primary crack tip. Auto-brightness contrast. Dashed red lines are the dark-bright splits of the nearby defects.



(d) SE at primary crack tip. Auto-brightness contrast.

Figure 6.42: ECCI analysis of the primary crack region of sample RJSK2.
(Cont. Next Page)



(e) ECCI ahead of primary crack tip.

Figure 6.42: ECCI analysis of the primary crack region of sample RJSK2.

6.4.3 Conclusions

- The fatigue crack can rotate the crystal locally on either side of it, due to a tearing mode (mode-III) component, causing a localised increase or decrease in the background BSE intensity on one side. The tearing mode component is reasonable, considering the crack path orientation and the cantilever bending (Ref [53]).
- According to Ref [42], the threading dislocations seen ahead of these tearing mode component cracks are likely screws (or related).
- A high dislocation density can manifest as a bright region in the ECCI micrographs; these can sometimes be captured in HR-EBSD ρ_{GND} maps.
- The observed dislocations range from purely non-threading to purely threading in appearance.
- Slip is highly planar at RT, with dislocations being found along specific parallel {111} slip planes. The slip ahead of a crack tip is predominantly of a slip system with a trace parallel to the crack path and often extends for microns

ahead of the tip.

- The frequent tearing mode observed with a primary crack is accompanied by a secondary slip system being active mainly on one side of that crack. The observed sub-cracks form on that side and follow the plane of that secondary slip system.
- Sub-cracks tend to form their own sub-cracks (i.e. sub-sub-cracks), which are associated with the slip system of the primary crack and form on one side of the sub-crack in the direction of the primary crack. Examples are in figs. 6.27 and 6.39. This behaviour and the previous point help explain the branching zig-zag {111} fracture path.
- Higher dislocation densities occur in the ECCI micrographs where the primary and sub-cracks meet. Both slip systems can be observed and are harder to distinguish unless there are non-threading dislocations.
- Comparisons between HR-EBSD ρ_{GND} maps with the RT Air ECCI micrographs tends to show different information. The trend is that where the dislocations density in ECCI is low, the ρ_{GND} map does not show it, but where the ρ_{GND} map shows high counts the ECCI micrograph often shows brighter intensity regions. This may indicate that the high density makes it challenging to identify individual dislocations, but they manifest as a general increase in BSE intensity in that region, as seen in fig. 6.34. Higher ρ_{GND} is also observed on the secondary slip system along the crack path (fig. D.9), and along nearby γ channels (fig. 6.34). Generally, the ECCI micrographs give more information about the deformation and the dislocation structures than the ρ_{GND} maps.
- The dislocations do not avoid the γ' phase, indicative of shearing mode failure, in addition to the observed {111} crack planes. Dislocations occur in the γ and γ' phases (see RJSK2). However, they are mainly found at the $\gamma - \gamma'$ interface in γ, likely due to γ's low strength, and more are found within the γ' precipitates than in the γ (bulk) which could be due to their lower dislocation mobility.

- Threading dislocations are often observed in pairs, especially at the $\gamma - \gamma'$ interfaces, which is understandable when considering the superdislocation mechanism for deformation (figs. 6.35 and 6.42c).
- Despite some dislocations having been captured under different channelling conditions. Assessing the $\underline{b}$ from these photos can be challenging as the same dislocations can appear as non-threading and then threading depending on the $\underline{g}$ used. Additionally, the observed BSE intensities in the ECCI micrographs are not trivial. The defects' super-dislocation nature and varying threading degrees complicate the observed BSE intensities and future ECCI defect simulations would be beneficial.

6.5 Intermediate Temperature

This section will investigate the intermediate temperature (IT) fatigue performance compared to room temperature (RT) fatigue (aim 9) and whether low p_{O_2} will affect this. The interplay between T, frequency (f), and p_{O_2} on the fractography (aim 10) will also be addressed.

6.5.1 Intermediate Temperature Rig

Figure 6.44 shows the setup for IT testing. A K-type thermocouple feedback loop with a control box controls the chamber's temperature. To avoid heating the piezoelectric actuator and other components, the horn is significantly longer and pressurised air is used to cool the bellow externally.

A standard USB webcam was used instead of the Thorcam due to a lack of space. However, the camera distortions and perspective are accounted for.

The samples had to be thinned via electropolishing due to a lack of coupling in the preliminary tests. After each electropolish, the thickness was tracked using the height micrometer to achieve values around $135 - 140\mu m$.

Air Specifics

The furnace controller and horn placement were adjusted to obtain a steady state temperature of 450 °C at the tip of the horn (fig. 6.43). The samples are placed in the horn tip and are assumed to be the tip's temperature as it acts as a heat bath compared to the significantly smaller fatigue sample. As the chamber window was open, significant temperature gradients occurred from the heat loss, and an offset of the demand temperature was required. The p_{O_2} is estimated to be $\approx$ 212 mbar (appendix C).

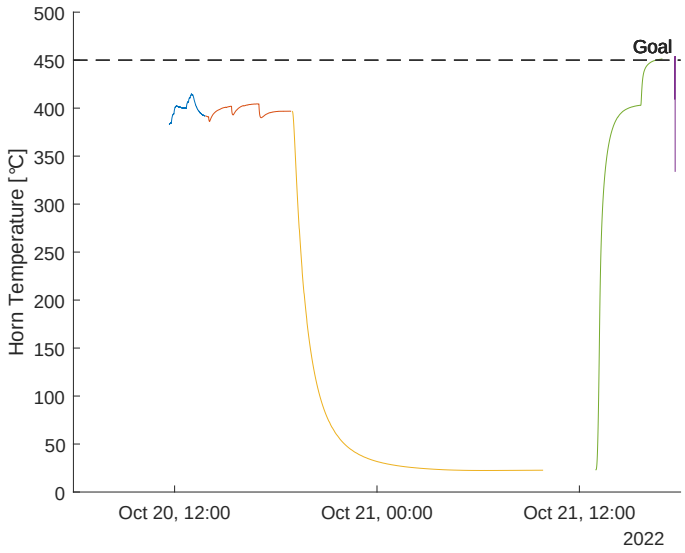


Figure 6.43: K-type thermocouple tracked the temperature of the tip of the horn as a function of time and changing chamber goal temperature. Goal horn temperature is $\approx$ 450 °C. Yellow & purple periods are turning the furnace off.

The bellow and adjustable height allowed the horn tip to be placed at the maximum temperature and to retract the horn whilst the furnace reached the desired temperature to minimise oxidation.

The resonant frequency of the actuator was tracked, and the fatigue was paused for a duration between 50 s to 100 s whenever the horn resonant frequency dropped too far due to self-heating.

Vacuum Specifics

To achieve a good vacuum, the chamber is baked out with the horn inserted and the window open to avoid byproducts being pumped. If successful, then $\leq 10^{-6}$ mbar pressure levels in the chamber are achievable e.g. 5.6 - 6.8 $\times 10^{-8}$ mbar when the furnace temperature is 650 °C. The p_{O_2} estimation is therefore $\approx$ 1.2 - 1.4 $\times$ 10^{-8} mbar (appendix C).

To minimise self-heating of the horn under vacuum, a similar horn was made from Inconel-718 rather than 304 stainless steel as its greater σ_y/E should minimise its hysteretic heating. Their thermal conductivity values of 9.3 W m^{-1} K^{-1} to 11 W m^{-1} K^{-1} and 16.2 W m^{-1} K^{-1} respectively.

However, under operation, the proprietary Branson power supply could not operate with this horn. So, a bespoke power supply had to be used and manually set the driving frequency operated at/near maximum sample bending. So, the most power was transferred into bending the sample for a given voltage (to reduce the risk of damaging the bespoke power source).

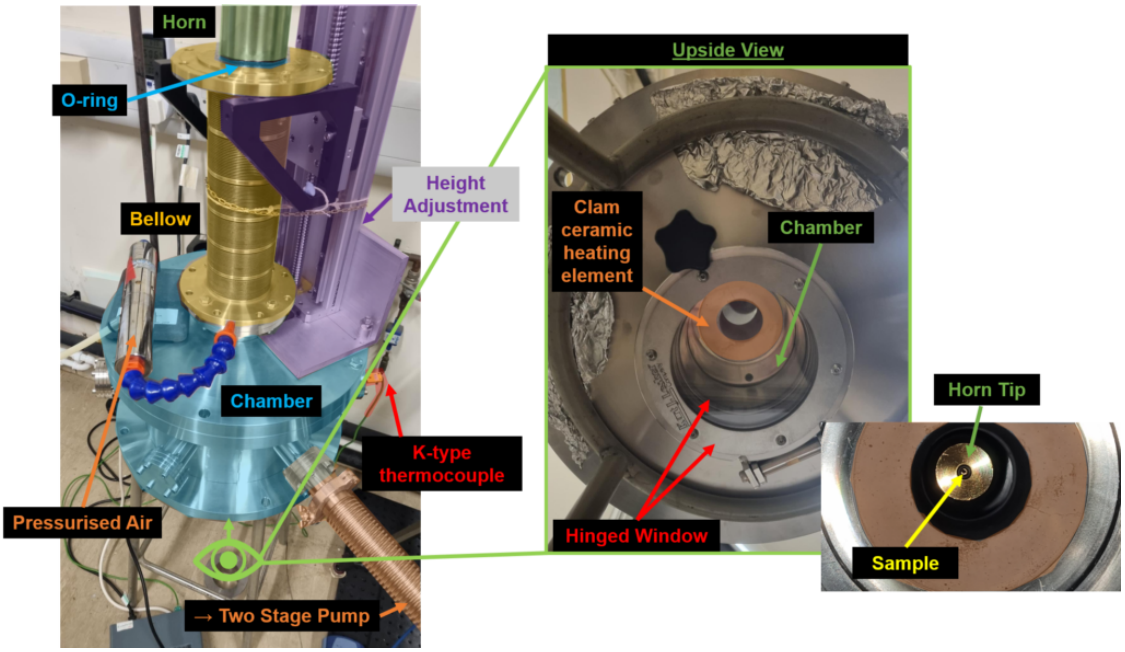


Figure 6.44: The intermediate temperature UFT rig setup. Including an upside view and what it looks like when the horn with a sample is inserted. The different components are labelled.

6.5.2 Intermediate Temperature Air

Fatigue Performance

The fatigue response with different temperatures can be accounted for in FEM by adjusting the $\underline{\underline{C}}$ tensor in ABAQUS (section 2.1.2) or by changing the temperature value in the CPFE model's UMAT. Using the former technique, the median stress-per-angle (ω) noticeably decreases and increases in variation (fig. 6.45) due to lower $\underline{\underline{C}}$ and thicknesses.

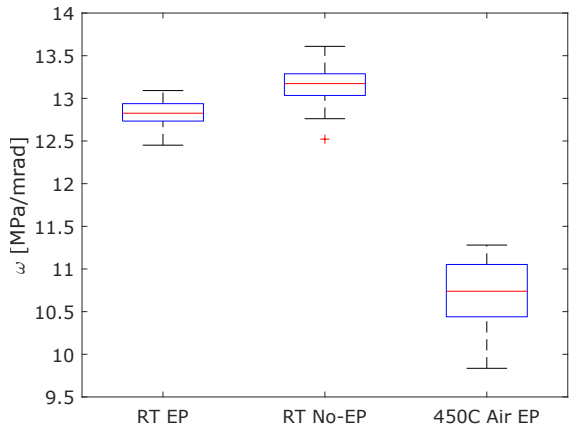
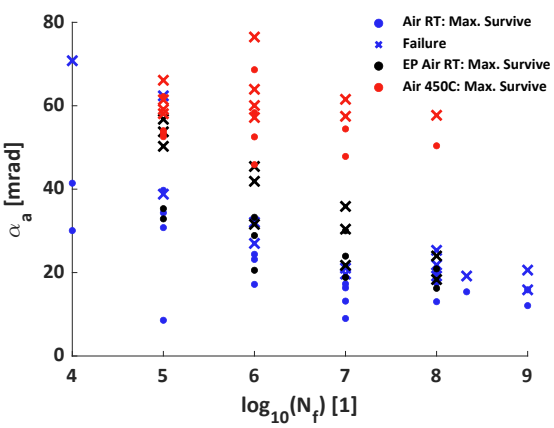
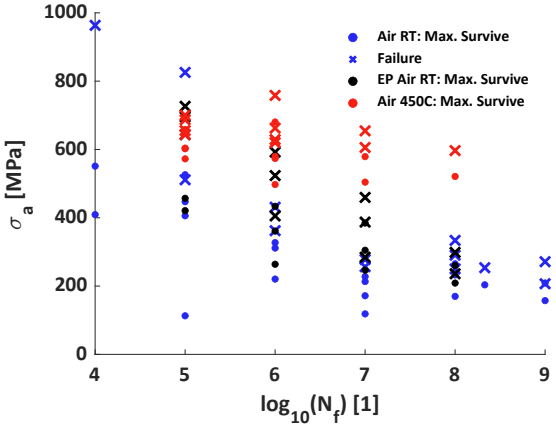


Figure 6.45: Box plot comparison of median ω values between RT EP & No-EP with those tested at 450 °C.

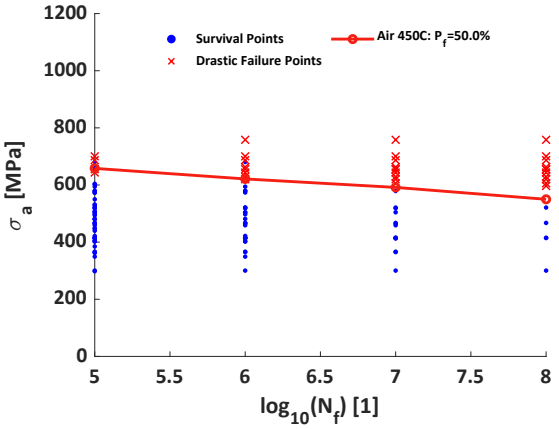
The greater ω variation tightens the spread in the S-N data from the A-N data (fig. 6.46). It is clear from fig. 6.46 that, in general, the in-air fatigue performance improves when going from RT to IT. However, this difference becomes greater with increasing N_f, becoming more appreciable to the RT EP air data at 10^5 cycles. The difference between the RT EP and 450 °C air curves ranges from 100 MPa to 271 MPa (for $N_f = 10^5 - 10^8$).



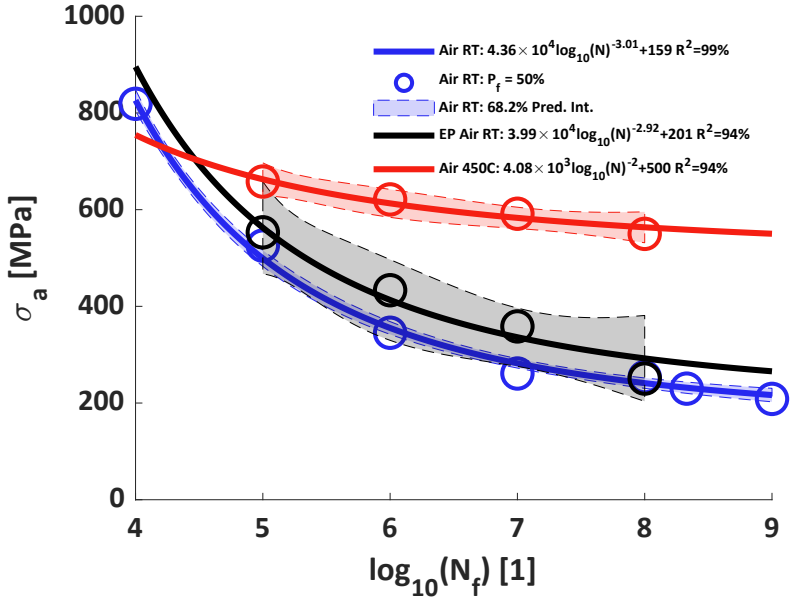
(a) A-N.



(b) S-N.



(c) S-N 450 °C propagated.



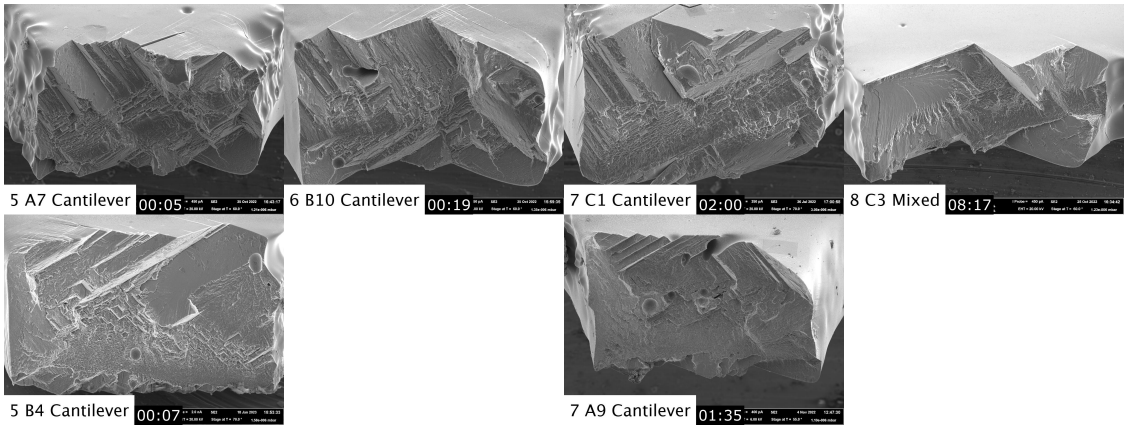
(d) S-N curves.

Figure 6.46: Fatigue response comparison between RT air (EP and no-EP) with EP IT air.

Oxidation Response

Figure 6.47 shows in its OM images that the surface oxidation tended to increase with increasing N_f (left-to-right in the columns), going from white $\rightarrow$ beige $\rightarrow$ brown $\rightarrow$ blue.

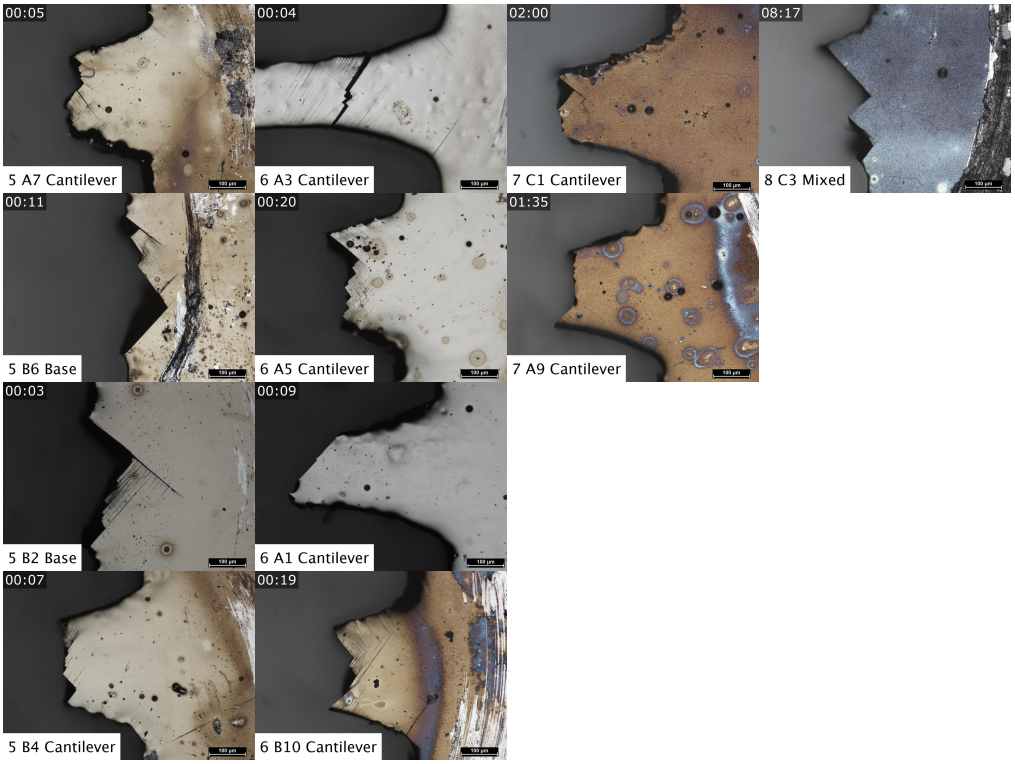
The variation in the oxidation amount in the lives 10^5 and 10^6 are likely due to variations in total time at temperature rather than chamber temperature.



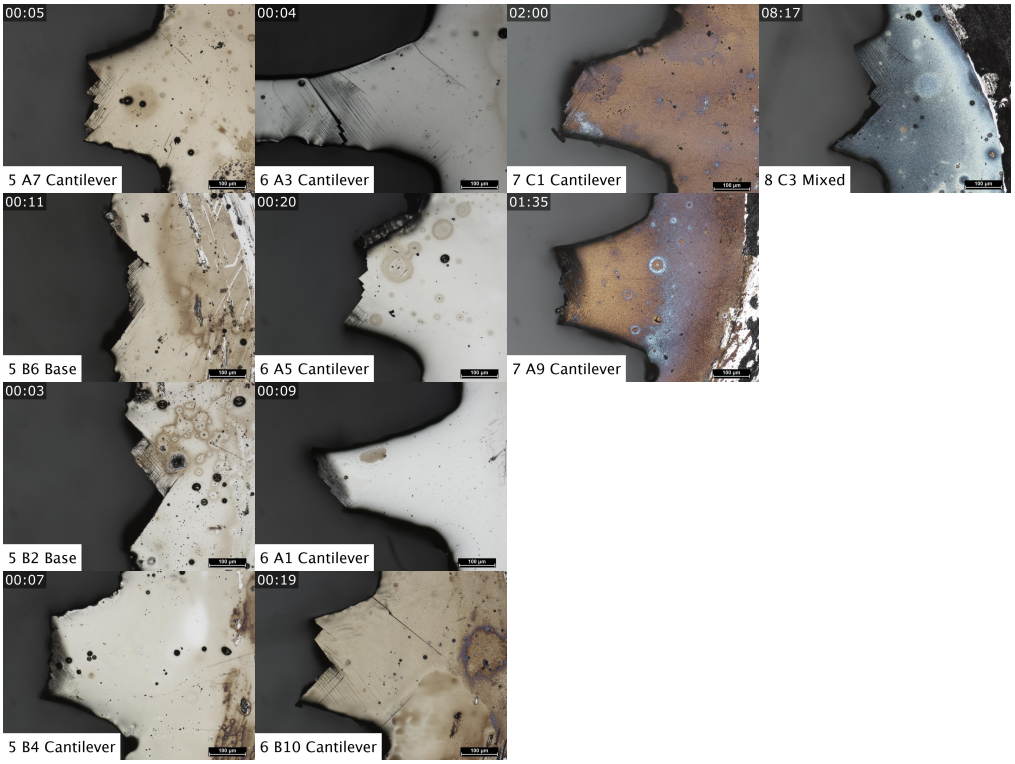
(a) SEM

Figure 6.47: IT air EP fractography Results. The time stamp indicates the estimated exposure time at temperature in hh:mm. Top-to-bottom indicates highest-to-lowest sample fatigue stress, the numbers and columns indicate the decade (i.e. $N_f = 10^x$), the letter-number combination is the sample ID, and the type of failure is at the end.

(Cont. Next Page)



(b) OM side 1



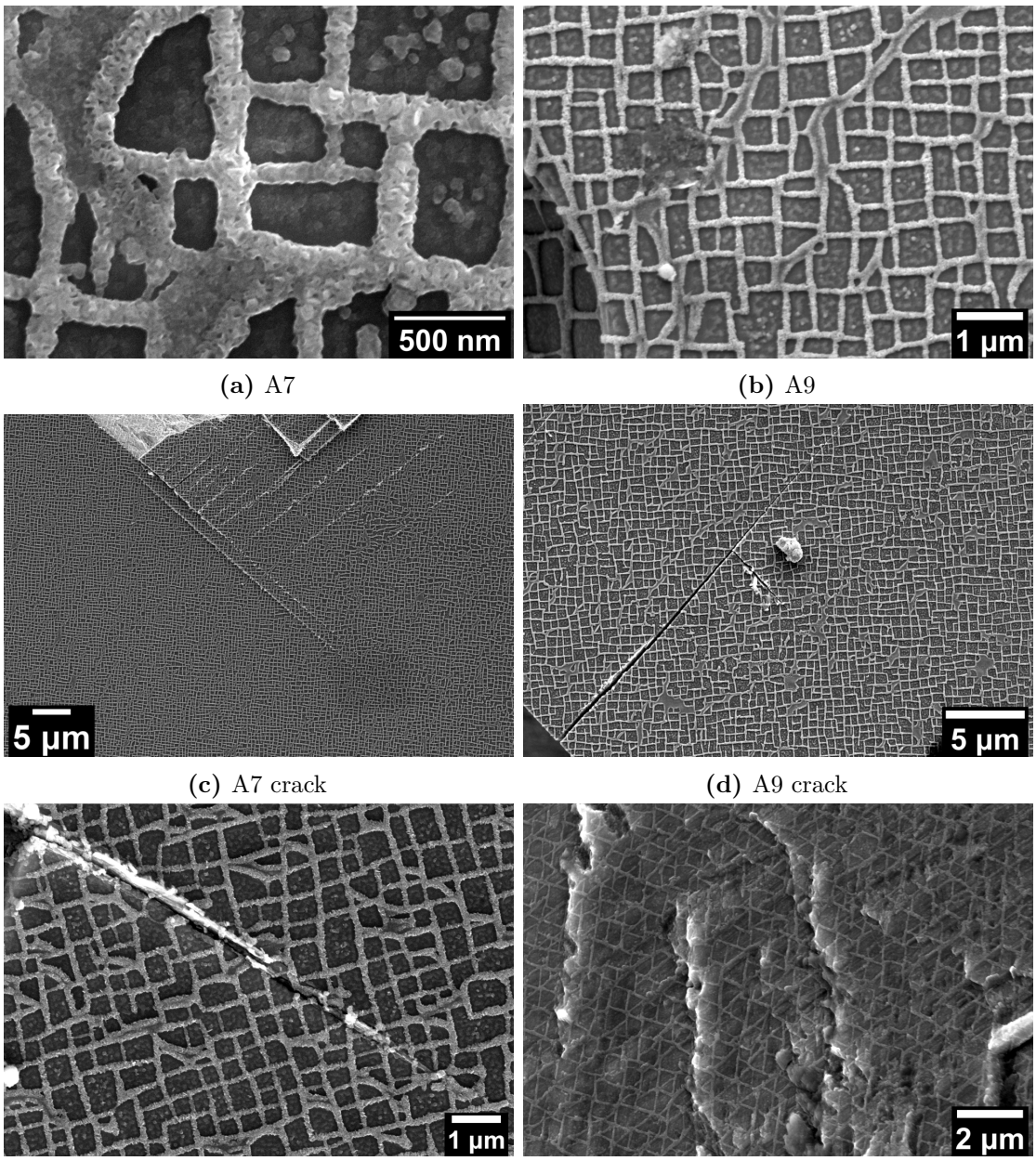
(c) OM side 2

Figure 6.47: IT air EP fractography Results. The time stamp indicates the estimated exposure time at temperature in hh:mm. Top-to-bottom indicates highest-to-lowest sample fatigue stress, the numbers and columns indicate the decade (i.e. $N_f = 10^x$), the letter-number combination is the sample ID, and the type of failure is at the end.

Figure 6.48 shows how the γ channels preferentially oxidised, raising them from the surface with a rough texture. The γ' still appears darker in colour but with small discrete protrusions from the surface within them. Similar to those seen in Ref [5] for a 1 h exposure in air at IT. Fracture surfaces that are oxidised also exaggerate the microstructure and can help identify whether the fracture is shearing or opening mode (e.g. fig. 6.48f).

High Ni and O counts are found along the oxidised γ channels of fig. 6.48's EDX count maps. NiO is the likely oxide of those protruding out of the channels as CMSX-4 fatigue at 450 °C showed similar oxidation [5, p. 130] and in the isothermal oxidation tests appears most like the transient stage where porous NiO forms over the γ channels and discrete thin Al-rich oxides over γ' like that observed in this work [5, §4.4.4, §4.5], specifically CMSX-4 with ≤ 1 h exposure in air at 550 °C [5, p. 91]. In the stable stage of oxidation, the oxidation seen covering the outer surface was still found to be NiO [5, §4.4.4]. The results appearing often like the short exposure times in the literature is not surprising considering: the 450 °C oxidation should be less compared to the same time at 550 °C; the relatively short duration of the fatigue tests (typically < 2 h, see estimated exposure times in fig. 6.47); and that the testing protocol was intended to minimise the exposure times at temperature. The oxidation is thought not to be Cr_2O_3 as it was absent in the similar oxidation of CMSX-4 [5, §4.5][24, p. 1690] and that the observed Cr counts in EDX could be partially due to peak overlapping with O in the EDX setup and analysis.

Oxides are found coming out from the fatigue cracks/slip bands on the surface. They appear in two ways: small and discrete for less open cracks and film-like for more open cracks.



(a) A7

(b) A9

(c) A7 crack

(d) A9 crack

(e) C1 crack

(f) C1 oxidised {111} fracture surface facet (fig. 6.56).

Figure 6.48: SEM images of the top/bottom surfaces of IT air EP samples, showing the oxidation.

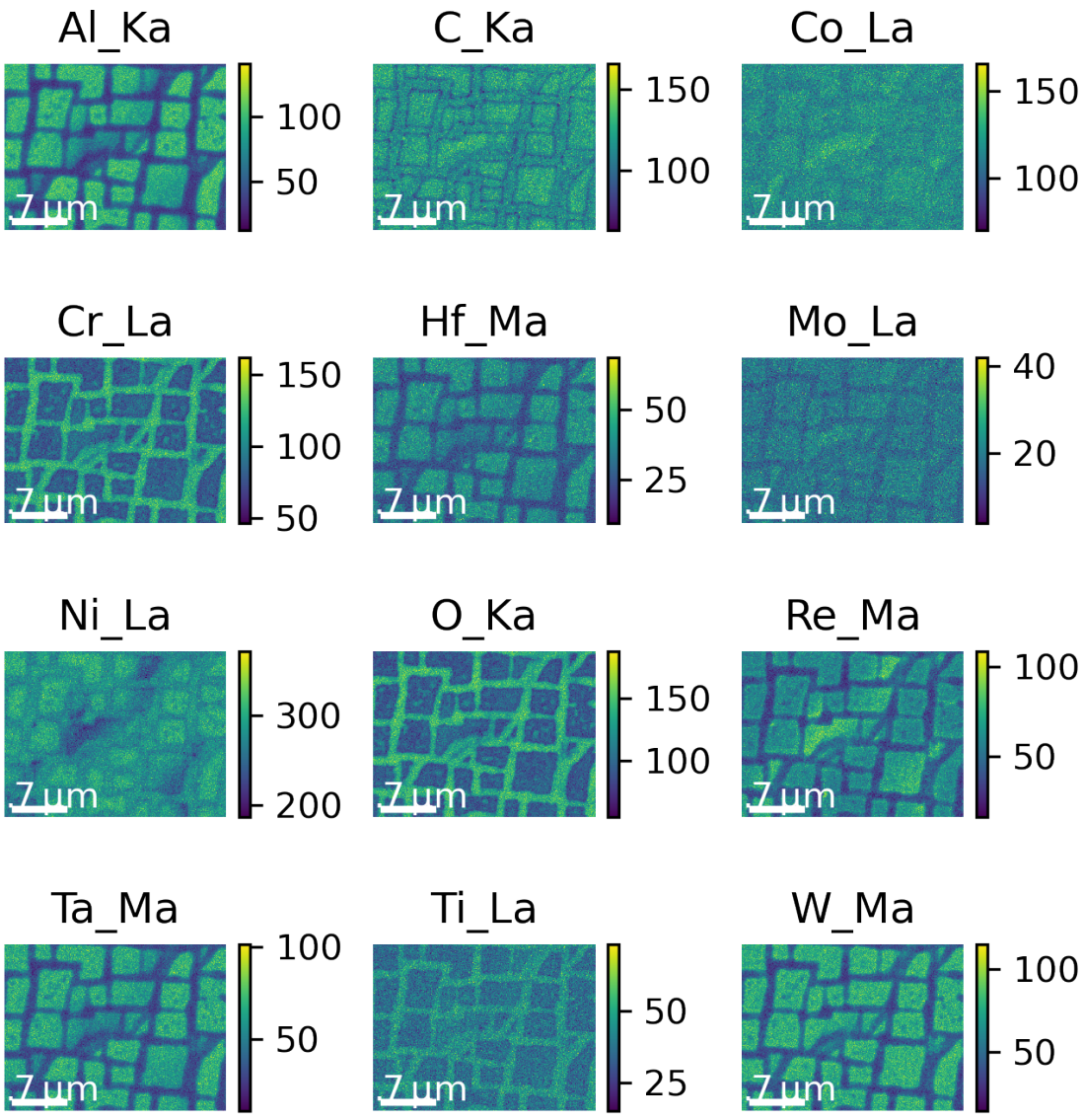


Figure 6.49: C3 EDX count maps with a down-sampling of 4.

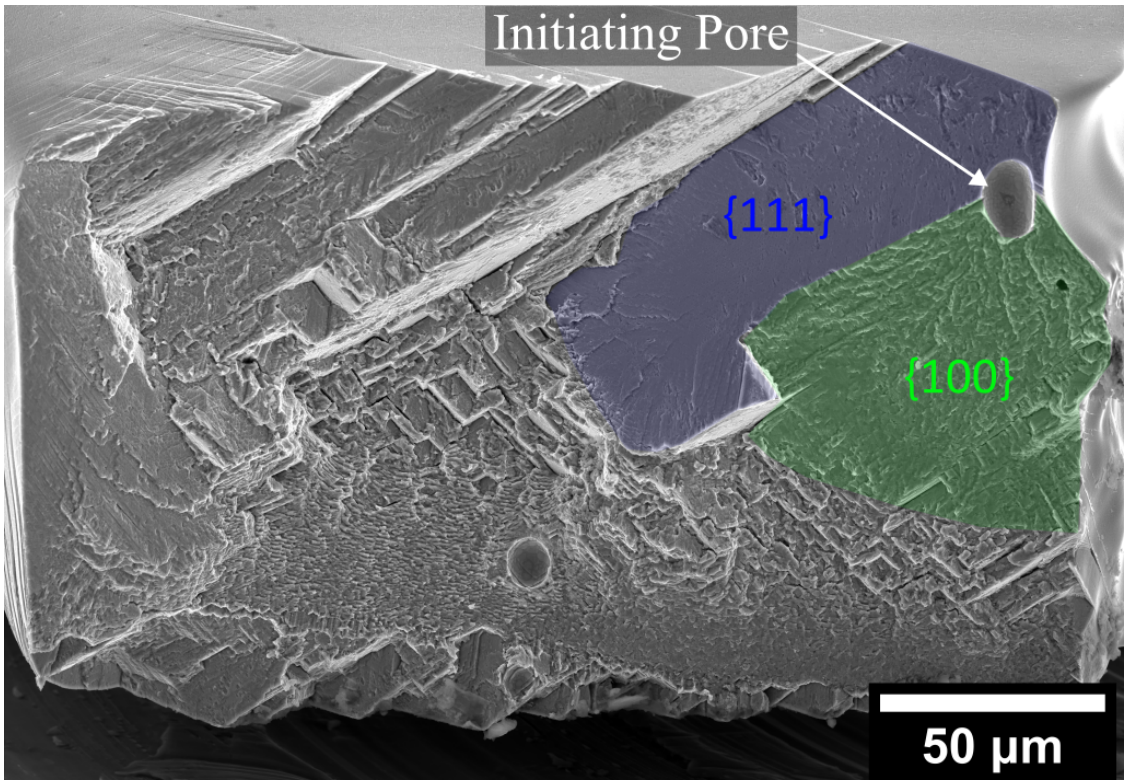
Fractography

Sample B4 ($N_f = 10^5$) is the clearest sample where the interplay between opening and shearing modes can be seen. Like the RT vacuum fractographs (section 6.3.4), there is a relatively smooth, circular feature around the suspected initiating pore with a near-normal orientation. Figures 6.50b and 6.50c in that region shows a (100) fracture plane microstructure, indicative of opening mode. Interestingly, initiating pores can contain both (100) and a {111} facets, which also occurred in some RT vacuum samples.

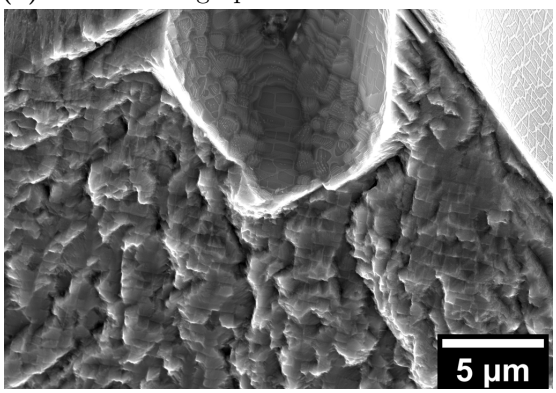
Using the OM and SEM fractographs (fig. 6.50a), the fatigue crack initiation likely started in the top right corner due to the lack of slip bands on that surface and the presence of a large pore.

Figure 6.50e shows a non-critical crack on the top surface that starts as shearing mode before briefly transitioning to opening mode for $\approx 2\,\mu m$.

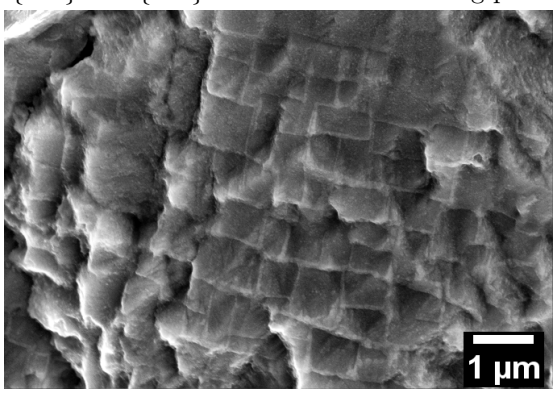
Towards the lower surface in fig. 6.50f, both a fine microstructure with facets near {100} planes (fig. 6.50h) and a smoother opening mode region exist (fig. 6.50g). The seamless transition between the two in fig. 6.50f indicates that the fine step region is also opening mode.



(a) Tilted fractograph with false colour to show {111} and {100} facets around initiating pore.

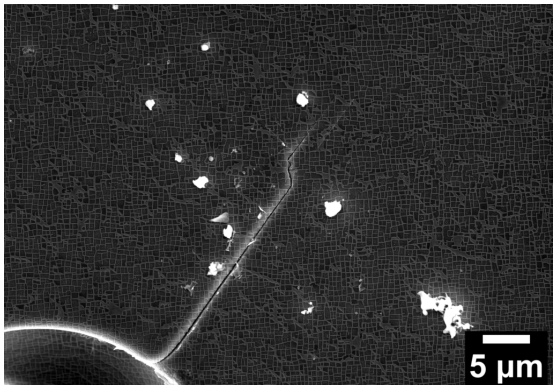


(b) Initiating pore.

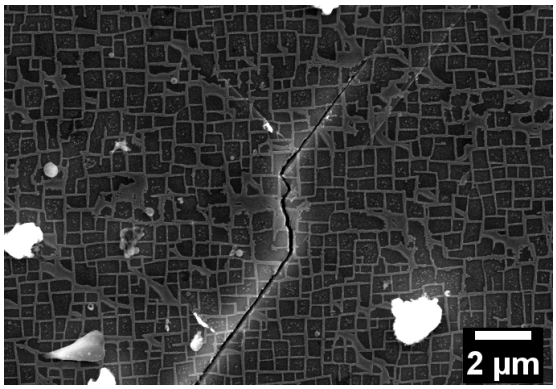


(c) Opening mode below pore.

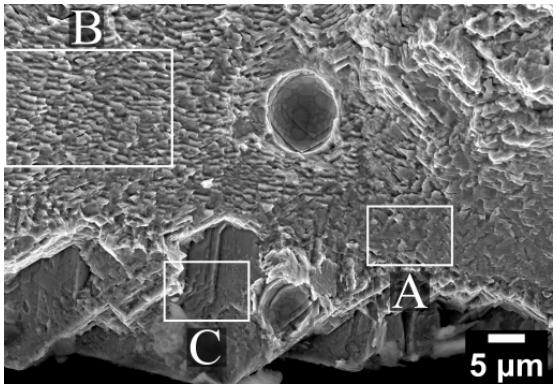
Figure 6.50: B4 ($N_f = 10^5$) fractographs an IT air EP sample.
(Cont. Next Page)



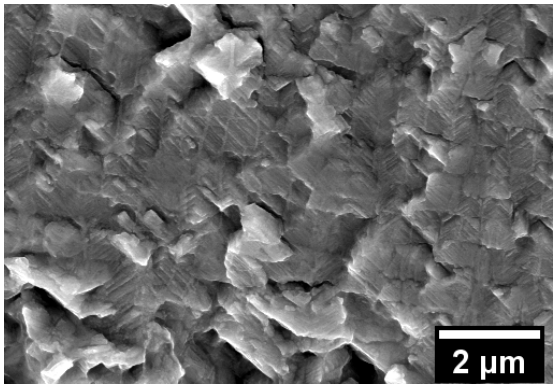
(d) Fatigue crack on the top surface.



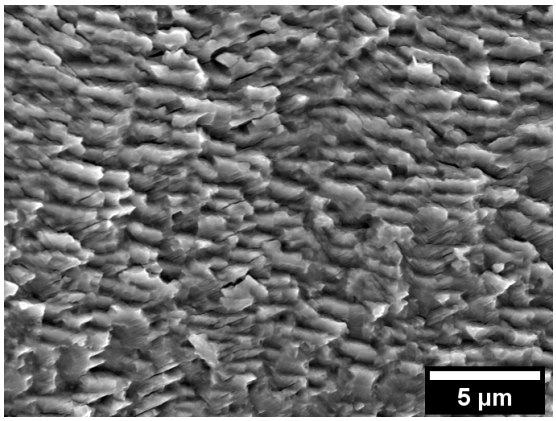
(e) Magnified fig. 6.50d showing the partial opening characteristic.



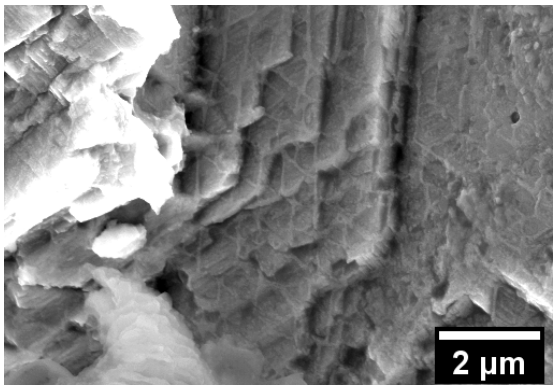
(f) Bottom region in fig. 6.50a.



(g) "A" - Smoother opening region.



(h) "B" - Fine steps.



(i) "C" - {111} exit facet.

Figure 6.50: B4 ($N_f = 10^5$) fractographs an IT air EP sample.

For **Sample A9** ($N_f = 10^7$), the top surface in fig. 6.51 is the initiation side based on the slip activity.

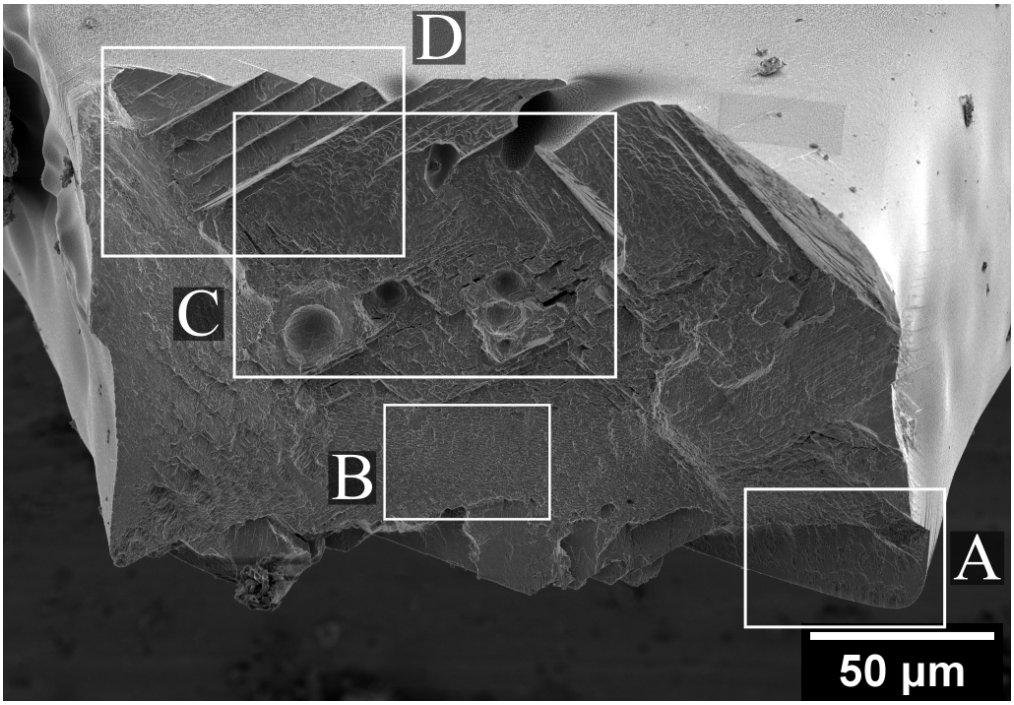
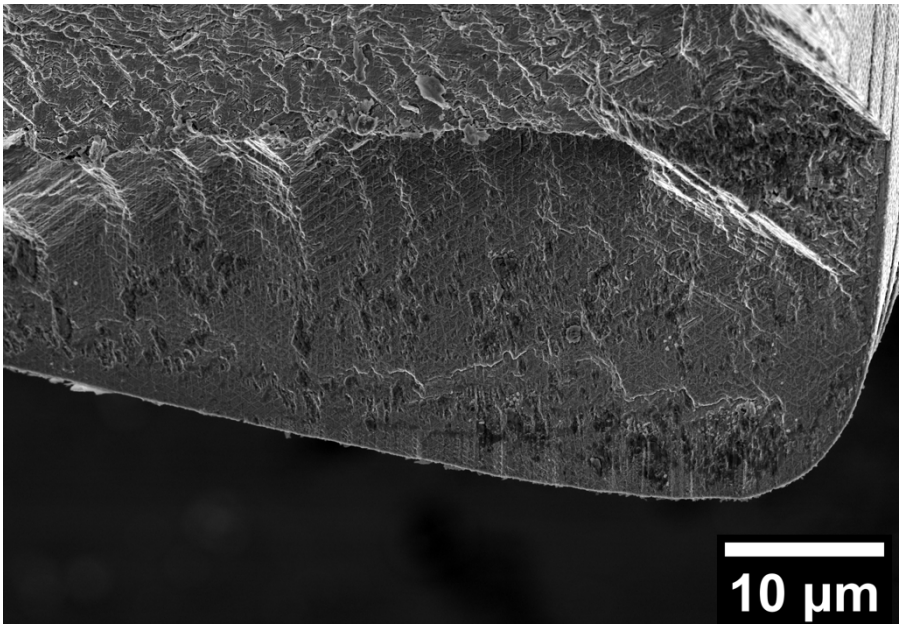


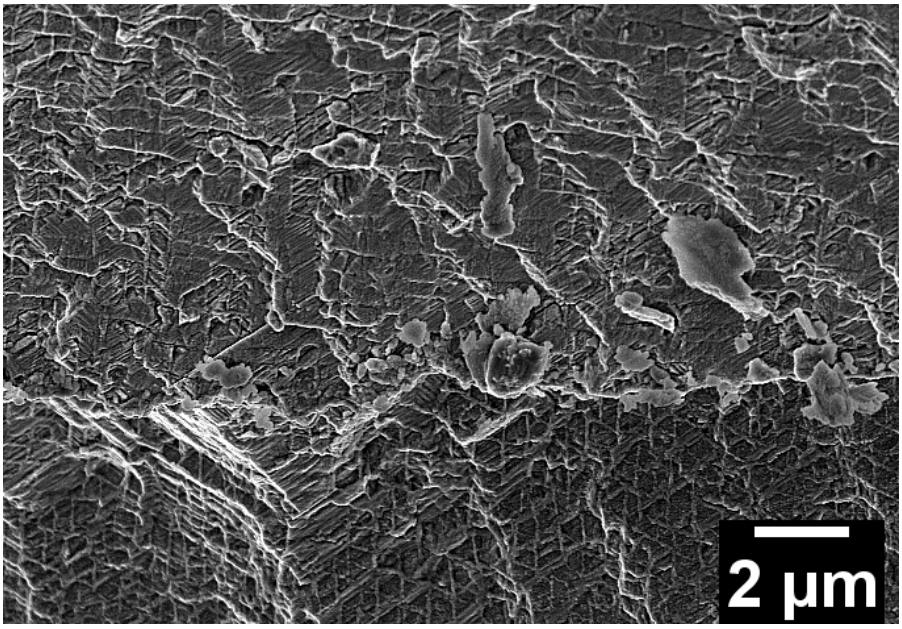
Figure 6.51: A9 ($N_f = 10^7$) low magnification fractograph (an IT air EP sample).

Despite being brown in colour in OM, in figs. 6.48b, 6.51 and 6.54a oxidation is noticeable but not thick enough to be plugging any surface pores.

A common feature among the samples in this test campaign is the large exit facets. In sample A9, a facet is found in the cantilever's corner (fig. 6.52a). It is likely an exit facet due to the prior justification for the top surface being initiation, but also because there are multiple of them and borders a rapid FCG rate region just above them. Under higher magnification, the tell-tale {111} fracture plane can be made out by mild oxidation.



(a) "A" fig. 6.51 - {111} facet.



(b) Possible top-to-bottom opening-to-shearing transition in fig. 6.52a.

Figure 6.52: Sample A9 region "A" in fig. 6.51.

Figure 6.53 shows the fine steps towards the end of fracture (similar in sample B4).

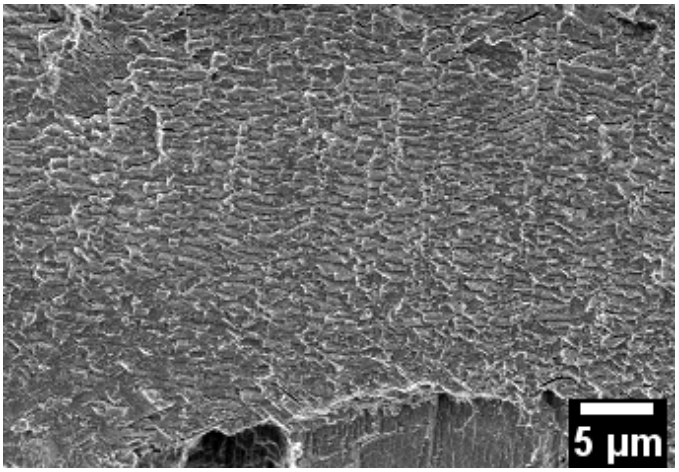
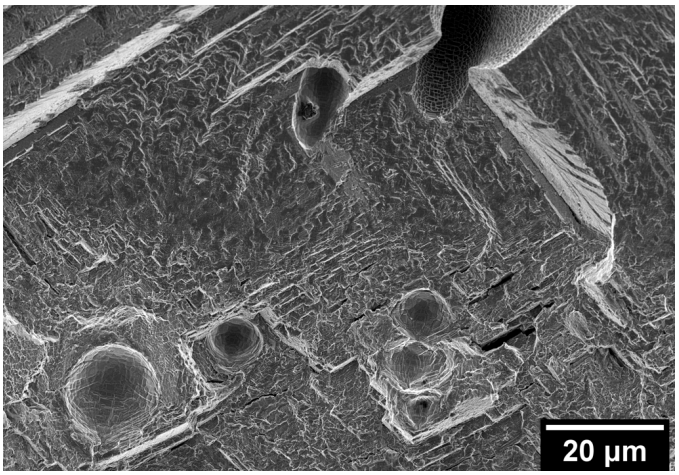
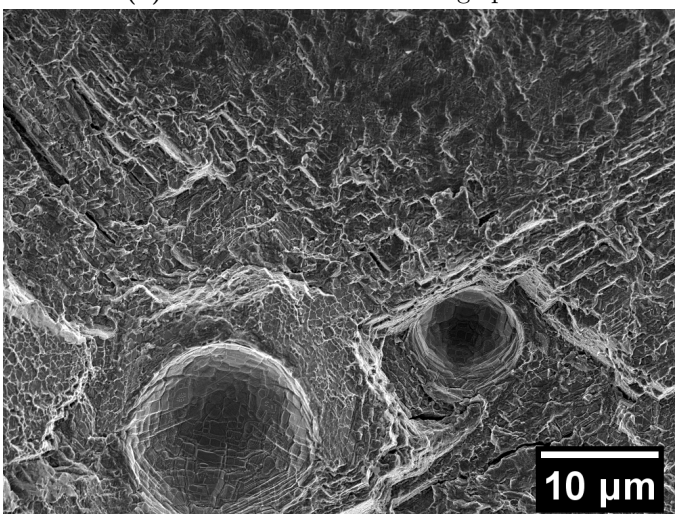


Figure 6.53: Sample A9 region "B" in fig. 6.51 where there are fine cuboidal steps.

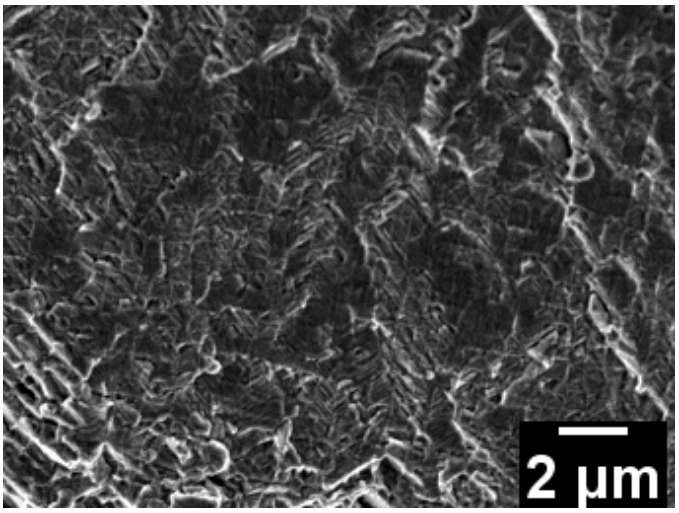
The large surface pore towards the top of fig. 6.51 is likely the initiating defect. Figure 6.54a shows the region around the pore, showing the nearby darker area and the brighter region it transitions to. The brighter region (fig. 6.54b) shows more ductility like those seen in the dimples for RT vacuum. The darker region (fig. 6.54c) appears more like opening mode fracture (via pseudo-cubic slip) than shearing mode fracture. The opening mode is not unexpected due to the (100) trace on the upper surface with which this region is in contact.



(a) "C" - Transition near large pore.



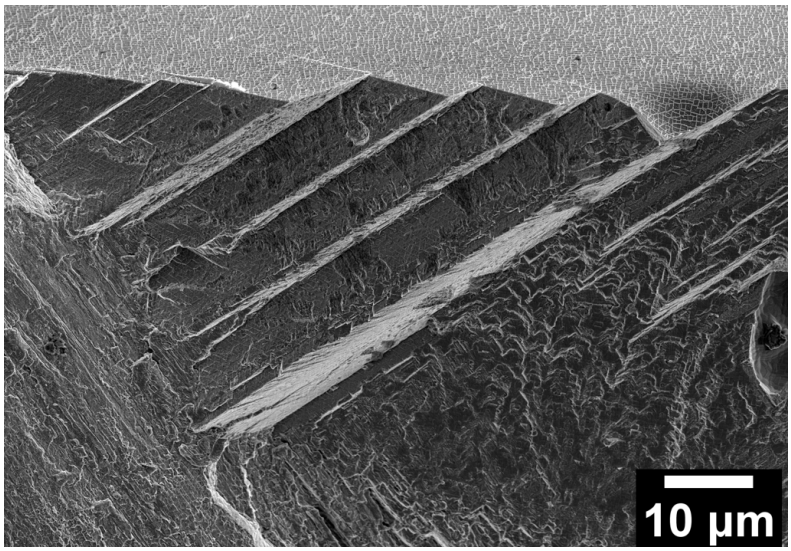
(b) Higher magnification of fig. 6.54a. Evidence of dimples in the lower brighter region.



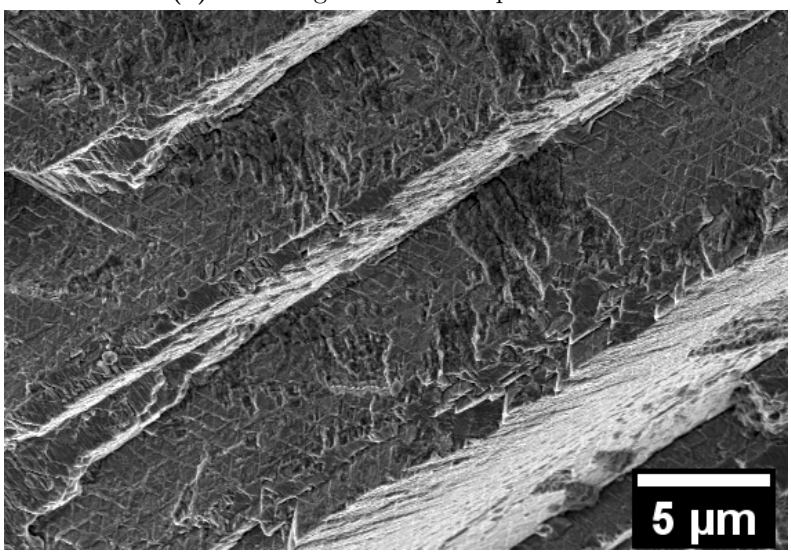
(c) Potential cubic slip in darker region near pore in fig. 6.54b.

Figure 6.54: Sample A9 region "C" in fig. 6.51 near potential initiating pore.

The rooftop fracture (fig. 6.55a) shows {111} surface traces and triangular γ channels on the fracture surface (fig. 6.55b). As the crack grew towards the bottom surface, the {111} facet showed greater ductility (fig. 6.55c). Opening mode fracture is seen closer towards the pore where the rooftop ends (fig. 6.55d).

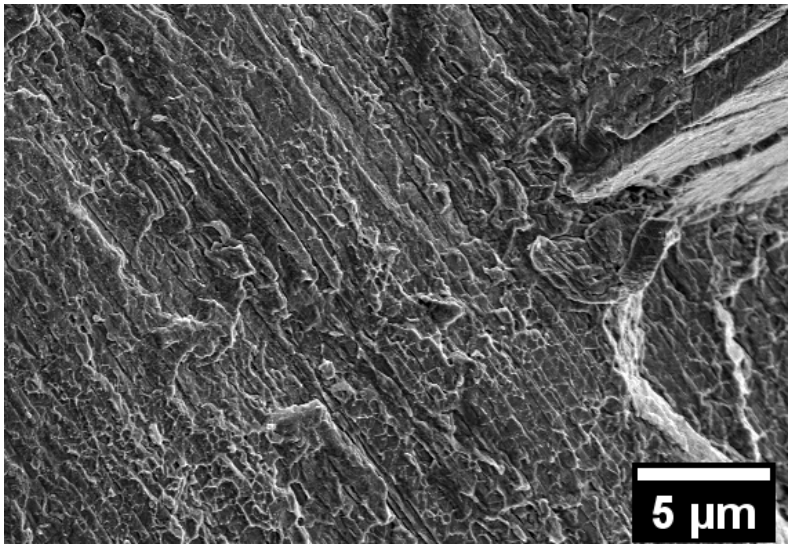


(a) "D" in fig. 6.51 - Rooftop fracture.

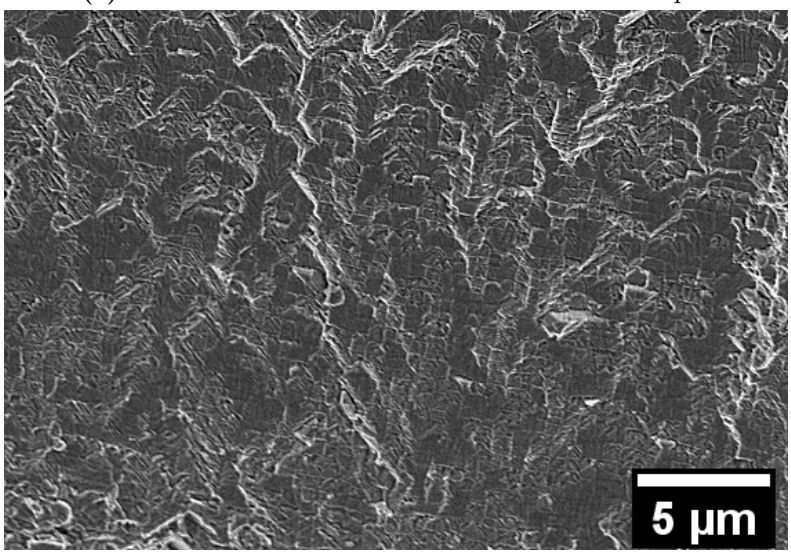


(b) Shearing mode facets of the rooftop.

Figure 6.55: Sample A9 region "D" in fig. 6.51 rooftop fractographs.
(Cont. Next Page)



(c) Ductile fracture towards bottom LHS of rooftops.



(d) Opening fracture adjacent to rooftop fracture.

Figure 6.55: Sample A9 region "D" in fig. 6.51 rooftop fractographs.

A relatively large {111} exit facet can be found near the corner in sample A9 and in virtually all the other samples in this condition. They exhibit islands of rough texture that appear to protrude from the surface (fig. 6.58). The cause of these protrusions was not explored in this work.

In Sample C1, the LHS rooftop faceting propagates south-easterly along a ⟨110⟩ direction (planar stress) before transitioning to cleavage steps when it becomes more triaxial in the centre, propagating in the same direction.

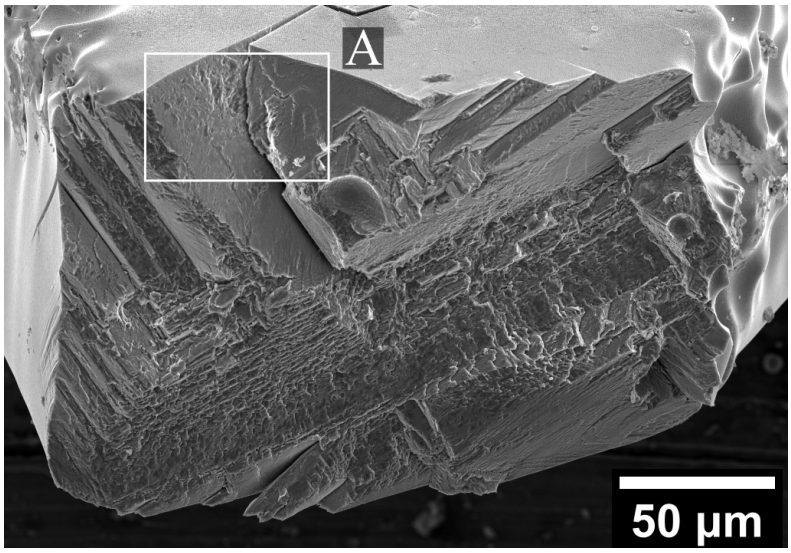


Figure 6.56: C1 SEM fracture surface fractograph.

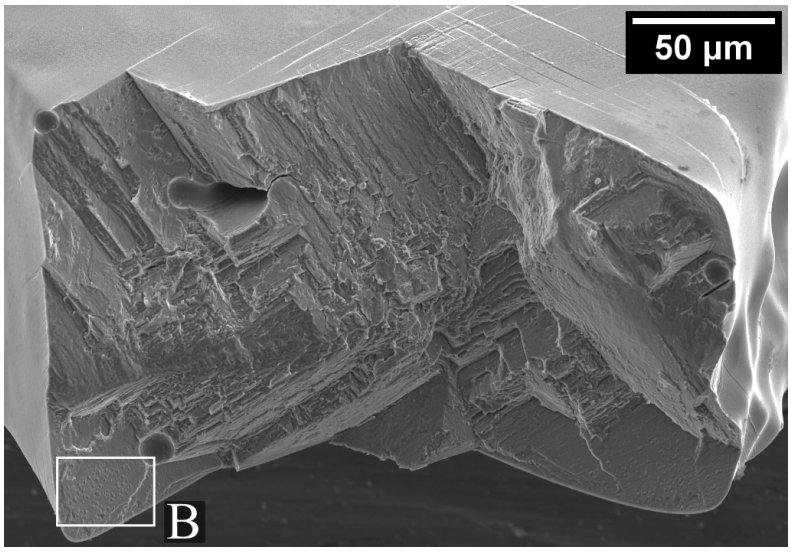
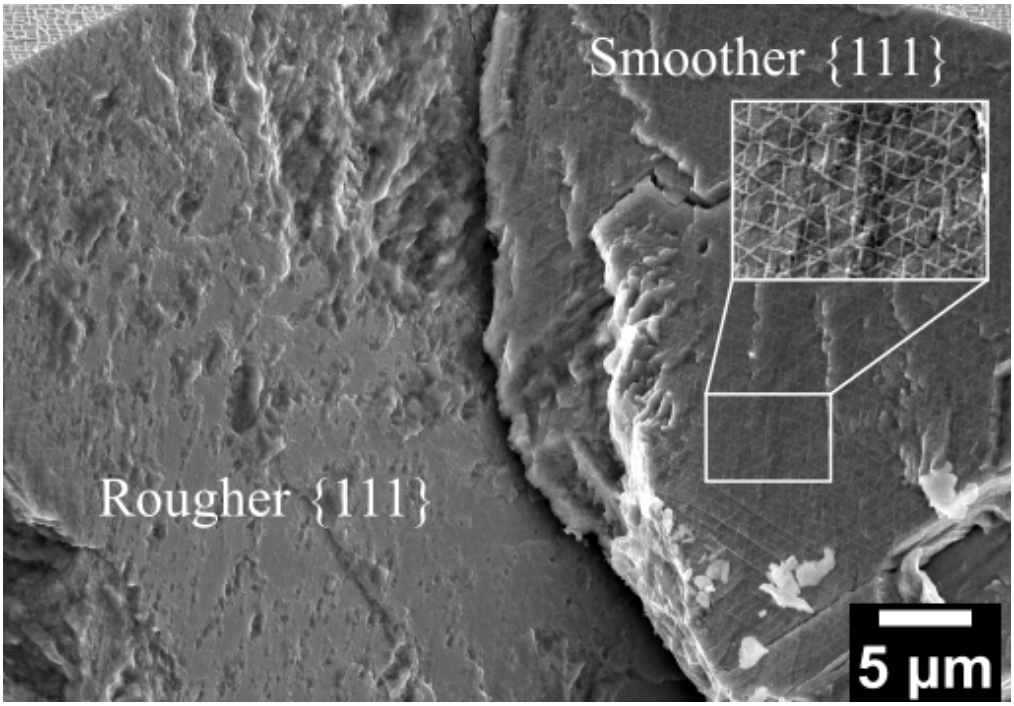
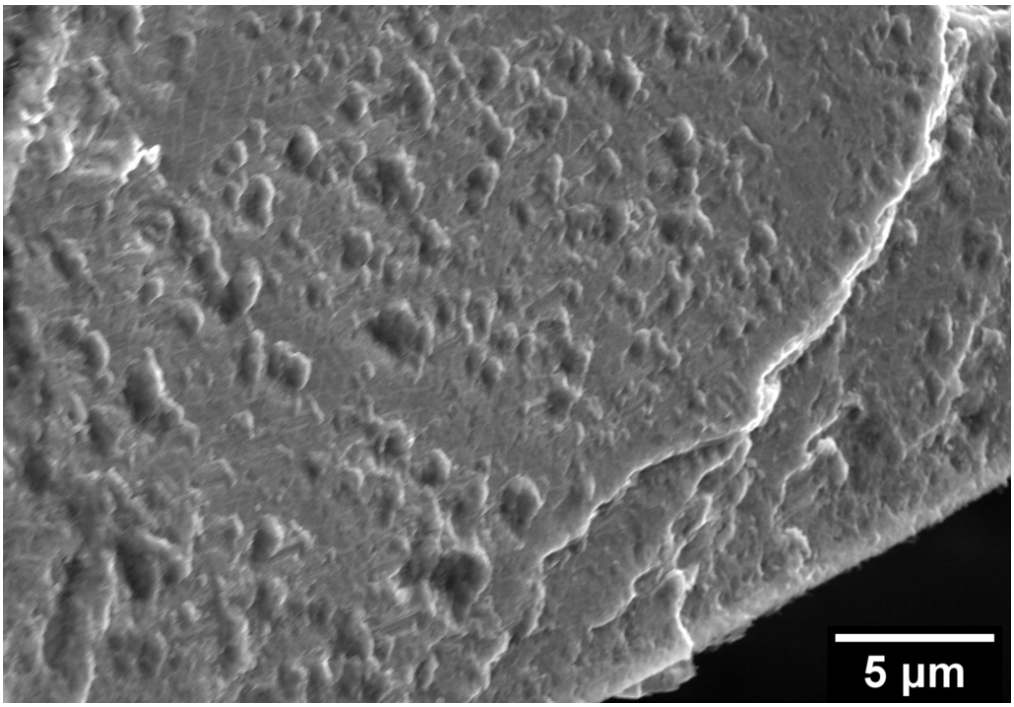


Figure 6.57: B10 SEM fracture surface fractograph.



(a) C1. Rougher and typical smooth {111} facets ("A" in fig. 6.48f).



(b) B10. {111} facet with protrusions ("B" in fig. 6.57).

Figure 6.58: SEM images of the {111} facet roughness for IT air EP.

6.5.3 IT Air Discussion

Of the six IT air samples who have had fractographs collected, 3/6 (B4, A9, & C3) were found to have extensive opening mode fracture. However, the opening fracture is not always visible on the top and bottom surfaces, which tend to transition to noticeably large {111} facets (shearing mode). The occurrence of opening mode fracture, despite being challenging to see visually, is thought to be due to the strengthening of the γ' (i.e. the anomalous yield effect) at IT compared to RT. A stronger SXNBS should exhibit a better fatigue performance.

Shearing mode fracture frequently occurred near the samples' edges and is partly due to plane stress conditions but also because:

- At IT, the opening and shearing modes co-exist [5].
- Complex ΔK behaviour due to multiple crack nucleation and changing neutral axis.
- Ultrasonic frequencies, in theory, promote planar slip [47].

However, it does appear that shearing is still significant in these samples, but that strengthening in the IT range is occurring, which can also manifest as opening mode fracture.

The SEM fractographs show that there are prominent shearing facets, but they tend to propagate to shorter distances (C3 being the exception) than those observed in RT tests. However, this is an artefact of the greater degree of rooftop-like shearing fracture, indicative of growth along $\langle 110 \rangle$ but the load axis being $\langle 100 \rangle$ as in Ref [45]. The rooftop morphology gives rise to the pseudo-opening mode fracture and can be distinguished from opening mode fracture by pseudo-cubic (i.e. γ-channel slip) in an SEM by the alternating {111} facets and surface traces.

IT air showed that extensive opening fracture occurred alongside shearing mode fracture. In samples B4 and A9 large pores near the initiation side are associated with an opening mode facet and also a shearing facet, much like RT vacuum but with

the (100) facet being less clear. Hence, like in Refs [42, 44, 57], lower ΔK conditions of the fatigue crack initiation promote opening mode. Despite the opening mode fracture being at times challenging to identify, observations of (100) traces on the surface from facets, square-like γ channels and fine steps all demonstrate its presence.

Opening mode has not been identified in all the samples. However, for this temperature, there is a complex mix and balance for opening and shearing fracture [5]. Therefore, the increase in σ_y causing the improvement in fatigue performance could still be occurring but not manifesting as opening mode in a large enough scale to be clearly seen. Alternatively, the fracture path is complex due to both mechanisms occurring simultaneously in some samples rather than a binary transition like in Ref [46] (fig. 2.12).

Fine steps have been observed in multiple samples under this condition (e.g., A9, B4, & C3). In the observed cases, it is associated with later-stage (100) fracture, with their facets orientated along cube directions rather than {111}. Therefore, the fine steps are likely opening mode fracture along the γ-channels in the <110><110> case as seen in Refs [45, 55] (figs. 2.14 and 2.16). The latter indicates that the load is no longer along $\langle 100 \rangle$, which is reasonable considering the extent of fracture by this point, unlike in a less fractured sample.

Generally, shearing steps (section 2.3.1 [59]), like in C1, have {111} facets smaller than the larger ones near the edges of the cantilever, which is thought to be due to plane vs triaxial stress [61]. Samples B10 and C3 show a lower degree of it.

Comparing RT vacuum with IT air:

- IT air generally shows a better performance than RT vacuum. Comparing their fracture surfaces, it is likely caused by the greater extent of opening mode or mixed mode fracture across the fracture surface in IT air. Whereas RT vacuum showed more shearing fracture facets.

- Both show some opening mode failure, but more shearing mode facets are found in the fracture surface of RT vacuum, with its opening mode being limited to an initial circular region. This is unlike IT air, where it can continue across a majority of the fracture surface but change appearance as the crack progresses.

Compared with literature data, the obtained 450 °C data is greater than conventional and ultrasonic frequency fatigue at 450 °C (fig. 6.59) and even at 750 °C. The obtained ultrasonic 450 °C data being greater than the confident ultrasonic 750 °C data for the same alloy and SXO (fig. 6.60) indicates that the greater performance cannot be solely a frequency effect. The increase in strength from the RT air tests in sections 6.2 and 6.3 (i.e. smaller risk-volume size effect) indicates that it is also happening here, but with the additional strengthening from being at 450 °C. Interestingly, the shape of the S-N curve resembles the 750 °C data more than the 450 °C data.

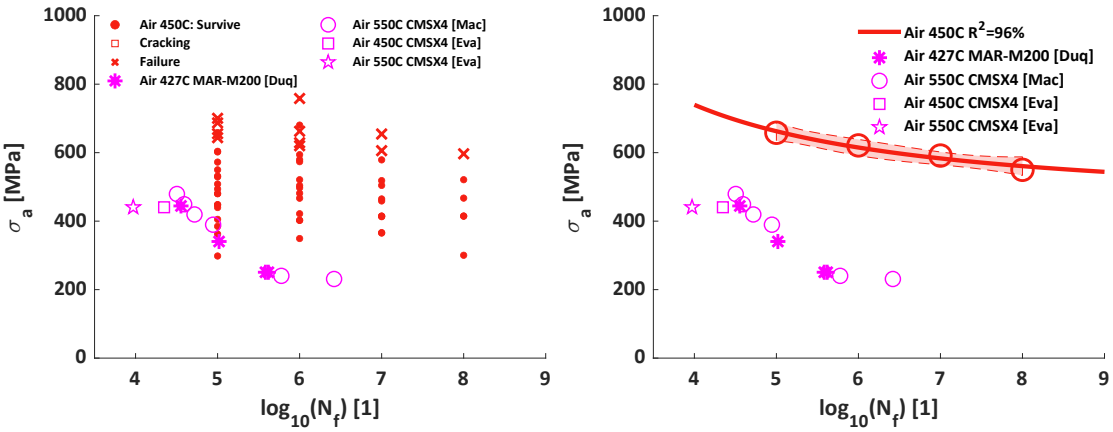


Figure 6.59: Comparison of IT fatigue data of the ⟨100⟩ SXNBSs in air at near 450 °C with the IT Air EP data collected in this thesis. Raw data and fitted 50% failure are shown. [Duq] is $R > 0$ uniaxial fatigue at 5 Hz from [93]. [Eva] is U-notched bend specimens at 0.25 Hz with $R = 0.1$ from [5]. [Mac] is $R = 0$ uniaxial fatigue on CMSX-4 done at 0.25 Hz for $N_f \leq 10^5$ and 100 Hz for $N_f > 10^5$ from [50].

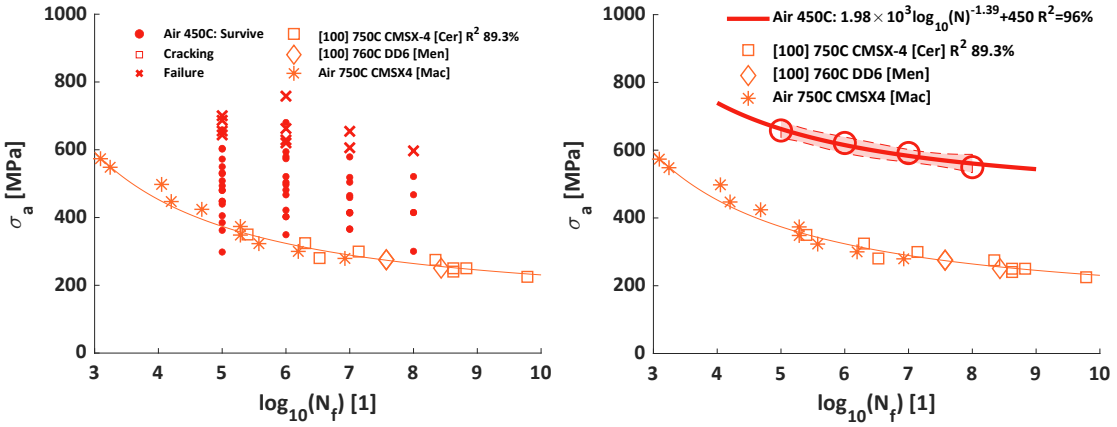


Figure 6.60: Same as fig. 6.59 but with literature data from near 750 °C. [Cer] ([11]) and [Men] ([88]) are uniaxial macroscale ultrasonic fatigue tests of ⟨100⟩ CMSX-4 and DD6, respectively. The conventional frequency CMSX-4 agrees with the ultrasonic frequency data well and so does the DD6 data. [Mac] is Ref [50].

The increase in σ_y from room temperature to 450 °C in the literature has been reported to be ≈ 28.8 MPa (804.8 MPa at 20 °C to 833.6 MPa 450 °C) [130]. Figure 6.61, normalises the fatigue curves by their σ_y values, which does not cause the results to overlap like seen in Ref [50]. This indicates that the increase in σ_y is not the sole cause for the increase in σ_y and that another mechanism(s) must be occurring for the significant improvement seen in this work [50]. The work in Ref [50] starts from above 550 °C and the highest frequencies used were 100 Hz, hence why the large difference in this work may have not been captured in Ref [50].

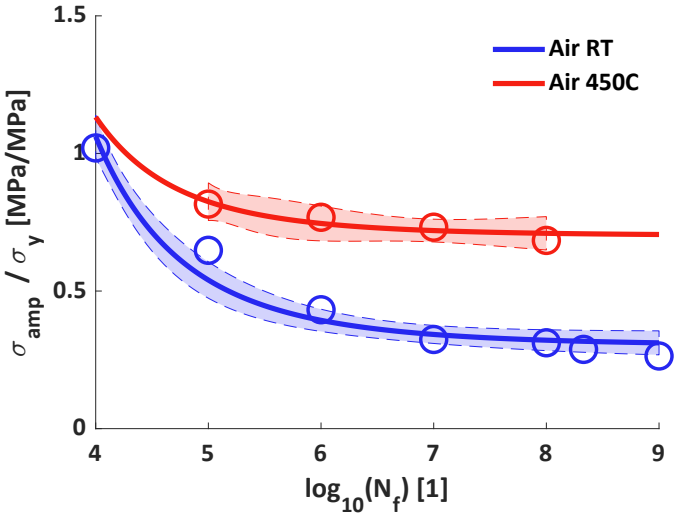


Figure 6.61: The results of the RT no-EP and 450 °C EP fatigue tests in this thesis when normalised by their respective σ_y values (values from Ref [130]).

6.5.4 Intermediate Temperature Vacuum

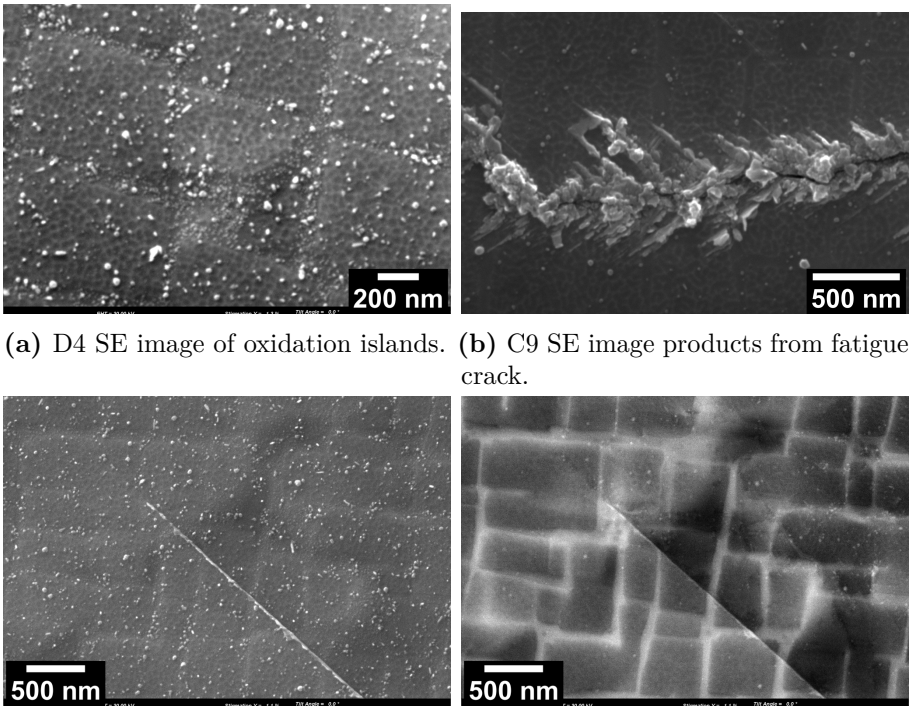
Performing this testing campaign was highly challenging compared to the other campaigns. A detailed explanation is discussed in appendix B.4. In brief, the bespoke power source could not track the resonant frequency of the fatigue rig and so the driving frequency (f_D) had to be manually decreased to maintain resonance. This was essential for preventing α_{amp} from decreasing with time and obtaining a linear $\alpha_{amp} - V$ response. This presented a challenge for achieving and maintaining a high enough α_{amp} to cause crack formation.

These samples are still useful in assessing the response of the mesocantilevers in this environment, especially for the two that generated visible fatigue cracks in this condition.

Environmental Response

Oxidation occurred despite being under low p_{O_2}. A very mild amount of oxidation occurred on the surfaces compared to in air tests, as indicated by their negligible colour change (fig. 6.67 & fig. 6.68). SEM micrographs in fig. 6.62 concur the low oxidation, showing that small sub-micron oxide islands preferentially occur along the γ-channels but also in γ', which agrees with Ref [5] with NiO forming first in γ at 450 °C air. These oxide islands do not appear in the high magnification EDX map taken at 5 kV (fig. D.3), and were also difficult to see in BSE images likely due to them being too small compared to the sampling volume.

Enhanced oxidation around the crack path is seen in multiple fatigue cracks, which is likely stress-assisted oxidation, as dislocations aid in the diffusion of oxygen and solute atoms by acting as fast diffusion pathways in the material, therefore enhancing oxidation rate (as seen by thicker oxide scales when the surface is under tensile load [5, §4.5]). The ribbon-like extrusions along {111} cracks in other testing conditions occur, but also a rougher and thicker oxide forms along the opening mode crack path, e.g., fig. 6.62b. Sometimes, this rough crack path oxide is so thick and wide that the underlying path is obscured.



(a) D4 SE image of oxidation islands.

(b) C9 SE image products from fatigue crack.

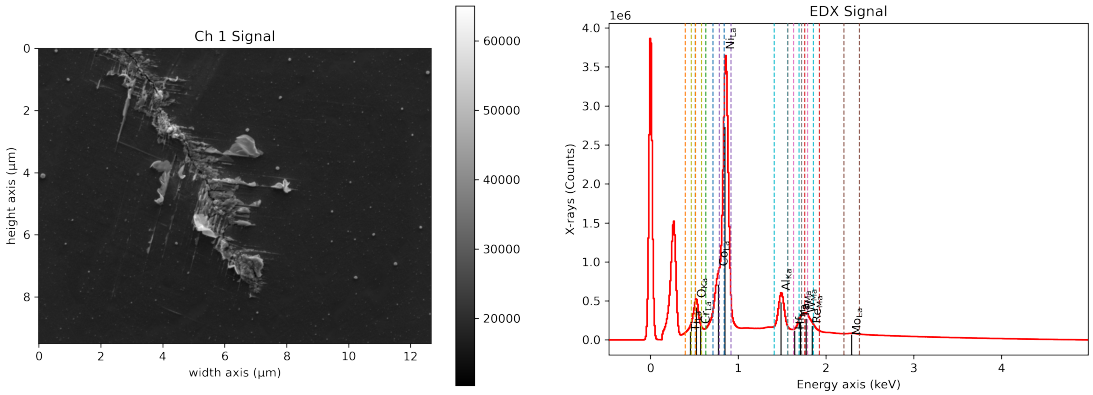
(c) D4 SE image of fatigue crack.

(d) D4 BSE image of fatigue crack.

Figure 6.62: Oxidation response of samples D4 & C9 tested at 450 °C under ultra-high vacuum.

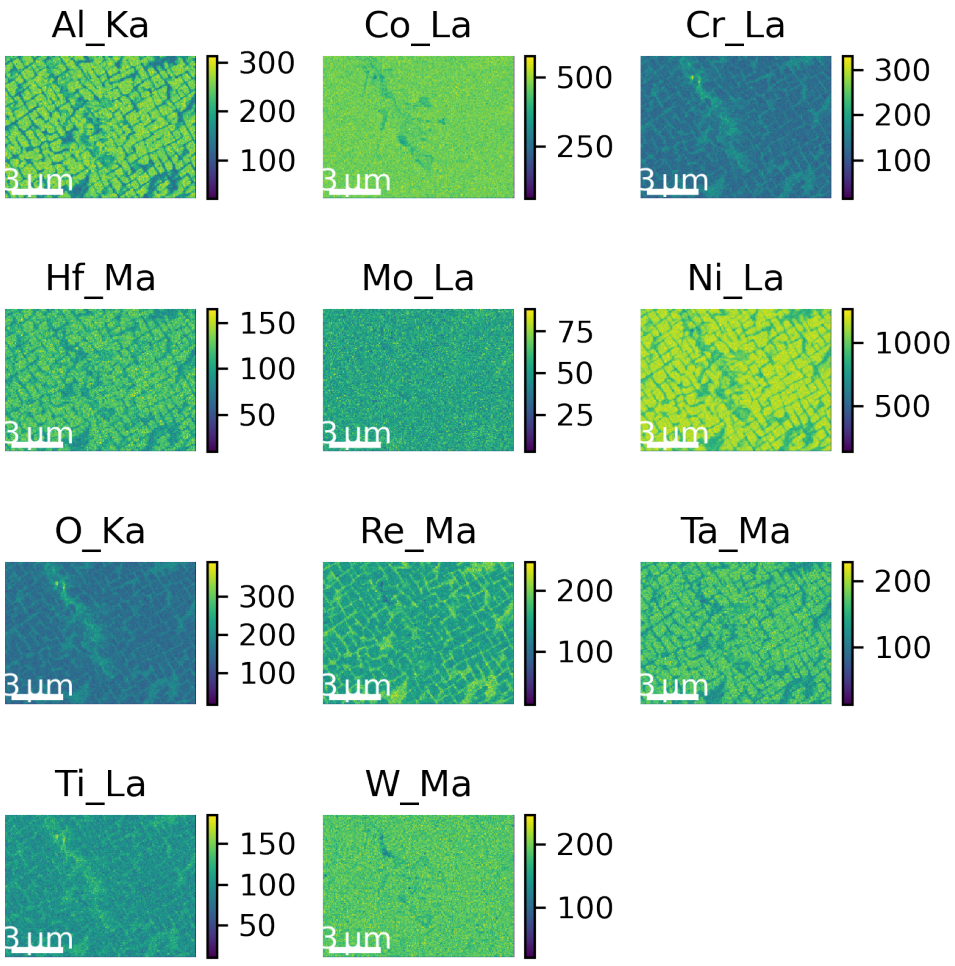
Figure 6.63 shows that the EDX analysis of the crack indicates that those features are oxides. Carbon has been neglected in the count analysis as it is likely a chamber contaminant, especially considering line scans and high exposures brightened the analysed region in SE imaging.

The at.% line scans show both the rough product (fig. 6.63d) and the ribbon-like product (fig. 6.63e), have a localised increase in O and a decrease in both Ti and Ni. The variation of the other elements in fig. 6.63e for the ribbon-like product is likely due to underlying chemical variation in the $\gamma - \gamma'$ microstructure.



(a) SE fatigue crack.

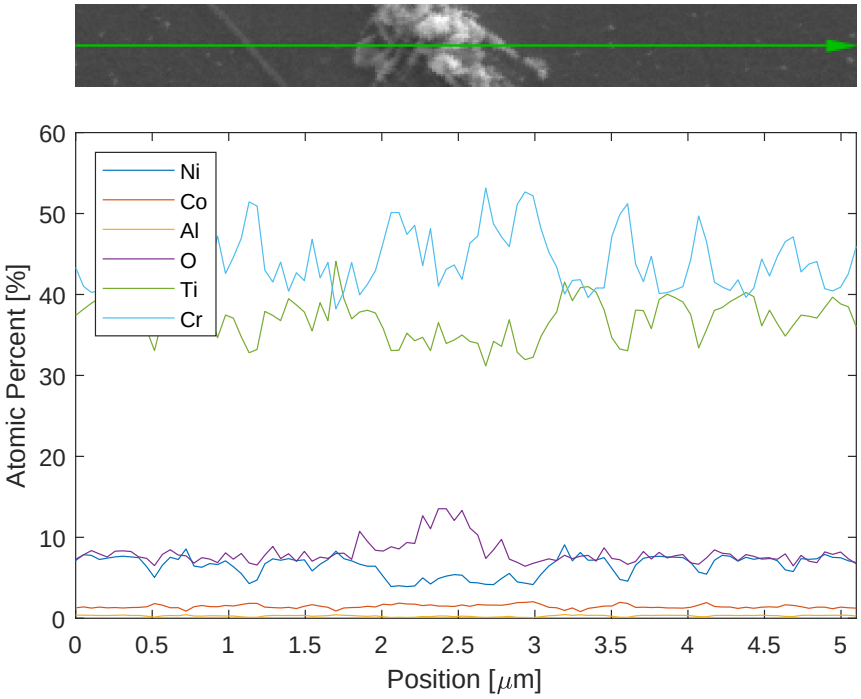
(b) EDX spectrum.



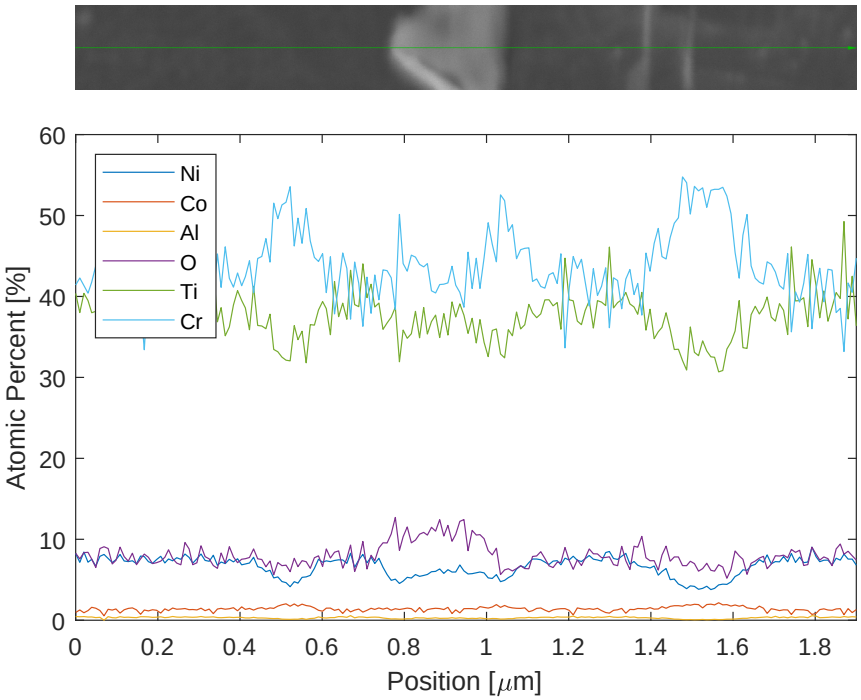
(c) Count Map.

Figure 6.63: EDX (5 kV) count maps for the oxidation products of a fatigue crack in C9. Down-sampling value of 10.

(Cont. Next Page)



(d) EDX line scan over rough product.



(e) EDX line scan over ribbon-like product.

Figure 6.63: EDX (5 kV) count maps for the oxidation products of a fatigue crack in C9. Down-sampling value of 5.

Fractured Samples

Samples C9 and D4 were the two samples with recorded fatigue cracks out of the 5 tested in total.

C9 showed multiple small fatigue cracks that initiated around pores. Their fracture paths, outlined brightly by the oxidation products, show substantial opening mode fracture, growing along the γ-channels and occasionally along $\{111\}$. It can be seen under low magnification and even better under higher magnification in fig. 6.66.

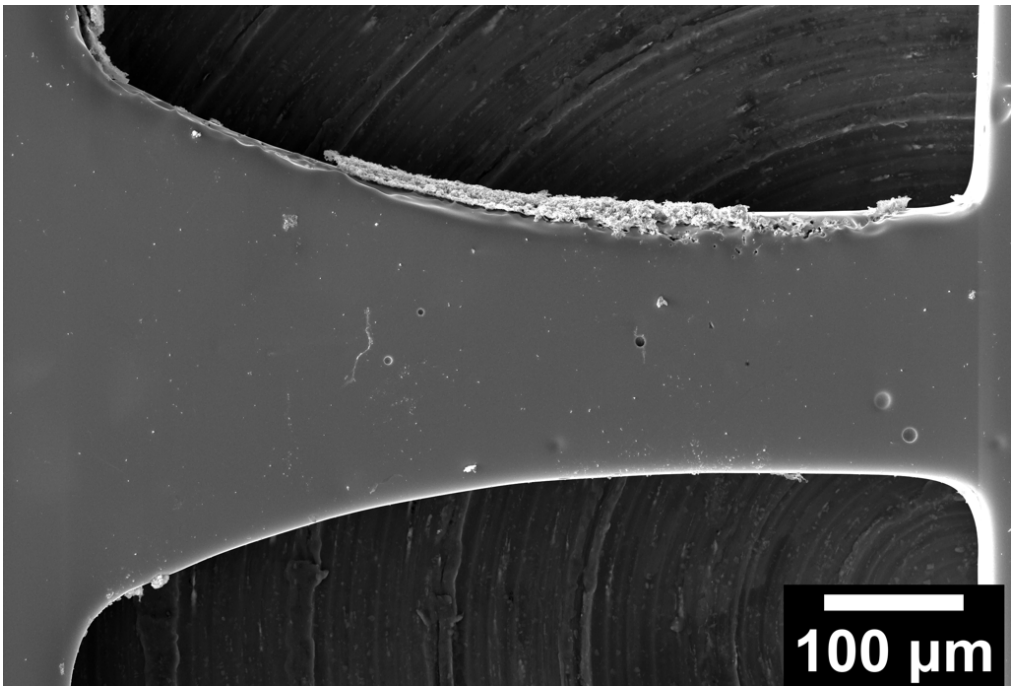


Figure 6.64: Sample C9 SE image of the initiated fatigue cracks under ultra-high vacuum at IT. The CD is rightwards.

It is hard to tell what mode the cracks initiate with as the mode within the pore can be obscured, and whether its initiation is surface or subsurface. The rough oxide can obscure the path, making it harder to discern it through the microstructure and if it is via pseudo-cubic slip or octahedral slip.

Figure 6.66a is a shallow surface pore (i.e., a dimple), where within it, pseudo-cubic opening fracture dominates and for a majority of the crack apart from the $\{111\}$ trace section towards the left.

As seen in the other opening crack paths, fig. 6.66a shows {111} slip traces extending out locally alongside the opening mode fracture path. This is an indicator of pseudo-cubic slip (section 2.1.3). Figure 6.65 shows a schematic of the pseudo-cubic slip with some of the slip along {111} planes cutting the precipitates despite the (100) fracture path. It could be that only a minority of the {111} slip causes the observed slip traces, with the majority being constrained within the γ phase.

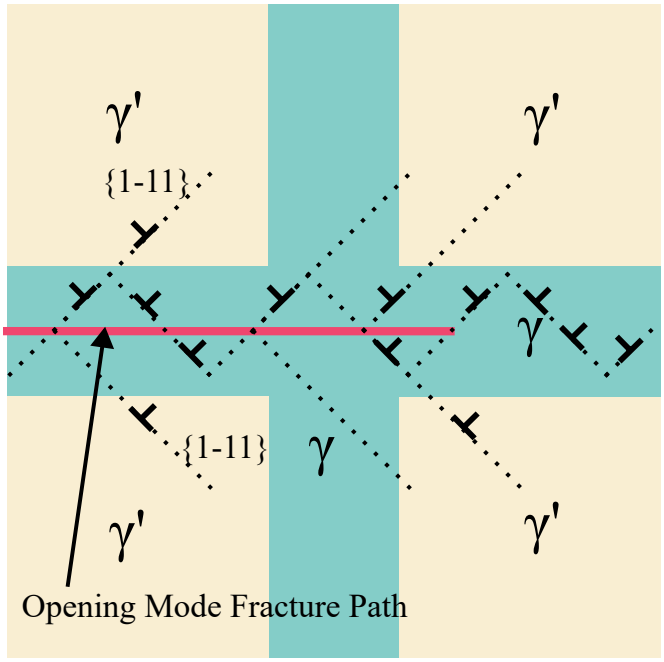
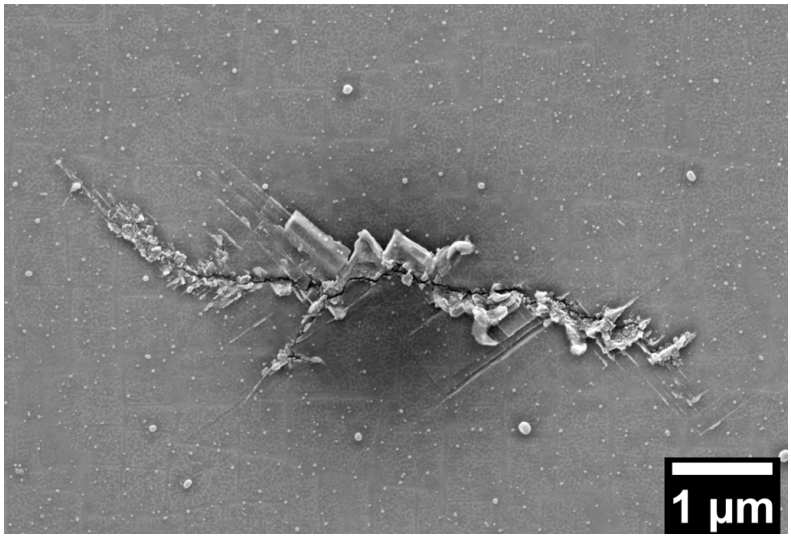


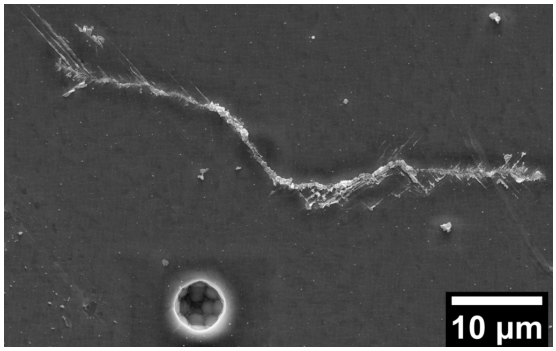
Figure 6.65: Schematic of opening mode crack path is occurring with pseudo-cubic slip at IT.

The two failure modes can both occur in a sample and even transition between them multiple times along the same crack. A good example is in fig. 6.66d, where the smaller crack shows opening mode, but its largest crack transitions to shearing mode for microns until reverting near its crack tip.

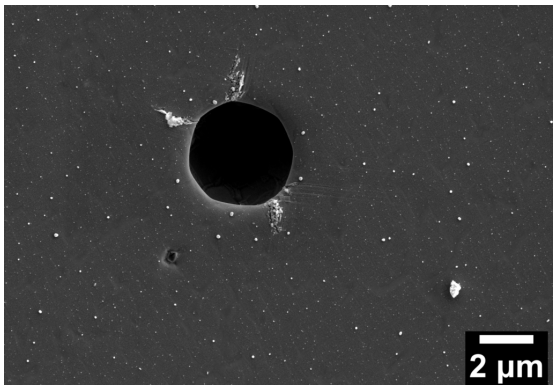
Figure 6.67 shows how the same fatigue cracks can be seen in OM, aided by the darker oxidation decorating the cracks.



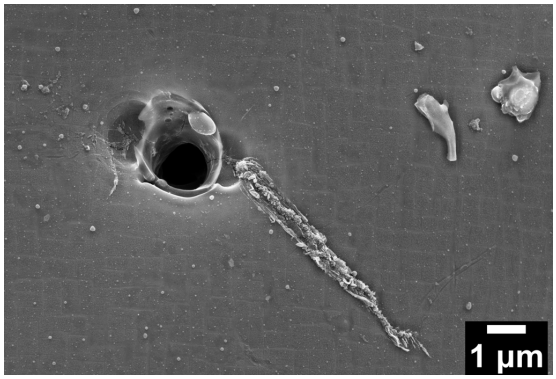
(a) Shallow surface pore.



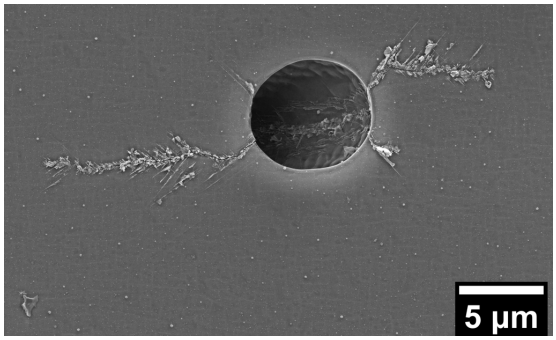
(b) Large crack with no surface pore.



(c) Small cracks from pore. Rotated ≈ 45° clockwise.

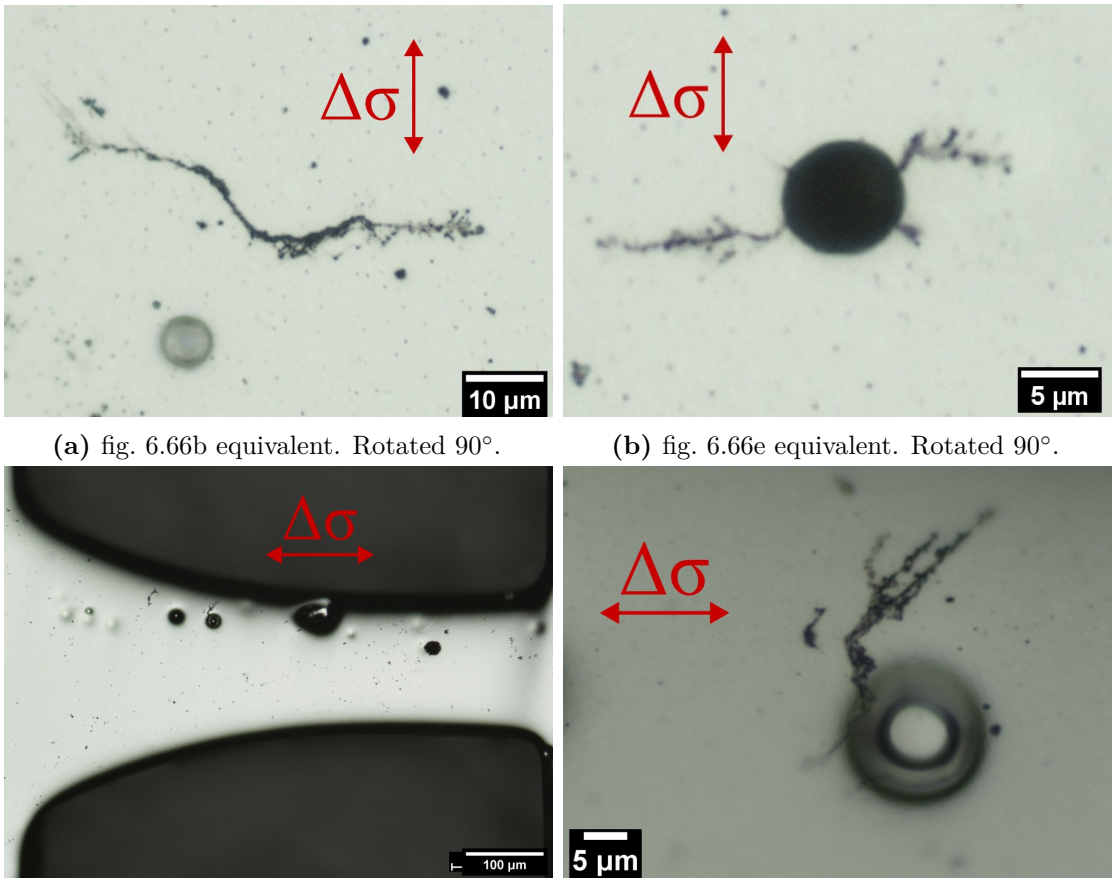


(d) Pore near side.



(e) Large surface pore.

Figure 6.66: Sample C9 SE images of the initiated fatigue cracks. The CD is downwards in the micrographs. CLAHE image contrast enhancement is used.



(a) fig. 6.66b equivalent. Rotated 90°.

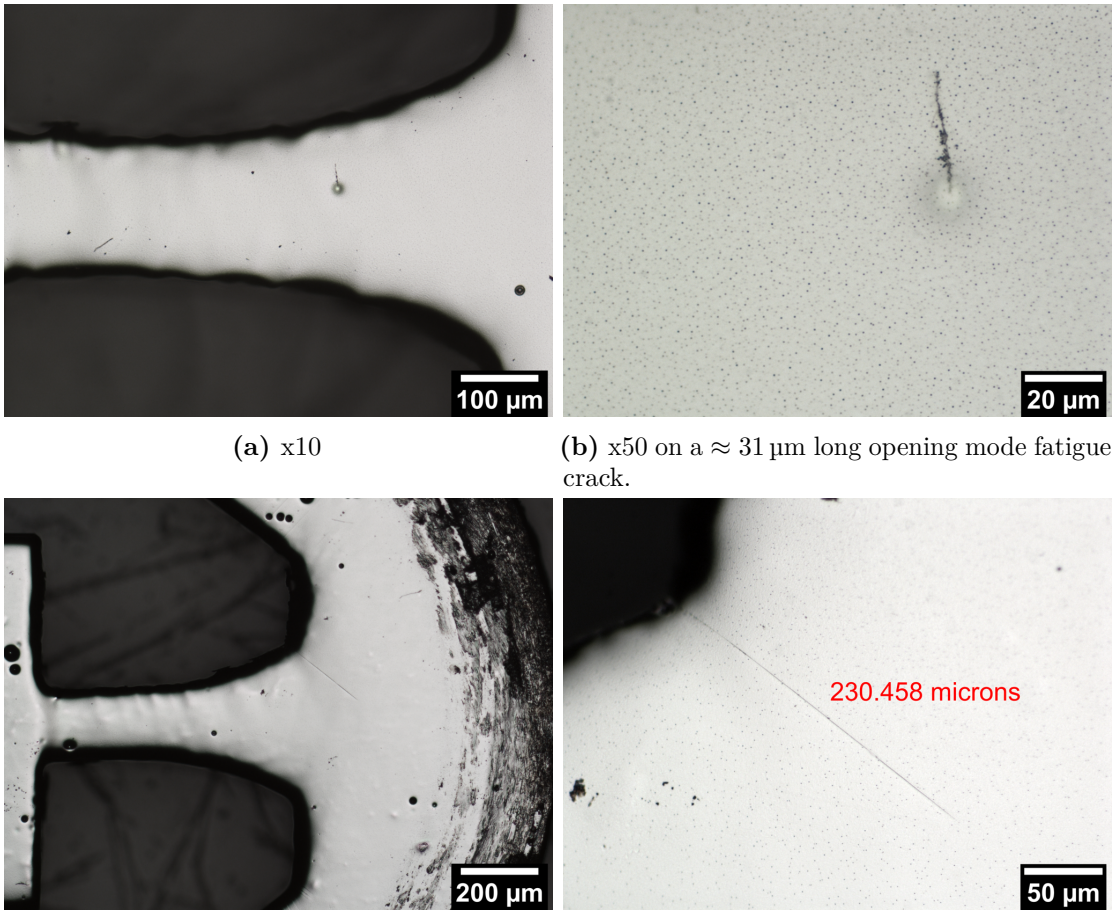
(b) fig. 6.66e equivalent. Rotated 90°.

(c) Other side of sample.

(d) Fatigue crack in fig. 6.67c.

Figure 6.67: Sample C9 OM images of the initiated fatigue cracks. The beam loading axis is annotated in each micrograph with $\Delta\sigma$.

Unlike C9, D4 has one small opening mode crack within the cantilever (fig. 6.68b) and one large shearing mode crack on the other side (fig. 6.68d).



(a) x10

(b) x50 on a ≈ 31 µm long opening mode fatigue crack.

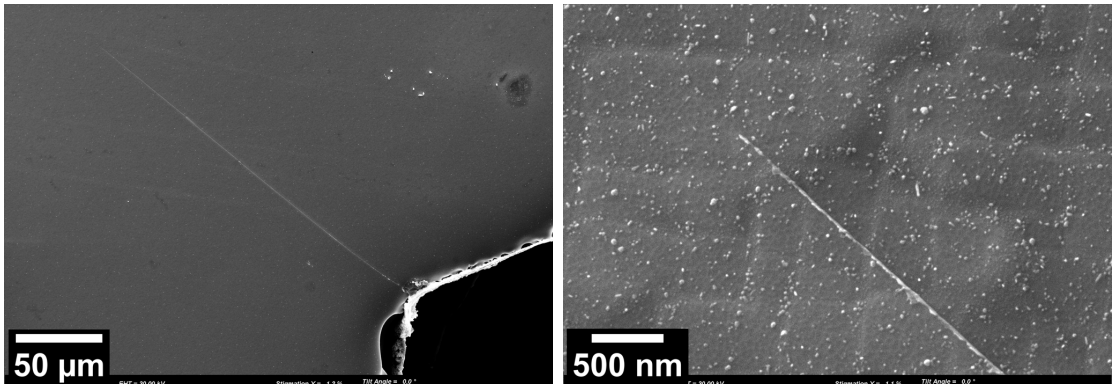
(c) x5

(d) x20 on a ≈ 230 µm long shearing mode fatigue crack.

Figure 6.68: Sample D4 OM images of the initiated fatigue cracks.

In the SEM, the large shearing crack in D4 (fig. 6.69) differs from the shearing cracks in C9 by having very short ribbon-like oxide with no extra octahedral {111} slip traces being active. Also, as the short opening crack appears like those in C9 under OM, it is deduced to be similar.

The difference in the crack decorations by the large-scale shearing mode crack and the numerous opening mode cracks indicates that the difference in mechanism between the two is a cause for this rather than the environment. Therefore, this could be a dislocation-based environment-fatigue interaction phenomenon.



(a) Low magnification. **(b)** High magnification around the crack tip.

Figure 6.69: Sample D4 SE images of the large shearing mode fatigue crack.

6.5.5 ECCI

Two physically short cracks of C9 were analysed using the ECCI technique outlined in section 5.3 (further details in appendix D.3.1), and were captured under $\underline{g} \approx [2\bar{2}0]$ and $\underline{g} = [020]$.

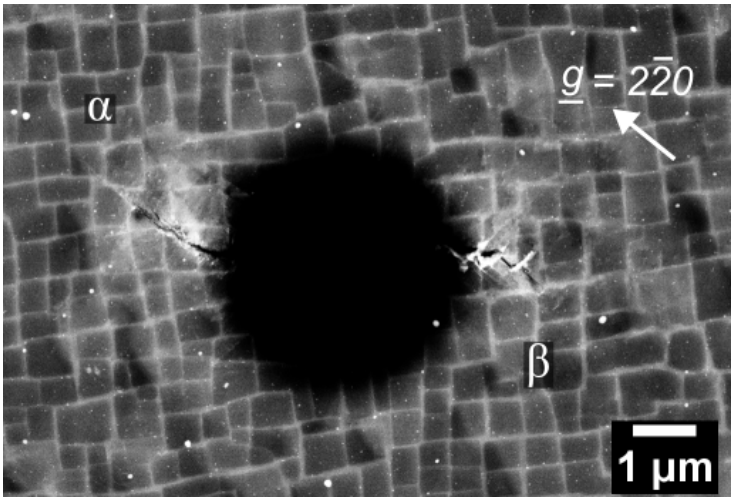
ECCI C9 - Pore A

Comparing fig. 6.71 with figs. 6.72 and 6.73, $\underline{g} = [020]$ expectedly shows a stronger defect contrast than $\underline{g} \approx [2\bar{2}0]$ due to its steeper and larger theoretical intensity profile, but also as it is slightly more off the optimal $\underline{g} = [2\bar{2}0]$ condition.

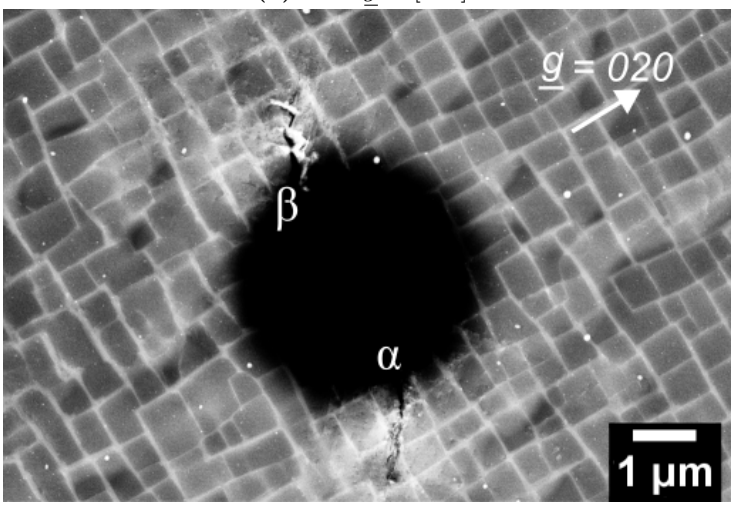
Both crack tips have many threading dislocations with a homogeneous distribution, especially for the crack α in fig. 6.73 ($\underline{g} = [020]$). In crack β (fig. 6.72), the dislocation lines can be partially seen (aka tails), suggesting they are less threading in orientation than those without tails. The inset in fig. 6.72a highlights that a larger proportion of the tail dislocations are in the γ-channels, they frequently occur as pairs (especially along the $\gamma - \gamma'$ interfaces), and their distribution is highly non-planar around the crack tip.

In crack α, the threading dislocations are observed in both $\underline{g}$ conditions, but the contrast is weaker with $\underline{g} \approx [2\bar{2}0]$. Without further higher magnification images, determining their bright-dark splits to estimate their $\underline{b}$ is challenging.

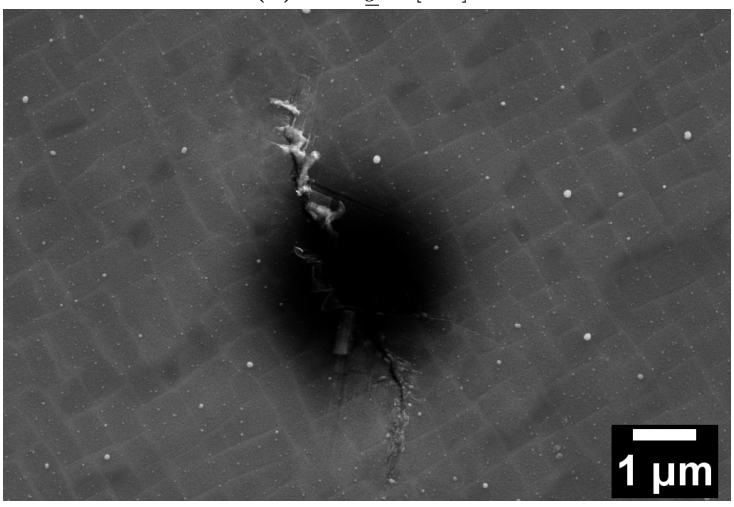
The dislocations with tails, however, have little-to-no visibility at $\underline{g} \approx [2\bar{2}0]$ (fig. 6.71b) but do so at $\underline{g} = [020]$ (fig. 6.72a). Using the $\underline{g} \cdot \underline{b}$ visibility criterion with $\underline{b} = \langle 110 \rangle$ suggests that these dislocations are associated with an FCC slip system where the following is the case $\underline{b}_{tails} \simeq \pm[1, 1, 0]$.



(a) BSE $\underline{g} \approx [2\bar{2}0]$.

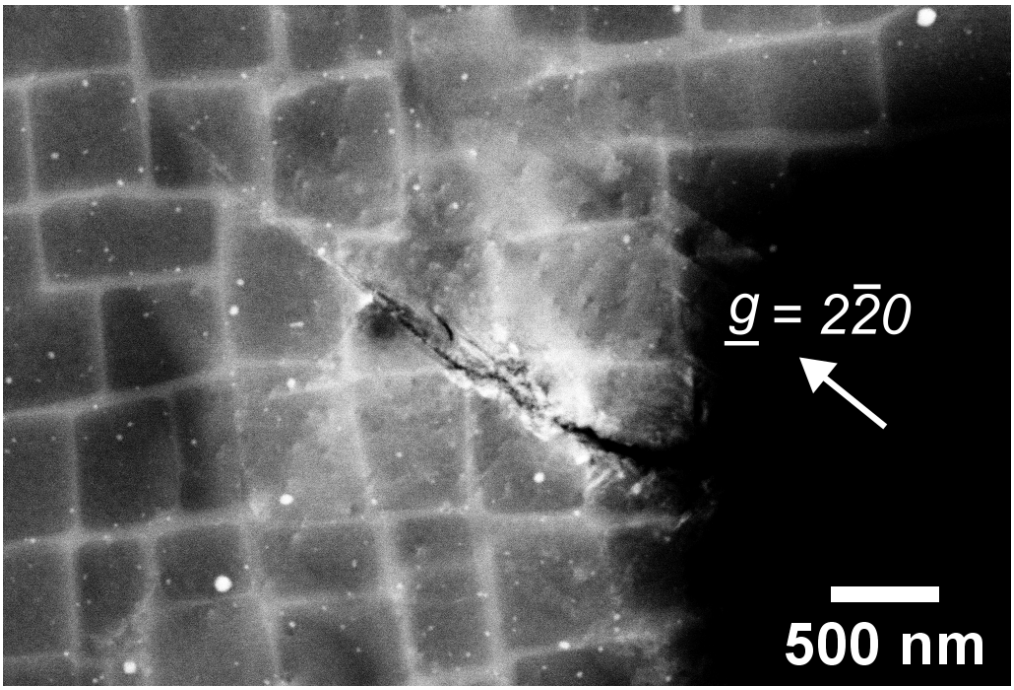


(b) BSE $\underline{g} = [020]$.

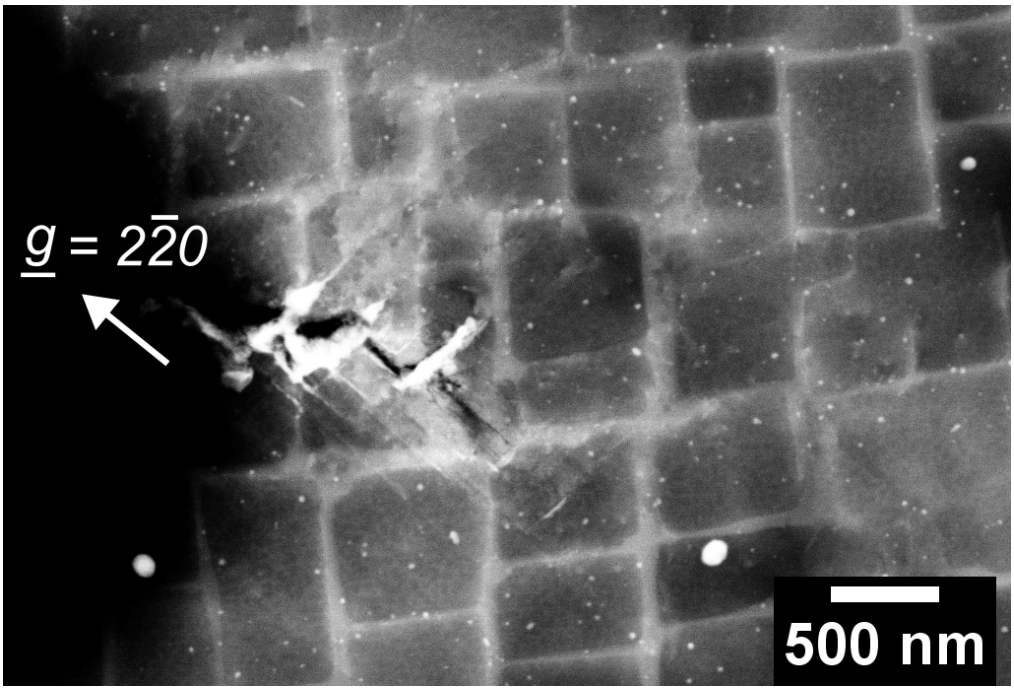


(c) SE $\underline{g} = [020]$.

Figure 6.70: ECCI of **pore A** at $\underline{g} \approx [2\bar{2}0]$ and at $\underline{g} = [020]$.

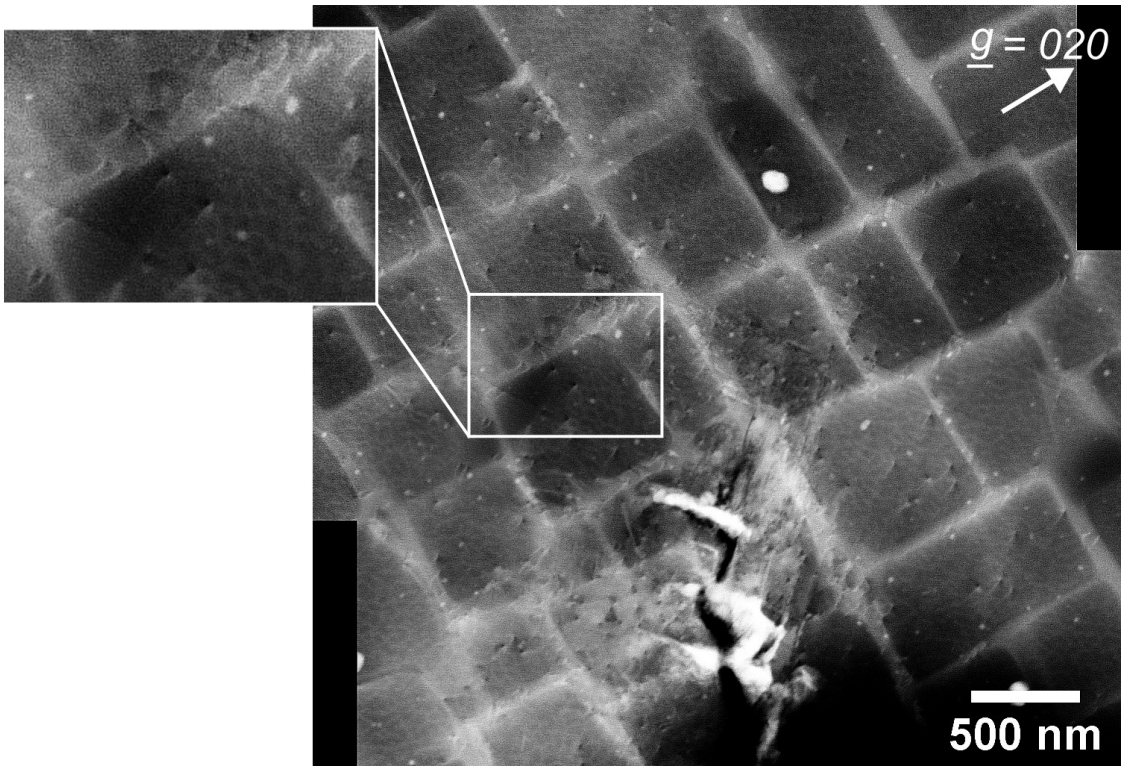


(a) Crack α.

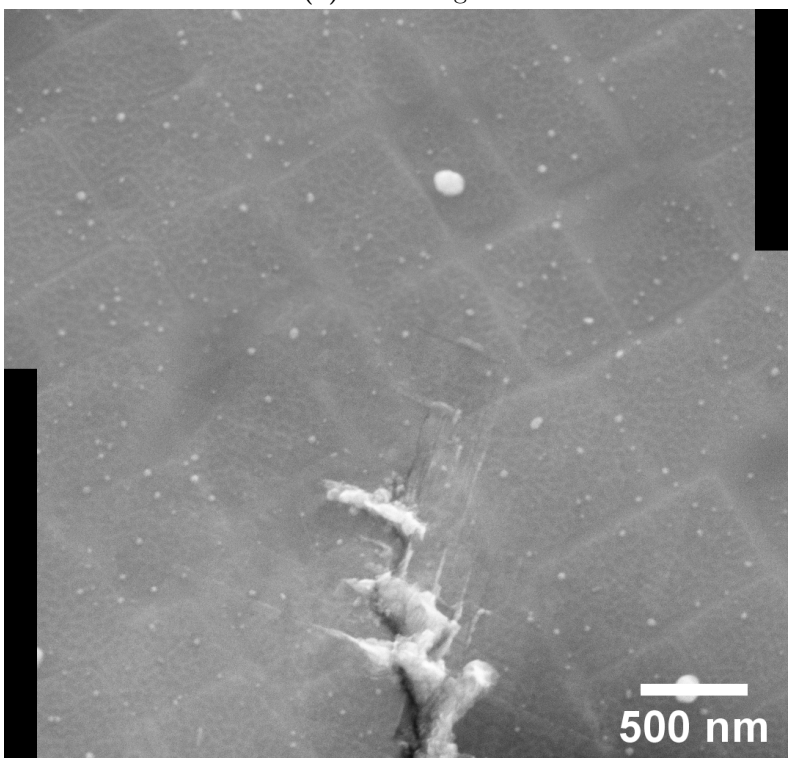


(b) Crack β.

Figure 6.71: ECCI of **pore A** at $\underline{g} \approx [2\bar{2}0]$.

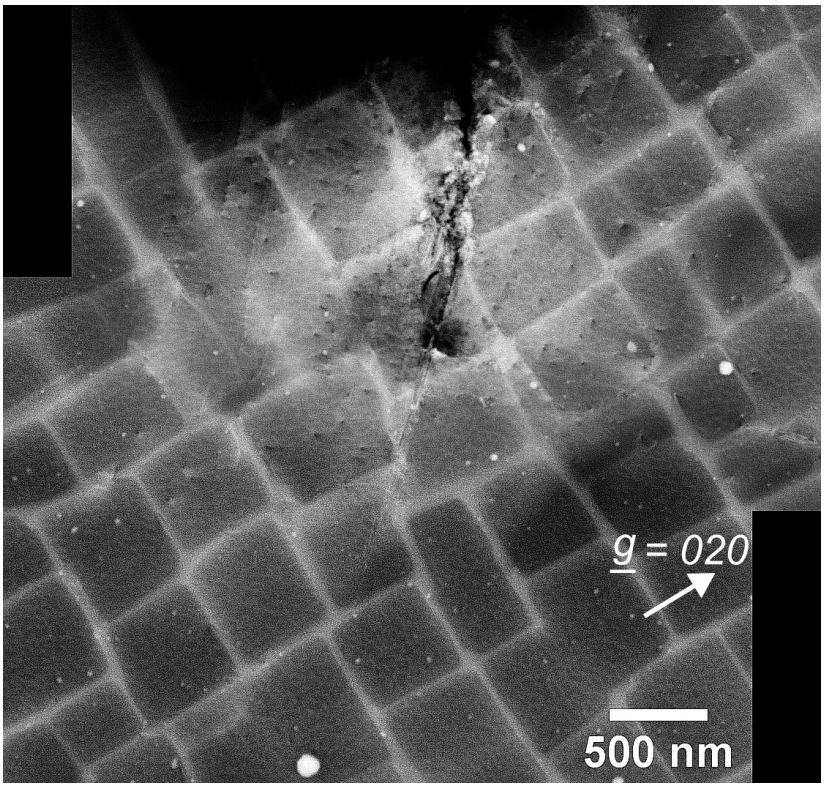


(a) BSE image.

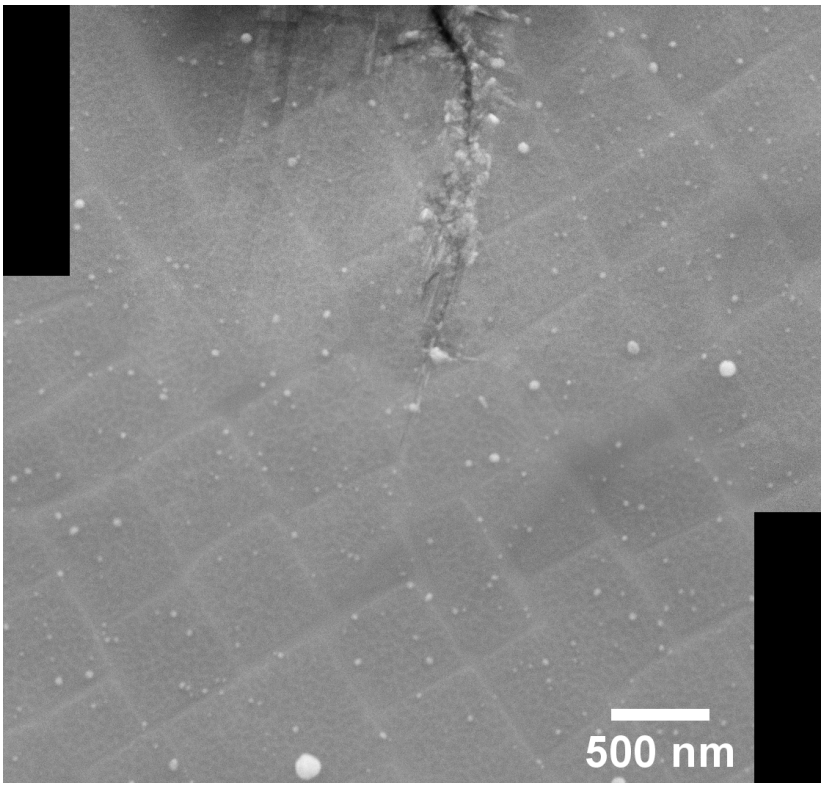


(b) SE image.

Figure 6.72: ECCI of crack β in **pore A** at $\underline{g} = [020]$.



(a) BSE image.



(b) SE image.

Figure 6.73: ECCI of crack α in **pore A** at $\underline{g} = [020]$.

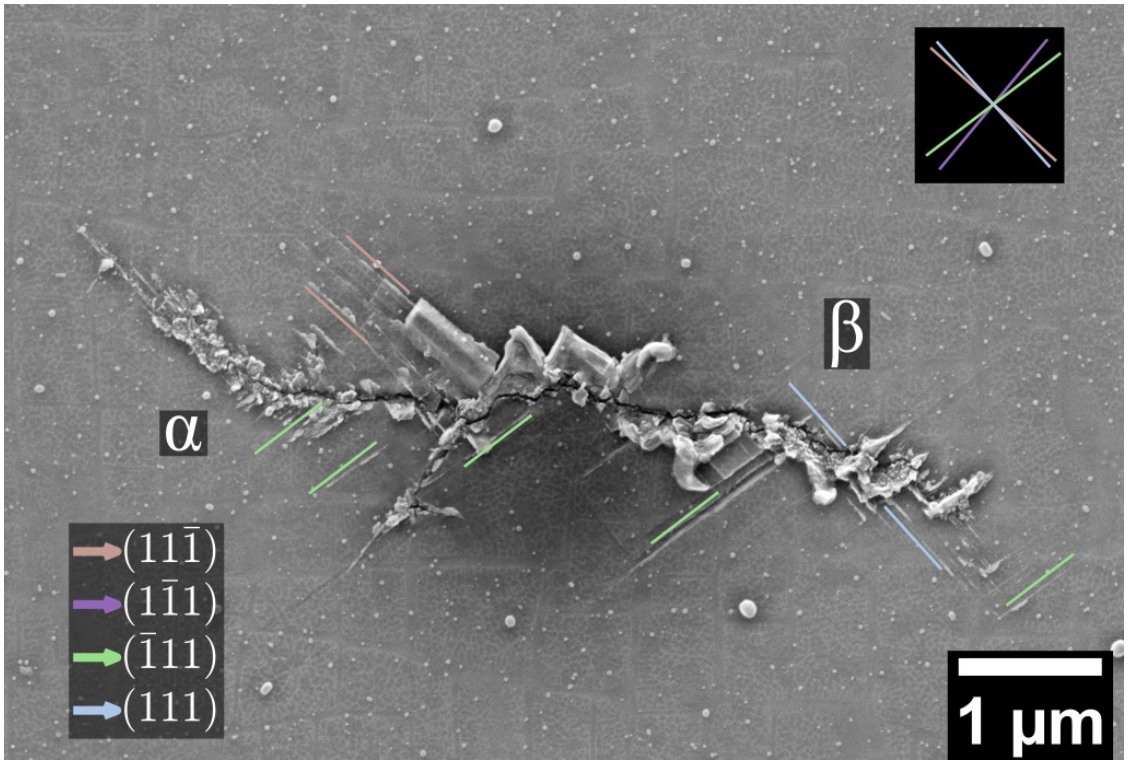
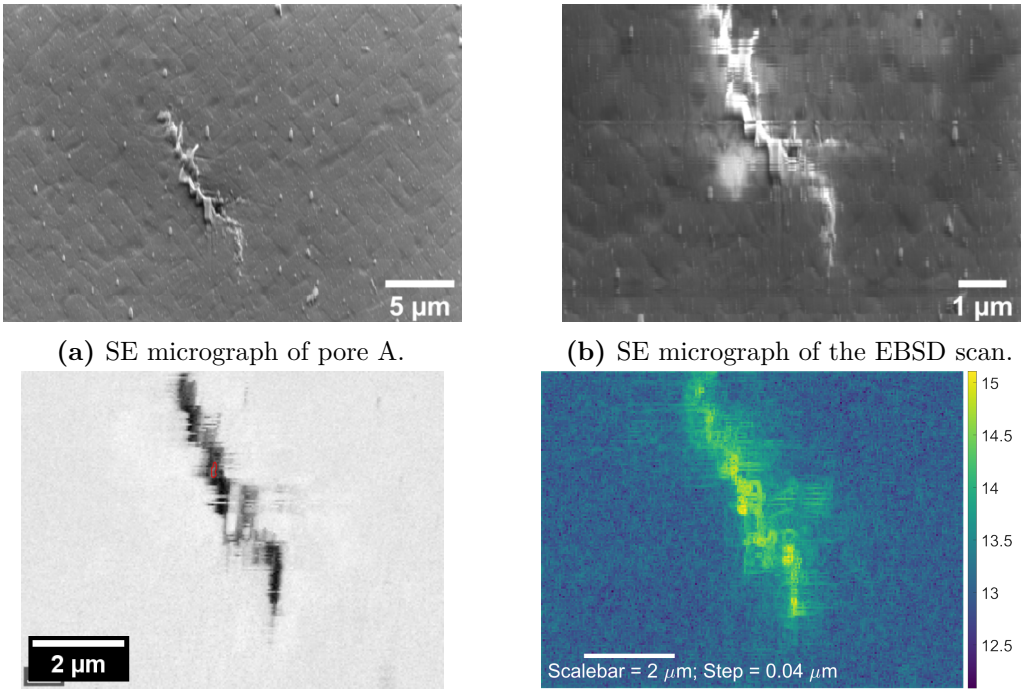


Figure 6.74: SE image slip traces of cracks α & β in **pore A**.

HR-EBSD was done on crack α (fig. 6.75) with a 40 nm step-size, 10 nA current, and a 20 kV voltage. Its orientation is similar to fig. 6.70b.

Scan jumps manifest as higher-density horizontal lines in the ρ_{GND} map. However, the ρ_{GND} indicates a localised density around the crack, but primarily where the Radon quality is poor (fig. 6.75c).



(a) SE micrograph of pore A.

(b) SE micrograph of the EBSD scan.

(c) Radon quality map.

(d) GND density map. Colour map range = $10^{12.09} - 10^{15.11}$.

Figure 6.75: C9 Pore A HR-EBSD results.

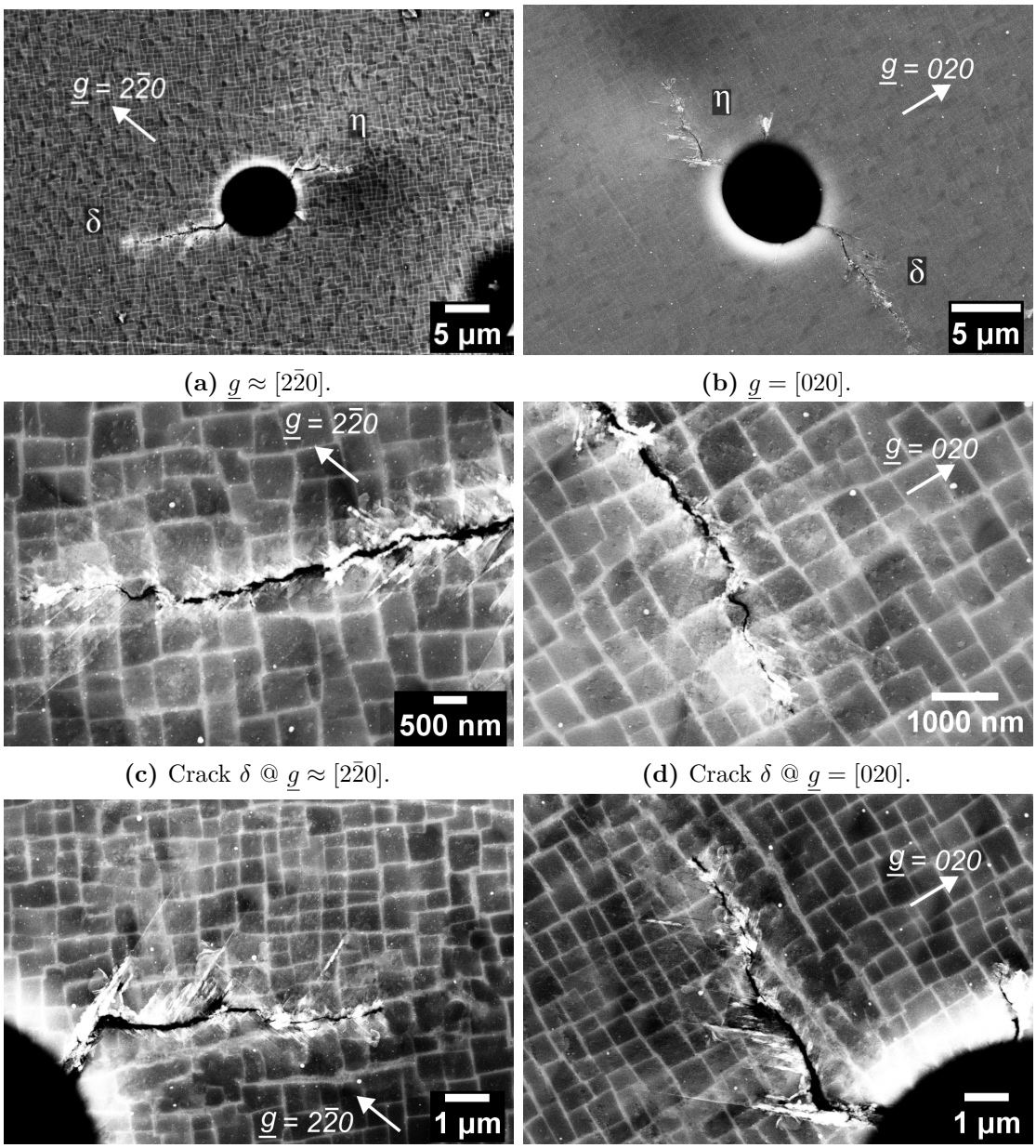
ECCI C9 - Pore E

Figure 6.76 shows how pore E, unlike pore A, starts with shearing mode before transitioning to opening mode on the surface. Like pore A, the dislocations are localised around the cracks and mostly homogeneously distributed about them compared to RT ECCI. Higher magnification images still show many threading dislocations and dislocations with tails mainly concentrated in γ and the $\gamma - \gamma'$ interfaces.

Figure 6.77a shows in its top RHS corner that inhomogeneous slip of threading dislocations occur along the $\{111\}$ slip traces of shearing mode cracks and on adjacent planes. In fig. 6.77a, the slip traces change from just $(\bar{1}11)$ in shearing mode to predominantly $(\bar{1}11)$ & $(11\bar{1})$ in opening mode.

As the opening crack progresses (fig. 6.77c), significantly fewer dislocations associated with shearing mode slip can be identified, with the distribution being highly homogeneous and significantly bright adjacent to the crack path (indicating a high dislocation density). Similar results can be seen in crack η's tip (fig. 6.78) but with more tail dislocations and a generally less clear dislocation structure. Hence,

cracks η & β share the trait of showing more tail dislocations. The side of the pore the crack is on may affect the active slip system(s), i.e. producing more distinct tail dislocations for cracks with growth along $[\bar{1}00]$.

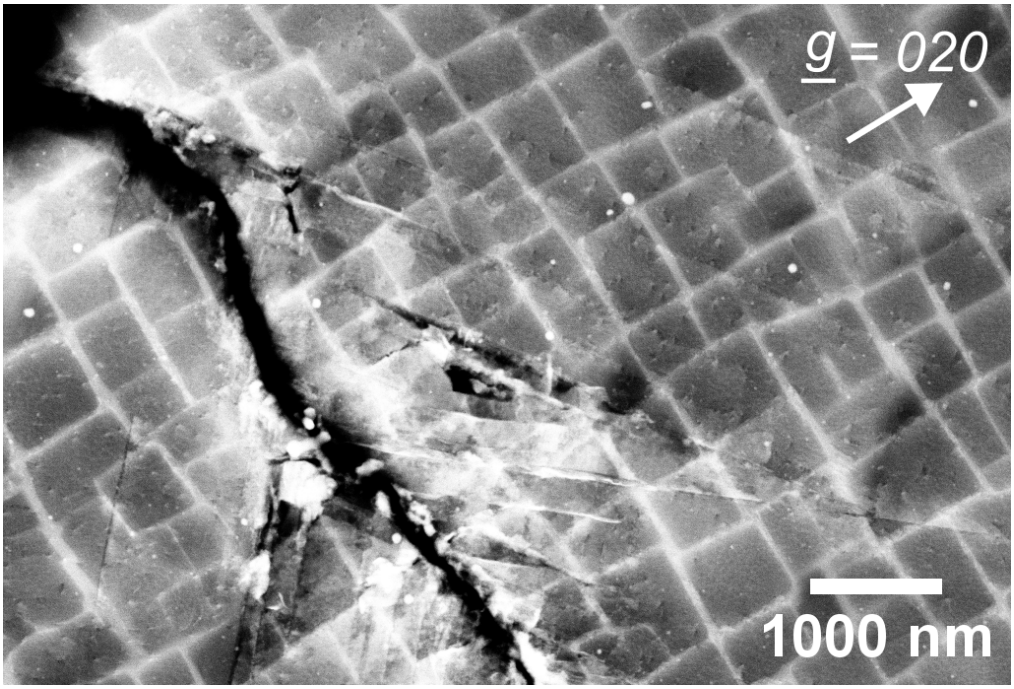


(a) $\underline{g} \approx [2\bar{2}0]$. **(b)** $\underline{g} = [020]$.

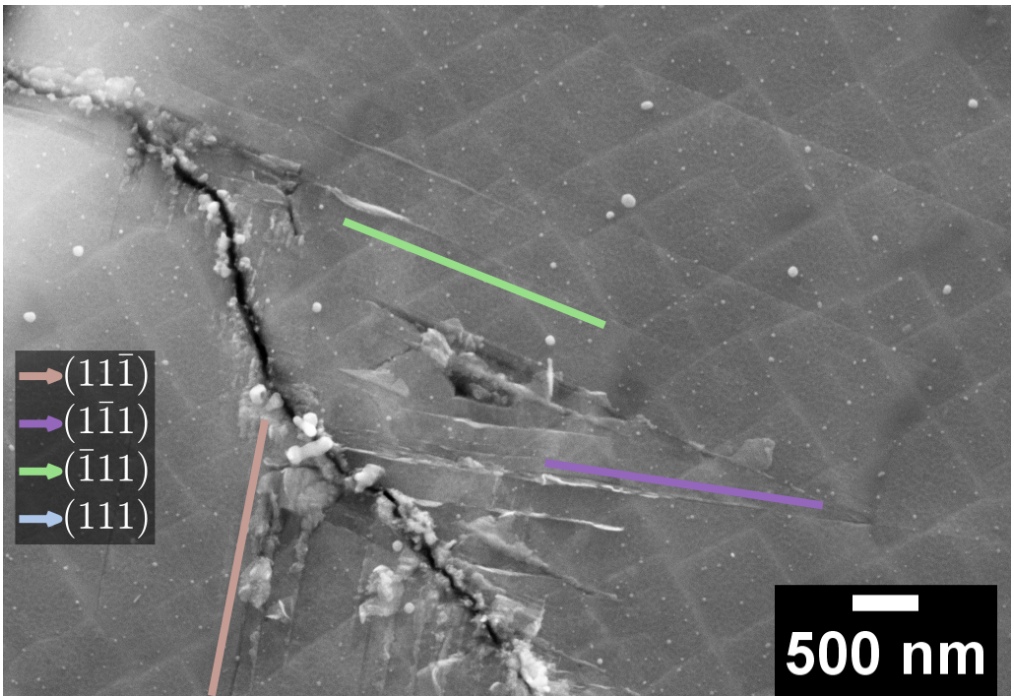
(c) Crack δ @ $\underline{g} \approx [2\bar{2}0]$. **(d)** Crack δ @ $\underline{g} = [020]$.

(e) Crack η @ $\underline{g} \approx [2\bar{2}0]$. **(f)** Crack η @ $\underline{g} = [020]$.

Figure 6.76: ECCI of **pore E**.

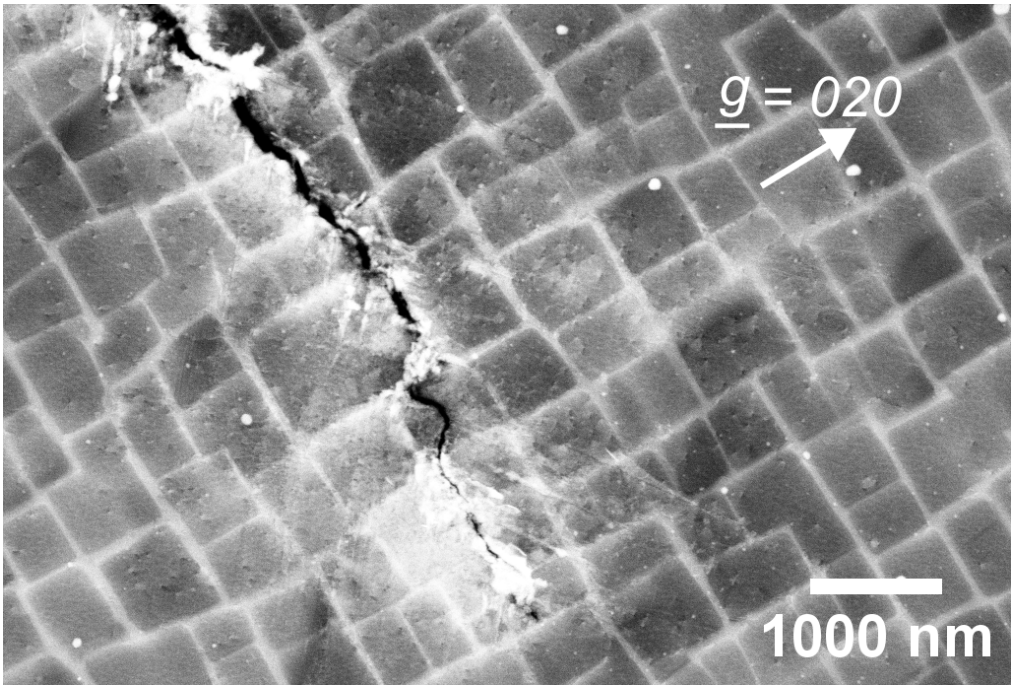


(a) Crack δ pt. I BSE.

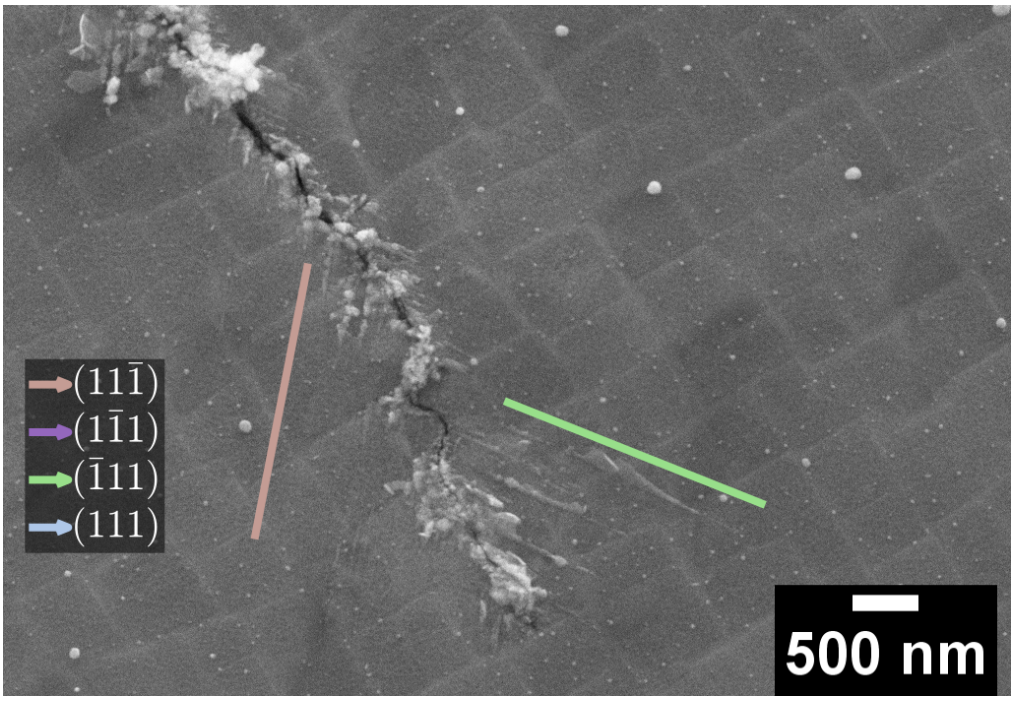


(b) Crack δ pt. I SE. ($\bar{1}$11) & (11$\bar{1}$) dominant.

Figure 6.77: Higher magnification ECCI of lower crack of **pore E** @ $\underline{g} = [020]$.
(Cont. Next Page)

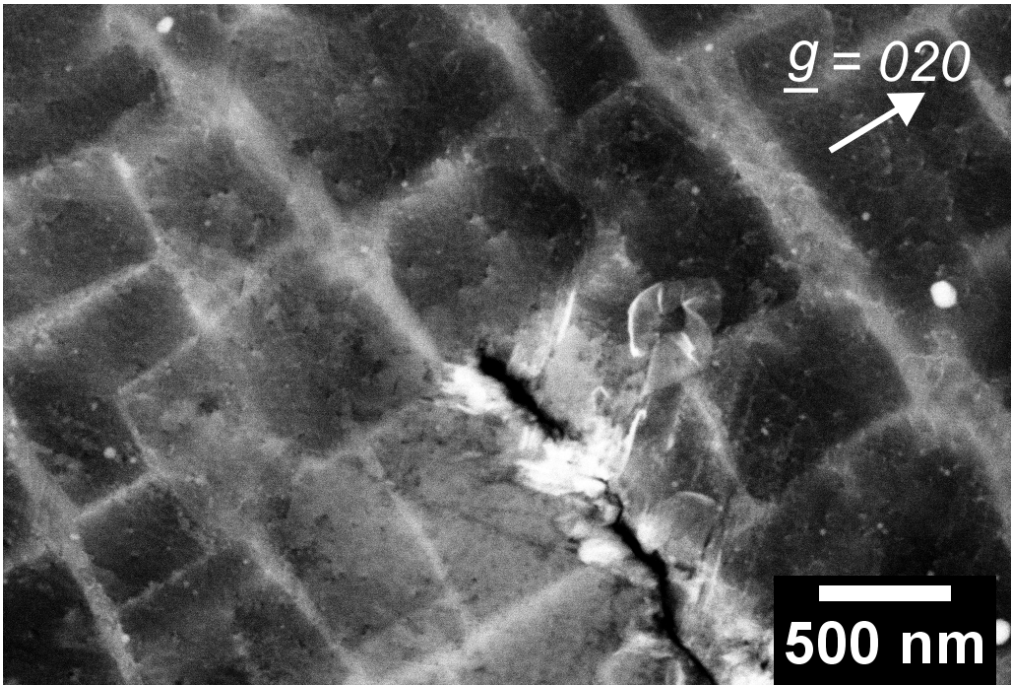


(c) Crack δ pt. II BSE.

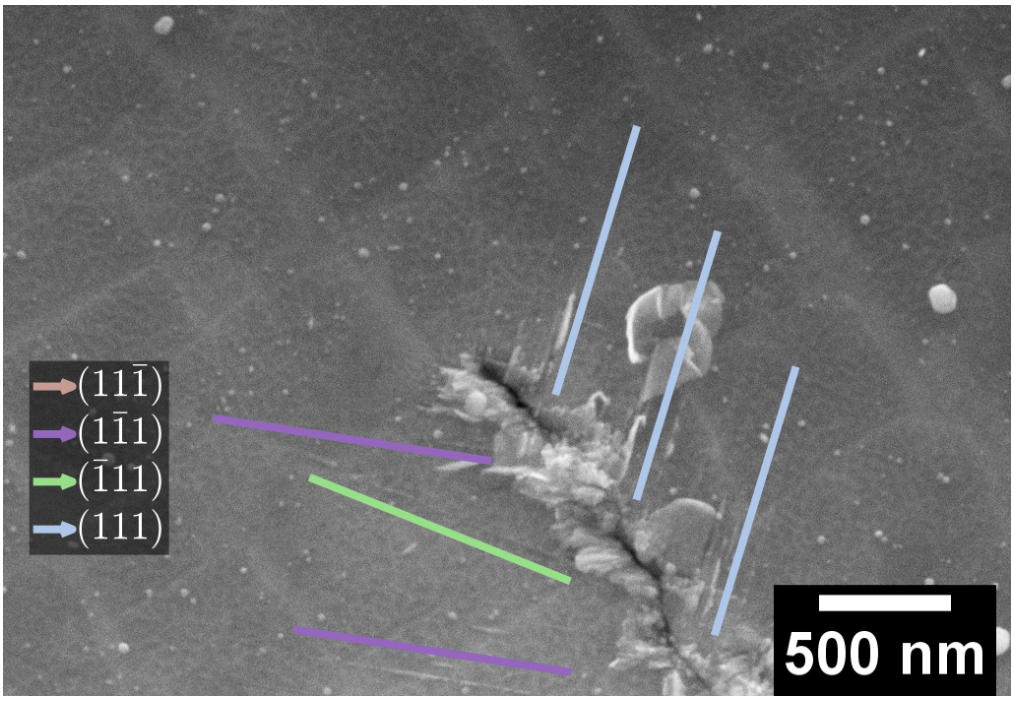


(d) Crack δ pt. II SE. ($\bar{1}$11) & (11$\bar{1}$) dominant.

Figure 6.77: Higher magnification ECCI of lower crack of **pore E** @ $\underline{g} = [020]$.



(a) Crack η tip BSE.



(b) Crack η tip SE. (1$\bar{1}$1) & (111) dominant.

Figure 6.78: Higher magnification ECCI of upper crack of **pore E** @ $\underline{g} = [020]$.

6.5.6 IT Vacuum Discussion

Much like IT air, a complex interplay exists between opening and shearing mode fractures, concurring with Ref [5, p. 140] for CMSX-4 at 450 °C. The physically short cracks in this condition especially showed this, switching between the two modes, and this is backed up by the dislocations in ECCI. This is interesting as shorter cracks should have a lower ΔK which promotes opening over shearing mode fracture [45].

Sample D4 shows both a complex short crack and a long shearing mode crack. These short complex cracks are not observed in IT air, indicating that it is promoted by the low p_{O_2}. The alternative is that they can also form in IT air, but in these tests, only long shearing-mode cracks formed or remained on the sample post-fracture.

The mild oxidation is not unexpected as NiO can form at a p_{O_2} of 10^{-19} mbar; however, but even a p_{O_2} of 1.25×10^{-3} mbar still reduces its extent [5]. As mentioned in section 6.5.4, the preferential oxidation over the fatigue cracks is most likely because of stress-assisted oxidation from dislocations around the crack tip and, in addition, potentially from the oxidation of the freshly exposed fatigue crack surfaces.

The difference in the crack decorations between the large-scale shearing mode crack (fig. 6.69) and the numerous opening mode cracks suggests that it is not caused by the environment but rather by their different mechanisms. Indicating a dislocation-based environment-fatigue interaction phenomenon or that the crack path changes the oxide topology.

In terms of non-critical sub-cracks, the IT vacuum (sample C9) exhibits a larger degree of opening mode fracture than the RT vacuum. Sometimes, showing an almost pseudo-cubic appearance due to two slip systems active on the crack tip at once. Figure 6.19d shows this, where the crack then propagates along these alternating {111} traces.

The difference between IT's air and vacuum propensity for pseudo-cubic crack paths for non-critical cracks may be an artefact of the vacuum samples not having

completely failed, and so is possibly more frequent in the main part of the cantilever or that, like the RT results, vacuum promotes pseudo-cubic slip compared to air. Evidence for the former point is found in sample A3 (OM side 2), but sample B4 has pseudo-cubic occurring briefly in a region nearer to the base. The latter point agrees with the trend in this thesis but is not documented in the literature.

The ECCI micrographs show more deformation information than HR-EBSD (fig. 6.75). However, like other ECCI-HR-EBSD comparisons, the ρ_{GND} map shows higher values near the crack path where the BSE intensity is higher. ECCI of both the cracks shows, compared to RT, that the dislocations are more localised around the cracks and mostly homogeneously distributed, as expected for higher temperatures but not of higher frequencies [48].

From the active slip traces in the opening sections of cracks δ and η, (figs. 6.77c and 6.78), then the combination of slip systems for cross-slip or a two edge slip system (with $\Sigma(\underline{b}) \parallel \pm[100]$) to occur are in table 6.5. Pore A was not included due to less clear slip traces with its strong opening region (fig. 6.74).

Table 6.5: Slip system combinations for the observed dominant co-active slip systems for the opening cracks for pore E. Note, "crack β v2" for the "Mode-I Edge" would only be edge dislocations if they are not threading i.e. $\underline{u} = [010]$.

	Cross-slip	Mode-I Edge
Crack δ	$[101](11\bar{1})$ & $[101](\bar{1}11)$	$[1\bar{1}0](11\bar{1})$ & $[110](\bar{1}11)$
Crack η	$[\bar{1}01](111)$ & $[\bar{1}01](1\bar{1}1)$	$[\bar{1}10](111)$ & $[\bar{1}\bar{1}0](1\bar{1}1)$

ECCI of pore E shows a transition between shearing and opening mode failure in fig. 6.77a. The initial shearing mode slip system has a $(\bar{1}11)$ trace, and these dislocations appear to be primarily threading. If their dislocation line vector is $\underline{u} = [001]$, the slip system could be the edge $[110](\bar{1}11)$ system, or two other mixed slip systems. This is further supported by this slip system having a high Schmid factor under axial tension (fig. 6.79) and that they cannot cross-slip (hence the more planar slip). Without clearer dark-bright splitting of those dislocations and

simulated contrasts, those dislocations are likely the $[110](\bar{1}11)$ edge slip system associated with the initial $\{111\}$ shearing mode behaviour.

In pore A the tail dislocations virtually disappeared under $\underline{g} = [2\bar{2}0]$ but not under $\underline{g} = [020]$, which if they have a $\underline{b}$ of $\pm[110]$ means they also have a relatively high Schmid factor (fig. 6.79). It also satisfies the $\underline{g} \cdot \underline{b}$ invisibility criterion but not the pure edge invisibility criterion $(\underline{g} \cdot (\underline{b} \times \underline{u}))$.

As pseudo-cubic slip is thought to be contained primarily within the γ channels, then as the tail dislocations occur there and near the opening crack portions, they could be the dislocations involved in the pseudo-cubic slip in the γ phase.

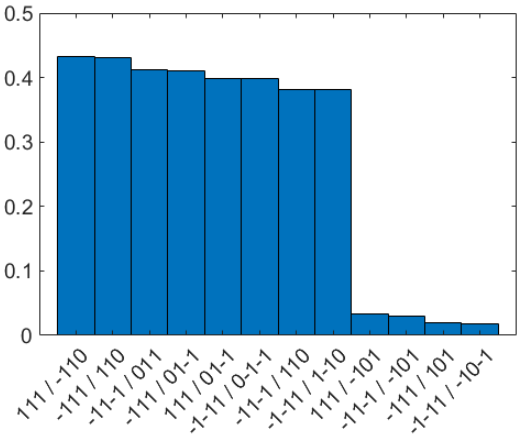


Figure 6.79: C9 MTEX slip analysis via Schmid factor for C9 using a uniaxial stress along the cantilever axis.

6.5.7 IT Conclusions

The conclusions from the IT discussions (sections 6.5.3 and 6.5.6) are:

- In air, IT outperforms RT (electropolished or not) in fatigue performance. This has been linked to a greater alloy σ_y via thermally activated γ' strengthening. A consequence of this is the observed pseudo-cubic slip and opening fracture paths along the γ channels. The increase in performance agrees with the expected σ_y increase in the general literature but disagrees with the results

from Ref [5], especially considering the lower degree of oxidation (less oxide plugging).

- Normalising the fatigue curves of the results by their respective σ_y values does not cause the results to overlap, which indicates that the increase in σ_y is not the sole cause of fatigue performance improvement.
- Both modes occurring at 450 °C fatigue in air and vacuum concur with the literature [5, 45, 54].
- In IT vacuum, the physically short cracks exhibit both shearing and opening mode fracture like in air, frequently transitioning between the two. ECCI micrographs show their expected planar and homogeneous slip, respectively. The two {111} slip bands involved in the opening mode fracture path indicate that pseudo-cubic slip occurs with occasional precipitate shearing. The change in slip traces from the shearing mode crack indicates different slip systems occur in opening mode to shearing mode.
- EDX and SE micrographs have confirmed that oxidation has occurred in both air and vacuum.
- The degree of oxidation in air is similar to what is reported in Ref [5] and indicates a short exposure as intended. Local oxidation around the crack path can be seen.
- In vacuum, the surface oxidation was, as expected, significantly less, allowing ECCI and HR-EBSD. With ECCI being more insightful. In air, the surface oxidation was too great for these techniques.
- Enhanced oxidation was observed on the cracks along the surface. Appearing rough and coarse around opening cracks and ribbon-like for shearing cracks. The ribbon-like products are seen in the ambient tests.
- Both vacuum and air tests at IT exhibited shear and opening fracture modes. Therefore, it is reasonable that the ECCI observations for the short cracks tested in vacuum are representative of both environments.
- For better defect characterisation, simulating the defect contrast in ECCI with software like *EMsoft* [131, 132] would be beneficial, not only to better

characterise appearances of $\langle 1\bar{1}0\rangle\{111\}$ dislocations but also of more complex dislocations in this material like those in Ref [6] (section 2.1.3).

6.6 Chapter Summary

The following points summarise this chapter and relate it back to the research aims:

- The S-N results show greater strength than expected from the macroscale fatigue results in the literature. A beneficial size-effect is likely due to the mesoscale samples' lower risk-volume (item 1).
- Bending fractographs of a SXNBS have been collected under different environmental conditions and under $R = -1$ (item 3). These fractographs will contribute to the interpretation and understanding of bending fractography for SXNBSs.
- The fractographs have shown how OM and SEM can distinguish the appearance of fatigue crack initiation. The SEM fracture surface micrographs show how their final fractures differ and progress (item 3).
- Ultra-high vacuum conditions have been observed to significantly improve the RT fatigue performance by promoting opening mode fracture that is absent under air, which only shows shearing mode fracture (item 7). Oxidation ahead of the crack tip in air is the proposed explanation behind the better fatigue performance under vacuum. The unexpected presence of opening mode under vacuum rather than air is proposed to be potentially from self-heating. The opening mode and the improved fatigue performance could be related. (item 8)
- Despite electropolishing the mesocantilevers, preferential fracture and critical failure came from the corners where the cantilever joins the base, indicating that the mesocantilever design is not ideal for a CD & FN of $\langle 100\rangle$. It is thought that the S-N within this chapter are comparable as they use the same design.

- ECCI has been highly insightful in capturing the dislocations associated with the plastic deformation in both the ambient conditions and IT vacuum; more appropriate than HR-EBSD (item 4).
  - The ambient fatigue tests show virtually all {111} shearing mode facets, as expected for high-frequency and low-temperature conditions [42]. The dislocations ahead of the crack tip are highly planar and occur on nearby parallel planes. Cracking and slip operating on a secondary slip system is frequent along a crack, as expected by simulation for this SXO, explaining the bifurcation and "zig-zag" fracture (item 4). The ECCI evidence of this bifurcation through dislocations is likely novel.
  - Planar threading dislocations ahead of a crack with a mode-III component have been observed in RT fatigue testing and associated with shear mode fracture (item 5). A mode-III component is not unexpected due to the nearly 45° crack orientation with the cantilever bending and as the literature of similar cracks showed mode-III components [53].
  - The IT vacuum fatigue cracks show the same behaviour for its shearing mode cracks but a significantly less planar and more homogeneous distribution of dislocations along and ahead of the opening mode cracks item 9. Opening mode fracture is significant in the fracture surfaces in air, more so than in vacuum. The physically short cracks in vacuum show that the transition between the two modes is frequent, agreeing with the complex interplay between the two modes at this temperature in Ref [5].
- Schmid factors have been used to correlate observed slip traces to identify the slip systems (item 4).
- IT fatigue tests show generally a higher fatigue strength than its RT counterparts, disagreeing with Ref [5] which found in the LCF regime a worse performance for CMSX-4 at 450 °C & 550 °C ($f = 0.25$ Hz, $N_f = 10^3$ to 10^4, & $R = 0.1$ c.f. $f = 20$ kHz, $N_f = 10^5$ to 10^8, & $R = -1$ in this work). However, the increasing fatigue performance with temperature (below the peak yield

strength temperature) agrees with the general literature [6, 35, 42, 50] (item 9). The normalisation of σ_{amp} by σ_y of the S-N curves does not cause them to overlap, indicating that the increase in σ_y is not the sole mechanism for the increase in fatigue performance. The larger extent of opening mode fracture compared to RT tests is proposed to be due to strengthening and related to the improved fatigue performance (item 9). The opening mode fracture surfaces in IT air are similar to RT vacuum, supporting that the RT vacuum features are opening mode.

- The IT tests show greater surface oxidation compared to RT conditions. The degree of oxidation in air appears mild (c.f. Refs [5, 22, 24, 52, 60, 73, 75]) , as expected for the relatively short exposure times at 450 °C (see fig. 6.47). However, it was enough to prevent HR-EBSD or ECCI. The oxidation in vacuum is expectedly very mild, so the aforementioned techniques are possible. The oxidation of the cracks under vacuum appears different, which is thought to be due to the oxidation of the freshly exposed cracks. The coarser oxide over the opening mode crack paths could be caused by its homogeneous dislocation distribution or by its opening path.

7

Single Crystal Orientation Testing & Modelling

Contents

7.1 Cantilever Design Development 237
7.2 Sample Preparation 243
7.3 S-N 247
7.4 Fractography 252
7.4.1 <100> 252
7.4.2 <110> 256
7.4.3 Fracture Surface Progression 259
7.4.4 LCF vs VHCF 270
7.5 Simulations vs Experiments 273
7.5.1 RJSN1 <110> 273
7.5.2 H8 <100> 276
7.6 <110> ECCI Micrographs 281
7.7 Discussion 304
7.8 Chapter Summary 311

This chapter will cover the testing & modelling of the mesocantilevers with different single-crystal orientations (SXOs). Comparisons will be made between experimental and simulated results and with the literature.

7.1 Cantilever Design Development

In chapter 6 the samples were prepared such that the cantilever direction (CD) and FN were near ⟨100⟩ (i.e. ⟨100⟩⟨100⟩). The cantilevers often cracked with shearing mode fracture at the corners where the cantilever attaches to the base (aka corner cracks), and was not improved by electropolishing in ambient conditions (section 6.2).

Original vs RJS Design

Initial FEM models assumed isotropic elasticity, which showed a suitable σ_{vm} distribution in the cantilever with no stress concentrations. However, when accounting for mechanical anisotropy for the ⟨100⟩⟨100⟩ SXO, σ_{vm} stress concentration occurred at the corners, with stresses higher or equivalent to the highest stress within the main cantilever body.

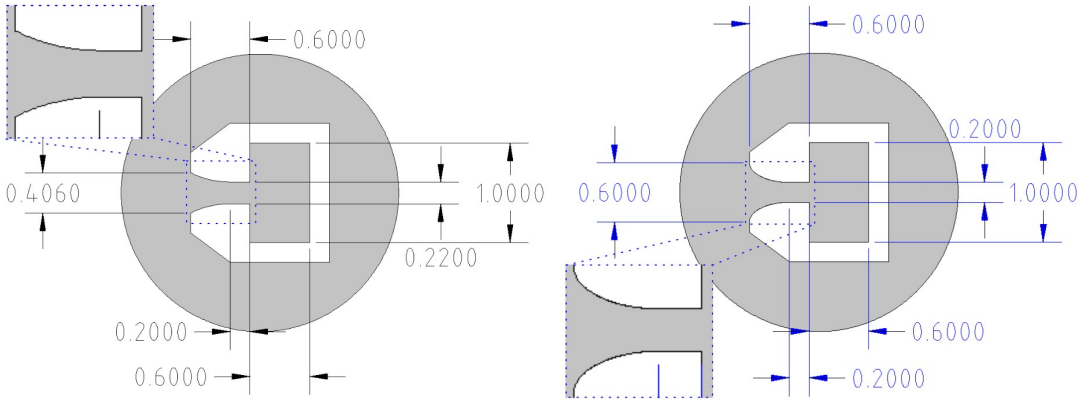
CPFE modelling was one method to account for the anisotropy. The Euler angles from EBSD and ideal orientations were inputted for the pre-defined CMSX-4 material. For brevity, C3D20 elements were used on a 40µm elements seed size, and the cantilever tip was deflected by 80µm in the work below. For consistency, the models used the ideal sample design dimensions rather than their measured dimensions.

Both the old and new designs in this subsection will use sample H8's SXO[1] to show how the stress concentration arises due to anisotropy and how the new (**RJS**) design was intended to improve it. Unique nodal data points are used for the displacements and loads, whereas integration points are used for stresses and strains.

Figure 7.1 shows how the new RJS design modifies the original by using an elliptical profile to form an additional tangent at the base to minimise the sudden change in geometry to combat the stress concentrations. Figure 7.2 shows this, with the RJS design significantly reducing the corner σ_{vm} stress concentrations, making the stress more uniform, and moving the peak stress region to within the main cantilever body. Similar changes occur for the total slip, with an even more

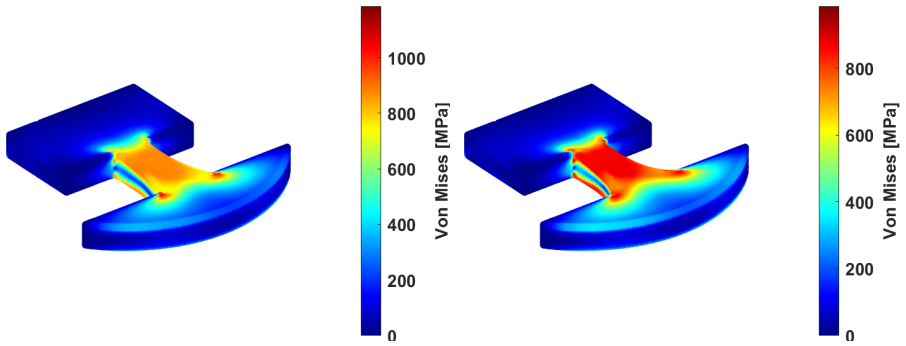
[1] Bunge Euler $[255.2°, 12.5°, 14.6°]$

significant improvement. Samples and simulations with the RJS design are prefixed with RJS.

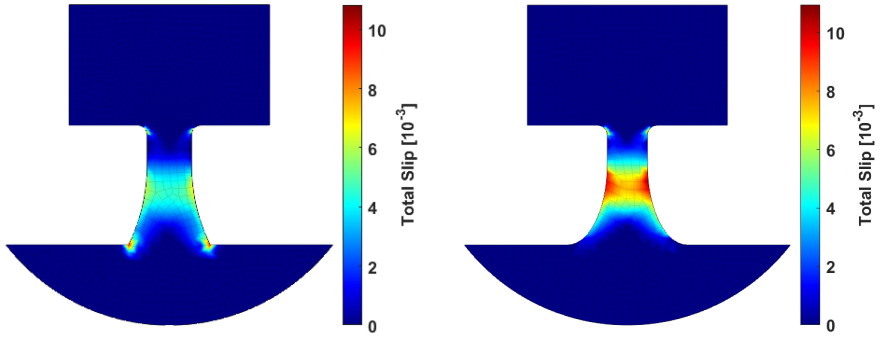


(a) Original design **(b)** RJS design

Figure 7.1: Original mesocantilever design vs new (RJS) design schematic drawings for machining (visualised in LibreCAD software). Units are in mm.



(a) Original - σ_{vm} distribution. **(b)** RJS - σ_{vm} distribution.

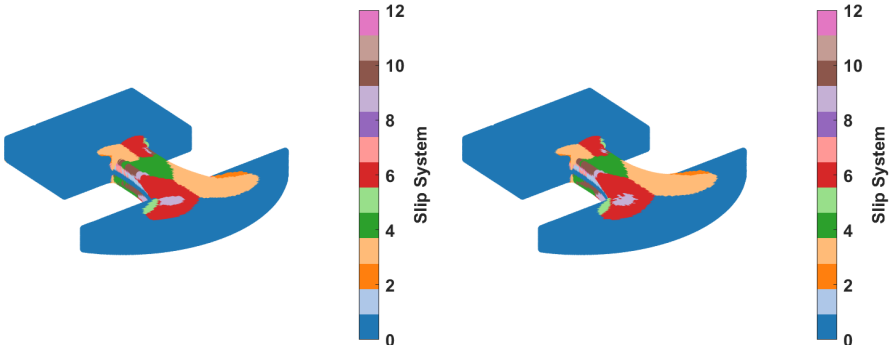


(c) Original - Total slip distribution. **(d)** RJS - Total slip distribution.

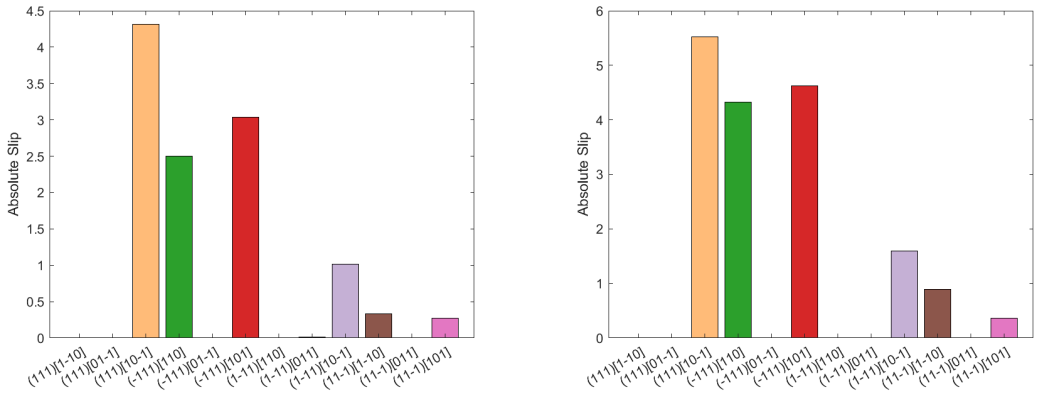
Figure 7.2: *Original*-vs-*RJS* mesocantilever designs in CPFE for sample H8 orientation. The total slip is the sum of the slip values from the unique nodal model data.

Analysing the CPFE results, fig. 7.3 shows similar active slip activity proportions in both designs, and the 3$^{\text{rd}}$ slip system ($(111)[10\bar{1}]$) dominates in both designs in the risk-volume. The risk-volume results are important to VHCF (see section 2.5.1) and indicate where fatigue initiation is more likely to occur. The top 10% σ_{vm} is chosen as the risk-volume due to Ref [68].
With the RJS design, the main changes are to the σ_{vm} and total slip distribution but less so the active slip systems and their relative dominance. Therefore, the changes in slip distribution and σ_{vm} should promote failure away from the corners and towards the cantilever itself, whilst the slip behaviour associated with fracture should be virtually unchanged.

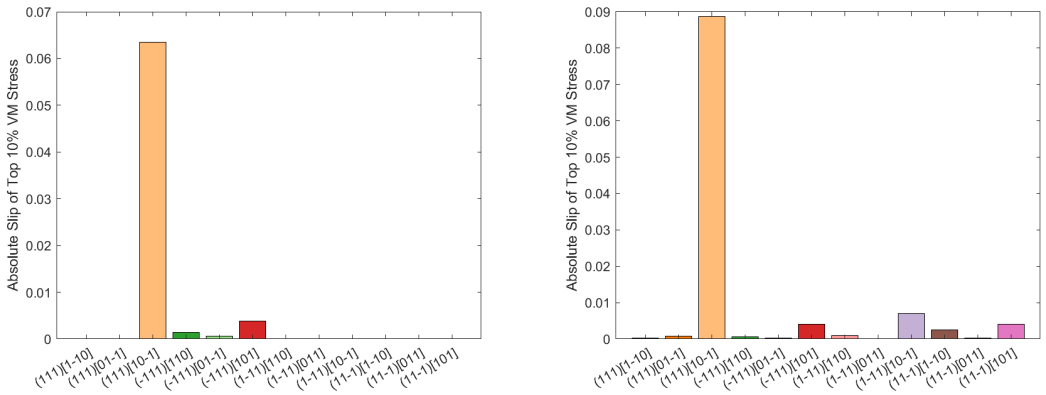
Therefore, comparing fractography results between the RJS $\langle 100 \rangle$ samples with the original design in chapter 6, their similarity in slip dominance explains their similar fracture paths, as shown later in section 7.4.



(a) Original - Dominant slip system map. **(b)** RJS - Dominant slip system map.



(c) Original - Σ(|slip per slip system|) for the whole volume. **(d)** RJS - Σ(|slip per slip system|) for the whole volume.

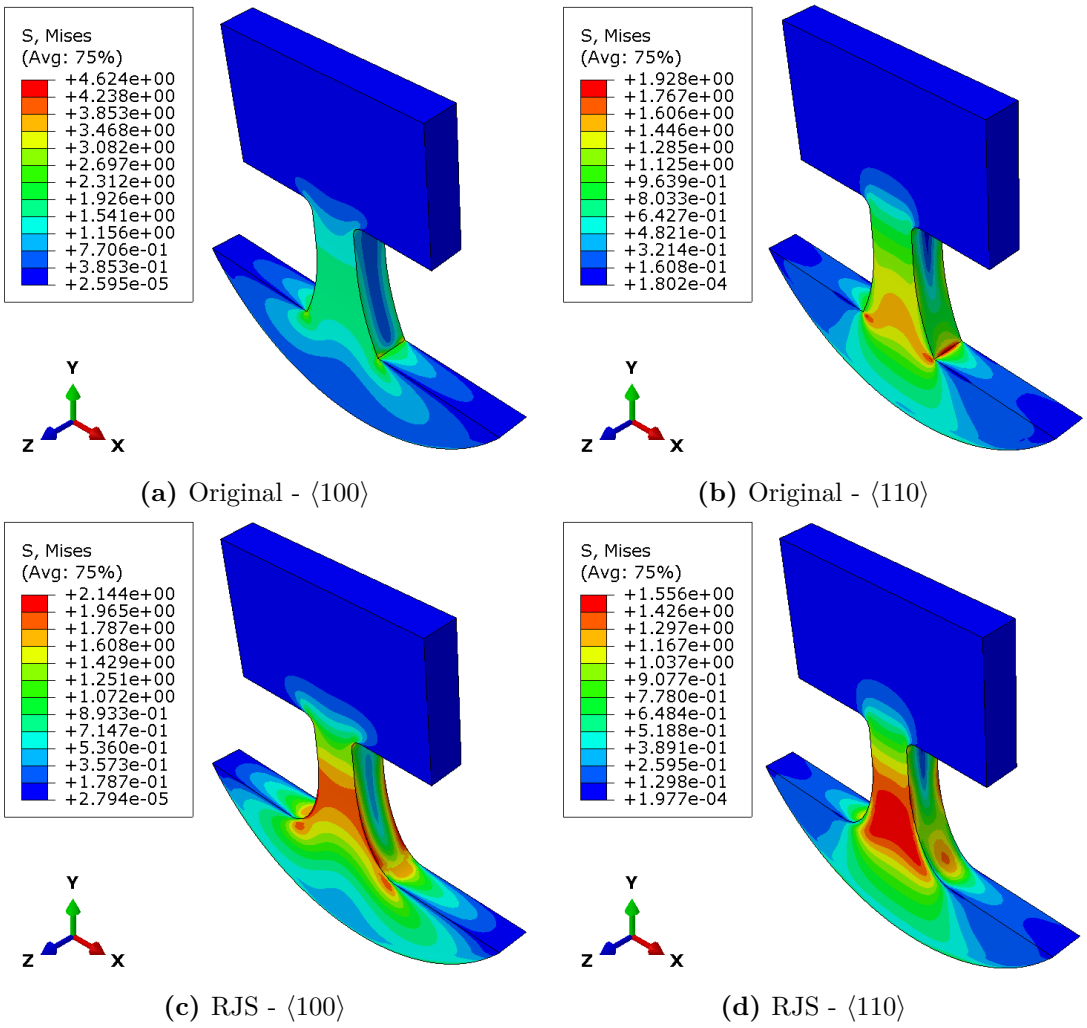


(e) Original - Σ(|slip per slip system|) for the risk volume. **(f)** RJS - Σ(|slip per slip system|) for the risk volume.

Figure 7.3: CPFE simulations for H8 using the integration point data to compare the original (1st column) and the RJS (2nd column) designs. Σ(|slip per slip system|) = sum of the absolute slip on each slip system. N.B. Slip system 0 (dark blue) is where no slip was calculated.

Ideal On-axis Orientations

Figure 7.4 shows that even the ⟨110⟩⟨100⟩ SXO used in this testing campaign shows a good σ_{vm} distribution, even better than for ⟨100⟩⟨100⟩ as it is less intense on the edges.



(a) Original - ⟨100⟩ **(b)** Original - ⟨110⟩

(c) RJS - ⟨100⟩ **(d)** RJS - ⟨110⟩

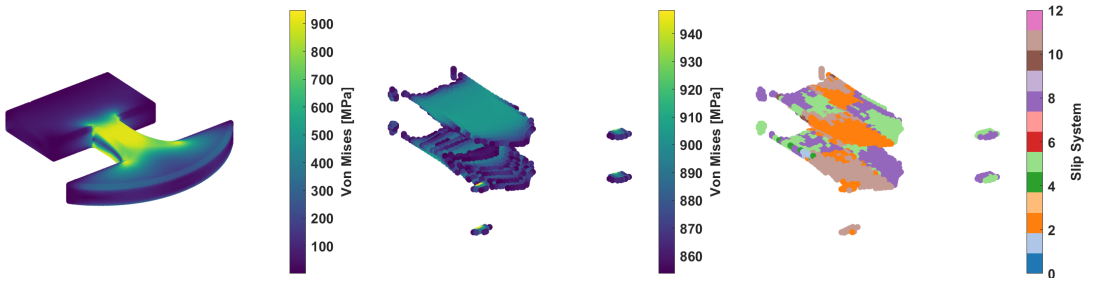
Figure 7.4: The of σ_{vm} stress field (in MPa) from direct-dynamic FEM simulations for the original and RJS designs with different SXOs by varying the CD but maintaining a ⟨100⟩ FN. A 20 µm global seed size was used. Visualised in ABAQUS CAE.

Repeating the same CPFE analysis with the on-axis ⟨100⟩ and ⟨110⟩ SXOs RJS models produces fig. 7.5, showing similar σ_{vm} distribution for the two orientations. Note that the stress state from static deflection is not identical to the more accurate direct-dynamic simulations.

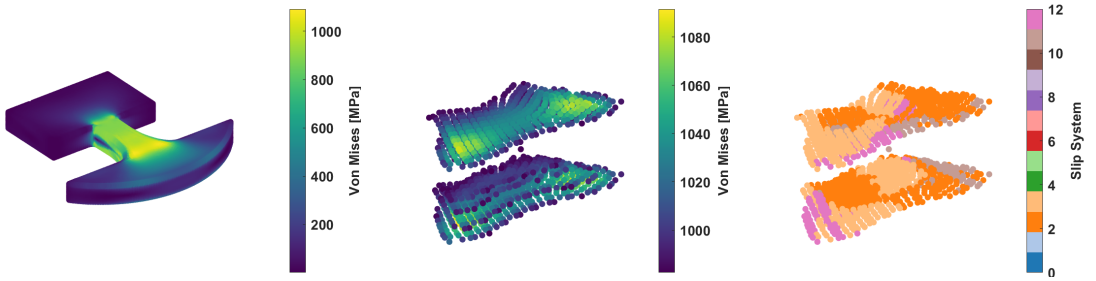
Analysing the slip systems of the two RJS SXOs, ⟨100⟩ has four dominant slip systems (on four different slip planes) compared to two slip systems (on two planes) for ⟨110⟩. For ⟨100⟩, the four active planes explain the experimentally observed "zig-zag" shearing fracture path (chapter 6) as they are ⟨100⟩ samples and because the path is alternating between at least two different slip planes. ⟨110⟩'s results mirror those in Ref [11] in that this orientation has in uniaxial fatigue and has two dominant slip systems if exactly on-axis. As this is bending deformation, that could be why the $(11\bar{1})$ slip systems are appreciable compared to the (111) systems.

If one alters the crystal orientation to keep the same CD but vary the FN, the σ_{vm} distribution can change along with the active slip systems involved with the cantilever deformation. However, in this work the FN is kept near ⟨100⟩.

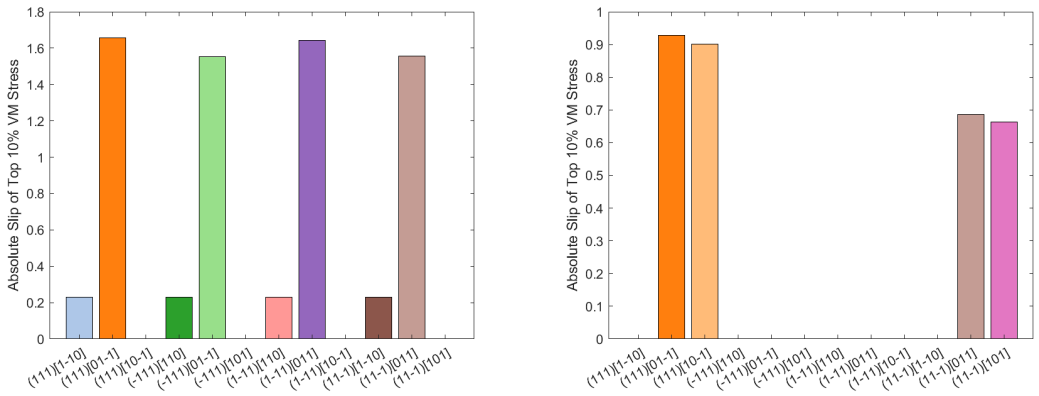
To summarise, this design is similar to the original but now improves the stress and slip distribution within the cantilever, reducing the corner stress concentration in ⟨100⟩ samples and is very suitable with ⟨110⟩ samples. Compared with the original design, this is done without significantly affecting the slip system activity, resonant frequency, and ω.



(a) RJS ⟨100⟩ SXO



(b) RJS ⟨110⟩ SXO



(c) RJS ⟨100⟩ SXO - Σ(|slip per slip system|) of the risk volume

(d) RJS ⟨110⟩ SXO - Σ(|slip per slip system|) of the risk volume

Figure 7.5: Analysis of the CPFE models of the RJS design with the ⟨100⟩ & ⟨110⟩ SXOs. The plots in (a) and (b) from left to right are the σ_{vm} of the whole sample, top 10% σ_{vm} risk volume, and this risk volume's dominant slip systems, respectively.

7.2 Sample Preparation

Figure 7.6 shows how a prepared foil can produce mesocantilevers with near ⟨100⟩ and ⟨110⟩ cantilever directions (CDs) with the same foil normals (FNs) by altering the rotation of the laser machining template. These orientations are akin to having the tensile axis of a uniaxial test along the ⟨100⟩ and ⟨110⟩ orientations, respectively. Additionally, the beam axis stress is typically the largest stress component in the

cantilevers. The samples were electropolished (EP) for 20 s (30 s for RJSK2 & RJSN3), short enough to improve the surface quality for HR-EBSD and ECCI.

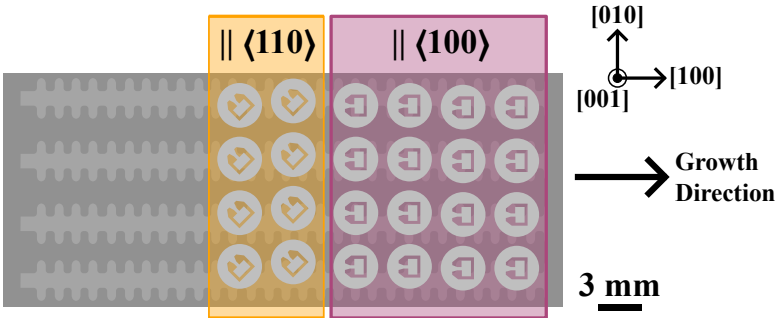
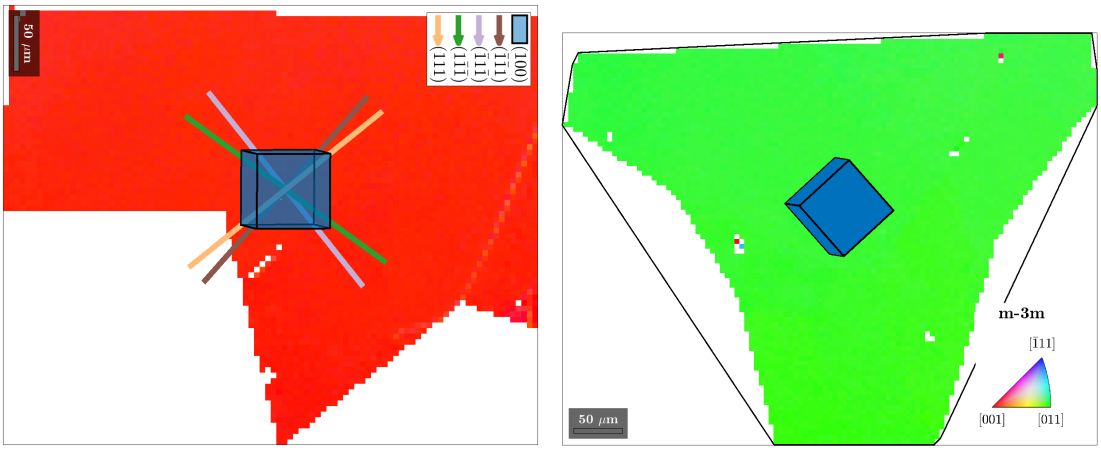


Figure 7.6: Schematic of how the ⟨100⟩ and ⟨110⟩ cantilevers were machined from a prepared foil.

Using MTEX [133] (a MATLAB crystallography toolbox) and EBSD data, the calculated disorientations have confirmed that the SXOs are close to their intended values (see figs. 7.7 and 7.8). Table 7.1 lists these disorientations values. Despite being from different foils, EDM and foil preparation have led to similar FN disorientation values. Apart from RJSM10, the CD disorientation values range is around 3.5°. The higher RJSM10 value is likely an outlier considering the manufacturing methodology from parallel EDM foils do produce consistent FN. Further supporting this is the low (3.4°) CD disorientation for RJSN1 from the same foil.

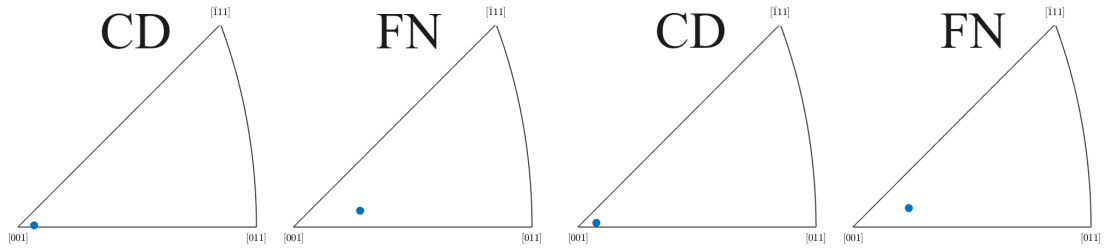
Table 7.1: Disorientation values of some of the samples from the thesis using the mean orientation in MTEX. I5 is rotation corrected as the EBSD map was approximately 4° to 6° from the CD axis.

Sample	CD SXO	CD [°]	FN [°]
H8	⟨100⟩	3.0	12.6
I5	⟨100⟩	3.5-3.9	10.9
C9	⟨100⟩	3.6	10.0
RJSM10	⟨100⟩	8.2	11.7
RJSN1	⟨110⟩	3.4	12.1

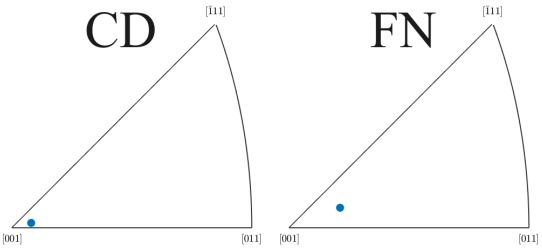


(a) H8 - ⟨100⟩ CD. **(b)** RJSN1 - ⟨110⟩ CD.

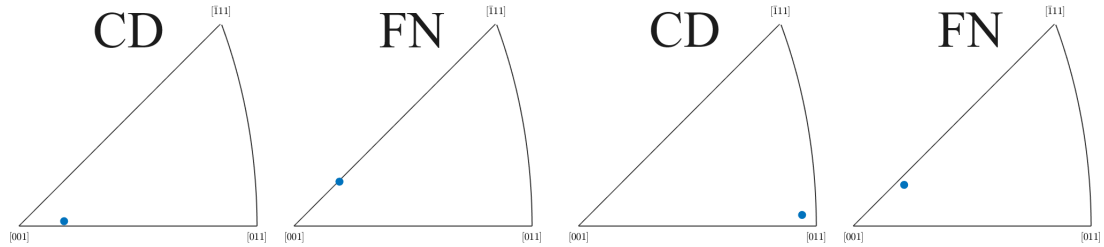
Figure 7.7: Physical SXOs represented as cubes (cubic crystal structure) superimposed onto the two cantilevers of different CD values, bright red is exactly ⟨100⟩and bright green is exactly ⟨110⟩. The cantilevers are rotated so their CDs pointed downwards.



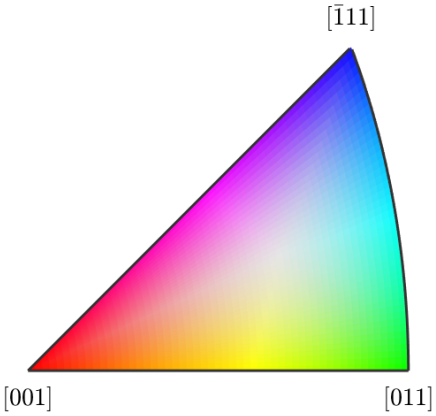
(a) H8 ⟨100⟩. **(b)** I5 ⟨100⟩.



(c) C9 ⟨100⟩.



(d) RJSM10 ⟨100⟩. **(e)** RJSN1 ⟨110⟩.



(f) Cubic inverse pole figure.

Figure 7.8: MTEX inverse pole figures for the samples in table 7.1. The sample was orientated so that the 1st column (y) for each sample was made near parallel to the CD and similarly, the 2nd column (z) is the measured FN.

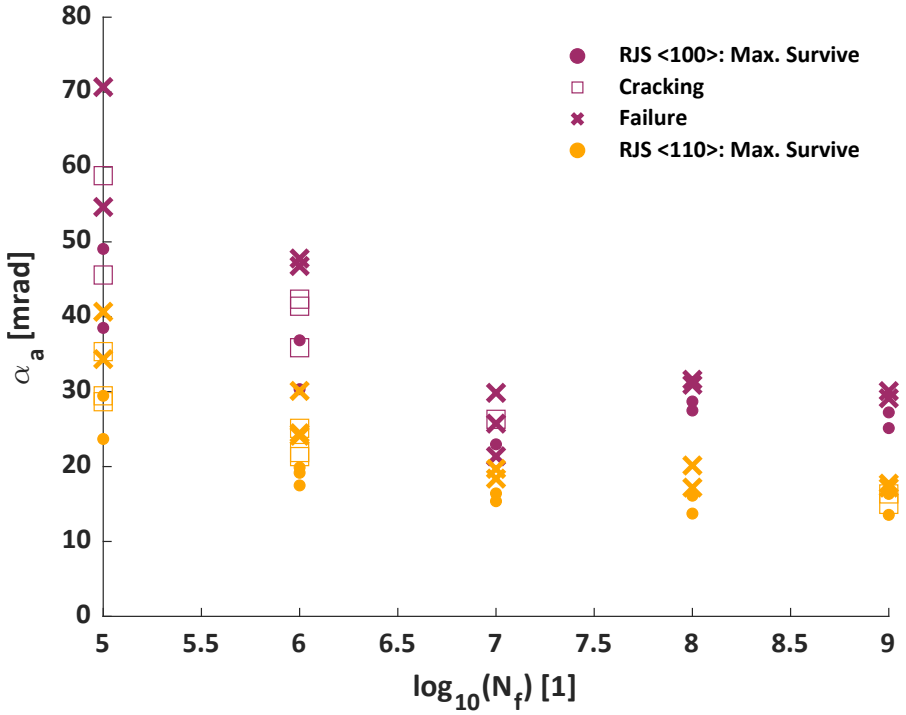
7.3 S-N

The A-N curves for the 11 ⟨100⟩ and 11 ⟨110⟩ CDs samples in fig. 7.9a show that the ⟨110⟩ has a greater value. However, this is an artefact of the single-crystal elastic anisotropy. Accounting for this using the linear-elastic stress-per-angle (ω) brings the two S-N curves together in fig. 7.9b. The Young's modulus of ⟨110⟩ is 230 GPa whereas it is 126 GPa for ⟨100⟩, which means that for the stress amplitude (σ_{amp}), the bending angle amplitude (α_{amp}) for ⟨110⟩ will be lower than ⟨100⟩'s by a factor of ≈ 1.83. This factor is seen in the FEM results where the ratio of the median average of the median ω values for the cantilevers is 1.84 with the ideal SXOs and lateral dimensions.

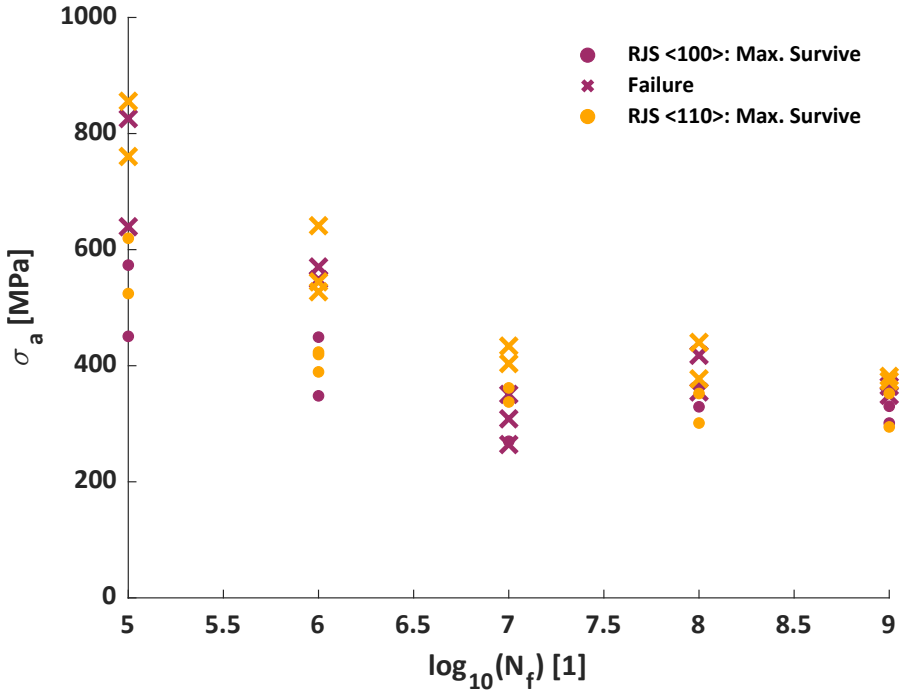
At $N_f = 10^7$ for RJS ⟨100⟩ in fig. 7.9b, two samples show a notably lower fatigue performance and quicker failure and are propagated. Localised decreases in the S-N data for one life have been observed in other materials for this UFR methodology.

Using the statistical analysis in section 4.1.6 on the data produces figs. 7.10 and 7.11, which shows how similar the fatigue responses of the two SXOs are. The difference between the fitted $P_f(50\%)$ curves varies from 0.31 MPa to 79 MPa with mean and median averages of 20 MPa and 15 MPa respectively. ⟨110⟩ shows a plateau at $N_f \geq 10^8$ and possibly even at $\geq 10^7$ when looking at the survival data only. For ⟨100⟩, a plateau may also be occurring.

The VHCF data for ⟨100⟩ is similar but becomes increasingly lower than ⟨110⟩. However, the prediction intervals show they are close. This is an artefact of the propagation of the two low $N_f = 10^7$ failure points as only 5 survival steps at $N_f = 10^9$ were done. Further tests at $N_f = 10^9$ may bring the ⟨100⟩ curve closer to the ⟨110⟩ curve by lessening the influence of those two points, as shown in the edited propagation analysis of fig. 7.12.

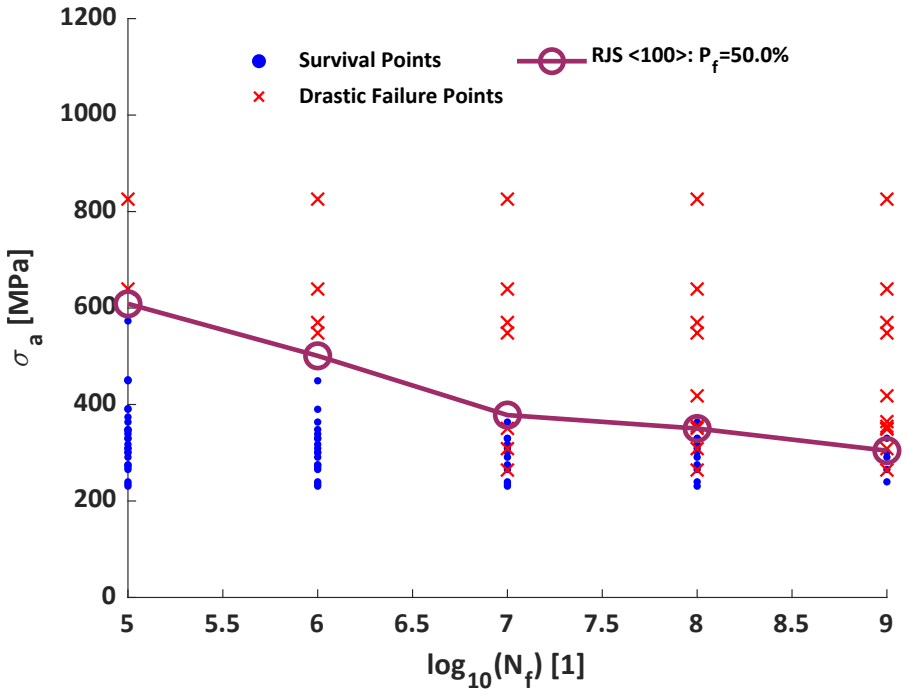


(a) A-N.

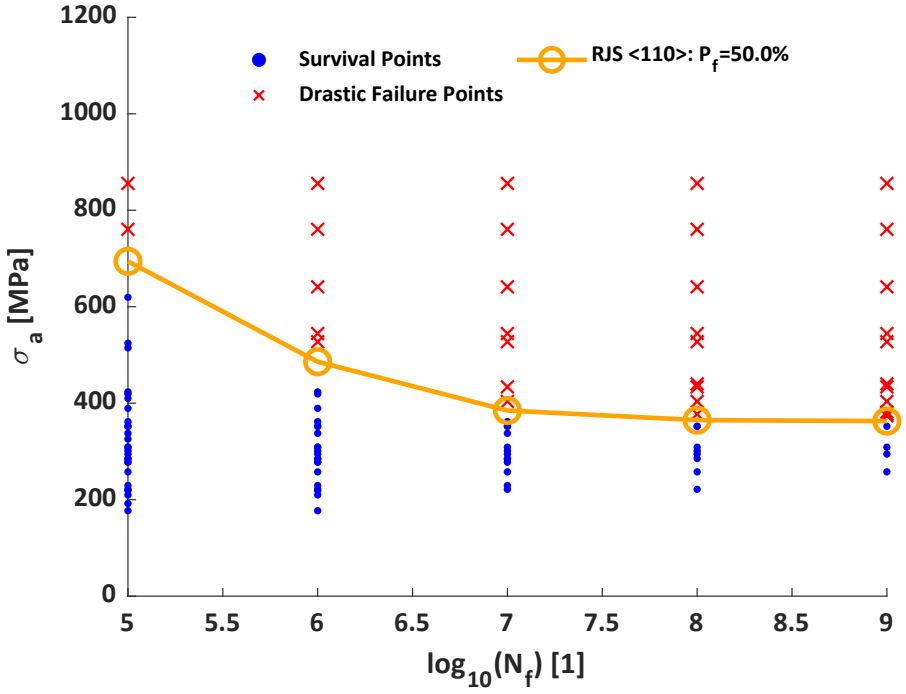


(b) S-N.

Figure 7.9: Ambient fatigue performance of with different SXOs. Both have FN ⟨100⟩ but different CDs.



(a) Propagated ⟨100⟩ plot



(b) Propagated ⟨110⟩ plot

Figure 7.10: Propagated data S-N curves for the two CD orientations. The drastic failure points and top 5 survival steps are propagated and shown along with the 50% probability of failure plotted.

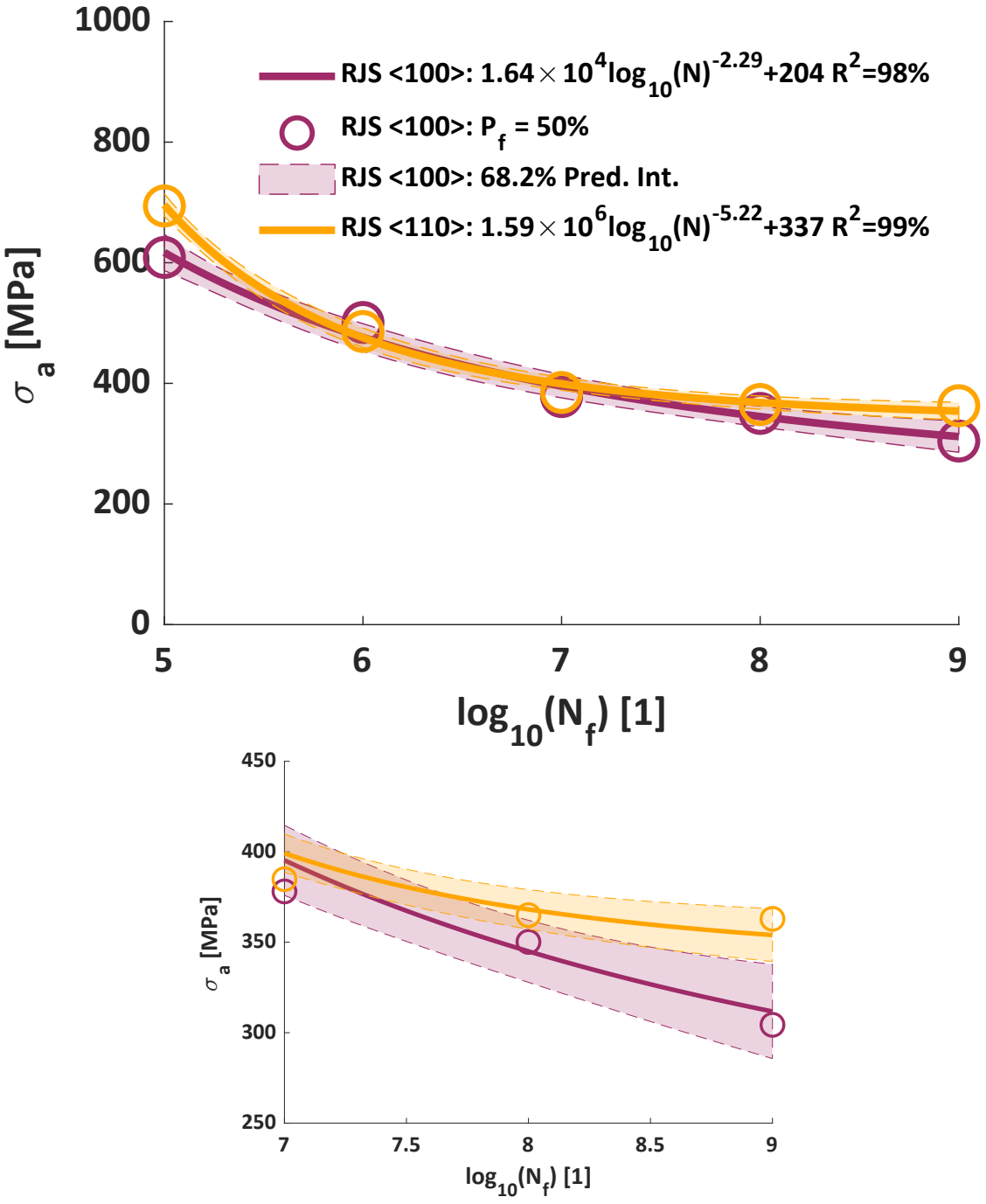


Figure 7.11: S-N with Basquin fitting of the RJS ⟨100⟩ and RJS ⟨110⟩ samples. The 50% probability of failure is fitted along with a shaded region representing ±1 standard deviation prediction interval.

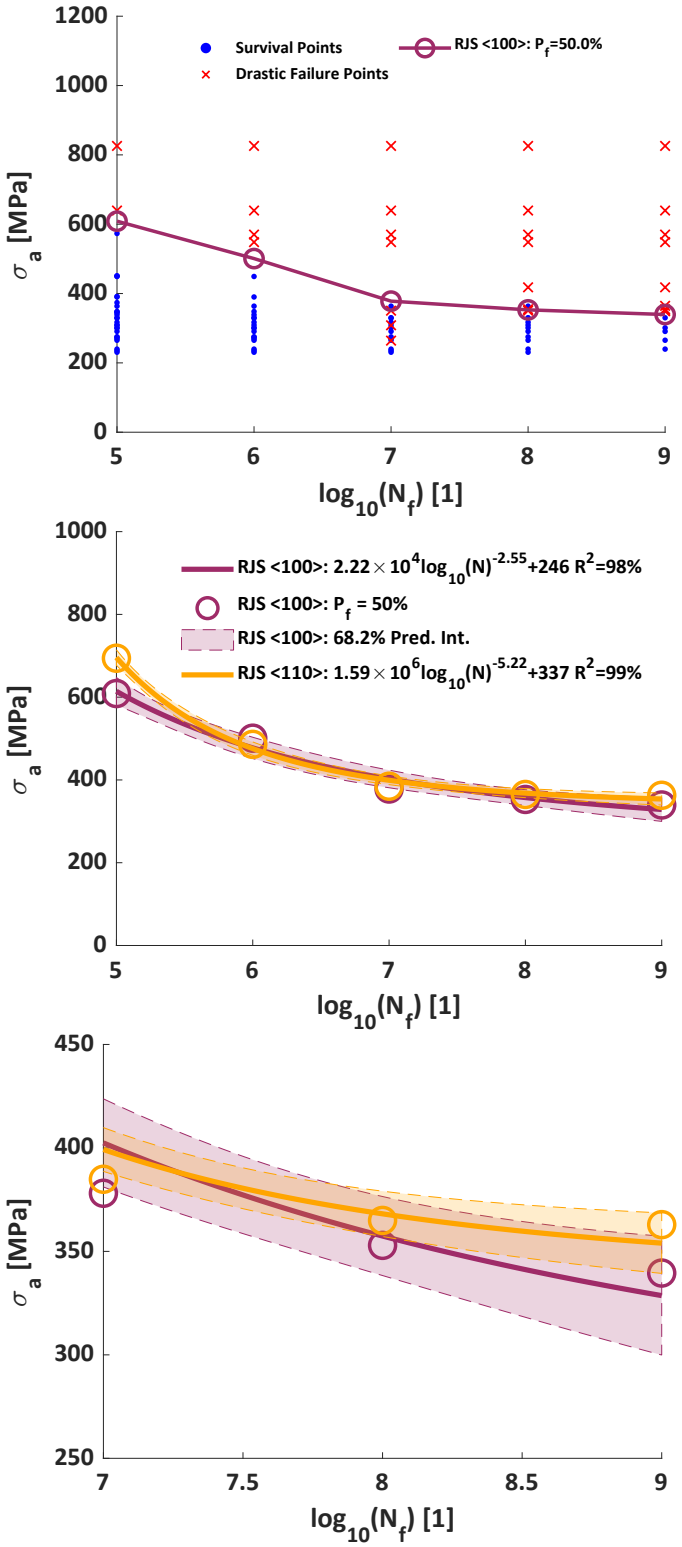
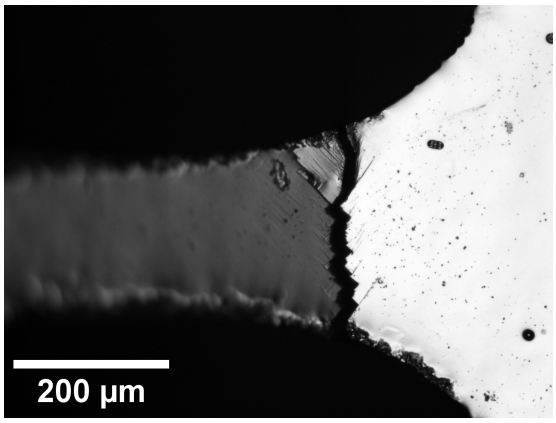


Figure 7.12: Edited propagation version of fig. 7.11 where the two lower $N_f = 10^7$ failure data points are not propagated forward.

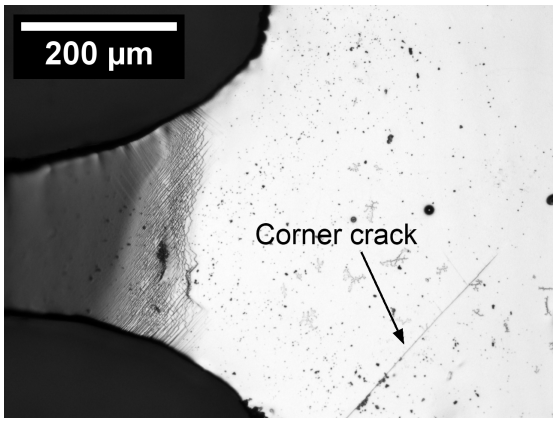
7.4 Fractography

7.4.1 <100>

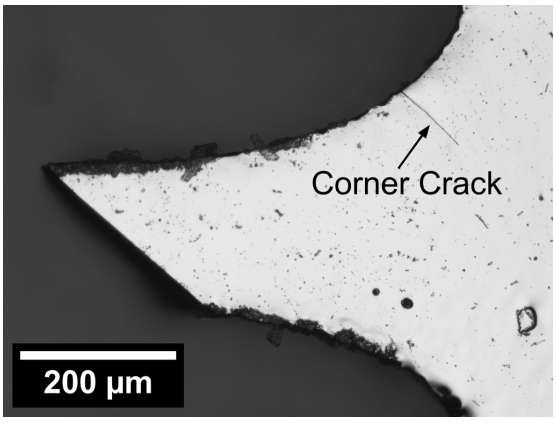
For the ⟨100⟩ SXO, failure is less dominated by corner cracks in the RJS design (c.f. original), occurring more within the cantilever's main body (e.g. fig. 7.13). Similar fracture features are shared between the two testing campaigns, like the "zig-zag" shearing fracture path and single {111} facet failures.



(a) RJSK2 initiation side with "zig-zag" {111} fracture path.



(b) RJSK2 exit side with corner crack.

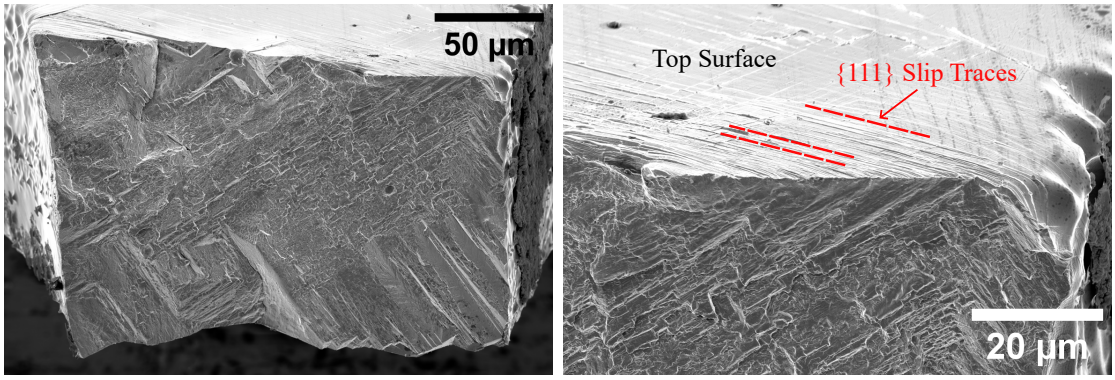


(c) RJSK4 initiation side with corner crack and a single {111} facet critical crack.

Figure 7.13: OM fracture images of RJSK2 and RJSK4 of the ⟨100⟩ SXO. These micrographs show how the failure is more dominated by fracture within the main body of the cantilever rather than corner cracks (if they form). The exit side shows significant amounts of slip and plastic deformation but no opening crack.

For both the mesocantilever designs in RT air, the crack paths in OM indicate purely shearing mode fracture. However, in some samples, small regions of the crack path appear to follow an opening mode direction. In RJSL9 (fig. 7.14b) and

RJSK2 (fig. 7.16), these regions are highly deformed, as shown by the extensive {111} slip traces, indicating a high σ_{amp} and two active {111} slip systems. However, as shown in RJSM8 fig. 7.15, this is likely just a finer version of the alternating {111} shearing mode fracture on two systems seen in RJSM8. This fracture does not appear like the opening mode observed in chapter 6 due to the long slip traces on the cantilever surface. Potentially, they are like the alternating facets seen in RJSM8 but on a finer scale.



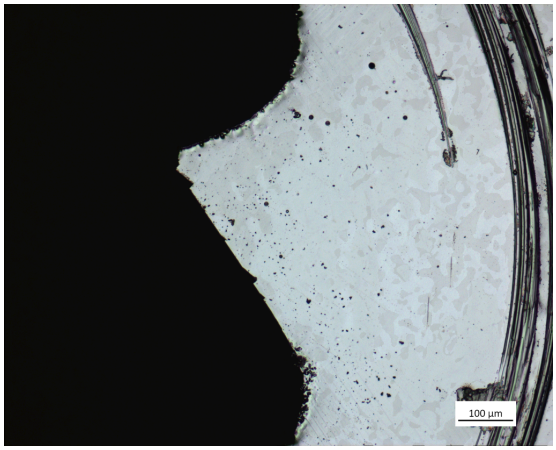
(a) Low magnification.

(b) Potential opening mode via fine {111} fracture.

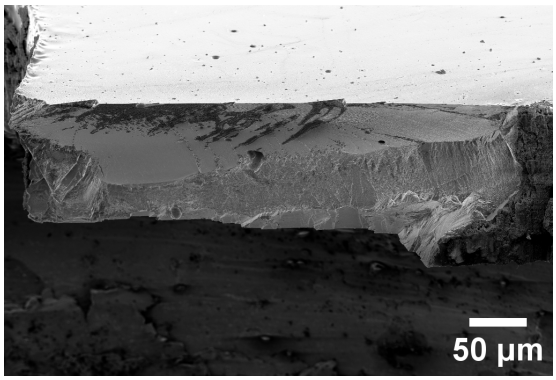
Figure 7.14: ⟨100⟩ RJSL9 cantilever SE fractography.

The crack paths in the main body of the cantilever following ⟨100⟩ macroscopically (e.g. fig. 7.16) can be explained by cracks switching fracture planes to follow the path of maximum surface σ_{vm}. Whereas {111} cracks closer to the base grow into decreasing σ_{vm}, and by switching planes, they won't grow into a greater stressed region; hence, they tend not to alternate.

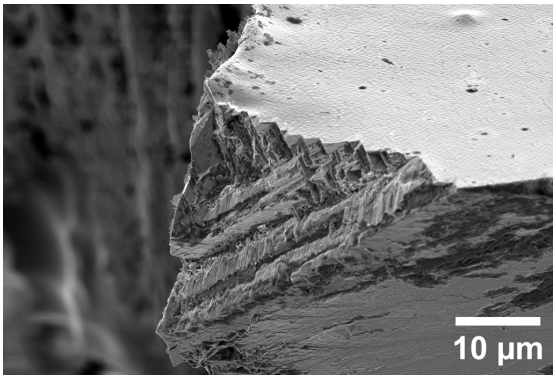
The crack path and growth mechanisms have been used to help explain fatigue performance, as the geometry of the fracture surface with respect to the deformation can cause roughness-induced crack closure. The crack closure reduces the ΔK at the crack tip [5, p. 20], thought to then reduce the FCGR and hence improve the fatigue life. This crack closure can be hard to evaluate, especially the complex shearing mode facets and the bending deformation employed in this work.



(a) Low magnification OM.

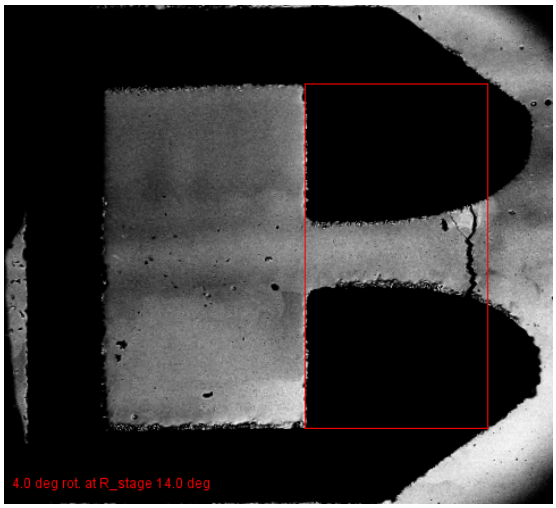


(b) Low magnification SE.

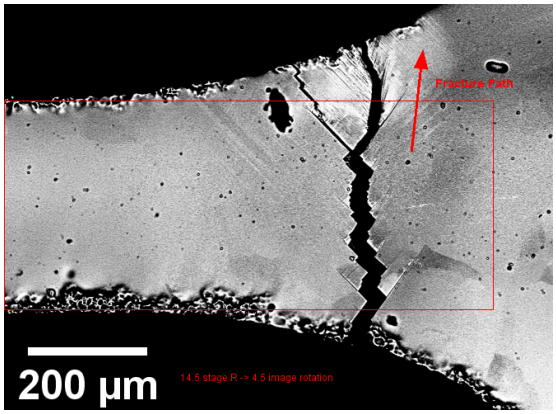


(c) Fine {111} path.

Figure 7.15: ⟨100⟩ RJSM8 cantilever fractography.



(a) Low magnification.



(b) Pseudo opening mode via fine {111} fracture.

Figure 7.16: ⟨100⟩ RJSK2 cantilever BSE fractography from ECCI session. The micrographs are rotated to make the cantilever face left, showing that the pseudo opening mode is off from the [100] axis.

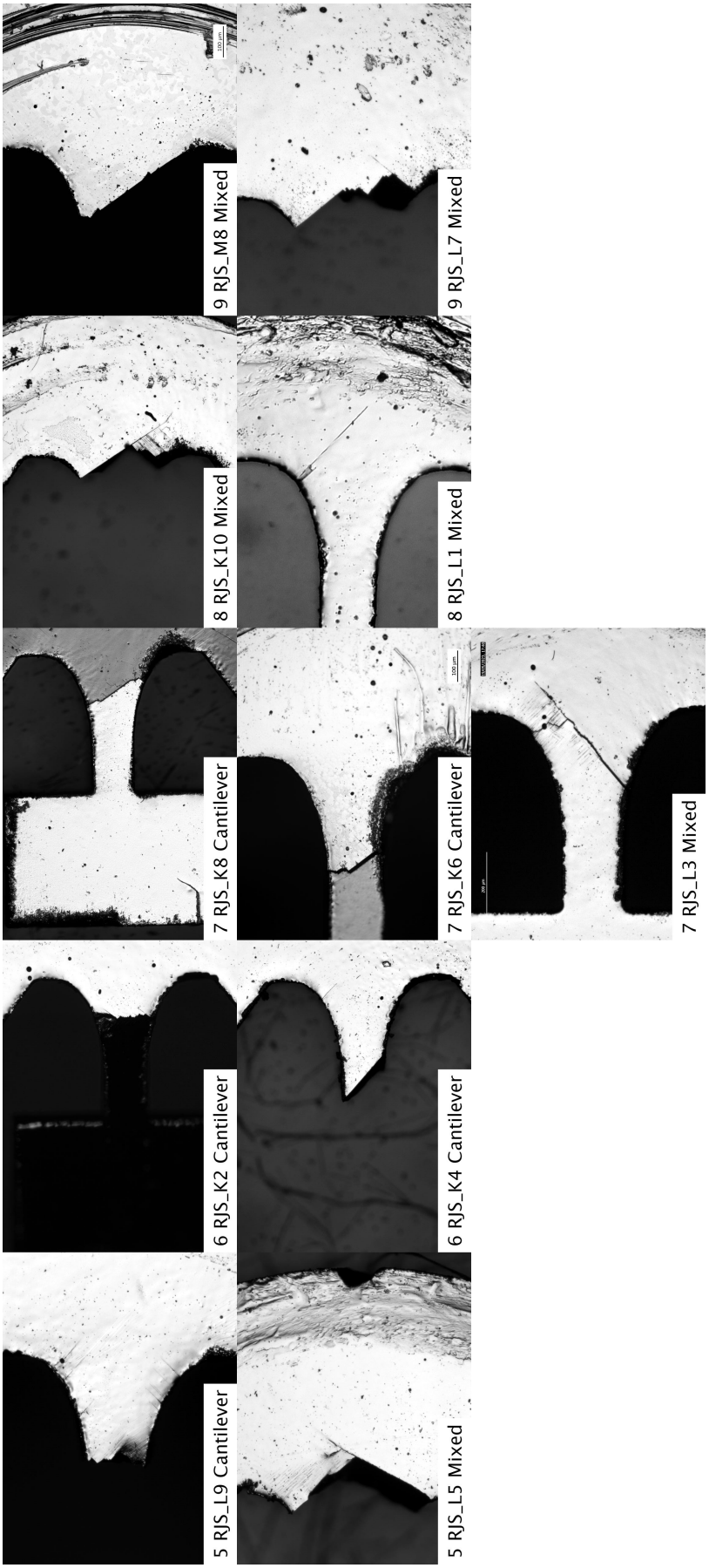


Figure 7.17: RJS ⟨100⟩ initiation side optical micrographs. Refer to figs. 7.2 and 7.4 for the σ_{vm} stress and slip distributions in these samples. Top-to-bottom indicates highest-to-lowest sample fatigue stress, the numbers and columns indicate the decade (i.e. $N_f = 10^x$), the letter-number combination is the sample ID, and the type of failure is at the end.

7.4.2 <110>

Figure 7.18 is a collation of the optical micrographs of the initiation side of the ⟨110⟩ SXO samples. Corner cracking does not occur in these samples; instead, if there is a crack, it is critical, and maybe some minor shearing mode cracks are coming from surface pores. Additionally, this SXO shows no evidence of an opening mode-like fracture paths or crack bifurcation like in the ⟨100⟩ SXO. The lack of bifurcation and propensity for secondary cracks makes the surface fracture paths virtually identical in multiple samples. There are two broad failure categories (see fig. 7.19), which the following will discuss (note that the planes are assuming that the initiation side has the same SXO as RJSN1):

1. $\{11\bar{1}\}$ primary cantilever fracture: This is the most common fracture with $^5/_{11}$ of the samples having it. It has clear initiation and exit sides exclusively within the main body of the cantilever, with the initiation side having just one facet and little slip; with the exit fracture and slip lines still following the same fracture plane. RJSO10 and RJSN1 are examples of this. Using MTEX on RJSN1, the fracture plane and slip traces are associated with the $\{11\bar{1}\}$ (shown later in fig. 7.40c). Minor cracks also fracture along this trace. The traces indicate that only a single slip system is potentially active in the sample.
   (a) A sub-case occurred where the initial fracture trace was along $\{111\}$ rather than $\{11\bar{1}\}$ (RJSO2 and RJSO4). In RJSO2, the slip traces and fracture path on the exit side indicate a change to the $\{11\bar{1}\}$ trace.
2. $\{111\}$ main facet nearer base: The fracture occurred primarily with a $\{111\}$ facet that initiates nearer to the base, progresses across, and a small $\{11\bar{1}\}$ joins the main crack. The exit side was also nearly identical and showed that the $\{111\}$ slip trace persists. Note only three samples fractured this way.

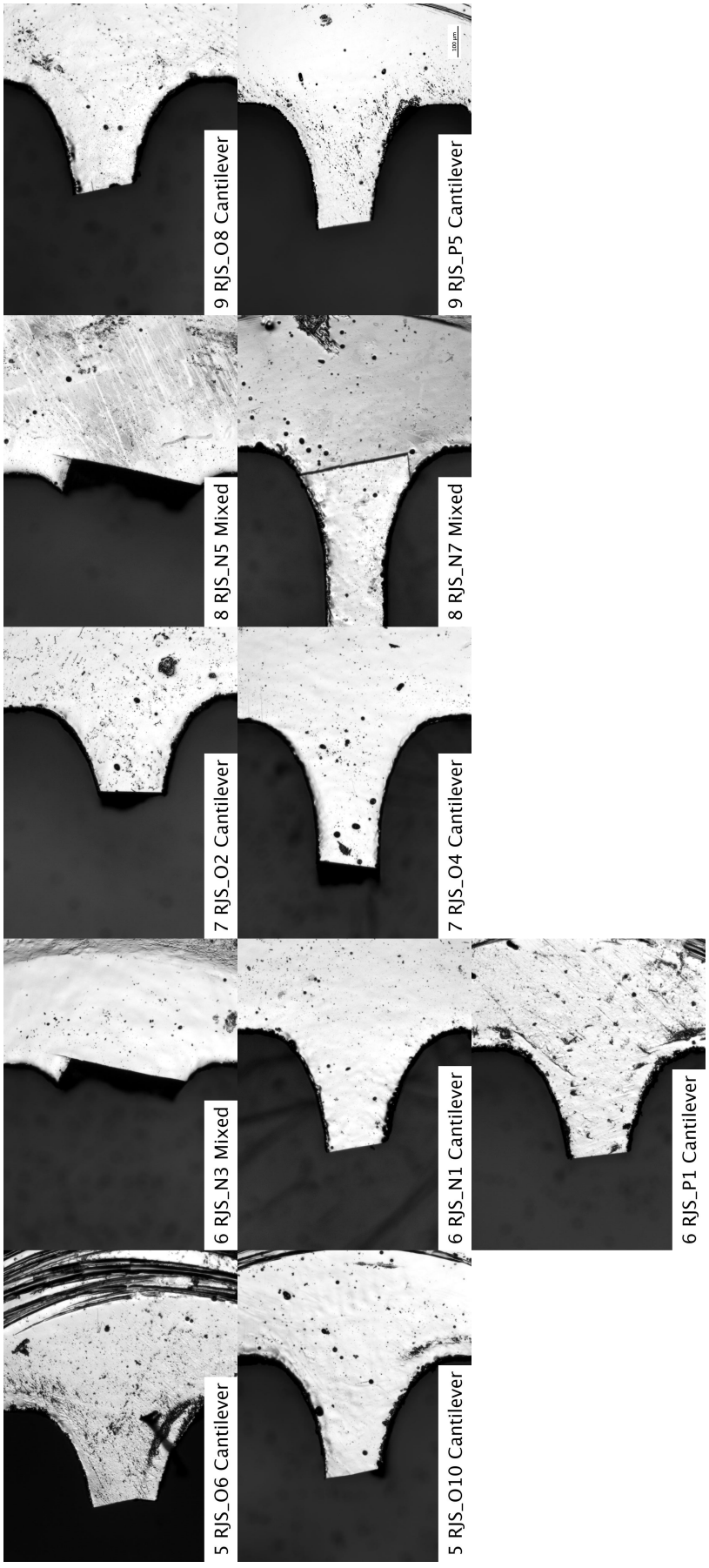
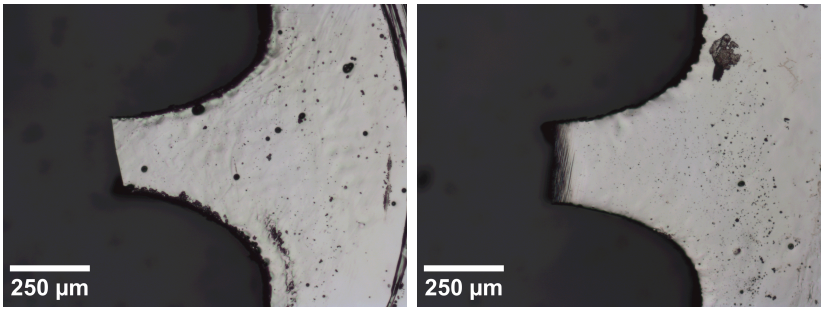
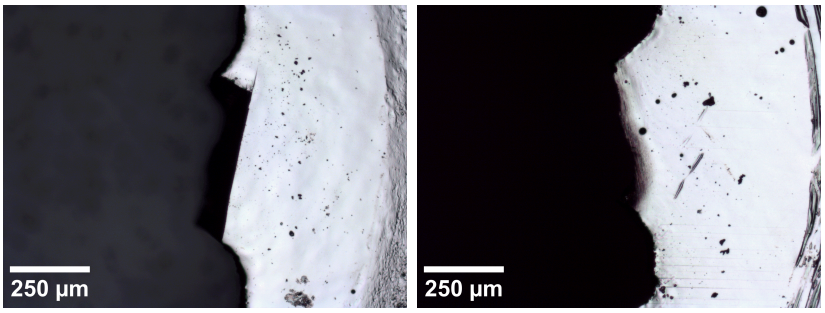


Figure 7.18: RJS ⟨110⟩ initiation side optical micrographs.



(a) Case 1 RJSO10.



(b) Case 2 RJSN3.

Figure 7.19: ⟨110⟩ fracture cases of the top and bottom surfaces from OM. 1st column is the initiation sides and the 2nd column is the exit sides.

The RJS design worked as intended as $^{8}/_{11}$ samples fractured within the main cantilever body, showing that the stress was more focused within that region. The repetition of fracture features indicates that crystallography dominates the fracture rather than irregularities in the design, as even those that initiate near the base appear highly similar.

The occurrence of corner and corner-like cracks in the ⟨100⟩ SXO but not in the ⟨110⟩ SXO, despite both having the same sample design and preparation, indicates that the crystal orientation is the dominant factor determining corner cracks formation. Corner cracking not being an issue for previous polycrystalline samples [41, 99, 100] with the original design indicates that it is more of an issue with the ⟨100⟩ SXO interacting with the mesocantilever geometry.

7.4.3 Fracture Surface Progression

With the RJS design, more samples failed with essentially one {111} shearing mode facet and fractured away from the base, making it easier to analyse the initial fracture behaviour and how it transitions with crack growth (see figs. 7.23 and 7.24). Figure 7.20 visually shows how the features in the fractography develop from initiation to final failure. Similar features are seen in both CD orientations. The ⟨100⟩ orientation, unlike the ⟨110⟩ orientation, has not exhibited pseudo-rooftop fracture in all the samples. ⟨100⟩ has shown rooftop fracture but not in the single facet cases (fig. 7.22).

An estimation of ΔK_I for the appearance of the fractographic features has been made by approximating the crack a mode-I crack, and taking the crack depth as the depth from the initiating surface when viewed directly along the cantilever axis (see fig. 7.21). From this, pyramids happen just below a ΔK_I of 14.2 MPa$\sqrt{\text{m}}$, pseudo-rooftop starts between 14.2-18.5 MPa$\sqrt{\text{m}}$, steps begin around 22.8 MPa$\sqrt{\text{m}}$, and smooth pseudo-rooftop at 56.5 MPa$\sqrt{\text{m}}$. From the literature, CMSX-4 at 300 & 450 °C was found to transition from opening mode fracture to shearing mode typically ranging from a ΔK_I of 14 MPa$\sqrt{\text{m}}$ to 23 MPa$\sqrt{\text{m}}$ [45, 54]; comparable to the transitions in regions this work.

For a single shearing mode facet to dominate across the fracture surface of a cantilever in the ⟨100⟩. Firstly, the FCGR along the {111} type plane needs to be sufficient to overcome the rate of dislocations leaving the slip plane; this is helped by the low temperatures. Secondly, the crack propagation direction and the greatest resolved slip system align large facets can form [44, p. 269]. Third, the cyclic work-hardening ahead of the plane of the fatigue crack remains sufficiently low with crack growth, reducing the need to change plane. For the initiation to be dominated with a single facet, then that indicates a strong favour of one slip plane, minimise zig-zag crack growth [42, p. 60] and additionally with its subsequent growth. This is supported in RJSK6 by the numerous slip traces along the same plane as the large facet on the exit side (top surface of micrograph) in fig. 7.23.

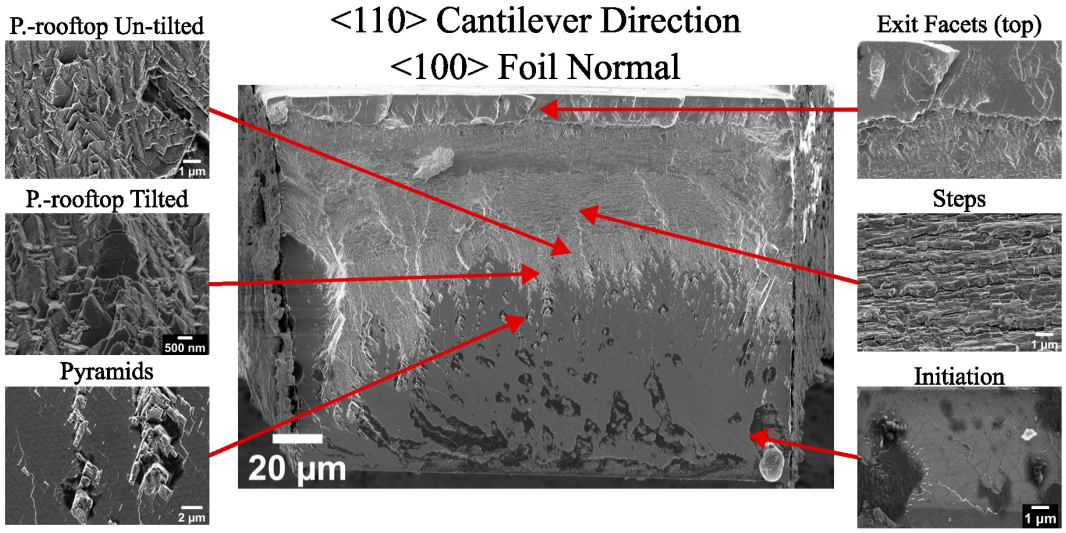


Figure 7.20: Diagram showing how the fatigue crack morphology changes with FCG, all from its initiation at the bottom to the exit facets at the top surface.

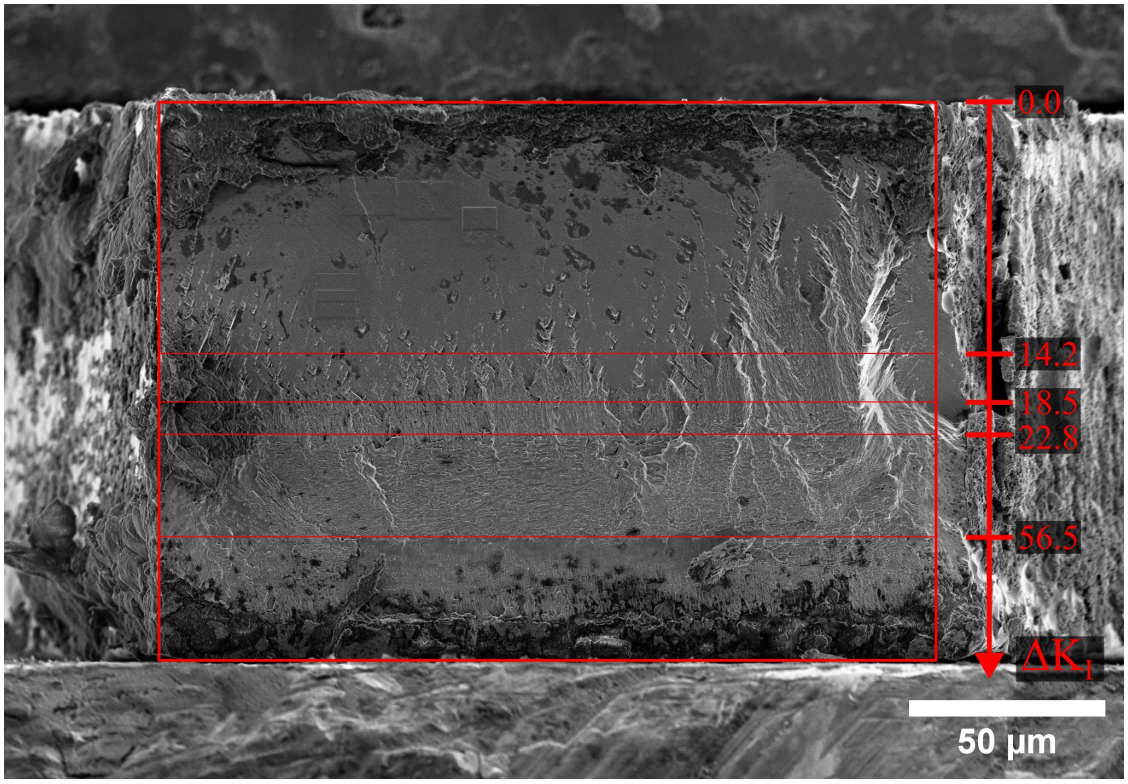


Figure 7.21: Mode-I stress intensity factor range estimation using the analytical solution from Ref [126] and the depth from the initiating surface viewed from along the cantilever axis (i.e. ⟨110⟩). Same sample as fig. 7.20 (i.e. RJSP5) but with mild surface contamination. The un-cracked axial stress was taken as the predicted un-cracked final fracture σ_{amp} (373.8 MPa), and the a thickness as 141.7 µm from the micrograph.

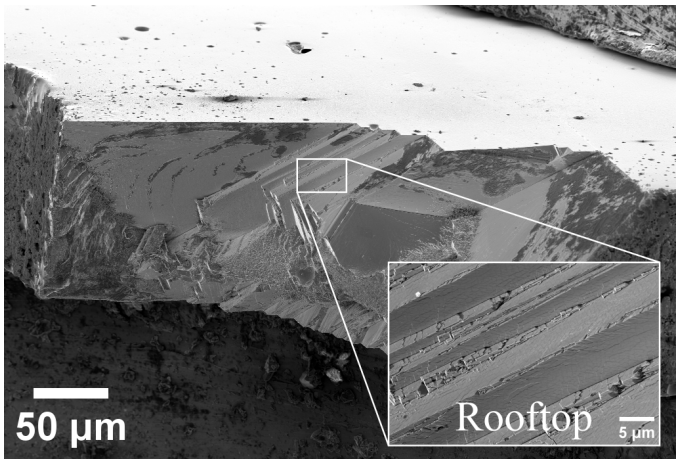
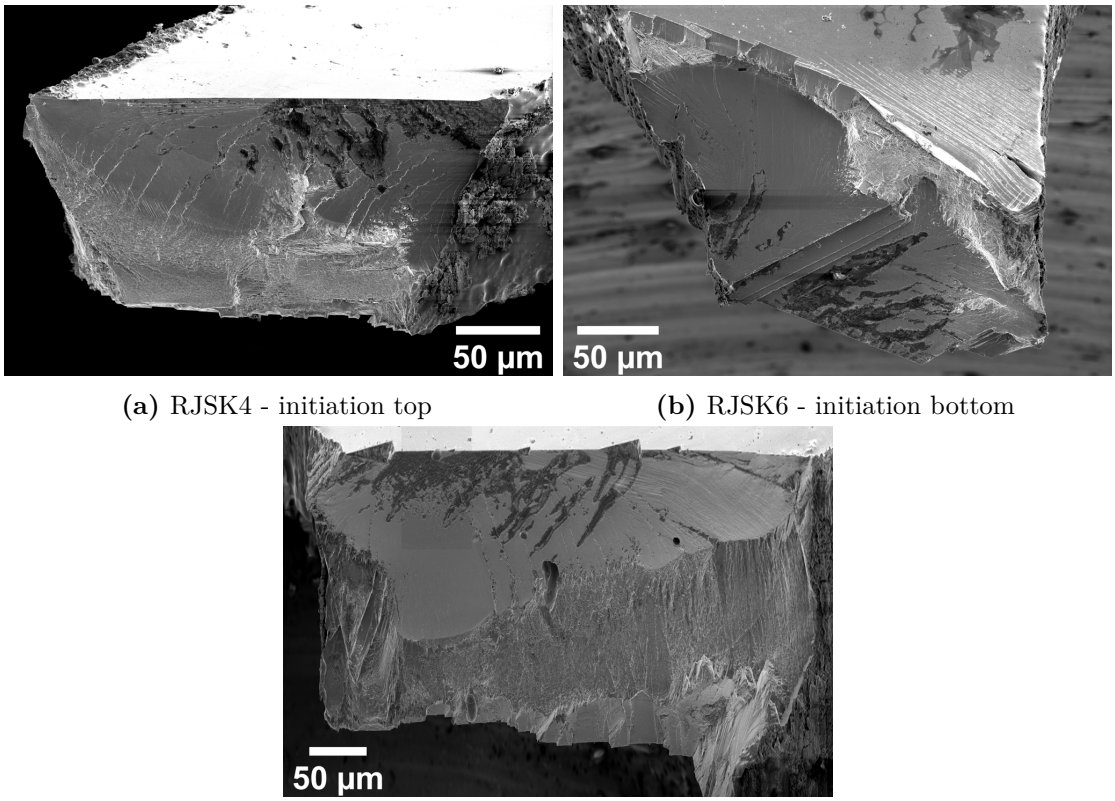


Figure 7.22: Example of rooftop fracture in RJSL7 with ⟨100⟩ SXO. The initiation side is on top.

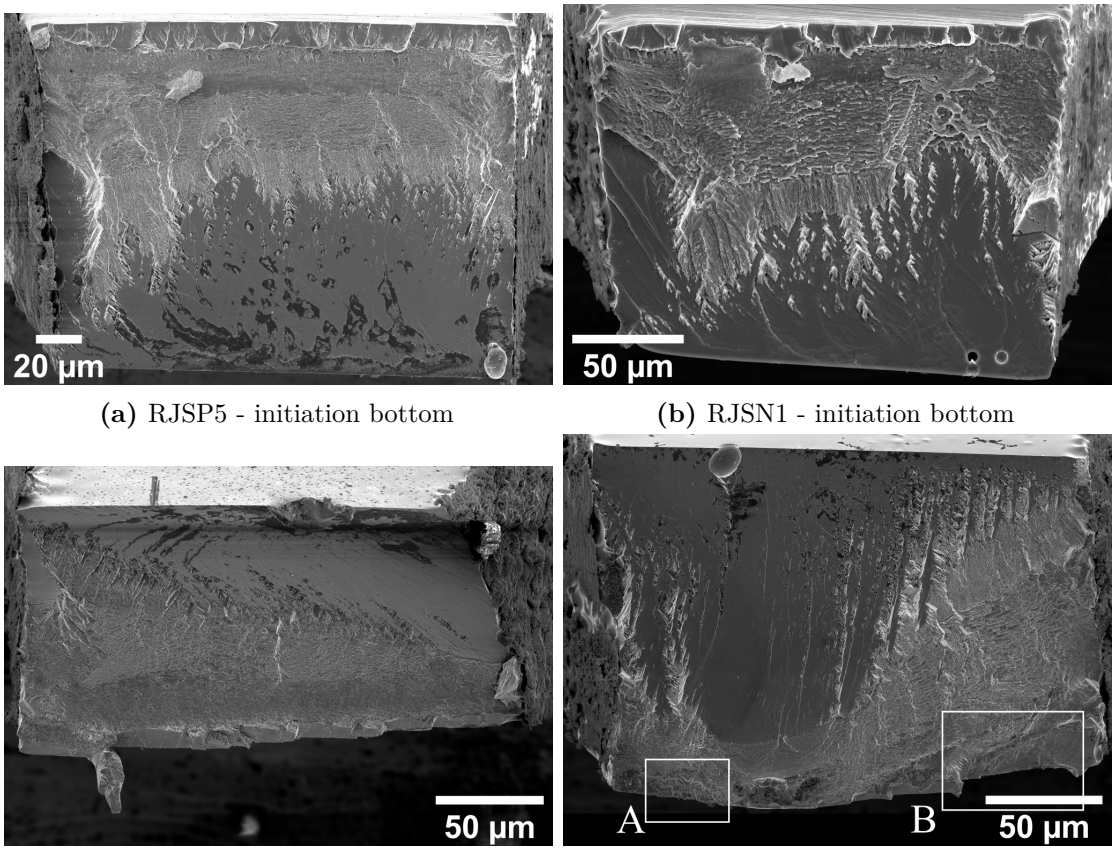


(a) RJSK4 - initiation top

(b) RJSK6 - initiation bottom

(c) RJSM8 - initiation top & 65° tilt correction

Figure 7.23: ⟨100⟩ single facet SE fracture micrographs at low magnification.



(a) RJSP5 - initiation bottom

(b) RJSN1 - initiation bottom

(c) RJSO8 - initiation top

(d) RJSO2 - initiation top

Figure 7.24: ⟨110⟩ single facet SE fracture micrographs at low magnification.

Initiation

Initiation is dominated by shearing mode, known from the {111} traces made with the samples (figs. 7.22 to 7.24) and shows the triangular γ' projections on the fracture surface (fig. 7.25). The initiation {111} facet is typically a large facet that extends across the fracture surface and still exhibits the triangular γ' projections, as shown best in the single facet fractographs (fig. 7.26).

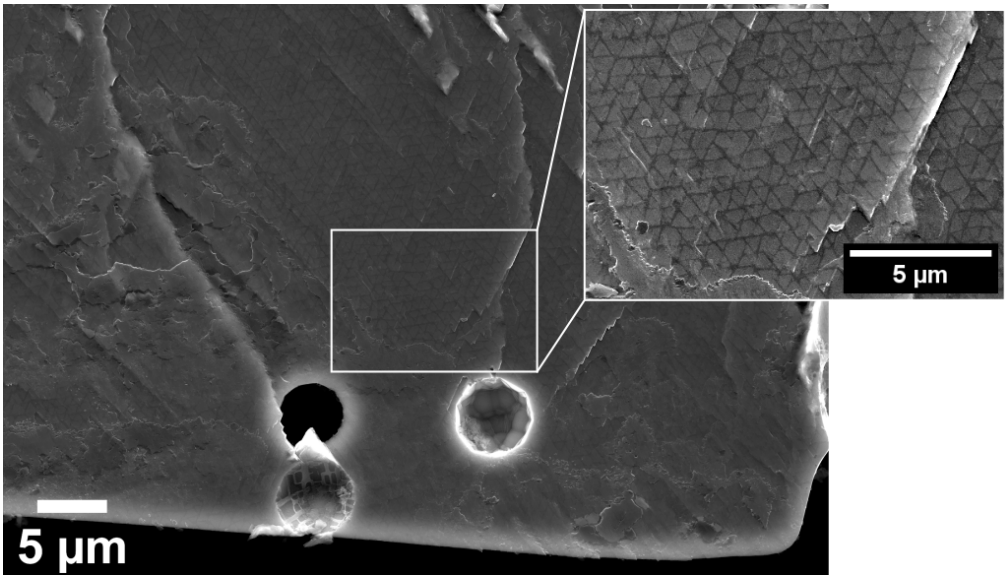


Figure 7.25: {111} initiation facet around pores in RJSN1 ($\langle 110 \rangle$).

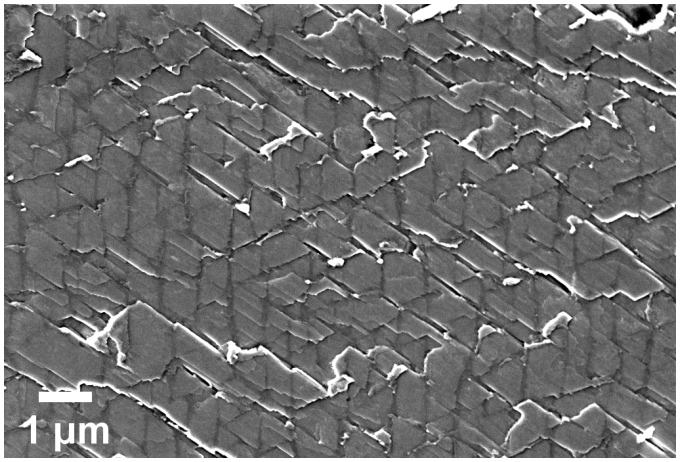


Figure 7.26: Triangular γ' projections still seen deep into the large {111} initiation facet in RJSK6 ($\langle 100 \rangle$).

Pyramids & Steps

All ⟨100⟩ SXO samples show the dominant {111} facet growing out in a smooth fashion before transitioning to a rougher topology and intercepting the exit facets. Figures 7.27 and 7.28 show this rougher topology is often shearing steps and can have an intermediate region where pyramid-like features made from {111} facets occur between it and the large initiation facet.

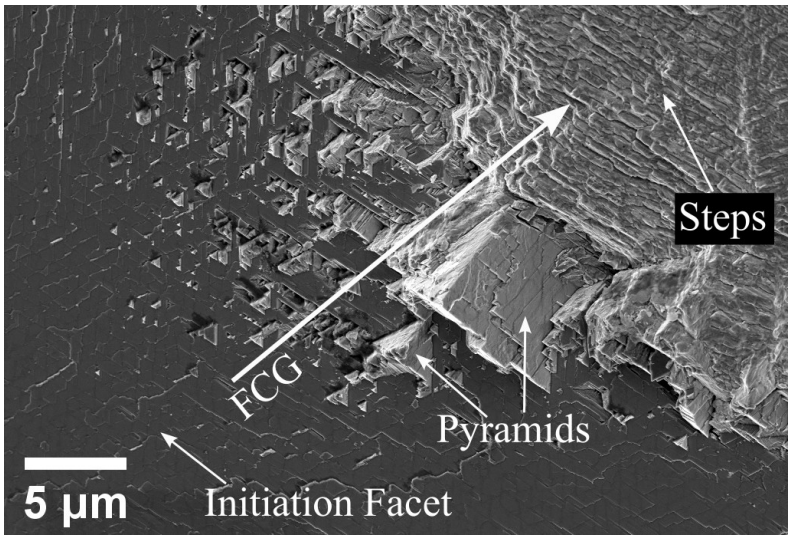
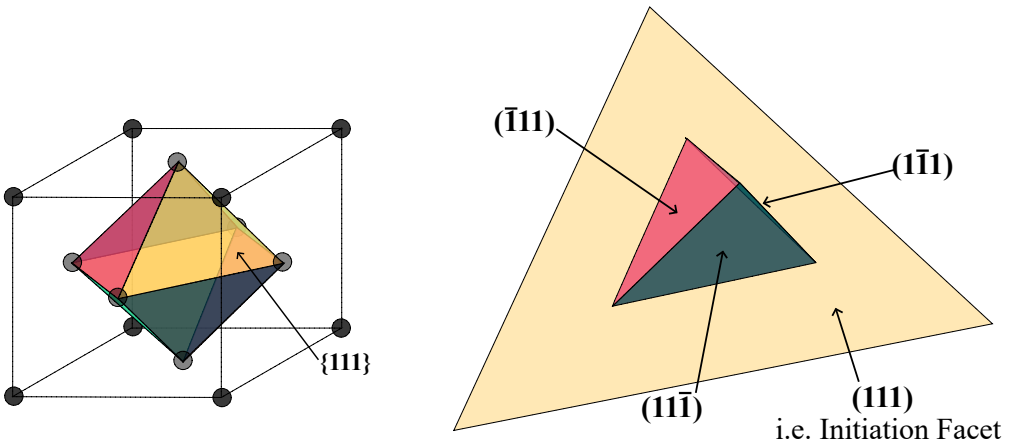


Figure 7.27: RJSK6 (⟨100⟩) fracture surface transition from the large {111} facet to "pyramids" and then shear steps as the crack grows along the FCG direction.



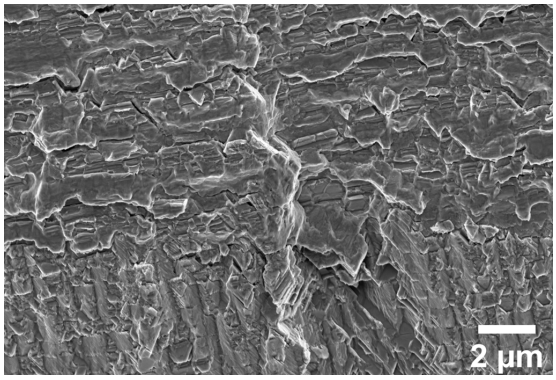
(a) The 8 FCC octahedral planes.

(b) The formation of a pyramid protruding from the {111} plane with octahedral planes.

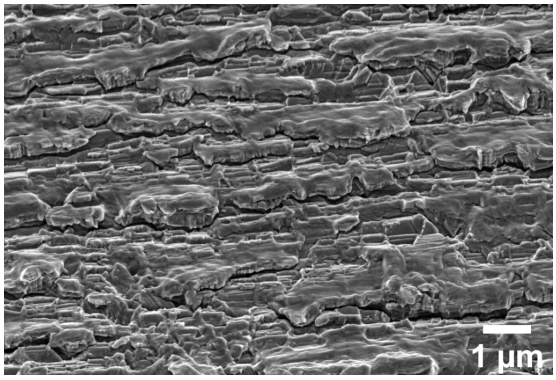
Figure 7.28: Schematic of how {111} shearing mode facets can form pyramids from the large initiation {111} facet.

The observed shearing steps indicate that the FCG direction is along ⟨110⟩ but loaded under ⟨100⟩ (fig. 2.20) [59]. This is reasonable considering how it is growing towards that direction in the ⟨100⟩ SXO samples and how it is growing out of the initiation facet plane, at a significant angle to the foil normal direction in the ⟨110⟩ SXO samples.

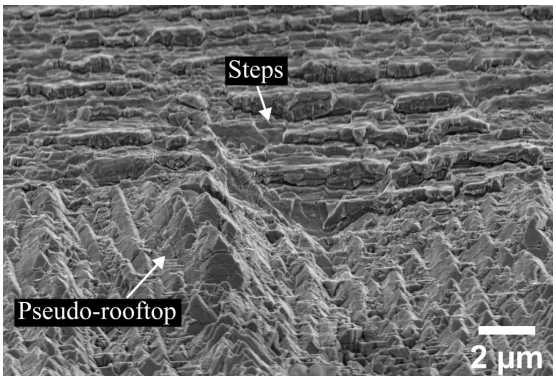
In RJSP5 (⟨110⟩), when tilted, the steps can be relatively smooth in appearance on specific faces, as shown in fig. 7.29. The top surfaces at ≈ 0° when tilted to 55° are approximately not visible, indicating that those surfaces are near the same {111} plane as the initiation facet. According to industry[2], the steps are related to the final fracture of SXNBSs, and the rounded nature has been observed before. The smooth-rounded nature is likely related to cross-slip.



(a) ≈ 0°.



(b) 35°.



(c) 55° steps at top.

Figure 7.29: RJSP5 (⟨110⟩) steps under different tilts.

[2]Private conversation with Jane Woolrich (Rolls Royce UTC).

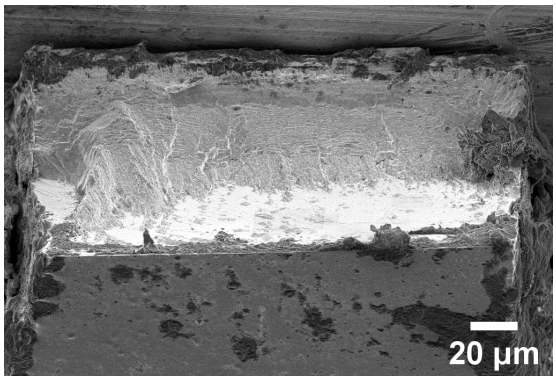
Pseudo-rooftop

Exclusively observed in the ⟨110⟩ SXO samples is the "pseudo-rooftop" region between the pyramids and the shearing step regions.

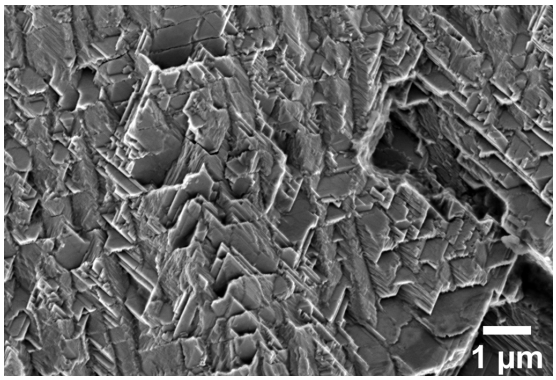
From tilted fractographs (fig. 7.30a), pseudo-rooftop occurs when the crack path travels out of the initiation facet's plane, continuing from the pyramids. It is likely near or at the conditions of growing along a [101] direction under primarily a [100] direction load, akin to the conditions which rooftop occurs in Refs [45, 53, 54], and because steps are thought to grow along ⟨101⟩. In figs. 7.30c and 7.30d, three different {111} planes occur, unlike the two used in rooftop; however, the third is less frequent.

In Ref [53], the CT tests of different orientations show that the pseudo-rooftop fracture is most like their <110><100> test, where the crack grows towards the ⟨100⟩ direction but loaded under the ⟨110⟩ direction (fig. 2.17). It also propagates at an angle to ⟨100⟩. It is, however, not similar in that the traces between the involved planes follow the crack direction, which is more like rooftop fracture; hence, pseudo-rooftop.

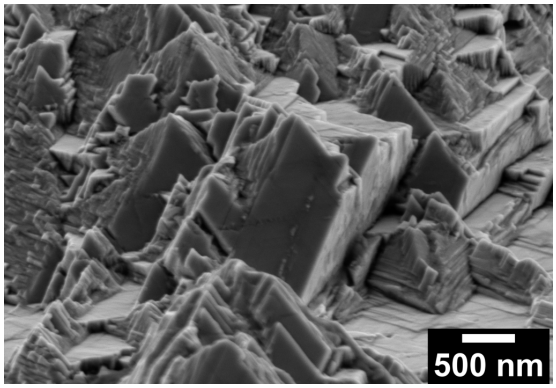
Due to their seamless transition, the mechanisms behind pseudo-rooftops are likely the same or similar to those for pyramid formation, with pyramids being the less extensive form returning to the original facet. Therefore, the ⟨110⟩ CD likely promotes pseudo-rooftop fracture by making the mechanism more extensive. The different SXOs have different loading directions and crack path directions, so they progress differently but share similarities (e.g. the crack progressing from {111} initiation facets).



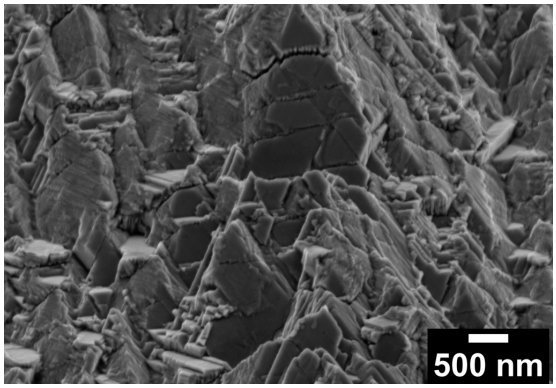
(a) 35° tilt low magnification.



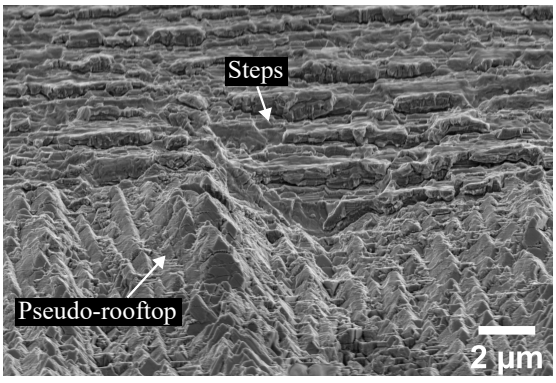
(b) 0° tilt in pseudo-rooftop region.



(c) 35° tilt transition from large {111} facet to pseudo-rooftop.



(d) 35° tilt transition deeper in pseudo-rooftop region.



(e) 55° tilt low magnification. Pseudo-rooftop at the bottom.

Figure 7.30: Pseudo-rooftop morphology example in RJSP5.

Post-step Region

Two interesting features have been observed after the steps in the samples, a smooth pseudo-rooftop region and fine globule features.
The smooth pseudo-rooftop is shown clearly in RJSP5 above the steps in fig. 7.31, appearing smoother compared to those in fig. 7.30e and sharing the same {111} fracture plane with the steps and the pseudo-rooftop fracture. Figure 7.32, from another perspective, is similar to fig. 7.30b.

It is likely caused by the higher ΔK above the steps, which also showed a relatively smooth surface, then switched back to pseudo-rooftop but smoother with the more cross-slip at the higher ΔK. This region likely occurs at the steps in RJSO8 and maybe in RJSK4.

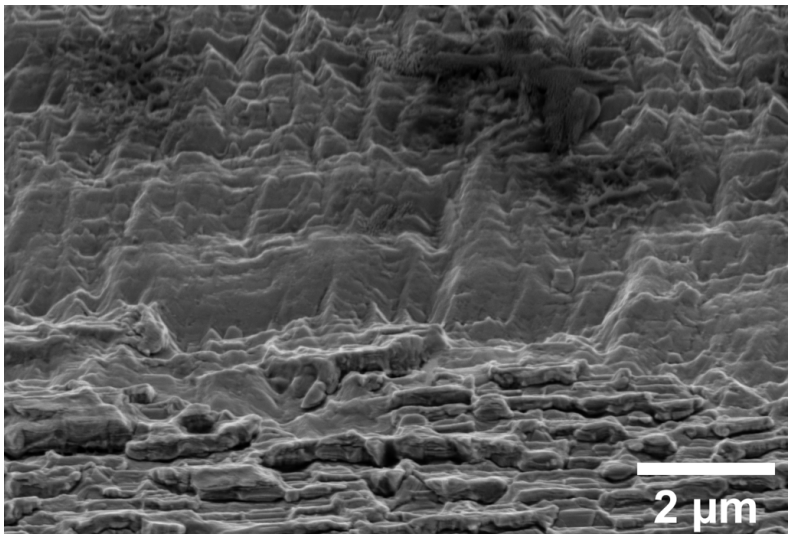


Figure 7.31: 55° tilt - Smooth pseudo-rooftop fracture at the top.

RJSN1 ($\langle 110 \rangle$) also shows some smooth pseudo-rooftop, it and RJSK4 ($\langle 100 \rangle$) show very fine globules after the steps (fig. 7.33).

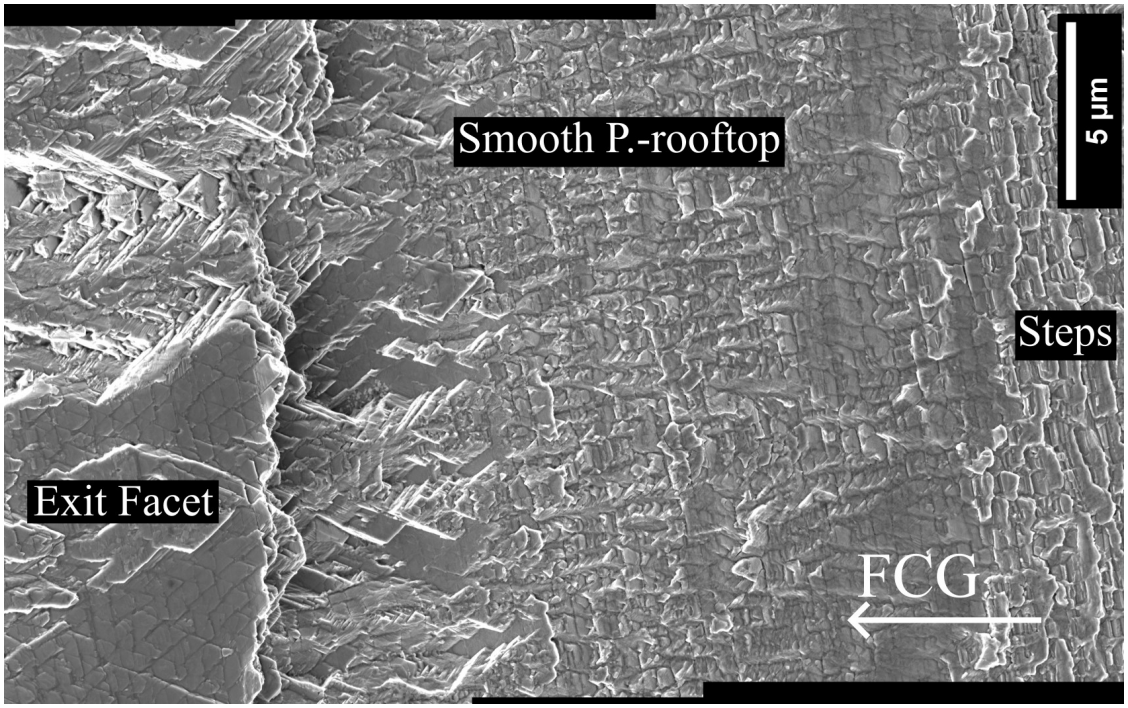


Figure 7.32: Annotated fractograph showing the smooth pseudo-rooftop and other morphologies in RJSP5.

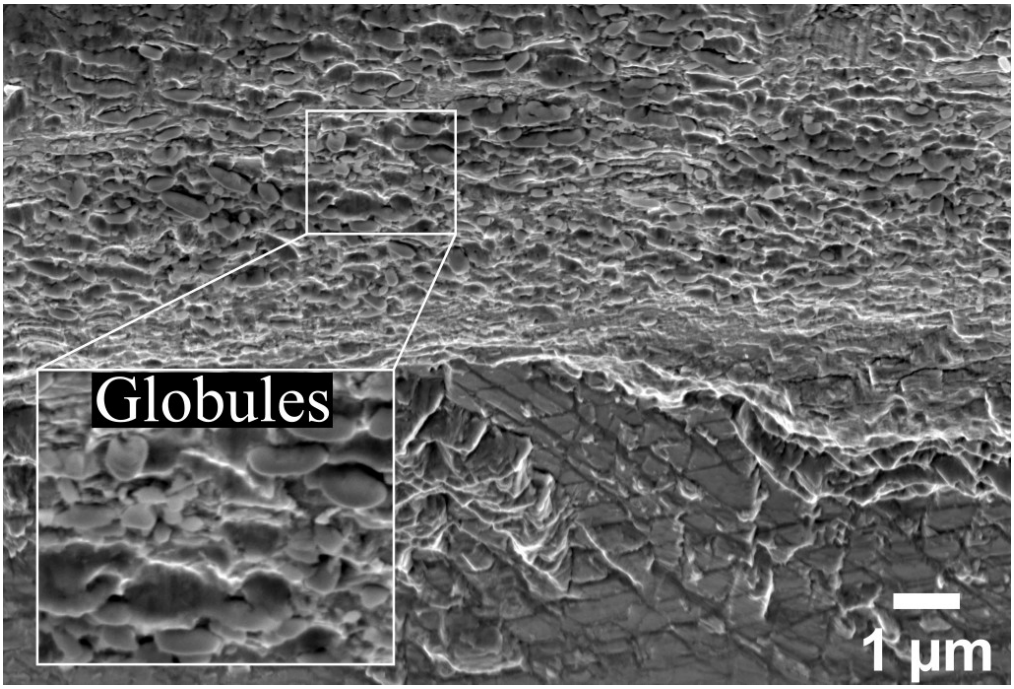


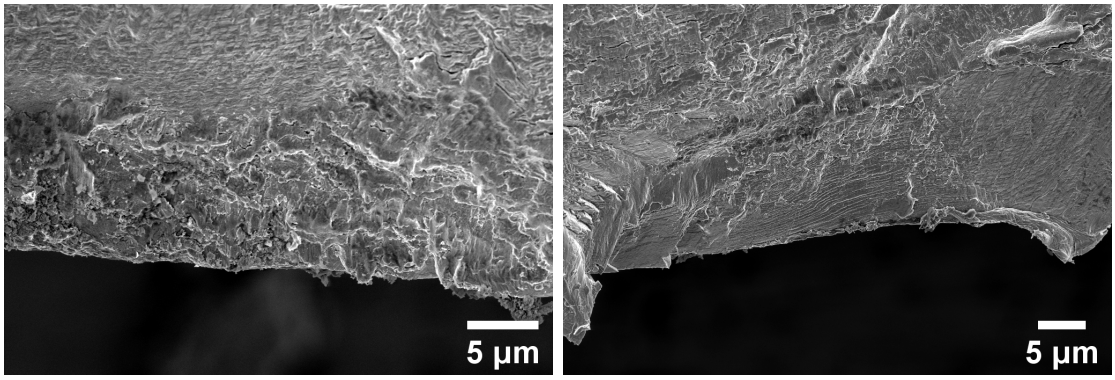
Figure 7.33: RJSN1 - Globular features before the exit facets. Round features observed after steps in RJSN1 towards the end of failure.

Exit Facets

The fracture surfaces of the ⟨100⟩ and ⟨110⟩ SXOs typically show exit facets (see section 6.1.1), and for the single {111} facet fractures, they tend to be parallel

to the initiating facet.

RJSO2 is an exception as it lacks typical facets (fig. 7.34). It has fewer exit facets, and they occur on a different {111} plane to the initiated crack. The initiated crack has grown through most of the sample, leading to a high ΔK, causing the high plasticity and surface roughness. It is also the likely cause of disparity in its fracture surface compared to the other three in fig. 7.24.



(a) "A" in fig. 7.24d. **(b)** "B" in fig. 7.24d.

Figure 7.34: Exit facet exceptions in RJSO2.

7.4.4 LCF vs VHCF

Due to the often easier-to-interpret fracture surfaces of the RJS design, the LCF and VHCF fracture surfaces collected in this campaign will be compared for each SXO to ascertain whether systematic changes occur or not.

The rooftop fracture is typically associated with a fast FCGR as there is little crack deflection with crack propagation, which in theory should promote shorter N_f. However, the alternating {111} crack paths could promote crack closure in the not necessarily pure mode-I cantilever deformation, so it would likely depend on the orientation and deformation of the cantilever.

<100>

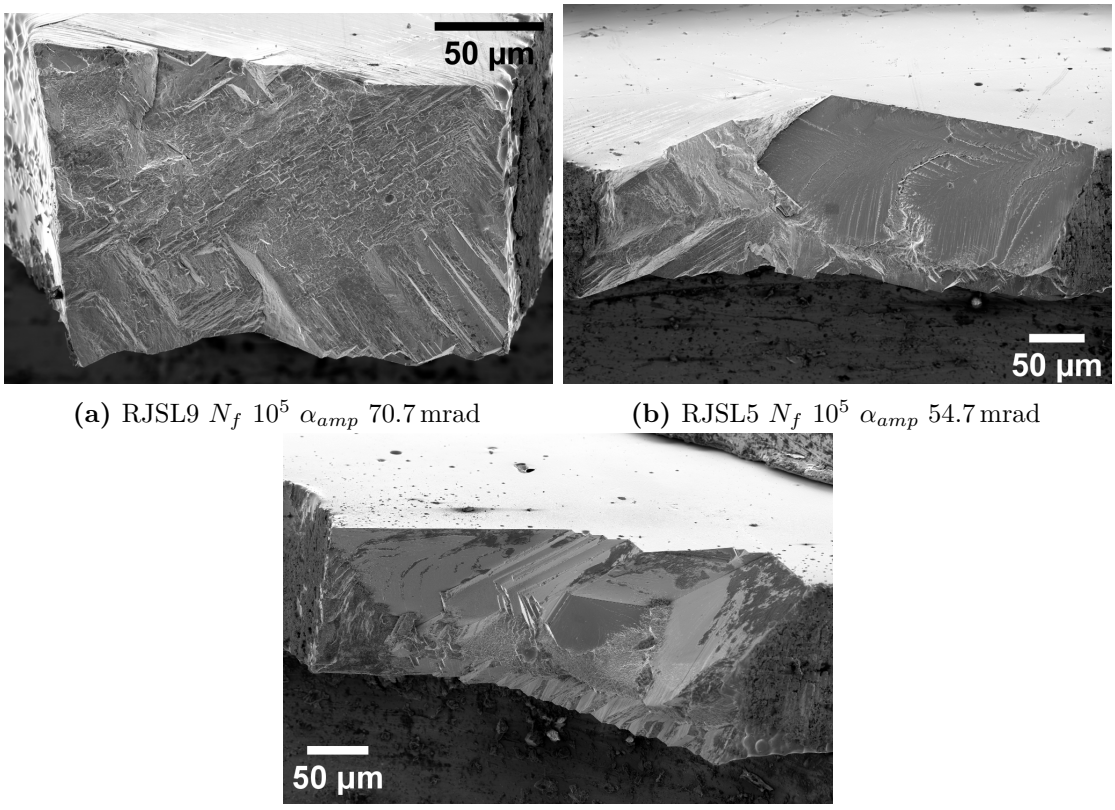
The LCF samples for this orientation show finer and more complex {111} facets compared to the VHCF samples. This trend is observed within the two tested at 10^5 cycles, as RJSL9 shows this more than RJSL5, failing at 70.7 mrad and 54.7 mrad

respectively. The more {111} facets, especially towards the top and bottom surfaces, is an indicator of multiple shearing mode crack initiations.

RJSL9 does not show a single large {111} facet, unlike RJSL5 and the other samples, with the general trend being that the lower the drastic failure bending angle amplitude (α_{amp}), the greater the initiation {111} facet's proportion on the fracture surface.

The exit facets appear larger for greater N_f, likely due to the lower crack growth rate of the main crack as N_f increases, enabling the initiated exit facets to grow larger before meeting the main crack. Similarly, this could be linked to why the initiation facet is larger with lower σ_{amp} as the maximum fatigue crack length before the final failure occurs in the cantilever becomes larger.

In the OM micrographs, the degree of slip traces on the exit side tends to decrease in extent, at least extending less into the material.



(a) RJSL9 N_f 10^5 α_{amp} 70.7 mrad

(b) RJSL5 N_f 10^5 α_{amp} 54.7 mrad

(c) RJSL7 N_f 10^9 α_{amp} 29.1 mrad

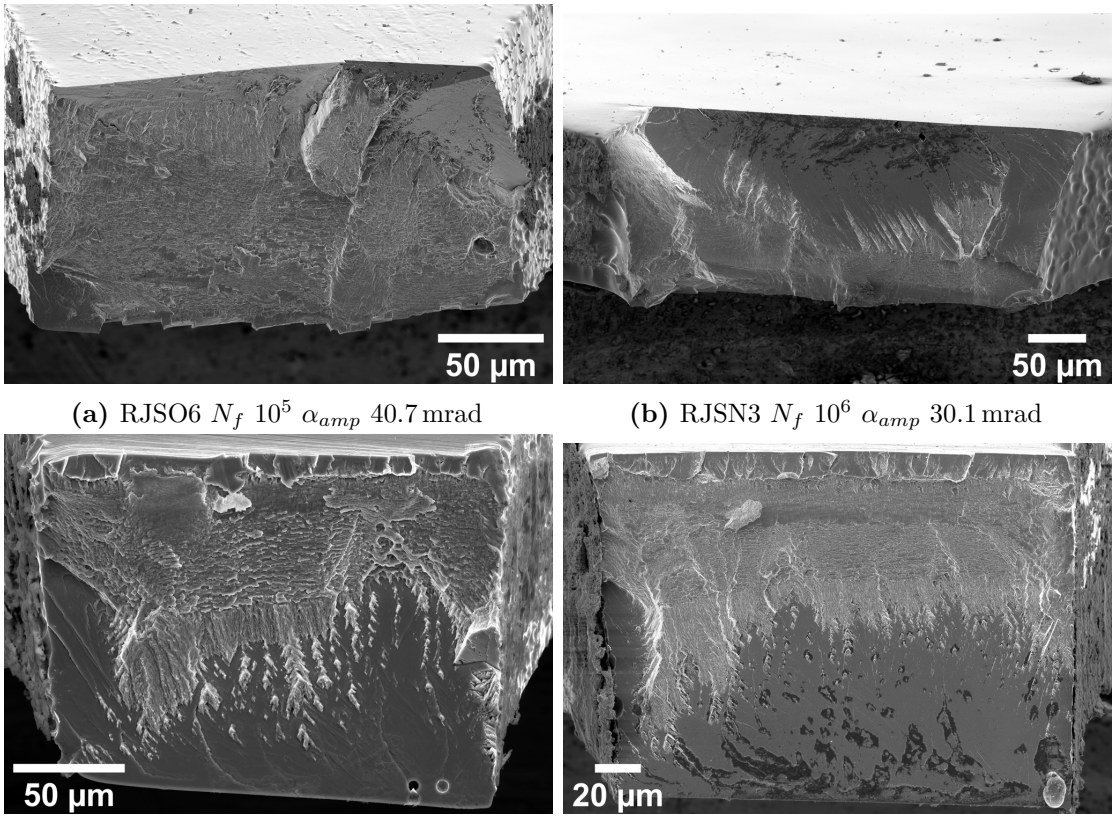
Figure 7.35: N_f comparisons for both ⟨100⟩ SXO.

<110>

A similar trend is seen as ⟨100⟩, as RJSO6 ($N_f = 10^5$) has a smaller degree of large {111} facets. RJSO6 is the only observed ⟨110⟩ sample with more than one large {111} facet. RJSO10 is also $N_f = 10^5$ but failed at a lower stress amplitude (σ_{amp}). Hence, the stress amplitude (σ_{amp}) may be sufficiently high for multiple {111} facets to initiate in RJSO6, unlike the other samples where this is not seen. In RJSO6, the initiation facets quickly transition to pseudo-rooftop and then to steps, consuming most of the fracture surface until the exit facets on the other side.

Despite not technically being LCF, RJSN1 which was a $N_f = 10^6$ test, shows a similar fracture behaviour to RJSO8 and RJSP5, which both are $N_f = 10^9$. They are all so similar it is difficult to distinguish any strong differences between them. Similar to ⟨100⟩, the 10^9 samples appear to show larger exit facets than the 10^5 and 10^6 samples, likely for the same reason. Directly comparing RJSN1 with RJSP5, the 10^9 RJSP5 appears to have a larger {111} initiation facet region, probably due to the slower FCG rate under the lower σ_{amp}. This comparison is complex to make with the other fracture surfaces as they are not as similar, the clearest example being RJSO2, which has a greater large {111} facet. This could be linked to the change of fracture plane of the exit facets compared to the initiation facet.

RJSN3 is a 10^6 test like RJSN1 but is of Case 2, showing similar features to RJSN1 & RJSP5. However, under the region where the crack deflects along a poor Schmid factor plane, a complex crack path occurs, likely due to multiple slip planes being active. RJSO6, on the other hand, has two surface crack paths along two high Schmid factor slip planes.



(a) RJSO6 N_f 10^5 α_{amp} 40.7 mrad

(b) RJSN3 N_f 10^6 α_{amp} 30.1 mrad

(c) RJSN1 N_f 10^6 α_{amp} 24.4 mrad

(d) RJSP5 N_f 10^9 α_{amp} 17.2 mrad

Figure 7.36: N_f comparisons for both ⟨110⟩ SXO.

7.5 Simulations vs Experiments

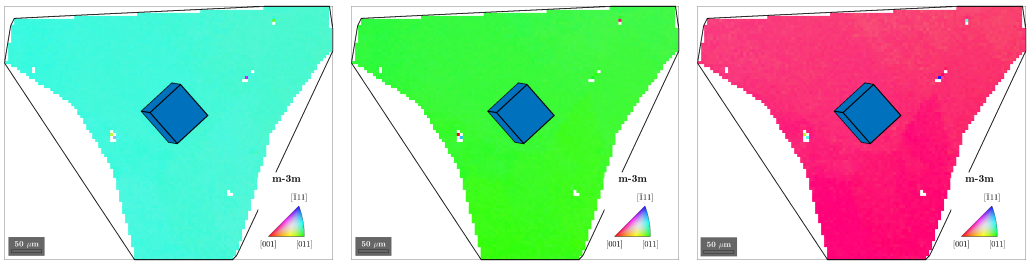
The following section shows and assesses the validity of the CPFE models and the slip traces from MTEX with experimental results using their EBSD derived orientations.

7.5.1 RJSN1 <110>

For RJSN1, EBSD confirms that the orientation is close to the intended ⟨110⟩ SXO (fig. 7.37).

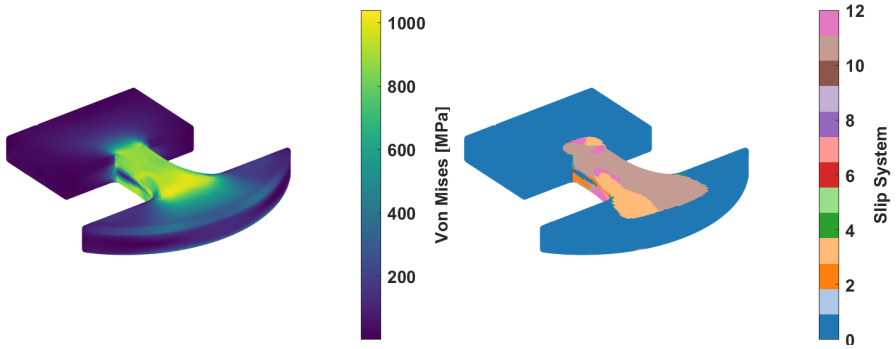
Analysing the CPFE for RJSN1 (fig. 7.38) produces fig. 7.39, showing that $(11\bar{1})[011]$ slip dominates the absolute slip sum (i.e. $|\Sigma(slip)|$) and that the edge GND densities are typically more dominant. Interestingly, the most dominant ρ_{GND} is $(11\bar{1})[101]$ rather than the most dominant slip system by absolute slip of $(11\bar{1})[011]$.

Uniaxial tension along the CD was used to estimate the Schmid factors for RJSN1 (fig. 7.40a); this is reasonable as opening mode fracture paths concur

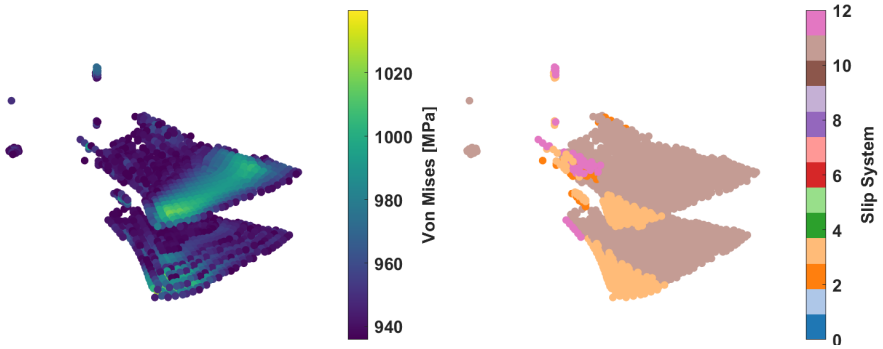


(a) X **(b)** Y **(c)** Z

Figure 7.37: EBSD MTEX plots for sample RJSN1's SXO. The cantilever's fracture surface is towards the bottom of the scan. Hence, the Y plot (b) the CD is close to ⟨110⟩ orientation.



(a) σ_{vm}. **(b)** Dominant slip systems.

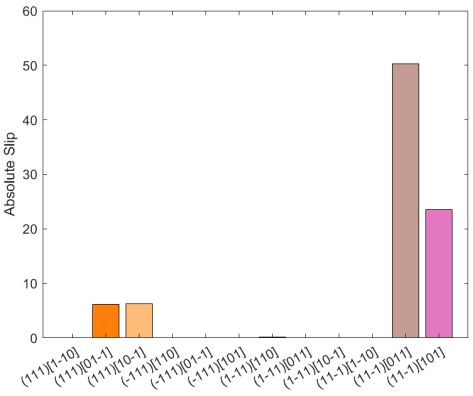


(c) Top 10% σ_{vm} risk-volume. **(d)** Dominant slip systems in risk-volume.

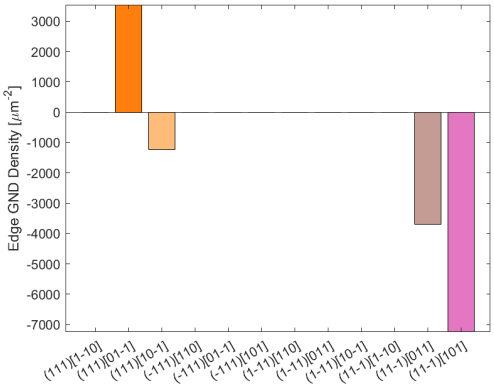
Figure 7.38: RJSN1 CPFE modelling scatter plots of integration points using the mean EBSD orientation. In **(b)**, slip system 11 (pale brown) is $(11\bar{1})[011]$, and slip system 3 (pale orange) is $(111)[10\bar{1}]$. Slip system 0 (dark blue) is where no slip was calculated.

with this (chapter 6).

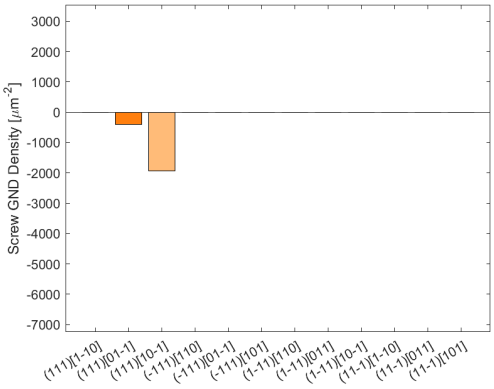
Comparing fig. 7.39a with fig. 7.40a, there is a clear difference in the bias of the distribution and a reorder of the top 4. Still, both predict that $\pm(11\bar{1})[011]$ will be the dominant slip system and have the same top 4 slip systems. The



(a) Absolute slip sum.



(b) Sum edge ρ_{GND}.



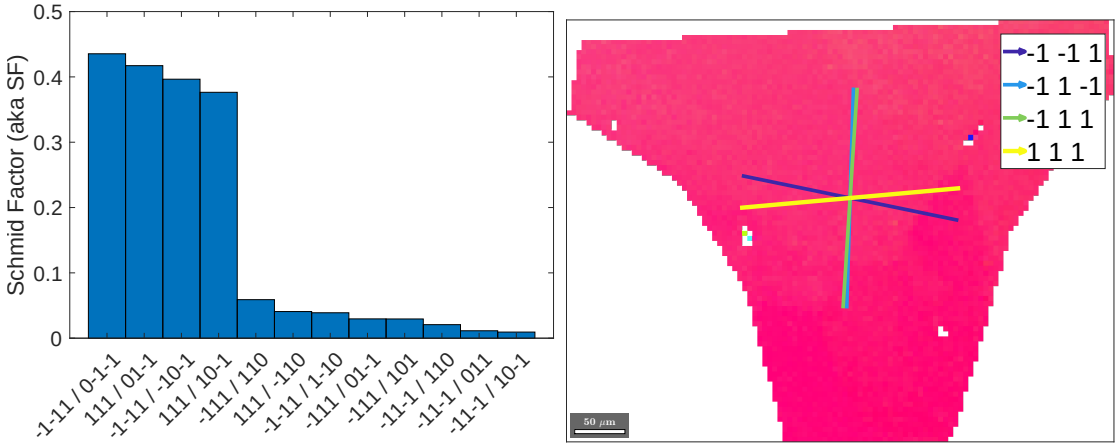
(c) Sum screw ρ_{GND}.

Figure 7.39: Pareto analyses of RJSN1 slip systems of the number of integration points in that slip systems or dislocation ρ_{GND}.

difference is likely because of uniaxial deformation in MTEX and the more accurate mode-I bending in CPFE.

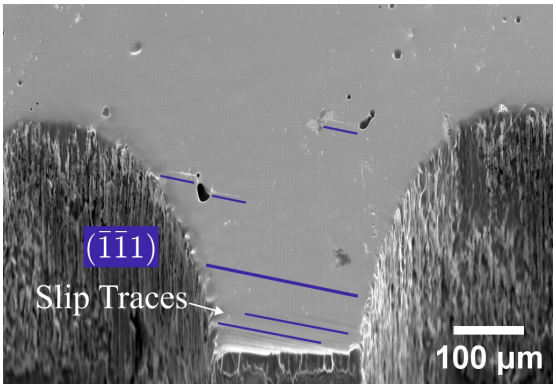
CPFE's stark dominance of $\pm(11\bar{1})[011]$ is concurred by $\pm(11\bar{1})$ slip traces in fig. 7.40c; agreeing with uniaxial literature stating that one slip system dominates for off-axis $\langle 110 \rangle$ tests [11].

These two techniques aid in understanding the deformation for RJSN1 in its ECCI (section 7.6).



(a) Schmid factors of the 12 FCC slip systems.

(b) All FCC slip traces.



(c) SE micrograph of EBSD scan.

Figure 7.40: MTEX slip system analysis and comparison with visible slip and fatigue cracks in SE image for RJSN1. The dominant $(\bar{1}\bar{1}1)$ slip trace in fig. 7.39 is also high in MTEX derived Schmid factor (fig. 7.40a) and is observed to be virtually the only slip trace in RJSN1 experimentally (fig. 7.40c).

7.5.2 H8 <100>

Sample H8 is a $\langle 100 \rangle$ sample tested at RT air with the original cantilever design. A post-fatigue EBSD scan (fig. 7.41) allows for its SEM fractographs to be correlated with slip traces, Schmid factors, and CPFE modelling.

CPFE predicts slip systems 3, 6, and 4 are the most dominant (fig. 7.42). In MTEX, these slip systems have high Schmid factors but are not in the same order, and more slip systems are active.

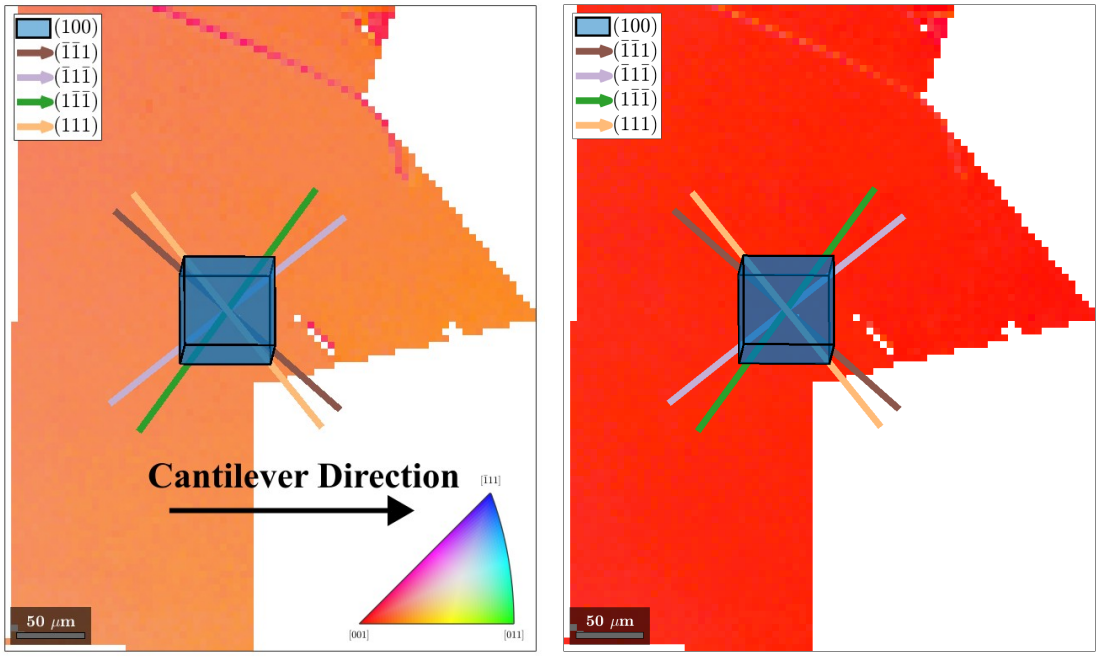
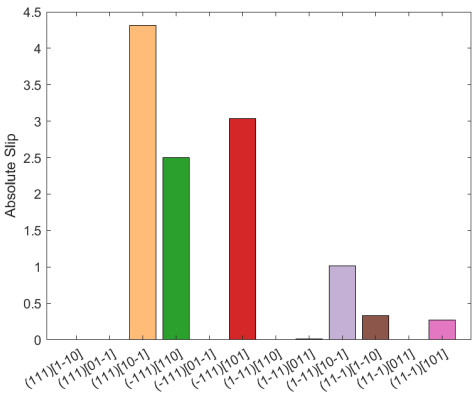
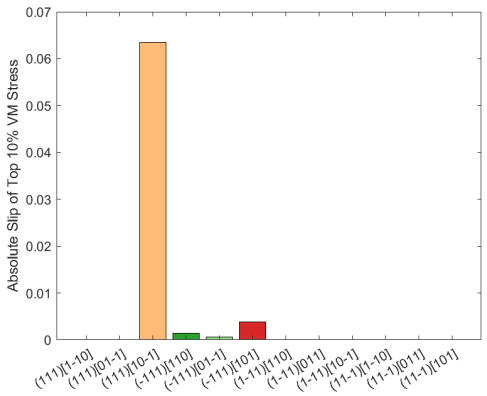


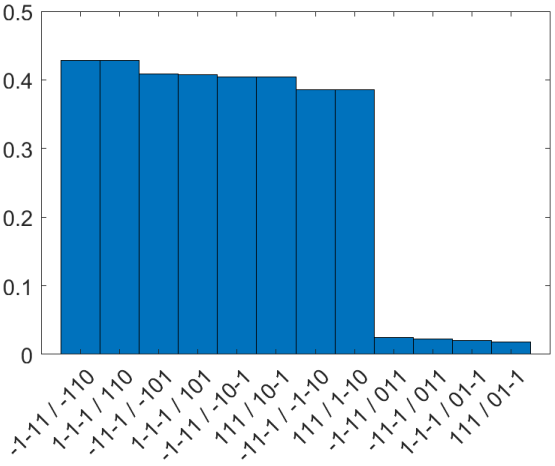
Figure 7.41: EBSD map of H8's initiation side. The four possible slip traces are superimposed. The two maps show the z-orientation (out-of-plane) and x-orientation (west). Hence, the CD is ≈ [100].



(a) Sum absolute slip whole sample.



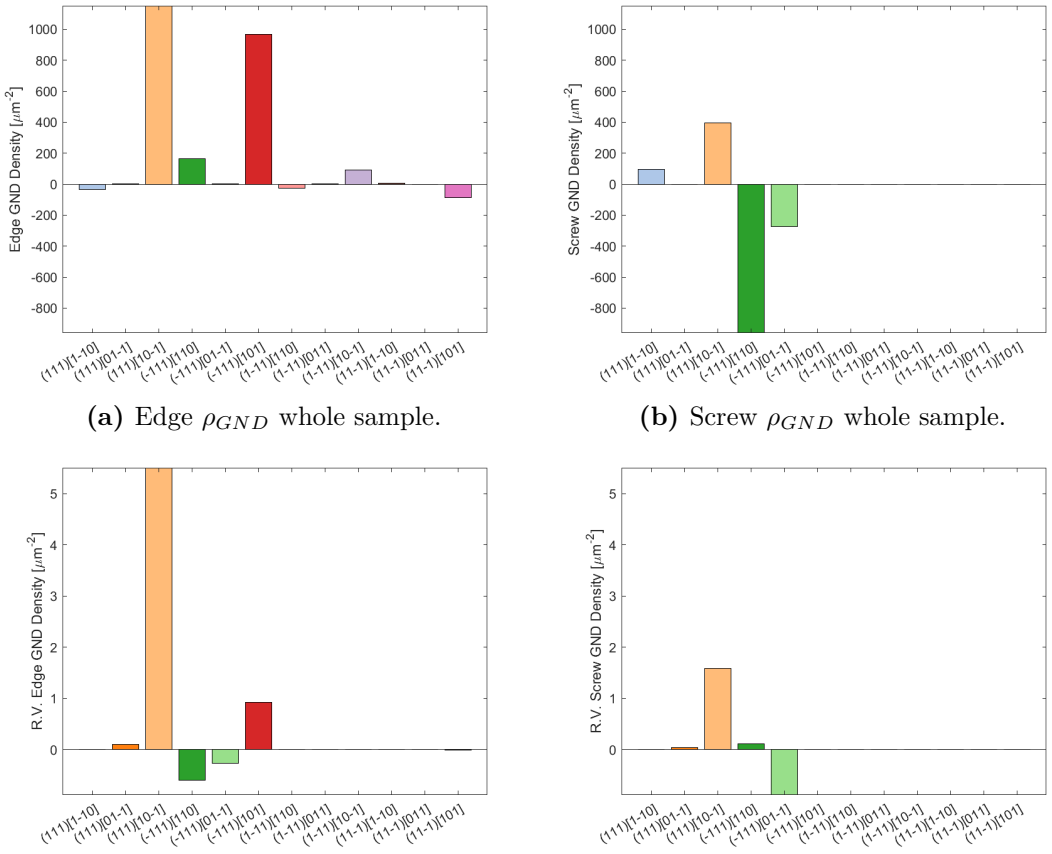
(b) Sum absolute slip risk-volume.



(c) MTEX Schmid factors.

Figure 7.42: CPFE sum absolute slip for H8 and MTEX Schmid factor with uniaxial stress along cantilever axis. The risk volume is the top 10% σ_{vm}.

In the risk-volume, the CPFE ρ_{GND} values show the 3$^{\text{rd}}$ slip system dominates for both edge and screw. For the whole volume, edge dislocations are dominated by the 3$^{\text{rd}}$ and 6$^{\text{th}}$ slip systems; however, for the screw dislocations, it is dominated by the 4$^{\text{th}}$ slip system. So, like the absolute slip sums above, systems 3, 4, and 6 are the most significant. Hence, the general population is likely more edge-dominated, especially for a (111) trace on the 3$^{\text{rd}}$ slip system, ($\bar{1}$11) trace is nearly equally likely to be 6$^{\text{th}}$ slip system edges or 4$^{\text{th}}$ slip system screws. The risk-volume results indicate that in high-stress regions like ahead of the fatigue cracks or at least their initiation conditions, the dislocations associated with its fracture are dominated by edge dislocations on the 3$^{\text{rd}}$ slip system. The stress state of a shearing mode fatigue crack is not trivial and depends on primary and secondary orientation. They are often inclined compared to the sample geometry and loading axis, which leads to mixed and complex stress intensity factor loadings. In addition to their inclination, the elastic anisotropy of SXNBSs, and their plastic anisotropy as slip is heterogeneous along {111} planes [134, §4.1][53, p. 641][135] adds to the complexity. Hence, the slip activity is important, as crystal plasticity FEM found that the crack path follows the {111} planes with the highest degree of slip [136, p. 17].



(a) Edge ρ_{GND} whole sample.

(b) Screw ρ_{GND} whole sample.

(c) Edge ρ_{GND} risk-volume.

(d) Screw ρ_{GND} risk-volume.

Figure 7.43: CPFE ρ_{GND} sums over each integration point on either the whole sample or within the top 10% σ_{vm} risk-volume.

In fig. 7.41, it is clear that the highest absolute slip from predicted by CPFE, slip system 3 $(111)[10\bar{1}]$ (*sandstone*), dominates the observed fracture paths. Slip systems 4 $(\bar{1}11)[110]$ and 6 $(\bar{1}11)[101]$ (both *green*) dominate the secondary crack system in the crack bifurcation, which is reasonable considering those slip systems are strong in the CPFE model. Slip system 9 $(1\bar{1}1)[10\bar{1}]$ (*lavender*) becomes more dominant where the crack path becomes more complex, likely because the local stress state deviates from the CPFE model. Hence, H8 show that the fracture paths and slip systems generally match closely to the uncracked CPFE model unless the local stress state deviates too much from the model.

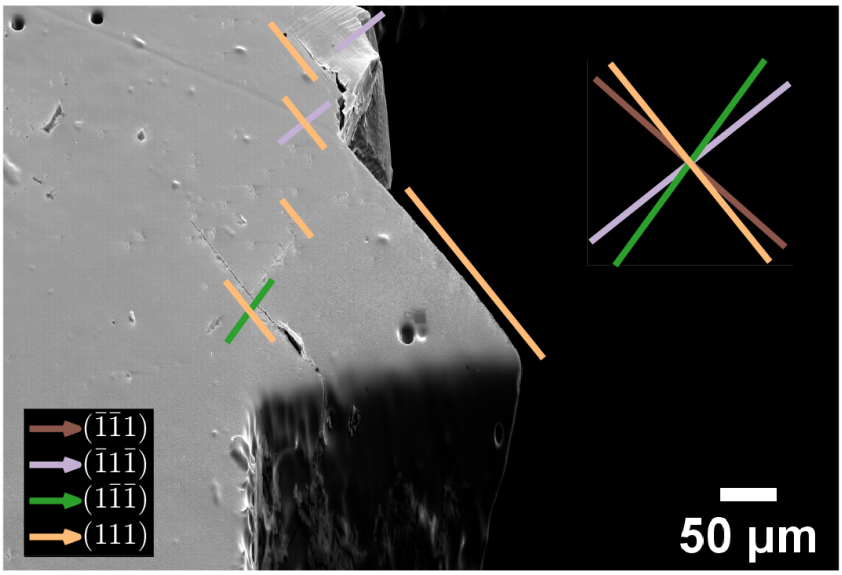


Figure 7.44: Annotated SE micrograph of H8's initiation side where the EBSD scan was taken from. The slip traces are superimposed and use the same colours as fig. 7.43. N.B. green and red in the bar plot have the same slip plane.

7.6 <110> ECCI Micrographs

ECCI micrographs have been collected for RJS samples of both ⟨100⟩ & ⟨110⟩ SXOs. However, the ⟨100⟩ samples have been discussed in chapter 6, as apart from the cantilever design, it shares the same SXO and environmental condition as the ambient tests with the original mesocantilever design.

Sample RJSN1 was the only ⟨110⟩ SXO sample with ECCI micrographs (all taken at 30 kV) and will be the focus of this section. It has the most straightforward fracture and slip traces as it is case 1 fracture. Figure 7.45 shows that unlike the other ⟨110⟩ SXO samples, it had $(11\bar{1})$ cracks coming from surface pores rather than just a critical fracture crack.

To analyse the slip traces and defect contrast in MTEX, the change in stage rotation in MTEX (ΔR_{mtex}) is set to match the rotation from the cantilever facing downwards to the ECCI condition. Stage tilt corrections are also applied to the SEM micrographs. Further details are in appendix D.4.

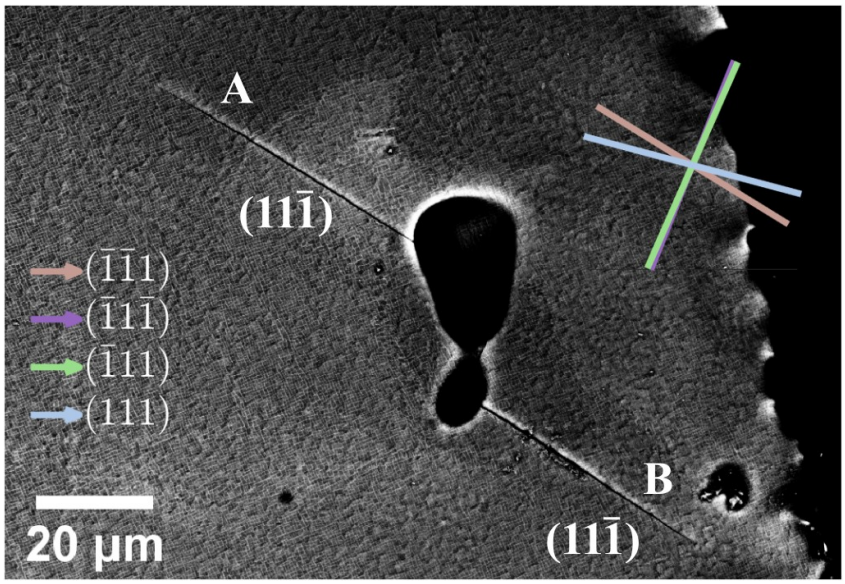
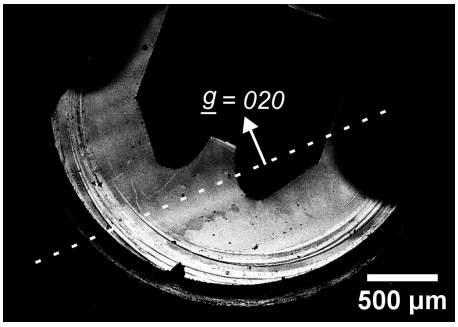
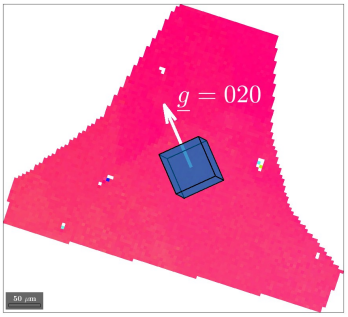


Figure 7.45: BSE micrograph ($\underline{g} = [020]$) of a casting pore with two (11$\bar{1}$) cracks called A and B.

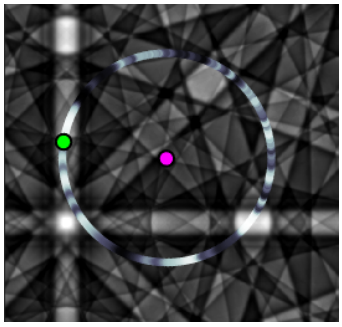
The results for the $\underline{g} = 020$ and $\underline{g} = 220$ diffraction conditions obtained using the novel ECCI protocol (see section 5.3) are summarised below in figs. 7.46 and 7.47 (see appendix D.3.5 for further details).



(a) ECP.

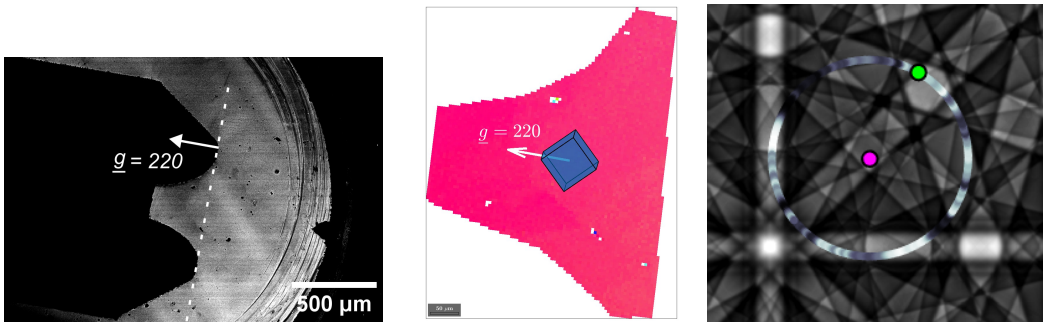


(b) Rotated EBSD map.



(c) Stereographic map.

Figure 7.46: RJSN1 ECCI diffraction condition under $\underline{g} = 020$. Done with a 10° T_{stage}.



(a) ECP. **(b)** Rotated EBSD map. **(c)** Stereographic map.

Figure 7.47: RJSN1 ECCI diffraction condition under $\underline{g} = 220$. Done with a 8.2° T_{stage}.

Crack A g=[020]

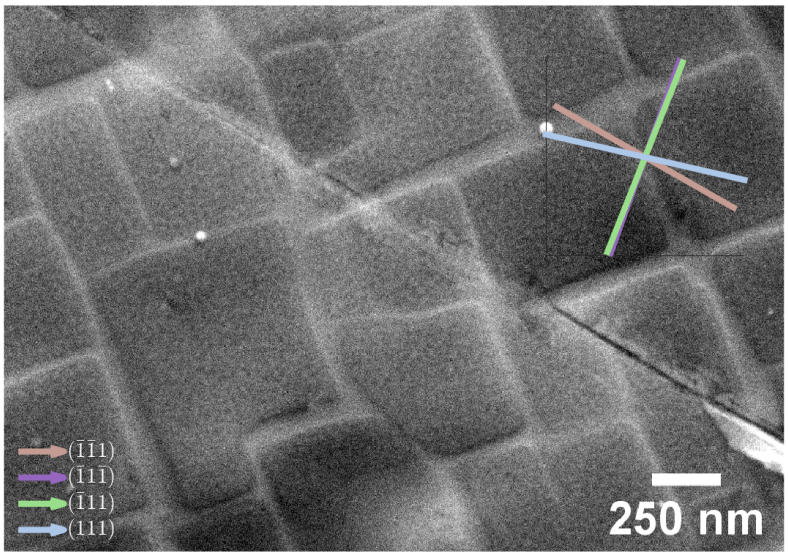
Figure 7.48 shows ECCI micrographs for crack A going into the cantilever's interior in fig. 7.45. Threading dislocations with a dark-bright split (*yellow*) are frequently seen in fig. 7.48b. Those whose splits nearly follow $\underline{g}$ could be screw dislocations.

Considering that CPFE modelling predicts that $(11\bar{1})[011]$ is the predicted dominant slip system (section 7.5.1), then those dislocations, in theory, should be visible as $\underline{g} \cdot \underline{b} = 020 \cdot 011 \neq 0$.

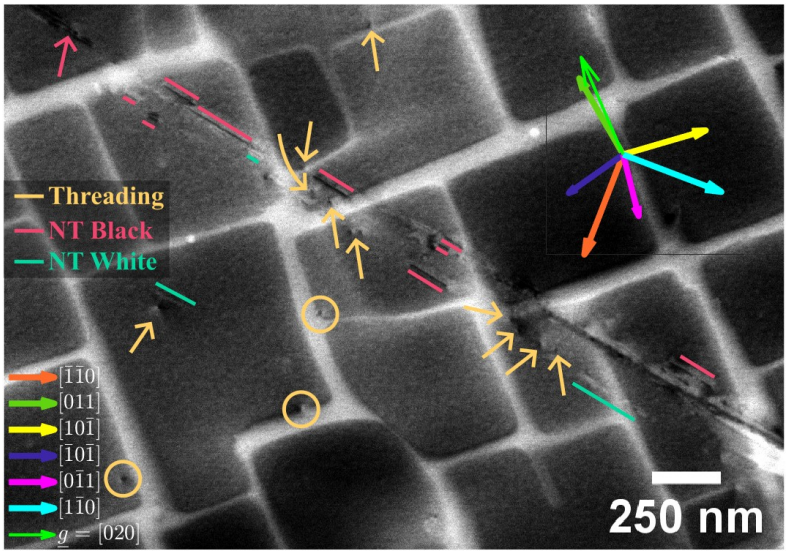
The bright and dark lines following along the $(11\bar{1})$ trace (*green* and *red*) could be the following features:

1. Non-threading dislocation line segments.
2. Isolated stacking faults (SFs) being bounded by threading dislocations with a $(11\bar{1})$ stacking fault plane (TEM [137]).
3. Microcracks in γ' [35].

Figure 7.49 shows evidence for the dark lines being SFs (2nd case) due to their dark, thick, and, importantly, straight features with nearby brightness. The extra contrast fringes are likely lost in the signal, so only one can be seen per SF. The exact identification of these SFs will not be made. They are unlikely to be microcracks as they only appear in the SE signal when under ECCI diffraction conditions.



(a) SE with slip traces.



(b) BSE with $\underline{g}$ and $\langle 110 \rangle$ $\underline{b}$ vectors.

Figure 7.48: RJSN1 ECCI micrographs under $\underline{g} = 020$.

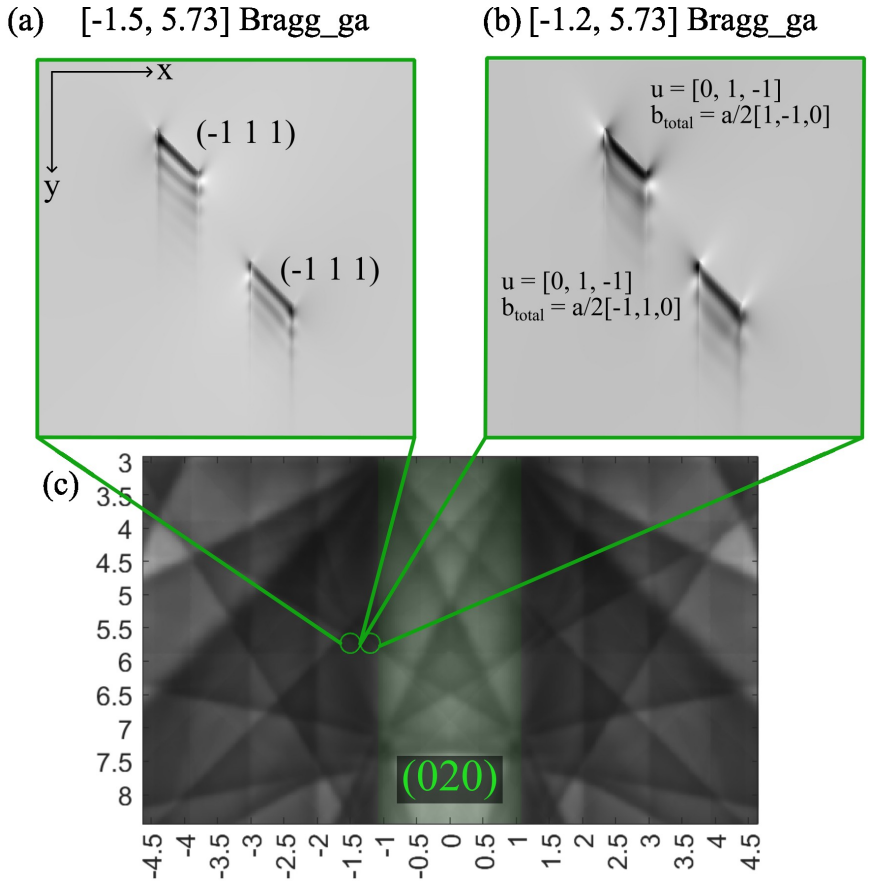


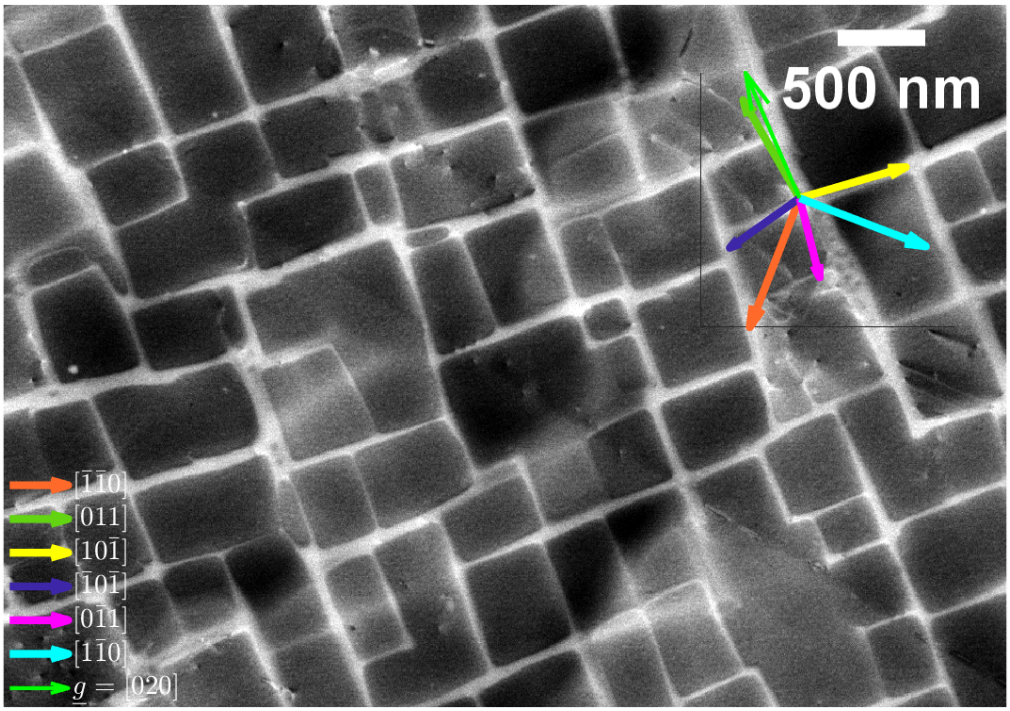
Figure 7.49: Simulated ECCI micrographs of two SFs imaged with deviation values of (a) $w = -0.5\xi_g$ and (b) $w = -0.2\xi_g$ [119] achieved with EMsoft v5.0 [131]. Their locations on a full stereographic projection are shown in (c). Positive w values invert the contrast of the SF as mentioned in Ref [138].

The white lines are less straight, thinner, and have more significant thickness variations, making them more likely dislocations (1st case). Similar bright lines have been in section 6.4, the high slip regions of samples RJSN1 and H8 (section 7.6). They appear as groups of at least two and so could be superlattice dislocation pairs in the slip bands (see Ref [139]).

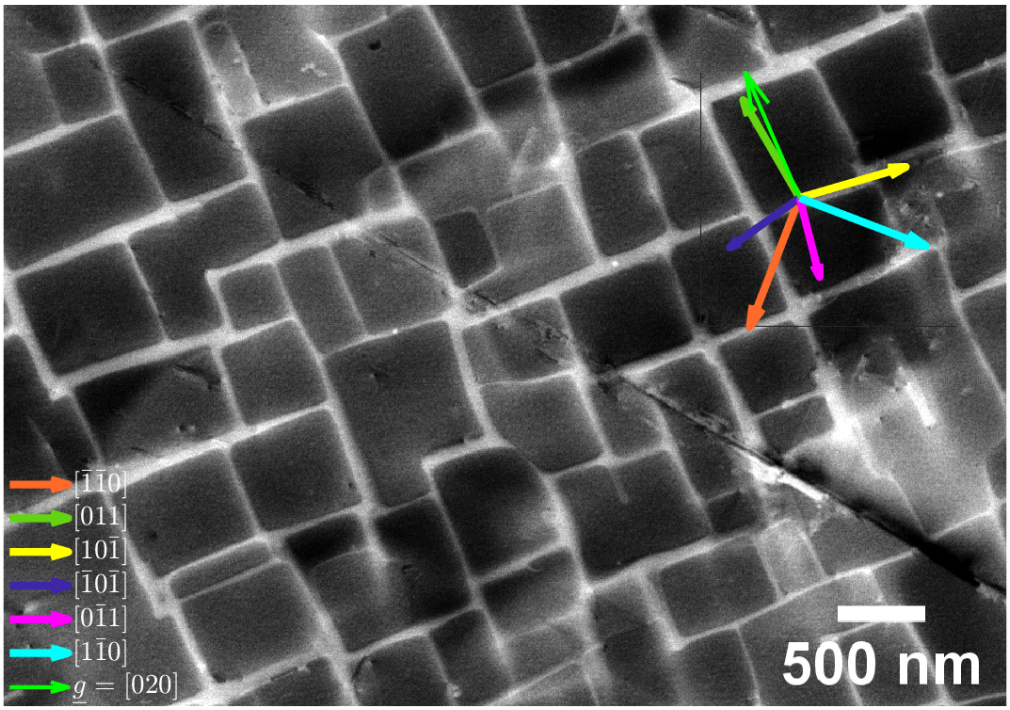
Figure 7.50b shows that the defects are primarily located on or very close to the crack tip's slip plane around the local area of the crack tip. Dislocations are sparse around it before becoming greater further away from the crack plane.

Figure 7.51 shows that the number of defects following along the crack's slip plane in adjacent parallel slip planes decreases further away from the crack. Additionally, the dark isolated SFs along the crack plane become less frequent further away from the physical crack tip, becoming almost absent in fig. 7.50a.

Little-to-no dislocations are seen in the γ phase. Instead, they are primarily at the γ' interfaces or within γ'.



(a) Further from crack tip.



(b) Closer to crack tip.

Figure 7.50: $\underline{g} = 020$ ECCI further from the crack tip in RJSN1.

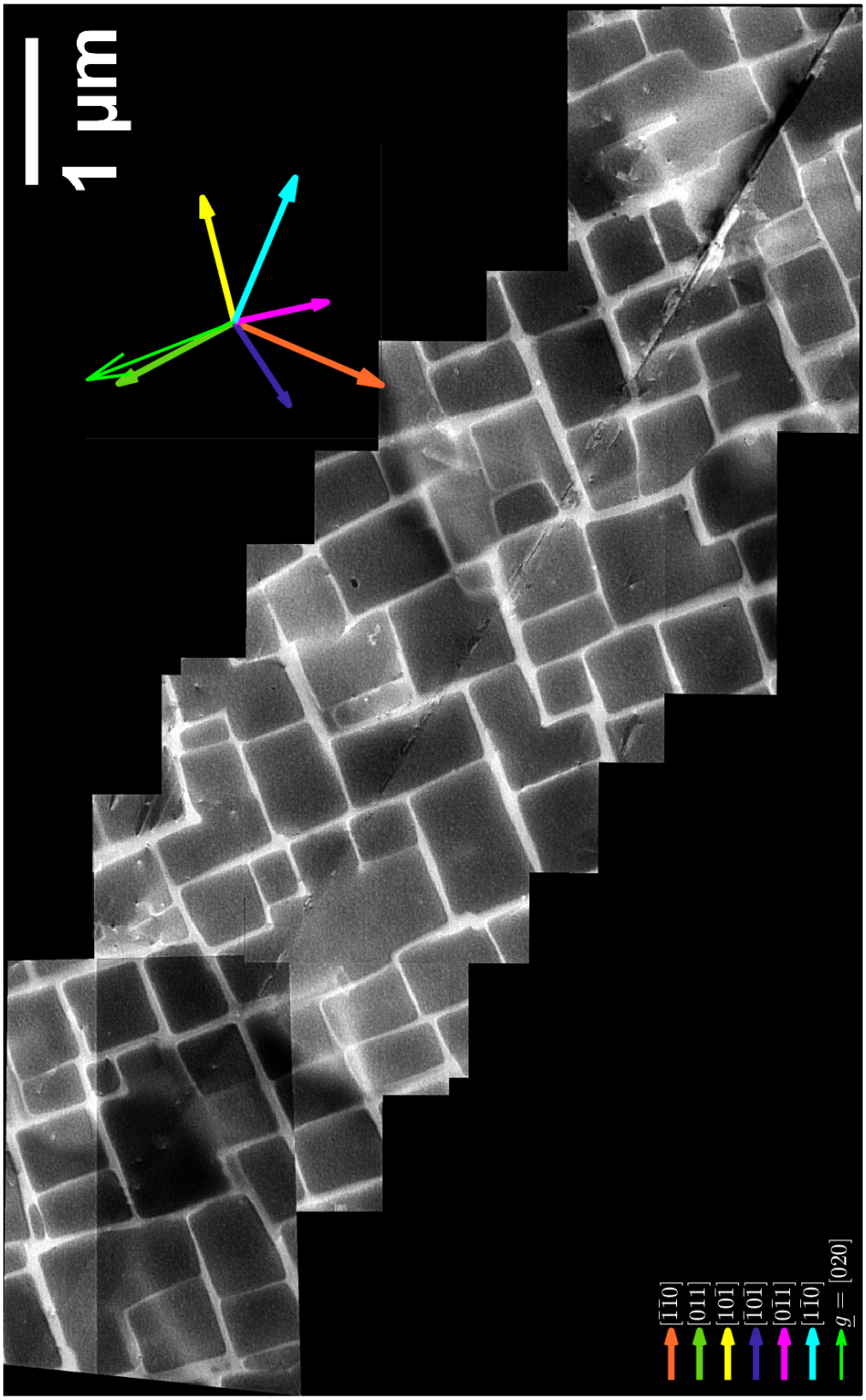


Figure 7.51: Stitched ECCI micrograph of the crack tip and ahead of it. CLAHE with a window of 11 followed by an automatic brightness-contrast adjustment.

Figure 7.52 shows a schematic of the potential dislocation structure occurring ahead of $(11\bar{1})$ fatigue cracks with example ECCI images of the defects. As the probe depth (t_g) is $\approx 100\,\text{nm}$ (appendix C.3), the exact nature of the dislocations deeper into the surface is hard to discern.

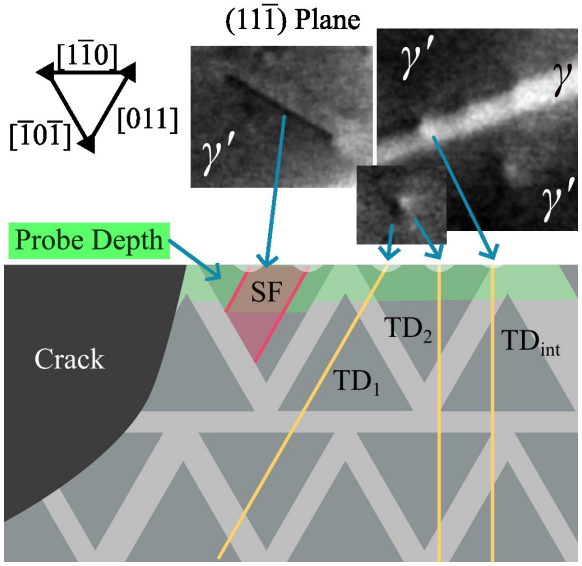


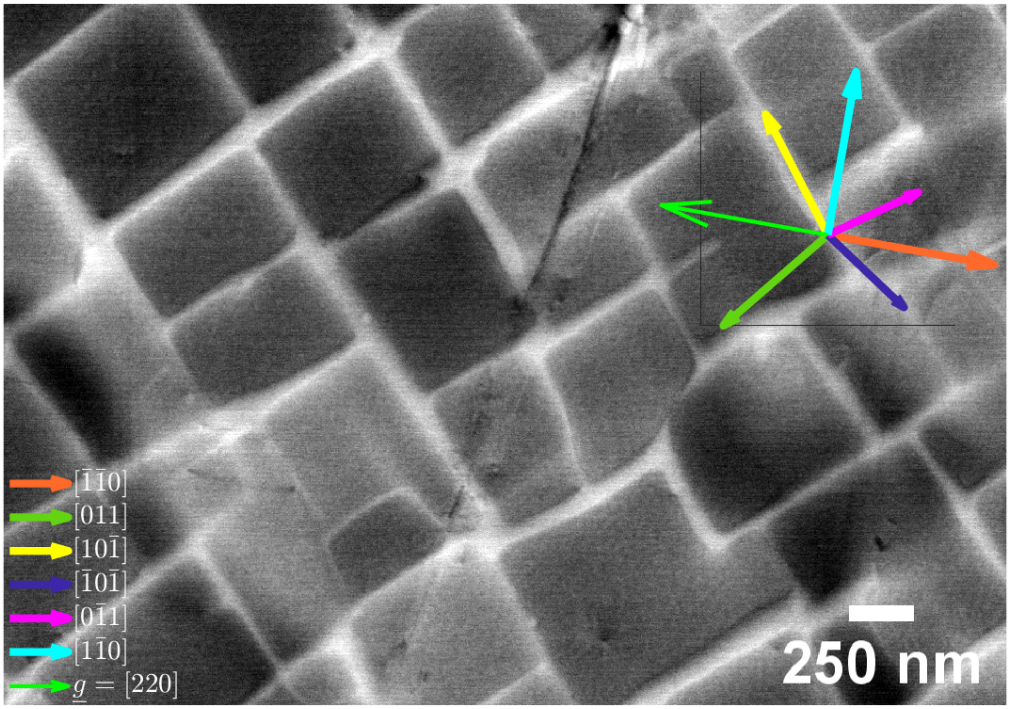
Figure 7.52: Schematic of the dislocations ahead of the fatigue crack for a ⟨110⟩ CD ⟨100⟩ FN orientated sample. Stacking fault (SF), threading dislocation (TD) are shown. TD_1 has a line vector parallel to a ⟨110⟩ direction, TD_2 is parallel to ⟨100⟩, and TD_{int} represents those at the interface. Without significant contrast of the dislocation line, it is challenging to determine their line vectors.

Crack A g=[220]

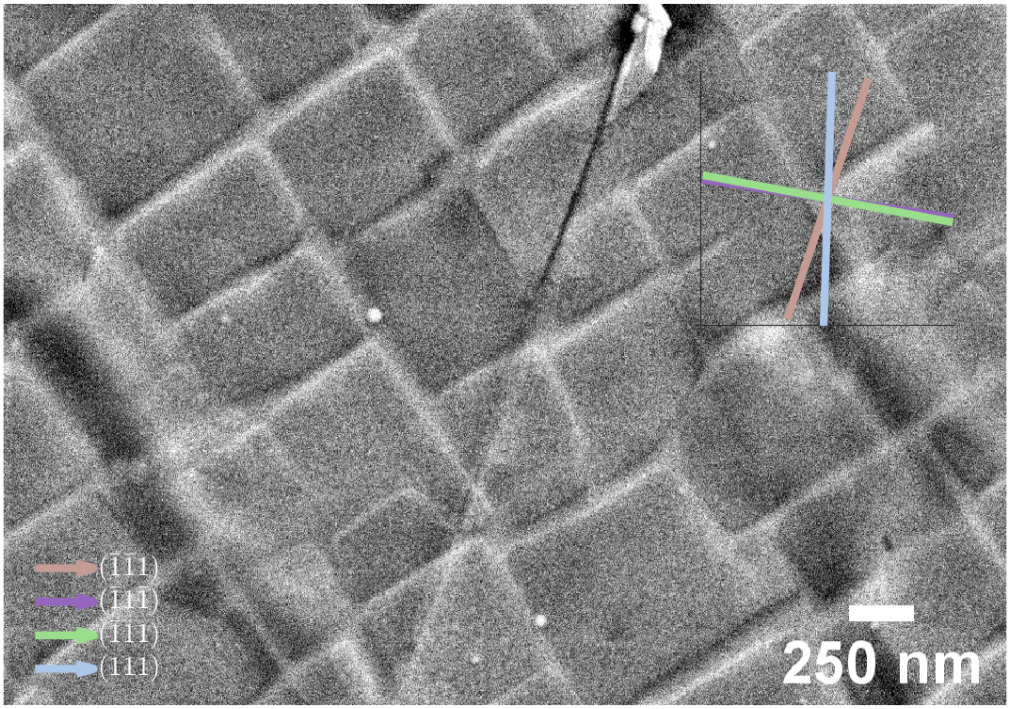
Figure 7.53 is the same region as fig. 7.48 but under $\underline{g} = 220$. The SEM experienced an issue between the $\underline{g} = 020$ and $\underline{g} = 220$ tests, reducing the flux, which decreased the signal-to-noise ratio, producing lower resolution/quality micrographs.

Figure 7.54 compares the two diffraction conditions. The threading dislocations can still be seen in γ' and the $\gamma - \gamma'$ interfaces. In some, their contrast split follows $\underline{g}$ in both, indicating threading screws. Not all of the threading dislocations are screws.

The non-threading bright dislocations following the $(11\bar{1})$ trace under $\underline{g} = [220]$ now have little-to-no contrast (c.f. $\underline{g} = [020]$), suggesting a $\underline{b}$ of $\pm[1\bar{1}X]$ (ignoring the poorer flux).



(a) BSE.



(b) SE.

Figure 7.53: Contrast enhanced and noise reduced micrographs taken under the $\underline{g} = 220$ condition for crack A's tip in RJSN1.

Some dark linear features (i.e., SFs) show weaker contrast in $\underline{g} = 220$, whereas some still show strong contrast, like those ahead of the crack path. Suggesting

some distortion component ($\underline{b}$) parallel to [010] or that it is a more complex defect. Those that lose contrast likely have a component parallel to $[\bar{1}10]$.

Both $\underline{g}$ conditions show primarily defects following the $(11\bar{1})$ trace, indicating slip on that plane and not the others, supporting its dominance in the CPFE model. Using $\underline{g} \cdot \underline{b}$, more dislocations should be visible compared to $\underline{g} = [020]$ apart from those of $\underline{b} = \pm[1\bar{1}X]$ or pure edges that satisfy $\underline{g} \cdot \underline{b} \times \underline{u} = 0$.

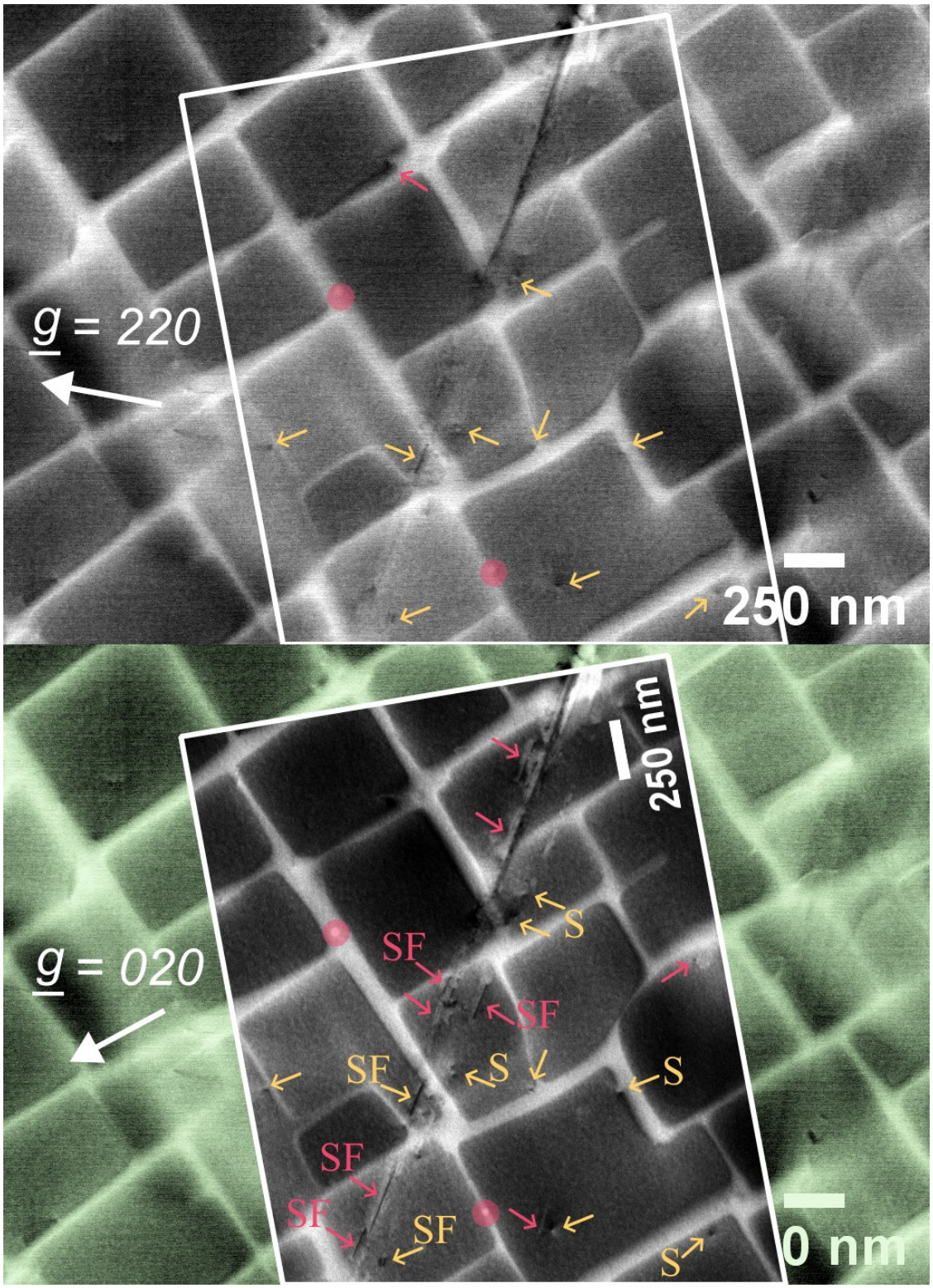
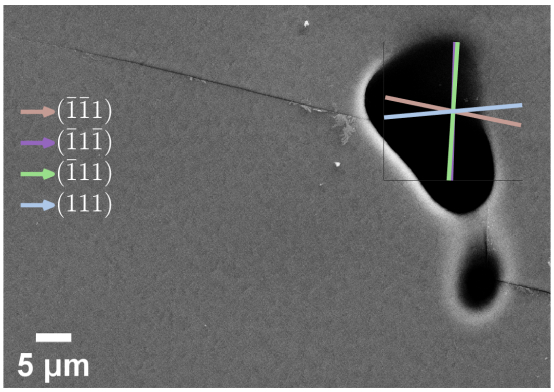


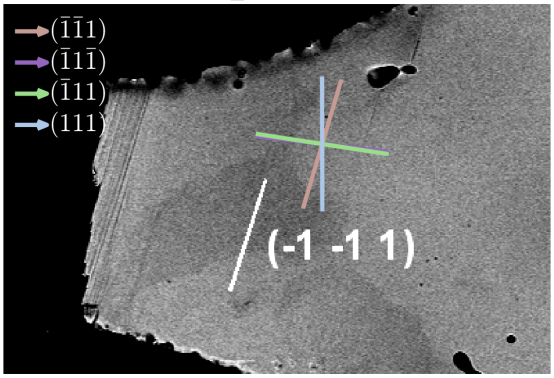
Figure 7.54: Comparison of $\underline{g} = 220$ and $\underline{g} = 220$ ECCI micrographs. *Red* arrows show features that lose contrast in the other $\underline{g}$, whereas *yellow* shows those with similar contrast amounts. Red circles highlight non-defect features. *S* stands for threading screw dislocations & *SF* is for stacking fault.

Low Schmid Factor Slip

In fig. 7.55a, a crack path between the two pores follows the trace of a low Schmid factor slip system (section 7.5.1) on either the $(\bar{1}1\bar{1})$ or $(\bar{1}11)$. Distinguishing between them visually is challenging because they are close to each other. The local deviation in the stress state between the two pores is probably the cause of the slip in the low Schmid factor slip system, making it a high Schmid factor slip system locally.



(a) $\underline{g} = 020$ SE.

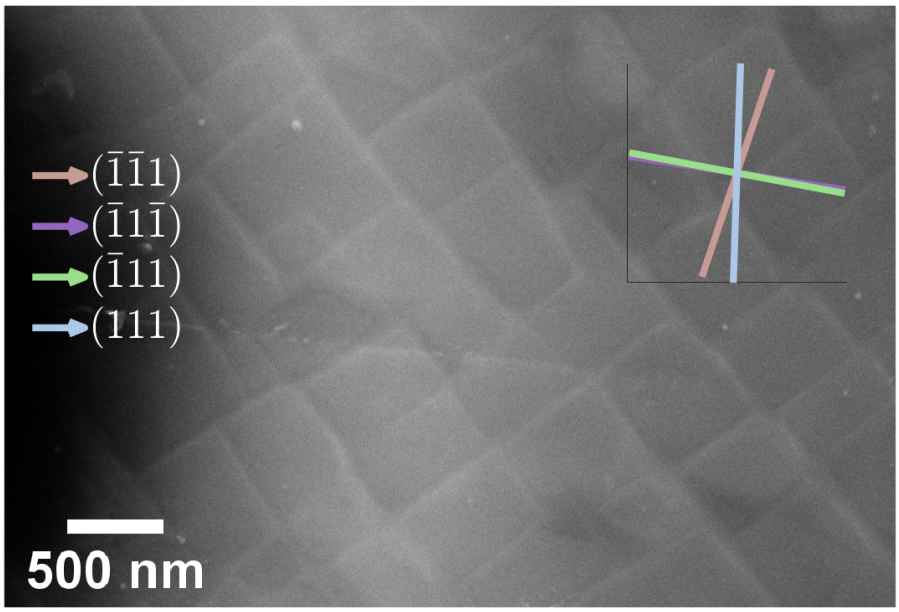


(b) $\underline{g} = 220$ BSE.

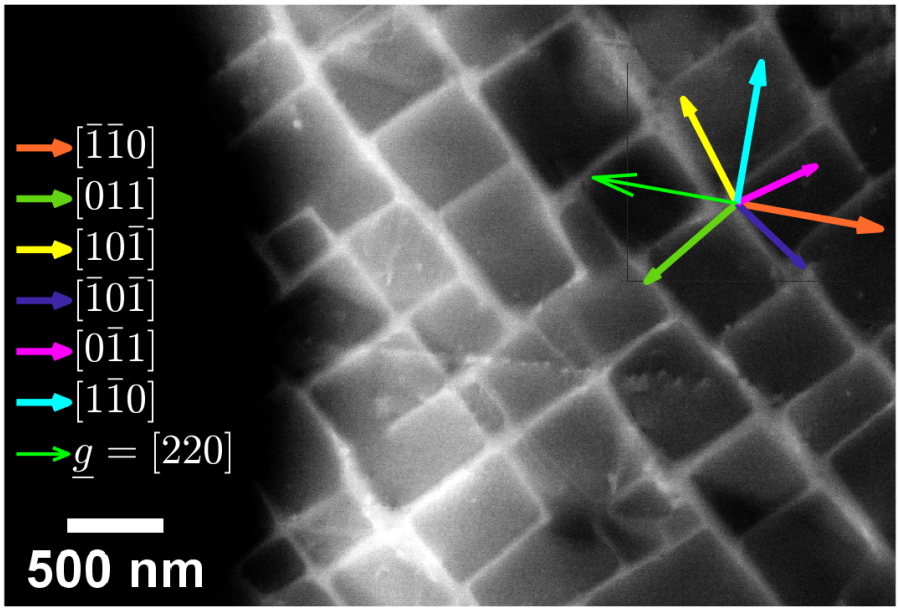
Figure 7.55: Annotated micrographs showing the orientation of the slip traces.

Figure 7.56a shows an example of this low Schmid factor slip seen near a surface casting pore in fig. 7.56b. The SE signal shows that it is more like a slip trace rather than a crack, as cracks can be seen when not under an ECCI diffraction condition. Features like this are usually found ahead of fatigue crack tips, likely a precursor for fatigue crack initiation.

Enhancing the micrograph around the slip band in fig. 7.57, the leftwards threading dislocations have a contrast-split closer to $\underline{g}$ unlike the rightward ones



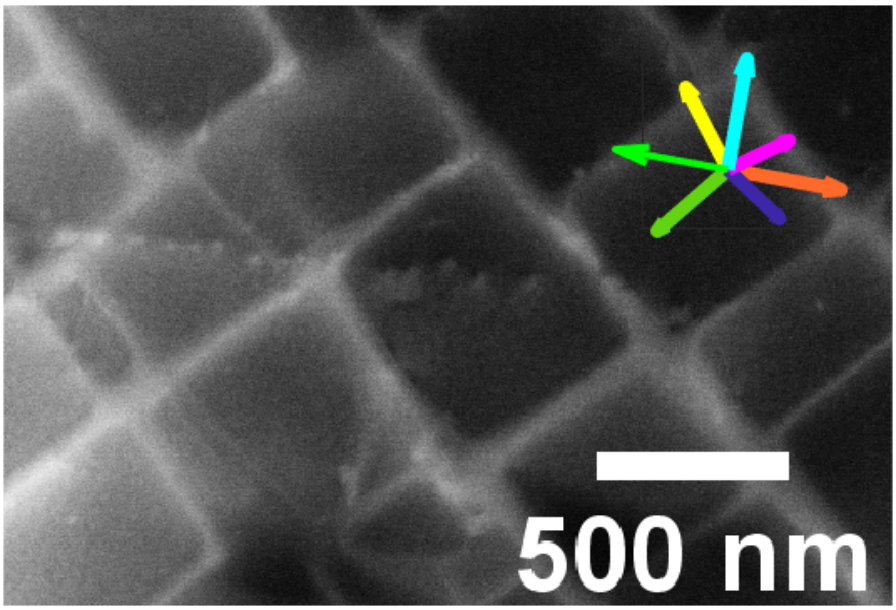
(a) SE micrograph.



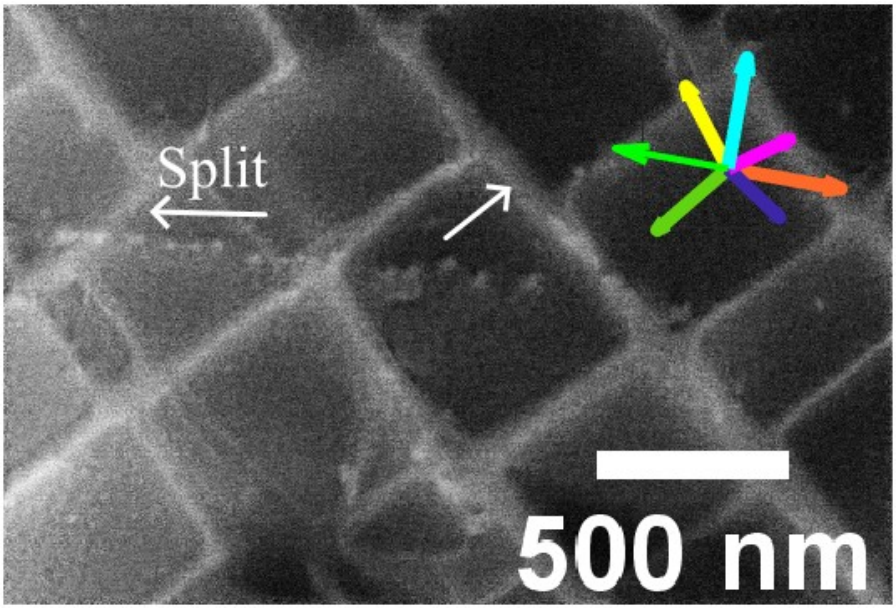
(b) ECCI micrograph + auto-brightness-contrast.

Figure 7.56: Low Schmid factor slip system of a $(\bar{1}1\bar{1})$ or $(\bar{1}11)$ trace coming from a pore on the left. $\underline{g} = 220$.

which are nearer to $[011]$ or $[0\bar{1}1]$.



(a) Crop with no further enhancements.



(b) CLAHE contrast enhancement with 11-pixel window. Contrast split vectors are annotated.

Figure 7.57: High magnification BSE of fig. 7.56b with CLAHE contrast enhancement.

No cracks were found to follow the low Schmid factor planes for crack A. ECCI micrographs do show dislocations alongside crack A (fig. 7.58), but their slip planes are hard to identify and are likely parallel to the $(11\bar{1})$ crack.

Wavy slip is seen in fig. 7.58, but these features do not tend to be involved around the crack tip or ahead of the crack plane. They appear like zigzag cross-

slipped dislocations in γ in TEM micrographs from uniaxial LCF at $\approx 800\,^{\circ}\mathrm{C}$ [137, 139] and uniaxial compression at RT [34]. The wavy slip could be related to the plastic zone, but the shearing mode fatigue crack's slip tends to be heterogeneous and parallel to the crack [135, p. 3112]

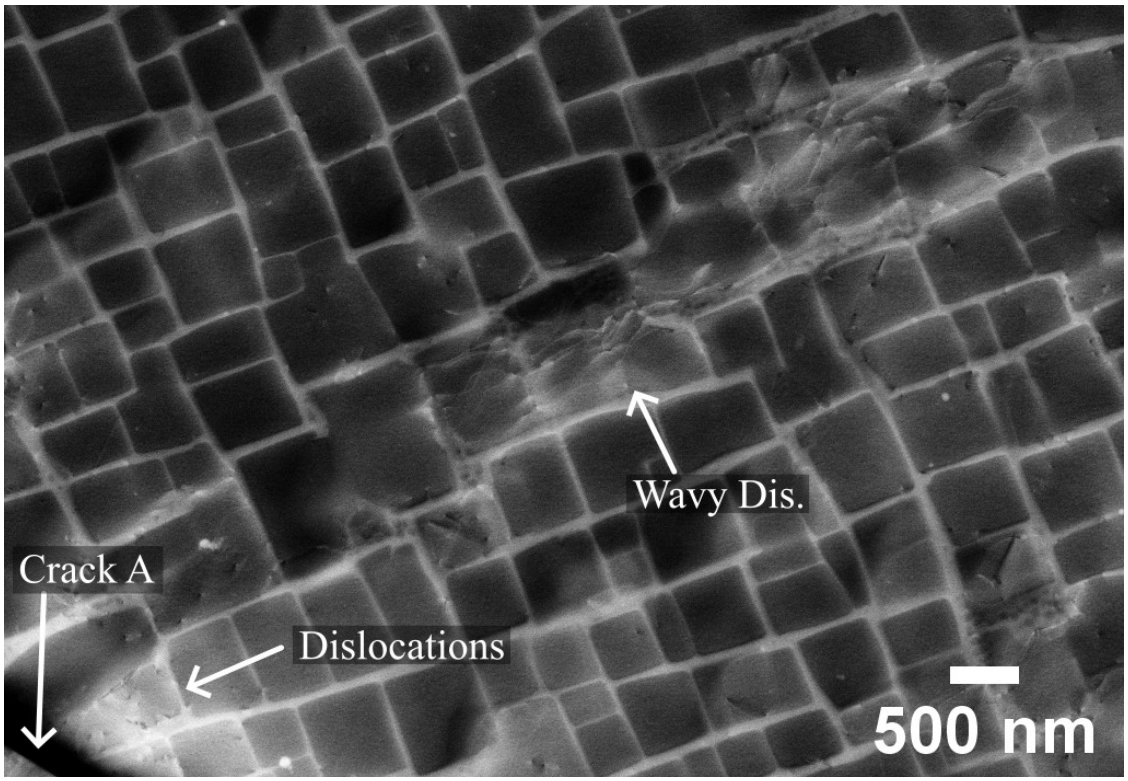
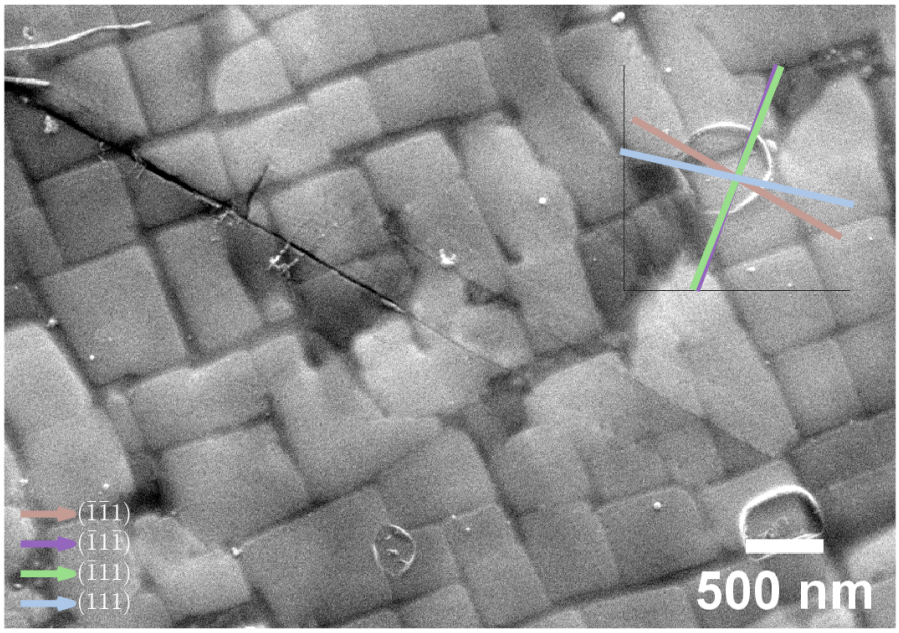


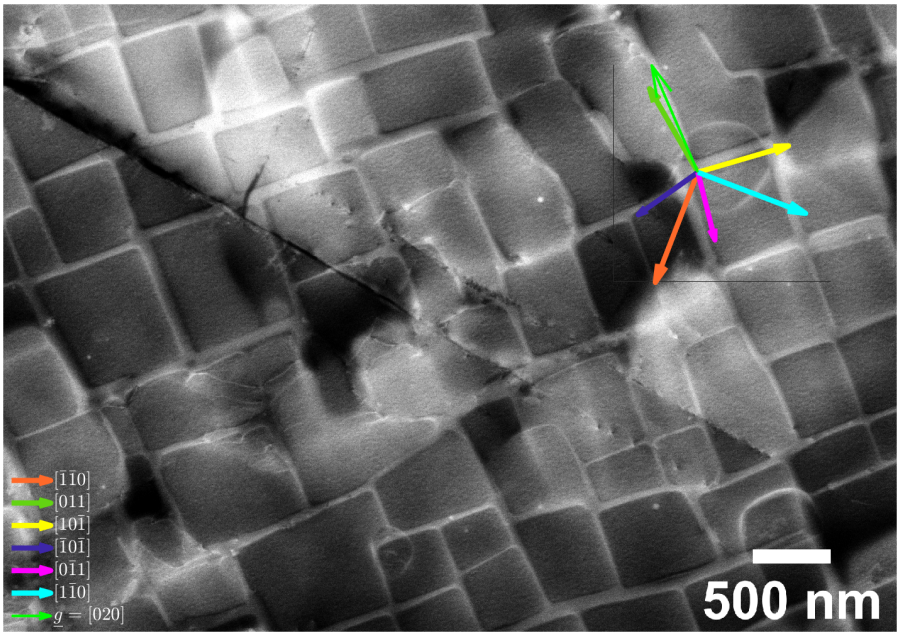
Figure 7.58: ECCI under $\underline{g} = 020$ alongside crack A as annotated. Wavy (zigzag) dislocations can be seen in the centre.

Crack B g=[020]

Crack B in fig. 7.45 does show a low Schmid plane sub-crack coming from a $(11\bar{1})$ crack in fig. 7.59. However, it is an arrested and relatively short sub-crack ($\approx$ 500 nm).



(a) SE.



(b) ECCI.

Figure 7.59: Micrographs of crack B under $\underline{g} = [020]$.

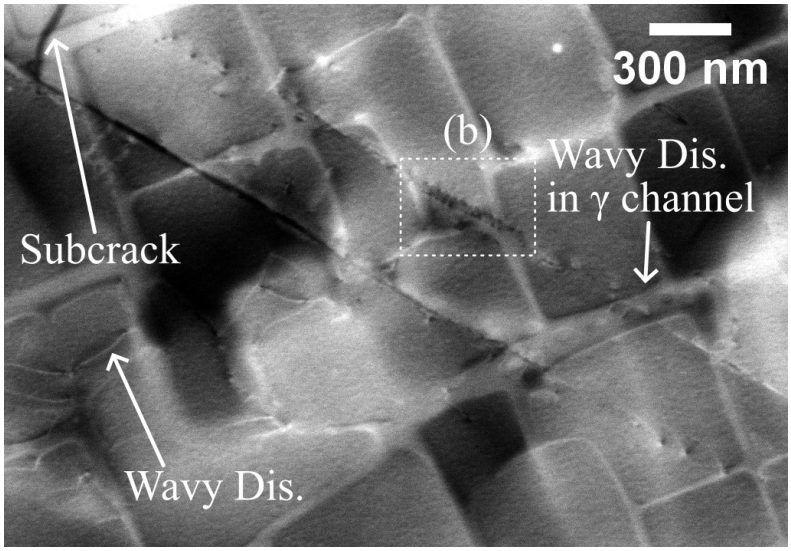
Where it has arrested, dislocations appear to have been emitted from the tip

back along the $(11\bar{1})$ (fig. 7.60), showing a collection of dipoles on two adjacent planes (darker band) briefly with threading dislocations before, and after it like ahead of the main crack tip. However, it is hard to ascertain the nature of these dipoles. They do not appear like non-threading dislocations in γ' in TEM [139].

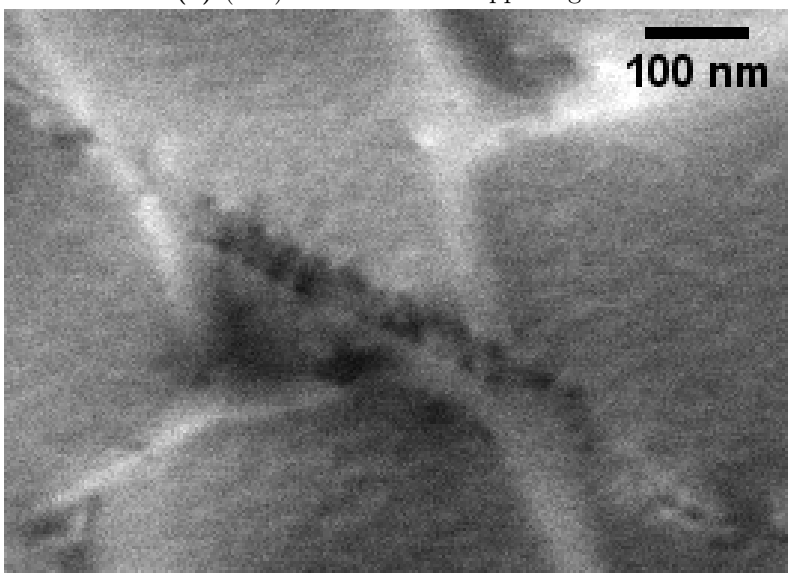
The arrested short crack also has dislocations seen continuing along the low Schmid factor plane but to a much lower degree than the $(\bar{1}\bar{1}1)$ slip.

This poor Schmid factor slip system is probably promoted because the crack is approaching the side of the cantilever, changing its local stress state. This supports the case for the observed case 2 fracture.

The defects along the two $(11\bar{1})$ slip bands in fig. 7.59 become much sparser beyond that figure, similar to what has been observed in other ambient test fatigue cracks and crack A in this sample. The threading dislocations from the main crack have the contrast splits parallel to $\underline{g}$, indicating pure screws. However, the threading dislocations along the sub-crack's parallel slip show a different contrast, possibly due to their source's different crack geometries. They could also be the same dislocation type as those seen in the dipoles.



(a) $(\bar{1}\bar{1}1)$ from sub-crack upper right.



(b) Dislocation dipoles magnified.

Figure 7.60: ECCI of sub-crack's dipoles along $(\bar{1}\bar{1}1)$ under $\underline{g} = [020]$.

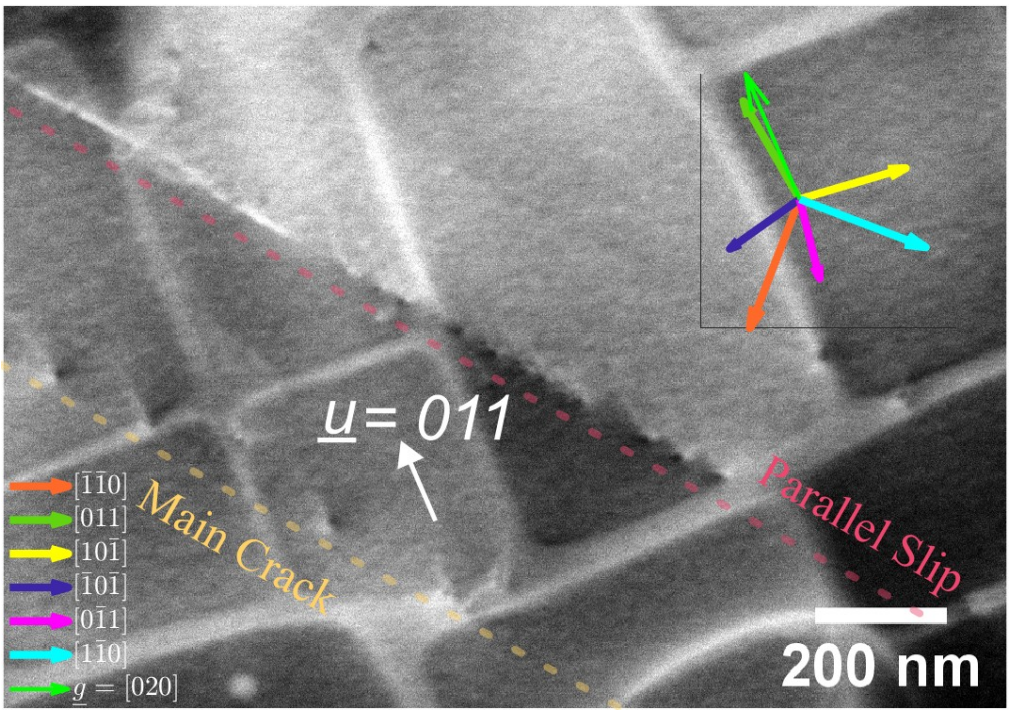


Figure 7.61: High magnification ECCI of threading dislocations along the two $(11\bar{1})$ slip bands of crack B's tip. Where $\underline{g} = [020]$. Both dislocations show brightness tails (i.e. $\underline{u}$) near parallel to [011].

High Slip Region on Exit Side

Figure 7.62 shows that RJSN1 has significant slip near the drastic failure fracture path on the exit side, as seen in many samples.

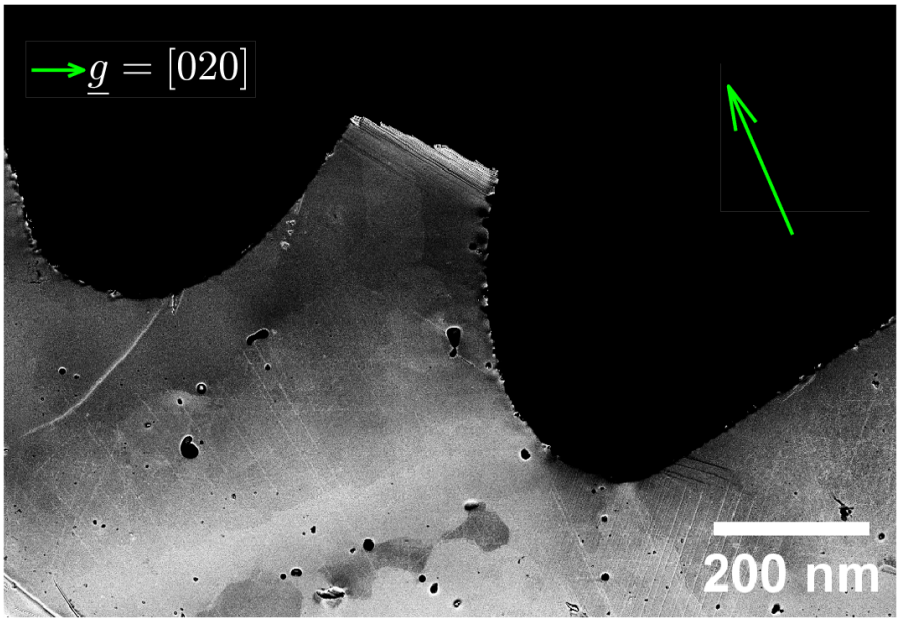
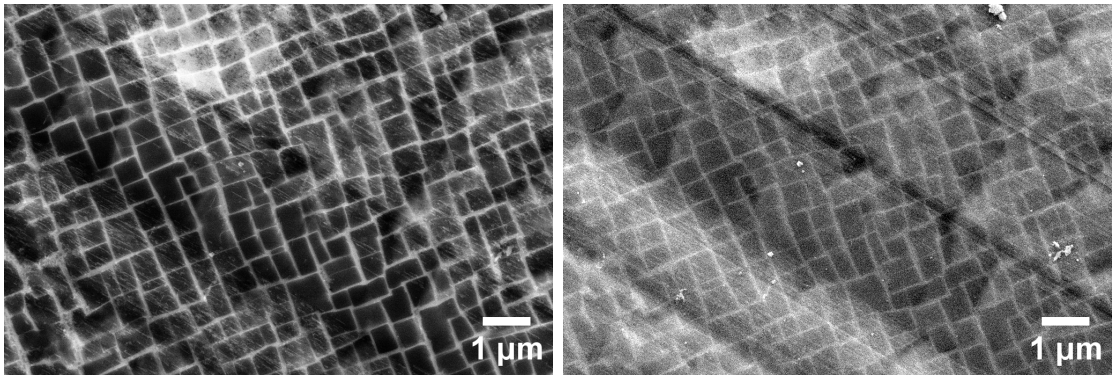


Figure 7.62: BSE micrographs with the high slip region can be seen near the top, appearing brighter due to surface topology. Taken under $\underline{g} = 020$.

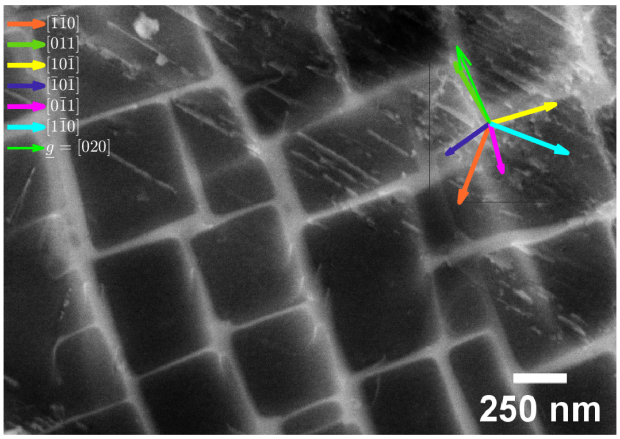
There are bands parallel to $(11\bar{1})$, either enriched or denuded in defects. In the enriched bands, many bright non-threading dislocations with traces parallel to $(11\bar{1})$ are seen primarily in the γ' phase (like crack A). They strongly resemble the dislocation pairs parallel and inside the slip bands of a fatigued SXNBS in TEM [139].

If these bright defects are like those in crack A in terms of visibility, they should have $\underline{b} = [X, -X, Z]$ for $\underline{g} \cdot \underline{b} = 0$ and no invisibility criterion for the pure edge case if $\underline{u} = [1, \bar{1}, 0]$. So for a octahedral slip on $(11\bar{1})$, they would be pure screws if $\underline{b} = [1\bar{1}0]$, or mixed for [011] and [101]. Therefore, if they show the same invisibility criterion as observed, they would be pure screws.

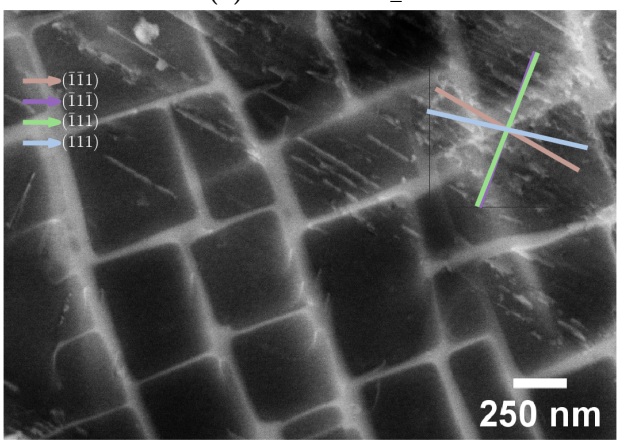
Unlike the dense bands, the denuded bands show virtually only dislocations with greater threading line vectors. They are bright, inclined, and seen at the $\gamma - \gamma'$ interfaces, with the dislocation lines parallel to $(\bar{1}11)$ or $(1\bar{1}1)$ so could be parallel to $[\bar{1}\bar{1}0]$ or [001].



(a) ECCI. **(b)** SE + auto-brightness-contrast.



(c) ECCI with $\underline{b}$.

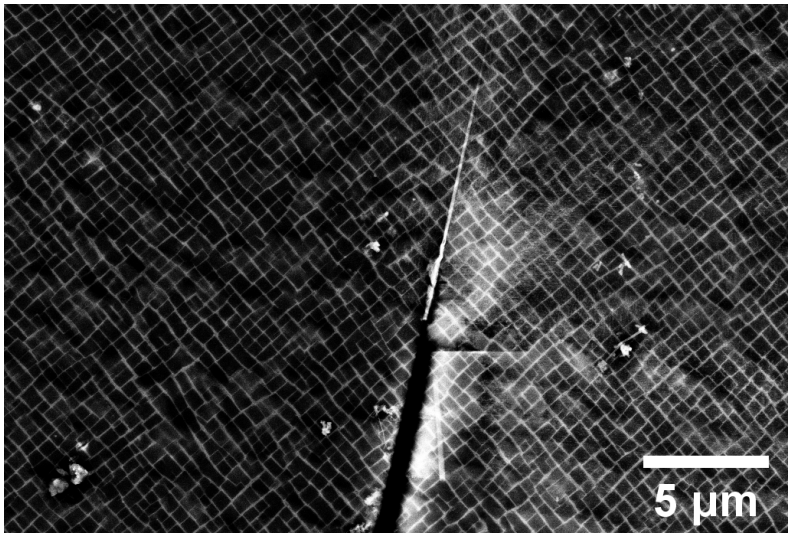


(d) ECCI with slip traces.

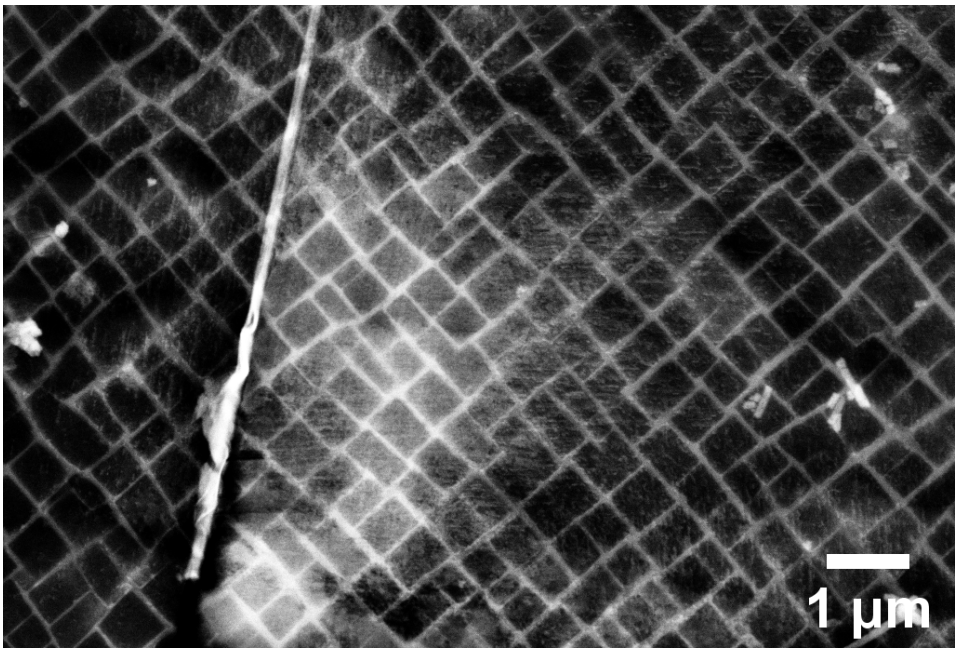
Figure 7.63: ECCI of high slip $(11\bar{1})$ slip bands near fracture surface for RJSN1 under $\underline{g} = [020]$. The denuded band appears darker compared to the dislocation denser bands. In (c) and (d), the denuded and dense regions are the bottom-left and the top-right regions, respectively.

More non-threading dislocations in high slip regions on the exit side have also been observed in a ⟨100⟩ SXO sample (e.g. H8 in fig. 7.64). However, under that SXO, the dislocations along two {111} traces are almost of equal proportions in the

region between the primary and sub-crack, as predicted by plasticity simulations. Outside of this region, the two systems can be seen separately. Unlike the virtually one slip system trace in RJSN1 ($\langle 110 \rangle$). Hence, the observed slip results in ECCI reflect those from crystal plasticity.

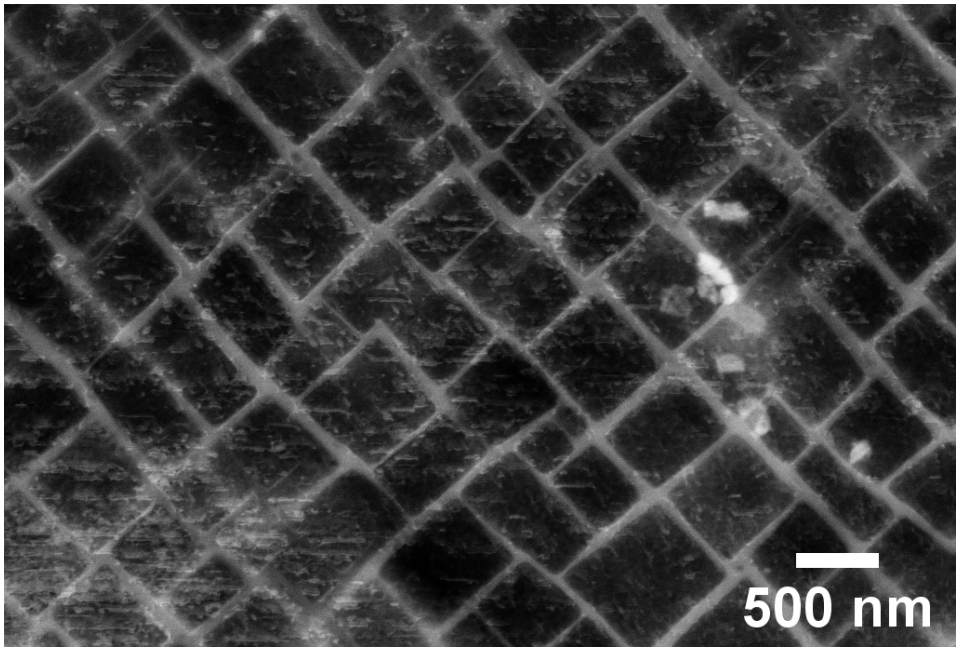


(a) Low magnification.

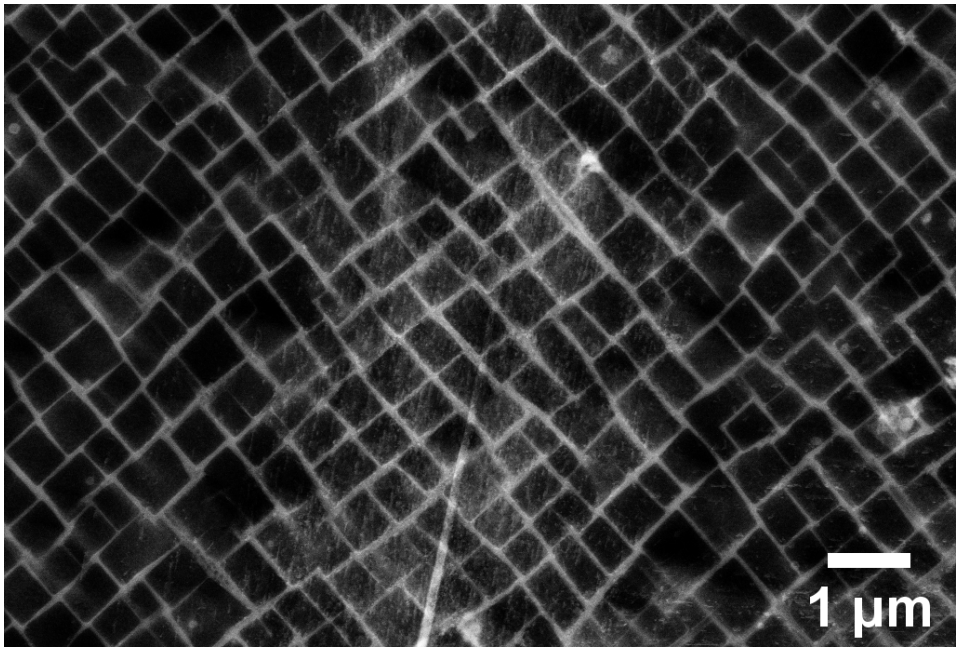


(b) Magnified BSE of the region of non-threading dislocations with two slip trace populations.

Figure 7.64: ECCI micrographs of H8 taken at T_{stage} 8° with unconfirmed $\underline{g}$ condition.



(c) Magnified BSE from rightwards region.



(d) Magnified BSE around main crack tip.

Figure 7.64: ECCI micrographs of H8 taken at T_{stage} 8° with unconfirmed $\underline{g}$ condition.

7.7 Discussion

CPFE vs Experimental

Uniaxial fatigue found multiple shearing octahedral slip systems active for ⟨100⟩, but only one for ⟨110⟩ if slightly off-axis (two if on axis) [11].

The on-axis SXO CPFE models in this work mirror their slip activity along the planes; however, often with more than one slip system being active per plane.

The off-axis ⟨110⟩ CPFE models of actual orientations (fig. 7.39) also show slip becoming dominated by one slip system and especially on one slip plane. Their surface fracture paths also showed the dominance of one slip plane (fig. 7.40) apart from when the local stress state deviates significantly (fig. 7.59).

The ⟨100⟩ CPFE models of sample orientations show that three significant slip systems activate, with the lesser two being on the same plane, i.e. two active planes (fig. 7.42). The dominant slip system's slip trace follows its sample's predominant crack path (fig. 7.44), and the secondary crack path involved in bifurcation follows the plane of the lesser two slip systems. Bifurcation behaviour has been observed frequently in chapter 6 and concurs with CPFE, only deviating when the crack becomes long enough. Bifurcation explains the "zig-zag" fracture path observed in the literature [48]. Multiple initiated shearing cracks for the ⟨100⟩ SXO are also observed in these tests, like in Ref [11].

Therefore, the CPFE models indicate well the crack path tendency (from the total slip) and a crack's initiation trace (from results within the risk volume). The surface crack path behaviour shares similarities with uniaxial fatigue results, but the bending cantilever will differ due to the different ΔK response with crack growth and stress states.

S-N Response

The two different SXOs behave similarly in their S-N response within error, as expected as the ⟨100⟩ and ⟨110⟩ primary SXOs have the same deformation mechanisms [11].

The similarity in the response is greater in the VHCF regime, which is likely in part a testing artefact of the geometric step increase in α_{amp}, as the step size is larger at larger α_{amp} (see section 4.1.5).

The consistency of the ⟨110⟩ curve's data is better than ⟨100⟩'s, with a lower spread in data and a better R^2-value for the 50% probability of failure ($P_f(50\%)$). It is likely due to its sample's greater fracture consistency and usually having only one crack initiate, making the failure α_{amp} more similar and well-defined.

Figure 7.65 compares the ⟨100⟩ SXO ambient tests between the original and RJS designs. The data consistency of RJS results is similar to the 20 No-EP samples and has significantly less spread than the 10 EP original design samples. This is likely due to RJS design's better cantilever stress distribution and less corner crack-dominated failure. Figure 7.65 shows that the $P_f(50\%)$ RJS results are comparable in value to the upper limit of the 68.2% prediction interval of the EP original design.

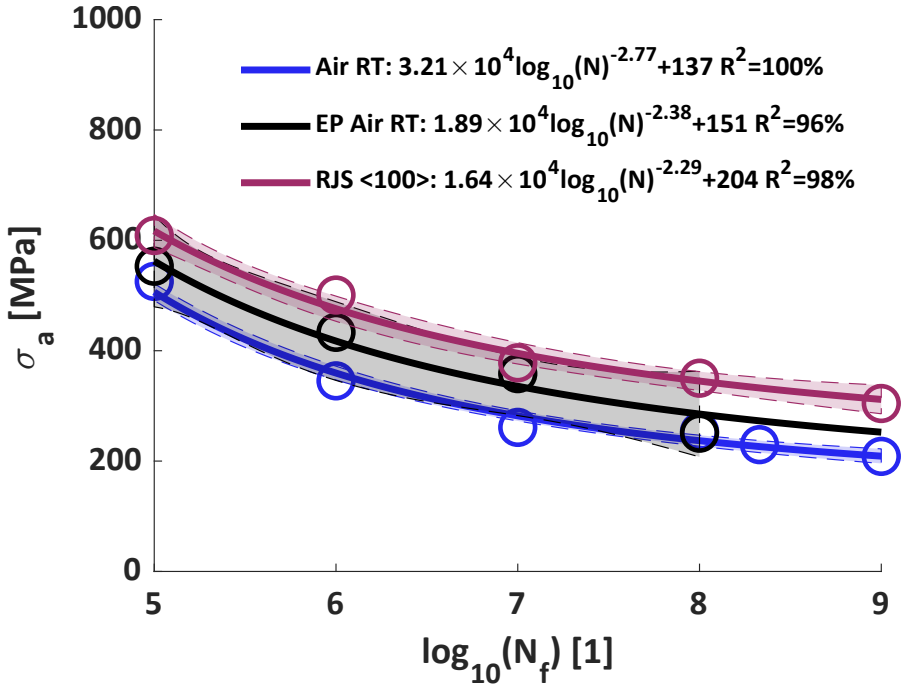


Figure 7.65: Original design EP vs No-EP fatigue data compared with the ⟨100⟩ RJS design data (EP).

Figure 7.66 shows that the S-N curves of both orientations are greater than those of similar SXNBSs near 750 °C [**11**]. Neglecting changes in R, fatigue frequency, specimen size, exact SXO, and fatigue test, this would be interesting as the fatigue strength at 750 °C should be greater than at RT. Figure 7.67 shows rotary bending at 700 °C from Ref [86] whose curves are more comparable to those in this thesis.

Their work suggests ⟨110⟩ has greater fatigue strength than ⟨100⟩; however, the R^2-value for their ⟨110⟩ is significantly lower.

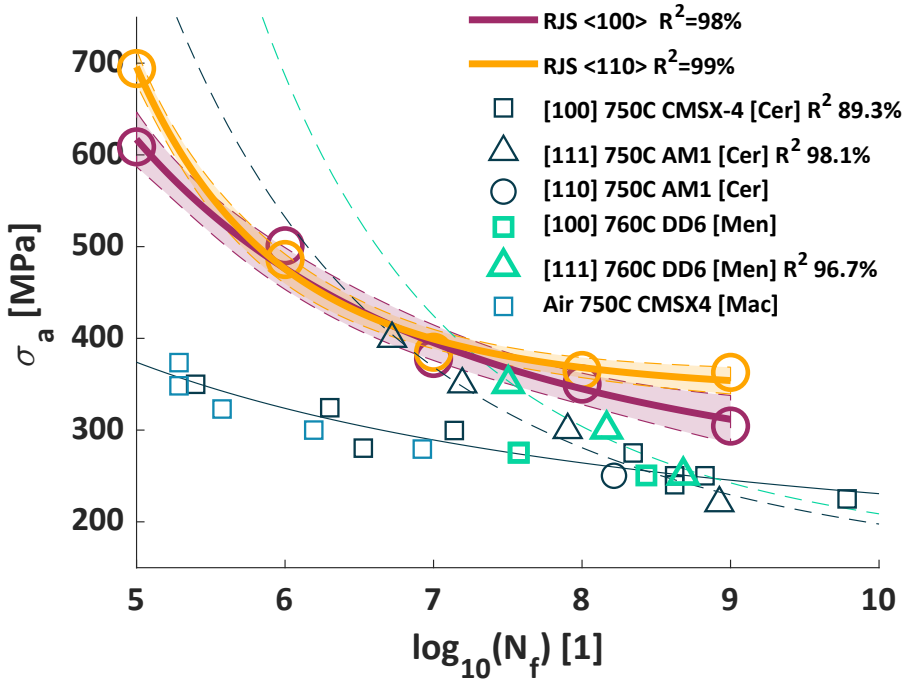


Figure 7.66: ⟨100⟩ & ⟨110⟩ RJS design data (EP) compared with uniaxial ultrasonic fatigue data for CMSX-4 and DD6 tested ≈ 750 °C for ⟨100⟩, ⟨110⟩, and ⟨111⟩. Basquin curve fits are added. [Mac] is low-frequency uniaxial fatigue from Ref [50]. [Cer] is Ref [11] and [Men] is Ref [88].

The greater than expected S-N curves indicate that a size-effect is occurring, most likely due to a lower risk-volume from bending fatigue and being meso-scale. Bending causes a reduction in risk-volume and increases the fatigue limit in the VHCF bending fatigue [105, p. 12], and this is likely why Ref [86] also shows greater values compared to the uniaxial tests.

In the literature, the FCGR is orientation dependent [11, 45, 53]. Figure 2.21a shows the RT Paris plot of CMSX-4, where the ⟨100⟩ and ⟨110⟩ SXOs in this work are most comparable to the <100><XXX> and <110><YYY> data. Refs [45, 53] show a significantly lower FCGR for <110> than <100>, suggesting a greater N_f for the same σ_{amp} (raising the S-N curve). However, in this work, although there is evidence of the ⟨110⟩ S-N curve being higher than ⟨100⟩, it is

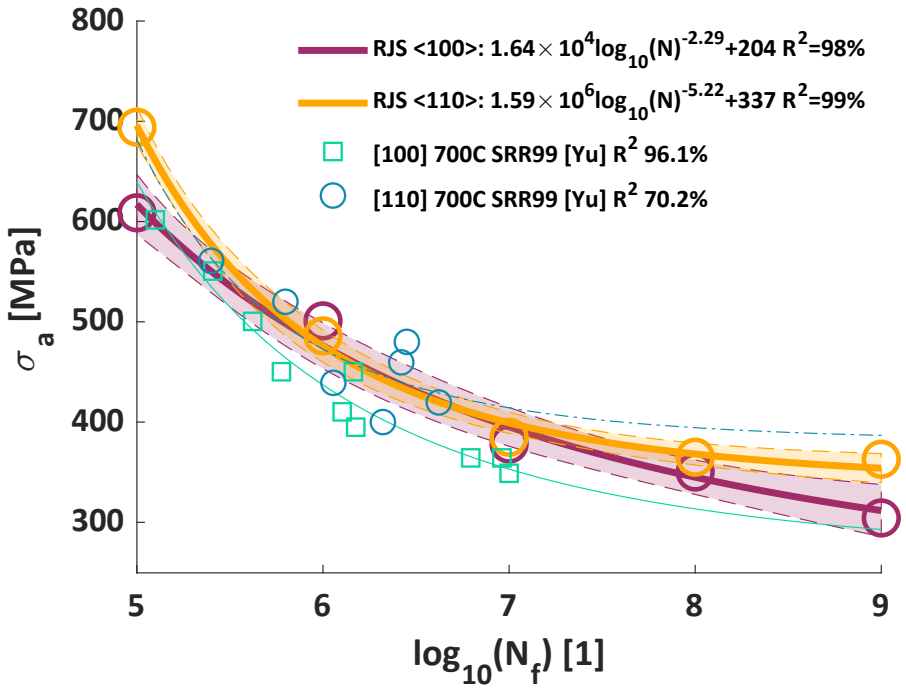


Figure 7.67: ⟨100⟩ & ⟨110⟩ RJS design data (EP) compared with rotary bending of SRR99 (SXNBS) at 700 °C from [Yu] [86]. ⟨111⟩ has been omitted for clarity and as it has a $R^2 = 61.7\%$ Basquin fit.

not as drastic as the FCGR difference. The smaller difference is either because the FCGR is not the sole factor in determining the S-N curve response and/or the greater coupling with crack growth in this fatigue technique causes failure rapidly after initiation. Making the S-N data more dominated by crack initiation than crack path. Further supporting the latter point, both ⟨100⟩ & ⟨110⟩ having heterogeneous slip is thought to give them similar VHCF initiation times, which take longer than the more homogeneous slip of ⟨111⟩ [11].

Therefore, this work indicates that the N_f for a given σ_{amp} for crack initiation in both SXOs are similar, especially in the VHCF regime. The slightly greater fatigue strength of ⟨110⟩ is indicated in Ref [86]. The greater measured value is unlikely to be due to a lower FCGR, as the fracture path tortuosity of ⟨110⟩ is visually lower than ⟨100⟩, which would reduce roughness-induced crack closure and so should have a greater FCGR. Supporting this, anecdotally, the time to failure was more rapid in the ⟨110⟩ orientation than in the ⟨100⟩ orientation. Differences in FCGR will only manifest in the S-N curves if the technique does not outweigh

the FCG portion of N_f after initiation.

Fractography

Shearing mode fracture exclusively occurs in both SXOs, akin to the ambient results in chapter 6 and as observed in Refs [11, 53].

The ⟨110⟩ orientation shows no corner cracks, and failure for ⟨100⟩ is less dominated by them. Therefore, indicating that the new mesocantilever design has improved in reducing the corner stress concentration and that the SX anisotropy is a significant factor in their formation. Design improvements could be made to promote further single fatigue crack initiation and no corner cracks in the ⟨100⟩ orientation.

The FCGR experiments show that the <110><100> orientation is purely opening mode at RT [45, 54]. However, in fig. 2.17 (Ref [53]), it shows only shearing mode cracks, similar to the ⟨110⟩ samples in this work, which show a single {111} facet throughout the central region (up until shearing steps, etc.). For both SXOs in this thesis, their features best match fig. 2.17 from Ref [53] out the related literature involving Sakaguchi.

For the ⟨100⟩ samples, <100><XXX> FCGR tests are most relevant, with the <100><100> tests, which involve all four {111} planes, describe initiation, exit facets, and internal facets well. However, unlike their later work, a large {111} facet forms at initiation rather than at higher ΔK (true in both SXOs), likely due to differences in fatigue testing and the pre-notch. "Rooftop" (i.e., <100><110>) has been observed when FCG direction is along ⟨110⟩ in the ⟨100⟩ samples.

For the ⟨110⟩ samples, <110><YYY> FCGR tests are most relevant. The crack path along the cantilever surface follows the trace of <110><110>. However, the observed cantilever fracture surfaces do not appear like those in fig. 2.17 for <110><YYY>.

As the FCGR tests involving Sakaguchi use the $R > 0$, a pre-notch, and controlled loading, differences in the observed fractography (especially with crack growth) are expected. The pre-notch likely causes changes in the crack formation and progression due to the different stress states around the pre-notch vs an initiation

facet.

The most similar bending fatigue on a SXNBS (DD6) was done with larger scale specimens, with different SXOs, at RT, and conventional frequencies [104]. Their clearest micrograph of the whole fracture surface is of an unspecified SXO. However, it does show roof-top-like alternating facets in the crack propagation zone on both sides of equal amounts, with then a rough final fracture zone near the original neutral axis. The two equally sized propagation zones indicate that fatigue cracks initiated on both surfaces at similar times, unlike this thesis, where one side is larger from crack initiation and growth primarily from that surface. Additionally, the final fracture zone appears different in this thesis.

The fractograph in Ref [104] had CD disorientations from $\langle 100 \rangle$ that are comparable to those in this thesis ($\approx 3.5°$) and appear similar too. Showing a mixture of a few large $\{111\}$ facets, smaller rooftop fractures, and occasionally four different $\{111\}$ facets meeting at a point. For the RJS $\langle 100 \rangle$ samples, the fracture is typically dominated by one or two large $\{111\}$ facets from the initiation side, followed by some rooftop fractures with limited four-plane intersections apart from the exit facets. No fractographs at or near the $\langle 110 \rangle$ orientation were captured.

The shearing steps found under both orientations have been associated with elevated temperatures ($> 650\,°C$) rather than RT [59], and they are not reported or shown in Ref [104].

The pseudo-rooftop style fracture could not be found in the literature fractographs, so it could be novel. Its formation is likely SXO dependent as it occurs with $\langle 110 \rangle$ but not with $\langle 100 \rangle$. The RT testing and the experimental technique could also influence its occurrence.

The surface topology tends to become rounder on a smaller scale towards the end of failure for some of the single crack failure samples. This feature was not seen in the reviewed literature, so extensive cross-slip under the higher stresses near

failure is the proposed cause.

The transition from a single large {111} facet to these other morphologies occurs near mid-thickness in RJSP5, which could be related to the dislocation pile-up [63]. However, this is not the case in the other samples, so it is more likely related to the ΔK and FCG direction.

Not shown, but {111} crack bifurcation into the fracture surface also occurs in RJSK4 as seen in Ref [62].

No cracks were found to initiate from the dendrite boundaries.

Plasticity in the Crack Tip Vicinity

The dislocations imaged ahead of a fatigue crack tip along the crack plane in ECCI are similar for both SXOs. However, slip in the ⟨110⟩ shows that it is dominated by those ahead of the crack, whereas ⟨100⟩ shows parallel slip traces locally on either side of the crack path. This is likely due to less crack bifurcation in ⟨110⟩ as demonstrated by the arrested crack in fig. 7.59.

Ref [83] suggests that octahedral slip interactions form SFs for the ⟨110⟩ orientation, and the dark linear features are proposed to be them based on appearance, simulations, and only being seen in ⟨110⟩ and not in ⟨100⟩. The bright linear features appear differently and are thought to be dislocation pairs.

7.8 Chapter Summary

The following summarises the main points of this chapter.

1. Rotating the sample design on the SX foil to obtain consistent and desired SXOs has been achieved. The mesocantilevers' CDs were within tolerance from ⟨100⟩ and ⟨110⟩, with nearly identical FN. The consistency of the SXO is highlighted by the highly similar failure in the ⟨110⟩ samples.

2. Accounting for mechanical anisotropy led to an improved cantilever design, which reduced "corner" cracking and improved the stress distribution. No corner cracks were observed with the ⟨110⟩ orientation, but the ⟨100⟩ showed less dominant corner cracks than in the original design; further optimisation may be needed.
3. S-N results indicate little difference in fatigue performance. If drastic failure occurs quickly after initiation, as expected with the fatigue testing method used, it would indicate that the initiation lifetimes are similar between the two orientations. These two points agree with the arguments proposed in Ref [11]. The slightly higher ⟨110⟩ S-N could be partly due to a lower average FCGR seen in the literature [45, 53]. A similar S-N response conflicts with other literature [20, 83, 86] especially considering if FCGR is a metric of performance [22, 42, 45, 53, 55], but that could be due to having a limited dataset, sample inconsistency, or other factors affecting the fatigue life. With increasing N_f, the proportion of fatigue life from initiation increases at the expense of propagation [38].
4. The fracture for both SXOs indicates shearing mode failure in both fractography and ECCI, showing a lot of similarities and differences. The ⟨100⟩ results with the RJS design are similar to those with the original design.
5. ECCI shows more similarities than differences between the two SXOs, with the main differences being a narrower plastic zone ahead of the crack tip (virtually one slip plane) for ⟨110⟩ and slip virtually occurring only along the dominated slip trace. Stacking faults (SFs) can be seen only in ⟨110⟩ as mentioned in Ref [83].
6. Deformation simulations agree well with the experimental observations and the literature [11, 42]. The octahedral slip estimations from CPFE are generally reflected in the surface fracture behaviour of the samples, apart from when the sample deviates from the models too much via extensive FCG and/or local stress state. This shows promise in understanding the fatigue fracture

behaviour for SX materials and potentially PX materials (e.g., oligocrystalline); especially if surface fatigue crack initiation is of interest.

7. Following the previous point, low Schmid factor slip for the ⟨110⟩ orientation has been observed in ECCI and fractography. It is postulated to occur when a crack's local stress state deviates enough from simulations.
8. The fractographs are more similar to Ref [104] than uniaxial fatigue despite not being ultrasonic. Unlike Ref [104], in this work, initiation is more dominated by one side of the cantilever surface, and a more detailed explanation of its progression is given. Additionally, this work also has fractographs of samples CDs close to ⟨110⟩. They exhibited pseudo-rooftop fracture, which was not seen in the reviewed literature.
9. Like the bending microcantilever fatigue, shearing mode is the dominant failure mode, and it similarly shearing mode exit side facets {111} form.

Therefore, aims 4, 11, 12, and 13 have been achieved.

8
Final Remarks

It is useful to bring together and summarise many of the aims and objectives achieved in this thesis.

Overall Conclusions

A large number of novel experimental data has been generated and analysed for the SXNBS CMSX-4. Accompanying this research was method development required by the nature of the samples and test conditions.

The effects of environment and SXO on the fatigue performance for CMSX-4 have been done, achieving many of the aims set out earlier in the thesis.
Novel data, such as the fractographs, were generated.
Interestingly, the fatigue life data indicates that even at RT, an ultra-high vacuum increases the fatigue strength compared to air. The increased fatigue strength in vacuum was accompanied by an increase in opening mode fracture features, but its occurrence was not predicted based on the literature. It is proposed that the improved fatigue performance under vacuum is the reduced embrittlement ahead of the fatigue crack tip caused by oxygen. This thesis found no definitive answer for the cause of the opening mode under vacuum, but a proposed potential cause is localised self-heating at the crack tip, as vacuum reduces the heat loss mechanisms

of the system.

As expected, the in-air fatigue strength improved when going from RT to IT (i.e. 450 °C) and was accompanied by appreciable amounts of opening mode fracture facets. The opening facets and increased fatigue strength are expected and related because the γ' precipitate strengthens with temperature, increasing the flow stress of the alloy ($\therefore \uparrow$ fatigue strength) and hindering dislocation cutting in the precipitates (promoting opening fracture). Ultrasonic frequencies are thought to hinder opening mode fracture despite elevated temperatures, and so this work shows that opening mode can occur even at lower temperatures than those previously investigated. These results will be useful in modelling the high-frequency fatigue response of regions of the high-pressure turbine blade under intermediate temperatures.

The fatigue performance at 450 °C under vacuum could not be assessed due to testing challenges. The already mild oxidation in the 450 °C air tests became minimal under vacuum and concentrated on the fracture path and slip planes. The coarse oxidation on the opening crack path could not be found in the literature. The very mild oxidation allowed HR-EBSD and ECCI to be performed and compared with the RT air samples. ECCI and HR-EBSD were performed on the RT air and IT vacuum samples, showing that ECCI was better at capturing the micromechanics at those low dislocation density conditions. The ECCI was able to distinguish between the dislocation behaviour change of in-homogeneous (planar) to homogeneous going from RT to 450 °C as mentioned in Ref [42]. It captured the mixed-mode behaviour of a crack transitioning from shearing to opening, showing the planar to homogeneous transition and that opening occurred by two concurrent octahedral slip systems. The oxidation under 450 °C vacuum over the opening crack path appears coarser than on the slip planes and is not observed with the shearing cracks. This indicates that the homogeneous dislocation behaviour affects the oxidation response.

It has been shown by EBSD that the SXO of the mesocantilevers can be highly

controlled and repeatable, achieving virtually identical orientations within the same foil, similar between different foils, and that the CD can be successfully targeted to near a desired crystallographic direction. This can open up the SXO effect on fatigue not just to CMSX-4 but to other SX samples that can be made into mesocantilevers.

The crack path behaviour for shearing mode fracture of the ⟨100⟩ & ⟨110⟩ SXOs is seen to differ in ECCI by the differences in plasticity around the crack paths, which has been correlated with the slip in un-cracked CPFE models. Showing that ECCI and modelling can be linked to explain the general differences in fracture behaviour. In Refs [22, 44, 45, 55], CMSX-4 samples loaded along ⟨110⟩ compared to ⟨100⟩ show different FCGRs. As the ⟨100⟩ & ⟨110⟩ SXOs show similar S-N curves and as the samples fracture quickly after fatigue crack initiation (due to the UFR setup), this indicates that the initiation lives of both orientations are similar. Supported by the increased similarity in the VHCF regime where initiation dominates the life. Knowing that the initiation is the same for shearing mode cracks despite differences in SXO will be helpful in lifing models in the VHCF regime.

Updating the mesoscale cantilever design to reduce corner cracking highlights the importance of accounting for the SX anisotropy for any small-scale testing.

Industrial Relevance

The improved vacuum performance compared to air at room temperature indicates that subsurface fatigue crack initiation and growth that act under vacuum conditions will be slower, leading to a greater N_f for the same stress, and hence be less of a concern in engine components. On the other hand, this reinforces the need to account for oxygen embrittlement of fatigue cracks even under ultrasonic frequencies and at room temperature conditions.

The intermediate temperature results indicate an improved fatigue performance at 450 °C compared to room temperature when oxidised mildly. Adding more data to the literature for CMSX-4 (and similar SXNBSs) that 450 °C improves fatigue

performance in this less studied lower temperature range .
The single-crystal orientation (SXO) studies indicate that primary orientation deviations of $< 5°$ from $\langle 100 \rangle$ towards $\langle 110 \rangle$ in the fabrication of the turbine blades are unlikely to lead to significant changes in fatigue performance of the component. The orientation consistency and repeatability offer promise for developing models based on experimental data for all SXOs and at different temperatures, which can then be used for more accurate fatigue simulations of the blades.
The novel ECCI methodology and results show their promise as an alternative to TEM in the industry when characterising the failure of components.

Future Work

The vacuum environments at RT and at 450 °C show promise of the effect that air has on the fatigue response, and it needs to be investigated in more detail. The mechanism behind the unexpected increase of opening mode fracture occurrence at RT and its correlation with the increased fatigue strength should be investigated. That mechanism could be relevant to the lower-end in-service temperatures that the high-pressure turbine blades experience and/or is related to an unknown testing artefact (e.g., highly localised self-heating). As the literature is less clear whether vacuum is beneficial or not to fatigue (c.f. air) around 450 °C, collecting S-N data at this condition and comparing it with its in-air counterpart will help clarify this [5, 22, 79, 93]. Additionally, a fracture surface comparison will show whether or not ultrasonic frequencies kinetically limit oxidation and other environmental effects during fracture. One could assess the effect of frequency on the environmental effects by recording the FCGR with ΔK at different frequencies as done in Ref [140]. Alternatively, one can calculate the exposure time (t_E) and the saturation time (t_S) of the fatigue experiment, knowing the FCGR, to assess whether ultrasonic fatigue is insensitive to species in the environment [79, 141]. Both results will be useful in the lower-end in-service temperature fatigue response predictions for the blades.

To better identify (quantitatively) the defects in ECCI, further ECCI micrographs

of the same cracks under different diffraction conditions ($\underline{g}$) combined with software like *EMsoft* can be used. Helping associate defects with fatigue cracks in different environmental conditions. For 450 °C air, an optimised procedure to plasma polish the surface oxidation away to allow for ECCI would be useful for comparison between air and vacuum, which the literature is unclear on [5, 22, 79, 93].

The SXO S-N response can be further improved by doing it as a function of temperature. Additionally, having a FN of ⟨110⟩ rather than ⟨100⟩ would allow CDs of ⟨100⟩, ⟨110⟩, and ⟨111⟩ to be achievable and with values in between, allowing for the full SXO to be assessed. Assessing more than one FN will allow the secondary orientation to be assessed, which is known to affect the FCGR and change the activities of different slip systems, but less is known for the fatigue life and/or initiation. The small specimen size allows many samples to be made, and this would be needed for a complete SXO S-N response at various temperatures. Achieving this will improve the blade lifing models due to the complexities such as growth deviations, stresses acting in directions other than ⟨100⟩, and complex stress states around features like cooling channels and the fir tree.
Accompanying these small-scale tests with ECCI can elucidate the dislocation mechanisms for fatigue as a function of temperature, life, and SXO. This will directly aid lifing models for CMSX-4 and indirectly aid SXNBS alloy development and creep-fatigue dislocation modelling.

More advanced CPFE modelling with more realistic cracks being added into the model and adding pores could allow one to explain for the less preferential slip observed in ECCI (when the crack deviates too far from the un-cracked model).

Mesoscale cantilevers are useful for comparison with more advanced CPFE models, as their size means that the fracture surface behaviour with crack growth can be analysed and compared with a model. The sample size is large enough to contain features relevant to macroscale samples (dendrite boundaries, pores, etc.), but its

smaller size reduces potential computation costs. Differences between predicted and experimental paths will show which aspects of the model are inaccurate.

Combining uncracked CPFE modelling and ECCI has shown to be useful in bridging experimental and predicted slip behaviour; this could also be beneficial for small-scale PX samples. It could also be possible to introduce cracks in these models in the future.

Further developments need to be done on the mesoscale cantilever design to fully remove the occurrence of corner cracking for a ⟨100⟩ CD. Alternatively, knowing that SXO anisotropy causes it, see whether it could be solved by changing the FN.

Developing the ECCI technique and code further for more accurate orientation determinations (e.g., full rotations under two different tilts) and for combining EBSD map data with the BSE images to allow for improved PX sample analysis will be the next major developments. This technique can be applied to more materials and applications than featured in this thesis.

The UFR was set to promote unstable fracture. However, combining that with further fatigue tests where stable fracture is promoted, the proportions of initiation and crack growth in the N_f can be quantified in the S-N data in this thesis.

Appendices

A

Room Temperature Oxidation (glaze)

A.1 Fretting Fatigue Literature

Fretting could be considered irrelevant; however, as shown in later RT air fatigue tests, it is the likely explanation for an observed oxidation phenomenon.

Yuen et al. (1984) [142] state in their paper that for Inconel-718, an oxide fretting mechanism causes a thickened oxide to form, which wedges the crack and decreases the ΔK of the crack. Unfortunately, no images of this thickened oxide are in that paper, and Yuen's thesis has poorly scanned micrographs of it [143]. However, more modern papers do have micrographs of the glaze formed in wear fatigue tests [127, 144–148].

Even at RT and small sliding velocities, high transient temperatures can cause significantly thick surface oxide formation [127, § 4.7.2]. The general process of this oxide is that the "oxide repeatedly ruptures, reforms, and compacts due to crack surfaces crushing together" [142].

Sengupta's thesis (1993) mentions how even a uniaxial CT fatigue test of CMSX-4 under $R > 0$, their zigzag and irregular crack path nature can "enhance oxide-induced crack closure due to relative abrasion between fracture surfaces" [42, p. 61].

A. Room Temperature Oxidation (glaze)

For the wear-tested PX Udimet 720Li in Watkins' thesis [127, § 4.7.2] the effect of temperature is discussed. For $T < 250\,°C$, a compacted wear debris oxide layer forms, but "further sliding" removes it. For $T > 250\,°C$ under heat and pressure, this layer sinters to form the smooth and more stable **nickel oxide glaze**. The glaze appears as "discrete islands that appear on top of the compacted oxide layer" which are "usually visible as smooth dark regions with a bluish tint to the eye [and] stand proud of the surrounding area". Finally, for $T > 400\,°C$ glaze becomes "self-healing".

The two forms of this oxide are shown in Ref [127] (Figure 4.7.2.2), where the glaze is the smooth & darker oxide and the compacted oxide has unsintered brighter appearing wear debris.

Fretting fatigue of PX Inconel 718 has shown that the reduction in friction from the glaze affects the fatigue strength, with room temperature (20 °C) significantly lower in fatigue life than 280 °C and 540 °C. Their results are from fretting fatigue though where "a glaze not only reduces friction and wear but also prevents the surface damage that can lead to the initiation of fretting fatigue cracks" [127, § 4.7.3], which differs from the results on fatigue as stated in Yuen et al.'s work [142].

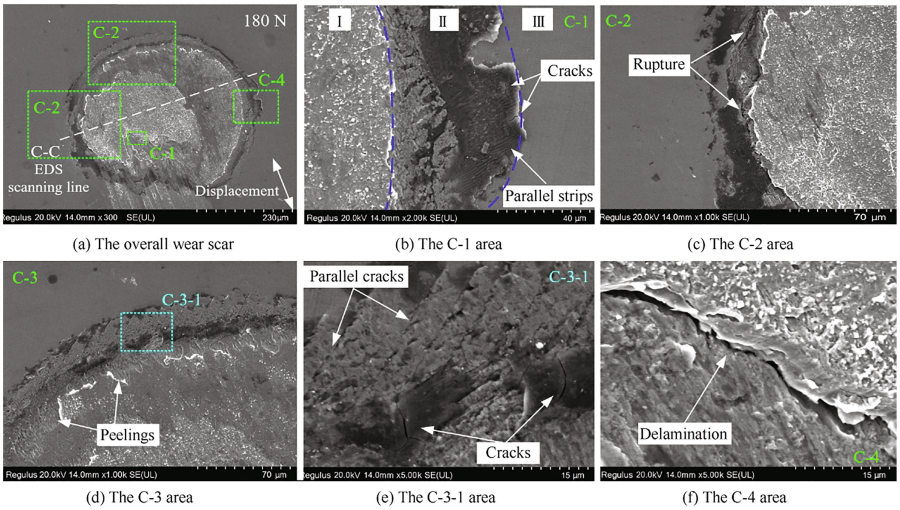
Higher temperatures have been reported to aid glaze formation and thus reduce the wear rate rather than increase it, with the data reported in [127, § 4.7.4.1] showing maximum removal rate at room temperature.

The oxide films in nickel alloys do not form below 0.5 - 1.0 mbar in air pressure, causing an increase in friction [127, § 4.7.4.3].

The greater the sliding velocity, the larger the debris particles and the greater the removal of debris, both stopping the particles from getting into wear tracks in fretting and forming the oxide layers [127, § 4.7.4.5]. This could impact the tests in this thesis, as when the cracks are short, the sliding velocity may be smaller than when it is larger, making it easier to form oxide layers initially on any steps on the

initiation fracture plane, but making it more challenging for the oxide layers to form as the crack grows.

Other examples of other micrographs showing the "glaze" and wear debris are shown in the following micrographs.



(a) The overall wear scar (b) The C-1 area (c) The C-2 area

(d) The C-3 area (e) The C-3-1 area (f) The C-4 area

Figure A.1: Micrograph of the compacted nickel oxides from a fret test. Figure from [146] (CC BY-NC-ND 4.0).

The rotary bending HCF work done by Shi et al. 2013 [58] on DD3 SXNBS @ 800°C 50 Hz in air shows on the {111} slip plane fractures a dark glaze-like phase (fig. A.2). However, they do not mention this dark phase outright, so it could also be the previously discussed glaze.

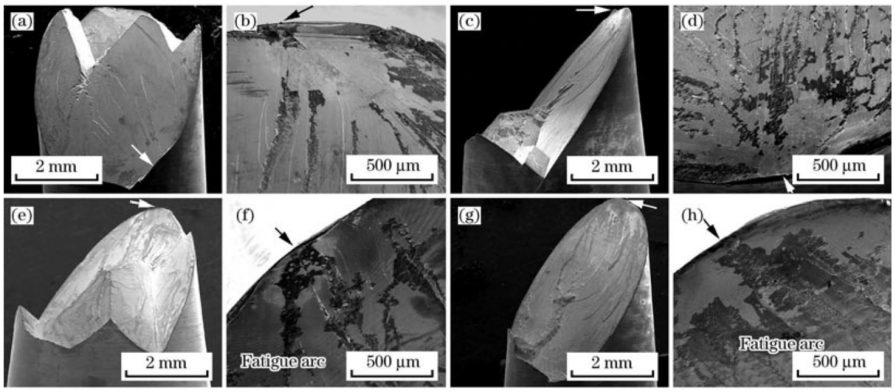


Figure A.2: Fractographs of the [001] loading direction orientated rotary bent samples. Figure from [58].

A.2 Experimental Observations

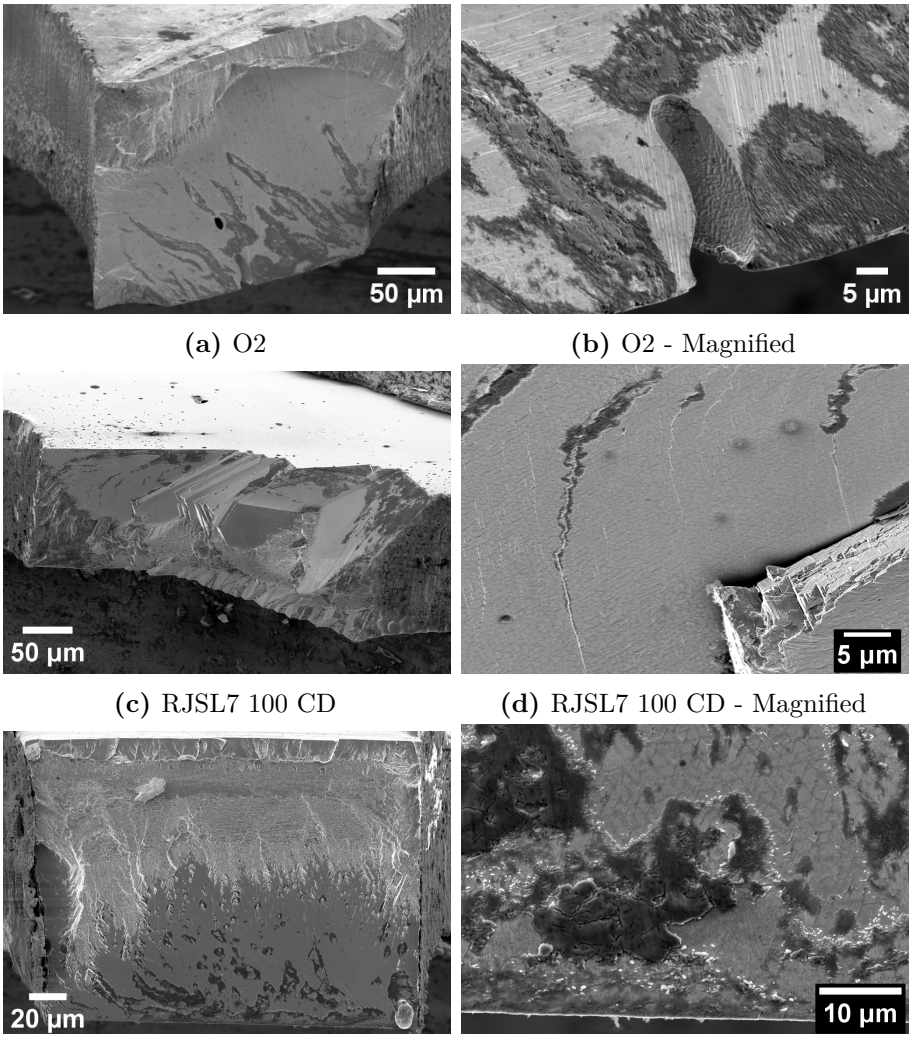
Across multiple samples in this ambient testing condition, darker islands of "finger-like" larger scale morphology were seen on {111} facets in a localised region. These features shared many similarities with the glaze in fretting fatigue. Therefore, this section will show when and where these features appear, give a detailed description, show EDX analysis results, and finally show that they are unlikely to be contaminants.

A.2.1 Occurrence & Description

Table A.1 shows when the glaze-like features have been observed using SE fractography, showing that it is observed only in the ambient conditions and with a significant proportion of the fracture surface ($^{19}/_{25}$). The distribution and extent of glaze can vary, as shown in fig. A.3. Observations using EDX, sample plasma cleaning, and FIB were done to rule out the possibility the glaze was a contaminant artefact.

Table A.1: Summary of glaze observations in fractography.

Condition	Fraction Observed	Sample IDs
RT air no-EP	4/8	O10,N5,M2,O2
RT air EP	6/6	J6,J4,I3,J10,I7,I9
RT vac. no-EP	0/6	-
RT air RJS 100 EP	3/5	RJS+ K6,M8,L7
RT air RJS 110 EP	6/6	RJS+ O6,N3,N1,O2,O8,P5
IT air EP	0/5	-



(a) O2 **(b)** O2 - Magnified

(c) RJSL7 100 CD **(d)** RJSL7 100 CD - Magnified

(e) RJSP5 110 CD **(f)** RJSP5 110 CD - Magnified

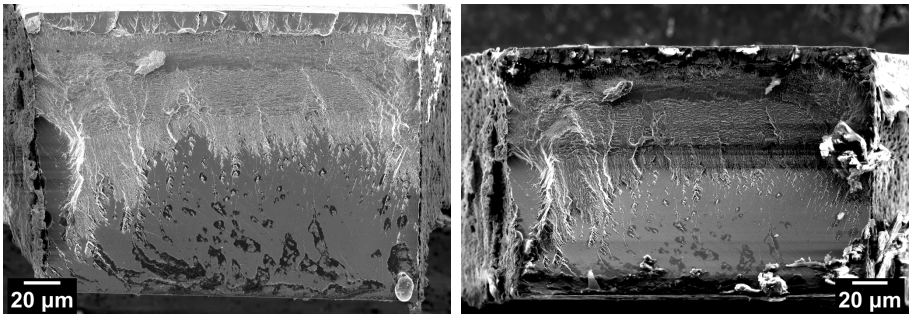
Figure A.3: Representative SE fractographs of the glaze-like features seen in RT air tests.

A.2.2 Characterisation

EDX

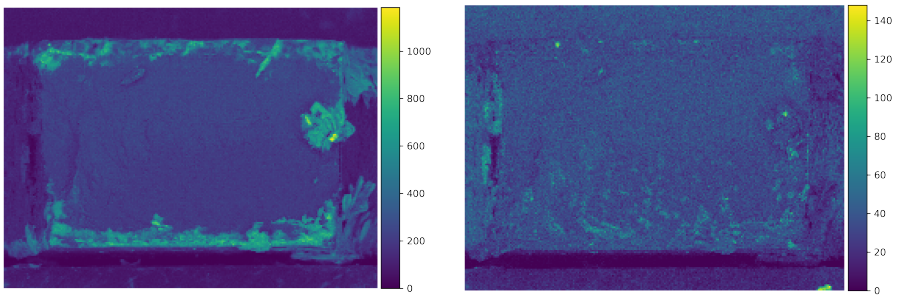
Significant focus has been put on sample RJSP5 because it is a good example of the oxidation features on its singular {111} facet (due to a ⟨110⟩ cantilever direction). Its analysis history is tilted fractography in the horizontal holder (HH); untitled fractography + 10 kV EDX in the vertical holder (VH); secondary ion mass spectrometry; plasma cleaned for 30 min; and finally, various tilt fractography + 4 kV EDX in the VH.

When changing holders (HH → VH), the sample was likely contaminated with hydrocarbons on its top and bottom surfaces when handling the sample with polynitrile gloves, the contamination is the dark charging regions in SE (fig. A.4) and in EDX show as high C:O. Figure A.4 shows that the oxide remains, appearing different from the contamination, and in EDX is differentiated by having a high O:C. Figures A.5, A.7 and A.8 highlight this count ratio difference as they show contaminant and oxide in the same map.



(a) HH low mag. **(b)** VH low mag.

Figure A.4: SE fractographs of sample RJSP5. The VH images (0°) were taken after the HH images (70°).

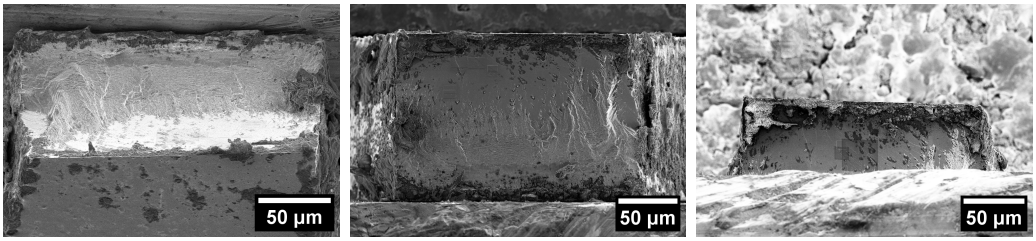


(a) C-Kα **(b)** O-Kα

Figure A.5: 10 kV EDX counts for RJSP5 under low magnification in the VH.

For the 4 kV EDX, the {111} facet normal incidence was found to be +35°, as shown in fig. A.6. Its SXO meant that in the VH, the normal incidence is ±35.3° or ±54.7°. EDX maps were acquired under each T_{stage} too.

Using 4 kV rather than 10 kV, the $\gamma - \gamma'$ microstructure is no longer visible in fig. A.7 unlike in fig. A.10, indicating that at 4 kV the excitation volume is small enough to not sample through the oxide glaze layer. The smaller bright



(a) −35° **(b)** 0° **(c)** 35°

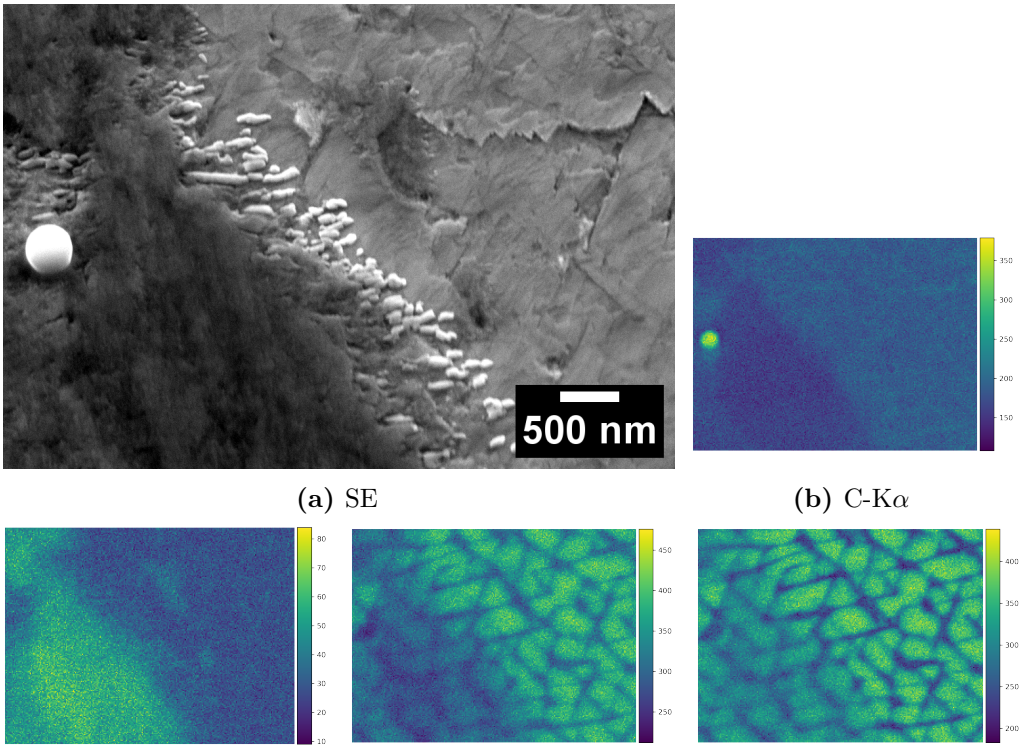
Figure A.6: RJSP5 post-FIB tilt investigation.

particles around the dark phase could not be discerned in EDX maps or line scans at 10 kV, showing the underlying $\gamma - \gamma'$ microstructure instead in fig. A.7, due to either them being too small compared to the excitation volume or that they are un-oxidised wear debris.

Figure A.8 is a 4 kV map of the glaze and small regions of C-containing contaminant. The contaminant not only morphologically looks different but has a significantly higher C-count and C:O ratio like that seen under low magnification. The large bright particle has a high Al-count and could be a larger version of the smaller ones seen.

Potential wear tracks (aka plowing) are seen on the glaze (fig. A.7a) like those in Refs [147, 148], and they roughly follow the crack growth direction (≈ vertical) if assuming the crack initiated from the large pore in the surface in the bottom right-hand corner in fig. A.4a.

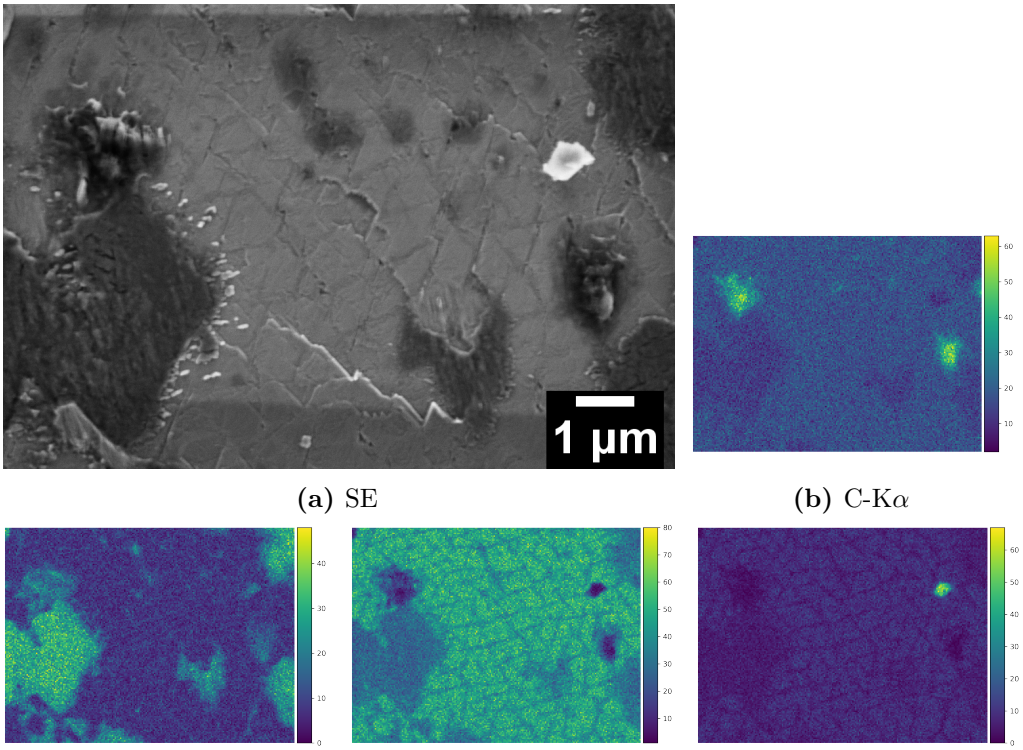
The glaze in a different region shows the same tracks along the same direction (N.B., the sample is rotated 180°). The bare superalloy between the glaze islands also shows tracks, so it could have been fretted and not formed a glaze, or the glaze has subsequently detached. The former is more likely, as underneath the dark oxide is a material that looks different than this marked superalloy region (shown later in figs. A.12 and A.13).



(a) SE **(b)** C-Kα

(c) O-Kα **(d)** Ni-Lα **(e)** Al-Kα

Figure A.7: 10 kV EDX count maps of sample RJSP5 under 20kx magnification.



(a) SE **(b)** C-Kα

(c) O-Kα **(d)** Ni-Lα **(e)** Al-Kα

Figure A.8: 4 kV EDX count maps of sample RJSP5 under 10kx magnification.

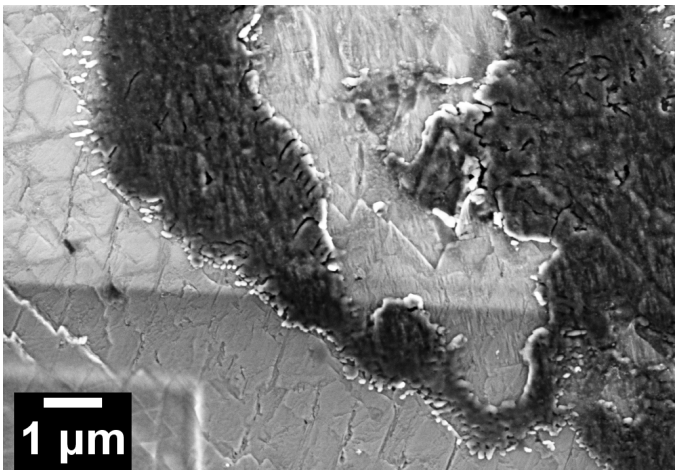


Figure A.9: $\times 10k$ magnification SE micrograph of 4 kV EDX map.

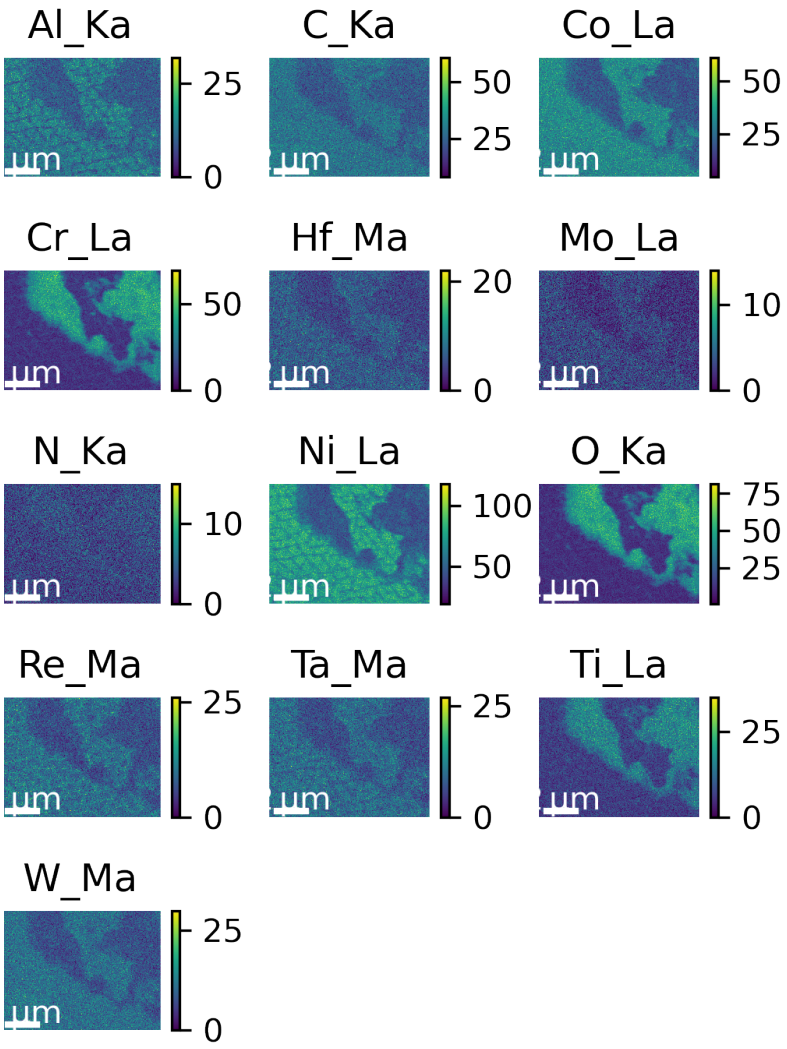
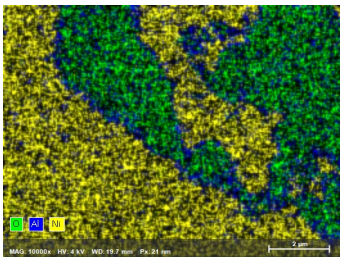


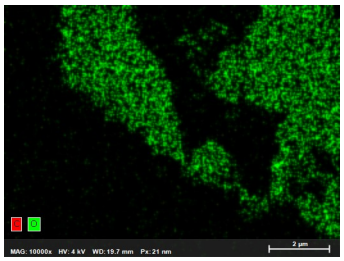
Figure A.10: EDX count maps for RJSP5 under $\times 10k$ magnification.

A. Room Temperature Oxidation (glaze)

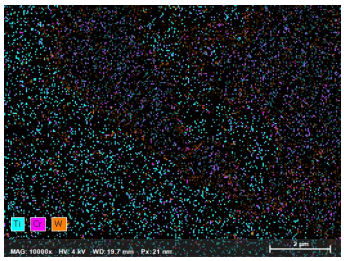
Quantification and phase analysis were done using *Bruker Esprit 2.3* software. Elements of significant counts and reasonable yields at 4 kV were chosen. The quantification in fig. A.11 showed that the small bright particles were Al enriched and that the general C:O ratio is very low (especially in the glaze). The software's three quantification modes tended to identify the bare superalloy (matrix), the glaze (dark), and often an extra Al-rich phase around the edges of the glaze (bright), coinciding with the small particles. The final phase quantification used the object mode that uses user-drawn ROI to identify phases. The quantification does indicate that the dark phase is an oxide glaze (enriched in Al−Ti−Cr), and the bare superalloy expectedly is Ni rich but low in O. The bright particles are generally intermediate between the two apart from their high Al−W but low Ti−Cr composition. However, unlike the other two regions, their non-flat topology could affect their counts and the calculated composition.



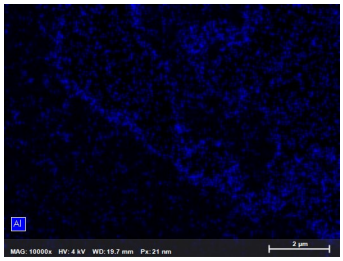
(a) O−Al−Ni smoothed.



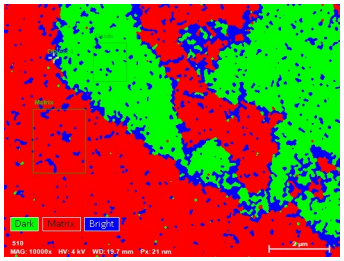
(b) C−O smoothed.



(c) Ti−Cr−W raw.



(d) Al smoothed.



(e) Phase Map.

	Atomic-% (norm.)	Area	Ch 1	Argus1	Argus2	Argus3	Argus4	O	Al	Ni	Ti	Cr	W	Co	C
■	Dark	32.9 %	--	--	--	--	--	26.53	7.45	0.85	4.41	2.90	1.84	0.03	0.06
■	Matrix	53.4 %	--	--	--	--	--	0.76	4.35	35.59	7.16	1.55	1.18	0.09	0.08
■	Bright	13.7 %	--	--	--	--	--	1.54	29.14	5.29	1.38	1.00	8.17	0.03	0.04
□	Unassigned	0.0 %	--	--	--	--	--	0.00	0.00	0.00	0.00	0.00	0.00	0.00	0.00

(f) Composition Output.

Figure A.11: RJSP5 post-FIB EDX atomic percent maps with 2x2 binning and absolute intensity. "Dark" in the table relates to the glaze, "matrix" refers to the bare superalloy, and "bright" refers to the smaller, brighter particles around the glaze.

FIB & Plasma Cleaning

Figure A.12 shows how one sample had a micrograph captured before the dark oxide phase could be fully removed by FIB, showing a less dark material underneath.

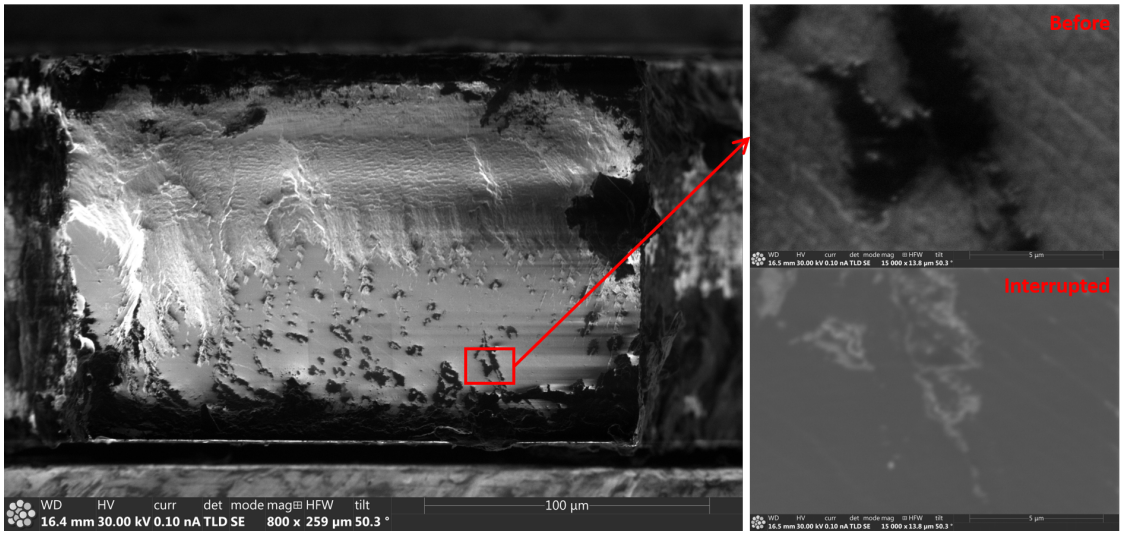
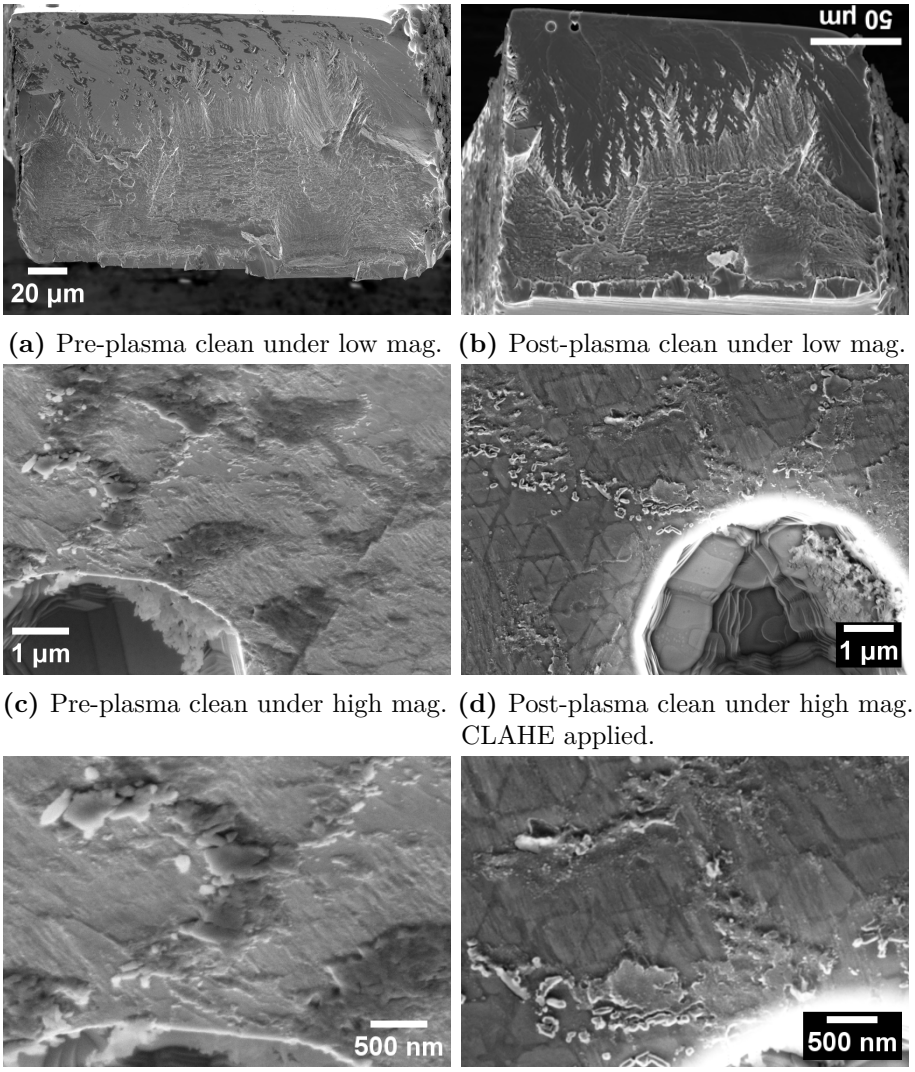


Figure A.12: Micrographs of RJSP5 explaining the in-situ process of the plasma-FIB milling process of the oxide. Collected with help from Yige Sun (Department of Materials, University of Oxford).

Another sample from the same test campaign showed a substantial, thick dark phase on top of its surface in the HH (no EDX), but after plasma cleaning for 1 h for ECCI a noticeable reduction in darkness occurred. Figure A.13 shows that it can look like a complete removal of the dark oxide under low magnifications. However, under high magnification of the same region, a raised material is in the same location as the dark phase before plasma cleaning. This material resembles the interrupted micrograph in fig. A.12, and EDX scans indicated a similar composition to the bare alloy.



(a) Pre-plasma clean under low mag. **(b)** Post-plasma clean under low mag.

(c) Pre-plasma clean under high mag. **(d)** Post-plasma clean under high mag. CLAHE applied.

(e) Crescent Before. **(f)** Crescent After.

Figure A.13: SE fractographs of sample RJSN1 before and after plasma cleaning.

A.2.3 Discussion

The observed microstructural features are thought to be an oxide glaze, as they resemble the oxide glazes in fretting fatigue literature for nickel alloys, appearing as dark raised islands with wear tracks and cracks, and as EDX suggests they are an oxide rather than a hydrocarbon contaminant.

The oxide glaze is only found in the largest {111} facet of each RT air fracture surface, although similar sized {111} facets in IT air should have a more stable glaze according to fret tests in Ref [127]. The lack of glaze for RT vacuum is expected due to the combination of low temperature and low p_{O_2}, as the chamber pressure is

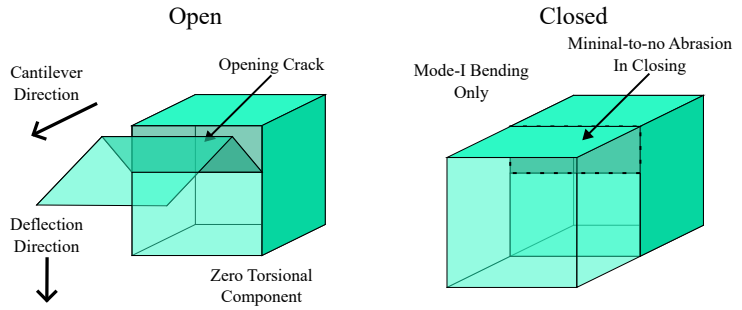
sufficiently below the minimum of 0.5-1.0 mbar for oxide films formation.

In terms of formation, using the above information, it is thought that the glaze forms because the large {111} facets self-fret under a sufficient p_{O_2} form a glaze. Ref [142] supports this with oxide thickening via fretting observed in a PX superalloy, and as the {111} facets can abrade one another in CMSX-4.

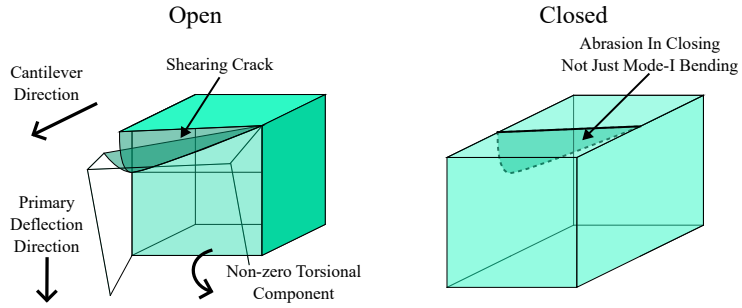
Figure A.14 is a schematic showing how opening mode cracks do not promote torsion or lateral movement of the crack against itself, as it promotes mode-I bending in the cantilever. Shearing cracks, on the other hand, also induce a torsional component to the bending alongside mode-I, manifesting as the observed "figures of eight"-like patterns in the laser deflection path. Therefore, the {100} facets of opening cracks will have less abrasion and glaze on them, and in samples where opening and shearing cracks coexist, like in IT air, the {100} facets reduce the overall torsional motion, reducing shear forces between shearing crack surfaces and reducing their formation of glaze. This is likely the reason for a lack of glaze at IT air. Ref [53] shows that stress intensity modes II and III can also occur on the crack with fractures like those seen in the mesocantilevers. Hence, these other modes can promote abrasion, unlike mode I.

The glaze being only on one large {111} facet could be due to them being the critical crack which initially dominates the cantilever deformation by bending and torsion, causing significant fretting on that facet. Once there are multiple {111} cracks, that reduces the torsion and shear force on that one facet, enhanced by facets of other {111} planes and by them being smaller, making the total crack path closer to being opening mode. Sample O8 of RT is a good example of this as it primarily comprises many small {111} facets and lacks a glaze.

Fractography and the FIB indicate that localised deviations of the {111} fracture plane along the large plane are where the glaze occurs. So, the glaze formation could be enhanced on these asperities of otherwise a planar surface. The similar EDX composition to the bare superalloy underneath the dark top layer indicates it is an asperity or unoxidised wear material, with the former being more likely.



(a) Opening



(b) Shearing

Figure A.14: Breathing opening and shearing mode cracks in ⟨100⟩ CD ⟨100⟩ FN sample. The opening crack would be in mode-I bending only, whilst the shearing would have some torsional component.

The potential poor adherence of the glaze to the fracture surface could skew the results to underestimating the fraction of samples exhibiting a glaze at RT air and their coverage on the surface. It could also be why plasma cleaning removed the darkness in fig. A.13 due to thermal coefficient mismatch or that sufficient mechanical agitation removed it.

A.2.4 Conclusions

1. The observed raised and isolated regions of a darker phase on large {111} facets on the fracture surface are an oxide glaze.
2. A mechanism has been proposed to explain their formation via fretting of {111} facets.
3. Their lack of glaze in the other environmental conditions is explained by the fracture causing less abrasion on a pair of {111} facets or due to insufficient p_{O_2} to form an oxide film.

4. Chemical analysis indicates that it is an oxide glaze rather than a (hydrocarbon) contamination.
5. Underneath the darker phase is a paler phase, which is likely asperities on the {111} phase where the glaze forms over.

B
Methods

Contents

B.1 Development: Laser Streak Length Measurement . . . 336
B.2 Convergence Studies 337
B.2.1 CPFE Convergence Study 338
B.3 Height Micrometer Part List 340
B.4 IT Vacuum Resonance Issues 341

B.1 Development: Laser Streak Length Measurement

Calibrating the camera via *Camera Calibrator* in MATLAB's Image Processing & Computer Vision toolbox was reasonably quick and easy. A chequered 4x7 calibration grid (10mm square length) grid was used with around 20 images. The camera intrinsics must also be calculated for image distortion correction. An angle limitation exists between the camera and the capture plane, so having it near-normal was desirable for fewer projection issues. Minimal difference between measuring from corrected images and manual pixel-to-mm calibration occurred for low-distortion lenses. Distortion correction is computationally expensive and slows the analysis rate. Reading frames from a long ".avi" video, correcting the frames, and performing

subsequent analysis, could take longer than recording the video.

The first computer vision-based method was done on fatigue videos of rolled steel samples. The rolling caused multiple parallel reflection lines. So, the first algorithms involved fitting shapes (e.g., ellipses, circles, rectangles) to these patterns from pre-recorded webcam videos.

The later smoother CMSX-4 samples had a more singular dot-like laser reflection. Allowing the one-line and two-dot methods to be used. Variation in the length of the laser line was observed and was called "wobbling". It is proposed that wobbling is due to the inconsistent frequency of the propriety power source for the UFR in combination with the camera frame rate. The variation was not significant enough to drastically affect the results but would lead to blurring the two bright ends of the laser streak and sometimes a range of values if it was unblurred. Using the bespoke power source with controlled frequencies led to less observed wobble.

B.2 Convergence Studies

Arutyunan converged the stress profiles and visually determined convergence [99, p. 68]. However, one can view convergence and ascertain the continuum value by the alteration of the x-axis to $1/node\,count$ [149] and $\log_4(mesh\,size)$ [150] and extrapolating via a linear fit to the continuum value (when $x = 0$). This extrapolation method has the benefit of justifying the degree of mesh fineness using the "true" value rather than the finest value, gives a %-error metric from this value, and allows the converged value to be predicted without having reached convergence (significant time reduction in assessing the degree of convergence).

The essential purpose for convergence is to have both the nominal stress and the hammer bending angle converge towards a value, thus causing the calculated ω value reported to be sufficiently accurate. The hammer bending angle converges the fastest, followed by axial stress and then Von Mises stress.

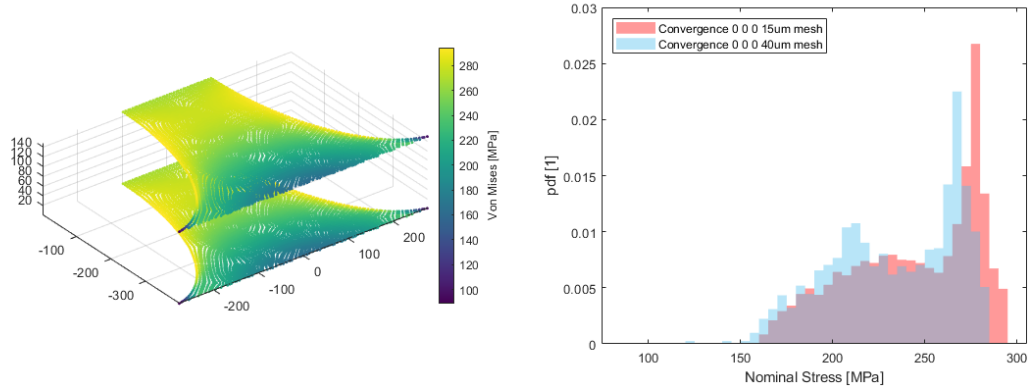
B.2.1 CPFE Convergence Study

A convergence study for the CPFE models of the RJS sample geometry has been performed using similar parameters in table 4.2. However, changes were made, that being: no calculation of slip or GND analysis; the model was purely elastic; a Bunge angle of [0°, 0°, 0°]; and the number of elements in the thickness was unrestricted (thus based on the seeded element size used). These conditions were used to minimise the time needed to perform the convergence study but should be a guide to the degree of accuracy for the CPFE models used.

The convergence criteria in this study is stress, so the region of the model to analyse and the subsequent metrics all affect the convergence study. Figure B.1a shows the area chosen in this study, being the top and bottom surface integration points of the main cantilever. The justification is that this region is under the highest stress compared to the subsurface and where fatigue failure is likely to initiate.

Figure B.1b shows two histograms of the surface stresses like in fig. B.1a of two different meshes, the location of the peak height changes with mesh refinement and bin width choice. Choosing the highest peak stress is more desirable than choosing the mean stress of the surface, as it inherently has to converge towards a bin value and because it represents the most frequent highest stress on the surface and is not biased by the lower stresses, which are of less concern in fatigue. The maximum stress can be chosen; however, this can be affected by stress singularities, but more importantly, it represents a less statistically significant volume.

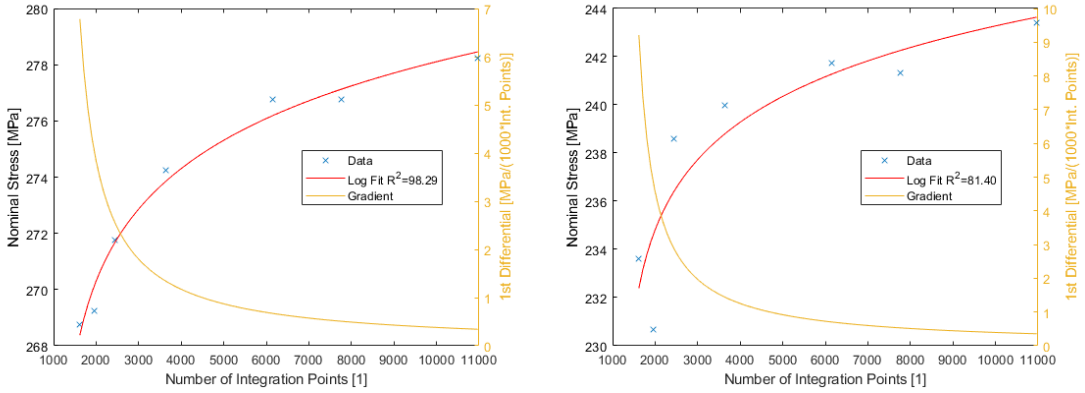
The more intuitive interpretation of convergence is shown in fig. B.2, showing how the mesh has not been fine enough for noise about the continuum value to have been achieved. It does, however, show a better fit to $y = a \cdot log(x+b)+c$ by selecting the highest peak in the histogram compared to choosing the mean, and it also shows the mean's lower stress bias. An exponential fit can also be applied, which gives a convergence value of 278 MPa (276.6-279.4 MPa 95% confidence interval) and $R^2 = 98.8\%$ for fig. B.2a.



(a) Von Mises scatter of the cantilever regions of interest.

(b) 5MPa histogram of Von Mises Stress of two different meshes.

Figure B.1: The choice of integration nodes to analyse and how to interpret the data for further analysis.



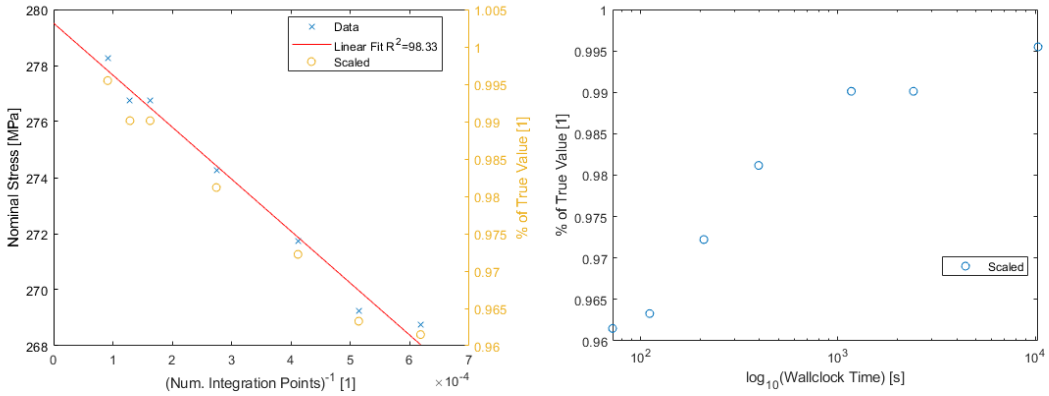
(a) Highest Peak (0.5MPa bin width).

(b) Mean.

Figure B.2: logarithmic fits for the nominal Von Mises stress against the number of integration nodes and the 1st differential of the fit.

In contrast, the less intuitive but more informative method is done by inverting the x-axis of fig. B.2 to produce a plot which shows a general linear trend. Similar to what was observed in fig. B.2, the highest bin stress offers a stronger linear fit than the mean stress (98.33% vs 83.31%); hence, that metric was chosen. When $x = 0$, the number of integration points is infinite (i.e. a continuum) and is approximate of the converged value, which for this is 279.5MPa (278.5-280.5MPa 95% confidence interval). The linear fit involves fewer parameters (two rather than three or four), which is likely the reason for its smaller 95% confidence interval range; hence its preference. It also produces a value that virtually concurs with the exponential

fitting method.



(a) Linear fit. **(b)** Time taken to run the model.

Figure B.3: Linear fitting method for assessing convergence (highest peak bin of 0.5MPa bin width used).

The final mesh size is chosen by comparing the computational run time for the FEM (see fig. B.2b) with the offset from the converged value. The 4$^{\text{th}}$ finest data point was found to be the best compromise (25.0µm input element size, 22.6µm characteristic element length), as it took a reasonable 6.6 minutes to run, which will only be longer with plasticity added, whilst still being 98.1% of the converged value. The finer mesh points took $>$ 19.5 minutes for only 99.0% and greater.

The consequence of this convergence study is that the conditions outlined in table 4.2 should be reasonably accurate for a design with no stress singularities based on these elastic results. This is especially the case considering the number of elements in the thickness is 10, greater than the six elements used in this convergence study.

B.3 Height Micrometer Part List

Table B.1: Mitutoyo height micrometer setup specification.

Part Description	Part ID
Probe	Mitutoyo 21AAA030 Needle Point (inch) steel L=.6"
Stand	Comparator Stand 235 mm
Digital Readout	Digimatic High Resolution /Functionality Indicator ID-H 30.4 mm / 1.2"
Gauge Block	0.50 mm Steel Gauge Block, Grade 1

B.4 IT Vacuum Resonance Issues

A main cause of this was the unusual non-linearity of the α_{amp} with input voltage relation that would develop despite occurring even at low α_{amp} values and no apparent damage when the samples were taken out. The non-linearity only worsened with increasing voltage, essentially plateauing in value to one where obtaining failure or cracking was not achievable.

After trying to achieve failure for a few samples, it was found that the f_D needed to be lowered dynamically (c.f. the frequency sweep value) during testing to achieve maximum α_{amp} for that voltage. If left for several minutes after operating, the optimum f_D would be close to return to its original value. If the fatigue duration was sufficiently long, a steady state optimum f_D would often be achieved, and conversely, for a short test, the transient decrease was small enough not to require in-situ optimisation.

The optimum f_D also changed with driving voltage, being different from the low voltage frequency sweeps. the value of f_D often decreased with increasing voltage, which led to the non-linearity. Hence, even though the short tests did not show a significant change in L during testing, having the constant f_D but increasing voltage meant that the power transfer progressively worsened, leading to the near plateau response.

C

Calculations & Equations

Contents

C.1 Pore Distribution Fitting Equations 342
C.2 Oxygen Partial Pressure 343
C.3 ECCI Probe Depth 344
C.4 Stage Tilt Correction 344
C.5 Plastic Zone 345

C.1 Pore Distribution Fitting Equations

$$s = \frac{x - \mu}{\sigma} \tag{C.1}$$

Where x is the value assessed, μ is the location parameter, and σ is the scale parameter.

The generalised extreme value (GEV) probability density function fit equation used by MATLAB$^{\text{TM}1}$ is:

$$y_{GEV} = \begin{cases} \sigma^{-1} \exp\left(-e^{-s} - s\right), & \text{for } k = 0 \\ \sigma^{-1}(1+sk)^{-1-k^{-1}} \exp\left(-(1+sk)^{k^{-1}}\right), & \text{for } sk > -1 \\ 0, & \text{otherwise} \end{cases} \tag{C.2}$$

Where k is the shape parameter. The first case is not considered as $k > 0$ in this work.

[1] `https://uk.mathworks.com/help/stats/generalized-extreme-value-distribution.html`

The extreme value (EV) probability density function fit equation used by MATLAB^{TM2} is:

$$y_{EV} = \sigma^{-1} \exp(s) \exp\left(-e^{s}\right) \tag{C.3}$$

The lognormal probability density function fit equation used by MATLAB^{TM3} is:

$$y_{LN} = \frac{1}{x\sigma\sqrt{2\pi}} \exp\left(\frac{-(\log x - \mu)^2}{2\sigma^2}\right) \tag{C.4}$$

Where x is the value assessed, μ and σ are the mean and the standard deviation of the logarithmic values, respectively.

C.2 Oxygen Partial Pressure

Ref [151] was used to estimate the p_{O_2} under the different conditions.

Room Temperature Air

First, assume that the ambient lab air has 50% relative humidity and is under room temperature and pressure. Based on sources the volume fraction of dry air that is $O_{2(g)}$ is 20.95 Vol.%. Then the initial p_{O_2} in ambient conditions is $p_{O_2} \approx (1013.25 - (23.37\frac{50}{100}))$mbar $\times \frac{20.95}{100} = 209.83$mbar, which in percentage pressure is $\approx \frac{207.28}{1013.25} = 20.71\%$.

Room Temperature Vacuum

Following from room temperature air, the initial air composition is 20.71% $O_{2(g)}$, so pumping the chamber at room temperature, to chamber pressures of 10^{-8}-10^{-6} mbar reduces the p_{O_2} down to 2.07×10^{-9} to 2.07×10^{-7}mbar.

Intermediate Temperature Air

Ignoring water vapour at 450 °C as the relative humidity cannot be calculated at this temperature, then the relative humidity is 0%, so at atmospheric pressure $p_{O_2} \approx 212$ mbar.

[2] https://uk.mathworks.com/help/stats/extreme-value-distribution.html
[3] https://uk.mathworks.com/help/stats/lognormal-distribution.html

Intermediate Temperature Vacuum

Also ignoring relative humidity like previously, using 20.95 Vol.% $O_{2(g)}$, then $p_{O_2} \approx 1.2$ - 1.4×10^{-8} mbar.

C.3 ECCI Probe Depth

The t_g from which the BSE signal returns to form the ECCI signal is related to the extinction distance (ξ_g) for a given diffraction vector ($\underline{g}$). The probe depth is reported to a factor of 5 [138] or 5-6 [119] times that of ξ_g. An equation to calculate ξ_g can be found in Ref [110, p. 333]. However, it is easier to use EMsoft to calculate it as done in Ref [152]. The ξ_g and t_g values for $\underline{g} = 200$ and $\underline{g} = 220$ in table C.1.

Table C.1: Extinction distance (ξ_g) calculations for $hkl = \{2, 0, 0\}$ and $hkl = \{2, 2, 0\}$ diffraction vector ($\underline{g}$) in Ni (γ) and Ni_3Al (γ'). In EMsoft V5.0 (Windows build-date 2023-06-08) [131], there are three cases for the EMxtalinfo executable; however, only cases 1 (Doyle-Turner/Smith-Burge with no absorption) & 3 (Weickenmeiner-Kohl with absorption) are written. For Ni, its inputs were $a = b = c = 3.524$ nm, space group 225, B=0.0035. An accelerating voltage of 30 kV and a camera length of 10 mm were used.

Phase	ξ_{200} [nm]	ξ_{220} [nm]	t_{200} [nm]	t_{220} [nm]
Ni Case 1	18.30	26.66	91.5	133.3
Ni Case 3	18.62	26.64	93.1	133.2
Ni_3Al Case 1	20.60	30.70	103.0	153.5
Ni_3Al Case 3	20.91	30.64	104.6	153.2

The ξ_g values for $\underline{g} = 200$ is comparable to the reported 18 nm calculated by Ref [31] which used Ref [110].

C.4 Stage Tilt Correction

To correct for stage tilt, the original image height (H_{orig}) is extended by the amount of stage tilt (θ) to become a new height of H_{corr}.

$$H_{corr} = H_{orig} \times {}^{1}/_{\cos\theta} \tag{C.5}$$

C.5 Plastic Zone

Refs [153–156] all mention and discuss the crack tip plasticity for SXNBSs. It is important to consider as "when investigating fracture processes in confined volumes, where crack tip plasticity predominates, it is important to follow and interpret the plastic zone evolution" [155, p. 19].

Compton & Martin (1984) state that for SXNBSs, "Measurements of crack tip plasticity have shown that the size of the plastic zone associated with a propagating fatigue crack is a complex function of the applied stress intensity, the temperature and the frequency of cycling" [156, p. 43]. Their paper uses a linear elastic fracture mechanics equation to calculate the plastic zone for CT tests of MAR-M-200 of <100><100> and compares it with experimental results from selected area electron channelling patterns.

$$r_p = \alpha \left(\frac{K_{max}}{\sigma_y} \right)^2 \tag{C.6}$$

Here, α has a value around 0.206 to 0.207.
Sengupta (1993) has a different metric for the plastic zone, where r_p is in m and N is the number of dislocations in the plastic zone, and the constant is in $^{m}/_{cycle^2}$.

$$r_p = 4.67 \times 10^{-12} N^2 \tag{C.7}$$

In the review paper by Ast et al. (2019), they give the Irwin **plane strain** plastic zone radius as:

$$r_p = \frac{1}{3\pi} \left(\frac{K_I}{\sigma_y} \right)^2 \tag{C.8}$$

The authors warn of smaller specimens having sizes comparable to r_p, a problem in most metals as the small-scale yielding approximation becomes invalid. However, as σ_y increases due to the size-effect, r_p also decreases.

Forest (2022) warns of the complexity of the crack paths in SXNBSs, stating that CMSX-4 can have a lot of shearing mode fracture that frequently branches and bifurcates, making continuum models and fracture mechanics challenging to do

[154, p. 461].

The most appropriate piece of literature relating to this work is that done by Wilkinson & Hirsch (1997), where the plastic zone was calculated for the SRR99 SXNBS [157], which can do both plane strain and plane stress [153]. The fatigue test was done at 650 °C with $R = 0.1$ and $f = 10\,\text{Hz}$ in a CT fatigue test. The plastic zone appears as a contrast around the wake of the crack and ahead of it, but the contrast ahead is weaker than the wake [112, 157].

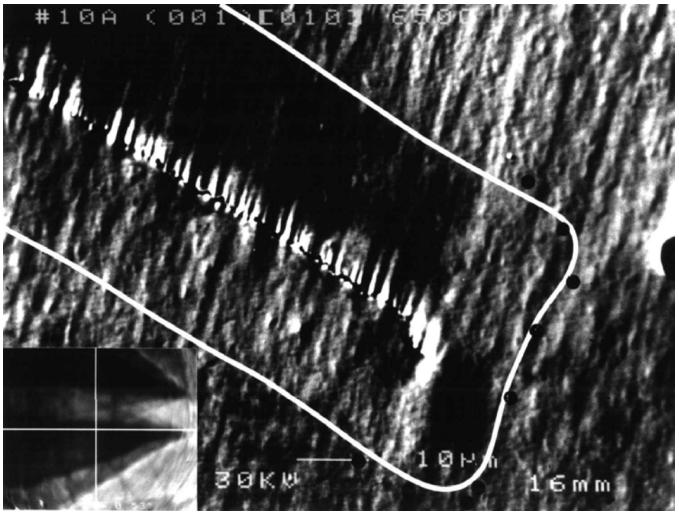


Figure C.1: ECCI of plastic zone imaged under $\underline{g} = 002$ where the crack plane is (001) with a [010] crack growth direction. Figure from [157].

In a review paper [153], it was stated that the r_p can also be defined as for a fatigued superalloy, where $^{da}/_{dn}$ is the FCG rate.

$$r_p = \left(\frac{da}{dn}\right)^{0.5} \tag{C.9}$$

In the book "Fracture Mechanics" by Anderson (2017) [158, § 2.8], the following is the equation for the plastic zone size on the crack plane using the Irwin approach for **plane stress**.

$$r_p = \frac{1}{\pi}\left(\frac{K_I}{\sigma_y}\right)^2 \tag{C.10}$$

The following is for **plain strain**:

$$r_p = \frac{1}{3\pi}\left(\frac{K_I}{\sigma_y}\right)^2 \tag{C.11}$$

Approximations

According to Ref [35, 42] the macroscale σ_y of CMSX-4 at RT is around 900 MPa to 950 MPa. Using the appropriate assumption that the bending stress is the dominant stress, essentially mode I loading, and approximating fracture to that of a single edge notched "homogeneous cantilever under Mode I loading" like in Ref [126]. For a 150 µm thick cantilever under maximum bending stress of 600 MPa, K_I as the crack grows through the cantilever to a length of a is shown below along with the Irwin plastic zone calculations.

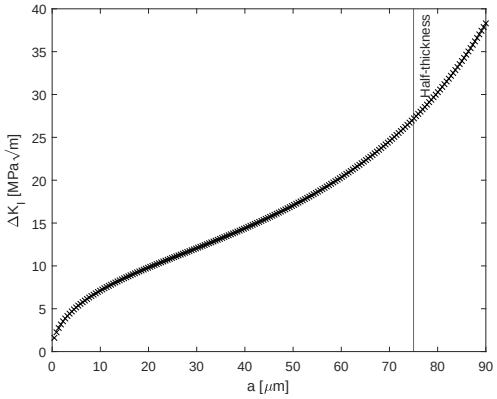


Figure C.2: K_I as a function of crack length a.

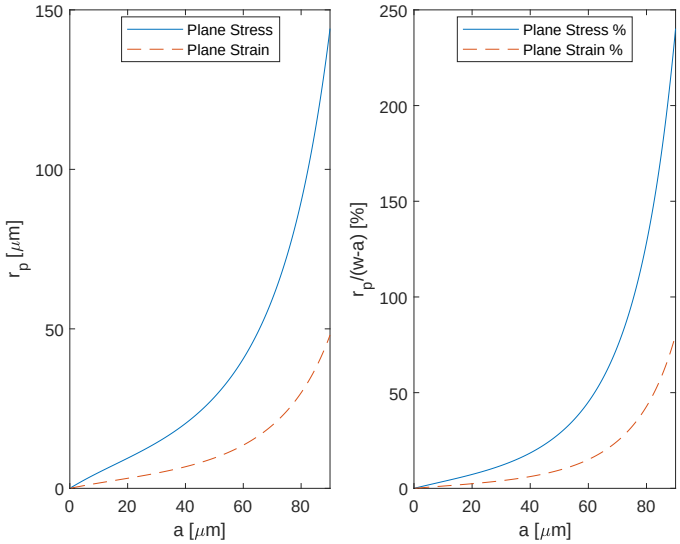


Figure C.3: Plastic zone size ahead of the crack tip as a function of crack length a in mode I loading.

D
Supplementary Micrographs

Contents

D.1 Radiographs 348
D.2 EDX 350
D.3 ECCI 351
D.3.1 C9 450C Vac 351
D.3.2 H8 352
D.3.3 I5 356
D.3.4 RJSN1 ECPs 359
D.3.5 RJSN1 Diffraction Conditions 359
D.4 MTEX Orientation on Micrographs 361

D.1 Radiographs

Figure D.1 shows how the cantilevers can be machined primarily within the darker dendritic or the brighter & more porous interdendritic areas. Figure D.2 shows that taking a 2D area fraction leads to overestimated mean area fraction porosity values of 1.99% for interdendritic, 1.79% for mixed, and 1.06% for dendritic. Hence, in the main thesis, a 3D estimate is taken, however, that assumes spheres with radii from the circular equivalent diameters of the pores in the 2D radiographs.

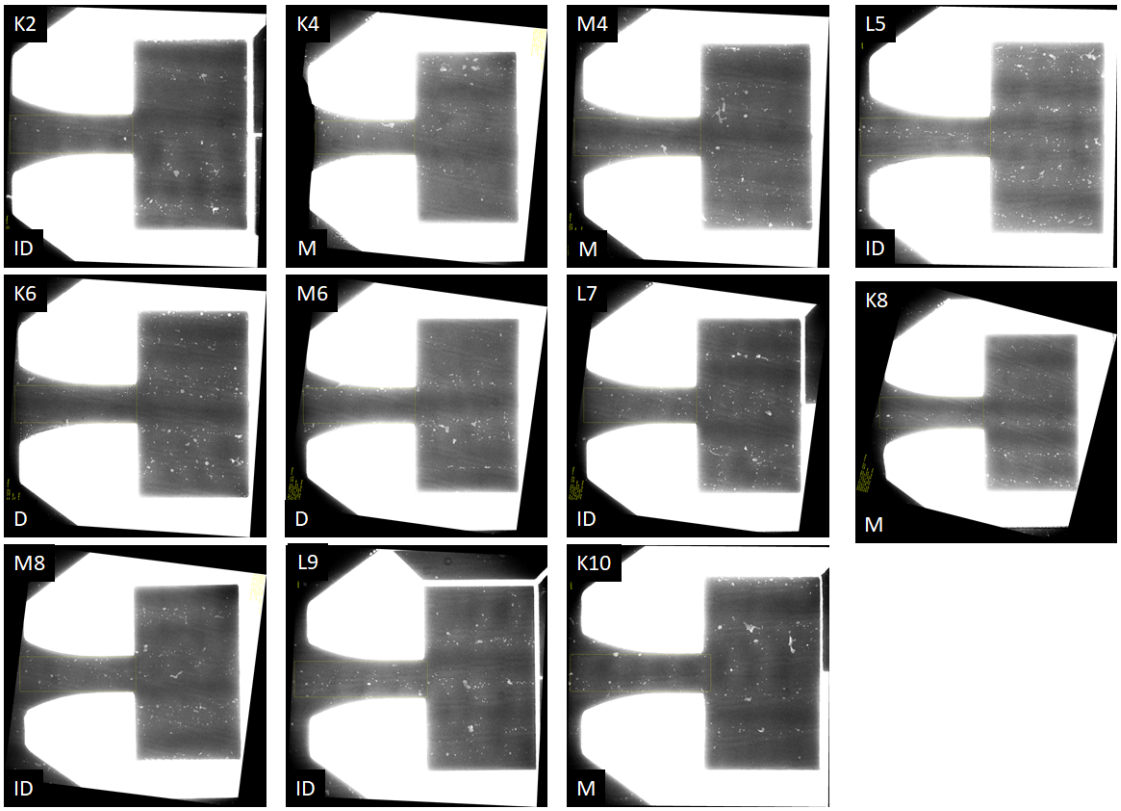


Figure D.1: Contrast-enhanced radiographs of 11 meso-cantilevers tested from the non-electropolished RT air campaign. The notations for the predominant microstructure within the cantilevers are **I** = interdendritic, **D** = dendritic, & **M** = mixed.

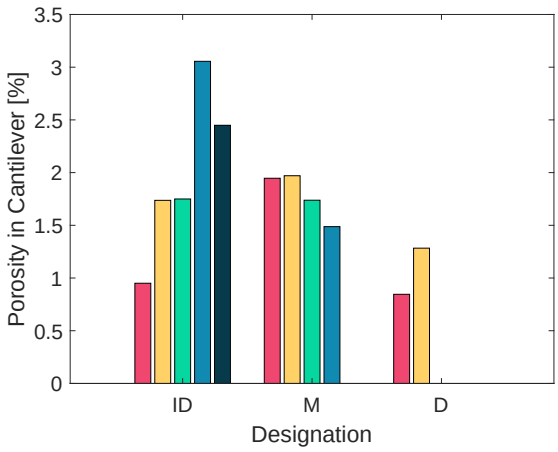
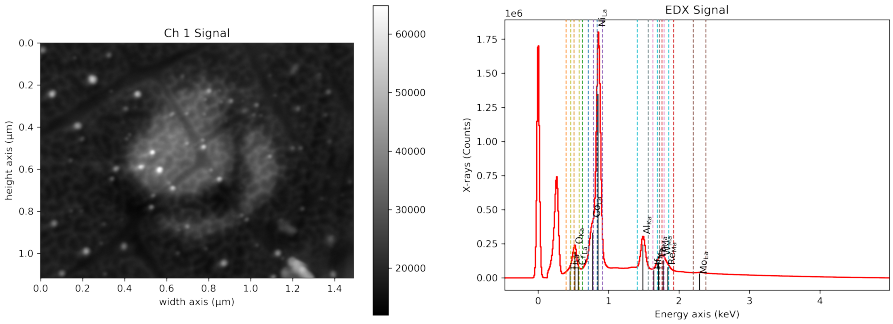
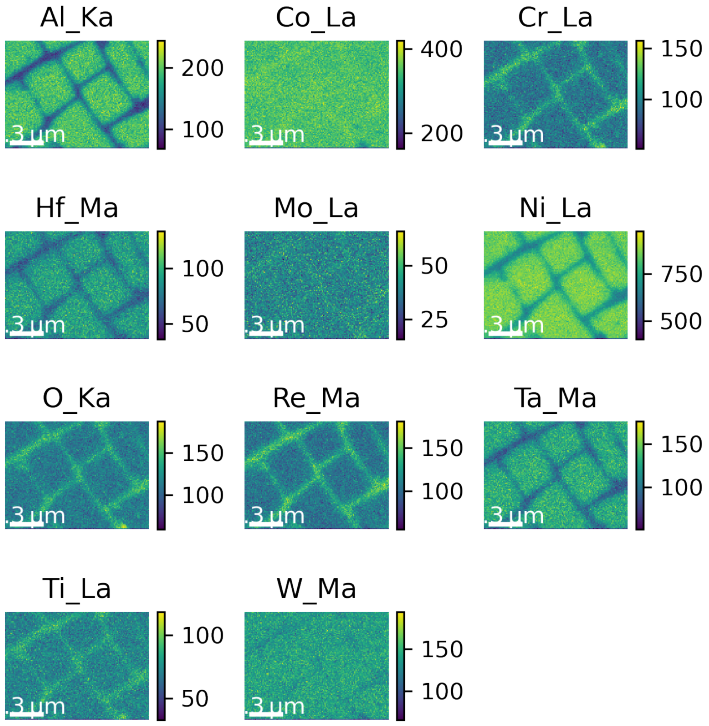


Figure D.2: 2D area fraction cantilever porosity in cantilever region of radiographs. "ID" is interdendritic, "M" is mixed, and "D" is dendritic.

D.2 EDX



(a) SE image. **(b)** Spectrum.

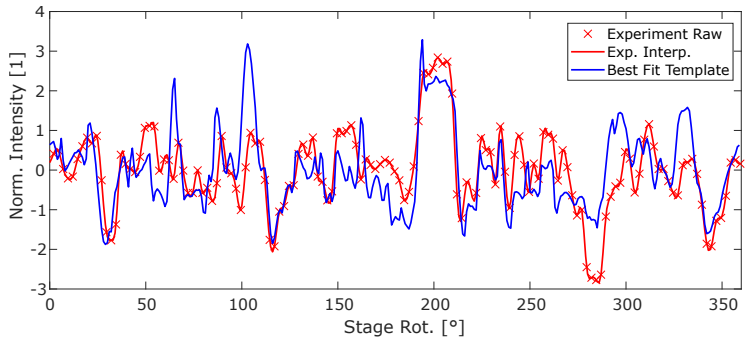


(c) Count maps.

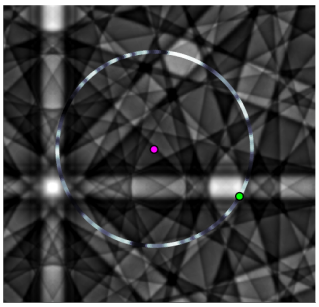
Figure D.3: EDX (5 kV) of microstructure of C9. Down-sampling value of 10.

D.3 ECCI

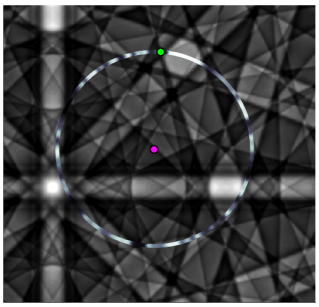
D.3.1 C9 450C Vac



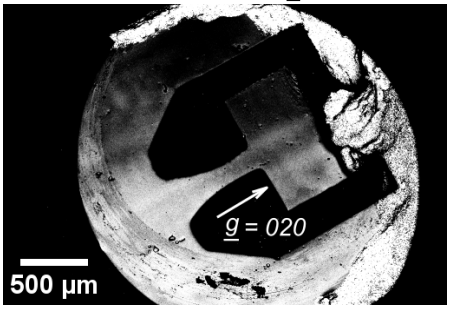
(a) Intensity profile matching.



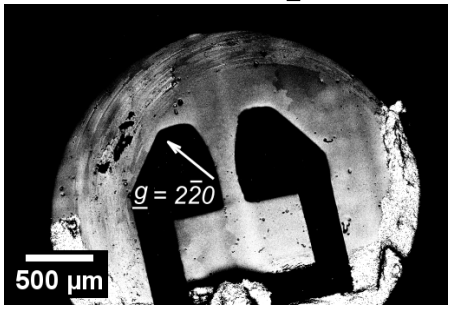
(b) R_{stage} 101° i.e. $\underline{g} = [020]$.



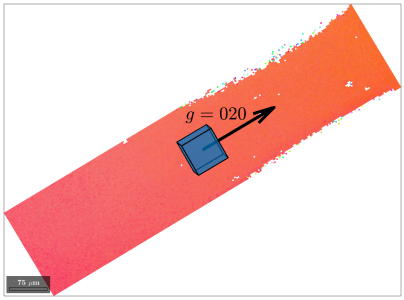
(c) R_{stage} 215° i.e. $\underline{g} \approx [2\bar{2}0]$.



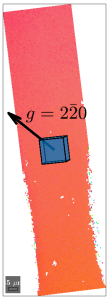
(d) $\underline{g} = [020]$



(e) $\underline{g} = [2\bar{2}0]$



(f) $\underline{g} = [020]$



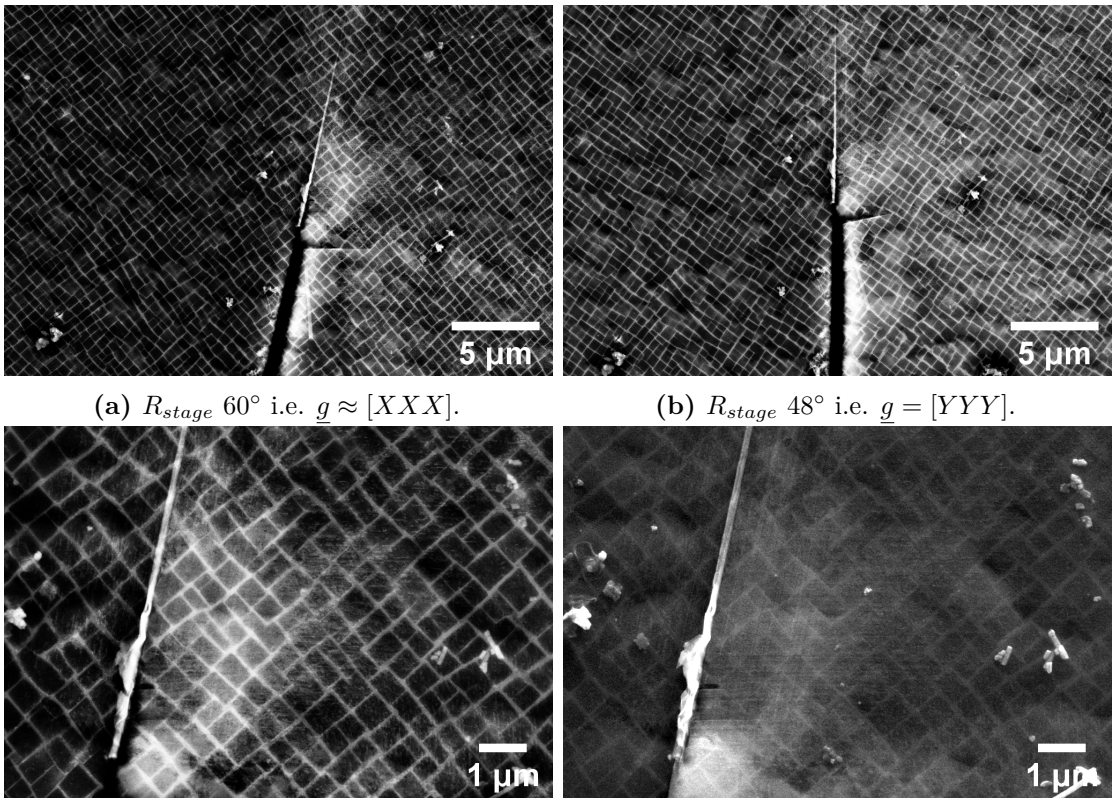
(g) $\underline{g} = [2\bar{2}0]$

Figure D.4: Identification of the two $\underline{g}$ conditions for sample C9. Done by combining the novel ECCI technique, BSE ECP micrographs, and the MTEX EBSD data. $T_{stage} = 10°$.

D.3.2 H8

The ECCI was collected on the exit side where generally there are more slip traces and plasticity. Figure D.5 shows the analysed shearing mode crack with a large degree of deformation and its sub-crack. Note that the two {111} active slip systems are parallel to the two crack paths.

In fig. D.5 and fig. D.6 one can observe a high degree of non-threading dislocations that are parallel with the sub-crack. They show strong contrast at R_{stage} 60°, virtually disappear under 48°, and show little-to-no contrast under 24°. Under 48°, many dark-bright splits are observed, likely the dislocations' surface relaxations from them entering the surface. Therefore, they are not completely non-threading.



(a) R_{stage} 60° i.e. $\underline{g} \approx [XXX]$.

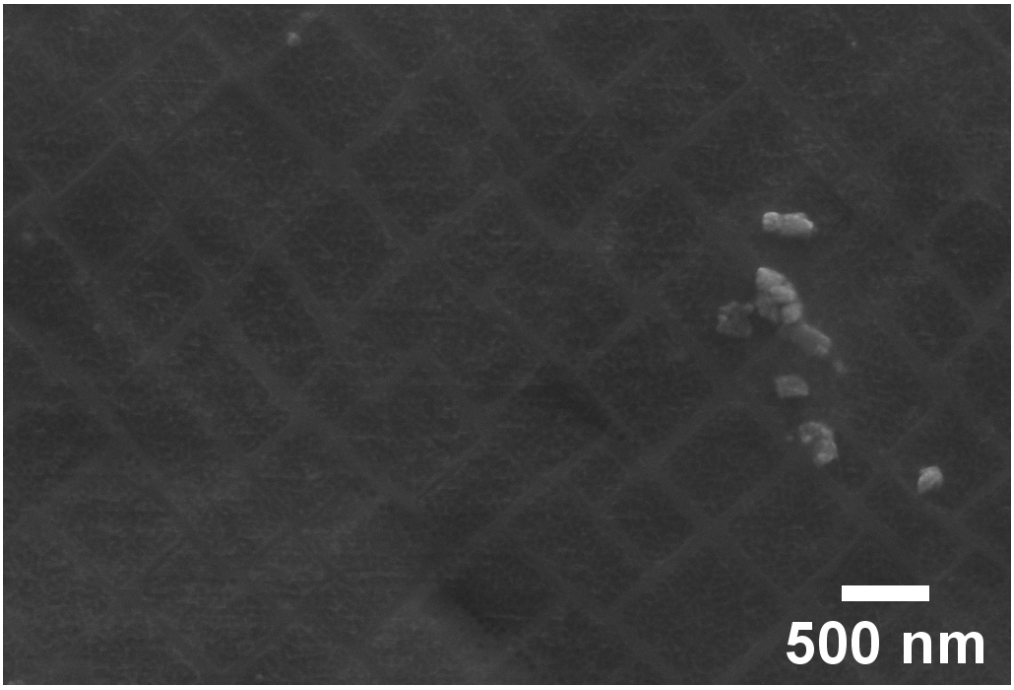
(b) R_{stage} 48° i.e. $\underline{g} = [YYY]$.

(c) R_{stage} 60° magnified BSE.

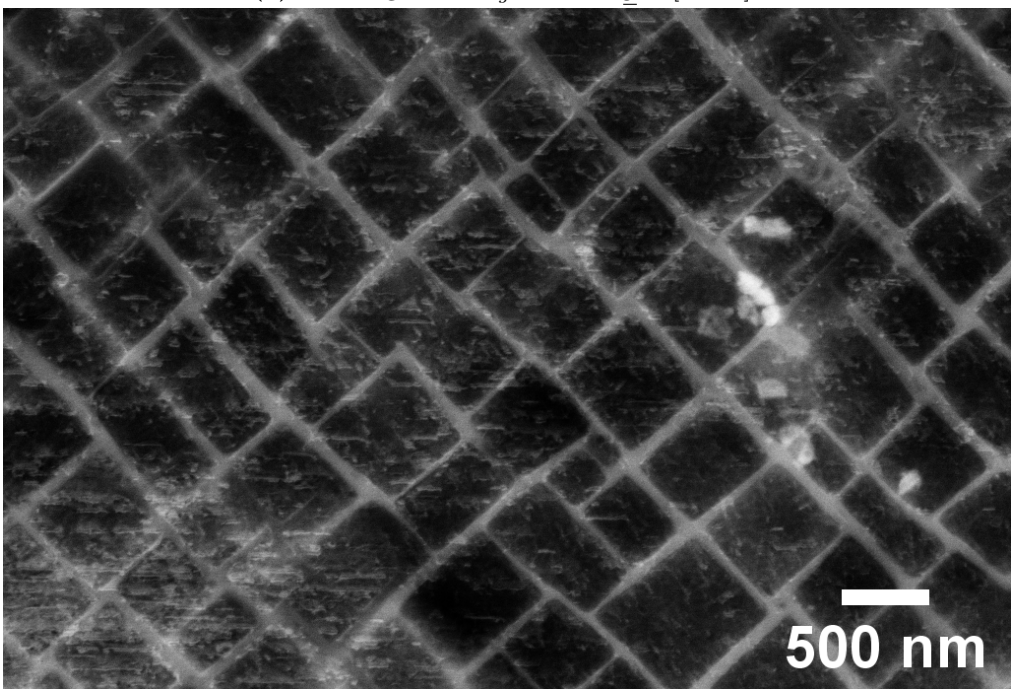
(d) R_{stage} 60° magnified & contrast-enhanced SE.

Figure D.5: BSE images collected *2023-07-24* on the Merlin SEM. T_{stage} 8°.

Figure D.7 focuses on the region ahead of the main crack path, where, similar to the previous region, many non-threading dislocations parallel to the main crack path occur.



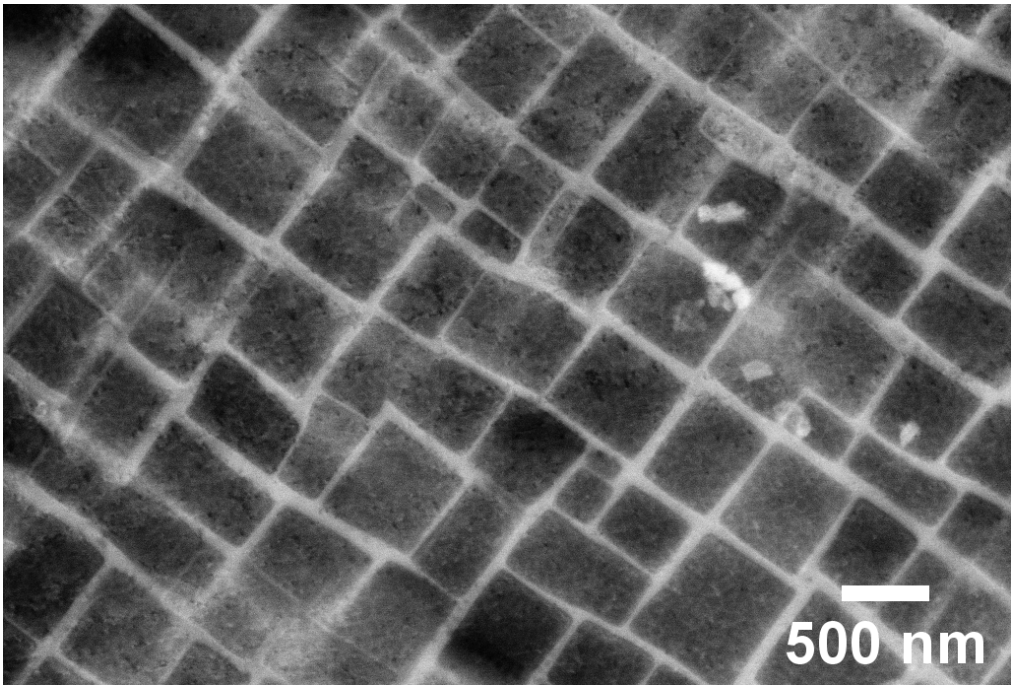
(a) SE image @ R_{stage} 60° i.e. $\underline{g} = [YYY]$.



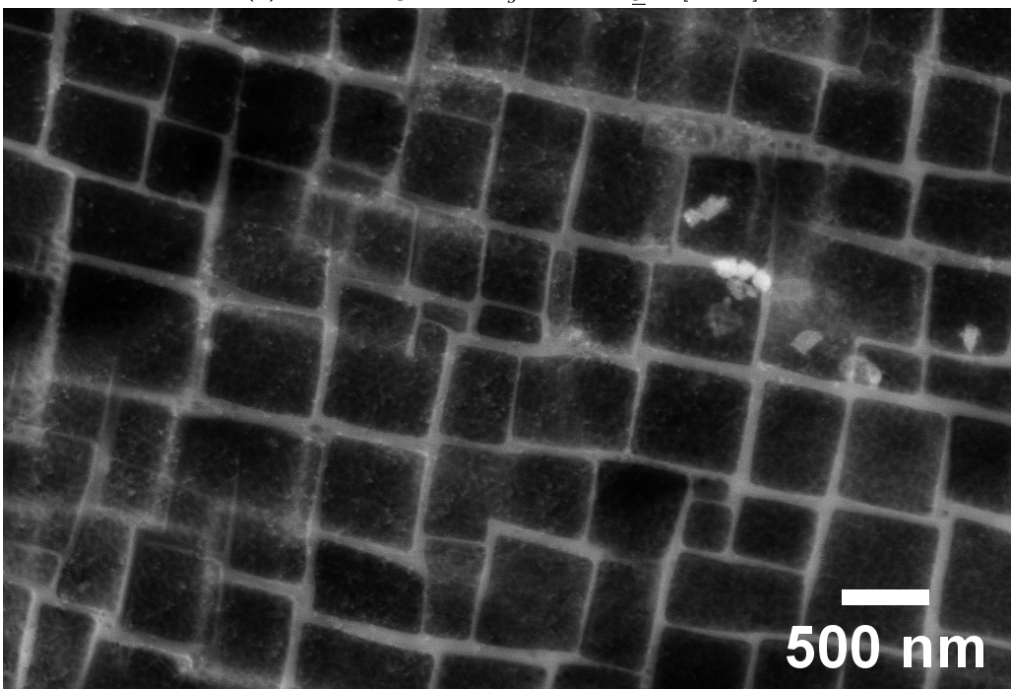
(b) BSE image @ R_{stage} 60° i.e. $\underline{g} \approx [XXX]$.

Figure D.6: Region 2.

These dislocations also have contrast when under 24°; however, their contrast appears greater, indicating a different $\underline{b}$ to show greater contrast under that $\underline{g}$.

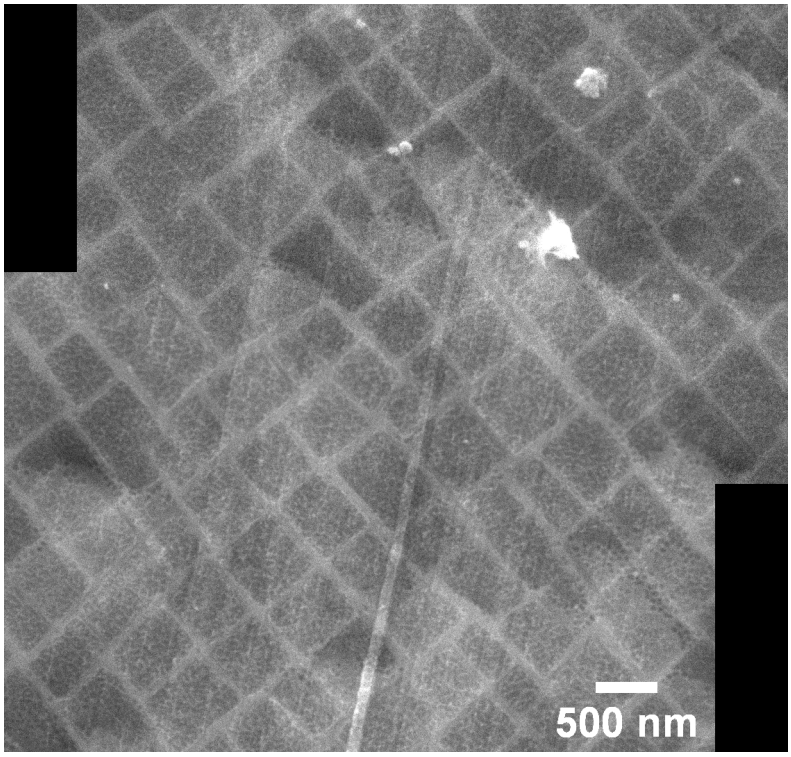


(c) BSE image @ R_{stage} 48° i.e. $\underline{g} \approx [YYY]$.

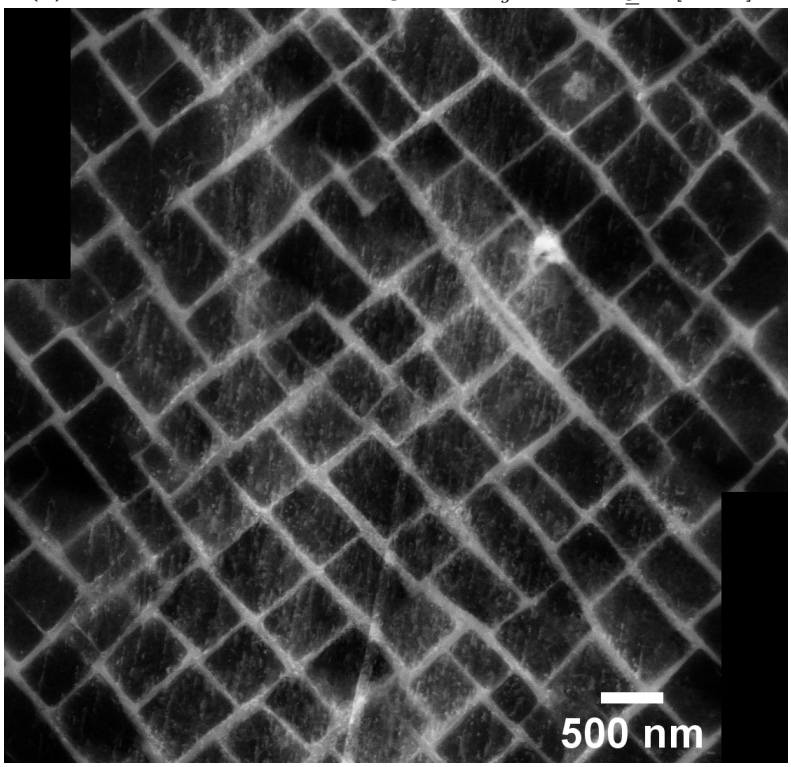


(d) BSE image @ R_{stage} 24° i.e. $\underline{g} \approx [ZZZ]$.

Figure D.6: Region 2.

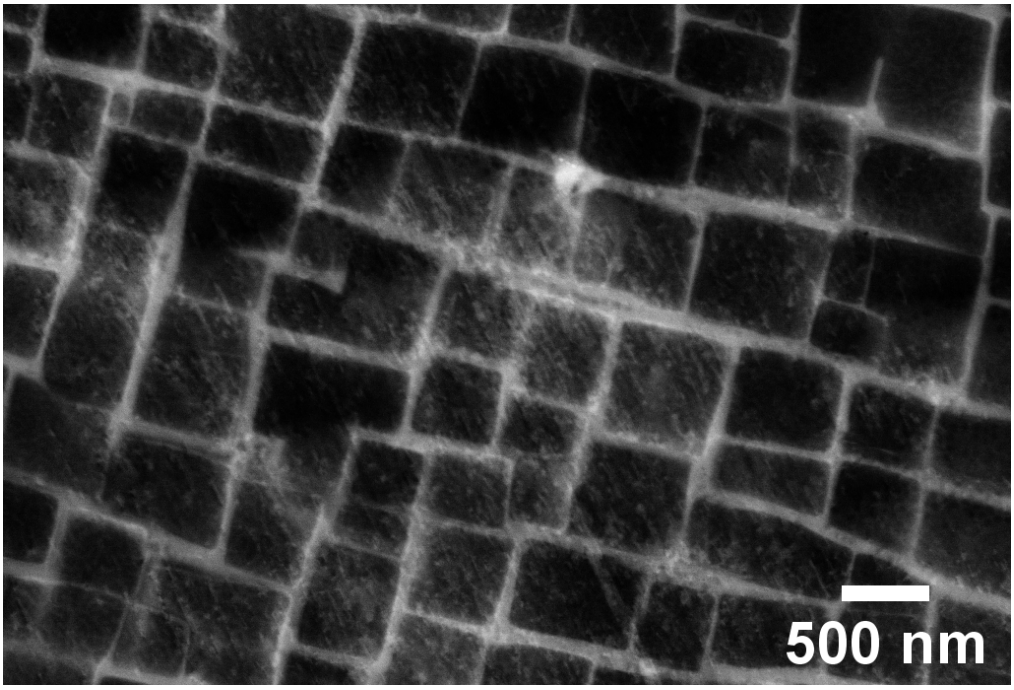


(a) Contrast-enhanced SE image @ R_{stage} 60° i.e. $\underline{g} = [YYY]$.



(b) BSE image @ R_{stage} 60° i.e. $\underline{g} \approx [XXX]$.

Figure D.7: Region 3.



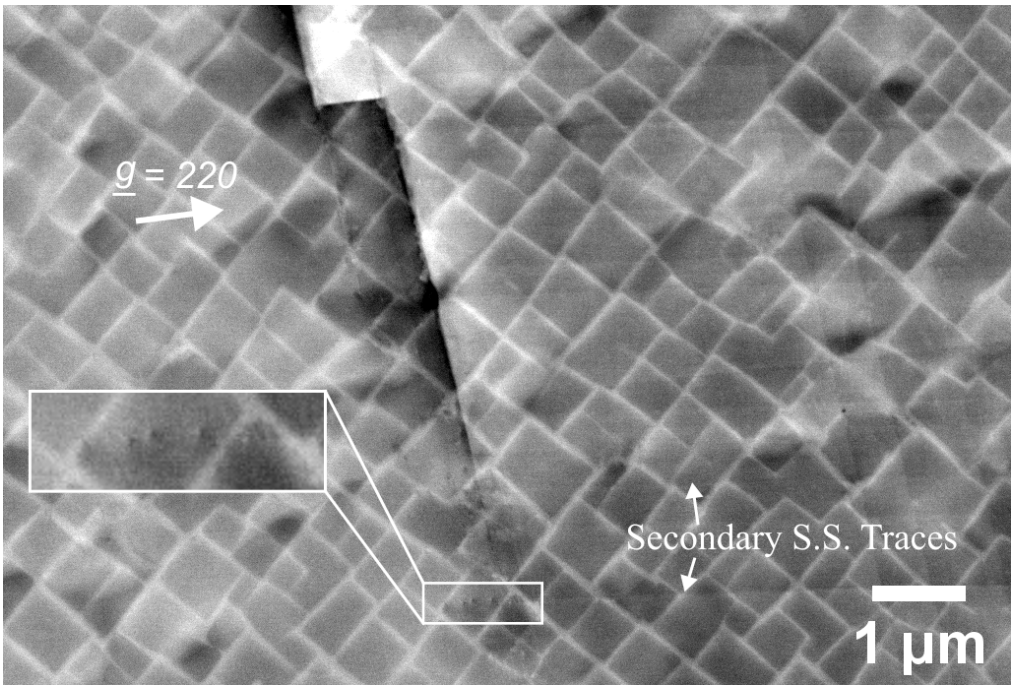
(c) BSE image @ R_{stage} 24° i.e. $\underline{g} \approx [ZZZ]$.

Figure D.7: Region 3.

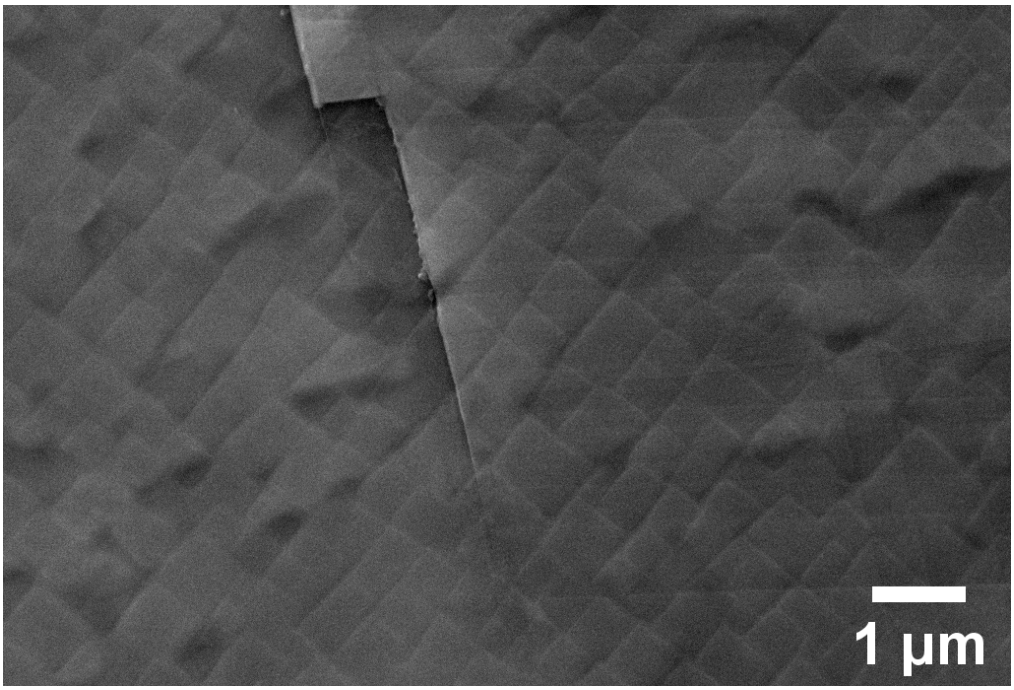
D.3.3 I5

Crack 1

Under higher magnification, fig. D.8a threading dislocations are seen coming from the main crack tip and on parallel nearby slip planes. The secondary slip system traces are seen in the BSE and SE image in fig. D.8 as near horizontal lines. The secondary slip lines occur only on one side of the main crack, which an SE micrograph (fig. D.9a) shows the slip trace bias and tearing mode (aka mode-III) component to the crack's propagation which is also seen in the rotations (fig. D.9c).



(a) BSE (i.e. ECCI).

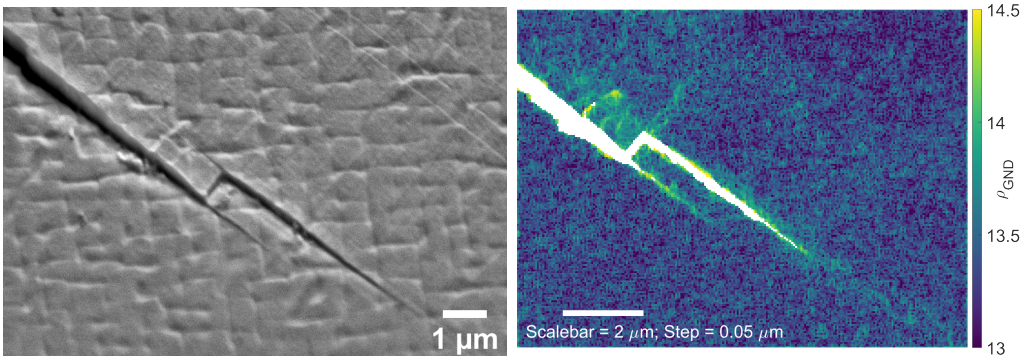


(b) SE.

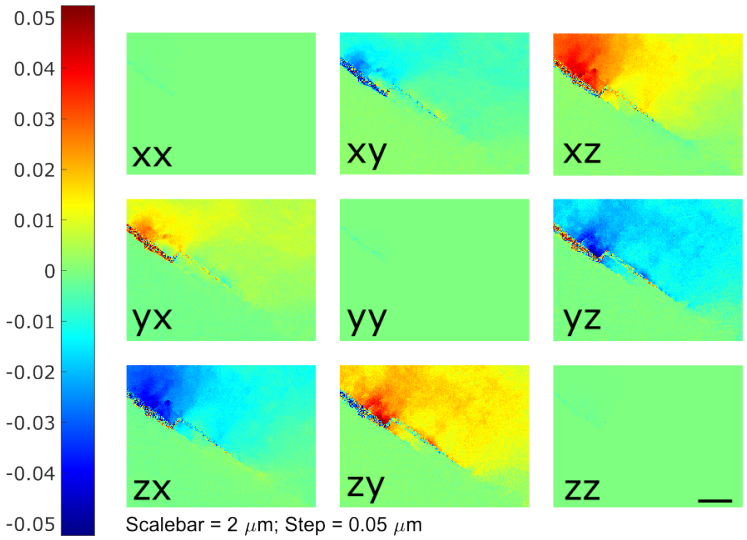
Figure D.8: High magnification electron microscope micrographs of crack tip 1 under diffraction condition ID 1.

The HR-EBSD results in fig. D.9 shows some slip on the secondary slip system, parallel to where the crack path changes direction in the ρ_{GND} map. This includes ahead of the crack tips, and even when it briefly changes direction, a higher localised but mild increase in ρ_{GND} is observed.

The fine slip bands with no height variation do not manifest as high ρ_{GND} regions, which is expected as dislocations have passed but have not been stored. If dislocations have stopped along a slip band, then its height is greater where more dislocations have passed.



(a) Correct SE micrograph at T_{stage} 70°. **(b)** ρ_{GND} map. Range = $10^{13} - 10^{14.5}$m^2.



(c) Rotations

Figure D.9: HR-EBSD analysis with a peak height mask of crack tip 1 (to exclude poor data at the crack itself). 2 µm scale bar, 45 nm step size.

D.3.4 RJSN1 ECPs

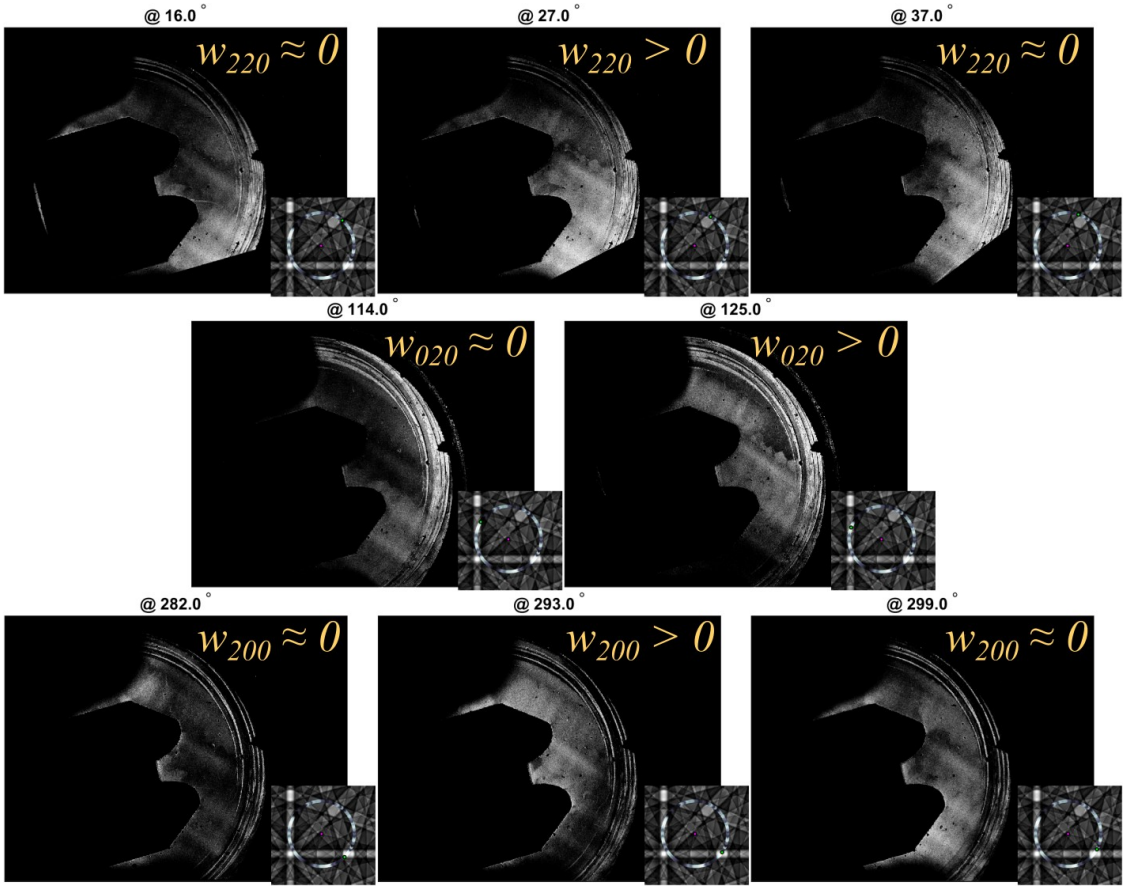
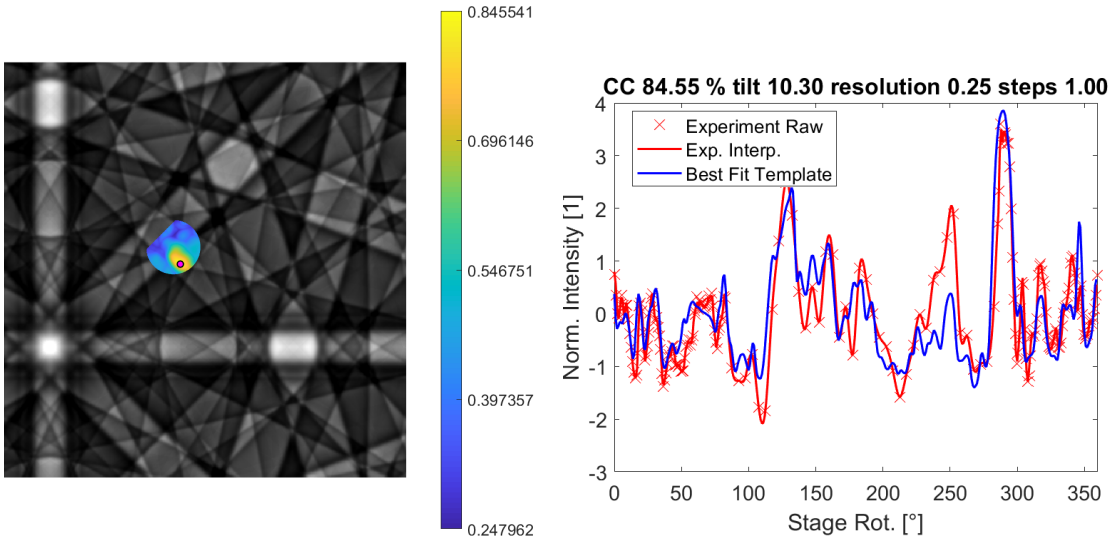


Figure D.10: ECPs for sample RJSN1 with the $\underline{g} = 220$, $\underline{g} = 020$, & $\underline{g} = 200$ bands per row with deviation parameters.

D.3.5 RJSN1 Diffraction Conditions

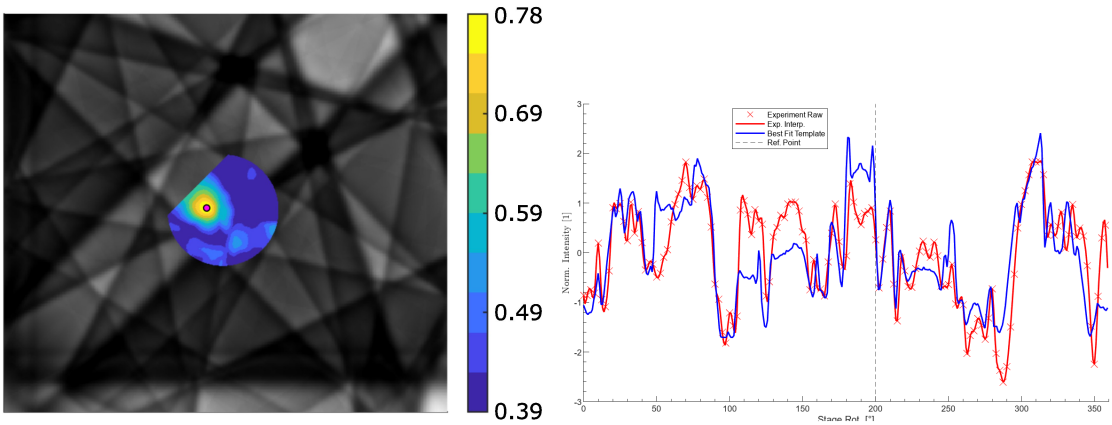
For the two $\underline{g} = 020$ & $\underline{g} = 220$ diffraction conditions, the results from the novel method are shown below, where both use a small circle of 2° from the EBSD determined orientation.

For $\underline{g} = 020$, an 84.6% CC solution was found 24.5 mrad from the mean EBSD orientation for a T_{stage} of 10.3° c.f. 10.0°. For $\underline{g} = 220$, a 78.4% CC solution was found 10.5 mrad from the mean EBSD orientation for a T_{stage} of 8.56° c.f. 8.2°.



(a) CC heat-map. **(b)** Matched intensity profile with experiment.

Figure D.11: Optimised results for RJSN1 for the $\underline{g} = 020$ session.

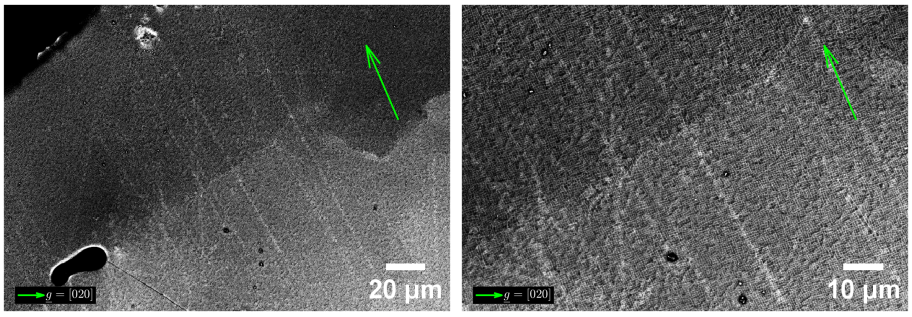


(a) CC heat-map. **(b)** Matched intensity profile with experiment.

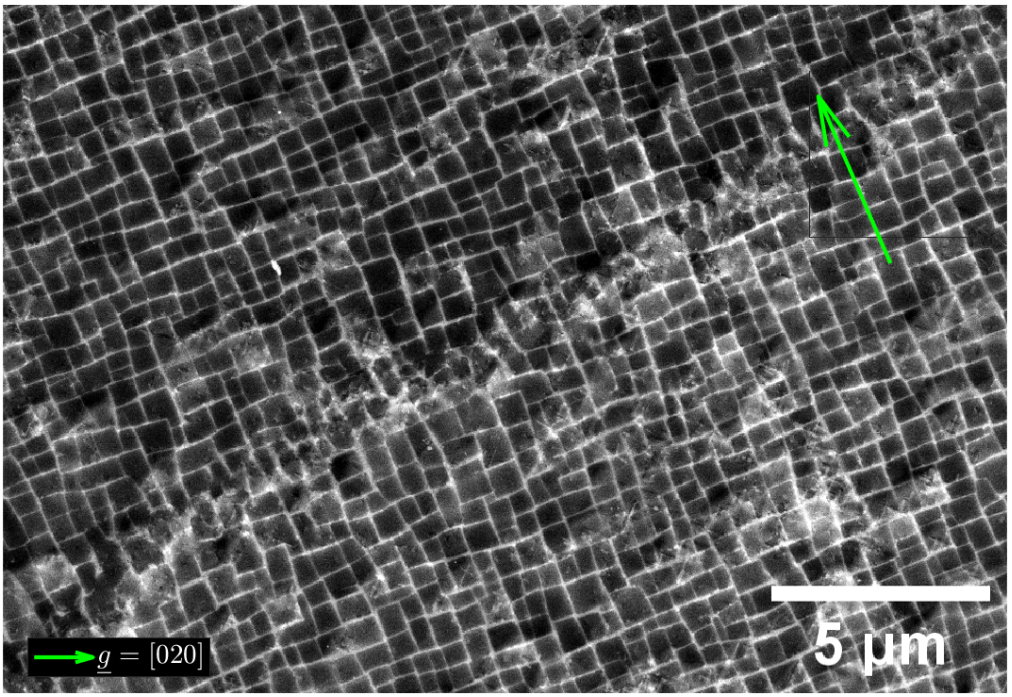
Figure D.12: Optimised results for RJSN1 for the $\underline{g} = 220$ session.

Dendrite Boundary

The very small misorientations between dendrites produce a contrast between them [31], and fig. D.13 uses this to show that dislocations are seen along a dendrite boundary. The accumulation is not too unreasonable considering that grain boundaries tend to act as barriers for dislocation motion in PX metals & alloys and are formed from an array of dislocations. In this work, no obvious fracture has been observed to initiate from dendrite boundaries.



(a) Low magnification. **(b)** Medium magnification.

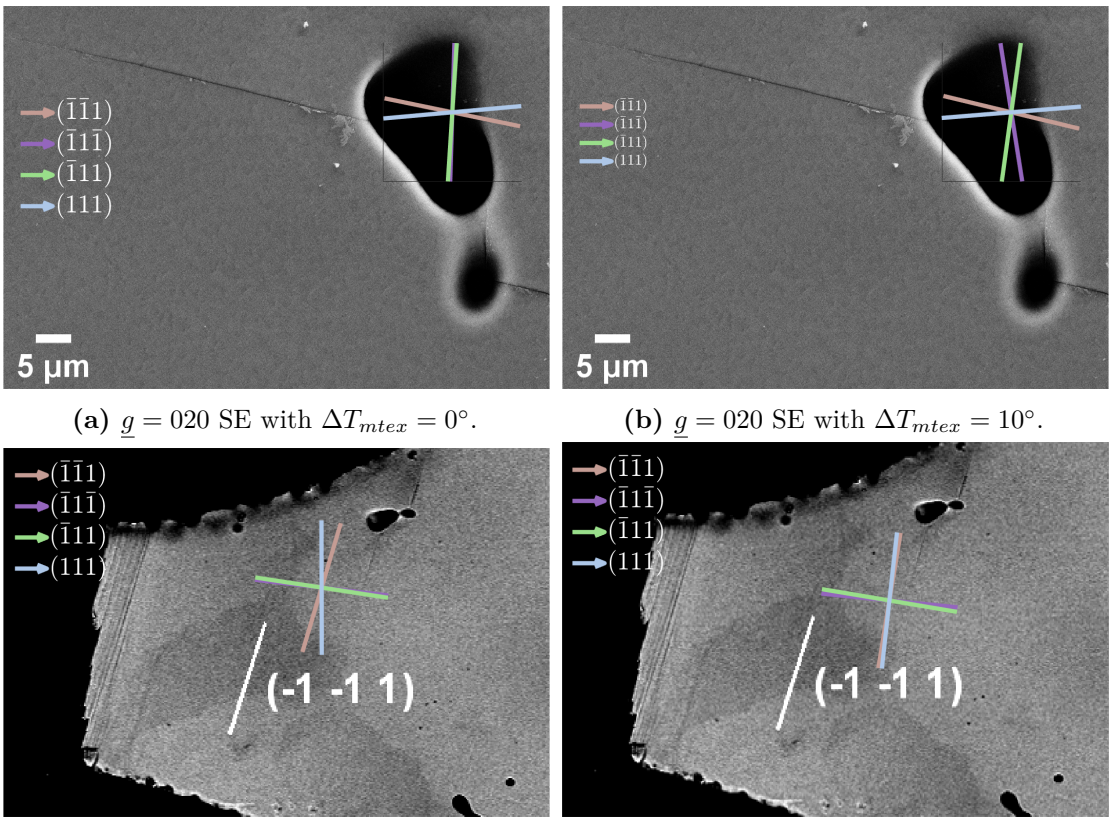


(c) High magnification. Dendrite boundary going from bottom-left to top-right corners of the micrograph.

Figure D.13: ECCI micrographs of a dendrite boundary in RJSN1 under $\underline{g}$ [020].

D.4 MTEX Orientation on Micrographs

Figure D.14 explains that with stage tilt corrected SEM micrographs ($^{H_{corr}}/_{H_{orig}} = 101.5\%$ for $\theta = 10°$, see eq. (C.5)) one does not need to tilt the EBSD map (change in stage tilt in MTEX (ΔT_{mtex})) in MTEX. The $(\bar{1}\bar{1}1)$ primary fracture trace is only consistent for the two different stage rotations when $\Delta T_{mtex} = 0°$. In (d) the slip traces and crack path follow no {111} trace well. Additionally, comparing sub-figures (a) and (b), the secondary crack/slip's trace between the two pores better follows either $(\bar{1}11)$ or $(\bar{1}1\bar{1})$ in (a) but follows no slip trace in (b).



(a) $\underline{g} = 020$ SE with $\Delta T_{mtex} = 0°$.

(b) $\underline{g} = 020$ SE with $\Delta T_{mtex} = 10°$.

(c) $\underline{g} = 220$ BSE with $\Delta T_{mtex} = 0°$.

(d) $\underline{g} = 220$ BSE with $\Delta T_{mtex} = 10°$.

Figure D.14: Annotated micrographs showing the orientation of the slip traces.

References

[1] *Global airline industry market size 2023*. en. URL: https://www.statista.com/statistics/1110342/market-size-airline-industry-worldwide/ (visited on 05/14/2024).

[2] Olga Miltcheva. *Aviation Value Chain*. en. Tech. rep. https://www.iata.org/en/publications/economics/reports/aviation-value-chain-brief-15-february-2024/. Feb. 2024. URL: https://www.iata.org/en/iata-repository/publications/economic-reports/aviation-value-chain/#:~:text=The%20airline%20industry%20is%20the,USD%20230%20billion%20in%202022. (visited on 05/13/2024).

[3] K Aainsqatsi. *Turbofan_operation.png*. June 2006. URL: https://commons.wikimedia.org/wiki/File:Turbofan_operation.svg (visited on 05/14/2024).

[4] A. Cervellon et al. "VHCF life evolution after microstructure degradation of a Ni-based single crystal superalloy". en. In: *International Journal of Fatigue* 104 (Nov. 2017), pp. 251–262. DOI: 10.1016/j.ijfatigue.2017.07.021. URL: https://linkinghub.elsevier.com/retrieve/pii/S0142112317303171 (visited on 05/14/2024).

[5] Angelos Evangelou. "Oxidation-fatigue mechanisms at moderate service temperatures in single crystal turbine blade materials". PhD Thesis. University of Southampton, Sept. 2017. URL: https://eprints.soton.ac.uk/420749/.

[6] Roger C Reed. *The Superalloys: Fundamentals and Applications*. en. Cambridge University Press, 2006.

[7] Rolls Royce. *The Jet Engine (Paperback)*. 2005.

[8] N. Kaewchoothong, K. Maliwan, and C. Nuntadusit. "Numerical simulations on flow and heat transfer in ribbed two-pass square channels under rotational effects". en. In: *IOP Conference Series: Materials Science and Engineering* 243 (Sept. 2017), p. 012004. DOI: 10.1088/1757-899X/243/1/012004. URL: https://iopscience.iop.org/article/10.1088/1757-899X/243/1/012004 (visited on 05/29/2024).

[9] Kamin Tahmasbi et al. "Dynamic frequency-dependent fatigue damage in metals: A state-of-the-art review". en. In: *Forces in Mechanics* 10 (Feb. 2023), p. 100167. DOI: 10.1016/j.finmec.2023.100167. URL: https://linkinghub.elsevier.com/retrieve/pii/S2666359723000021 (visited on 01/01/2024).

[10] Takehiro Okura. *Materials for Aircraft Engines*. en. https://www.colorado.edu/faculty/kantha/teaching/supplementary-material/aircraft-propulsion/reports/materials. 2015. URL: https://www.colorado.edu/faculty/kantha/content/materials-aircraft-engines (visited on 05/15/2024).

[11] Alice Cervellon, Chris J. Torbet, and Tresa M. Pollock. "Crack initiation anisotropy of Ni-based SX superalloys in the very high cycle fatigue regime". en. In: *Materials Science and Engineering: A* 825 (Sept. 2021), p. 141920. DOI: 10.1016/j.msea.2021.141920. URL: https://linkinghub.elsevier.com/retrieve/pii/S0921509321011862 (visited on 10/24/2023).

[12] Duoqi Shi et al. "An orientation-dependent creep life evaluation method for nickel-based single crystal superalloys". en. In: *Chinese Journal of Aeronautics* 35.1 (Jan. 2022), pp. 238–249. DOI: 10.1016/j.cja.2021.03.003. URL: https://linkinghub.elsevier.com/retrieve/pii/S1000936121000388 (visited on 05/07/2024).

[13] Cyrus B. Meher-Homji and George Gabriles. "Gas Turbine Blade Failures - Causes, Avoidance, And Troubleshooting." en. In: *Proceedings of the 27th Turbomachinery Symposium*. Meher-Homji, Cyrus B.; Gabriles, George (1998). Gas Turbine Blade Failures - Causes, Avoidance, And Troubleshooting.. Texas A&M University. Turbomachinery Laboratories. Available electronically from https : / /hdl .handle .net /1969 .1 /163404. Texas A&M University: Texas A&M University. Turbomachinery Laboratories, 1998, pp. 129–180. DOI: https://doi.org/10.21423/R1RD4R. URL: https://oaktrust.library.tamu.edu/bitstream/handle/1969.1/163404/Vol27015.pdf?sequence=1&isAllowed=y (visited on 05/15/2024).

[14] M. Spodniak et al. "FEM analysis of natural frequencies of jet engine iSTC-21v turbine blade". en. In: *2019 IEEE 17th World Symposium on Applied Machine Intelligence and Informatics (SAMI)*. Herlany, Slovakia: IEEE, Jan. 2019, pp. 287–292. DOI: 10.1109/SAMI.2019.8782781. URL: https://ieeexplore.ieee.org/document/8782781/ (visited on 05/15/2024).

[15] Stefanie Stanzl-Tschegg. "Very high cycle fatigue measuring techniques". en. In: *International Journal of Fatigue* 60 (Mar. 2014), pp. 2–17. DOI: 10.1016/j.ijfatigue.2012.11.016. URL: https://linkinghub.elsevier.com/retrieve/pii/S0142112312003581 (visited on 10/25/2023).

[16] Youshi Hong and Chengqi Sun. "The nature and the mechanism of crack initiation and early growth for very-high-cycle fatigue of metallic materials – An overview". en. In: *Theoretical and Applied Fracture Mechanics* 92 (Dec. 2017), pp. 331–350. DOI: 10.1016/j.tafmec.2017.05.002. URL: https://linkinghub.elsevier.com/retrieve/pii/S0167844217301581 (visited on 05/14/2024).

[17] R Morrissey and P Golden. "Fatigue strength of a single crystal in the gigacycle regime". en. In: *International Journal of Fatigue* 29.9-11 (Sept. 2007), pp. 2079–2084. DOI: 10.1016/j.ijfatigue.2007.04.003. URL:

https://linkinghub.elsevier.com/retrieve/pii/S0142112307001569 (visited on 05/14/2024).

[18] B. A. Cowles. "High cycle fatigue in aircraft gas turbines—an industry perspective". en. In: *International Journal of Fracture* 80.2-3 (Apr. 1996), pp. 147–163. DOI: 10.1007/BF00012667. URL: http://link.springer.com/10.1007/BF00012667 (visited on 05/14/2024).

[19] R. K. Mishra and Vinay Kumar. "Investigation of Turbine Blade Failure in a Turboprop Engine: A Case Study". en. In: *Journal of Failure Analysis and Prevention* 22.2 (Apr. 2022), pp. 458–463. DOI: 10.1007/s11668-022-01334-8. URL: https://link.springer.com/10.1007/s11668-022-01334-8 (visited on 05/14/2024).

[20] Chris Bullough et al. "The characterisation of the single crystal superalloy CMSX-4 for industrial gas turbine blading applications". en. In: vol. 5. LIEGE, BELGIUM, Sept. 1999, pp. 861–878. URL: https://www.researchgate.net/publication/259778979_The_characterization_of_the_single_crystal_superalloy_CMSX-4_for_industrial_gas_turbine_blading_applications.

[21] Alexander Epishin et al. "Investigation of Elastic Properties of the Single-Crystal Nickel-Base Superalloy CMSX-4 in the Temperature Interval between Room Temperature and 1300 °C". en. In: *Crystals* 11.2 (Feb. 2021), p. 152. DOI: 10.3390/cryst11020152. URL: https://www.mdpi.com/2073-4352/11/2/152 (visited on 06/28/2023).

[22] M. D. Miller et al. "Effect of environment on notch fatigue behaviour in CMSX-4". en. In: *Materials Science and Technology* 23.12 (Dec. 2007), pp. 1439–1445. DOI: 10.1179/174328407X213198. URL: http://www.tandfonline.com/doi/full/10.1179/174328407X213198 (visited on 01/02/2024).

[23] B. Pyttel, D. Schwerdt, and C. Berger. "Very high cycle fatigue – Is there a fatigue limit?" en. In: *International Journal of Fatigue* 33.1 (Jan. 2011), pp. 49–58. DOI: 10.1016/j.ijfatigue.2010.05.009. URL: https://linkinghub.elsevier.com/retrieve/pii/S0142112310001362 (visited on 01/16/2024).

[24] A. Evangelou et al. "Oxidation behaviour of single crystal nickel-based superalloys: intermediate temperature effects at 450–550°C". en. In: *Materials Science and Technology* 34.14 (Sept. 2018), pp. 1679–1692. DOI: 10.1080/02670836.2018.1471436. URL: https://www.tandfonline.com/doi/full/10.1080/02670836.2018.1471436 (visited on 01/03/2024).

[25] Jean Charles Stinville et al. "Fatigue deformation in a polycrystalline nickel base superalloy at intermediate and high temperature: Competing failure modes". en. In: *Acta Materialia* 152 (June 2018), pp. 16–33. DOI: 10.1016/j.actamat.2018.03.035. URL: https://linkinghub.elsevier.com/retrieve/pii/S1359645418302337 (visited on 12/08/2023).

[26] N. K. Arakere and G. Swanson. "Effect of Crystal Orientation on Fatigue Failure of Single Crystal Nickel Base Turbine Blade Superalloys". en. In: *Journal of Engineering for Gas Turbines and Power* 124.1 (Jan. 2002), pp. 161–176. DOI: 10.1115/1.1413767. URL: https://asmedigitalcollection.asme.org/gasturbinespower/article/124/1/161/461738/Effect-of-Crystal-Orientation-on-Fatigue-Failure (visited on 09/12/2023).

[27] U. Bruckner et al. "The influence of the dendritic structure on the gamma/gamma'-lattice misfit in the single-crystal nickel-base superalloy CMSX-4". In: *Materials Science and Engineering: A* 247.1 (1998), pp. 23–31. DOI: https://doi.org/10.1016/S0921-5093(97)00856-3. URL: https://www.sciencedirect.com/science/article/pii/S0921509397008563.

[28] R.A. Hobbs et al. "Solidification Characteristics of Advanced Nickel-Base Single Crystal Superalloys". en. In: *Superalloys 2004 (Tenth International Symposium)*. TMS, 2004, pp. 819–825. DOI: 10.7449/2004/Superalloys_2004_819_825. URL: http://www.tms.org/Superalloys/10.7449/2004/Superalloys_2004_819_825.pdf (visited on 11/29/2023).

[29] Hong Zhang et al. "Tensile properties, strain rate sensitivity and failure mechanism of single crystal superalloys CMSX-4". en. In: *Materials Science and Engineering: A* 782 (Apr. 2020), p. 139105. DOI: 10.1016/j.msea.2020.139105. URL: https://linkinghub.elsevier.com/retrieve/pii/S0921509320301933 (visited on 08/22/2023).

[30] Alireza Mirak and Mohamad Fathi. "Effects of solidification rate and heat treatment on microstructure characterization and hot tensile strength of single crystal CMSX-4 superalloy". en. In: *Materials Characterization* 194 (Dec. 2022), p. 112449. DOI: 10.1016/j.matchar.2022.112449. URL: https://linkinghub.elsevier.com/retrieve/pii/S1044580322007318 (visited on 11/30/2023).

[31] Sabin Sulzer et al. "On the assessment of creep damage evolution in nickel-based superalloys through correlative HR-EBSD and cECCI studies". en. In: *Acta Materialia* 185 (Feb. 2020), pp. 13–27. DOI: 10.1016/j.actamat.2019.07.018. URL: https://linkinghub.elsevier.com/retrieve/pii/S1359645419304586 (visited on 06/28/2023).

[32] Jian-Min Zhang et al. "Young's modulus surface and Poisson's ratio curve for cubic metals". en. In: *Journal of Physics and Chemistry of Solids* 68.4 (Apr. 2007), pp. 503–510. DOI: 10.1016/j.jpcs.2007.01.025. URL: https://linkinghub.elsevier.com/retrieve/pii/S0022369707000133 (visited on 11/30/2023).

[33] A Sengupta et al. "Tensile behavior of a new single-crystal nickel-based superalloy (CMSX-4) at room and elevated temperatures". en. In: *Journal of Materials Engineering and Performance* 3.1 (Feb. 1994), pp. 73–81. DOI: https://doi.org/10.1007/BF02654502. URL: https://doi.org/10.1007/BF02654502.

[34] Hong Zhang et al. "Dependence on temperature of compression behavior and deformation mechanisms of nickel-based single crystal CMSX-4". en. In: *Journal of Alloys and Compounds* 866 (June 2021), p. 158878. DOI: 10.1016/j.jallcom.2021.158878. URL: https://linkinghub.elsevier.com/retrieve/pii/S0925838821002851 (visited on 08/22/2023).

[35] Tianjian Wang et al. "Effect of temperature on tensile behavior, fracture morphology and deformation mechanisms of Nickel-based single crystal CMSX-4". en. In: *Journal of Alloys and Compounds* 912 (Aug. 2022), p. 165175. DOI: 10.1016/j.jallcom.2022.165175. URL: https://linkinghub.elsevier.com/retrieve/pii/S0925838822015663 (visited on 08/22/2023).

[36] Z.H. Tan et al. "Temperature dependence on tensile deformation mechanisms in a novel Nickel-based single crystal superalloy". en. In: *Materials Science and Engineering: A* 776 (Mar. 2020), p. 138997. DOI: 10.1016/j.msea.2020.138997. URL: https://linkinghub.elsevier.com/retrieve/pii/S0921509320300861 (visited on 08/22/2023).

[37] H Mughrabi. "Specific features and mechanisms of fatigue in the ultrahigh-cycle regime". en. In: *International Journal of Fatigue* 28.11 (Nov. 2006), pp. 1501–1508. DOI: 10.1016/j.ijfatigue.2005.05.018. URL: https://linkinghub.elsevier.com/retrieve/pii/S0142112306001034 (visited on 01/16/2024).

[38] T. Straub et al. "Small-Scale Multiaxial Setup for Damage Detection Into the Very High Cycle Fatigue Regime". en. In: *Experimental Mechanics* 55.7 (Sept. 2015), pp. 1285–1299. DOI: 10.1007/s11340-015-0027-z. URL: http://link.springer.com/10.1007/s11340-015-0027-z (visited on 01/18/2024).

[39] Yukitaka Murakami et al. "Essential structure of S-N curve: Prediction of fatigue life and fatigue limit of defective materials and nature of scatter". en. In: *International Journal of Fatigue* 146 (May 2021), p. 106138. DOI: 10.1016/j.ijfatigue.2020.106138. URL: https://linkinghub.elsevier.com/retrieve/pii/S0142112320306708 (visited on 11/15/2023).

[40] Christopher Massimo Magazzeni et al. "Bayesian optimized collection strategies for fatigue strength testing". en. In: *Fatigue & Fracture of Engineering Materials & Structures* 46.1 (Jan. 2023), pp. 228–243. DOI: 10.1111/ffe.13859. URL: https://onlinelibrary.wiley.com/doi/10.1111/ffe.13859 (visited on 10/31/2023).

[41] Christopher Massimo Magazzeni. "Towards local property assessment of advanced manufactured microstructures: a case study in linear friction welded titanium". en. PhD thesis. Oxford: University of Oxford, 2022. URL: http://dx.doi.org/10.5287/ora-rywmwyy0x (visited on 10/24/2023).

[42] Abhijit Sengupta. "Kinetics of gamma prime precipitation and fatigue crack growth behavior of a single crystal nickel-based superalloy (CMSX-4)". English. ISBN: 979-8-208-54921-6 Publication Title: ProQuest Dissertations and Theses 9418245. Ph.D. United States – Michigan: Wayne State University, 1993. URL: https://www.proquest.com/dissertations-theses/kinetics-gamma-prime-precipitation-fatigue-crack/docview/304081566/se-2?accountid=13042.

[43] X. Wu et al. "A continuously distributed dislocation model for fatigue cracks in anisotropic crystalline materials". In: *International Journal of Fatigue* 23 (Jan. 2001), pp. 201–206. DOI: 10.1016/S0142-1123(01)00131-1. URL: https://www.sciencedirect.com/science/article/pii/S0142112301001311 (visited on 12/05/2023).

[44] Richard W. Neu. "Crack paths in single-crystal Ni-base superalloys under isothermal and thermomechanical fatigue". en. In: *International Journal of Fatigue* 123 (June 2019), pp. 268–278. DOI: 10.1016/j.ijfatigue.2019.02.022. URL: https://linkinghub.elsevier.com/retrieve/pii/S0142112318307291 (visited on 09/12/2023).

[45] Shiyu Suzuki, Motoki Sakaguchi, and Hirotsugu Inoue. "Temperature dependent fatigue crack propagation in a single crystal Ni-base superalloy affected by primary and secondary orientations". en. In: *Materials Science and Engineering: A* 724 (May 2018), pp. 559–565. DOI: 10.1016/j.msea.2018.03.090. URL: https://linkinghub.elsevier.com/retrieve/pii/S0921509318304490 (visited on 09/06/2023).

[46] Zhiwu He et al. "Temperature effect on the low cycle fatigue behavior of a directionally solidified nickel-base superalloy". en. In: *Materials Science and Engineering: A* 676 (Oct. 2016), pp. 246–252. DOI: 10.1016/j.msea.2016.08.064. URL: https://linkinghub.elsevier.com/retrieve/pii/S0921509316309777 (visited on 09/15/2023).

[47] G. R. Leverant and M. Gell. "The influence of temperature and cyclic frequency on the fatigue fracture of cube oriented nickel-base superalloy single crystals". en. In: *Metallurgical Transactions A* 6.2 (Feb. 1975), p. 367. DOI: 10.1007/BF02667291. URL: https://link.springer.com/10.1007/BF02667291 (visited on 09/18/2023).

[48] Abhijit Sengupta and Susil K. Putatunda. "Influence of dynamic strain aging on the near-threshold fatigue crack growth behavior of a new single crystal nickel-based superalloy". en. In: *Scripta Metallurgica et Materialia* 31.9 (Nov. 1994), pp. 1163–1168. DOI: 10.1016/0956-716X(94)90569-X. URL: https://linkinghub.elsevier.com/retrieve/pii/0956716X9490569X (visited on 12/13/2023).

[49] Lu Zhang. "Cyclic deformation, fatigue crack initiation and crack growth in a nickel-based single-crystal superalloy". en. thesis. Loughborough University, Jan. 2019. DOI: 10.26174/thesis.lboro.8323382.v1. URL: https://repository.lboro.ac.uk/articles/thesis/Cyclic_deformation_fatigue_crack_initiation_and_crack_growth_in_a_nickel-based_single-crystal_superalloy/8323382/1 (visited on 12/01/2023).

[50] D. W. MacLachlan and D. M. Knowles. "Fatigue behaviour and lifing of two single crystal superalloys: FATIGUE BEHAVIOUR OF SINGLE CRYSTAL SUPERALLOYS". en. In: *Fatigue & Fracture of Engineering Materials & Structures* 24.8 (Aug. 2001), pp. 503–521. DOI: 10.1046/j.1460-2695.2001.00392.x. URL: http://doi.wiley.com/10.1046/j.1460-2695.2001.00392.x (visited on 09/15/2023).

[51] Y. Liu et al. "High cycle fatigue behavior of a single crystal superalloy at elevated temperatures". en. In: *Materials Science and Engineering: A* 454-455 (Apr. 2007), pp. 357–366. DOI: 10.1016/j.msea.2006.11.045. URL: https://linkinghub.elsevier.com/retrieve/pii/S092150930602452X (visited on 09/12/2023).

[52] C. Busse et al. "Criteria evaluation for the transition of cracking modes in a single-crystal nickel-base superalloy". en. In: *Theoretical and Applied Fracture Mechanics* 106 (Apr. 2020), p. 102453. DOI: 10.1016/j.tafmec.2019.102453. URL: https://linkinghub.elsevier.com/retrieve/pii/S0167844219305841 (visited on 09/06/2023).

[53] Motoki Sakaguchi et al. "Stage I Fatigue Crack Propagation in a Single Crystal and a Directional Solidified Ni-Base Superalloy". In: *Superalloys 2016*. _eprint: https://onlinelibrary.wiley.com/doi/pdf/10.1002/9781119075646.ch68. John Wiley & Sons, Ltd, 2016, pp. 639–646. DOI: https://doi.org/10.1002/9781119075646.ch68. URL: https://onlinelibrary.wiley.com/doi/abs/10.1002/9781119075646.ch68.

[54] Xiaosheng Chen, Dianyin Hu, and Motoki Sakaguchi. "Temperature dependent transition from Mode I to crystallographic cracking in a Ni-base single crystal superalloy". en. In: *Theoretical and Applied Fracture Mechanics* 124 (Apr. 2023), p. 103795. DOI: 10.1016/j.tafmec.2023.103795. URL: https://linkinghub.elsevier.com/retrieve/pii/S0167844223000472 (visited on 01/17/2024).

[55] Xiaosheng Chen and Motoki Sakaguchi. "Transition behavior from Mode I cracking to crystallographic cracking in a Ni-base single crystal superalloy". en. In: *International Journal of Fatigue* 132 (Mar. 2020), p. 105400. DOI: 10.1016/j.ijfatigue.2019.105400. URL: https://linkinghub.elsevier.com/retrieve/pii/S0142112319305043 (visited on 09/12/2023).

[56] Vasilis Karamitros, Duncan W. MacLachlan, and Fionn P.E. Dunne. "Modelling of short crack growth in single crystal Ni gamma-gamma' microstructure". en. In: *Acta Materialia* 240 (Nov. 2022), p. 118305. DOI: 10.1016/j.actamat.2022.118305. URL: https://linkinghub.elsevier.com/retrieve/pii/S135964542200684X (visited on 01/15/2024).

[57] Motoki Sakaguchi et al. "Effect of rafted microstructure and its temperature dependency on fatigue crack propagation in a single-crystal Ni-base superalloy". en. In: *Fatigue & Fracture of Engineering Materials & Structures* 46.2 (Feb. 2023), pp. 590–602. DOI: 10.1111/ffe.13888. URL:

https://onlinelibrary.wiley.com/doi/10.1111/ffe.13888 (visited on 09/14/2023).

[58] Zhen-xue Shi et al. "Influence of Cast Dimension on Rotary Bending High Cycle Fatigue Properties of Single Crystal Superalloy". en. In: *Journal of Iron and Steel Research International* 20.12 (Dec. 2013), pp. 98–102. DOI: 10.1016/S1006-706X(13)60222-8. URL: http://link.springer.com/10.1016/S1006-706X(13)60222-8 (visited on 09/12/2023).

[59] M.R. Joyce, X. Wu, and P.A.S. Reed. "The effect of environment and orientation on fatigue crack growth behaviour of CMSX-4 nickel base single crystal at 650 °C". en. In: *Materials Letters* 58.1-2 (Jan. 2004), pp. 99–103. DOI: 10.1016/S0167-577X(03)00423-3. URL: https://linkinghub.elsevier.com/retrieve/pii/S0167577X03004233 (visited on 09/12/2023).

[60] Frans Palmert et al. "Fatigue crack growth behaviour of an alternative single crystal nickel base superalloy". en. In: *International Journal of Fatigue* 109 (Apr. 2018), pp. 166–181. DOI: 10.1016/j.ijfatigue.2017.12.003. URL: https://linkinghub.elsevier.com/retrieve/pii/S0142112317304437 (visited on 09/15/2023).

[61] Jack Telesman and Louis J. Ghosn. "The unusual near-threshold FCG behavior of a single crystal superalloy and the resolved shear stress as the crack driving force". en. In: *Engineering Fracture Mechanics* 34.5-6 (Jan. 1989), pp. 1183–1196. DOI: 10.1016/0013-7944(89)90279-8. URL: https://linkinghub.elsevier.com/retrieve/pii/0013794489902798 (visited on 09/15/2023).

[62] Lena Eisenhut et al. "Effect of a dislocation pile-up at the neutral axis on trans-crystalline crack growth for micro-bending fatigue". en. In: *International Journal of Fatigue* 94 (Jan. 2017), pp. 131–139. DOI: 10.1016/j.ijfatigue.2016.09.015. URL: https://linkinghub.elsevier.com/retrieve/pii/S0142112316302894 (visited on 01/04/2024).

[63] Steven Lavenstein et al. "High frequency in situ fatigue response of Ni-base superalloy René-N5 microcrystals". en. In: *Acta Materialia* 144 (Feb. 2018), pp. 154–163. DOI: 10.1016/j.actamat.2017.10.049. URL: https://linkinghub.elsevier.com/retrieve/pii/S1359645417309084 (visited on 01/11/2024).

[64] S. Stekovic. "Low Cycle Fatigue and Fracture of a Coated Superalloy CMSX-4". en. In: *Fracture of Nano and Engineering Materials and Structures*. Ed. by E. E. Gdoutos. Dordrecht: Springer Netherlands, 2006, pp. 275–276. DOI: 10.1007/1-4020-4972-2_135. URL: http://link.springer.com/10.1007/1-4020-4972-2_135 (visited on 09/15/2023).

[65] Q. Chen, N. Kawagoishi, and H. Nisitani. "Evaluation of fatigue crack growth rate and life prediction of Inconel 718 at room and elevated temperatures". en. In: *Materials Science and Engineering: A* 277.1-2 (Jan. 2000), pp. 250–257. DOI: 10.1016/S0921-5093(99)00555-9. URL: https://linkinghub.elsevier.com/retrieve/pii/S0921509399005559 (visited on 12/01/2023).

[66] H. Mayer. "Recent developments in ultrasonic fatigue". en. In: *Fatigue & Fracture of Engineering Materials & Structures* 39.1 (Jan. 2016), pp. 3–29. DOI: 10.1111/ffe.12365. URL: https://onlinelibrary.wiley.com/doi/10.1111/ffe.12365 (visited on 10/25/2023).

[67] Zebang Zheng, Mei Zhan, and M.W. Fu. "Microstructural and geometrical size effects on the fatigue of metallic materials". en. In: *International Journal of Mechanical Sciences* 218 (Mar. 2022), p. 107058. DOI: 10.1016/j.ijmecsci.2021.107058. URL: https://linkinghub.elsevier.com/retrieve/pii/S002074032100744X (visited on 01/11/2024).

[68] A. Tridello et al. "Size-effect in Very High Cycle Fatigue: A review". en. In: *International Journal of Fatigue* 153 (Dec. 2021), p. 106462. DOI: 10.1016/j.ijfatigue.2021.106462. URL: https://linkinghub.elsevier.com/retrieve/pii/S0142112321003200 (visited on 01/11/2024).

[69] Johannes Ast et al. "Interplay of stresses, plasticity at crack tips and small sample dimensions revealed by in-situ microcantilever tests in tungsten". en. In: *Materials Science and Engineering: A* 710 (Jan. 2018), pp. 400–412. DOI: 10.1016/j.msea.2017.10.096. URL: https://linkinghub.elsevier.com/retrieve/pii/S0921509317314247 (visited on 01/22/2024).

[70] Patrick Grünewald et al. "Fatigue crack growth in micro specimens as a tool to measure crack–microstructure interactions". en. In: *Fatigue & Fracture of Engineering Materials & Structures* 43.12 (2020). _eprint: https://onlinelibrary.wiley.com/doi/pdf/10.1111/ffe.13354, pp. 3037–3049. DOI: 10.1111/ffe.13354. URL: https://onlinelibrary.wiley.com/doi/abs/10.1111/ffe.13354 (visited on 01/15/2024).

[71] Shun-Peng Zhu et al. "Recent advances on size effect in metal fatigue under defects: a review". en. In: *International Journal of Fracture* 234.1-2 (Apr. 2022), pp. 21–43. DOI: 10.1007/s10704-021-00526-x. URL: https://link.springer.com/10.1007/s10704-021-00526-x (visited on 01/11/2024).

[72] Wen Jiang et al. "The effect of porosity size and oxidation on the HCF property of nickel-based single crystal superalloy at 980 ℃". en. In: *Theoretical and Applied Fracture Mechanics* 120 (Aug. 2022), p. 103423. DOI: 10.1016/j.tafmec.2022.103423. URL: https://linkinghub.elsevier.com/retrieve/pii/S0167844222001719 (visited on 09/18/2023).

[73] A. Cervellon et al. “Very High Cycle Fatigue of Ni-Based Single-Crystal Superalloys at High Temperature”. en. In: *Metallurgical and Materials Transactions A* 49.9 (Sept. 2018), pp. 3938–3950. DOI: 10.1007/s11661-018-4672-6. URL: https://link.springer.com/10.1007/s11661-018-4672-6 (visited on 08/29/2023).

[74] Yawei Li et al. “High temperature VHCF of a 3rd generation Ni-based single crystal superalloy with different casting pore sizes”. en. In: *International Journal of Fatigue* 175 (Oct. 2023), p. 107804. DOI: 10.1016/j.ijfatigue.2023.107804. URL: https://linkinghub.elsevier.com/retrieve/pii/S0142112323003055 (visited on 01/02/2024).

[75] Luciana Maria Bortoluci Ormastroni. “Crack Initiation Mechanisms in Very High Cycle Fatigue at High Temperatures of Nibased Single Crystal Superalloys : Transition from Internal Sites to the Surface”. Thesis. Köln-Porz: Ecole Nationale Superieure de Mechanique et de Aerotechnique, 2023. URL: https://elib.dlr.de/191246/ (visited on 01/02/2024).

[76] Eralp Demir, Dierk Raabe, and Franz Roters. “The mechanical size effect as a mean-field breakdown phenomenon: Example of microscale single crystal beam bending”. In: *Acta Materialia* 58.5 (Mar. 2010), pp. 1876–1886. DOI: 10.1016/j.actamat.2009.11.031. URL: https://www.sciencedirect.com/science/article/pii/S1359645409008106 (visited on 01/10/2024).

[77] C. Motz, T. Schöberl, and R. Pippan. “Mechanical properties of micro-sized copper bending beams machined by the focused ion beam technique”. en. In: *Acta Materialia* 53.15 (Sept. 2005), pp. 4269–4279. DOI: 10.1016/j.actamat.2005.05.036. URL: https://linkinghub.elsevier.com/retrieve/pii/S1359645405003253 (visited on 02/01/2025).

[78] Alejandro Barrios et al. “Comparison of the low and high/very high cycle fatigue behaviors in Ni microbeams under bending”. en. In: *Journal of Materials Research* 36.11 (June 2021), pp. 2337–2348. DOI: 10.1557/s43578-020-00097-y. URL: https://link.springer.com/10.1557/s43578-020-00097-y (visited on 10/23/2023).

[79] J. K. Tien and R. P. Gamble. “The room temperature fatigue behavior of nickel-base superalloy crystals at ultrasonic frequency”. en. In: *Metallurgical Transactions* 2.7 (July 1971), pp. 1933–1938. DOI: 10.1007/BF02913426. URL: https://link.springer.com/10.1007/BF02913426 (visited on 01/17/2024).

[80] Subra Suresh. *Fatigue of Materials*. en. Second edition. Cambridge core. Cambridge: Cambridge University Press, Oct. 1998. DOI: 10.1017/CBO9780511806575. URL: https://www.cambridge.org/core/product/identifier/9780511806575/type/book (visited on 09/13/2024).

[81] N. Schneider et al. "Frequency effect and influence of testing technique on the fatigue behaviour of quenched and tempered steel and aluminium alloy". en. In: *International Journal of Fatigue* 93 (Dec. 2016), pp. 224–231. DOI: 10.1016/j.ijfatigue.2016.05.013. URL: https://linkinghub.elsevier.com/retrieve/pii/S0142112316301153 (visited on 02/02/2025).

[82] Heinz Parkus. *Thermoelasticity.* eng. Blaisdell book in solid mechanics. Waltham, Mass: Blaisdell Pub. Co., 1968.

[83] Bin Hu et al. "Orientation Dependence of High Cycle Fatigue Behavior of a Oriented Single-Crystal Nickel-Based Superalloy". en. In: *Metals* 11.8 (Aug. 2021), p. 1248. DOI: 10.3390/met11081248. URL: https://www.mdpi.com/2075-4701/11/8/1248 (visited on 09/12/2023).

[84] S X Li, E G Ellison, and D J Smith. "The influence of orientation on the elastic and low cycle fatigue properties of several single crystal nickel base superalloys". en. In: *The Journal of Strain Analysis for Engineering Design* 29.2 (Apr. 1994), pp. 147–153. DOI: 10.1243/03093247V292147. URL: http://journals.sagepub.com/doi/10.1243/03093247V292147 (visited on 09/12/2023).

[85] Chengli Dong et al. "Life modeling of anisotropic fatigue behavior for a single crystal nickel-base superalloy". en. In: *International Journal of Fatigue* 61 (Apr. 2014), pp. 21–27. DOI: 10.1016/j.ijfatigue.2013.11.026. URL: https://linkinghub.elsevier.com/retrieve/pii/S0142112313003411 (visited on 09/12/2023).

[86] Jinjiang Yu et al. "Anisotropy of high cycle fatigue behavior of a Ni-base single crystal superalloy". en. In: *Materials Science and Engineering: A* 566 (Mar. 2013), pp. 90–95. DOI: 10.1016/j.msea.2013.01.001. URL: https://linkinghub.elsevier.com/retrieve/pii/S0921509313000221 (visited on 09/16/2023).

[87] A. Cervellon et al. "Crack initiation mechanisms during very high cycle fatigue of Ni-based single crystal superalloys at high temperature". en. In: *Acta Materialia* 188 (Apr. 2020), pp. 131–144. DOI: 10.1016/j.actamat.2020.02.012. URL: https://linkinghub.elsevier.com/retrieve/pii/S1359645420301130 (visited on 02/02/2025).

[88] Y. Meng et al. "Orientation dependence of nickel-based single crystal superalloys in VHCF regime". en. In: *International Journal of Fatigue* (July 2024), p. 108502. DOI: 10.1016/j.ijfatigue.2024.108502. URL: https://linkinghub.elsevier.com/retrieve/pii/S0142112324003608 (visited on 07/21/2024).

[89] D. J. Duquette and M. Gell. "The effect of environment on the mechanism of Stage I fatigue fracture". en. In: *Metallurgical Transactions* 2.5 (May 1971), pp. 1325–1331. DOI: 10.1007/BF02913355. URL: https://link.springer.com/10.1007/BF02913355 (visited on 01/05/2024).

[90] B.L. Boyce, J.R. Michael, and P.G. Kotula. "Fatigue of metallic microdevices and the role of fatigue-induced surface oxides". en. In: *Acta Materialia* 52.6 (Apr. 2004), pp. 1609–1619. DOI: 10.1016/j.actamat.2003.12.032. URL: https://linkinghub.elsevier.com/retrieve/pii/S1359645403007419 (visited on 01/15/2024).

[91] Saurabh Gupta et al. "Improved very high cycle bending fatigue behavior of Ni microbeams with Au coatings". en. In: *Acta Materialia* 161 (Dec. 2018), pp. 444–455. DOI: 10.1016/j.actamat.2018.09.037. URL: https://linkinghub.elsevier.com/retrieve/pii/S1359645418307493 (visited on 01/15/2024).

[92] Ebiakpo Kakandar et al. "A computational and experimental comparison on the nucleation of fatigue cracks in statistical volume elements". en. In: *International Journal of Fatigue* 137 (Aug. 2020), p. 105633. DOI: 10.1016/j.ijfatigue.2020.105633. URL: https://linkinghub.elsevier.com/retrieve/pii/S014211232030164X (visited on 01/18/2024).

[93] D. J. Duquette and M. Gell. "The effects of environment on the elevated temperature fatigue behavior of nickel-base superalloy single crystals". en. In: *Metallurgical Transactions* 3.7 (July 1972), pp. 1899–1905. DOI: 10.1007/BF02642576. URL: https://link.springer.com/10.1007/BF02642576 (visited on 09/15/2023).

[94] A. Defresne and L. Remy. "Fatigue behaviour of CMSX 2 superalloy [001] single crystals at high temperature II: Fatigue crack growth". In: *Materials Science and Engineering: A* 129.1 (1990), pp. 55–64. DOI: https://doi.org/10.1016/0921-5093(90)90344-3. URL: https://www.sciencedirect.com/science/article/pii/0921509390903443.

[95] L. Rémy et al. "Effects of microstructure in high temperature fatigue: Lifetime to crack initiation of a single crystal superalloy in high temperature low cycle fatigue". en. In: *International Journal of Fatigue* 57 (Dec. 2013), pp. 37–49. DOI: 10.1016/j.ijfatigue.2012.10.013. URL: https://linkinghub.elsevier.com/retrieve/pii/S014211231200312X (visited on 02/03/2025).

[96] T. Straub et al. "A method for probing the effects of conformal nanoscale coatings on fatigue crack initiation in electroplated Ni films". en. In: *Thin Solid Films* 526 (Dec. 2012), pp. 176–182. DOI: 10.1016/j.tsf.2012.11.011. URL: https://linkinghub.elsevier.com/retrieve/pii/S0040609012014873 (visited on 10/23/2023).

[97] Eva K. Baumert et al. "Fatigue-induced thick oxide formation and its role on fatigue crack initiation in Ni thin films at low temperatures". en. In: *Acta Materialia* 67 (Apr. 2014), pp. 156–167. DOI: 10.1016/j.actamat.2013.11.057. URL: https://linkinghub.elsevier.com/retrieve/pii/S1359645413009154 (visited on 09/18/2023).

[98] M Nazmy et al. "Environmental effects on tensile and low cycle fatigue behavior of single crystal nickel base superalloys". en. In: *Scripta Materialia* 48.5 (Mar. 2003), pp. 519–524. DOI: 10.1016/S1359-6462(02)00506-7. URL: https://linkinghub.elsevier.com/retrieve/pii/S1359646202005067 (visited on 01/04/2024).

[99] Arutyun Arutyunyan. "Microscale and Ultrafast High Cycle Fatigue Testing of Titanium". en. PhD thesis. Oxford: University of Oxford, 2019. URL: https://ora.ox.ac.uk/objects/uuid:857ceea6-56d3-4726-abff-216a7fd2837e (visited on 10/24/2023).

[100] Rory Rose. "Ultrasonic Fatigue Testing". en. MA thesis. Oxford: University of Oxford, 2021.

[101] Steven Lavenstein and Jaafar A. El-Awady. "Micro-scale fatigue mechanisms in metals: Insights gained from small-scale experiments and discrete dislocation dynamics simulations". en. In: *Current Opinion in Solid State and Materials Science* 23.5 (Oct. 2019), p. 100765. DOI: 10.1016/j.cossms.2019.07.004. URL: https://linkinghub.elsevier.com/retrieve/pii/S1359028619300890 (visited on 01/17/2024).

[102] Ali Riza Durmaz et al. "Micromechanical fatigue experiments for validation of microstructure-sensitive fatigue simulation models". en. In: *International Journal of Fatigue* 160 (July 2022), p. 106824. DOI: 10.1016/j.ijfatigue.2022.106824. URL: https://linkinghub.elsevier.com/retrieve/pii/S0142112322000998 (visited on 01/18/2024).

[103] Erik Natkowski et al. "Fatigue lifetime prediction with a validated micromechanical short crack model for the ferritic steel EN 1.4003". en. In: *International Journal of Fatigue* 152 (Nov. 2021), p. 106418. DOI: 10.1016/j.ijfatigue.2021.106418. URL: https://linkinghub.elsevier.com/retrieve/pii/S0142112321002760 (visited on 01/18/2024).

[104] Hao Lu et al. "Effect of orientation deviation on random vibration fatigue behavior of nickel based single crystal superalloy". en. In: *International Journal of Fatigue* 177 (Dec. 2023), p. 107930. DOI: 10.1016/j.ijfatigue.2023.107930. URL: https://linkinghub.elsevier.com/retrieve/pii/S0142112323004310 (visited on 10/23/2023).

[105] Jie Wan et al. "A novel methodology for bending ultrasonic fatigue testing in the VHCF regime". en. In: *International Journal of Fatigue* 170 (May 2023), p. 107562. DOI: 10.1016/j.ijfatigue.2023.107562. URL: https://linkinghub.elsevier.com/retrieve/pii/S0142112323000634 (visited on 10/23/2023).

[106] Ajay Harish. *Tips for Meshing a CAD Model for Structural Analysis | SimScale*. en. June 2023. URL: https://www.simscale.com/blog/mesh-cad-model-structural-analysis/ (visited on 11/07/2023).

[107] Todd Thompson, Jinqiang Liu, and Chao Hu. "A comparative analysis of step loading and staircase testing for fatigue strength estimation of an engine component". en. In: *Fatigue & Fracture of Engineering Materials & Structures* 46.2 (Feb. 2023), pp. 667–681. DOI: 10.1111/ffe.13898. URL: https://onlinelibrary.wiley.com/doi/10.1111/ffe.13898 (visited on 09/12/2023).

[108] Yue Su et al. "High temperature in-situ SEM observation and crystal plasticity simulation on fretting fatigue of Ni-based single crystal superalloys". en. In: *International Journal of Plasticity* 127 (Apr. 2020), p. 102645. DOI: 10.1016/j.ijplas.2019.102645. URL: https://linkinghub.elsevier.com/retrieve/pii/S074964191930628X (visited on 09/06/2023).

[109] Chris Hardie et al. "A robust and efficient hybrid solver for crystal plasticity". en. In: *International Journal of Plasticity* 170 (Nov. 2023), p. 103773. DOI: 10.1016/j.ijplas.2023.103773. URL: https://linkinghub.elsevier.com/retrieve/pii/S0749641923002577 (visited on 11/01/2023).

[110] Ludwig Reimer. *Scanning Electron Microscopy*. en. Ed. by Peter W. Hawkes and Helmut K. V. Lotsch. 2nd ed. Vol. 45. Springer Series in Optical Sciences. Berlin, Heidelberg: Springer Berlin Heidelberg, 1998. DOI: 10.1007/978-3-540-38967-5. URL: https://doi.org/10.1007/978-3-540-38967-5 (visited on 11/02/2023).

[111] T. Ben Britton et al. "Probing Deformation and Revealing Microstructural Mechanisms with Cross-Correlation-Based, High-Resolution Electron Backscatter Diffraction". en. In: *JOM* 65.9 (Sept. 2013), pp. 1245–1253. DOI: 10.1007/s11837-013-0680-6. URL: http://link.springer.com/10.1007/s11837-013-0680-6 (visited on 10/06/2023).

[112] Angus J. Wilkinson and Peter B. Hirsch. "Electron diffraction based techniques in scanning electron microscopy of bulk materials". en. In: *Micron* 28.4 (Aug. 1997), pp. 279–308. DOI: 10.1016/S0968-4328(97)00032-2. URL: https://linkinghub.elsevier.com/retrieve/pii/S0968432897000322 (visited on 11/04/2023).

[113] Gert Nolze. "Fundamentals and applications of EBSD". en. In: *Fundamentals and applications of EBSD*. Fujian University. URL: https://www.researchgate.net/publication/277403952_Fundamentals_and_applications_of_EBSD (visited on 11/08/2023).

[114] Brent L Adams and Joshua Kacher. "EBSD-Based Microscopy: Resolution of Dislocation Density". en. In: *Computers, Materials & Continua* 14.3 (2009), pp. 185–196. DOI: 10.3970/cmc.2009.014.185. URL: http://www.techscience.com/cmc/v14n3/22513.

[115] Qiwei Shi et al. "Calibration of crystal orientation and pattern center of EBSD using integrated digital image correlation". en. In: *Materials Characterization* 178 (Aug. 2021), p. 111206. DOI: 10.1016/j.matchar.2021.111206. URL: https://linkinghub.elsevier.com/retrieve/pii/S1044580321003363 (visited on 10/04/2023).

[116] Shigeto Yamasaki. "Observation and Measurement Using the Electron Channeling Pattern Function". en. In: *Scientific Instrument News* 19 (2023).

[117] N.S. De Vincentis and D.P. Field. "Factors affecting Confidence Index in EBSD analysis". en. In: *Ultramicroscopy* 225 (June 2021), p. 113269. DOI: 10.1016/j.ultramic.2021.113269. URL: https://linkinghub.elsevier.com/retrieve/pii/S0304399121000590 (visited on 10/04/2023).

[118] Yoosuf N. Picard et al. "Future Prospects for Defect and Strain Analysis in the SEM via Electron Channeling". en. In: *Microscopy Today* 20.2 (Mar. 2012), pp. 12–16. DOI: 10.1017/S1551929512000077. URL: https://academic.oup.com/mt/article/20/2/12/6820801 (visited on 06/28/2023).

[119] Stefan Zaefferer and Nahid-Nora Elhami. "Theory and application of electron channelling contrast imaging under controlled diffraction conditions". en. In: *Acta Materialia* 75 (Aug. 2014), pp. 20–50. DOI: 10.1016/j.actamat.2014.04.018. URL: https://linkinghub.elsevier.com/retrieve/pii/S1359645414002572 (visited on 05/16/2023).

[120] M. A. Crimp, B. A. Simkin, and B. C. Ng. "Demonstration of the g · b x u = 0 edge dislocation invisibility criterion for electron channelling contrast imaging". en. In: *Philosophical Magazine Letters* 81.12 (Dec. 2001), pp. 833–837. DOI: 10.1080/09500830110088755. URL: https://www.tandfonline.com/doi/full/10.1080/09500830110088755 (visited on 11/10/2023).

[121] Y.N. Picard et al. "Theory of dynamical electron channeling contrast images of near-surface crystal defects". en. In: *Ultramicroscopy* 146 (Nov. 2014), pp. 71–78. DOI: 10.1016/j.ultramic.2014.07.006. URL: https://linkinghub.elsevier.com/retrieve/pii/S0304399114001296 (visited on 08/24/2024).

[122] G. L'hôte et al. "Rotational-Electron Channeling Contrast Imaging analysis of dislocation structure in fatigued copper single crystal". en. In: *Scripta Materialia* 162 (Mar. 2019), pp. 103–107. DOI: 10.1016/j.scriptamat.2018.10.050. URL: https://linkinghub.elsevier.com/retrieve/pii/S1359646218306791 (visited on 12/03/2023).

[123] C. Lafond et al. "Electron CHanneling ORientation Determination (eCHORD): An original approach to crystalline orientation mapping". en. In: *Ultramicroscopy* 186 (Mar. 2018), pp. 146–149. DOI: 10.1016/j.ultramic.2017.12.019. URL: https://linkinghub.elsevier.com/retrieve/pii/S0304399117303947 (visited on 05/16/2023).

[124] C Trager-Cowan et al. "Advances in electron channelling contrast imaging and electron backscatter diffraction for imaging and analysis of structural defects in the scanning electron microscope". en. In: *IOP Conference Series: Materials Science and Engineering* 891.1 (July 2020), p. 012023. DOI: 10.1088/1757-899X/891/1/012023. URL: https://iopscience.iop.org/article/10.1088/1757-899X/891/1/012023 (visited on 05/16/2023).

[125] C. Lafond et al. "Towards large scale orientation mapping using the eCHORD method". In: *Ultramicroscopy* 208 (Jan. 2020), p. 112854. DOI: 10.1016/j.ultramic.2019.112854. URL: https://www.sciencedirect.com/science/article/pii/S0304399119301044 (visited on 11/10/2023).

[126] Masoud Sistaninia and Otmar Kolednik. "A novel approach for determining the stress intensity factor for cracks in multilayered cantilevers". en. In: *Engineering Fracture Mechanics* 266 (May 2022), p. 108386. DOI: 10.1016/j.engfracmech.2022.108386. URL: https://linkinghub.elsevier.com/retrieve/pii/S0013794422001424 (visited on 09/11/2023).

[127] Shaun Gareth Watkins. "Wear fatigue in nickel superalloys." en. PhD thesis. Swansea University Prifysgol Abertawe, 2015.

[128] O.M. Horst et al. "Exploring the fundamentals of Ni-based superalloy single crystal (SX) alloy design: Chemical composition vs. microstructure". en. In: *Materials & Design* 195 (Oct. 2020), p. 108976. DOI: 10.1016/j.matdes.2020.108976. URL: https://linkinghub.elsevier.com/retrieve/pii/S0264127520305104 (visited on 02/07/2025).

[129] Satoshi Utada, Lucille Despres, and Jonathan Cormier. "Ultra-High Temperature Creep of Ni-Based SX Superalloys at 1250 °C". en. In: *Metals* 11.10 (Oct. 2021), p. 1610. DOI: 10.3390/met11101610. URL: https://www.mdpi.com/2075-4701/11/10/1610 (visited on 02/07/2025).

[130] Chinnapat Panwisawas et al. "Prediction of recrystallization in investment cast single-crystal superalloys". In: *Acta Materialia* 61.1 (Jan. 2013), pp. 51–66. DOI: 10.1016/j.actamat.2012.09.013. URL: https://www.sciencedirect.com/science/article/pii/S1359645412006350 (visited on 12/01/2023).

[131] Marc De Graef. *EMsoft-org/EMsoft: Public EMsoft repository.* 10.5281/zenodo.3489720. URL: https://github.com/EMsoft-org/EMsoft (visited on 08/09/2024).

[132] M. De Graef. "Electron Channeling Contrast Image (ECCI) Simulations". en. In: *Microscopy and Microanalysis* 18.S2 (July 2012), pp. 682–683. DOI: 10.1017/S1431927612005260. URL: https://academic.oup.com/mam/article/18/S2/682/6934487 (visited on 05/16/2023).

[133] G. Nolze and R. Hielscher. "Orientations – perfectly colored". en. In: *Journal of Applied Crystallography* 49.5 (Oct. 2016), pp. 1786–1802. DOI: 10.1107/S1600576716012942. URL: https://scripts.iucr.org/cgi-bin/paper?S1600576716012942 (visited on 07/10/2024).

[134] Motoki Sakaguchi et al. "Crystal plasticity assessment of crystallographic Stage I crack propagation in a Ni-based single crystal superalloy". en. In: *International Journal of Fatigue* 123 (June 2019), pp. 10–21. DOI: 10.1016/j.ijfatigue.2019.02.003. URL: https://linkinghub.elsevier.com/retrieve/pii/S0142112319300325 (visited on 09/06/2023).

[135] D. J. Duquette, M. Gell, and J. W. Piteo. "A fractographic study of Stage I fatigue cracking in a nickel-base superalloy single crystal". en. In: *Metallurgical Transactions* 1.11 (Nov. 1970), pp. 3107–3115. DOI: 10.1007/BF03038426. URL: https://link.springer.com/10.1007/BF03038426 (visited on 01/05/2024).

[136] Vasilis Karamitros, Duncan W. MacLachlan, and Fionn P.E. Dunne. "Mechanistic fatigue in Ni-based superalloy single crystals: A study of crack paths and growth rates". en. In: *Journal of the Mechanics and Physics of Solids* 158 (Jan. 2022), p. 104663. DOI: 10.1016/j.jmps.2021.104663. URL: https://linkinghub.elsevier.com/retrieve/pii/S0022509621002957 (visited on 01/15/2024).

[137] Liu Liu et al. "Investigation on low cycle fatigue behaviors of the [001] and [011] oriental single crystal superalloy at 760 °C". en. In: *Materials Science and Engineering: A* 734 (Sept. 2018), pp. 1–6. DOI: 10.1016/j.msea.2018.07.078. URL: https://linkinghub.elsevier.com/retrieve/pii/S0921509318310128 (visited on 08/23/2024).

[138] A. J. Wilkinson et al. "Electron channelling contrast imaging of interfacial defects in strained silicon-germanium layers on silicon". en. In: *Philosophical Magazine A* 68.1 (July 1993), pp. 59–80. DOI: 10.1080/01418619308219357. URL: http://www.tandfonline.com/doi/abs/10.1080/01418619308219357 (visited on 08/29/2024).

[139] Pengfei Wang et al. "Deformation mechanisms of low cycle fatigue of a fourth generation Ni-based single crystal superalloy". en. In: *Journal of Materials Research and Technology* 24 (May 2023), pp. 2053–2063. DOI: 10.1016/j.jmrt.2023.03.148. URL: https://linkinghub.elsevier.com/retrieve/pii/S2238785423006129 (visited on 09/03/2024).

[140] G. Henaff, K. Marchal, and J. Petit. "On fatigue crack propagation enhancement by a gaseous atmosphere: Experimental and theoretical aspects". en. In: *Acta Metallurgica et Materialia* 43.8 (Aug. 1995), pp. 2931–2942. DOI: 10.1016/0956-7151(95)00002-D. URL: https://linkinghub.elsevier.com/retrieve/pii/095671519500002D (visited on 02/13/2025).

[141] M.R. Achter. "The adsorption model for environmental effects in fatigue crack propagation". en. In: *Scripta Metallurgica* 2.9 (Sept. 1968), pp. 525–527. DOI: 10.1016/0036-9748(68)90187-7. URL: https://linkinghub.elsevier.com/retrieve/pii/0036974868901877 (visited on 02/13/2025).

[142] J. L. Yuen, P. Roy, and W. D. Nix. "Effect of oxidation kinetics on the near threshold fatigue crack growth behavior of a nickel base superalloy". en. In: *Metallurgical Transactions A* 15.9 (Sept. 1984), pp. 1769–1775. DOI: 10.1007/BF02666360. URL: https://link.springer.com/10.1007/BF02666360 (visited on 08/23/2023).

[143] James Lum Yuen. "Near Threshold Corrosion Fatigue Crack Growth Behavior of a Nickel Base Superalloy in Air and Inert Environments". English. ISBN: 9798661973917. Ph.D. United States – California: Stanford University, June 1982. URL: https://www.proquest.com/docview/303245112/abstract/10CBAC8747334B3BPQ/1 (visited on 01/22/2024).

[144] Tao Liu et al. "A Review of Research Progress on the Fretting Fatigue Mechanism and Protection Measures of Metal Matrix Composites". en. In: *Coatings* 13.2 (Feb. 2023), p. 365. DOI: 10.3390/coatings13020365. URL: https://www.mdpi.com/2079-6412/13/2/365 (visited on 08/29/2023).

[145] Kaili Feng and Tianmin Shao. "The evolution mechanism of tribo-oxide layer during high temperature dry sliding wear for nickel-based superalloy". en. In: *Wear* 476 (July 2021), p. 203747. DOI: 10.1016/j.wear.2021.203747. URL: https://linkinghub.elsevier.com/retrieve/pii/S0043164821001368 (visited on 08/29/2023).

[146] Weijie Kuang et al. "Fretting wear behaviour of machined layer of nickel-based superalloy produced by creep-feed profile grinding". en. In: *Chinese Journal of Aeronautics* 35.10 (Oct. 2022), pp. 401–411. DOI: 10.1016/j.cja.2021.10.007. URL: https://linkinghub.elsevier.com/retrieve/pii/S1000936121003691 (visited on 08/29/2023).

[147] Ibrohim Rustamov, Fei Guo, and Zixi Wang. "Experimental investigations into fretting wear and damage mechanisms of Inconel X-750 alloy". en. In: *Journal of Mechanical Science and Technology* 33.10 (Oct. 2019), pp. 4701–4713. DOI: 10.1007/s12206-019-0818-8. URL: http://link.springer.com/10.1007/s12206-019-0818-8 (visited on 08/29/2023).

[148] Ibrohim A. Rustamov et al. "Fretting Wear Behavior and Damage Mechanisms of Inconel X-750 Alloy in Dry Contacts". en. In: *Advances in Materials Science and Engineering* 2019 (Mar. 2019), pp. 1–15. DOI: 10.1155/2019/7079819. URL: https://www.hindawi.com/journals/amse/2019/7079819/ (visited on 08/29/2023).

[149] Łukasz Skotny. *Correct mesh size – a quick guide!* en. July 2017. URL: https://enterfea.com/correct-mesh-size-quick-guide/ (visited on 10/30/2023).

[150] Tong Pin and Theodore H.H. Pian. "On the convergence of the finite element method for problems with singularity". en. In: *International Journal of Solids and Structures* 9.3 (Mar. 1973), pp. 313–321. DOI: 10.1016/0020-7683(73)90082-6. URL: https://linkinghub.elsevier.com/retrieve/pii/0020768373900826 (visited on 10/30/2023).

[151] *What is Partial Pressure of Oxygen and How Do You Calculate It?* URL: https://www.processsensing.com/en-us/blog/o2-sensor-working-principle-partial-pressure-of-oxygen.htm (visited on 03/14/2024).

[152] E. Pascal et al. "Dislocation contrast in electron channelling contrast images as projections of strain-like components". en. In: *Materials Today: Proceedings* 5.6 (2018), pp. 14652–14661. DOI: 10.1016/j.matpr.2018.03.057. URL: https://linkinghub.elsevier.com/retrieve/pii/S2214785318306461 (visited on 07/26/2024).

[153] Agah Ugˇuz and John W. Martin. "Plastic zone size measurement techniques for metallic materials". en. In: *Materials Characterization* 37.2-3 (Aug. 1996), pp. 105–118. DOI: 10.1016/S1044-5803(96)00074-5. URL: https://linkinghub.elsevier.com/retrieve/pii/S1044580396000745 (visited on 04/15/2024).

[154] Samuel Forest. "Crystal plasticity and damage at cracks and notches in nickel-base single-crystal superalloys". en. In: *Nickel Base Single Crystals Across Length Scales*. Elsevier, 2022, pp. 457–469. DOI: 10.1016/B978-0-12-819357-0.00025-1. URL: https://linkinghub.elsevier.com/retrieve/pii/B9780128193570000251 (visited on 04/15/2024).

[155] J. Ast et al. "A review of experimental approaches to fracture toughness evaluation at the micro-scale". en. In: *Materials & Design* 173 (July 2019), p. 107762. DOI: 10.1016/j.matdes.2019.107762. URL: https://linkinghub.elsevier.com/retrieve/pii/S0264127519301996 (visited on 04/15/2024).

[156] J.S. Crompton and J.W. Martin. "Crack tip plasticity and crack growth in a single-crystal superalloy at elevated temperatures". en. In: *Materials Science and Engineering* 64.1 (May 1984), pp. 37–43. DOI: 10.1016/0025-5416(84)90071-5. URL: https://linkinghub.elsevier.com/retrieve/pii/0025541684900715 (visited on 04/15/2024).

[157] A. J. Wilkinson. "Examination of fatigue crack plastic zones using scanning-electron-microscope-based electron diffraction techniques". en. In: *Philosophical Magazine Letters* 74.3 (Sept. 1996), pp. 145–152. DOI: 10.1080/095008396180290. URL: http://www.tandfonline.com/doi/abs/10.1080/095008396180290 (visited on 04/15/2024).

[158] Ted L. Anderson. *Fracture mechanics: fundamentals and applications*. eng. Fourth edition. Boca Raton, Fla. London New York: CRC Press, Taylor & Francis Group, 2017.